In-Situ Proton Irradiation Creep of FM Steel T91

by

Cheng Xu

A dissertation submitted in partial fulfillment
of the requirements for the degree of
Doctor of Philosophy
(Nuclear Engineering and Radiological Sciences)
in the University of Michigan
2014

Doctoral Committee:

Professor Gary S. Was, Chair
Professor Michael Atzmon
Professor J. Wayne Jones
Professor Lumin Wang

For my parents and grandparents

Ming Quan Xu (徐明泉), Jin Xiu Wang (王锦秀)

Fang Jin Mei (方金美), Song Mei Xiang (宋梅香)

Acknowledgements

I would like to thank my advisor, Dr. Gary Was for this guidance and assistance throughout my doctoral program. His knowledge, wisdom, and support has fostered my critical thinking, improved my skills, and pushed me through the many challenges of the graduate program. Because of his guidance, I have improved both as an engineer and a researcher.

My fellow research group members have also provided invaluable support and encouragement throughout my graduate program. Their feedback in discussing research problems and ideas have helped me greatly in the laboratory. I would like to thank: Zhijie Jiao, Elaine West, Janelle Wharry, Mike McMurtrey, Pantip Ampornrat, Deepak Kumar, Vani Shankar, Gokce Gulsoy, Tyler Moss, Kale Stephenson, Yugo Ashida, Peng Wang, Liz Beckett, Stephen Raiman, Shyam Dwaraknath, Anthony Monterrosa, and Justin Hesterberg. I am exceedingly grateful to Anne Campbell for her assistance in developing the unique experimental setup for irradiation creep experiments. I would also like to acknowledge Micah Hackett for our in depth discussion on irradiation creep mechanisms and various details regarding FM alloys. I am also forever indebted to Ovidiu Toader and Fabian Naab, of the Michigan Ion Beam Laboratory, for their patience, dedication, and hours of hard work helping me with proton irradiation creep experiments. I am also thankful for the assistance of Alex Flick, and Rob Blackburn for dedication to the smooth operation of the laboratories.

The staff at the Electron Microbeam Analysis Laboratory have also provided me with the tools and expertise necessary to conduct dislocation loop analysis by helping with microscope troubleshooting, dislocation imaging techniques, and FIB: Kai Sun and Haiping Sun. I would

also like to thank Scott Braswell at Nanotech User Facility for his assistance with TEM analysis at University of Washington.

To Dr. Lou Mansur, Dr. Frank Garner, Dr. and Dave Gelles, for their insights and experience in the field of irradiation creep of FM steels, and having the patience to engage in many technical conversations with me over the years. Their guidance have helped me build a better understanding of irradiation creep mechanisms and their contributions to the field have paved the way for my research.

Finally, to my family – mom, dad and my grandparents– thank you for all your support and understanding throughout my life. For giving me the freedom and tools to pursue my dreams. I would not be able to achieve what I have without your hard work to provide me with the best opportunities available. You are what made me the person I am today, and this thesis is dedicated to you.

This research was supported by the U.S. Department of Energy awards NERI 08-055 DE-FG07-07ID14894.

Table of Contents

List of Figures

List of Tables

List of Appendices

CHAPTER 1 INTRODUCTION

The ever increasing world energy demands combined with the need to reduce long lived actinides in radioactive waste have motivated the nuclear community to design and construct next generation fast reactors to close the nuclear fuel cycle. The Generation IV fast reactors proposed will be operating at higher temperatures, and be subjected to higher irradiation dose than any current reactors in service. Therefore, the accurate prediction of materials performance with limited in-reactor data becomes a vital element in ensuring the safe and efficient operation of these next generation nuclear power plants.

Ferritic-martensitic (F-M) steels are currently the leading candidate material for next generation fast reactors cladding and core internals [1]–[3]. These alloys were developed in the 1960s for the power industry, and its properties have been continuously improved upon to the present day. F-M alloys have better thermal conductivity, lower thermal expansion coefficient, and are more resistant to radiation induced swelling compared to stainless steels currently used in light water reactors [4]. These advantages make them especially suited for Generation IV fast reactor designs, with operating temperatures as high as 600°C and estimated radiation damage in excess of hundreds of displacements per atom (dpa). This has motivated concentrated efforts in the nuclear community to understand the fundamental mechanisms behind irradiation creep of F-M alloys under fast reactor conditions.

F-M alloys are iron based alloys with 7-15% chromium, low carbon (<0.1%) and additions of Mo, W, Nb, V, Ti, and N. The microstructure of F-M alloys includes a body centered cubic (bbc) matrix formed into martensitic lathes grouped together inside prior-austenitic grain boundaries (PAG). It has a higher concentration of dislocation network density, and various different carbides decorating its grain boundaries [1]. The complex microstructure contributes to the general radiation resistance and high temperature strength of these materials. The microstructure

complexity of the alloy also makes it difficult to describe its creep deformation mechanisms from fundamental physical principles.

A myriad of irradiation creep mechanisms have been proposed by researchers throughout the years to provide a theoretical description of irradiation creep deformation [5]. The I-creep mechanism proposed by Gittus, and later expanded by Heald et al. [6] described a physical process dominated by dislocation glide locked by obstacles which are subsequently overcome by dislocation climb. This description has met some success in describing creep behavior in stainless steels with its direct relationship to void swelling. However, I-creep is unsatisfactory in describing the creep in F-M steels where the void swelling is orders of magnitude smaller than stainless steels. Stress Induced Preferential Absorption (SIPA) and Stress Induced Preferential Nucleation (SIPN) are then proposed to explain irradiation creep without swelling [5]–[8]. SIPA and SIPN hypothesize that the applied stress will further influence the bias of sinks for interstitial and vacancy depending on the orientation of the sinks to the tensile axis. Therefore, the excess vacancies created by irradiation damage can be preferentially absorbed in unaligned sinks instead of being forced to neutral sinks to create voids. SIPA describes the creep deformation as preferential dislocation climb by interstitials to create extra half planes in the tensile direction. In contrast, SIPN proposes that creep deformation is caused by extra dislocation loops nucleating to cause elongation in the tensile direction. However, there is a lack of experimental data for stress induced anisotropic microstructure in F-M alloys, and the relevant data available for other materials are often inconsistent [9].

In addition, theoretical considerations of irradiation creep mechanism do not preclude the combination of more than one mechanism. Thermal creep has been discussed as a factor influencing SIPA by Preferential Emission (PE) in the review paper by Matthews et al [5]. The same paper also discussed the possibility of combining SIPA with traditional climb-glide mechanism in the form of Preferential Absorption Glide (PAG). In light of the complexity of irradiation creep theory, a systematic set of irradiation creep experiments are needed in order to narrow down the dominating mechanism from all the theoretical possibilities.

Irradiation creep studies have been done on cladding material at various doses, temperatures, and stresses using many different methods [10]. The most comprehensive set of neutron irradiated empirical creep data for F-M alloys are those conducted by Toloczko et al in FFTF [11], [12], and those by Ando et al in HFIR [13]. The neutron irradiations established that F-M

steel minimal creep rates have very little temperature dependence, and has a stress exponent between 1 and 1.5. The dose rates for neutron irradiation creep experiments are mostly estimated values since they are highly dependent on the location of the samples, and the operation history of the reactor. These neutron irradiation creep studies have contributed to the development of empirical models to describe irradiation creep deformation, but the large time and money investment needed for neutron experiments makes them inadequate for the systematic exploration of possible theoretical creep mechanisms. In addition, long term neutron irradiation creep experiments fails to capture the changing microstructure in the primary creep regime, where valuable insight could be gained from directly observing the microstructure during its development towards steady state.

Ion irradiation creep experiments have also been conducted on various materials in order to overcome limitations in gathering data from neutron irradiated samples. McElroy et al [5,11] irradiated nickel and 321 stainless steel using 4MeV protons while subjecting the samples under stress at high temperatures. Their study showed irradiation enhanced the creep rate of both nickel and stainless steel. The stress dependence of irradiation creep was found to be linear below 150MPa, and becomes exponential beyond 150MPa at 500^{o}C. Large dislocation loops were also observed in the proton irradiation creep samples, but the total loop density and loop size were not affected by the applied tensile stress. Tanigawa et al. [15]also irradiated Fe-15Cr-20Ni ternary alloys with 4MeV nickel ions to observe the Frank loop anisotropy on different {111} planes. The experiments showed a strong dependence of Frank loop concentration on the resolved normal stress affecting the plane. In addition, a higher resolved shear stress seemed to promote the nucleation of small perfect loops. In contrast, TEM investigation done by Chen et al. [16] on an ODS alloy PM2000 irradiated with helium showed no remarkable changes in dislocation microstructure. In general, studies on irradiation creep microstructure are not completely consistent and often gave contradictory response. [9] However, much of the inconsistency could be attributed to the wide variety of materials studied at vastly different conditions. An in depth study on the irradiation creep deformation, and its relationship to microstructure development for F-M alloys by ion irradiation would be valuable for understanding the fundamental mechanism behind irradiation creep.

The objective of this thesis is to understand the mechanism behind irradiation creep of F-M alloy T91. This study proposes to systematically examine the irradiation creep rates by proton

irradiation, and describe the temperature dependence, dose rate dependence, and stress dependence of F-M steel T91. TEM investigation of the irradiation creep samples aims to capture surviving microstructure evidence that can help identify the dominating mechanism of irradiation creep for the material. Chapter 2 of this work will cover all relevant background for F-M alloy T91, theoretical creep mechanisms, and both neutron and ion irradiation creep experimental data for all relevant alloys. Chapter 3 presents the detailed objective of this work. Chapter 4 describes the unique experimental setup that was developed for this work and the analysis procedure employed in this work. Chapter 5 includes all strain rate data, microstructure images, analysis, and results from the experiments. Chapter 6 discusses the implications of the experimental results in light of possible theoretical descriptions leading up to a conclusion on what is the dominating irradiation creep for F-M alloys in Chapter 7 along with any additional work that may be pursued in the future.

CHAPTER 2 BACKGROUND

This chapter is a review of published literature of both theoretical and experimental insight into the irradiation creep of F-M alloys. The first section focuses on creep theories, including the unique phenomenon of irradiation creep, and the various mechanisms proposed to describe irradiation creep deformation. The second section outlines the various properties of F-M alloys and their complex microstructure in both as received, and irradiated conditions. The third section provides a review of creep experiments in published literature, which illuminates the current knowledge available for irradiation creep of F-M alloys, and highlights the gaps in understanding in the field that led to the current thesis topic and experimental conditions.

2.1 Introduction to Creep

Creep is the time dependent plastic deformation of a material at high temperature. The phenomenon usually occurs at temperatures higher than one third of the melting point with stresses well below the yield point. This phenomenon is understood to be volume conservative and stress dependent, which separates it from other irradiation effects such as swelling, and growth. Creep deformation is the product of defect diffusion induced by the applied stress, combined with irradiation induced defects and accelerated diffusion rates; causing an increase in dislocation mobility that ultimately leads to plastic deformation. Creep is often the primary mode of failure for a material during high temperature operations, and is the life limiting factor for many structural components in a nuclear reactor.

In general, creep is measured by the engineering strain of a material over time. A typical creep curve for a metal is shown in Figure 2.1. Creep strain can be typically separated into three distinct stages. First stage is known as primary creep, where the strain rate over time continuously decrease as the material strain hardens and the microstructure develops under stress. Once the microstructure has stabilized, the strain rate will cease to decrease and reach a steady state regime where the strain rate becomes a constant. This is known as secondary creep, which is generally accountable for the majority of the creep lifetime of a material. Since the secondary creep rate is a constant, it is often the value recorded to describe the characteristic creep rate of a material at a given condition. However, some materials such as FM steels often do not have well defined secondary regime where the creep rate is constant. Instead, the secondary regime is reduced to a point of inflection where the creep rate is at its minimum. Past the

secondary creep is the tertiary creep regime, where the material starts to neck and crack which ultimately leads to an increase in strain rate ending in failure.

Creep tests are usually conducted under constant load and constant temperature to obtain the complete creep curve, and the corresponding minimal creep rate for the test condition. The creep rates are generally measured in strain per second, and tests are performed over a large combination of temperatures and stress to describe the overall creep behavior. For engineering applications, the creep lifetime observed experimentally are normalized to the temperature into a Larson Miller parameter, and plotted against the applied stress.

Discussions of creep mechanisms beyond empirical fits will require more complex descriptions of the physics behind the deformation. At an atomistic level, high temperatures or irradiation will generate a significant number of point defects that make it possible for atoms to migrate to sinks under the influence of an applied stress. How these point defect migrations ultimately lead to macroscopic deformation is still under investigation. Many creep theories have been proposed to adequately explain various aspects of creep behavior, and new experimental techniques have provided empirical data to help refine the existing theories. This chapter will systematically break down each irradiation creep theory viable for F-M alloys, and the related data that support or dispute them.

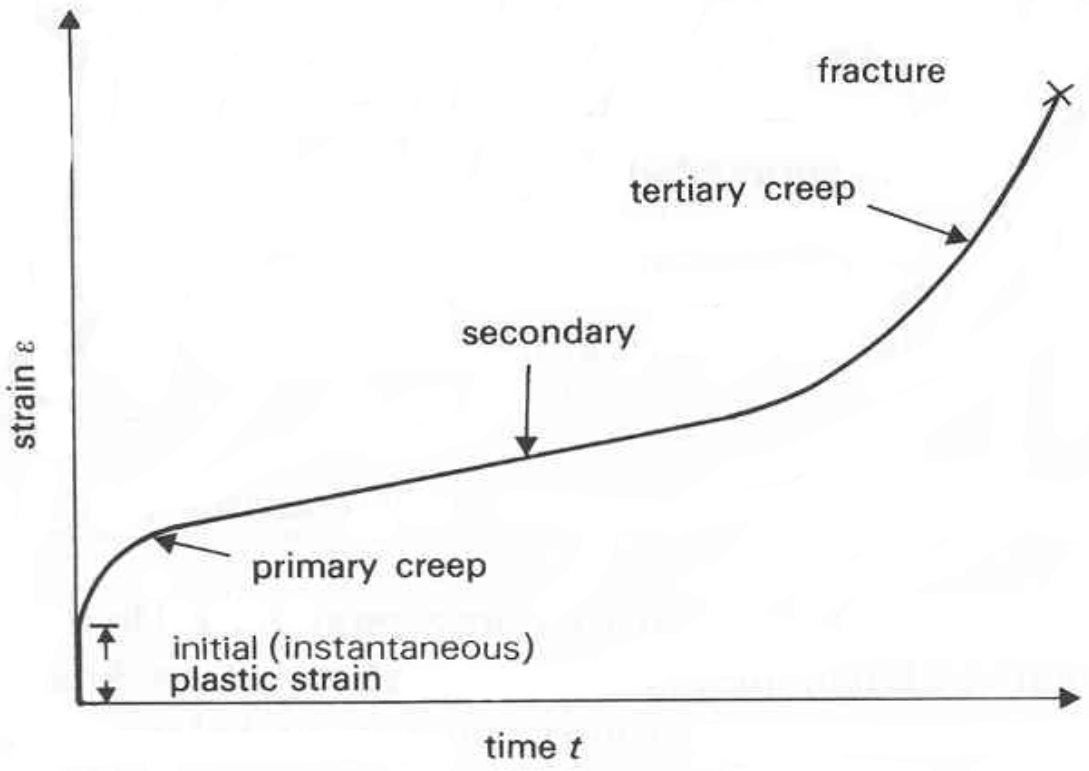

Figure 2.1 Typical creep curve of metal.

2.2 Thermal Creep vs Irradiation Creep

It is important to first understand thermal creep behavior of a material before undertaking an in depth discussion of irradiation creep. Thermal creep mechanisms provide the framework and additional experimental data that may provide better comprehension of irradiation creep. Secondly, thermal creep isolates the effects of temperature and stress on the deformation behavior, providing valuable insight and foundation in explaining irradiation creep. Lastly, at higher temperature and stress, it is likely that thermal creep may operate along with irradiation creep in contributing to strain; therefore, it is important to understand the interaction between the two mechanisms.

Thermal creep is understood to be caused by the higher vacancy contribution resulting from high temperatures. Those vacancies will facilitate the diffusion of atoms to sinks under the influence of the applied tensile stress. At low stresses, the creep strain rate is linearly dependent on the applied stress, and exponentially dependent on the temperature. This is taken to be evidence for the operation of a purely diffusion mechanism, with the activation energy being either matrix self-diffusion or grain boundary diffusion. At higher stresses, dislocation movement will start to dominate the creep deformation, and the stress dependence of strain rate increases to 3-8. Due to the higher stress exponent, this regime is called the power-law creep. At significantly higher stresses, usually around half of the yield stress, power-law breakdown (PLB) occurs and the stress exponent will increase to 10-15 combined with a drop in activation energy. This is commonly explained as transition from climb controlled creep to glide controlled creep with contribution from dynamic recrystallization. This complex thermal creep behavior is illustrated by creep deformation map as shown by Figure 2.2 for stainless steel 316.

Empirically, thermal creep rate $\dot{\varepsilon}$ was derived using the following phenomenological equation:

$$\dot{\varepsilon} = A\sigma^m exp\left(\frac{-Q}{kT}\right) \tag{2.1}$$

A is a fitting constant, Q is the activation energy, k is the Boltzmann constant, T is the temperature, σ is the applied stress, and m is the stress exponent.

In contrast, irradiation creep occurs at much lower temperatures than thermal creep. This is because irradiation creep is not initiated by the excess vacancy population resulting from high temperature; instead irradiation damage cascades create an excess of both interstitials and vacancies even at low temperatures. Due to the higher point defect density, and the more mobile nature of interstitials, irradiation creep exhibits distinctly different behavior than those of thermal creep. Firstly, irradiation creep has been observed to show very little temperature dependence compared to the exponential dependence of thermal creep. This is consistent with the fact that point defects are generated by irradiation damage instead of temperature. Secondly, irradiation creep rate is often many orders of magnitude higher than thermal creep under the same conditions. Lastly, irradiation creep is consistently found to have a linear stress dependence over a wide range of conditions. At first glance, this would seem to suggest irradiation creep is just diffusion creep enhanced by the extra point defect density from the irradiation damage. However, since the extra point defect density created by irradiation damage is homogenously distributed over the material, there is no extra driving force for atoms to diffuse in one direction versus the other under irradiation. Therefore, diffusion creep does not adequately explain why irradiation creep rates are orders of magnitude higher than those under thermal conditions.

Empirically, irradiation creep is most commonly described using the following phenomenological equation:

$$\frac{\dot{\varepsilon}}{\sigma^m} = B_o + D\dot{S} \tag{2.2}$$

B_o is called the creep compliance, $\dot{S}$ is the steady state swelling rate, D is the creep swelling coupling coefficient, and m is the stress exponent. Table 2.1 highlights the major difference between thermal creep behaviors and irradiation creep.

Table 2.1 Comparison of thermal creep and irradiation creep behavior

	Diffusion Creep	Power-law Creep	Power-law Breakdown	Irradiation Creep
Temperature Dependence	Exponential	Exponential	Exponential	Negligible
Stress exponent	1	3-8	>10	~1
Point defects	Vacancy	Vacancy	Vacancy	Interstitial + Vacancy
Microstructure defects	None	Dislocation lines	Dislocation lines	Dislocation lines, Dislocation loops

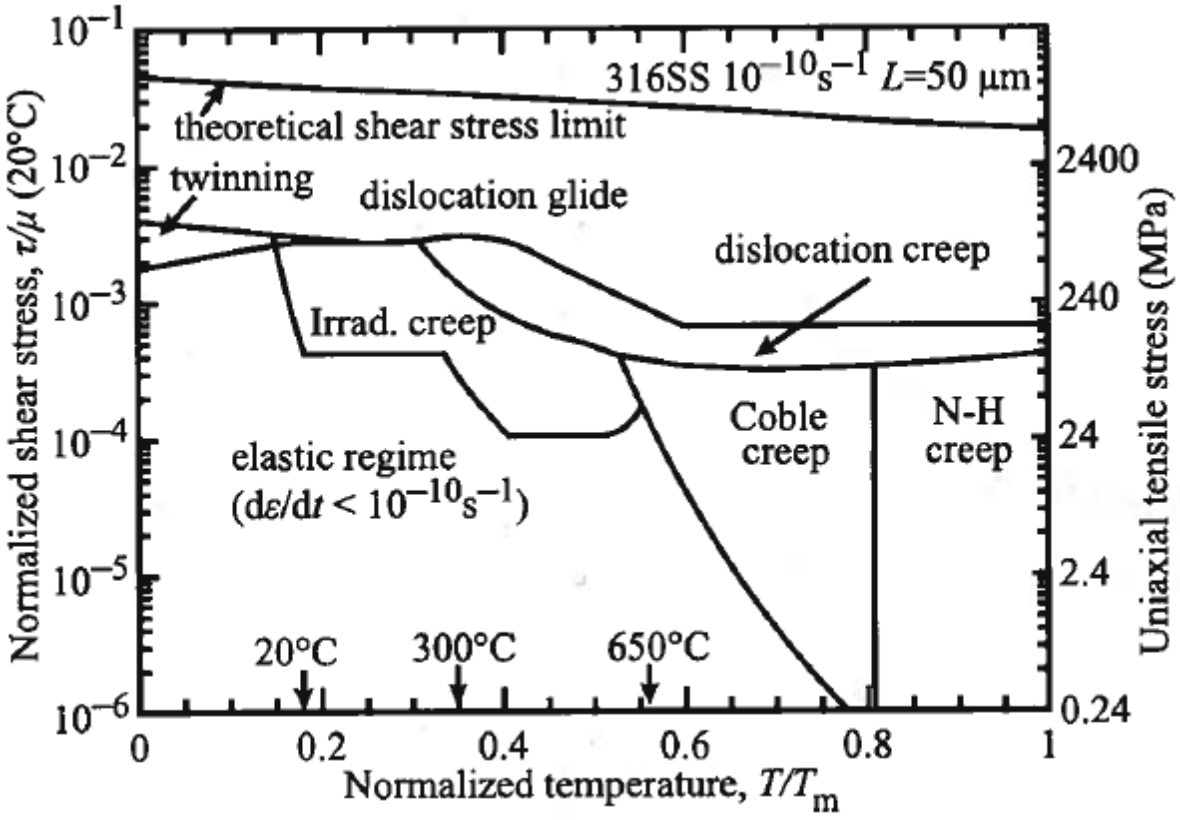

Figure 2.2 Creep deformation map of 316 stainless steel [17]

2.3 Irradiation Creep Mechanisms

Irradiation creep has been extensively studied, and theories proposed to explain its behavior since it was first observed in uranium fuel in the 1950s [18]. Irradiation creep occurs at temperatures below those of thermal creep, and could be the major contributor to the total strain of fuel cladding inside a reactor. The development of irradiation creep models has closely followed the irradiation creep experiments, in the hopes of achieving a satisfactory scientific understanding behind the deformation process. However, the complex nature of the problem yielded an abundance of viable models, each with its own strengths and weaknesses. This chapter will systematically review the irradiation creep theoretical models that are applicable to F-M steels.

2.3.1 I-Creep

One of the earliest irradiation creep mechanism is proposed by Gittus et al [19] commonly referred to as I-creep. This theory proposes a macroscopic deformation mechanism by dislocation climb and glide. The segments of dislocation lines in the material will get pinned by defect clusters or precipitates in the matrix, while the unpinned portion of the dislocation will bow out under the applied tensile stress. The elastic deformation from the bowed out dislocation lines become permanent plastic strain when the lines become unpinned and glide throughout the matrix. The natural interstitial bias that dislocations have will then absorb the excess of interstitials from the irradiation damage, and cause the dislocation to climb over the obstacle pinning them in place, enabling the glide process. Once the dislocation climbs over the obstacle, it is free to glide to a free surface or grain boundary to cause deformation.

This irradiation creep mechanism is described by the Orowan equation with the dislocation bowing directly proportional to the applied tensile stress [19]:

$$\dot{\varepsilon}_{I-creep} = \frac{\sigma}{E} b \rho v_d \tag{2.3}$$

In the equation, σ is the applied tensile stress, E is the elastic modulus, b is the magnitude of the Burgers vector of the dislocation, ρ is the dislocation density, and $v_d$is the climb velocity of the dislocation as described below:

$$v_d = \frac{1}{b}\left(z_i^d D_i C_i - z_v^d D_v C_v\right) \tag{2.4}$$

The climb velocity is a flux balance of interstitials and vacancies that the dislocation line absorbs. The z denotes the sink strength of the dislocation for either interstitials (i) or vacancies (v). The D is the diffusion coefficient and C is the concentration of the point defects. The superscript d denotes dislocations, and subscripts v and i denotes vacancies and interstitials.

In this theoretical description, the dislocations will absorb more interstitials than vacancies. The excess vacancies will likely to cluster into voids and cause swelling. This fits well with the empirical description of irradiation creep where the minimum creep rate is linearly proportional to the swelling rate. In that regard, the I-creep model is fairly successful in describing the irradiation creep behavior of austenitic stainless steels. However, FM alloys exhibit orders of magnitude lower stress free swelling rate compared to the austenitic steels but have comparable irradiation creep rates. The lack of voids is the main argument against I-creep as the dominant irradiation creep mechanism in FM alloys, yet the large density of lathe boundaries and precipitates in FM steels could act as neutral sinks in place of void formation as seen in austenitic steels.

If I-Creep is dominating the irradiation creep of FM steels, it should occur accompanied by void swelling between the temperatures of 300^{o}C to 500^{o}C at all stress, and dose rate conditions. The viability of I-creep as a dominant irradiation creep mechanism will depend on careful microstructure analysis, and calculation of neutral sink densities of the material after irradiation creep testing.

2.3.2 Stress Induced Preferential Absorption (SIPA)

Stress induced preferential absorption, commonly abbreviated as SIPA, is a diffusion driven mechanism built upon the sink bias theory of I-creep. In addition to the inherent interstitial bias from dislocations described by I-creep, SIPA proposes that the addition of an applied external stress will further bias the point defects toward sinks of certain orientations. SIPA mechanism by itself will cause the climb of network dislocations which contributes to irradiation creep strain.

There has been some debate within literature regarding the origin of the stress induced bias. Heald et al.[20] proposed the SIPA mechanism as changes in interaction energy between dislocation and point defect under applied stress. Bullough and Willis [21] further modeled the bias as a point defect in a crystalline structure with anisotropic elastic constants later coined as SIPA-I. Savino et al [8] describes a more complicated SIPA model developed by Woo et al. [22] which predicts a reduction in energy barrier for point defect migration in one direction of the stress field versus the other. This allows interstitials to migrate easier in one direction versus the other, causing anisotropic diffusion. This SIPA mechanism predicts anisotropic diffusion rates of point defects on top of the stress induced interstitial bias; therefore it is termed SIPA-AD. The difference in the two SIPA models is reflected in their description of the sink strength and sink bias. SIPA-AD is observed to predict higher climb rates compared to SIPA-I [8].

In the SIPA creep description, the strain rate is only a function of dislocation climb. The creep rate of this mechanism will be a function of how fast the interstitials are absorbed at the aligned dislocation lines, denoted by subscript A.

$$\dot{\varepsilon}_{SIPA} = b\rho_A v_{d_A} \tag{2.5}$$

The SIPA strain rate, $\dot{\varepsilon}_{SIPA}$, is a function of the density of aligned dislocations ρ_A, the Burgers vector of the dislocations b, and the climb velocity of the dislocations v_{dA}. The climb velocity is a function of the point defect diffusivity, point defect concentrations, and the interstitial bias induced by the applied stress. In addition, the positive climb from interstitial absorption will be offset by the negative climb from vacancy absorption which is related to the swelling rate. By taking all the point defect flux into account, the total climb velocity is described by Mansur et al. as the following [23].

$$\nu_{d_A} = \frac{\Omega}{b}\sum_{j}^{3}\left(z_i^{dj}D_iC_i - z_v^{dj}D_vC_v\right) - \left(z_i^{dn}D_iC_i - z_v^{dn}D_vC_v\right)$$

$$= \frac{2}{3}\frac{\Omega}{b}\left[\Delta z_i^d D_i C_i - \Delta z_v^d D_v C_v\right] \quad (2.6)$$

Where *Di* is the interstitial diffusivity, *Dv* is the vacancy diffusivity, *Ci* is the interstitial concentration, and *Cv* is the vacancy concentration. *Ω* is the atomic volume and *b* is the Burgers vector of the dislocation. The term Δz_i^d is the difference in the sink strength for interstitials between aligned and unaligned dislocations, derived in the equation below [8].

$$\Delta z_i^d = z_i^d\left[\frac{5\sigma(2-\upsilon)}{2\mu\epsilon_o(7-5\upsilon)} + \frac{5\sigma(1+\upsilon)}{2\mu\epsilon_o(7-5\upsilon)}\right] \quad (2.7)$$

In this formulation, z_i^d describes the sink strength of dislocations for interstitials. The expression within the brackets describes the effect of stress on aligned and unaligned dislocations. Again, the superscript *d* denotes dislocations, and subscripts *v* and *i* denotes vacancies and interstitials. The σ is the applied tensile stress, μ is the shear modulus, ϵ_o is the relaxation volume, and υ is the Poisson's ratio.

For an isotropic material, the dislocation orientations will be distributed evenly amongst the three orthogonal directions. For irradiation creep, where the diffusion is dominated by interstitials, the preferential vacancy emission term is dropped and described in a separate mechanism as preferential emission (PE). The aligned dislocation density ρ_A is assumed to be 1/3 of the total dislocation density ρ. The total creep rate then becomes the following form:

$$\dot{\varepsilon}_{SIPA} = \frac{2}{9}\rho\Omega\left[\Delta z_i^d D_i C_i\right] \quad (2.8)$$

where *Di* is the interstitial diffusivity, *Ci* is the interstitial concentration, *Ω* the atomic volume, *b* the Burges vector, ρ the dislocation density and Δz_i^d the difference in interstitial sink strength between the aligned and unaligned dislocations. SIPA is considered to be one of the most promising irradiation creep theories to explain many of the experimental observations for conditions where little to no swelling is observed [5]. This mechanism should occur under all

stress, temperature, and dose rate conditions during irradiation. Because the mechanism relies on dislocation climb by interstitials, SIPA will not occur under purely thermal conditions due to the low thermal interstitial concentration. Due to the anisotropic nature of the interstitial diffusion described in this mechanism, it is expected that loop growth would also be anisotropic if SIPA is dominating. Therefore, a systematic analysis of dislocation loop size as a function of the applied tensile stress is necessary to demonstrate the viability of this mechanism.

2.3.3 Preferential Emission (PE)

Although irradiation creep is generally considered to be independent of temperature, under certain conditions, thermal effects could still influence the irradiation creep rate. As an augmentation to the SIPA mechanism, preferential emission (PE) is proposed as the vacancy equivalent mechanism to SIPA [5, 23]. The hypothesis is that the applied external stress will also affect the vacancy diffusion to sinks of different orientation to the tensile axis. The major difference between the PE mechanism and the SIPA mechanism is that the vacancy concentrations in question are thermally induced rather than irradiation induced.

The deformation mechanism for PE is dislocation climb; therefore the governing equation for irradiation creep rate of PE is the same as SIPA described by equation 2.6. However, the climb velocity will change due to the difference in point defect concentration.

$$\nu_{d_A} = \frac{\Omega}{b}\sum_{j}^{3}\left(z_v^{dj} D_v C_v^o - z_v^{dn} D_v C_v^o\right)$$

$$= \frac{2}{3}\frac{\Omega}{b}\left[\Delta z_v^d D_v C_v^o\right] \tag{2.9}$$

Note that C_v^o is the thermal vacancy concentration and not the vacancy concentration from irradiation. *Dv* is the vacancy diffusivity, *Ω* is the atomic volume, and *b* is the dislocation Burgers vector. The term Δz_v^d is the difference in the sink strength for thermal vacancies in an externally applied stress field [5][8].

$$\Delta z_v^d = z_v^d \left[\exp\left(\frac{\sigma\Omega}{kT}\right) - 1\right] \tag{2.10}$$

The z_v^d term describes the sink strength of dislocations for vacancies. The σ is the applied stress, k the Boltzmann constant, and Ω is the atomic size. This expression for vacancy sink strength is different than those in SIPA because the anisotropic vacancy diffusion in this formulation is no longer driven by the interstitial diffusion. Instead, the vacancy anisotropic emission is hypothesized to be driven by the external stress modifying the exponential temperature dependence. The total creep rate under this formulation takes the following form:

$$\dot{\varepsilon}_{PE} = \frac{2}{9}\rho\Omega C_v^o z_v^d \left[\exp\left(\frac{\sigma\Omega}{kT}\right) - 1\right] \tag{2.11}$$

where the z_v^d term describes the sink strength of dislocations for vacancies, and C_v^o is the thermal vacancy concentration. The σ is the applied stress, T the temperature, k the Boltzmann constant, Ω is the atomic size, and ρ the dislocation density. The preferential emission distinguishes itself from other mechanisms by its exponential temperature dependence in the thermal vacancy concentration. It accounts for the migration of vacancies under both thermal and irradiation conditions, but only dominates in regimes where thermal defects are larger than irradiation defects. PE itself has no direct dependence on the dose rate, but its strain contribution depend on the ratio of thermal defects to irradiation defects, which is a function of the dose rate. It could potentially explain any thermal effect present in irradiation creep that is not captured by other mechanisms. One should note that this mechanism also has exponential stress dependence. However, because the stress term is normalized by the temperature, the term inside the exponent mimics linear behavior with respect to stress under fast reactor conditions.

2.3.4 Preferential Absorption Glide (PAG)

Building on the I-creep climb glide model and coupling it with SIPA diffusion, Mansur et al. [23,24] introduced a climb glide irradiation creep model that could operate in the absence of swelling. This model has dislocation glide as the major deformation mechanism, but the rate controlling climb velocity is dictated by the SIPA mechanism. The added stress dependence from

dislocation interstitial bias of SIPA to the climb glide model makes it one of the few irradiation creep mechanisms that predicts a stress dependence that is higher than linear.

For F-M steels with high dislocation densities, the dislocation network itself will act as the main obstacles for dislocation glide. Under that description, the creep rate from dislocation movement will be determined by how fast the dislocations can climb past dislocation lines that are spaced a length "l" apart. This can be written as the formula below [17]:

$$\dot{\varepsilon}_{PAG} = \frac{\sigma}{E}\frac{\nu_d}{l} \tag{2.12}$$

where the *E* is the elastic modulus, and σ is the applied stress. The dislocation line spacing "l" is approximated as $(\pi\rho)^{-1/2}$ [23], while the dislocation climb velocity ν_d shares the same form as that of SIPA described in equation 2.8. By combining equations 2.8 and 2.9, the PAG creep rate becomes:

$$\dot{\varepsilon}_{PAG} = \frac{4}{9}(\pi\rho)^{1/2}\frac{\Omega}{\mathrm{b}}\frac{\sigma}{E}\left[\Delta \mathrm{z_i^d D_i C_i}\right] \tag{2.13}$$

similar to eqn 2.8, *Di* is the interstitial diffusivity, *Ci* is the interstitial concentration, *Ω* the atomic volume, *b* the Burges vector, ρ the dislocation density and Δz_i^d the difference in interstitial sink strength between the aligned and unaligned dislocations. Since the PAG mechanism presupposes the operation of SIPA, there is a stress condition where the dislocation glide will start to dominate over the dislocation climb. A critical stress is found by equating the PAG creep rate and the SIPA creep rate, yielding the equation:

$$\sigma_{crit} = \frac{\mathrm{Eb}}{2}\left(\frac{\rho}{\pi}\right)^{1/2} \tag{2.14}$$

At stress above the critical stress, PAG is thought to dominate the creep mechanism, while SIPA dominates the creep at lower stress. This mechanistic switch from climb to climb enabled glide is only a function of the elastic strain and the dislocation network density. However, as the microstructure continuously evolves in the material under irradiation, the SIPA PAG relationship becomes increasingly complex. Definitive testing of these models require detailed microstructure determination in tandem with macroscopic creep strain data. [23]

The flexibility of the PAG theory allows more complex microstructure features to be considered as obstacles to dislocation glide. Accurate theoretical calculations of the creep rate depend on microstructure analysis at specific test conditions that corresponds to the measured creep rate. If the dislocation networks are the dominant obstacle for dislocation motion, PAG will differentiate itself from other irradiation creep mechanisms by its unique quadratic stress dependence.

2.3.5 Stress Induced Preferential Nucleation (SIPN)

Stress induced preferential nucleation (SIPN) is an irradiation creep mechanism proposed to explain primary creep deformation by the anisotropic distribution of dislocation loops. The applied tensile stress will enhance the nucleation of interstitial loops on planes that are aligned perpendicular to the tensile stress direction. This anisotropy in the number of interstitial loops will cause an effective strain in the tensile direction as the loops grow in size.

Anisotropy in dislocation loops at low dose have been qualitatively confirmed independently by microscopic observations [7], [25], [26]. However, deriving a strain from microscopic observations has proven to be difficult. The most comprehensive attempt to quantify SIPN strain is developed by Brailsford et al [27] and reviewed by Matthews et al.[5] The derivation is based on a probabilistic approach. It is assumed that a dislocation loop is formed when a point defect clusters reaches *n* atoms, then the probability of dislocation forming on a specific orientation i takes the following form:

$$p_i = \left. exp\left(\frac{\sigma_i n\Omega}{kT}\right) \middle/ \sum_{j=1}^{n_0} exp\left(\frac{\sigma_j n\Omega}{kT}\right) \right. \tag{2.15}$$

where σ_i is the resolved stress on the ith set of loops, n is the number of atoms in the loops, Ω the atomic volume, k is the Boltzmann constant, and T is the temperature. This probability function is then applied to the dislocation loops by defining f_i as the excess fraction of interstitial loops in the ith direction. For a simple cubic system where there is a total of three loop directions, and it

is assumed that one set of loops is perfectly perpendicular to the tensile axis and the other two are perfectly parallel, f_i takes the following form:

$$f_1 = \left.(exp\left(\frac{\sigma_1 n\Omega}{kT}\right) - 1)\right/(exp\left(\frac{\sigma_1 n\Omega}{kT}\right) + 2)$$

$$f_2 = f_3 = 0$$

(2.16)

Where n is the number of interstitials making up the loop, Ω is the atomic volume, k is the Boltzmann constant, and T is the temperature. Brailsford et al [27] defines the interstitial loops that are perpendicular to the tensile axis as "aligned". If f is the excess fraction of aligned loops, then, the concentration of aligned loops is the following:

$$N_{AL} = \frac{1}{3}(1 - f)N_L + fN_L \tag{2.17}$$

Combining the previous equations will yield the following form for strain due to SIPN.

$$\varepsilon_{SIPN} = \frac{2}{3} f\pi b r_L^2 N_L \tag{2.18}$$

Once again, b is the Burgers vector, r_L is the average radius of the dislocation loop, and N_L is the dislocation loop concentration. The SIPN strain rate could be obtained by taking the time derivative of equation 2.18, yielding the following:

$$\dot{\varepsilon}_{SIPN} = \frac{4}{3} f\pi b N_L r_L \dot{r_L} \tag{2.19}$$

This expression can further reduced by simplifying f. It is understood that for x<1, exp(x) ~ x+1. Therefore, equation 2.19 can become the following.

$$\dot{\varepsilon}_{SIPN} = \frac{4}{9}\frac{\sigma n\Omega}{kT}\pi b N_L r_L \dot{r_L} \tag{2.20}$$

Furthermore, the dislocation loop concentration N_L can be expressed in terms of an area density, by defining ρ_L as the loop line length per volume with the expression that $\rho_L=2\pi r_L N_L$. The simplified form of the strain rate becomes the following:

$$\dot{\varepsilon}_{SIPN} = \frac{2}{9}\frac{\sigma n b \Omega}{kT}\rho_L \dot{r_L} \tag{2.21}$$

The loop growth rate $\dot{r_L}$ can be expressed in terms of point defect concentrations similar to the previous mechanisms discussed. Dislocation loops are biased sinks, so its growth will be directly related to the interstitial and vacancy flux under irradiation. The description for the point defect flux is described in the expression for climb velocity shown in equation 2.9. By expressing the loop growth rate in terms of point defects, the final form of the SIPN strain rate equation takes the following form:

$$\dot{\varepsilon}_{SIPN} = \frac{2}{9}\frac{\sigma n b \Omega}{kT}\rho_L \left[z_i^d D_i C_i - z_v^d D_v C_v\right] \tag{2.22}$$

In the final form of the equation, z_v^d term describes the sink strength of dislocations for vacancies, z_i^d term describes the sink strength of dislocations for interstitials, C_i is the interstitial concentration, and C_v is the vacancy concentration. The σ is the applied stress, n is the number of atoms per dislocation loop, T the temperature, k the Boltzmann constant, Ω is the atomic size, and ρ the dislocation density. There has been much debate on the significance of SIPN contribution to irradiation creep. The major argument against the mechanism is it consistently under-predicts the creep strain by factors of 2-4 [5]. The other argument is that since the mechanism is based only upon loop nucleation, it will only affect the primary creep regime; and once the loop nucleates, SIPN will no longer contribute to the creep strain. Traditional nucleation theory predicts that loop nucleation still occurs during steady state creep, it's just the nucleation rate has reached an equilibrium with loop annihilation rates either due to unfaulting or loops growing into dislocation networks. However, since bcc steels have such high stacking fault energy, the loops do not annihilate through unfaulting. In addition, interstitial emission was also found to be unlikely due to unfavorable energetics. Therefore, SIPN mechanism has been criticized for unable to achieve equilibrium. However, the anisotropy described by SIPN can still contribute to irradiation creep strain and have an effect on the measured creep rate.

2.3.6 Method for Identifying Irradiation Creep Mechanisms

The irradiation creep mechanisms outlined above all have complicated theoretical basis derived from first principles. In order to correctly identify the mechanism through experiments, variables must be isolated that will demonstrate significant changes in experimental results due to the dominance of different creep mechanisms.

For every creep mechanism, the independent variables that may affect irradiation creep strain rates are temperature, dose rate, and stress. By isolating the individual effects of these variables and then measure the changes in strain rates, different creep mechanisms could be identified through their unique dependencies on the variables.

In addition to strain rate data through macroscopic experiments, microscopic analysis would also yield valuable microstructure evidence for the dominance of certain mechanisms. The existence of voids would point to the dominance of an I-creep type mechanism. If dislocation bowing is observed, then dislocation glide is active thus pointing to either I-creep or PAG. Anisotropic loop size would be a clear indication of SIPA, and any anisotropic loop distribution will be evidence for SIPN. The individual creep mechanisms and their theoretical response to each variable are outlined in Table 2.2.

Table 2.2 Irradiation creep mechanisms and their major characteristics.

	I-creep	PE	SIPA	PAG	SIPN
Temperature Dependence	None	Arrhenius	None	None	None
Stress Exponent	1	1	1	2	1
Dose Rate Dependence	Linear	None	Linear	Linear	Linear
Microstructure Evidence	Voids and bowing dislocations	None	Anisotropic loop size	Bowing dislocations	Anisotropic loop distribution

2.4 Ferritic Martensitic (FM) Steels

Before one can fully understand and analyze the irradiation creep behavior of ferritic martensitic (FM) alloys, it is important to have knowledge of the general behavior of the FM alloys. This section will review the basic properties of FM steels, including their composition, physical metallurgy, and overview their mechanical behavior. The key microstructure features of FM alloys will also be discussed in detail, as well as the changes that develop under irradiation. This chapter will provide the relevant background information unique to designing an irradiation creep experiment for FM steels and the related analysis. The review will focus primary on T91 as the prototypical FM steel since it is the material used most extensively in this project. However, the theories and properties of outlined in this review can be generalized to all FM steels unless otherwise stated.

2.4.1 Composition

Ferritic martensitic (FM) steels are the primary candidate materials for this application, since they have already proven themselves in the high corrosion, high temperature environments of the petrochemical and turbine industry. They were first developed in 1930, after it was discovered that low carbon (less than 0.1%) high chromium (7-12%) steels exhibited both oxidation and corrosion resistance with superior properties at elevated temperatures. The 12Cr FM steel designated as HT9 developed by Sandvik was demonstrated to show great swelling resistance in comparison to 316 Stainless Steel in FFTF reactor. Later, 9Cr FM steels such as T91 and T92 were developed to optimize the chromium content to suppress alpha phase formation. Concurrently, reduced activation steels such as F82H were being developed for fusion applications. Although the FM steels generally exhibit very similar mechanical behaviors, different minor alloying elements will impact the swelling and creep performance of these steels. Consequent efforts were made to control the alloying elements to achieve improved creep resistance by attaining the following conditions:

- Optimizing the δ-ferrite content by additions of austenite stabilizing elements.
- Maximize the solid solution strengthening.
- Stabilize the martensite dislocation structure and the $M_{23}C_6$ type precipitates.
- Enhance precipitation strengthening of fine particles that are resistant to coarsening.

The alloy elements and their weight percent of T91 is tabulated in (Table 2.3), and the general effects of common alloys addition to FM steels are discussed below [28].

Carbon addition of 0.2-2%wt is the definition for iron to be classified as steel. In general, the addition of carbon increases hardness and strength but reduces ductility and weldability. For ferritic martensitic steels, carbon is most crucial in the formation of martensite. Martensite is formed by rapidly quenching an austenitic (γ) phase iron to room temperature, freezing the solid solution carbon atoms in a newly formed lattice with high strain energy, resulting in more strength. As observed the Fe-C double phase diagram, Figure 2.3, the γ phase forms a closed loop with the maximum at about 2%wt carbon. This loop exists in most iron binary phase diagrams, and its vertex gives an upper limit to the amount of alloying that can be done before the iron ceases to have the potential to be martensitic. The maximum alloy percentage for every single alloying element is tabulated in Table 2.4.

Chromium is the essential alloy addition for corrosion and oxidation resistance. In high amounts, it will form a protective passive film of chromium oxide that prevents further oxidation. The chromium will also react with carbon to form carbide precipitates. This precipitation increases strength by precipitation hardening, but lowers corrosion resistance since it reduces the formation of chromium oxide. It also makes chromium a ferrite former since it reduces the amount of carbon, an austenite stabilizer, in the steel. From the Fe-Cr equilibrium diagram, Figure 2.4, we can see that no austenite will form at chromium compositions higher than 12%. However, adding austenite stabilizers such as Ni and Mn will extend the γ phase loop and adding ferrite forming elements will contract it. The combined contribution of all alloying elements were transformed into a Cr equivalent weight representing ferrite formers, and Ni equivalent weight representing austenite stabilizers using the following equations:

$$Ni\ equivalent\ (wt\%) = (\%Ni) + (\%Co) + 0.5(\%Mn) + 0.3(\%Cu) + 30(\%C) + 25(\%N)$$
$$Cr\ equivalent\ (wt\%) = (\%Cr) + 2(\%Si) + 1.5(\%Mo) + 5(\%V) + 1.75(\%Nb) + 0.75(\%W) + 1.5(\%Ti) + 5.5(\%Al) + 1.2(\%Ta) + 1.2(\%Hf) + 1.0(\%Ce) + 0.8(\%Zr) + 1.2(\%Ge) \quad (2.23)$$

The competing ferrite formers and austenite stabilizers are tabulated in Table 2.5. The equivalent weights determine whether the final composition of the normalized steel will be austenite, martensite or a combination of them with traces of δ-ferrite. The final phases of the steel as a function of the equivalent weights are documented in the Scheaffler-Schneider diagram as shown in Figure 2.5.

Molybdenum and Tungsten are the major alloying component for high temperature components since they exhibit very little temperature dependent expansion and softening. At 1-2%wt addition, the steel will show significant increase in creep strength and hardenability. They also improve resistance to hydrogen corrosion and overall weldability of the steel. However, they are both ferrite formers so their effects must be offset by other austenite stabilizers.

Cobalt and Nickel are the most effective austenite stabilizers that may be added to the alloy. They are unique elements in that they do not have a closed γ phase loop in dual phase with iron. Therefore, a large amount of these elements can theoretically be added to the alloy. However, these elements are very expensive to be used for heavy alloying. Furthermore, these two elements also yield high radioactivity after neutron activation and should be minimized for safe nuclear application. In addition, nickel has been recently identified as the source for helium generation in fast reactor conditions through n-α reaction. Helium is known to stabilize void nucleation in steels; thus high nickel content could also be detrimental for irradiation swelling behavior, negating one of the major advantages for FM steels for nuclear applications.

Copper is an austenite stabilizer that is generally used in between 0.2-0.5% wt. to provide atmospheric corrosion resistance. An addition of 1-1.5%wt can also result in precipitation hardening for the alloy, increasing strength but lowering ductility.

Nitrogen is also an austenite stabilizer that can be added. However, the amount of addition that is needed to be effective is usually excessive to be practical. Nitrogen will also react with other elements to be described below, that will cause precipitation hardening to reduce ductility and toughness.

Manganese is another austenite stabilizer that is often used in alloys. With a γ phase loop vertex at 13%wt, a large amount of this element may be added. At small amounts, usually 0.2%wt, it will react with sulfur impurities to prevent the formation of FeS, which have a relatively low melting point. At higher alloying amounts, manganese provides solid-solution

hardening, decreases ferrite grain size and increases hardenability. However, a large amount of manganese leads to embrittlement during thermal ageing and irradiation.

Aluminum and Silicon are added to take oxygen out of the steel by forming SiO_2 or Al_2O_3. They provide oxygen corrosion resistance at the expensive of forming ferrites. Silicon will also provide solid solution strengthening at 0.5-1%wt while aluminum will form AlN to provide precipitation strengthening.

Niobium, Tantalum, Titanium, and Vanadium are all ferrite formers that inhibit austenite grain growth during reheating so the microstructure can be controlled. However, they also react with nitrogen to form nitrides; providing precipitation hardening and reduce ductility and toughness.

Hydrogen, Oxygen, Phosphorus, and Sulfur are all trace elements that could not be eliminated during manufacturing. Hydrogen will rapidly diffuse through the metal to create internal defects and pressure to cause blistering, flaking, and embrittlement. Oxygen will react with iron to create oxides that reduce ductility and toughness. Phosphorus will segregate to grain boundaries promote brittleness and intergranular failure. Sulfur will react with iron to form FeS that has a low melting point. These elements are all uniquely detrimental to the strength of the metal and should be reduced as much as possible.

ASTM standard [29] requires that for T91, the material should be supplied in the normalized and tempered condition. Tempered material shall be normalized at 1038^{o}C minimum as a final heat treatment. Tempering temperature for T91 was defined at 732^{o}C minimum and 807^{o}C maximum. The material should be held at the tempering temperature for at least 1hr/in of cross section. The heat treatment requirements ensure that the resulting material meets the ASTM requirement on grain size, inclusions, and carbide density as well as yield strength, total elongation and hardness.

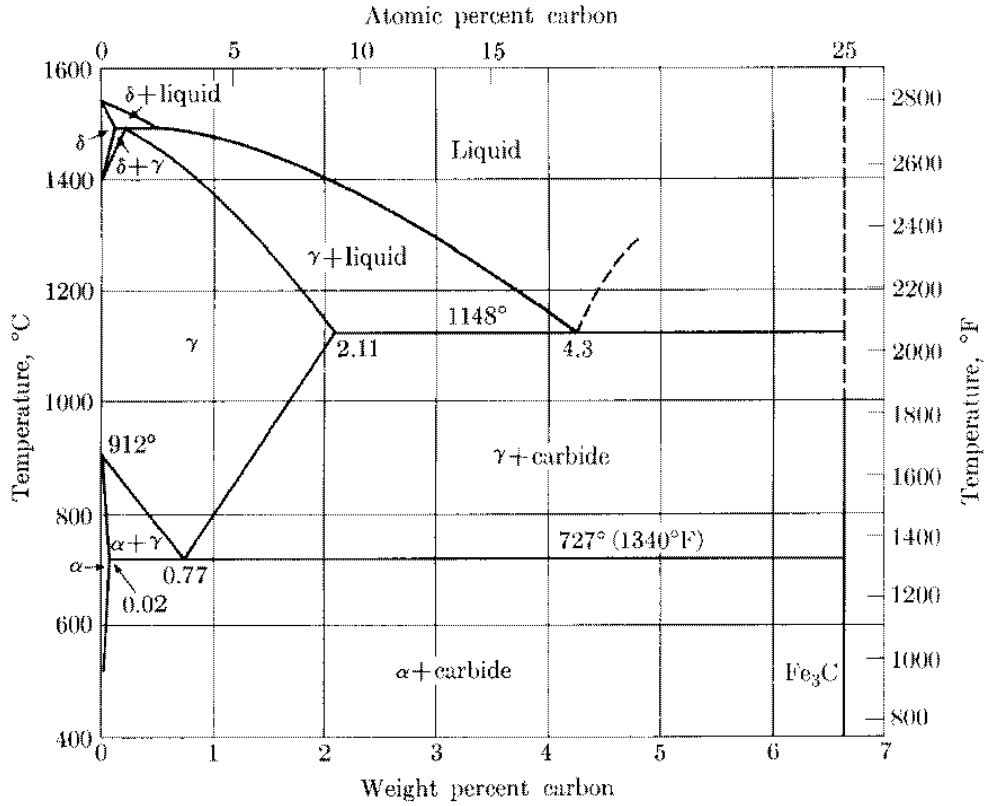

Figure 2.3 Binary phase diagram of Fe-C. [30]

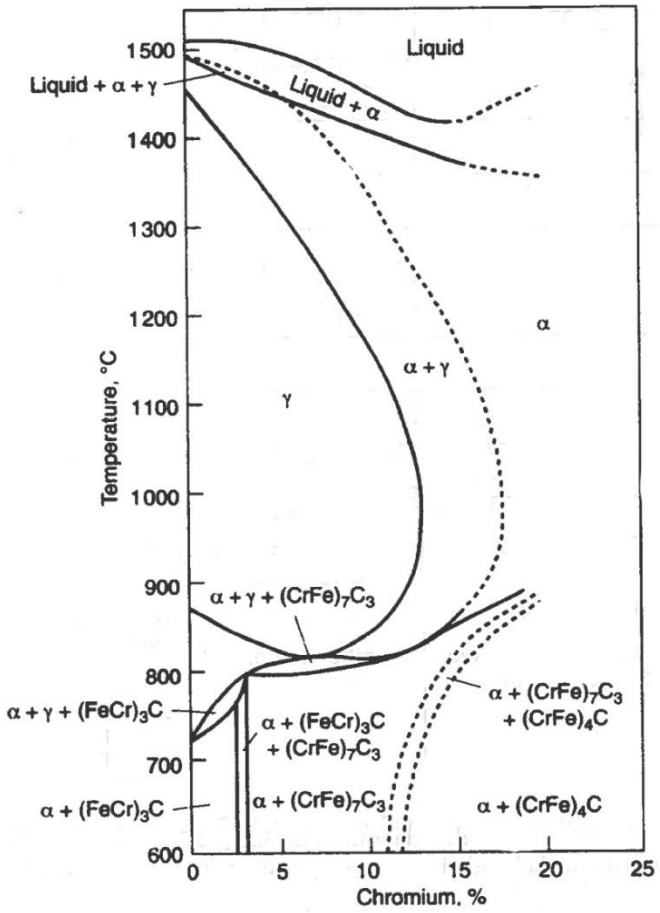

Figure 2.4 The effect of chromium on Fe-Cr alloys containing 0.1% C. [1]

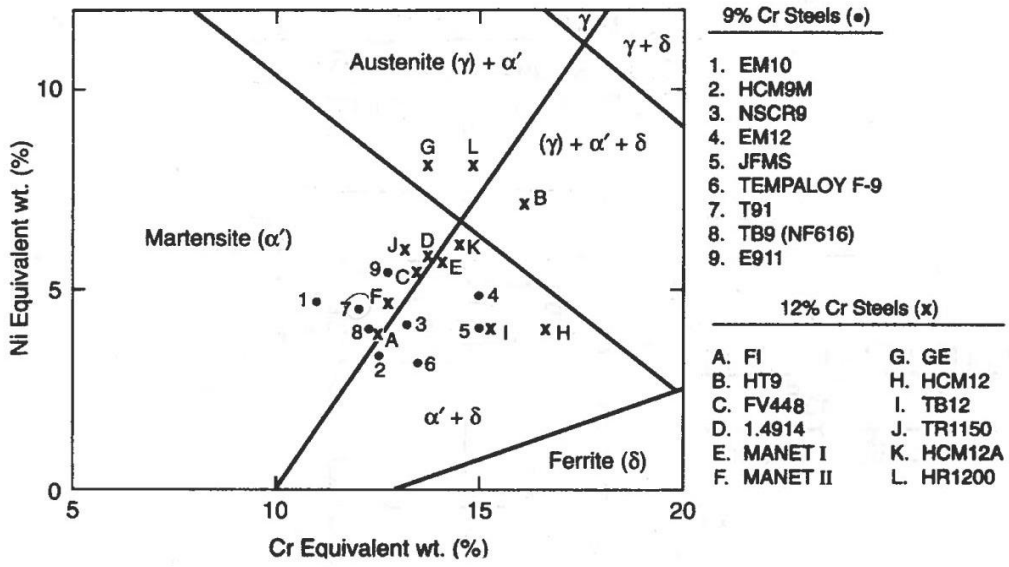

Figure 2.5 Scheaffler-Schneider diagram shows the final phase of the material as the function of nickel and chromium equivalent weight. T91 is fully martensitic. [1]

Table 2.3 Percent weight composition of T91 as defined by ASTM standard. [29]

Composition	Weight %
Cr	8-9.5
C	0.08-0.12
Mo	0.85-1.05
Mn	0.30-0.60
Si	0.20-0.50
V	018-0.25
Ni	0.40 Max
Cu	N/A
Nb	0.06-0.1
Al	0.04 Max
N	0.03-0.07
P	0.02 Max
S	0.01 Max
Fe	Bal

Table 2.4 γ-loop vertex of alloying elements. [30]

Element Addition	Weight Percent
C	2.11
Co	N/A
Cr	12.5 – 30 dependent on Ni, Mn
Cu	8.5
Mn	13
Mo	3
N	2.8
Nb	2.6
Ni	N/A
Si	2.15
Ta	3
Ti	0.6
V	1.5
W	1

Table 2.5 Competitive alloy elements

Ferrite Formers	Si	Mo	V	Al	Nb	Ta	Ti	W	Cr
Austenite Stabilizers	C	Mn	N	Cu	Co	Ni			

2.4.2 Microstructure

The overall microstructures of various FM steels in the normalized condition are generally similar in nature. They all have lath martensite of about 1μm wide and 5μm long. Depending on the composition, the matrix will also have δ-ferrite instead of being fully martensitic. Within the martensite matrix are various types of precipitates such as carbides, nitrides, and intermetallic phases of different compositions. The precipitates will be favorably located at a variety of grain boundaries, including prior austenitic grain boundaries (PAGB), martensite lath boundaries, ferrite boundaries, and sub-grain boundaries. In addition to the grains and precipitates, FM steels also consist of dislocations with a density of 10^{14} m^{-2}. The complex nature of FM steels warrants an in depth exploration of the individual components contributing to its microstructure. [1]

Martensite laths are the major matrix component making up the constitution of ferritic martensitic steels. The long lath structure is result of the shearing caused by a rapid transformation from fcc austenite to bcc iron upon quenching, trapping the carbon in its octahedral site, which causes asymmetric strain in the distorted bcc lattice. M.A. Shtremel et al. [31] characterized five different types of lath boundaries based on the double shift model proposed by Kurdyumov – Sachs [32] for the formation of martensite. Similarly oriented crystals (type 1-1) and crystals that have the same first shift but different second shift (type 1-2) will exhibit low angle boundaries. Incoherent twin boundaries are created when two crystal first shifts in different direction, but have a second shift which reduced their relative rotation (type 1-6). The remaining two types of lath formation (type 1-3/5, type 1-4) will cause regular Σ33 and Σ41 grain boundaries. For low carbon steels (<0.3%) such as FM steels, the laths inhabit the {111} plane and mostly form packets with low angle grain boundaries in between them, with very little observed twins.

Since martensite lath is formed by quenching from austenite, the grain structure of the austenite prior to quenching will be retained. These grain boundaries stop the growth of lath packets and any precipitation that exists in the austenite matrix will impede the packet growth, creating a finer microstructure. The boundaries also act as nucleation sites for precipitates, resulting in a preference for coarser $M_{23}C_6$ precipitates to be located on the prior austenitic grain boundaries. Because manipulation of the austenitic grains before quenching will not affect the

final overall martensitic microstructure, controlling the austenite is a feasible method of improving the mechanical behavior of FM steels. [33]

One major microstructure advantage of the FM steel is its ferrite sub-grains with high dislocation density and stable fine precipitates that block the movement of sub-grain boundaries and dislocations. A study done by G.Gupta et al [34]showed a significant increase in creep strength of T91 by increasing the sub-grain density within the FM steel.

Dislocations are another major contributor to the microstructure of ferritic martensitic steels. Their presence in the austenite phase act as nucleation sites for the martensitic transformation. After the martensitic transformation, there will be stress relaxation from the shift, creating new dislocations in the martensite. The dislocations found within martensite under normal heat treatment are curvilinear, entangled, and uniformly fill the volume of the martensite. [35] Few straight dislocations may also be found within the material and exhibit a clear screw characteristic. The dislocation density are on the order of $10^{15}m^{-2}$ and the burgers vector equal to $\frac{1}{2}$ a_o <111> that are typical of bcc structure. [36] The dislocation structures of the different variants of FM metals are generally similar, but they will undergo transformation under heat treatment, deformation, and irradiation.

Precipitation is one of the most complex features to quantify within the material. Depending on composition, different precipitates may form; each with a different crystal structure, individual composition, and distribution within the material. Under heat treatment, these precipitates will evolve and cause various changes in the mechanical characteristic of the material. In general, precipitates can be obstacles for dislocation motion, cause precipitation hardening and secondary hardening. They also impede grain and sub-grain growth, thus providing microstructure stability during tempering and aging. However, due to the differences between various types of precipitates, they will cause vastly different properties in the material.

Carbide precipitates are the most stable and dominant precipitation in FM steels. At room temperature, $M_{23}C_6$ (M = Cr, Fe, Mo) is the most common precipitate in the steels. These precipitates have an fcc structure with a lattice parameter of around 1.06 nm, which increases with Mo content and decreases with Fe content. The typical composition of this precipitate is $(Cr_{16}Fe_6Mo)C_6$. Any addition of nitrogen tends to inhibit the precipitation of this phase. In general, $M_{23}C_6$ will favorably precipitate on grain boundaries, then incoherent twins, and coherent twin boundaries. They will nucleate at the grain boundary with a set orientation to the

grain, and then grow into other grains. The intergranular precipitation happens at high Σ grain boundaries or large angles due to low Σ lattice misorientation. [37] For FM steels, these coarse $M_{23}C_6$ precipitates will be preferentially located at prior austenitic grain boundaries, martensite lath boundaries, and fine intra-lath particles. [1] It is observed in FM steel F82H, that the $M_{23}C_6$ carbide size range from 10 – 500 nm with an average size of 45 nm. [36] Another study on HT-9 puts equiaxed 150 nm sized $M_{23}C_6$ on the prior austenitic grain boundaries and elongated 30x200 nm $M_{23}C_6$ at the lath boundaries. [38] These $M_{23}C_6$ carbides will cause intergranular corrosion and decrease ductility; however, it will also impede grain boundary sliding, thus improving creep strength.

Another precipitation in competition with $M_{23}C_6$ is the MC (M = Ti, Zr, Hf, V, Nb, Ta) precipitate. These are also fcc precipitates with a much smaller lattice parameter of 0.44 nm. This is a more stable phase than $M_{23}C_6$, thus their formation is promoted to hinder $M_{23}C_6$ formation, reducing the decrease in ductility and corrosion susceptibility caused by $M_{23}C_6$. These carbides tend to form two types of distribution depending on method for formation. The first type is a coarse distribution of 1 – 10 μm in size during solidification. However, these carbides will be annealed out during standard treatment. Therefore, the only distribution of interest for FM steels is the fine dispersion of secondary precipitate during aging. These MC carbides are usually 5 – 50 nm in size and tend to be located inside grains on dislocations, and stacking faults. [37] In FM steels, they are mainly found on martensitic lath boundaries either as fine precipitates or undissolved particles.

The M_6C (M = Mo, Cr, W, Fe, Nb, V) type precipitation, also called η-carbide, could also found in ferritic martensitic steels. The typical composition of this carbide is $(Fe_{39}Cr_6Mo_4Si_{10})C_6$, with Mo being the most representative element. This carbide requires at least three different types of atoms and the number of carbon is variable in a unit cell. This carbide has a diamond cubic structure with a lattice parameter of 1.07 – 1.22 nm. [1] An addition of nitrogen will replace the carbon in this phase, reducing the lattice parameter, and favor this precipitation instead of $M_{23}C_6$ since it can dissolve more nitrogen. Similar to $M_{23}C_6$, these carbides are found on prior austenitic grain boundaries, and martensitic lath boundaries. Figure 2.6 illustrates the stability of different carbide phases as a function of the equivalent chromium content of the alloy. [1]

In FM steels that are heavily alloyed with ferrite formers, the difference in composition of the ferrite and austenite phase will cause precipitation of M_2C (M=CrN, Mo, W) during tempering. These carbides have a hexagonal crystal structure with a lattice parameter a= 0.478 nm and c = 0.444 nm. Under the microscope, these carbides are easily identified by their needle like structure. They tend to form on grain boundaries or the ferrite region of duplex steels depending on their composition. These precipitates will promote the formation of intermetallic compounds during aging, increasing creep strength by precipitation strengthening. [1]

In T91, fcc V_4C_3 are also observed dispersed throughout the matrix. [34] These carbides have an fcc structure with a lattice parameter of 0.42 nm. These carbides form as platelets on the {100} plane but will grow as spheres on grain and lath boundaries. In austenitic steels, it was found the V_4C_3 carbides form on grain boundaries with its nucleation closely associated with stacking faults. [39] However, in martensitic steels, it is proposed that V_4C_3 are formed by V diffusion into the M_3C cementite during tempering, finally dissolving the cementite to form the more stable V_4C_3. [40] This carbide is advantageous in that it can trap hydrogen to reduce hydrogen embrittlement and fracture.

Finally, two other carbide precipitate of interest are M_7C_3 and M_3C (M=Cr, Fe). M_3C cementite are carbides found in as received FM steels before normalization. They form as 50nm platelets of high iron content around MX precipitates since the MX depletes the Nb and V element in the matrix around it. However, these M_3C precipitates disappear during normalization by diffusion of Nb and V in the austenite matrix, replaced by the more stable $M_{23}C_6$ precipitate upon tempering. [38] M_7C_3 precipitates are carbides that are often found in steels of very high carbon to chromium ratios such as 300 series stainless steel. [37] These two carbides should not appear in FM metals under normal conditions. If they are observed, then it is helpful to look back into the heat treatment history and composition of the steel to find the source of error.

It is inevitable that nitrogen will be present in the steel during the manufacturing process. Nitrogen may also be added purposefully as an austenite stabilizer, and improve mechanical and corrosion resistance in the steel. Its presence in the steel will give rise to nitride precipitates that we can observe under the microscope. The primary nitride precipitate is of the type MN (M=Zr, Ti, Nb, $(Cr,Fe)_2$). It shares most of its properties with MC carbide, except they have a smaller lattice parameter and are more stable. Due to their stability, they will not dissolve during solution annealing, providing better microstructural control during heat treatment. The other nitride of

interest is the Z-phase nitride of composition (CrVNb)N. They are large plate particles that precipitate out in the matrix during creep at temperatures higher than 600^{o}C. They have a tetragonal crystal structure with lattice parameters a = 0.286 nm and c = 0.739 nm. It is also observed at NbC will form along with the Z-phase in Nb stabilized steels such as T91, suggesting NbC is more stable than the Z-phase. [1], [37] In general, nitride precipitates enhance creep strength and provide precipitation strengthening. However, their effects are limited since the addition of nitrogen impedes the precipitation of $M_{23}C_6$ and intermetallic phases because they do not dissolve nitrogen.

The most common intermetallic phase precipitates found in FM steels are the Laves (Fe_2Mo, Fe_2Nb, Fe_2Ti, and $Fe_2(MoW)$), and Chi (χ) (Fe–Cr–Mo and Fe–Cr–Ti) phase precipitates. The Laves phase have a hexagonal crystal structure with lattice parameters a = 0.474 nm and c = 0.773 nm. They are located on the prior austenitic grain boundaries, martensite lath boundaries, and within laths. χ-phase have a bcc structure with lattice parameter a = 0.892. They form inside martensite laths and in δ-ferrite of duplex steels.[1] These intermetallic phases are undesirable in that they deplete alloying elements such as Cr, Mo, and Nb from the matrix, reducing overall ductility and corrosion resistance. However, they do provide precipitation hardening in the steel, increasing creep resistance.

Each alloying element will cause vastly different microstructure properties once combined in the steel. One of those properties is the martensite formation temperature. It is observed that all the alloying additions to the steel will lower the martensite formation temperature, causing residual austenite to be present at room temperature, and decreasing overall strength. Therefore, the alloying elements must be optimized to yield the highest possible martensite formation temperature. Another physical property of interest is the transition temperature from α to γ upon heating. Alloying elements such as Ni, Mn, and Cu will lower this temperature while ferrite formers such as Si, Mo, V, and Al all increase it. This temperature needs to be high enough (typically above 760^{o}C) to prevent re-austenization during tempering. This limits the amount of Ni and Mn that can be alloyed into the steel as an austenite stabilizer. Other stabilizers such as N and Co are either not efficient in removing the ferrite without an excessive quantity, or can easily become radioactive under heavy neutron flux.

Typical heat treatment of FM metals start with austenization at 1040 ^{o}C, then air cooled and tempered at 760 ^{o}C. The microstructure evolution of the material with respect to temperature

is as follows: at heating less than 350 °C, fine dispersion of Fe_3C precipitates, with the possibility of M_7C_3 formed due to Cr alloying. At temperatures between 450 – 500° C, fine needles of M_2X nucleate at dislocations within martensite lath to retard softening. At slightly elevated temperature of 500–550° C, M_7C_3 and M_2X precipitates coarsen and rapid decrease in hardness ensues. From 550 - 650° C, $M_{23}C_6$ grows to replace M_7C_3 and M_2X on martensite laths and PAGB. At temperatures higher than 650 °C, sub-grains form across martensite laths and dislocation density decrease. Finally at temperatures higher than 750 °C, virtually all carbons precipitate as $M_{23}C_6$, and elongated sub-grains evolve into equiaxed sub-grains with little trace of original lath structure.[2] After the heat treatment, the microstructure will no longer change at any annealing temperature below 500 °C due to low thermal diffusion of these elements in the steel. However, at temperatures higher than 600 °C the none-equilibrium phase will become unstable and dissolve, changing the microstructure. [38]

Under standard heat treatment, T91 was observed to have a tempered martensite structure with 3-5% volume fraction of δ-ferrite despite theory suggesting it being fully martensitic with prior austenitic grain boundaries (PAGB) clearly visible. The tempered martensite laths form sub-grains in the matrix enclosed by the PAGBs. Coarse dispersion of $M_{23}X_6$ and M_2X precipitates are observed along with fine dispersion of $M_{23}X_6$, MX, M_2X, M_6X, and V_4C_3 precipitates. The carbides and carbonitride precipitates concentrates on martensite-ferrite boundaries, lath boundaries, and PAGBs. The dislocation densities are measured to be around $3x10^{14}$ m^{-2}. Prior austenite grain size is around 10 μm, lath width is around 0.46 μm. The linear carbide densities are: 1.74 μm^{-1} on PAGB, 4.4 μm^{-1} for lath boundaries, and 3.8 μm^{-1} for sub-grain boundaries.[2], [34], [41] The microstructure features of T91 are shown below in Figure 2.7-8.

In general, FM alloys will have large PAG grains that contain lath packets with large $M_{23}C_6$ carbides on its grain boundaries. Each lath packet will have its own distinct orientation and contain multiple martensitic laths that form small angle boundaries with each other. Within the martensitic laths, dislocation lines, sub-grains, small carbides and other precipitates may be observed. A diagram of the FM steel microstructure is illustrated in Figure 2.9. The complex microstructure of FM steels causes it to have higher strength than none-coldworked austenitic steels, and have higher irradiation resistance in general.

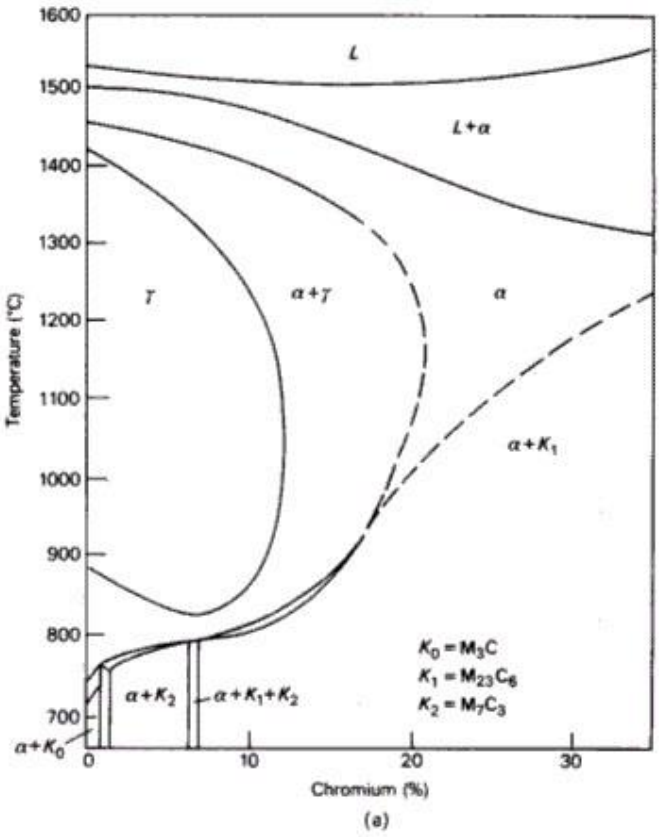

Figure 2.6 Phase diagram of precipitation as a function of equivalent chromium content. [1]

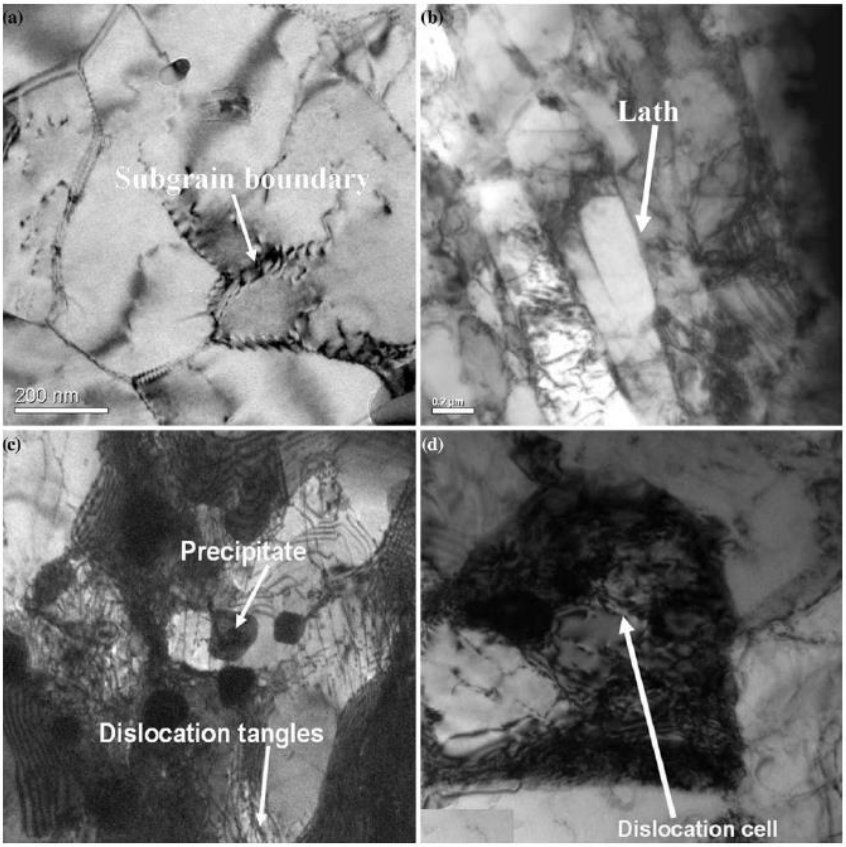

Figure 2.7 TEM images of unirradiated T91 (a) sub-grains (b) martensitic lath, (c) carbide precipitates, and (d) dislocation cells. [34]

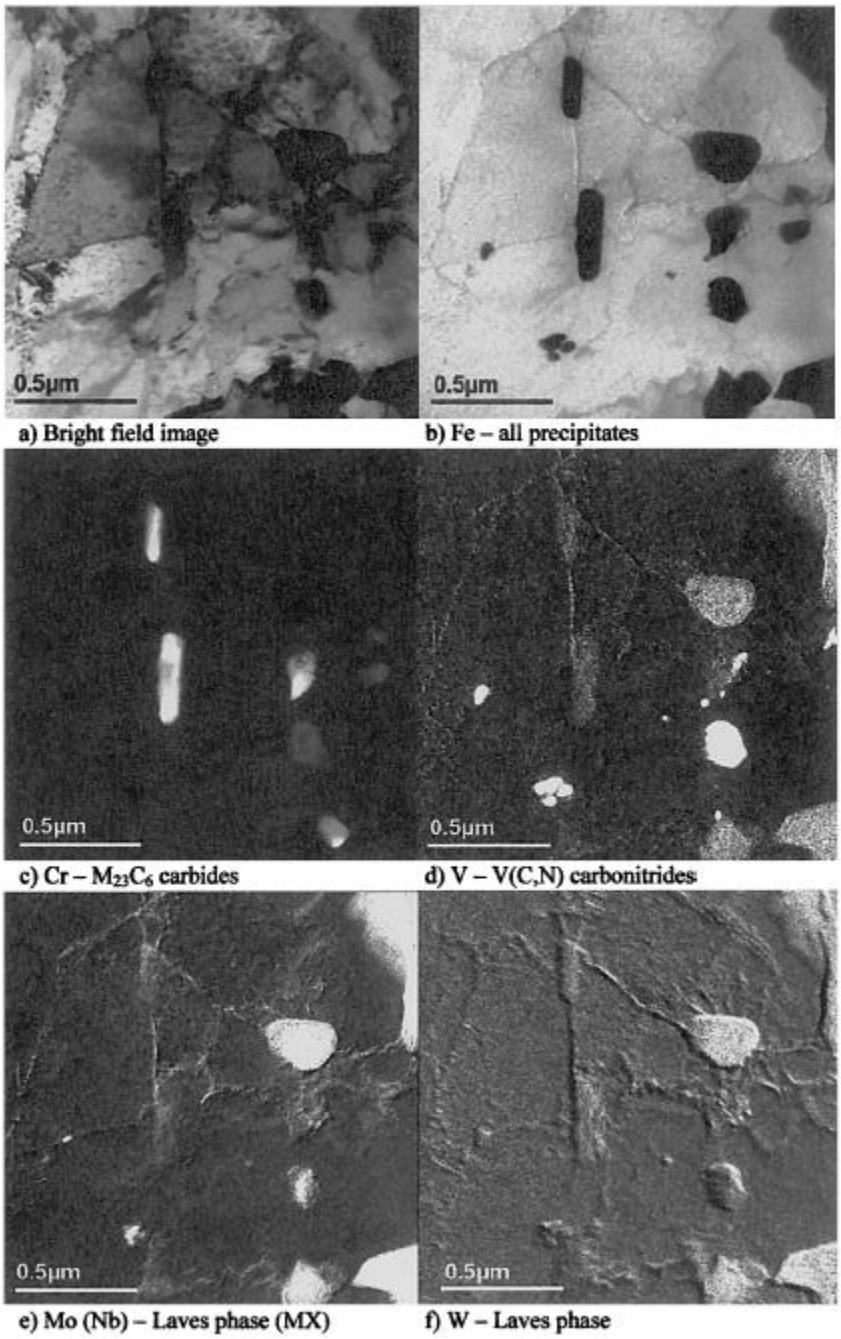

Figure 2.8 Typical precipitation in FM steels. [42]

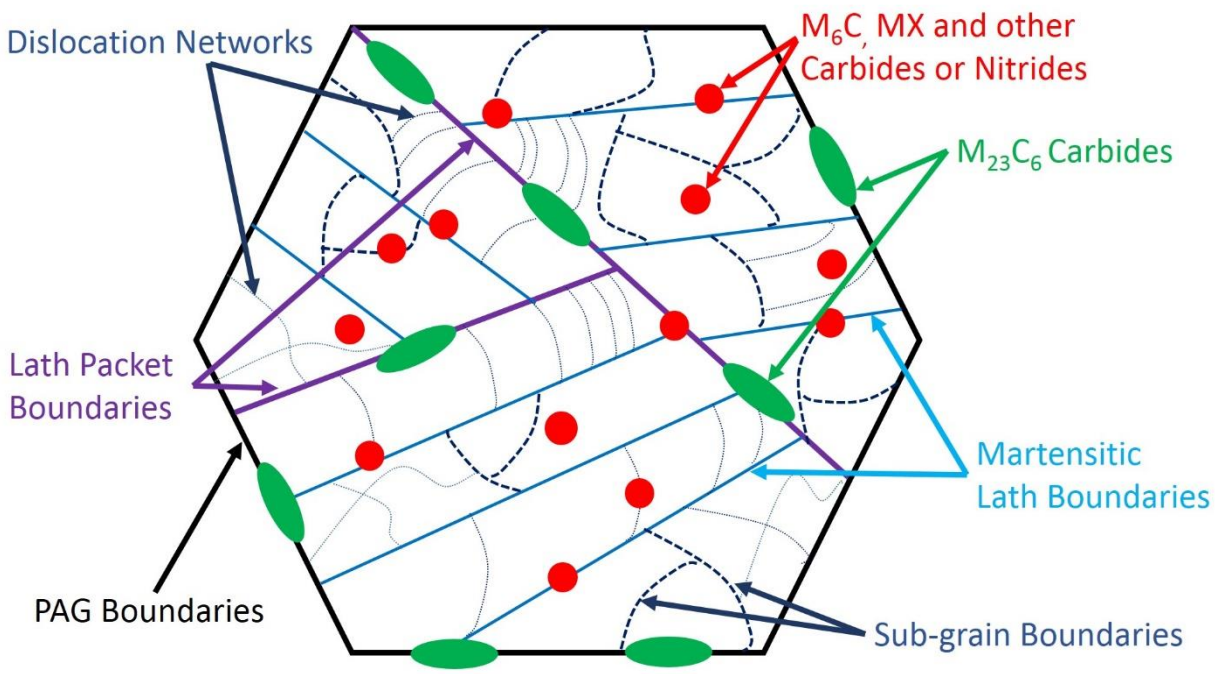

Figure 2.9 Schematic of FM steel microstructure.

2.4.3 Physical Properties

In order to fully characterize the behavior of FM steels, it is important to understand many of its inherent physical properties. The ones of special interest are density, melting point, emissivity, thermal expansion coefficient, specific heat, and thermal conductivity.

Typical steel density will vary from 7.60 g/cm^3 to 8.06 g/cm^3 depending on composition [43]. Measurements conducted on a 0.225 cm^3 piece of T91 confirmed the density of T91 to be 7.68 g/cm^3. Reduced activation FM steel F82H has a density of 7.89 g/cm^3 due to its higher W content [44]. Other FM steels should have similar densities since the only difference are minor alloying elements. Austenitic stainless steels will have a higher density of around 8.0 g/cm^3 due to their fcc closed packed structure instead of the body centered tetragonal crystal structure of martensite.

The melting temperature of FM steels is generally found to be at 1300^{o}C, although some can go as high as 1500 ^{o}C [43]. Increase in carbon or chromium content will reduce the melting point as shown in the binary phase diagrams, Figure 2.3.

Knowing the emissivity of the metal is important in determining the sample temperature using a pyrometer during proton irradiation. However, the emissivity of the metal varies greatly depending on the surface finish and angle of incidence. An oxidized surface will have an emissivity of 0.8 while a polished surface will have an emissivity of around 0.1. From past experiments conducted at Michigan Ion Beam Laboratory, the emissivity of FM steels after electropolish will have an emissivity of 0.13 during irradiation.

Thermal properties such the thermal expansion coefficient, specific heat, and thermal conductivity are all essential parameters for a creep experiment due to the high temperature conditions involved. These parameters are all temperature dependent and have been characterized by independent studies. N. Yamanouchi et al [42] compared the thermal properties of modified 9Cr alloy T91, 12%Cr alloy HT9, and reduced activation FM steel F82H. It was found that the thermal expansion coefficients of all three are similarly around 10 ppm/K at room temperature, with the T91 value being slightly higher. As temperature increases, the thermal expansion coefficients also increase. At 1000K, the coefficients of F82H and HT9 are around 12 ppm/K and T91 is roughly 15 ppm/K. Figure 2.10 suggests that a linear interpolation of the data is an adequate estimate of the coefficient of expansion in those temperature ranges. In that report,

the specific heat and thermal conductivity were also documented using laser flash techniques. The specific heat shows a slight increase from 500 J/kgK at room temperature to 700 J/kgK at 1000K, Figure 2.11. The thermal conductivity is measured to be roughly 30 W/mK, independent of temperature. These data are independently verified by A.F. Tavassoli et al [45] and S.J. Zinkle et al [46].

In another experiment conducted by A.F. Tavassoli et al [47] compared the thermal properties of T91, F82H and Eurofer. The heat capacities of the three steels are very similar, suggesting very little difference between the thermal properties of distinct FM steels. There is also a significant drop of heat capacity of F82H at temperatures higher than 700^{o}C, Figure 2.12. Although no explanation was given for this anomaly, the temperature corresponds to the transition temperature between γ and α phase; suggesting that this drop in heat capacity may be caused from the phase transformation from martensite back to ferrite.

The physical properties of FM steels are important background information for experimental design. Thermal conductivity and thermal expansion values are used to benchmark the experimental setup, and provide the basis for heat transfer calculations to achieve temperature control during irradiation.

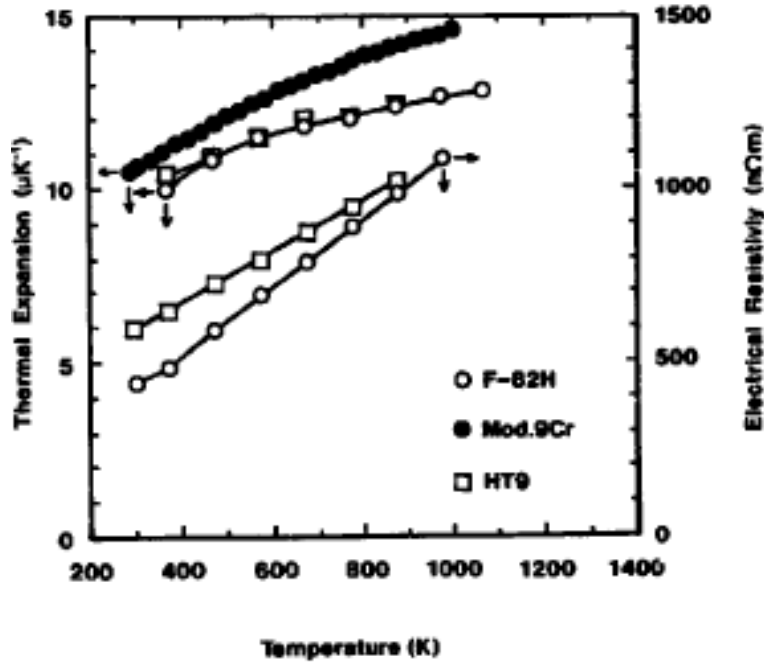

Figure 2.10 Thermal expansion coefficients of T91, HT9, and F82H as a function of temperature. [42]

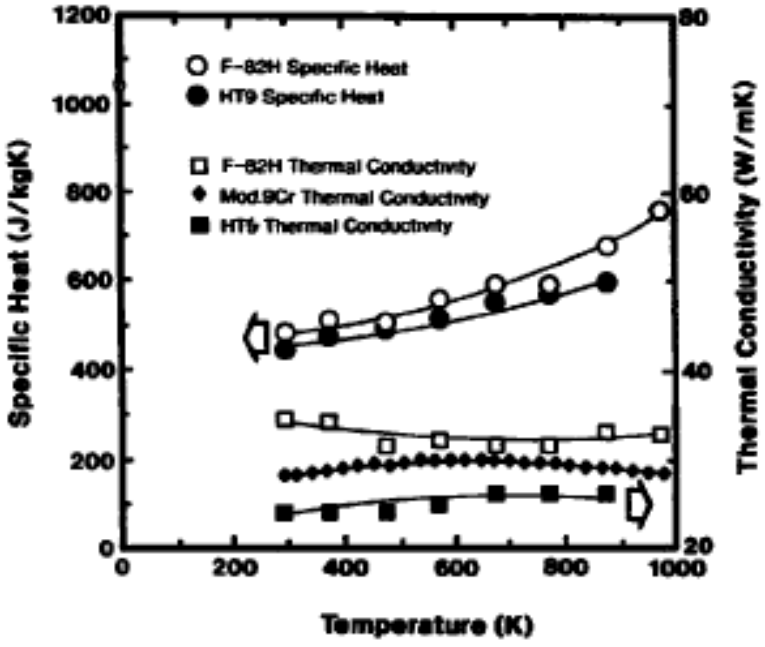

Figure 2.11 Thermal conductivity of T91, HT9, and F82H as a function of temperature.[42]

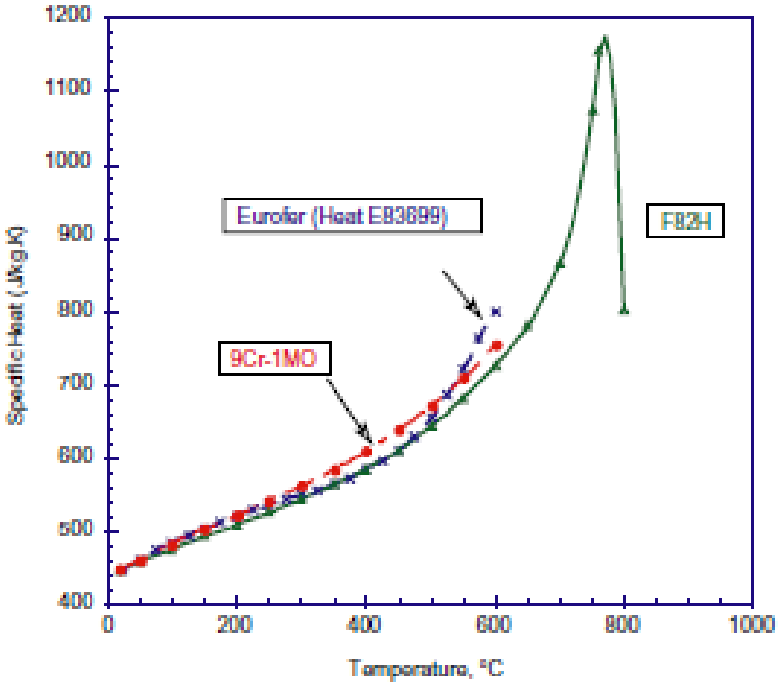

Figure 2.12 Specific heats of T91, F82H and Eurofer as a function of temperature. [47]

2.4.4 Mechanical Properties

For creep tests, the specimens will be loaded under high temperature environment; therefore it is important to understand the mechanical properties of FM steels under various loading conditions. A variety of tests are conducted to accurately measure the yield stress, ultimate tensile stress, total elongation, uniform elongation, and elastic modulus of FM metals.

An in depth exploration on the elastic properties of FM steels was done by K. Sawada et.al. [48] Three different tests were compared at different temperatures: conventional tensile tests were performed at a constant strain rate of $5x10^{-6}$ s^{-1} to obtain the stress strain curve; at temperatures higher than 973K, abrupt stress loading (ASL) tests was done at $1x10^{-2}$ s^{-1} and compared against results of the ultrasonic pulse method.

Conventional tensile test results show the elastic modulus of T91 varies greatly with temperature, dropping from 220 GPa at room temperature down to 70 GPa at 1000K. Results from ASL tests also show a decreasing trend of elastic modulus at high temperatures, however the values of the elastic modulus are higher than those obtained by tensile tests and correspond better with ultrasonic testing. The ultrasonic testing corresponds well with conventional tensile test at lower temperatures, but does not show such a significant drop at higher temperatures as shown in Figure 2.13. The dramatic drop of elastic modulus at higher temperatures from conventional tensile test and ASL is attributed to inelastic deformation caused by bending of martensitic lath boundary, shear stress relaxation at grain boundaries, and the onset of creep under loading greater than 100MPa. This inelastic deformation is time dependent, making it more significant at lower strain rates. To eliminate the inelastic contribution, ASL testing needs to achieve an even higher strain rate to obtain a true elastic modulus at high temperatures. Furthermore, these tensile tests were performed on tensile bars and not thin foils as those in creep testing. Since inelastic deformation is highly dependent on the geometry of the sample, further work is required to achieve sufficient confidence in the elastic modulus obtained to be applicable in thin foil creep samples.

Other tensile properties of interest for T91 are also explored by M. Matijasevic et al. [49] in their neutron irradiation experiment of FM metals. To characterize properties of T91 before

irradiation, tensile tests were done in an electro-mechanical testing machine (INSTRON 8500) at a strain rate of $10^{-4}s^{-1}$ over a variety of temperatures. The yield stress of T91 was found to be 544MPa, and ultimate tensile strength of 684 MPa at room temperature. There is a consistent decrease in yield stress and ultimate tensile strength as temperature increases. A linear decrease in elongation to failure is also observed with increasing temperature in T91, Figure 2.14. This data is reproduced by Y. Dai et al. [50] in another irradiation experiment in SINQ.

In another experiment conducted by G. Gupta et al [41], the ultimate tensile strength and yield stress was tested to be lower than those found by M. Matijasevic et al. At room temperature, T91 has a yield stress of 370 MPa and ultimate tensile stress of 482 MPa. Strain to necking is 5% and total elongation is 18% at failure. The difference in yield stress may be explained by the addition of 0.17 weight percent of Cu that is found in T91 sample used in G. Gupta's experiment that was absent in M. Matijasevic and Y.Dai's material.

The data compiled by S.J. Zinkle et al [46] also showed that tensile properties for F82H are similar to those of T91, Figure 2.15. The yield stress and ultimate tensile stress at room temperature are respectively 520 and 650MPa. As temperature increases to 700^{o}C, they drop down 150MPa and 220MPa. The elastic modulus decreases linearly from 193 to 160GPa as temperature increases from 450 to 700^{o}C; similarly the shear modulus also drops from 75 to 60.5GPa for that temperature range. The Poisson's ratio has a constant value of 0.29 for temperatures lower than 500^{o}C, but will slowly increase to 0.31 at 700^{o}C.

Understanding the as received mechanical properties of FM steels will inform the loading conditions of irradiation creep experiments to avoid viscoplastic behavior at high temperatures. The next section will describe in detail the thermal creep response of FM steels, specifically at stresses levels below the yield stress, and temperatures less than half of melting.

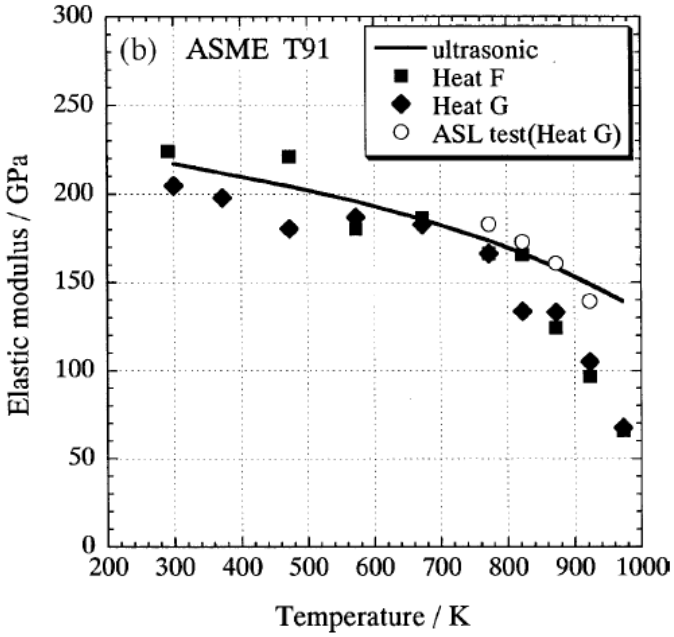

Figure 2.13 Elastic modulus results of tensile tests, ASL tests, and ultrasonic tests at various temperatures. [48]

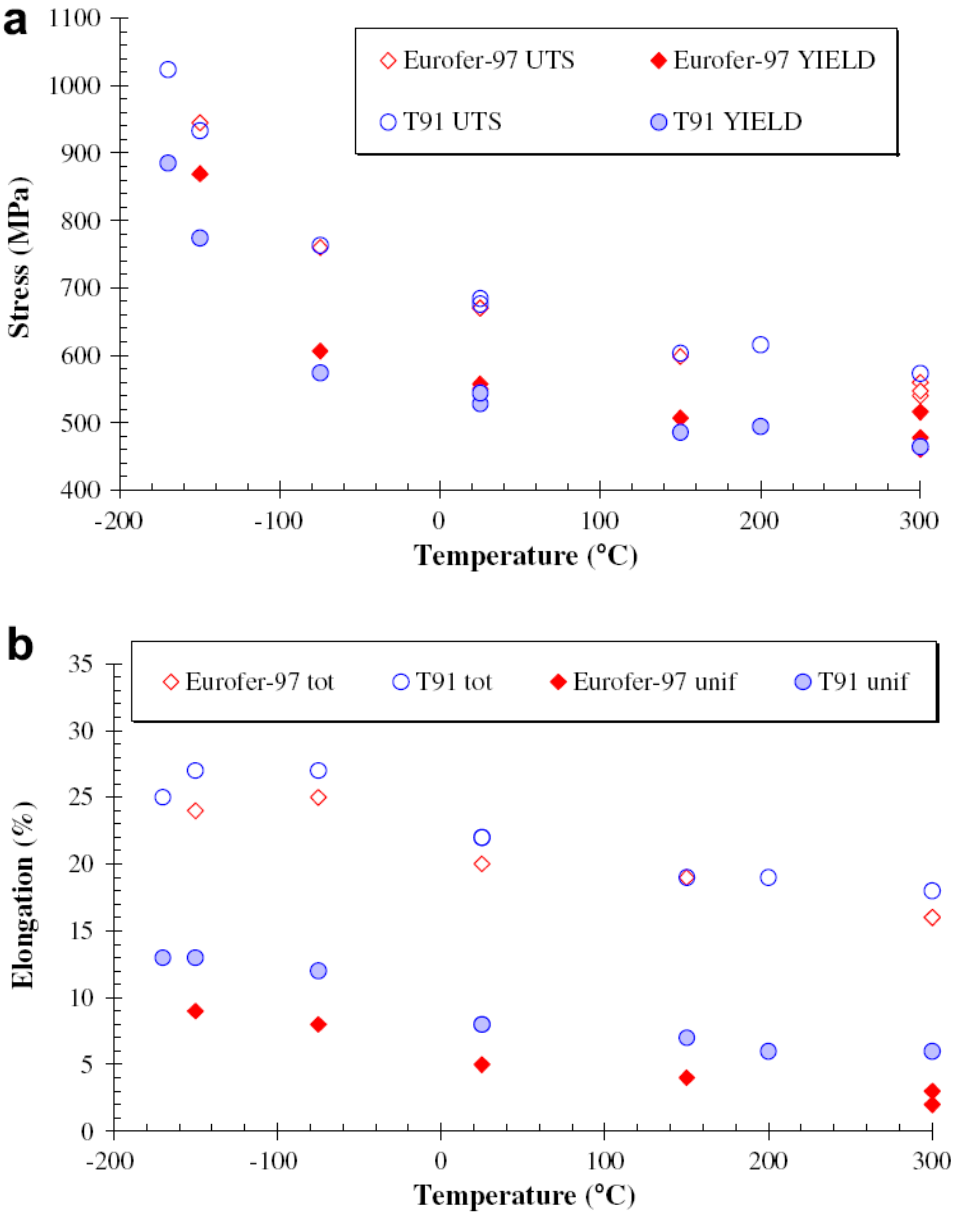

Figure 2.14 (a) Yield stress and ultimate tensile strength of T91 versus temperature. (b)The total elongation and uniform elongation of T91 versus temperature. [49]

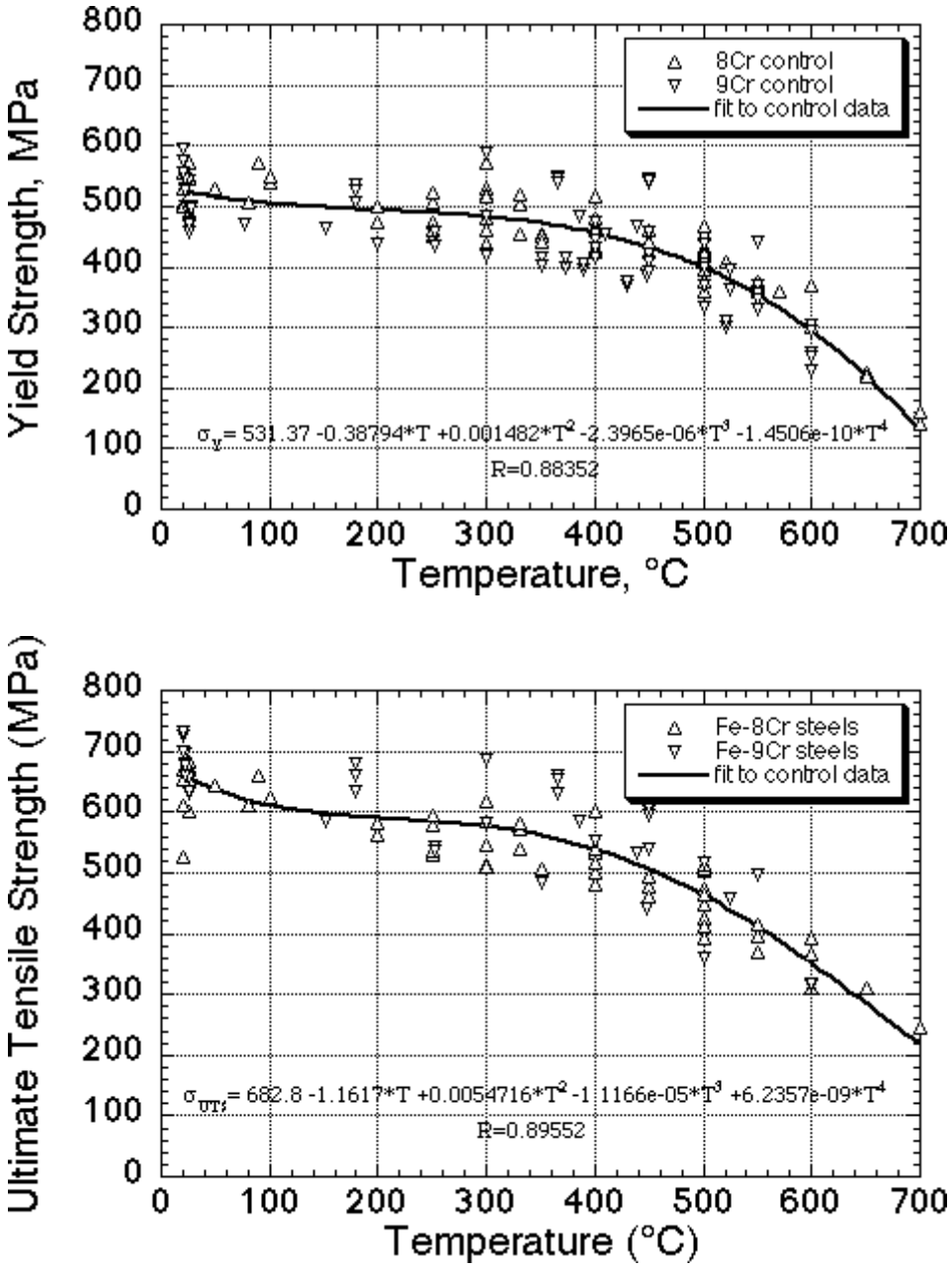

Figure 2.15 Yield stress and ultimate tensile stress of F82H up to 700°C. [46]

2.4.5 Thermal Creep

Thermal creep of FM steels has been studied extensively using different experimental techniques and approaches. Although the fundamental mechanisms for thermal creep behavior is still under debate, the empirical creep rates and dependencies are generally in agreement with each other within an order of magnitude.

Generally, thermal creep tests are conducted in one of two ways, each with their unique sample geometry. Creep rupture tests use pressurized tubes subjected to high temperature in order to get a correlation between time to rupture and applied stress. Constant load tests use tensile specimens combined with a strain measuring device to track the strain over time. Both tests have been done for FM steels and the results are reviewed in this chapter.

Majority of the macroscopic thermal creep data for 9Cr-1Mo FM steels pressure tubes are compiled by Haney et al [51]. The minimum creep rate as a function of applied stress are plotted for 625°C, 600°C and 500°C as shown in Figure 2.16-18. The minimum creep rate shows near linear stress dependence at low stress levels, and power law stress dependence with n = 10-18 past a certain threshold stress. The threshold stress is also a function of temperature, being as low as 50-90MPa at 625°C and increases up to 170-210MPa at 500°C. By comparing the time to rupture and minimum creep rates, the paper asserts that measuring the minimum creep rate is an accurate predictor of total creep lifetime through the Monkman-Grant relationship.

The creep rupture data is independently verified by Choudhary et al [52] for the Indian Prototype Fast Breeder Reactor (PFBR) program. The program tested T91 and P91 steels at narrower temperatures range of 550°C to 600°C, but higher stress levels of 125-275MPa. Due to the large amount of data points at high stress, this study narrowed down the stress exponent in the power law regime to n=12. The minimum creep rate as a function of stress for this study is shown in Figure 2.19. For 550°C, the empirical equation from this study predicts a minimum creep rate of $2.3 \times 10^{-9} s^{-1}$ for an applied stress of 200MPa. In addition to macroscopic creep data, Choudhary et al [52] also showed SEM micrographs of thermally crept samples at 52 hours, 2360 hours, and 8520 hours. The general martensite lath microstructure of FM alloys is retained after thermal creep, but precipitates on the grain boundaries were observed to coarsen due to long term creep exposure.

Constant load tests on uniaxial tensile specimens were conducted by Gupta et al [34] to explore the effect of grain boundary engineering on thermal creep response of T91. Two different heat treatment of T91 were subjected to thermal creep tests between temperatures of 500°C and 615°C under loads of 150-255MPa. This study once again confirmed power law stress dependence of thermal creep, along with finding the activation energy of thermal creep to be around 700kJ/mol. In addition, this study confirmed that increased sub-grain boundary density could increase the thermal creep resistance of T91. TEM analysis of the creep samples show sub-grain formations to be the dominant microstructure features; suggesting the operation of a dislocation driven thermal creep mechanism.

To evaluate the viability of 9Cr-1Mo steels as core internals for VHTR, Shrestha et al [53] further investigated the thermal creep behavior of FM steels at higher temperatures. Thermal creep tests on uniaxial tensile specimens were performed at temperatures between 500°C – 750°C. Linear stress dependence is observed for stress below 50MPa at temperatures higher than 700°C, and power law dependence is observed for higher stress and lower temperature conditions. The power law exponent is found to be around n=9-11, while the activation energy is around 510±51 kJ/mol. The study analyzes the data by using a modified Bird-Mukherjee-Dorn (BMD) equation. [54] The BMD equation is a semi-empirical formula that is a function of temperature, applied stress, Burgers vector, elastic modulus, and grain size. In addition, the author modified the BMD equation to introduce a threshold stress to account for the interaction of dislocations with large amounts of incoherent particles. The threshold stress is found to vary between 56-136MPa depending on the temperature, and its implementation reduced the stress exponent down to n=5 and activation energy down to 225±24 kJ/mol. This lead the author to conclude that power law creep in FM steel is the result of dislocation climb. TEM analysis of creep samples observed elongated grains and denuded zones, which the author attributes to the operation of Nabarro-Herring (NH) creep. Although the modified BMD analysis could yield stress exponents and activation energies that are in agreement with certain theoretical thermal creep mechanisms, the entire analysis is based on the assumption of an accurate threshold stress. Unfortunately, the theoretical basis for the existence and quantity of threshold stress is not well established. The author presents four separate calculations of the threshold stress available in literature, and they range from 5MPa up to 190MPa. The high uncertainty associated with the

threshold stress cast doubt into the claim that Nabarro-Herring (NH) and dislocation climb is the dominant thermal creep mechanism for FM steels.

Thermal creep behavior of FM steels has been extensively studied and the empirical results are in good agreement with each other. It is accepted that thermal creep follows power law stress dependence at high stress and linear stress dependence at lower stress. The temperature dependence of thermal creep follows Arrhenius behavior with activation energy around 500-700 kJ/mol. Microstructure analysis points to dislocation climb and sub-grain formation due to dislocation motion as possible mechanisms of creep deformation. The thermal creep rates measured in both tensile and pressure tube experiments are in agreement with each other, and provide the basis of comparison to creep rates measured for irradiation creep.

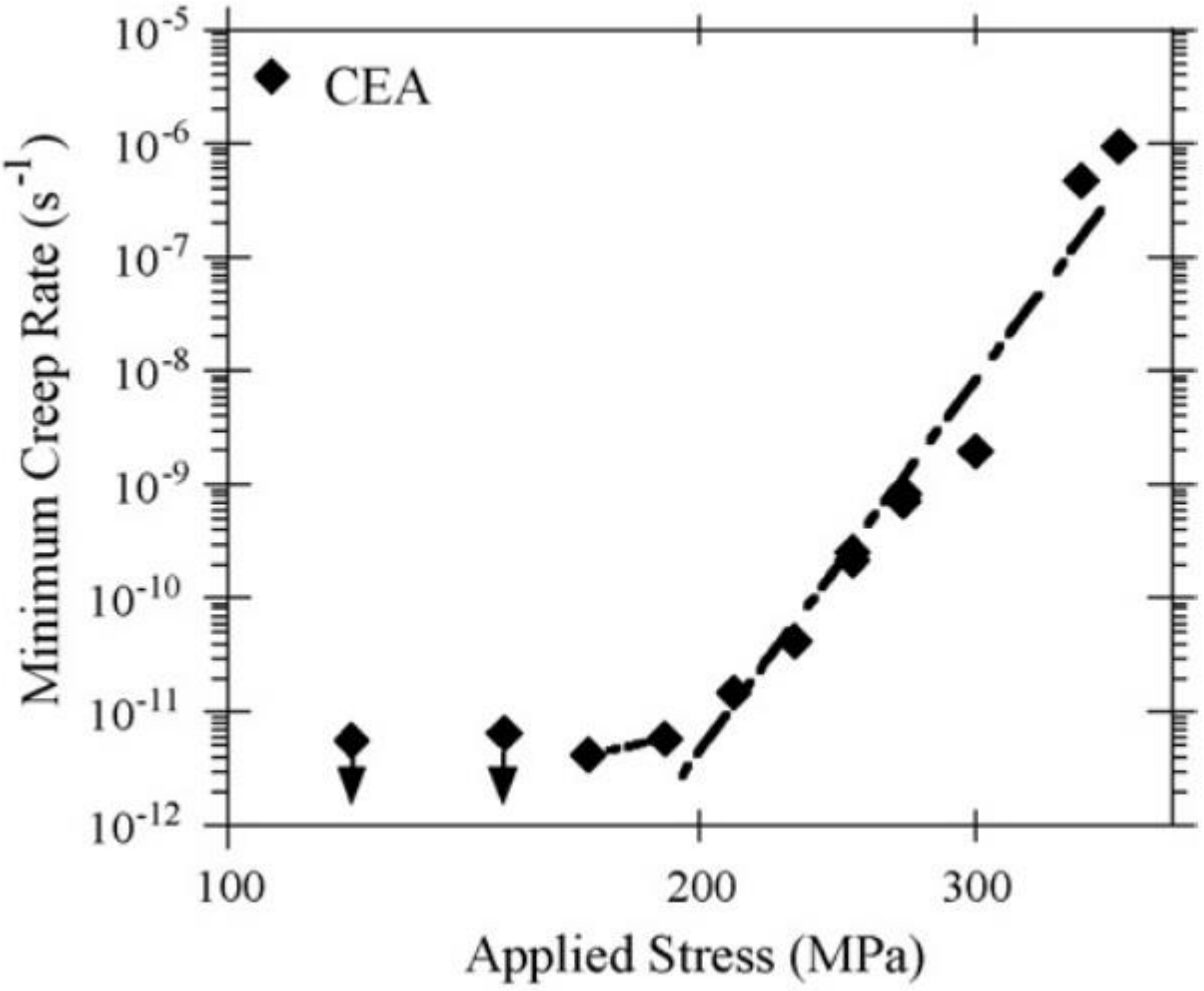

Figure 2.16 Minimum thermal creep rate as a function of applied stress for FM steel T91 at 500°C. [51]

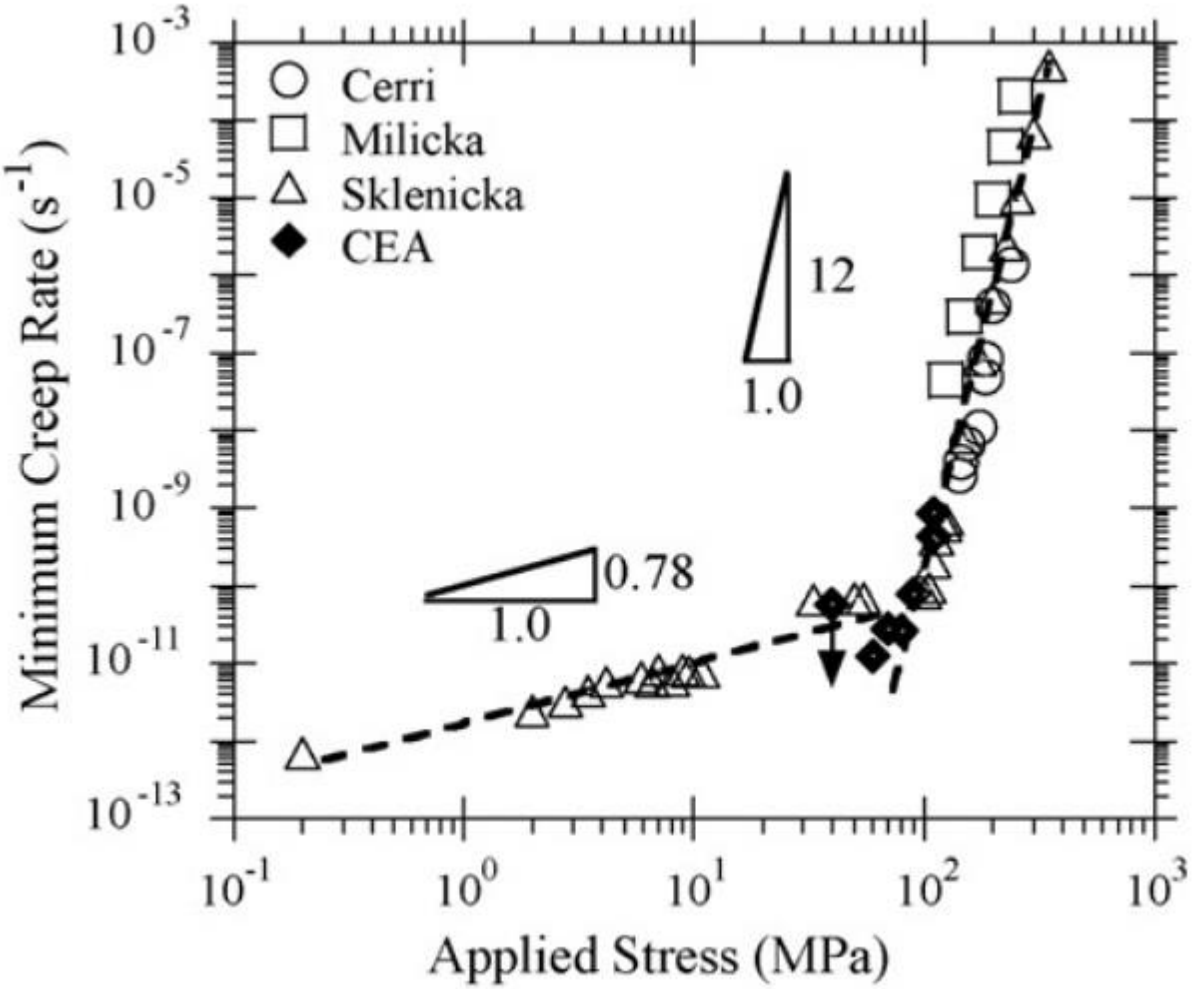

Figure 2.17 Minimum thermal creep rate as a function of applied stress for FM steel T91 at 600°C. [51]

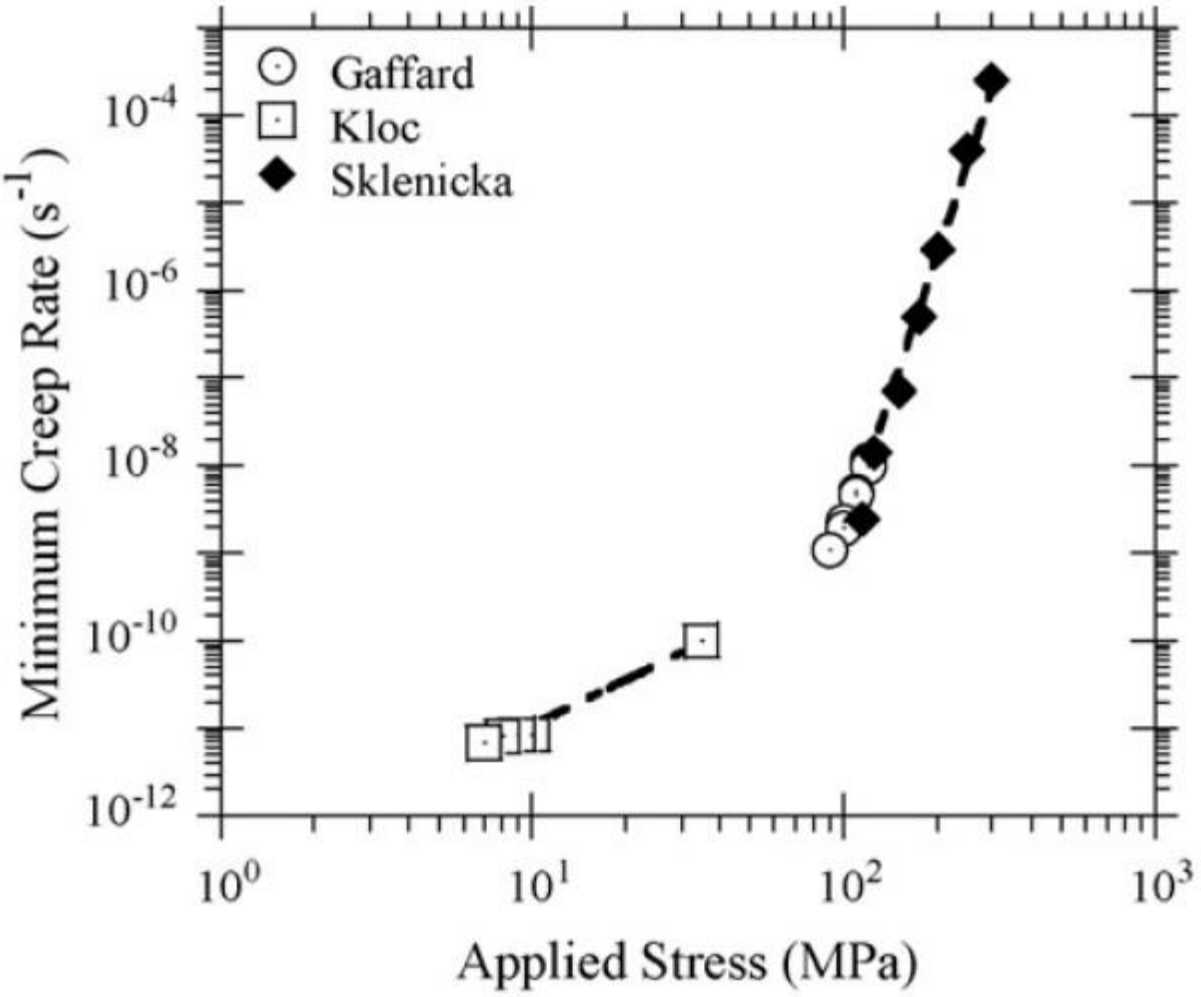

Figure 2.18 Minimum thermal creep rate as a function of applied stress for FM steel T91 at 625°C. [51]

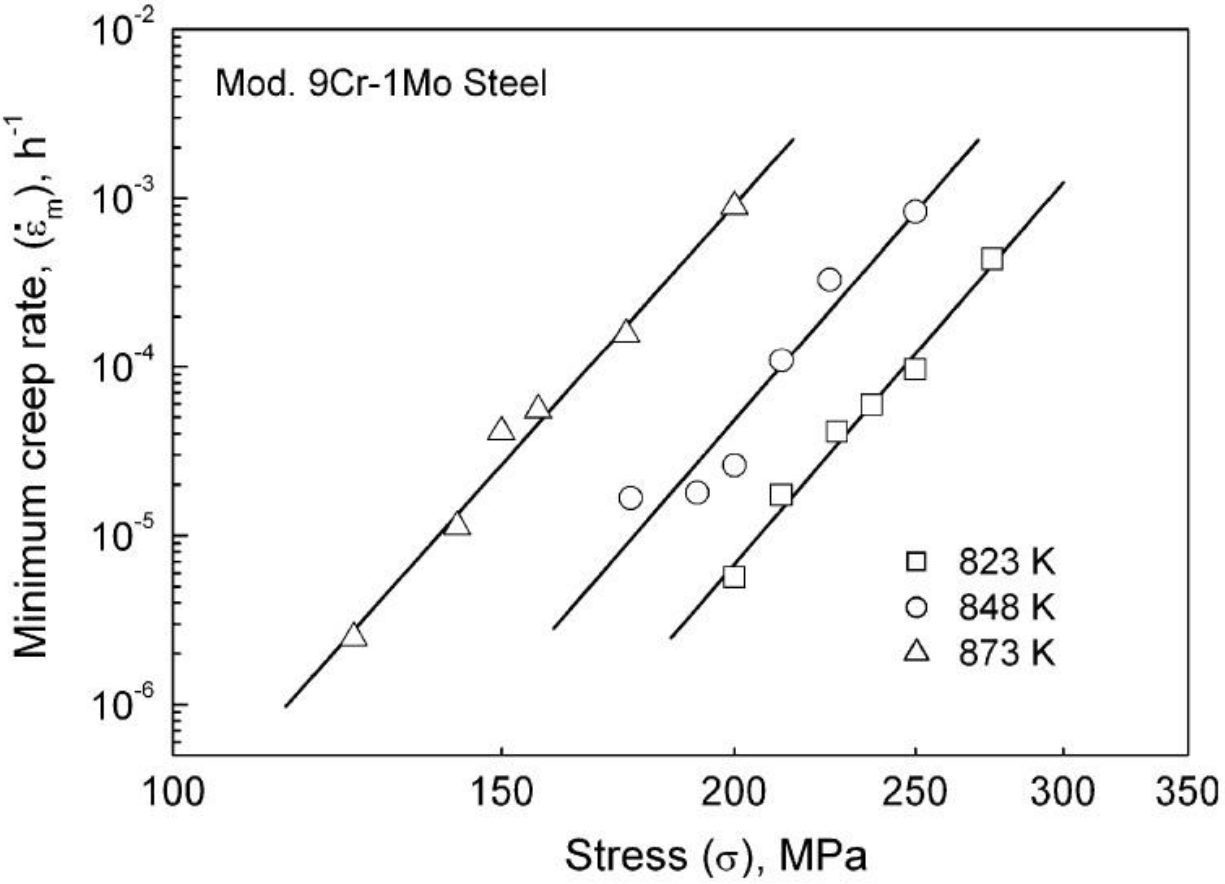

Figure 2.19 Minimum thermal creep rate as a function of applied stress for FM steel between 550°C-600°C. [52]

2.5 Irradiation Creep Experiments

Irradiation creep experiments can fall into two major categories, reactor experiments and ion irradiation experiments. Reactor experiments are conducted in test reactors such as EBRII or FFTF by exposing pressurized tube samples to high temperature and high neutron flux environments. The diameter strain of the pressure tubes are measured after the samples have reached a certain dose, and plotted against time. Neuron irradiation creep experiments provide valuable empirical data for realistic materials behavior in reactor environments. However, there is difficulty in maintaining constant temperature and neutron flux conditions inside a reactor for a long period of time. In addition, reliable monitoring of the temperature and flux inside reactor also pose unique challenges. The high costs of irradiations, radioactivity concerns for post irradiation analysis, along with lack of irradiation facilities also make neutron irradiation creep experiments problematic.

To confront these difficulties inherent in neutron irradiation experiments, several ion irradiation creep experiments have been designed to explore specific aspects of irradiation creep behavior. Ion irradiations usually have more precise control over the temperature and damage rate compared to neutron irradiations. In addition, the low activation of ion irradiated samples and their relatively cheap and fast turnaround time make these techniques especially suited for exploring fundamental mechanisms of irradiation creep. By targeting specific conditions unique to each irradiation creep mechanism, ion irradiations can produce large data sets to separate the different mechanisms in a statistically significant manner. Limitations for ion irradiations include low overall dose, small depth of penetration, and charged ions will generate different damage cascades in comparison to uncharged neutrons. However, self-consistent ion irradiations could provide valuable insights into the fundamental mechanisms of irradiation creep.

This chapter will review both the neutron irradiation creep and ion irradiation creep experiments available in open literature. The background information will highlight the results of these experiments and analyze the major conclusions from the data. In depth discussion of the inconsistencies or gaps in understanding between these varied experiments will also be performed.

2.5.1 Neutron Irradiation Creep Experiments

Neutron irradiations have been performed on various FM steels of different compositions to support fast reactor programs in the past. The FM steels tested ranged from 12Cr FM steels such as HT9, different variants of 9Cr steels such as T91 and P91, and other reduced activation FM steels intended for fusion applications. This section will focus on both the macroscopic strain rates measured in those experiments, as well as the microstructure of the samples resulting from long term irradiation creep exposure.

T91 Irradiations in FFTF

The most comprehensive set of irradiation creep study available for T91 are those conducted by Toloczko et al [55], [56] in FFTF. Two types of pressure tubes were fabricated from two heats of T91. The bigger pressure tube has dimensions of 6.86mm OD x 5.76mm ID x 28.2mm with a wall thickness of 600μm. The smaller pressure tube has dimensions of 4.57mm OD x 4.17mm ID x 22.4mm with a wall thickness of 200μm. The tubes were pressurized with helium to various stresses and irradiated in FFTF at ~400°C, ~500°C, 550°C, and ~600°C at a dose rate of 0.8-1.7x10^{-6}dpa/s.

At 400°C, five different stress levels were tested for their irradiation creep behavior along with two stress free tubes to quantify the irradiation swelling behavior. Figure 2.20 shows the creep curves of T91 in FFTF at 400°C. No clear creep transient was observed in the 400°C condition. The dose dependence of creep strain is not linear due to the effects of stress enhanced swelling. The stress dependence of the creep rate is roughly linear at 400°C. The creep behavior at 500°C deviates from those of 400°C. A clear creep transient started to present itself at stresses above 100MPa at 500°C. At doses past the transient, the creep strain showed linear dose dependence as shown in Figure 2.21. The creep rate at 500°C for T91 retains its linear stress dependence for stress below 140MPa. The creep strain as a function of dose for 550°C condition is plotted in Figure 2.22. Data at 550°C was only available at three different stresses at three different doses. The lack of data made analysis on the linearity of dose and stress dependence difficult, but evidence suggest the stress dependence is slightly none-linear at 550°C. Large creep transients were also observed to develop at 550°C for stresses below 100MPa. At 600°C, the creep rates were observed to be higher than those of lower temperatures. Large creep transient

were once again observed at below 100MPa. Figure 2.23 shows the creep curve for 600°C for T91. The strain as a function of dose deviates from linearity at higher dose, but still retains its linear stress dependence.

This study provided the only in-reactor data for T91 across a wide temperature, stress, and dose range that are necessary for understanding the mechanisms behind irradiation creep behavior. Analyses of the creep strains suggest that creep rates generally have linear stress dependence, and very small temperature dependence. Figure 2.24 plots the strain rate data as a function of stress compared to thermal creep data for T91 under the same conditions. Irradiation clearly enhances the creep behavior of T91 compared to thermal conditions. However, the microstructure data for this study have not been extensively analyzed; therefore there is insufficient data to draw any conclusion on the underlying mechanisms responsible for irradiation creep in this study. In addition, there is not enough data at low dose to study the transient creep behavior that is observed in this study. A complementary study for T91 at low dose with sufficient microstructure analysis will be invaluable to explore the problem of irradiation creep mechanism.

HT9 and 9Cr1Mo Irradiated in FFTF and PFR

HT9 was one of the first FM steels to be used and tested in fast reactor environments that showed marked improvement in swelling resistant compared to austenitic steels. HT9 has been extensively studied in FFTF to quantify its irradiation creep resistance by Toloczko, and Garner et al. [11], [12], [55]–[57] The HT9 creep tubes were pressurized by helium up to 200MPa hoop stress. The irradiation temperature were kept between 375^{o}C to 750^{o}C in FFTF and the samples were irradiated up to maximum dose of ~200dpa. The pressure tubes were periodically discharged and their diameter strain was measured before reinsertion into the reactor.

In a study comparing HT9 and 9Cr1Mo to austenitic steel PCA provided a comprehensive analysis of the creep rates as a function of stress and dose.[12] Figure 2.25 plots the irradiation creep strain as a function of total fluence for austenitic PCA and FM steels HT9 and 9Cr1Mo with applied stress up to 200MPa. The creep strain found for HT9 and 9Cr1Mo are very similar, while the PCA are factors of 4-8 larger. This difference in creep rates can also be seen in the stress dependence of the irradiation creep strains plotted in Figure 2.26. From the stress dependence plots, it is also observed that the stress dependence of the creep strain increase

dramatically when temperature is above 550°C. The dramatic increase at higher temperatures could be evidence that thermal creep is significant above 550°C. Analysis of the creep compliance at 400°C showed PCA to have a compliance of $B=9.8x10^{-6}MPa^{-1}dpa^{-1}$, about factor of 5 greater than the compliance of $B=2.1x10^{-6}MPa^{-1}dpa^{-1}$ found for HT9. Analysis of the creep swelling coupling coefficient found that for both austenitic PCA and FM HT9, the coefficient D is found to be around $0.6x10^{-2}MPa^{-1}$. Based upon that observation, the crystalline structure is determined to be not very important in the creep-swelling relationship.

In a follow up study on the same experiment, Toloczko et al [11], [56] analyzed more carefully the irradiation creep stress dependence of HT9 and 9Cr1Mo by taking into account the stress free swelling data from both immersion density and TEM void counting. By looking at the swelling data, evidence of stress enhanced swelling was observed for HT9 but not for 9Cr1Mo as shown by Figure 2.27. By taking into account the swelling contributions, creep compliance B and creep-swelling coefficient D were calculated for 9Cr1Mo as $0.5x10^{-6}MPa^{-1}dpa^{-1}$ and $0.7\text{-}1.0x10^{-2}MPa^{-1}$ respectively. However, HT9 stress dependence was found to be closer to ~2 instead of linear as shown in Figure 2.28. This study confirmed the magnitude of creep compliance and stress swelling coefficient for FM steels under neutron irradiation. However, the greater than linear stress dependence of HT9 at high dose complicates mechanistic analysis since it contradicts majority of existing theoretically irradiation creep mechanisms.

The HT9 creep samples irradiated in FFTF were also compared to those irradiated in the Prototype Fast Reactor (PFR) in a joint US/UK creep study. [58] It was found that the swelling behavior of the stress free HT9 tubes showed very different behavior in the two reactor environments. The HT9 tube showed positive swelling in FFTF but negative swelling in the PFR irradiations. It is recognized that swelling is dependent upon irradiation history, but no further explanation is given for the discrepancy in swelling in the two reactors. It was also found that the creep compliance and creep swelling coefficient of the HT9 irradiated in PFR fell within the range of $B= 0.25\text{-}1.0x10^{-6}MPa^{-1}dpa^{-1}$ and $D=0.6x10^{-2}MPa^{-1}$. These values are typical of those found in previous irradiation creep studies on FM steels.

The in-reactor studies on HT9 showed that FM steels share similar creep rate in different reactor environments. The irradiation creep stress dependence for HT9 is between linear and quadratic, with minimum temperature dependence at below 550°C. The combination of stress free swelling, stress enhanced swelling, and irradiation creep complicates the analysis of in-

reactor studies. Therefore, a systematic study of the irradiation creep in the absence of swelling would be valuable to help narrow down the specific irradiation creep mechanism operating in FM steels.

MA957 Irradiated in FFTF

Irradiation creep and swelling study have been performed on an ODS alloy MA957 by Toloczko et al [59], [60] in FFTF. MA957 is a 14Cr ferritic steel with ~5nm yttrium oxide particles finely dispersed throughout its matrix. The stock rods of MA957 were formed from hot extruded powders followed by a combination of hot and cold working. Some of the stock rods were then swaged and annealed down to 5.84mm OD x 5.08mm ID x 6.73mm pressure tubes. The rest were drawn and annealed down to 6.86mm OD x 5.74mm ID x 28.1mm pressure tubes. The samples were irradiated in FFTF from 400°C – 600°C up to 110dpa for six different stress levels. The diameter of the pressure tubes were measured before and after each irradiation cycle using a scanning laser profilometer.

The irradiation creep rates were calculated for MA957 as a function of temperature and stress. The irradiation creep curve for every temperature and stress are plotted in Figure 2.29. At 400°C, the stress dependence was observed to be linear at stress below 121MPa. At 500°C, the stress dependence is linear only at stress below 87MPa. At higher temperatures, the large transient in primary creep makes it difficult to draw conclusions on creep rates with only two data points per each stress condition. The creep compliance was found to be between $5x10^{-7}$ $MPa^{-1}dpa^{-1}$ and $1.5x10^{-6}$ $MPa^{-1}dpa^{-1}$.

Microstructure analysis of the ODS alloy after irradiation creep showed that creep rate was not significantly affected by the size and density of dispersed oxides. Because of this lack of creep dependence on dislocation obstacles, the authors dismissed the traditional dislocation climb and glide as the dominating irradiation creep mechanism. [60] However, the ODS particles do improve the high temperature creep strength of the material. The improvement in creep strength at high temperature is reflected by the creep compliance in comparison to HT9 plotted in Figure 2.30.

This study provided the much needed data for in-reactor irradiation creep behavior for ODS alloys. The data set was sufficient to draw conclusions on the stress dependence, temperature dependence, and dose dependence of irradiation creep strain. However, the lack of

low dose transient data caused difficulty in drawing conclusions about the creep behavior at higher temperatures. In addition, although these experiments provided evidence against the conventional dislocation climb glide as the dominating mechanism for irradiation creep, there is still insufficient data to narrow down which mechanism is dominating.

12Cr-2W and 9Cr-2W Irradiated in FFTF/MOTA

Low activation ferritic steels of various chromium contents were irradiated in FFTF to provide materials database for fusion reactor design. The irradiation creep data of these samples were compiled by Kohyama et al [61], and compared to 316SS austenitic steels and 2.25Cr-1W bainitic steels. The samples were machined into pressure tubes that are 19.8mm in length, outer diameter of 3.57mm with a wall thickness of 0.25mm. The creep tubes were exposed to fast neutron flux in FFTF for a total exposure time of 300.4 equivalent full power days. The total dose accumulated varied between 25dpa ($5.8x10^{22}n/cm^2$) to 36dpa ($8.5x10^{22}n/cm^2$).

The analysis of the creep rates of the different steels found linear stress dependence at 430°C for all stress levels. At temperatures higher than 430°C, linear stress dependence was still observed at low stress regime, but switches to weakly quadratic stress dependence at stresses higher than 60MPa. The study claims that 9-12% Cr steels showed the best creep resistance, while the 7-8% Cr showed the worst creep resistance. However, given the uncertainty of ±0.04% strain in the calculated creep strains, only the experiments at 520°C showed significant difference between strain rates of steels at different Cr content. Similar to other neutron irradiation experiments, the strain rate was fitted to the empirical creep equation (Equation 2.2) with stress exponent of n=1.5. Creep compliance was found to be around $2x10^{-6}$dpa/s up to $1.5x10^{-6}$dpa/s at 600°C.

The author comments on the difficulty of establishing an in-reactor creep equation with functional dependence on all the variables for irradiation creep. Therefore, there is no mention of any irradiation creep mechanisms in this study. The difficulty arises from the lack of data available that is needed to separate out the combined deformation behaviors of irradiation creep, stress enhanced swelling, and thermal creep. To truly understand the irradiation creep mechanism by itself, creep experiments designed to avoid any swelling contribution and thermal creep contribution are needed.

F82H Irradiated in HFIR

Irradiation creep of reduced activation FM steel F82H have been irradiated in High Flux Isotope Reactor (HFIR) at 573 to 773K up to a dose of 5 dpa. Ando et al. [13] examined the irradiation creep strain of the samples from this experiment and calculated the creep compliance for each temperature and stress conditions. The F82H creep tubes were 21.85mm long with an inner diameter of 4.17mm with a wall thickness of 2mm. The tubes were pressurized with helium to achieve hoop stresses between 0-400MPa.The creep tubes were irradiated in HFIR for an accumulated 224 equivalent full power days, with a dose rate ranging from 2.17×10^{-7}dpa/s to 3.08×10^{-7}dpa/s. Stress free creep tubes were also irradiated in the reactor to monitor swelling in the material. The tube diameter was measured before and after irradiation by laser micrometer with a precision of ±250nm to obtain the diameter strain.

Irradiation creep strain appears to be linear at stress levels below 200MPa at 573K, but increase dramatically at higher stress levels. At 773K, creep strain is linear below 100MPa, but deviates from linearity at stresses above. The author explains this phenomenon as contribution from thermal creep; however, thermal creep strains for FM steels at these temperatures are orders of magnitude lower than irradiation creep. The paper does not offer any detailed calculation to explain how thermal creep combines with irradiation creep at lower temperatures. Instead, the creep rates are simply fitted to the empirical creep equation (Equation 2.2) with a stress exponent of n=1.5. Microstructure analysis was absent in this study, however the author claimed that the strain of F82H irradiated in HFIR at 573K, 400MPa and 5dpa is similar to FM steels irradiated in FFTF at 703K, 60MPa, and 60dpa. It is speculated that the microstructure of those two studies will be also be very similar based on the similar macroscopic strain. Based upon the anisotropic dislocation burgers vector found for the FFTF irradiation [62], the author mentions SIPA to be the irradiation creep mechanism that can explain the irradiation creep rate. However, in light of lack of microscopic analysis for this irradiation, a more rigorous study is needed to confirm that assertion.

316SS Irradiated in EBR-II

Irradiation of 316SS in EBR-II have yielded microstructure results that may be generalized to FM steels and shed light upon the underlying irradiation creep mechanism. Independent studies by both Brager et al [25] and Okamoto et al [7] both focused on the effect of

stress on the neutron irradiated 316SS pressure tubes from EBR-II. Although the results from austenitic steels are not readily comparable to those of FM steels, the exploration of stress effects on neutron irradiated microstructure has a direct implications on the mechanistic understanding of irradiation creep in general.

Thin walled pressure tubes made from 316SS were manufactured with a 5.84mm OD, 0.38mm wall thickness and 2.54cm in length. The tubes were irradiated in EBR-II at 500±20^{o}C to neutron fluence of 2.0-3.0x10^{22}n/cm^{2}. After irradiation, TEM samples were taken in the middle of the tube wall, and electrochemically polished in such a way that a primary axis of sample image is perpendicular to the hoop stress direction. The samples were imaged on the <110> zone axis with g=<111> direction to image the <111> loops. The dislocation loop density, dislocation loop size, void size, and void density as a function of the resolved stress are measured and calculated.

Many conclusions are drawn from this extensive analysis of the effect of stress on the microstructure of neutron irradiated 316SS. It was found that the application of stress on the cold-worked sample reduced the dislocation density to the level that are comparable to the annealed state. The application of the stress also enhanced the nucleation of voids and Frank loops. The Frank loop density is mainly a function of the resolved normal stress they were subjected to, while the void density is mainly a function of the applied hydrostatic force. The nucleation of voids were found to be sensitive to the starting microstructure while the nucleation of loops were not a function of the cold work. The dislocation loop size were found to be controlled by unfaulting of the loops by interaction with other microstructure components. Finally, the microstructure of voids and loops were found to evolve together, therefore swelling and irradiation creep for 316SS are directly related.

This study empirically confirmed the operation of stress enhanced dislocation loop nucleation and hinted at the possibility of stress enhanced dislocation loop growth. However, the interaction between void evolution and dislocation loop evolution that are found in 316SS is not directly applicable to FM steels. How the anisotropy of dislocation loops will evolve under stress in the absence of swelling is not immediately clear from this study. In addition, it is also not clear how the stress state for each dislocation loop family was accounted for due to the complex nature of biaxial loading in pressure tube samples. This study qualitatively provide evidence for SIPN and SIPA for 316SS, but the result can't be fully transferred to FM steels.

2.5.2 Ion Irradiation Creep Experiments

Many ion irradiations have been done on different steels under different conditions. This section will focus mainly on ion irradiations done on FM steels that are comparable to those of neutron irradiations. However, ion irradiations experiments on other materials will also be highlighted if the experimental setup or the results can be generalized to draw specific insights regarding irradiation creep mechanisms in FM steels.

Nickel Alloy and 321SS Accelerator Irradiation

One of the earlier attempts to study irradiation creep using proton irradiations was by Hudson et al. [14] The study used 4MeV protons generated by a Harwell Van der Graff Accelerator to cause irradiation damage in thin film specimen around 25 μm in thickness. The proton damage was calculated to create uniform damage in the sample at a dose rate of $1x10^{-7}$dpa/s. The temperature of the sample was continuously measured using an infrared pyrometer from 400ºC to 600ºC. The samples were loaded to a tensile stress of 20-250MPa using a special loading rig with an LVDT attachment to measure the total strain of the sample under irradiation.

Series of interrupted tests were done on the nickel alloy to explore the effect of irradiation on creep behavior. The experiment started with thermal creep testing followed by periods of irradiation and subsequently alternating periods of thermal creep and irradiation creep at varying damage rates. [14] The interrupted irradiation creep test confirmed that proton damage consistently enhance the creep rate and the enhancement exhibits a linear dependence on damage rate. However, the decrease in creep rate as a function of time was shown to be faster for the irradiated condition compared to the thermal condition. Therefore, it is possible that the thermal creep rate of the same alloy post irradiation would be lower than the thermal creep rate of an as received sample. The major concern for this study is the short time interval used for each irradiation. Each data point for this experiment is taken over a few hours at most, therefore the strain rates measured could be influenced by many other transient effects. The fact that each sample undergoes many different irradiation damage conditions, any systematic comparisons of irradiation conditions are difficult to conduct for these type of experiments.

Similar irradiation creep tests were conducted for 60% cold worked 321 stainless steel. The irradiations are conducted at 400°C-600°C, at $1.2x10^{-6}$dpa/s between 50-200MPa. The irradiation creep below 150MPa is a linear function of the applied stress. At higher stress, the creep rate deviates from linearity and shows power law stress dependence similar to thermal creep. Irradiation enhancement of creep rate was also observed at stress below 100MPa. The temperature dependence was found to be minimal below 520°C. The experiments conducted on 321 stainless steel also suffer the shortcoming of putting a single sample through multiple irradiation creep conditions in short intervals.

This experiment demonstrated the viability in conducting in-situ proton irradiations on loaded thin-film samples. It also illustrated the advantage of fast turnaround time possible in proton irradiations. With each irradiation condition only taking 3-5 hours, proton irradiation was able to obtain temperature, dose rate, and stress dependence of irradiation creep in a fraction of the time necessary for neutron irradiations. However, by choosing to change conditions on the same sample, it is difficult to draw conclusions from any microstructure analysis done on the samples.

DIN 1.4914 (MANET) Proton Irradiation

Proton irradiation creep experiments were conducted on DIN 1.4914 (MANET) by Jung et al [63] at Julich compact cyclotron with 6.2 MeV protons. DIN 1.4914 is a 12Cr martensitic alloy similar to HT9 in composition. The samples are thinned down to 50μm and bombarded with 6.2MeV protons at a damage rate of around $3x10^{-6}$dpa/s. The irradiations were done at 793K with a tensile stress of 50-200MPa. The strain and resistivity were analyzed during beam-off periods. The sample microstructures were then analyzed using energy dispersive X-ray analysis (EDX) and TEM after irradiation.

The strain and resistivity measurements have significant scatter, but qualitative behavior can be reproduced. Reduction in strain was found for stress below 50MPa, and that behavior was explained by precipitation and densification. The study also claimed that irradiation did not significantly enhance creep rates at stress above 200MPa. Resistivity changes observed under irradiation indicated precipitation and segregation in the material. TEM and EDX examination showed $M_{23}C_6$ type carbides around 0.5 μm in diameter, with niobium and vanadium precipitates

at around 0.3 μm. Smaller precipitates of around 20-150nm were also observed along the PAG boundaries, but were not able to be identified using EDX.

This study demonstrated the possibility of conducting proton irradiation creep experiments on thin film FM steels. However, the results of the experiments are highly quantitative. Lack of in-situ strain measurements also limited the major benefit of proton irradiations. Similar to the proton irradiations done by Hudson et al on nickel and 321 stainless steels [14], this experiment showcased the potential of in-depth analysis of irradiation creep mechanism by proton irradiation, but did not fully take advantage of the novel experimental method.

19Cr ODS and PM2000 Cyclotron Irradiation

Two ODS alloys were extensively studied by Chen et al. [64], [65] using α particles to cause irradiation damage. The two alloys tested are the industrially developed PM 2000, and an advanced 19Cr ODS developed by Kyoto University named K1. Both alloys were manufactured by mechanical alloying in a high energy mill with ODS power consolidation using hot compression. The steels were then hot and cold rolled with a final heat treatment to obtain a uniform Y_2O_3 particle distribution inside the matrix. The average grain size for PM2000 is around 1mm in diameter, the ODS particle size around 28±8nm with a density of $5.1x10^{20}/m^3$. In comparison, the K1 steel has much smaller grain size on the order of 200nms, and ODS particle of 2.1±0.5nm with density of $1.2x10^{24}m^{-3}$. The samples were cut by spark erosion along the rolling direction to 300μm thickness in a dog-bone shape, and then mechanically polished down to 100μm thickness using 2400 grit SiC paper.

In-situ irradiation creep experiments were conducted at the Compact Cyclotron of Forschungszentrum Juelich with 24MeV $^4He^{++}$ ions. The $^4He^{++}$ ions both cause irradiation damage at a dose rate about $4.4x10^{-6}$dpa/s, and He-implantation rate around 0.019 appm per second. The irradiation damage of the irradiation creep samples were calculated to about 0.75 dpa total. Strain of the samples were measured by a Linear Variable Displacement Transducer (LVDT).The samples were subjected to ion irradiation until strain rate becomes constant, and then a uniaxial stress is applied to the samples between 20-250MPa. Strains as a function of dose were recorded and the strain rates calculated from the measurements. The strain rates are fitted to

the empirical irradiation creep equation as shown by Equation 2.2. The creep compliance, B_o is also found and compared to other experiments in existing literature as shown in Figure 2.31.

The creep compliance can vary from $5x10^{-7}$ $MPa^{-1}dpa^{-1}$ to $2x10^{-5}$ $MPa^{-1}dpa^{-1}$. No clear temperature dependence on the creep compliance is observed.[64] Irradiation creep of 19Cr ODS has linear stress dependence up to 250MPa between 573 and 773K. Microstructure observations of the irradiated samples showed no major change in the ODS particle size and distribution after irradiation creep. Dislocation loops of $½a_o<111>$ and $a_o<100>$ are observed along with helium bubbles of 1.1±0.2 nm with a density of around $10^{23}m^{-3}$. Using inside and outside contrast technique, all dislocation loops are determined to be interstitial in nature. No difference in loop density and size were readily observed as a function of orientation, therefore the author dismisses the operation of SIPN and SIPA as the dominate irradiation creep mechanism.

The analysis of this set of experiment is complicated by the fact that there is simultaneous He implantation as well as irradiation damage operating at the same time. The presence of helium bubbles will greatly confound the effect of SIPN or SIPA, since it will affect the ratio of neutral and biased sinks within the material. In addition, each sample in this set of experiments are subjected to multiple loading conditions, so the final microstructure of the samples is the result of multiple transient conditions that could have erased any evidence of SIPN and SIPA that might exist. In addition, the fact that He is implanted in the sample ensures that irradiation damage caused by the He ions is not fully penetrating the sample. This makes it difficult to relate macroscopic strain rate to the irradiated microstructure since the irradiation damage changes dramatically across the thickness of the sample. The creep compliance and the general dislocation loop nature found in this experiment provide significant insight and confirmation of empirical data for irradiation creep of ODS FM alloys. However, more experiments and theoretical studies are needed to confirm the author's assertion regarding the operation of certain irradiation creep mechanisms.

F82H Cyclotron Irradiation

Irradiation creep experiment on F82H was conducted using a cyclotron accelerator at National Institute for Materials Science by Nagakawa et al [66]. Thin wires of 0.7mm diameter were manufactured from F82H through repetition of annealing at 780°C in vacuum and swaging

at room temperature followed by normalization at 940°C for 40 minutes, and tempering at 750°C for 1 hour. The wire is then electro-chemically polished down to 0.15mm diameter of 12mm in length in the center to define the gage section. The thin wire was attached to a grip and torque coil with a mirror reflecting a laser lens to an encoder. The samples were loaded through the torque coil by a magnet to induce large shear stress in the sample. The sample temperatures were controlled by shooting jets of helium at the sample, and measured by a K-type thermocouple as well as an infrared pyrometer monitoring near the gage length of the sample. The 17MeV proton beam generated by the cyclotron caused an average displacement rate of $2x10^{-7}$dpa/s with a total dose of 0.2dpa in the F82H samples.

The irradiation creep stress dependence in this study is also observed to be n=1.5. For stress under 30MPa, contraction was observed in the samples. This was attributed to the precipitation, defect clustering and solute segregation from the onset of irradiation. It was also speculated, that increase in elastic modulus at the surface of the specimen could also lead to the reduction of elastic strain under torsion. The strain rate measured in this study is also several factors larger when compared to neutron data on the same alloy irradiated at HFIR by Ando et al[13]. The large creep rate is explained to be the result of different defect production between proton cascade and neutron cascade. The author comments qualitatively on the possibility of SIPN and SIPA enabled climb and glide as the dominating irradiation creep mechanism in this study. However, no calculations or analysis were attempted to relate those mechanisms to the observed creep strain.

This study developed a novel experimental method for studying irradiation creep in FM steels and showed that proton irradiations are useful in reproducing stress dependence of FM steels that are found in neutron irradiations. However, using shear stress instead of tensile stress to load the sample makes it difficult to compare with other existing experiments. Furthermore, SIPN and SIPA mechanisms both rely on the change in interstitial bias based on the stress field, and there is currently no intuitive quantitative description of how an applied shear stress can change the interstitial bias of a material.

2.5.3 Summary

Despite the wealth of in-reactor and accelerator experiments that have been conducted on FM and similar steels in the past, there still exists a large gap between our fundamental understand of irradiation creep mechanisms and experimental observations. In order to bridge that gap in understanding, experiments specifically tailored to narrow down theoretical mechanisms are needed in addition to those that explore purely empirical relationships. With that motivation in mind, the existing data in literature falls short in the necessary data needed to quantitatively link specific creep mechanisms to the macroscopic and microscopic observations for a single alloy. Experiments that aim to bridge the gap in knowledge should have the following capabilities:

- Consistent alloy composition, heat treatment and geometry of the sample throughout entire experiment matrix.
- Ability to isolate the entire dose rate, temperature, and stress dependence of irradiation creep strain rate.
- Ability to isolate irradiation creep from other strain contributions mechanistically (swelling, growth, thermal creep) through experiments or calculation based upon known theory.
- Ability to capture transient microstructure features of irradiation creep samples to relate to the observed irradiation creep strains.

In light of the capabilities required for an experiment to adequately address irradiation creep in the framework of theoretical mechanisms, the advantage of accelerator based ion irradiations become immediately apparent. Accelerators can easily isolate temperature, dose rate, and stress conditions of an experiment as compared to in a reactor where the neutron flux and temperature is interlinked by virtue of the position of the sample in the core. In addition, ion irradiations do not generate helium through n-α reactions, thus mitigating the combined effects of swelling to those of irradiation creep. Lastly, the low activation and faster damage rate of ion irradiations will make it practical for post irradiation microstructure analysis to be done in a timely manner. These observations provide motivation for a comprehensive study on irradiation creep mechanisms by ion irradiations coupled with in depth microstructure analysis.

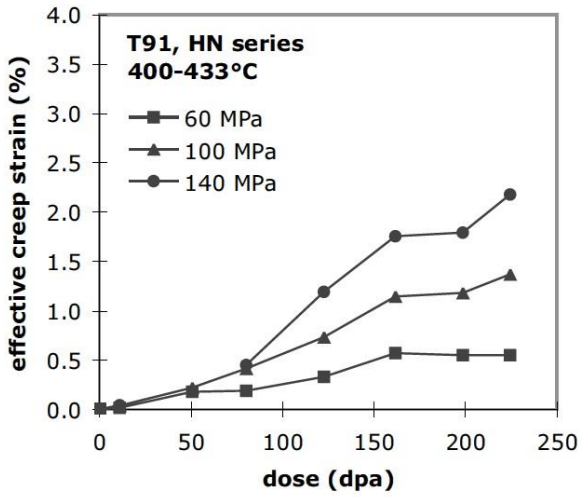

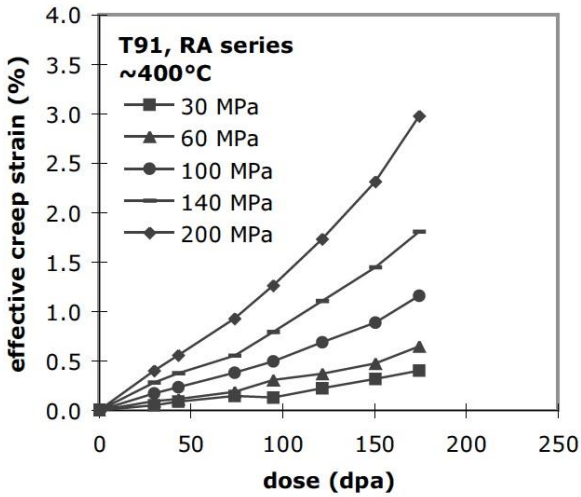

Figure 2.20 Irradiation creep curve of T91 at ~400°C in FFTF. [55]

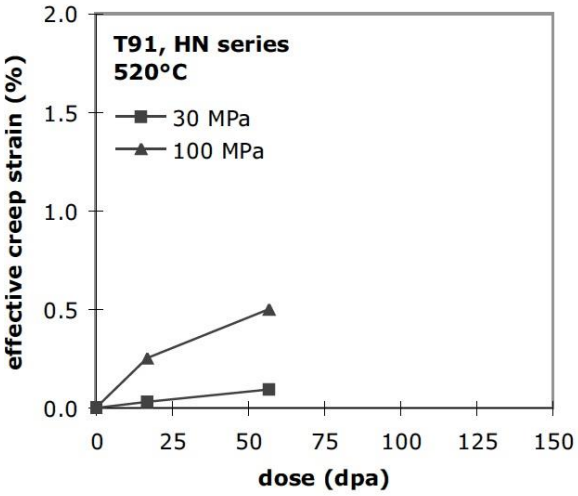

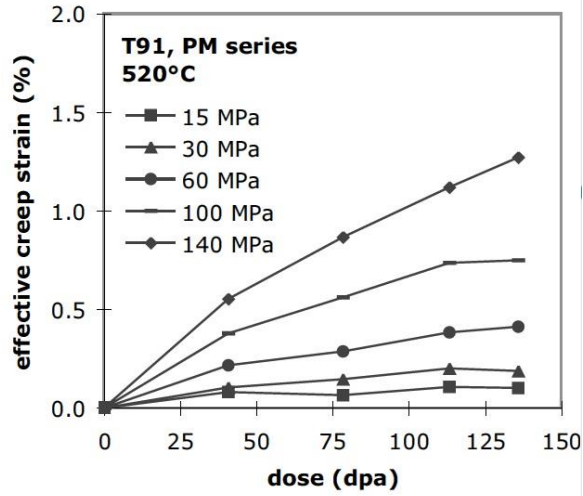

Figure 2.21 Irradiation creep curve of T91 at ~500°C in FFTF. [55]

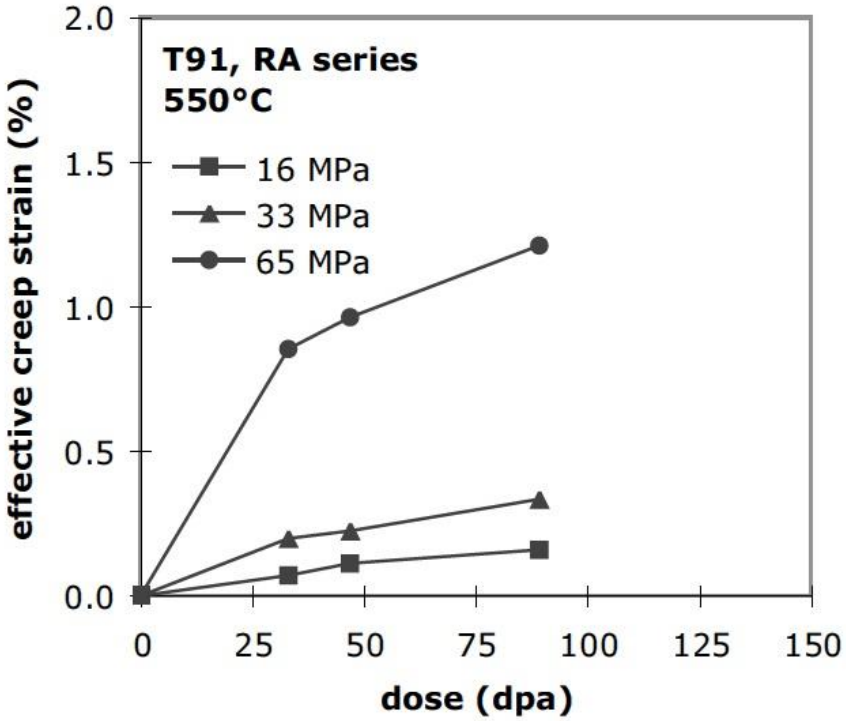

Figure 2.22 Irradiation creep curve of T91 at 550°C in FFTF. [55]

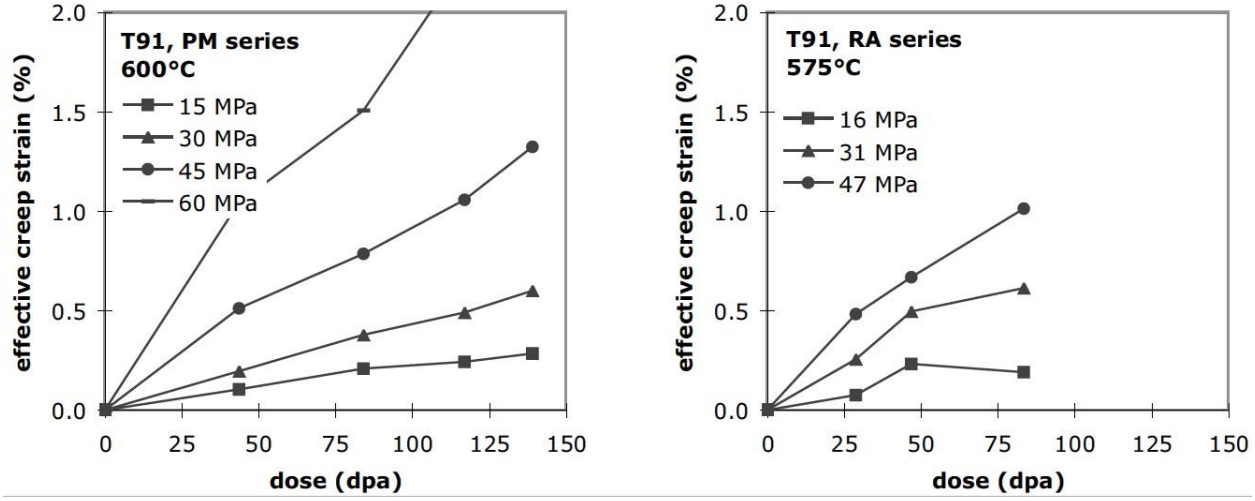

Figure 2.23 Irradiation creep curve of T91 at ~600°C in FFTF. [55]

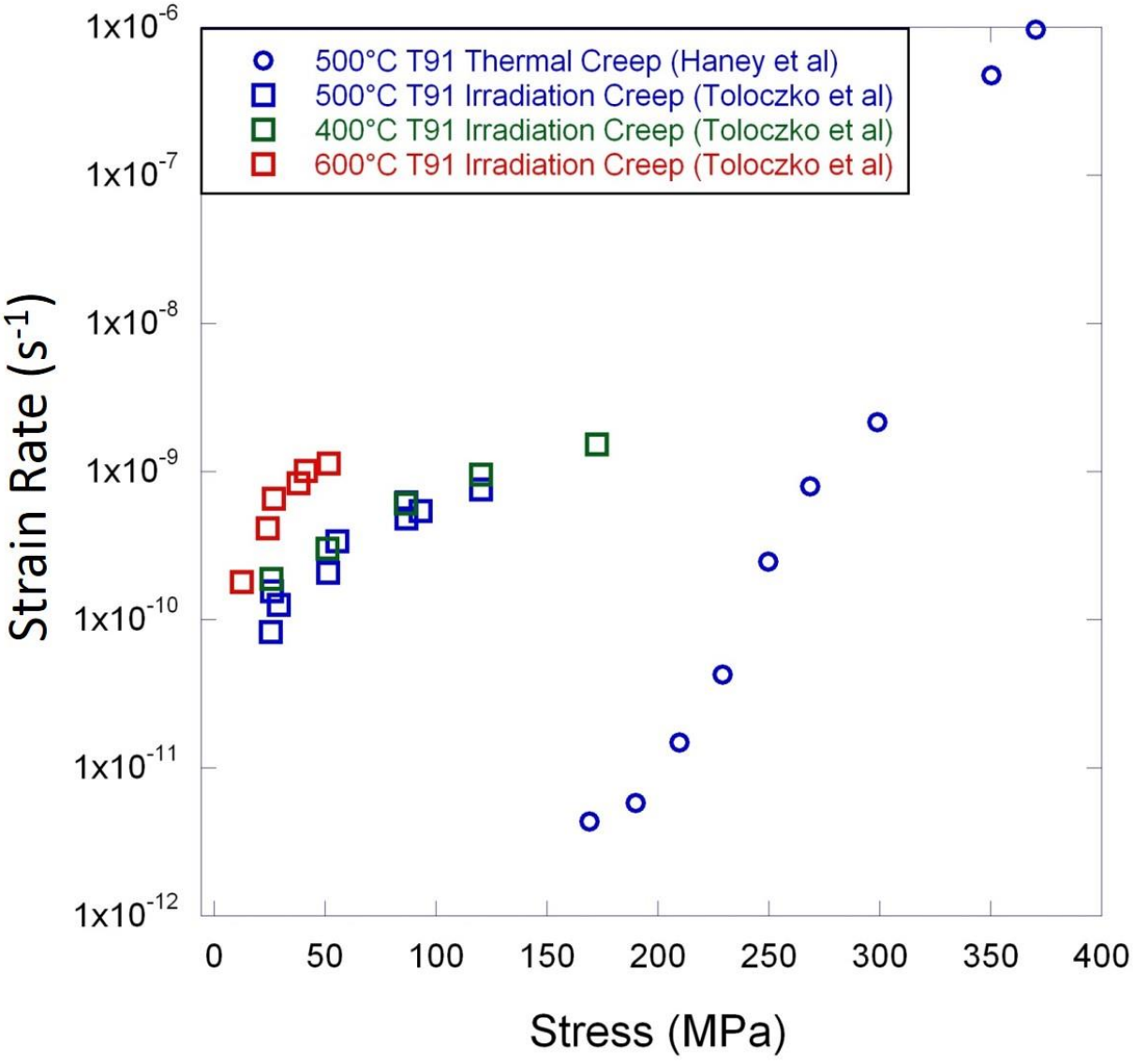

Figure 2.24 Irradiation creep rate and thermal creep rate behavior of T91 as a function of applied stress. [51], [55]

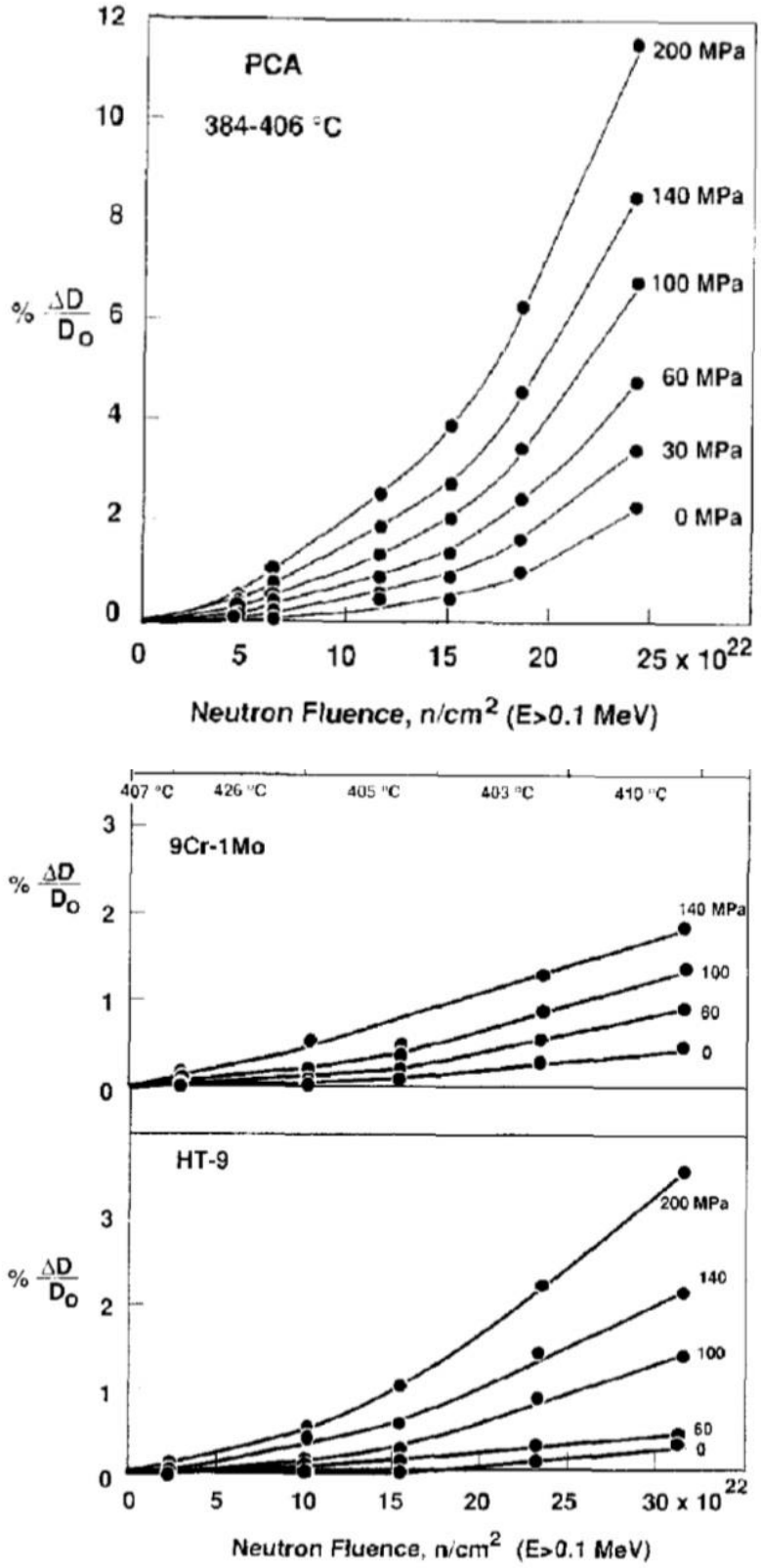

Figure 2.25 Irradiation creep strain of HT9, 9Cr1Mo, and PCA as a function of fluence. [12]

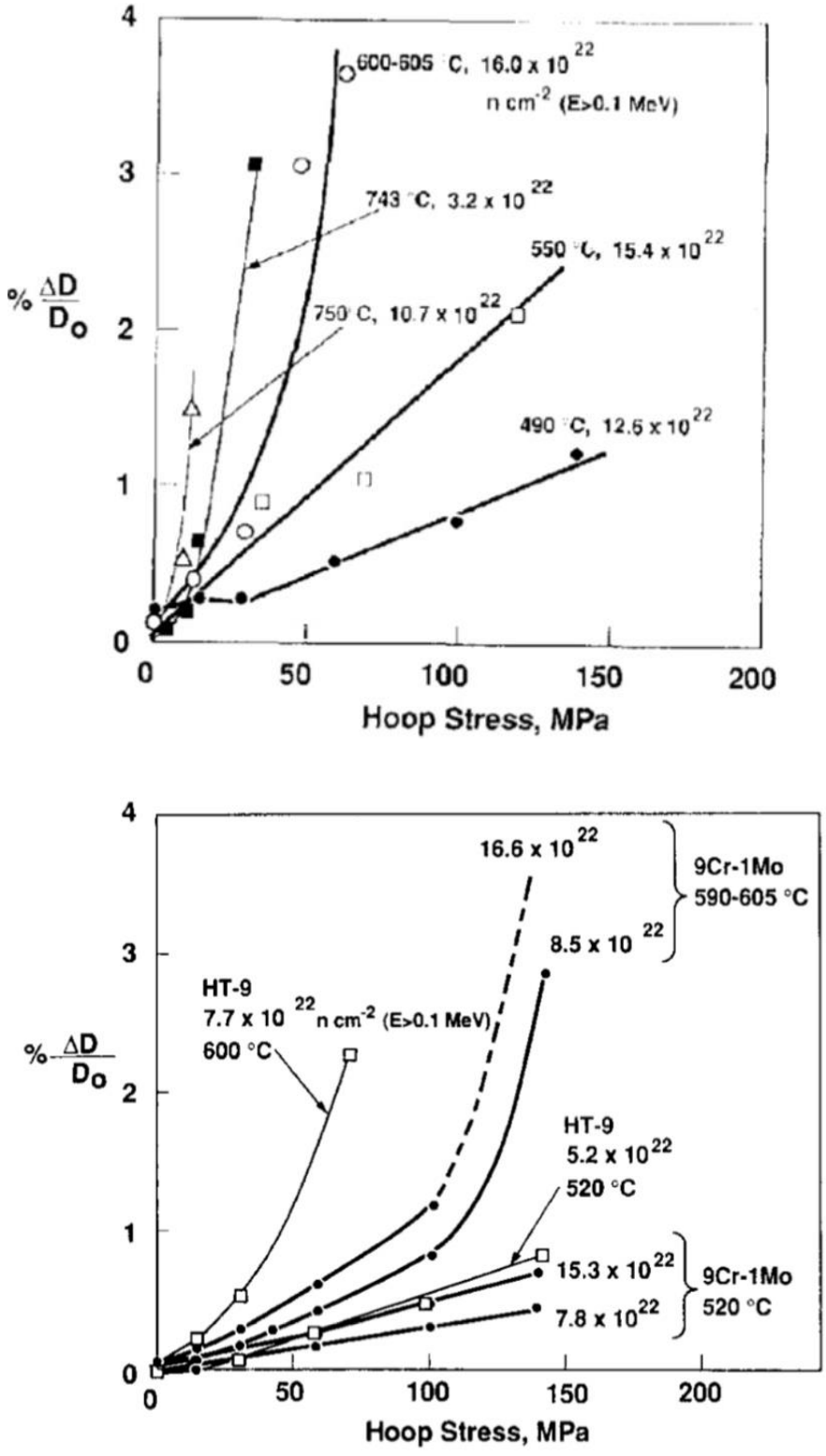

Figure 2.26 Irradiation creep stress dependence of HT9, 9Cr1Mo, and PCA irradiated in FFTF. [12]

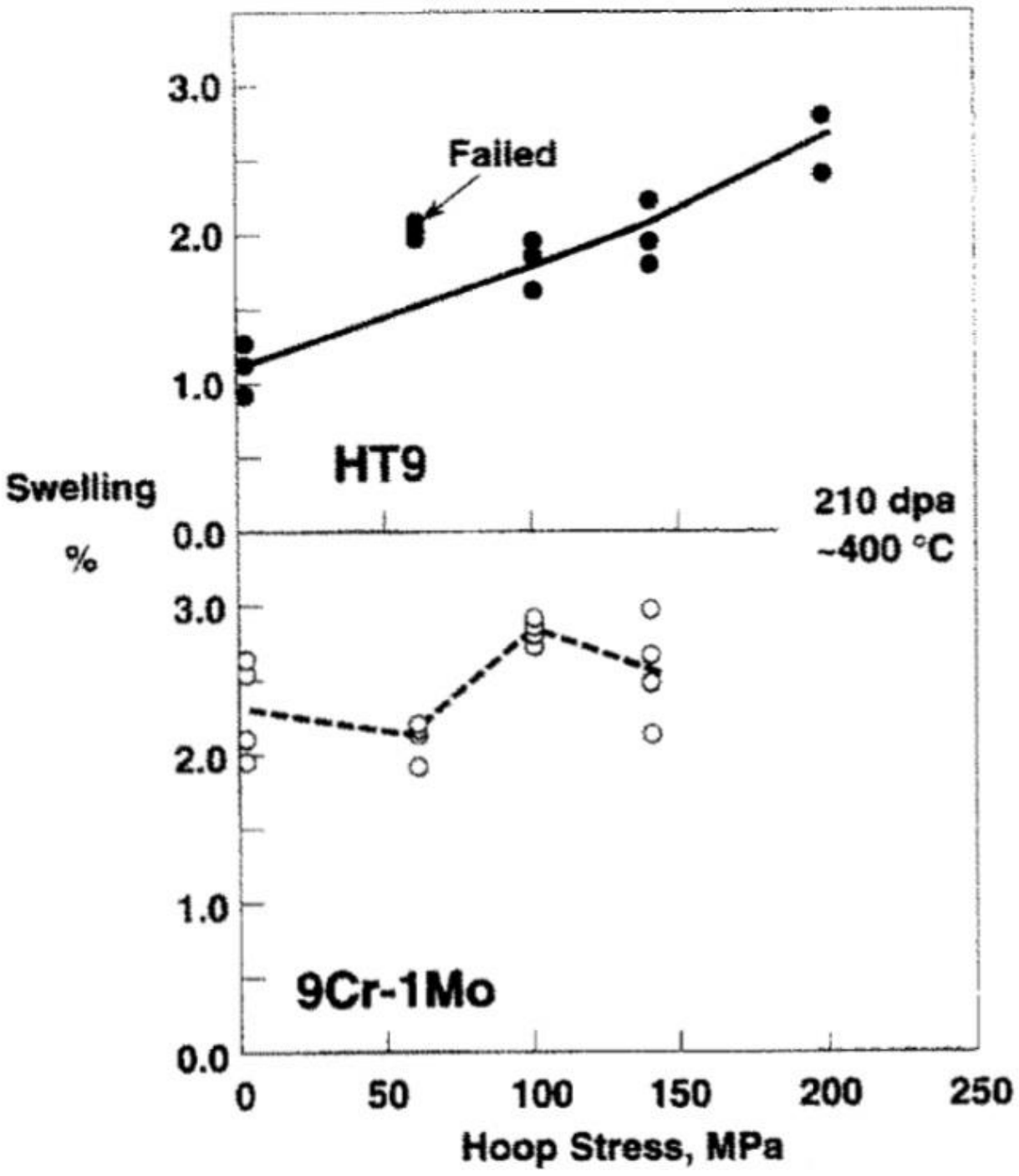

Figure 2.27 Irradiation swelling as a function of applied hoop stress for HT9 and 9Cr1Mo irradiated in FFTF. [56]

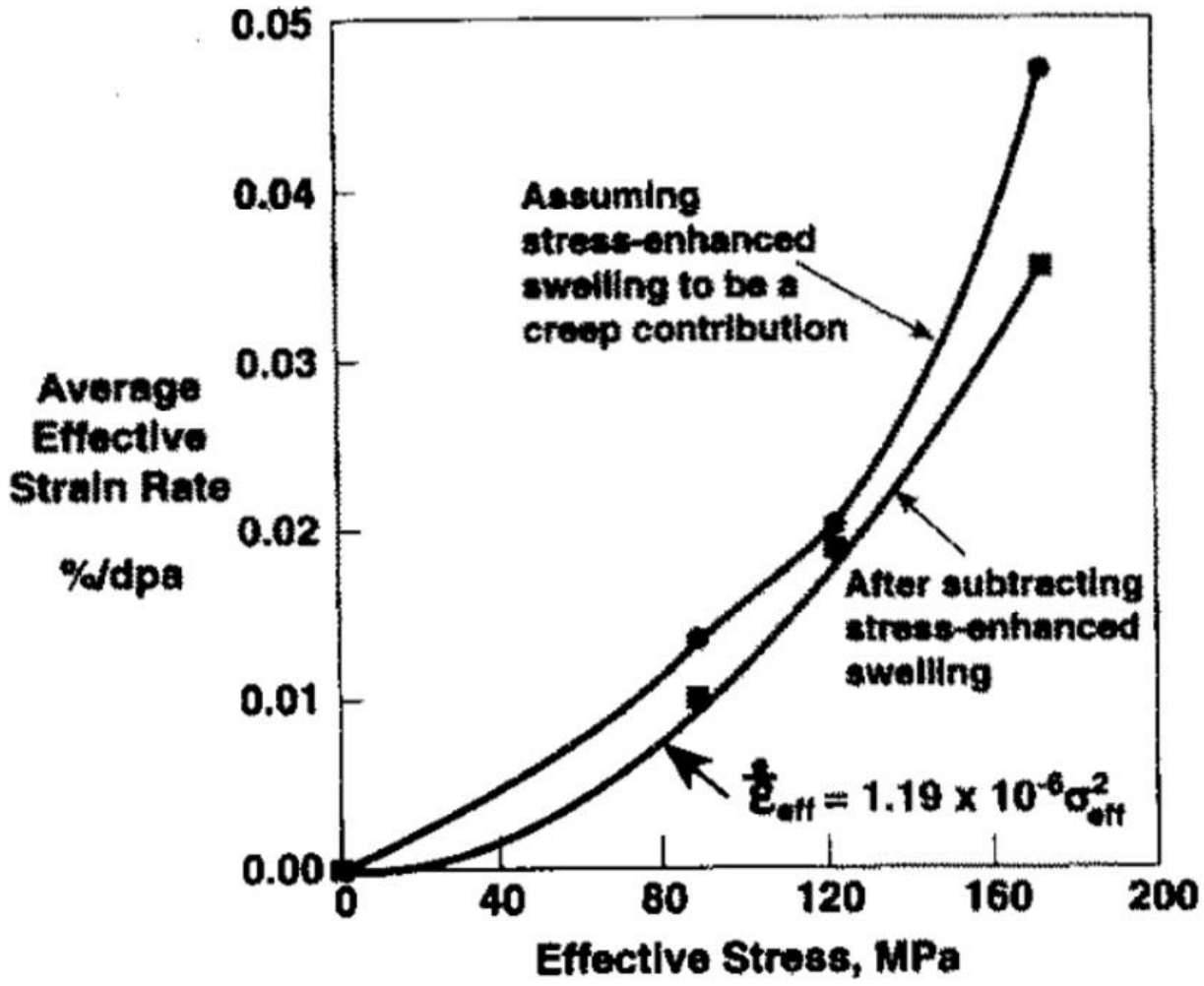

Figure 2.28 Irradiation creep stress dependence of HT9 after accounting for stress enhanced swelling. [56]

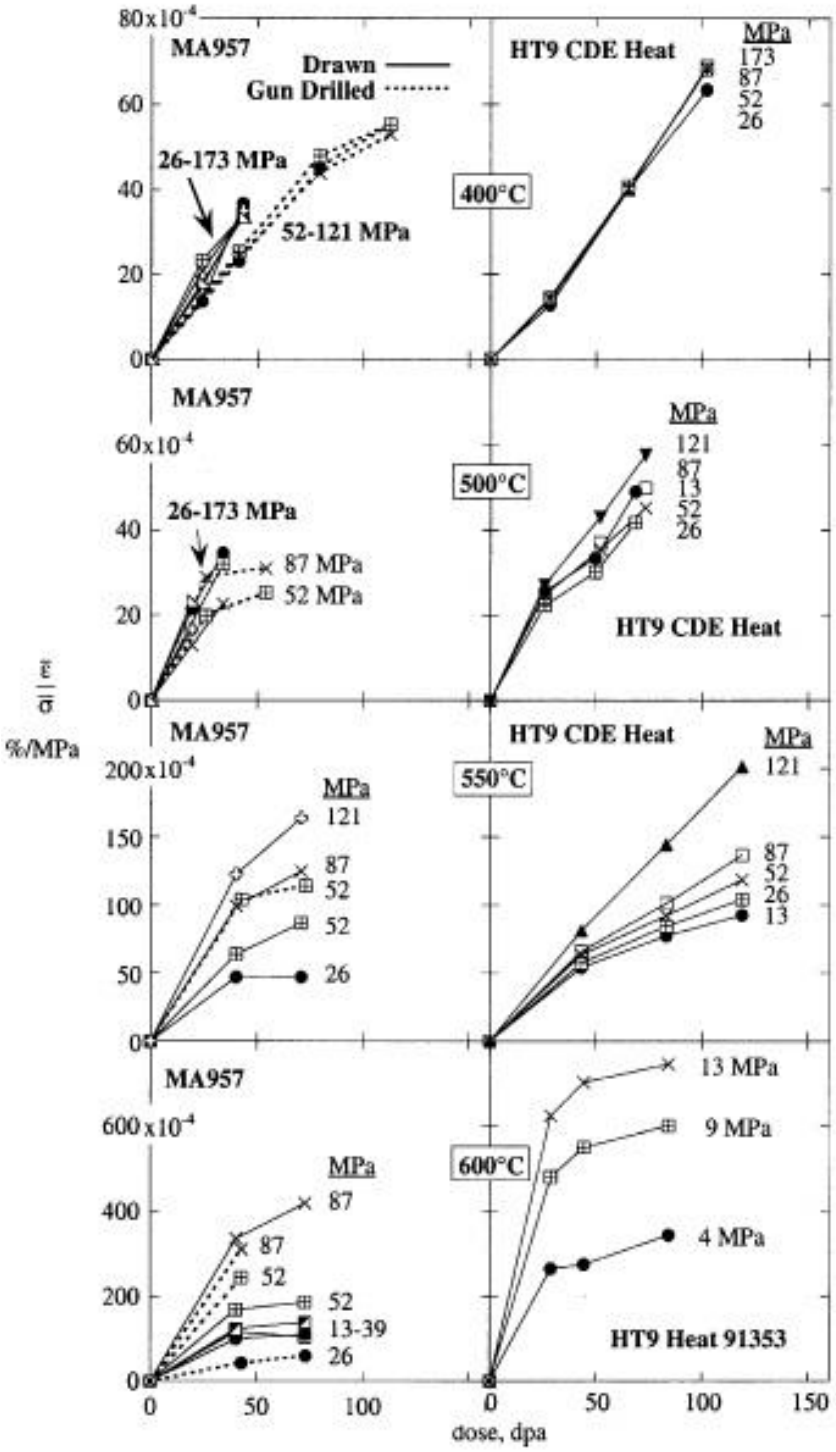

Figure 2.29 Biaxial stress-normalized creep as a function of dose observed in MA957 and HT9 during irradiation at 400-600°C. [59]

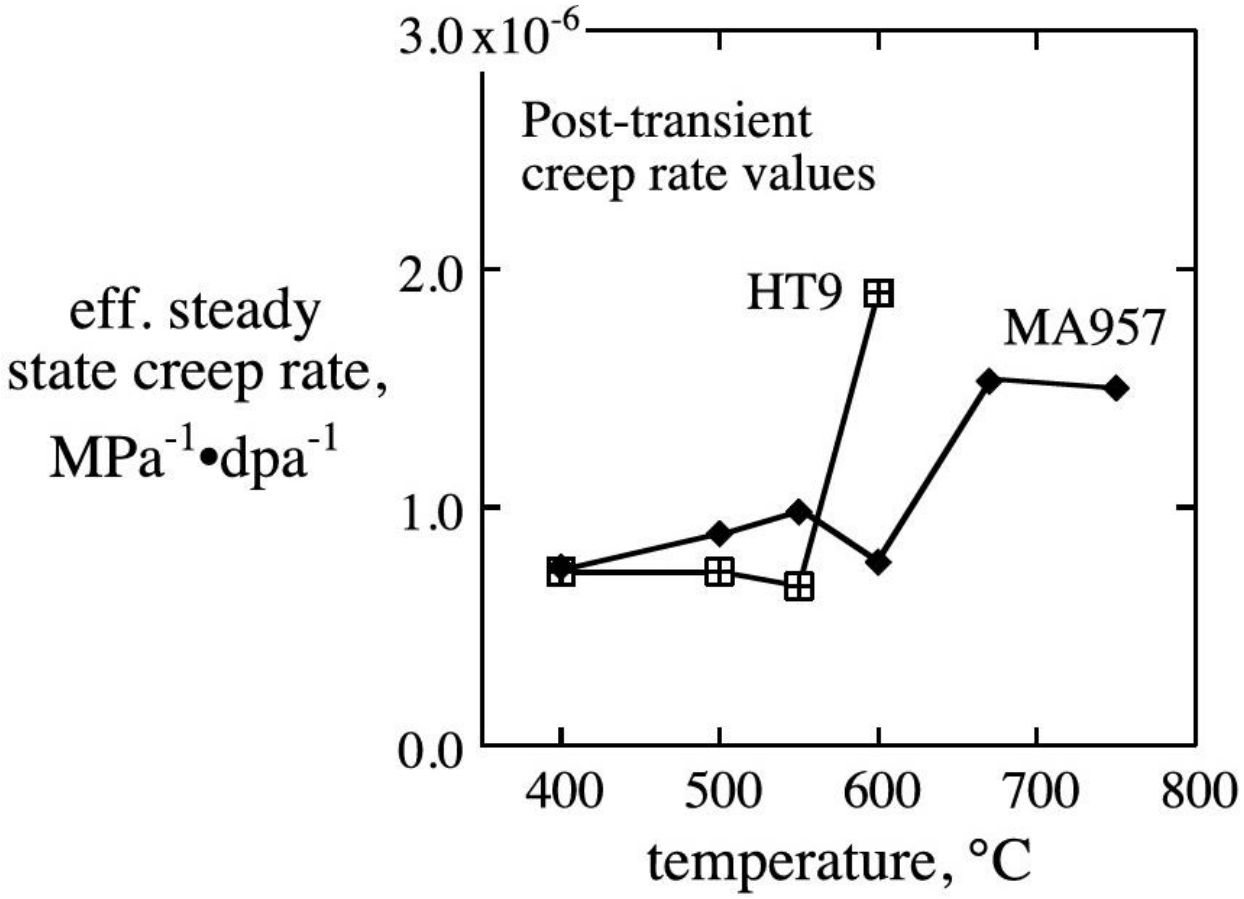

Figure 2.30 Steady state creep rate values of HT9 and MA957 as a function of irradiation temperature. [60]

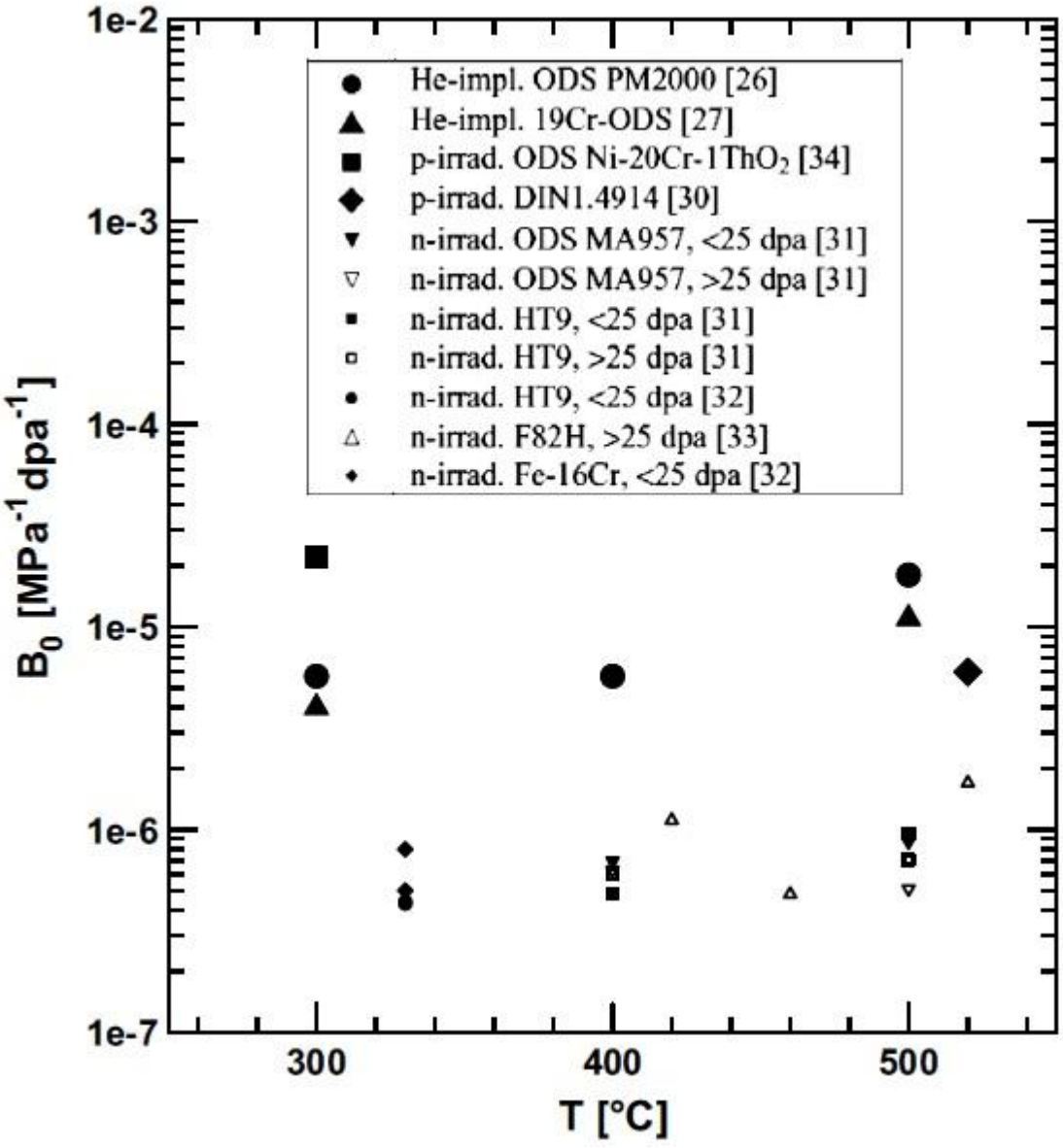

Figure 2.31 Irradiation creep compliance of FM and ODS steels under various conditions. [65]

CHAPTER 3 Objective

The objective of this thesis is to determine the mechanism of irradiation creep in ferritic-martensitic (FM) alloys. This will be accomplished by the combined efforts of newly developed experimental techniques and analysis methods to bridge the gap between empirically observed irradiation creep characteristics with those predicted by theoretical mechanisms. The results of the analysis will be used to judge whether observations are consistent with specific irradiation creep theories. This consistency will be assessed through the examination of macroscopic creep rate dependencies on experimental variables such as stress, dose rate, and temperature. In addition, microstructure data will be used to complement the strain rate analysis to provide empirical evidence demonstrating the dominance of specific irradiation creep mechanisms in FM alloys.

Due to the many possible mechanisms that have been proposed to explain irradiation creep in FM steels, this thesis will focus on identifying unique characteristics observed from experiments over a wide range of conditions to separate the potential mechanisms. In order to achieve measurable irradiation creep strain for all conditions, the first sub-objective is to design and test a brand new experimental setup that is capable of achieving the necessary experimental conditions for a mechanistic study.

Second sub-objective is to conduct consistent experiments to measure irradiation creep in FM alloys. The alloys will be irradiated with 3.2 MeV protons over a wide range of irradiation conditions. The experiments are designed to cover the temperature, stress and dose rate ranges that are applicable to fast reactor operations:

Temperature Dependence – Three experiments at 400^{o}C, 450^{o}C, and 500^{o}C for T91 to dose of 1dpa (FC), at a constant dose rate of $3.4x10^{-6}$dpa/s (FC) and stress of 160MPa.

Dose Rate Dependence – Three experimental conditions at $3x10^{-6}$dpa/s (FC), $3.4x10^{-6}$dpa/s (FC), and $5x10^{-6}$dpa/s (FC) for the same T91 sample at 500^{o}C and 160MPa.

Stress Dependence – Seven experimental conditions at ~15MPa, 100MPa, 120MPa, 140MPa, 160MPa, 180MPa and 200MPa irradiated for T91 at a constant dose rate of 3.4×10^{-6}dpa/s (FC) under 450^{o}C. All experiments were irradiated to a dose of 1dpa (FC) with exception of 100MPa condition that was irradiated to 2dpa (FC) due to low strain rate.

The third sub-objective is to develop reliable and consistent analysis methods for irradiation creep microstructure features specifically aimed at quantifying anisotropy as a function of applied stress. The results of the detailed microstructure analysis will provide quantifiable relationship between microstructure features and macroscopic strain under the paradigm of known irradiation creep theories.

Final sub-objective is to combine the strain rate measurements and microstructure data in comparison to those described by I-creep, SIPN, SIPA, PE, and PAG creep theories. Inconsistencies between observations and theoretical mechanisms will be highlighted to narrow down the possible dominating irradiation creep theories. The remaining theories that are found to be consistent with empirical observations will be considered, and developed into a comprehensive mechanistic picture of how irradiation creep occurs in FM alloys.

CHAPTER 4 Experimental

This chapter will describe in detail the experimental techniques and measurement methods used in this thesis. The chapter is organized into sections for each step in the experimental procedures: (1) alloys and sample preparation, (2) irradiation creep experiments, (3) irradiation creep strain rate analysis, (4) irradiation creep microstructure analysis.

4.1 Alloy and Sample Preparation

This thesis will focus mainly on the irradiation creep of FM steel T91. Due to the unique experimental setup designed for this thesis project, novel sample preparation techniques were also developed to meet experimental requirements. This section describes in depth the design criteria for irradiation creep samples, the rationalizations behind the sample design, and the method of sample manufacturing necessary to meet the requirements.

4.1.1 Alloy Composition and Processing

T91 is a modified 9Cr-1MoVNb martensitic alloy developed for its high temperature strength, and swelling resistance. The ingot used in this thesis project was developed by Bethlehem Lukens Plate Mill with heat number of #C2269 and plate number of #A9532. [67] The composition of the T91 heat is outlined in Table 4.1. The plate was heated up to 1066^{o}C for 46 minutes to fully normalize the microstructure into the austenite phase. The material was then air cooled down to room temperature to reach a fully martensitic phase. A tempering treatment at 790^{o}C for 42 minutes was used to recover ductility and promote carbide growth, followed by air cooling to room temperature to reach the final state. The end result was a plate of tempered martensitic steel with carefully controlled microstructure through heat treatment.

The tempered martensitic steel microstructure of T91 consists of prior austenite grain boundaries (PAG) that were around 10 μm in size and martensite lathes around 0.5 μm in width

and 5 μm in length. Metallography of the T91 as-received samples were done using Villella's reagent with 1 gram picric acid, 5ml of hydrochloric acid, and 100ml of ethanol at room temperature for 30 seconds. [68] Figure 4.1 shows the T91 as received condition etched with Villella's reagent imaged in scanning electron microscope (SEM). The martensite lathes were clearly visible in the etched condition as well as the PAG boundaries. The microstructure features were more prominently shown in bright field transmission electron microscope (TEM) image as shown in Figure 4.2. The PAG boundaries and lathes were once again clearly visible as well as the carbides on the grain boundaries.

Following the heat treatments, the alloys were machined to size by electrical discharge machining (EDM). EDM was chosen as the method of machining for two reasons. First, it cut the material using high frequency sparks applied across a 10 μm copper wire without introducing cold work. Second, due to the thin copper wire used, EDM was capable of cutting materials evenly to a thickness of 100 μm. These two requirements were necessary to achieve the necessary sample geometry shown in Figure 4.3.

The sample geometry was selected in consideration of the complicated stress and temperature state of the material under irradiation. For accurate strain rate measurements, it was imperative that the sample had a clearly defined gage length that will have even temperature and proton flux distribution. Therefore, the sample gage length had to be wide enough to make sufficient contact with the heat sink, and long enough to ensure the entire irradiated area had a constant cross sectional area. The final dimension of 8mm x 3mm rectangular gage length was chosen. In order to ensure that majority of the strain measured will be in the irradiated region, and the sample did not fracture outside of the gage length, a dog-bone shaped sample geometry was chosen. Mechanical FEM analysis using Solidworks ® was conducted to ensure that no significant stress concentration will occur in the sample under uniaxial load of 200MPa. The FEM results are shown in Figure 4.4.

4.1.2 Sample Preparation

The irradiation creep experiments required a sample that was less than 35μm in thickness to ensure full proton penetration through the entire sample in order to avoid hydrogen implantation and achieve constant dose rate during irradiation. A series of polishing steps were

required to take the 100µm thick sample after EDM, and reduced it down to a final 35µm sample thickness in the gage length.

EDM machining typically left a 10-15µm thick damage layer on the sample surface due to the high temperature spark used in the process. However, due to the delicacy of the thin samples, mechanical polishing was not recommended to remove the EDM layer. Instead, a series of electropolishing steps were used with different polishing rigs to control the final thickness of the sample.

During electroplishing, the samples were immersed in a bath of 500mL of 90% methanol and 10% perchloric acid solution in a 6 inch diameter beaker. The beaker itself was submerged in a bath of dry ice to maintain a nominal temperature of -40^{o}C. Inside the beaker, a magnetic stirrer bead rotating at ~650rpm was used to create circular flow inside the solution. The sample itself was clamped in a specially machined polishing rig made from PVC plastic, with a polishing window to limit the area of exposure as shown in Figure 4.5. A platinum cathode mesh was made to surround the openings of the rig to ensure even polishing from both sides. An anode made from 1mm stainless sheet metal was inserted into the rig to make electrical contact with the sample. Both the anode and cathode were connected to the electropolishing machine with an applied potential of 20V as verified by a digital multi-meter. As the potential was applied, electrical current caused removal of atoms from the anode to the cathode at a fixed rate. The rate of removal was dependent upon the voltage applied, rate of agitation, and alloy composition. For T91 used in this project, the rate of removal was experimentally determined to be around 20µm on both sides per minute as shown in Figure 4.6.

To remove the EDM layer, the largest window rig was first used to expose majority of the sample to the cathode. The rig was lowered into the solution at and polished for 1 minute to remove around 20µm from each surface to reduce the entire sample thickness down to around 60µm. The sample was then immediately cleaned off in acetone, methanol, and ethyl alcohol to remove any residual perchloric acid to avoid corrosion. The sample thickness was then verified using a micrometer before being put back into the rig with a smaller window to polish only the gage length. The rig was once again lowered into the polishing solution for around 30 seconds to reach thickness of around 40µm. After cleaning and measuring with the micrometer of the sample thickness, a final polish of around 5-10 seconds achieved the target thickness of 35µm

for the sample. The final sample were cleaned in acetone, methanol, and sonic jet cleaned in ethyl alcohol for 5 minutes and stored in plastic membrane box after air drying.

The accuracy of the sample thickness using this sample preparation method was verified by SEM imaging. Cross section of a T91 dummy samples that were electropolished down to 15μm as measured by micrometer were imaged under SEM, as shown in Figure 4.7. The SEM images showed the sample preparation method could achieve a sample thickness with error of around ±2μm.

Table 4.1 Composition of T91 as provided by manufacturer [67]

	Cr	Mo	Mn	Si	V	Ni	Cu
Wt%	8.37	0.9	0.45	0.28	0.22	0.21	0.17
At%	8.89	0.52	0.45	0.55	0.23	0.20	0.15
	C	Nb	Al	N	P	S	Fe
Wt%	0.1	0.076	0.022	0.048	0.009	0.003	Bal
At%	0.05	0.045	0.045	0.189	0.016	0.005	Bal

a)

b)

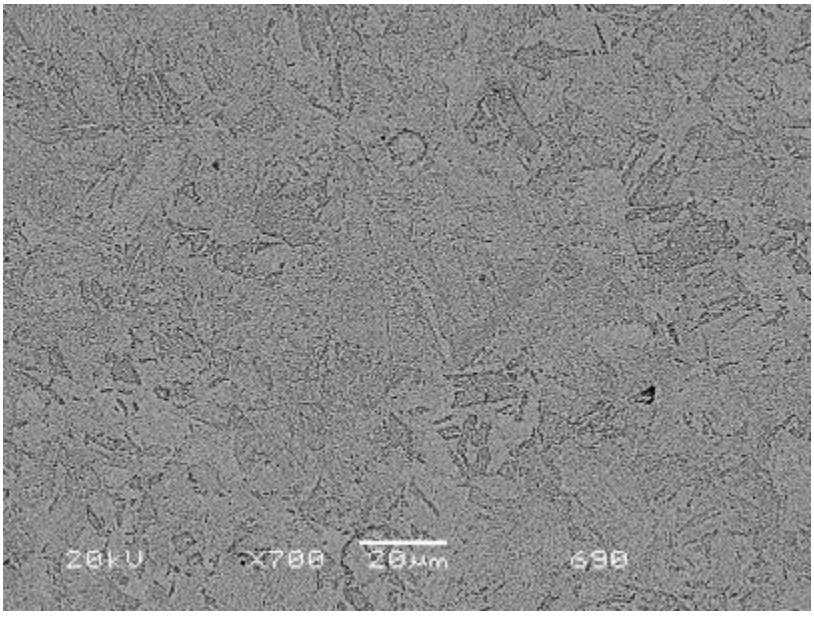

Figure 4.1 T91 as received condition etched by Villella's Reagent seen under SEM a) EBSD mode and b) SE mode.

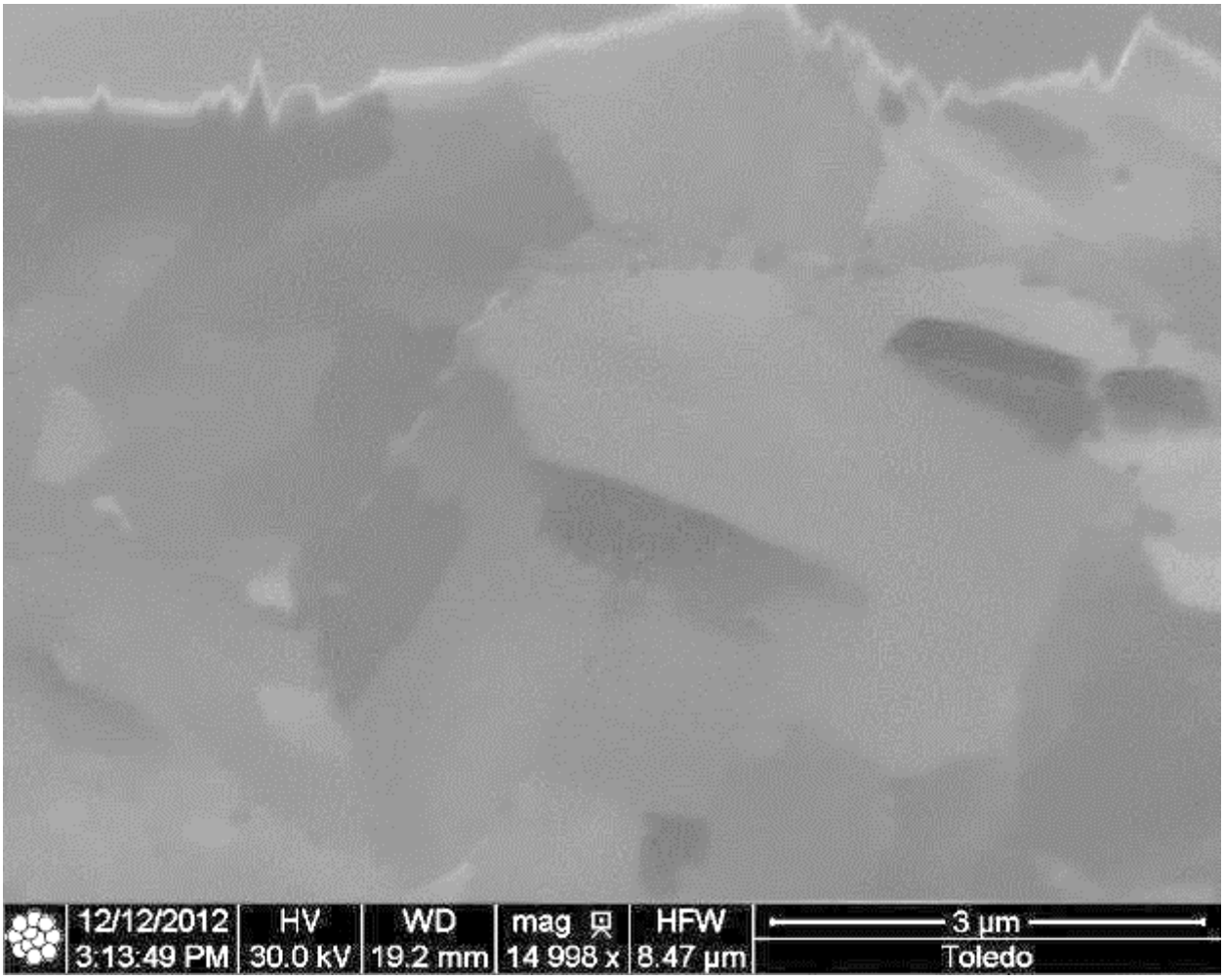

Figure 4.2 T91 irradiation creep sample after Focused Ion Beam (FIB) machining and imaged using heavy ions.

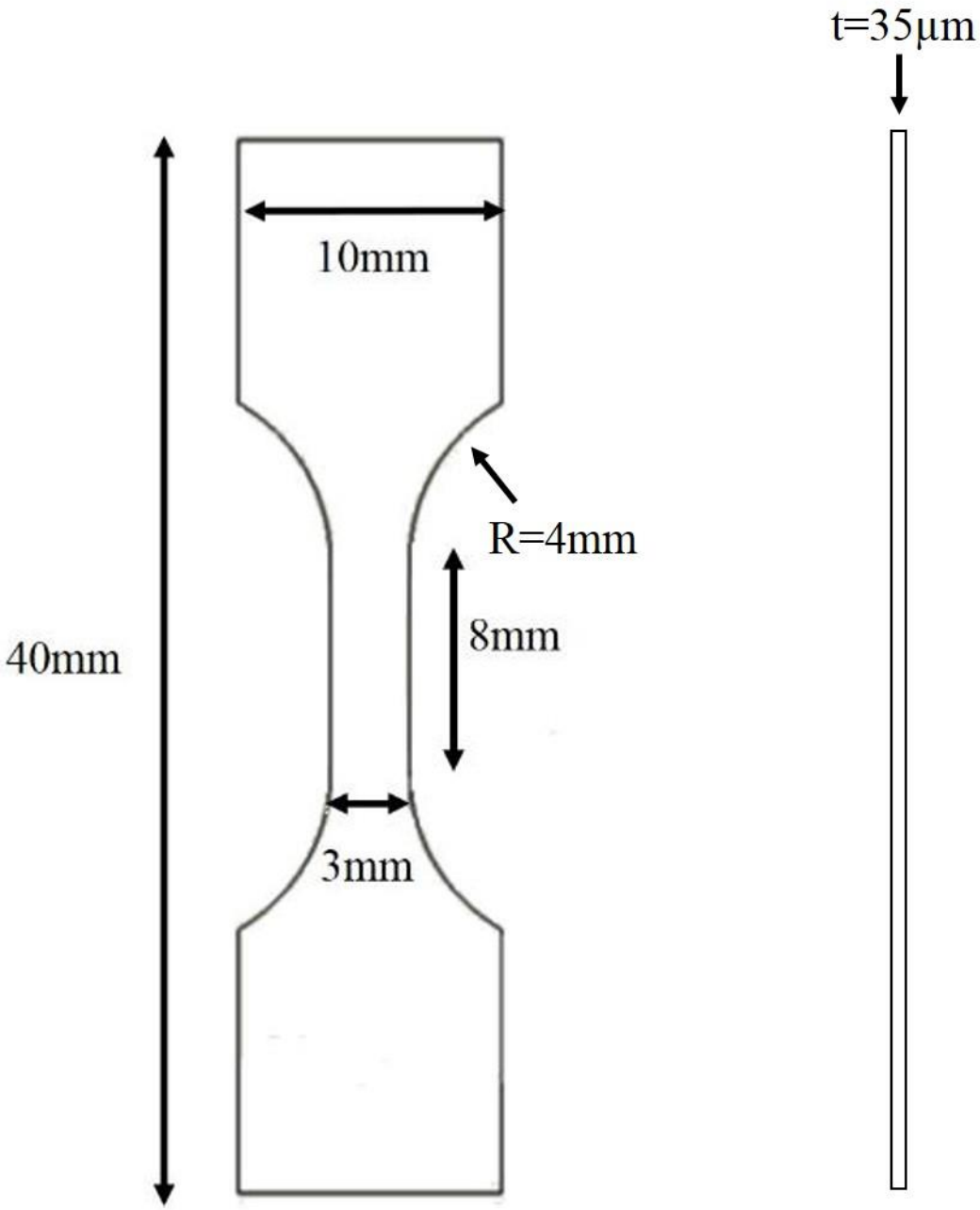

Figure 4.3 T91 dog-bone sample dimension after Electro-Discharge Machining (EDM).

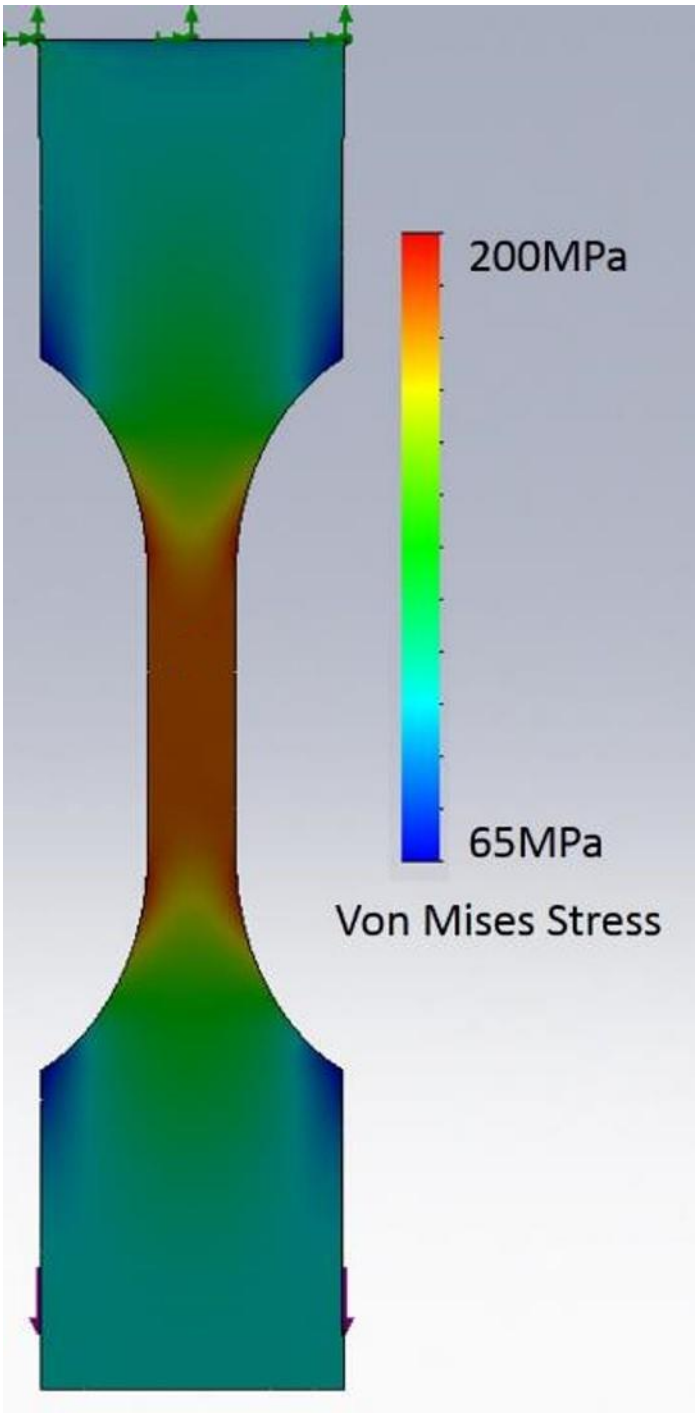

Figure 4.4 T91 dog-bone sample under 200MPa simulated loading analyzed using Solidworks®. Stress distributions within the sample under uniaxial load are shown as different colors.

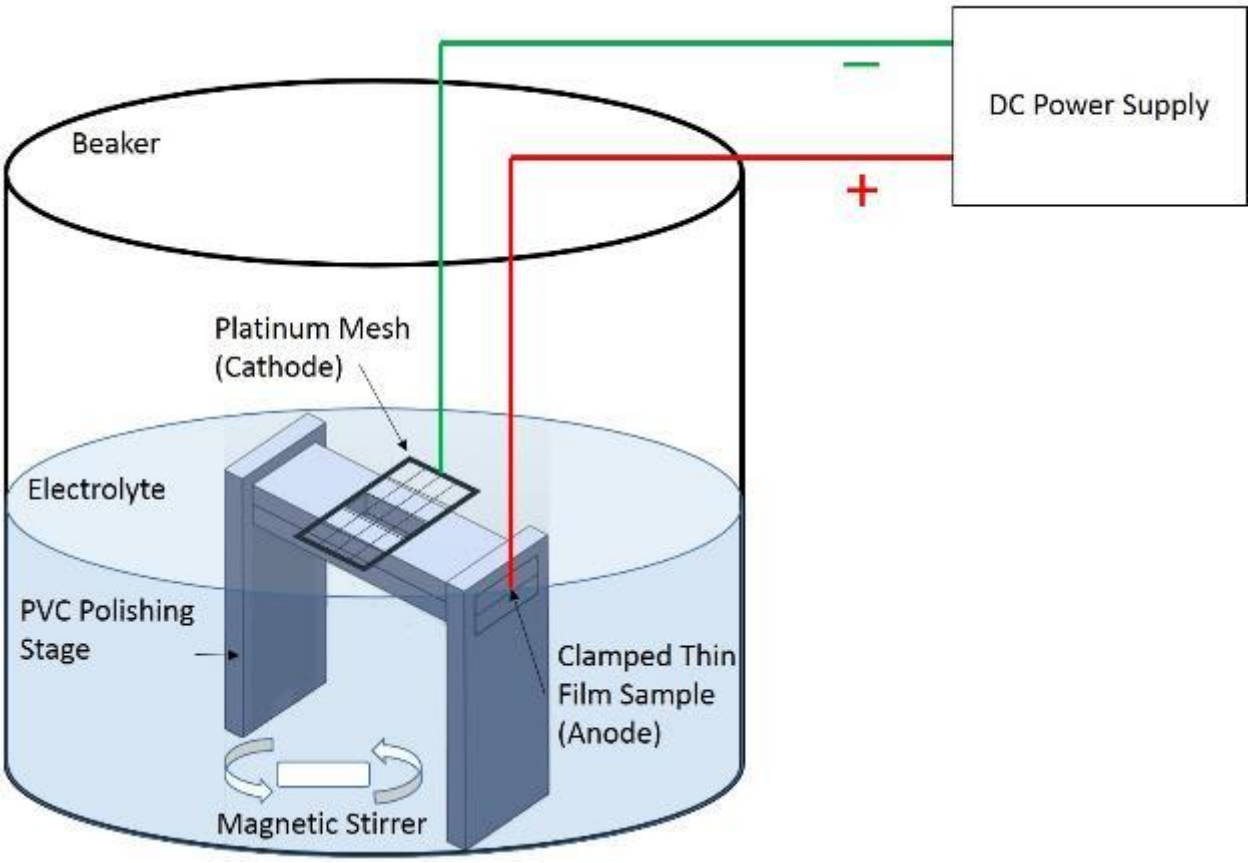

Figure 4.5 Electropolishing setup used to reduce 100µm EDM T91 samples down to 35µm final thickness.

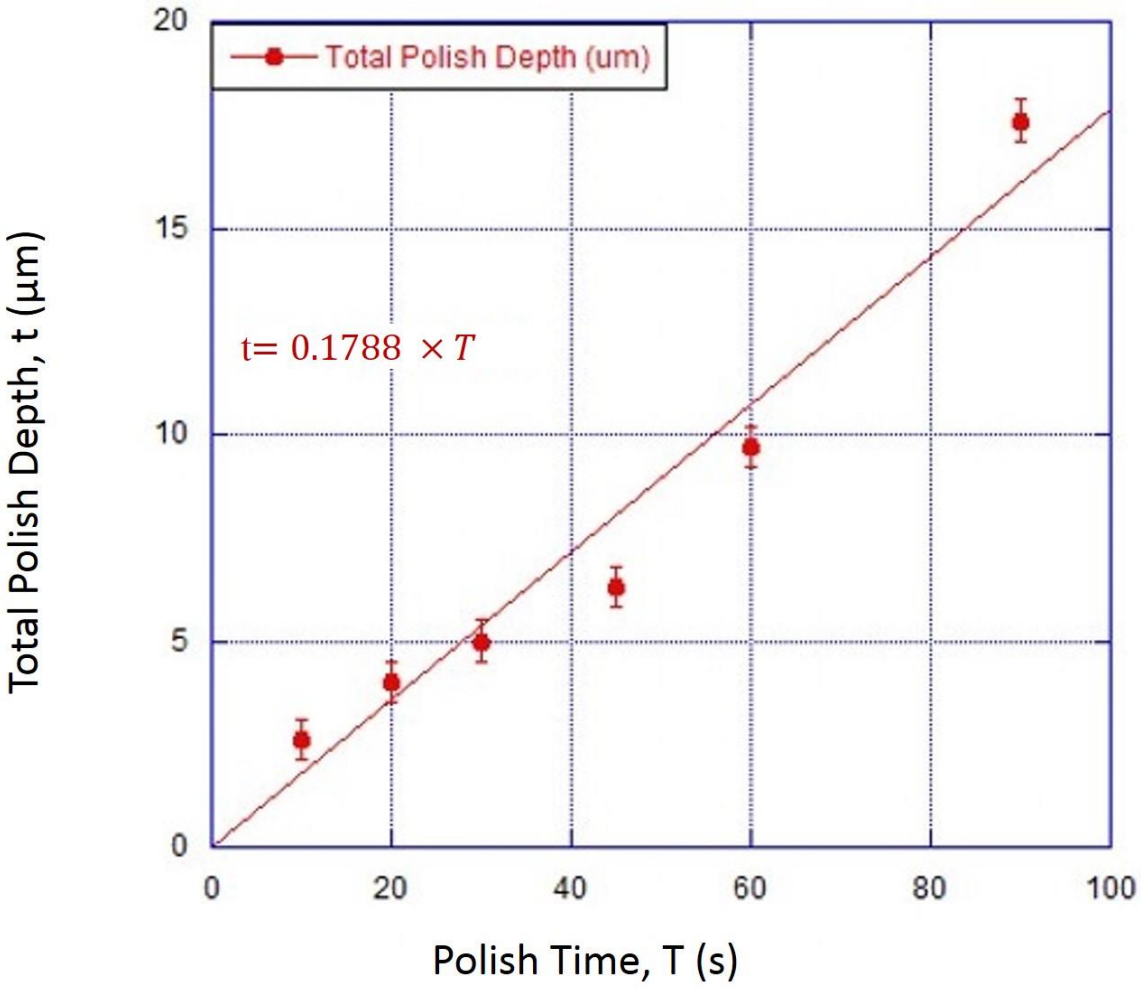

Figure 4.6 Electropolishing rate as a function of time for T91 at -40°C and 20V. The reduction in thickness is measured by contact profilometry on one side of the sample.

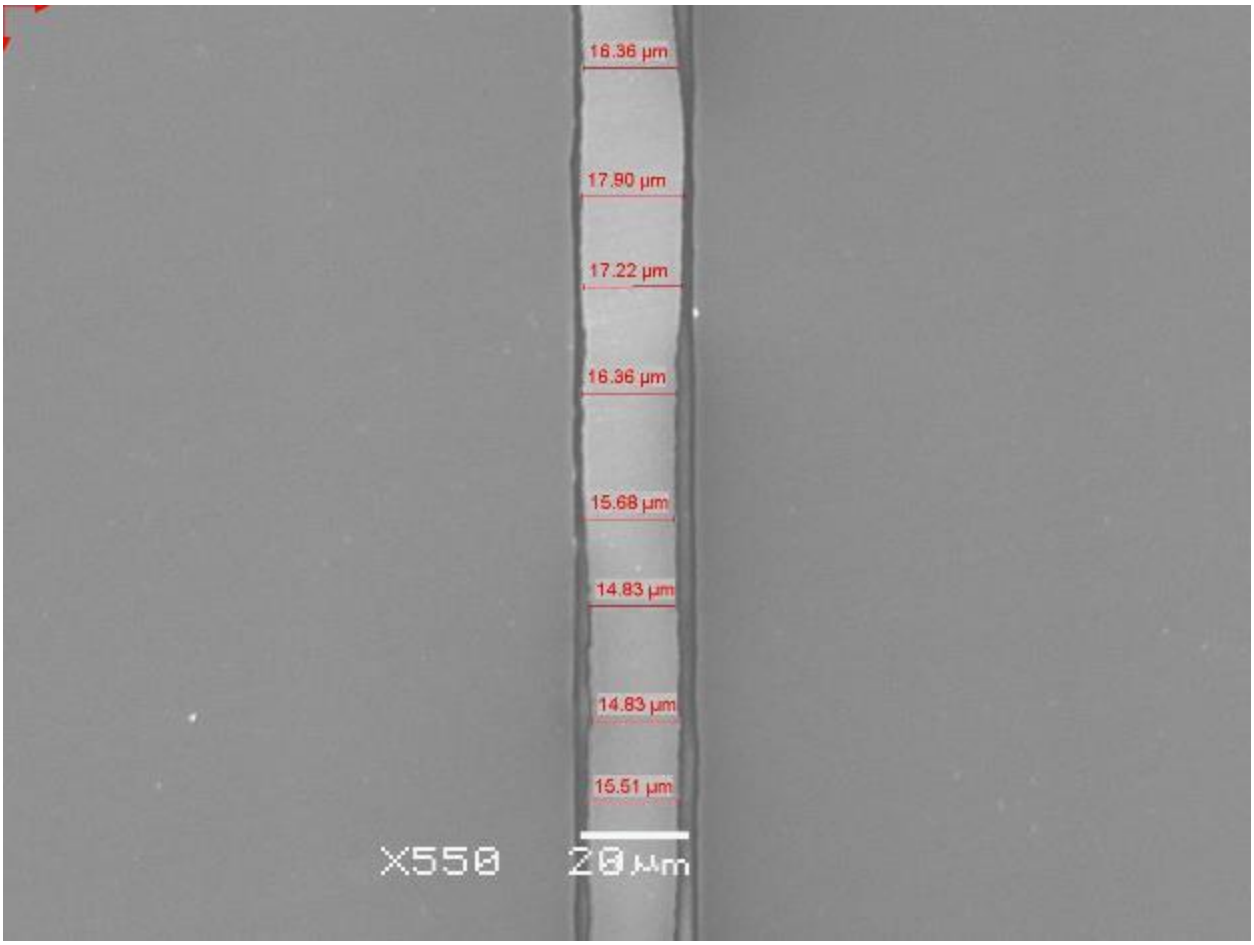

Figure 4.7 SEM image of electropolished dummy sample with target thickness of 15µm. The thickness variation is on the order of ± 2µm.

4.2 Irradiation Creep Experiments

This section explains the unique experimental setup utilized to conduct irradiation creep experiments using the General Ionex Tandetron accelerator in the Michigan Ion Beam Laboratory. There were many special considerations that were required for a successful irradiation creep experiment. Many significant changes and design decisions were made over this project to achieve the capabilities necessary for irradiation creep. This section will delve into each component of the experimental setup, including the irradiation beam line, irradiation chamber, irradiation stage, temperature monitoring, dose rate monitoring, stress monitoring, strain monitoring, and the procedure for setting up the experiment.

4.2.1 Irradiation Beam Line

The General Ionex Tandetron at Michigan Ion Beam Laboratory (MIBL) is a tandem accelerator that is capable of generating 3.4MeV protons for irradiation damage. The protons were generated by passing hydrogen gas through high voltages to create hydrogen plasma in the Torvis source. The negatively charged hydrogen ions were then accelerated out of the source through an extractor, bent with a magnet, and enters the tandem chamber. Inside the tandem chamber houses a high voltage generator column capable of providing 1.7MV of positive voltage. As the hydrogen ions were accelerated to 1.7MV in the center of the tandem chamber, their electrons were stripped off by nitrogen gas and turns into positively charged protons. These positively charged ions were then accelerated once again from the 1.7MV positive potential down to the ground state in the target chamber, reaching a maximum total of 3.4MeV of energy to the protons as they strike the target.

To ensure the proton beam strikes the target evenly, the high energy protons first entered a bending magnet as they exit out of the tandem chamber, so they may be directed down one of the three beam lines. The irradiation creep experiment used the 15 degree beam line, which had four quadruple lenses to focus the ion beam down to 3mm x 3mm spot size. The ion beam then went through a raster scanner that raster-scan across the samples at a frequency of 2061 Hz in the vertical direction and 255 Hz in the horizontal direction. The raster-scanning allowed the experimenter to control the irradiation area and beam current density. Figure 4.8 shows the raster

pattern of the proton beam during irradiation. The entire beam line from the source to the scanner must be at a pressure below 10^{-7} torr to ensure the steel samples did not oxidize under high temperature. Therefore, two cryopumps were attached to the beam line with bellows to achieve the necessary vacuum with minimum pump vibration. Two faraday cups were also attached to the two ends of the beam line to measure the ion beam current at both the low energy and high energy end. Figure 4.9 shows an overview of the accelerator and the components attached to the beam line to provide 3.2MeV protons necessary for irradiation creep experiments.

4.2.2 Irradiation Creep Chamber

Irradiation creep experiments required very specific instrumentation to achieve the necessary measurements. Due to space limitations in the shielded target chamber, design choices were made to the chamber to accommodate all the instrumentations. Figure 4.10-11 shows the entire target chamber designed for irradiation creep experiments. The design was composed of two large vacuum chambers, one upper and one lower. The upper chamber has total of 8 ports, which includes four 6 inch ports and four 1-1/3 inch ports.

The 6 inch ports acted as connections to other major components. The port in the front of the chamber acted as the connection to the accelerator beam line, and held the chamber in place. The bottom port connected to the bottom chamber where the stress was applied, and stress strain monitoring instruments were housed. The back port held the flange for the irradiation creep stage where the sample was attached. The top port was a viewing port necessary for the proper assembly of the irradiation creep experiment.

The 1-1/3 inch ports were functional viewing ports designed specifically to allow optic access to the sample during irradiation. The top left port was angled 20 degrees from the horizontal to provide a visual line of sight for the 2D infrared thermal pyrometer used for in-situ temperature monitoring. The front right port was angled 30 degrees from the chamber to provide a visual line of sight to the sample gage length for the laser speckle extensometer (LSE) used for in-situ strain monitoring of the sample gage length. The bottom left port was used as a connection to a turbo pump that will be used to pre-vacuum the chamber before exposing the entire accelerator to the creep chamber.

The lower chamber was designed to hold enough tungsten weights to provide the necessary tensile stress, and the instrumentations needed for conducting irradiation creep

experiments. The chamber had two 6 inch ports on top and bottom. The top port connected to the upper chamber, and the bottom port connected to a flange with a feed-through that could be raised and lowered. The feed-through housed the linear variable differential transducer (LVDT), and was how the samples are loaded inside the chamber. The bottom chamber also had a side window port that was large enough to allow manual adjustment of equipment in the bottom chamber by hand. Finally, the small port to the side was designed to interface with a 10 pin electronic feed through that allowed wires from the LVDT and load cell to connect to electronics outside of the vacuum chamber.

The irradiation creep chamber defined the spatial constraints of the irradiation creep experimental setup. Every component that was required for the irradiation creep experiment must be able to operate reliably under the conditions inside the irradiation chamber. The next sections will describe in detail each major component that goes into the irradiation chamber that made irradiation creep experiments a possibility.

4.2.3 Irradiation Creep Stage

The irradiation creep stage functioned mainly as the sample mount during irradiations. In order to be able to control the temperature, dose rate, and stress of the sample during irradiation, the stage was designed with specific capabilities and limitations in mind. The complete irradiation creep stage is shown in Figure 4.12. The stage was built on a 6 inch vacuum flange with three holes machined along the center line of the flange. The two ¾ inch diameter holes on the side were attached to 10 pin electronic feed through for connection of aperture and thermocouple wires. The single 1 inch hole in the middle was welded to a 2 inch 316 stainless tubing. The tubing was then braised to a cylindrical copper block about ¾ inch in thickness. The copper block was machined with a central 1-1/4 inch hole as the housing for a cartridge heater, and four 1/16 inch air tunnels for air cooling. These components made up the base portion of the irradiation creep stage, and will require significant effort to make any changes to the design.

Smaller components were machined to attach to the irradiation creep stage designed to be removable and flexible enough to accommodate any changes that might arise. The most important of these components was the shim block. The purpose of the shim block was to provide the best thermal conductance between the sample and the copper block for the entire duration of the irradiation, so the sample temperature can be well controlled. The shim block was

made of 316 stainless steel to prevent any high temperature interaction between the stage and the liquid indium. To contain the liquid indium, 8mm x 2.8mm reservoir was machined in the middle of the shim block. The reservoir was slightly raised by 1mm to define the sample gage length location during the irradiation. The reservoir was also slightly beveled on top to allow the thin film sample to drape over the reservoir, thus minimizing the chance of indium leak during irradiation. The thickness of the shim was chosen such that its bottom flat surface maintained good thermal contact with the copper block. Figure 4.13-14 illustrates the shim block and the FEM results of the shim deflection as a function of thickness.

Above the shim, a mounting block was machined to attach a mounting post directly on top of the reservoir. This mounting post allowed the clamped sample to be attached to the irradiation creep stage via a pin-hole mechanism. This method was chosen such that the sample will always be hanging freely under gravity, thus minimizing any shear stress that might occur during handling or irradiation. Figure 4.15 shows a schematic of the sample mount and sample stage.

Three holes were drilled and threaded into the copper stage for installation of the aperture using aperture posts. The location of the aperture posts must not interfere with the line of sight of the stinger and the LSE. The aperture posts were also electrically and thermally isolated from the rest of the stage by ceramic pieces. The aperture served two major functions. First, the size and location of the aperture defined the area where the ion beam will hit during the irradiation. Secondly, it independently measured the irradiation ion beam current density during the irradiation. The aperture was made with four tantalum sheet metals fixed to zirconium blocks. Each sheet was connected to a wire in the feed through so the ion current hitting that specific sheet can be independently measured. The four aperture sheets combined will make a window with which the ion beam will pass through and hit the target sample. The window size and location can be adjusted during the setup procedure. For irradiation creep experiments, the window size was designed to be 5mm x 5mm to cover the sample gage length. The aperture design is shown in Figure 4.16.

The irradiation creep stage was the medium through which the sample will interact with the rest of the experimental setup. The components of the stages are all designed to ensure that the sample will be irradiated at a constant ion beam current density, temperature, and uniaxial

tensile stress during the experiments. The next sections will go over how these variables can be accurately measured during irradiation creep experiments.

4.2.4 Temperature Control and Monitoring

Temperature was controlled during irradiation by a combination of approaches. A 300W Watlow FIREROD ® resistance cartridge heater that was capable of heating the stage to a maximum of 760^{o}C was inserted into the back of the copper stage as a primary means of external heating. In addition, cooling channels inside the copper block were fixed to pressurized air hose to continuously remove heat from the copper stage by air flow. By using these two methods, the indium heat sink can be guaranteed to stay in the liquid state with or without irradiation. The liquid indium was crucial for irradiation creep experiments due to its ability to provide heat conductance between the sample and the stage without adding any friction to the sample that can affect the sample strain rate.

The temperature was monitored in-situ by two methods. Before the proton beam was applied, the temperature was monitored through a front thermocouple attached to the shim, and a back thermocouple attached near the heater. The front thermocouple was made of J-type iron and constantan wires of 0.005" in diameter. It was insulated with ceramic beads to prevent them from shorting to the stage and each other. The back thermocouple was a coated J-type probe from Omega® that was inserted into a back port machined in the copper stage. The thermocouple measurements were used to preheat the sample to irradiation temperature and calibrate the 2D infrared pyrometer before irradiation started. Under thermal conditions, the two thermocouples measure temperatures very close to each other as shown by Figure 4.17.Once ion beam strikes the target, the front thermocouple was no longer reliable due to its distance from the irradiated region, and only the 2D pyrometer was used as the temperature measurement for the sample. The back thermocouple was still measured throughout the irradiation, to ensure the stage temperature did not drop below the solidus temperature of indium in the event of a power loss.

The IRCON^{TM} Stinger thermal imaging system is a 2D infrared pyrometer that was mounted at a 30 degree angle with a direct line of sight to the sample. Area of interest (AOI) were set up on the thermal image through the Stinger software. Eight AOIs were created on the irradiation creep sample, with each AOI making a rectangle approximately 2mm x 1.5mm in length, numbered 1 to 8 from top to bottom. As an example, a Stinger image from a 450^{o}C

irradiation is shown in Figure 4.18. Each AOI had a user-assigned emissivity which correlates to the temperature reading of that AOI. Typical emissivity values for electropolished T91 ranged from 0.11 – 0.14, consistent with other proton irradiation experiments [69]. Therefore, each AOI was calibrated before irradiation to the thermally stabilized condition to match the readings from the thermocouples.

The irradiation creep experiment uses both thermocouple and 2D infrared pyrometer to monitor and control the sample temperature during irradiation. This redundancy allows accurate, and consistent temperature control throughout the irradiation such that the sample temperature was maintained with ±10°C. During irradiation, the sample temperatures of the irradiated region, typically around 4-6 AOI were consistent with each other, typically within 5°C of the target temperature. The AOI outside of the irradiated region would have much lower temperatures. For AOI at the lowest positions, temperatures could be as much as 20°C lower than the target temperature. Therefore, AOI 4-6 were reported as the irradiation creep temperature, while the other AOI were used to monitor indium stability or beam shifts during irradiation. Figure 4.19 plots the temperature distribution of the different AOI during irradiation.

4.2.5 Dose Rate Control and Monitoring

The irradiation dose rate is directly related to the current of the proton beam incident on the irradiation stage. The beam current was measured by collecting the total charge incident on the stage that was electrically grounded. This was made possible by electrically isolating the entire creep chamber from the rest of the beam line by a ceramic isolator, effectively making the creep stage as a Faraday cup to measure all the positively charged protons that hit it. The charge measured from the stage is passed through a charge integrator that assigns one "count" for every micro-Coulomb of charge collected, or 10^6 counts/C. The number of counts is recorded, and then is used to determine the irradiation dose rate according to the following equation:

$$\frac{dpa}{s} = \frac{R_D\left(\frac{Displacements}{ion \cdot Angstrom}\right)\times 10^8\left(\frac{Angstrom}{cm}\right)\times Counts\times 10^{-6}\left(\frac{Coulomb}{Count}\right)}{q\left(\frac{Coulomb}{ion}\right)\times A(cm^2)\times N\left(\frac{atoms}{cm^3}\right)\times time(s)} \tag{4.1}$$

Where N is the atomic density, q is the charge per incident ion, A is the irradiation area defined by the aperture, and R_D is the displacement rate determined by SRIM.

SRIM 2006^{TM} is an acronym for Stopping and Range of Ions in Matter, developed by J.F. Ziegler [70] that uses Monte Carlo method to simulate the penetration and total displacement produced per unit length per incident ion. The SRIM code required input of displacement energy of each species of atom in the target material. ASTM E 521-89 [71] recommends displacement energy of 15eV used for Si, 60 eV for Mo, and 40 eV for all other species present in the alloys (e.g. Fe, Cr, Ni, W, V, Mn). The SRIM calculations were selected to be detailed calculations taking into account secondary knockoff atoms (as opposed to the "quick" mode that used simple Kinchin-Pease approximation) with full damage cascades using total of 1,000,000 incident ions. Recent studies on the application of SRIM code suggest the simple Kinchin-Pease (KP) approximation was the more appropriate method for comparison of dose rates between ion and neutron irradiations, reducing the dose calculations by full cascade by roughly half [72]. However, for historical consistency of other ion irradiations, the result of the detailed SRIM calculation will still be used as default value in this project. In any comparison to neutron irradiation results, the dose and dose rates of both methods will be reported for clarification purposes.

SRIM detailed calculation for 3.2MeV protons perpendicularly incident on HT9 a penetration depth of around 40μm, with peak damage occurring at a depth of around 37μm. The damage profile of SRIM simulation is illustrated in Figure 4.20. For samples that were 35±2μm in thickness, the damage profile was fairly flat at an average of 5.6×10^{-5} displacements/angstrom-ion, with the exception of last 2μm in the back where the damage was factor of 5 higher than the rest of the sample thickness. Because the higher damage was limited close to the surface sink where radiation damage was unlikely to accumulate, the difference in damage would not adversely affect the bulk irradiation creep. For the purpose of this study, the dose rate was calculated using the average damage profile across the sample thickness.

In addition to the beam current measured on the stage, the current density was also measured by the apertures. The aperture system as described in section 4.2.3 was used to define the irradiation area and to actively control the ion beam current density during irradiation creep experiments. The four tantalum pieces that made up the aperture window were individually connected with wires to a charge integrator that measures the current density the same way stage

current was measured. The individual measurements were essential to ensure the raster-scanned proton beam overlap all the apertures by at least full beam diameter of 3mm, so the sample can be evenly irradiated. For an irradiation area of 5mm x 5mm in irradiation creep experiments, the total area scanned was 12mm x 12mm. A schematic of this beam overlap onto the aperture is shown in Figure 4.21. Since current was directly proportional to area, the stage aperture current ratios were roughly 1:5. For a typical irradiation creep experiment, the stage current was maintained at 2μA for a dose rate of $3.4x10^{-6}$dpa/s by Equation 4.11 using damage rate calculated by SRIM detailed mode. The total current was maintained at 12μA with aperture current at 10μA.

4.2.6 Stress Application and Monitoring

A special load train was designed specifically for the application of constant stress in an irradiation creep experiment. Design decisions were made to ensure uniaxial tensile stress on the sample while allowing the sample to strain freely with minimum vibration. Tungsten blocks were chosen as the means to apply weight to the sample due to their high density. Set of seven tungsten blocks of various masses were manufactured by Midwest Tungsten Service: 2 lbs, 3/2 lbs, 1 lb, 1/2 lb, 1/4 lb, 1/8 lb, and 1/16 lb. The weights were machined to rectangles that fit inside the bottom creep chamber with a 1/4 inch diameter hole drilled through the very center.

A weight rod was used to attach the weights to the sample via a pin saddle connection as shown in Figure 4.22-23. The weight rod came in two parts. The top part was about 1 inch in length with two #4-40 threads on its top and bottom. The top thread connected to a flat head screw that sat into the loading pin that was connected to the sample clamp. The bottom thread was connected to a miniature load cell by Measurement Specialties ™ [73]. The miniature load cell took in 5V input and outputs 0.5 – 4.5V as a function of force measured in Newton. Figure 4.24 plots the calibration of the load cell voltage output as a function of tungsten weight mass. With the input of sample cross sectional area, the stress of the sample was measured in real time by the load cell.

The second half of the weight rod connected to the load cell on top, and was attached to a LVDT rod on the bottom that will be lowered into the LVDT coil as the sample strains. The LVDT rod was thermally isolated from the rest of the weight rod by a ceramic stopper and a #4-40 nut that keeps the tungsten weights on the rod. The LVDT coil was attached in a cylindrical

tower designed to align and protect the LVDT if the sample fails. Inside the cylindrical tower, a base with a 1 inch spring was attached to catch the tungsten weights, allowing for partial loading during setup, and protect the LVDT from ever been crushed by the tungsten weights. Figure 4.25 illustrates the bottom of the weight rod in both the fully loaded and fully unloaded configuration.

The design for tungsten dead weight can provide 0-200MPa uniaxial stress on a 35μm sample. The stress was measured in real time by the load cell, and the load train provided a method for the implementation of an LVDT for strain measurement. The next section will describe in detail the method for strain measurement with both the LVDT and LSE.

4.2.7 Strain Monitoring

The strain of the irradiation creep sample over time was the main output of interest for this project. The measurement techniques needed to be consistent and reliable under irradiation, high temperature, and vacuum chamber environments. The equipment used for strain measurement also needed to fit the limited space available in the irradiation creep chamber. All these considerations informed the choices made for the type of instruments and the experimental setup for these instruments.

Two methods were used for the monitoring of the irradiation creep experiment. The primary method was through Laser Speckle Extensometer (LSE). The secondary method was through Linear Variable Differential Transducer (LVDT). The LSE is an optical strain measurement device mounted outside of the vacuum chamber, and it measured the strain in the gage length with submicron resolution. The LVDT is an electro-mechanical strain measurement system that rests inside the bottom vacuum chamber and measured the entire strain of the load-train. Both measurement techniques came with their own unique advantages and challenges. The details of their implementation will be thoroughly discussed below.

The LSE is a laser optical strain measuring system developed by Messphysik™ [74]. The instrument came in two parts, the laser and the camera. The LSE utilized a 532nm wavelength green laser that shined upon the sample surface. The laser light was then reflected back and captured by the camera as a series of speckle patterns. The initial speckle patterns were analyzed and stored by the LSE software. The LSE software will take the video image, and process the image as a sub-matrix of discrete functions that are named “correlation functions” obtained by Fast Fourier Transformations (FFT). This effectively transformed the speckle patterns into a

locational center of mass that can be tracked over time. The LSE used two speckle boxes spaced 5mm apart vertically on the sample to measure the sample strain during irradiation. The strength of the correlation function for each pattern was described by a correlation peak as shown in Figure 4.26. Any peak that was higher than value of 50 was deemed to have a good correlation and tracked the patterns consistently. However, as the sample strains, the quality of the correlation function will degrade over time. When the correlation peak dropped below 20, the LSE can no longer reliably track the strain resulting in excessive noise. Therefore, the experimenter must monitor the LSE correlation peaks during irradiation to ensure reliable strain measurements over time. The schematic for how the LSE works is illustrated in Figure 4.27.

The LSE had a theoretical strain resolution of 0.1μm, which translated to a $5.6x10^{-14}s^{-1}$ strain rate solution over 100 hours for a 5mm gage length. However, this resolution limit did not take into account external factors such as pump vibration, and light saturation caused by the glowing sample at high temperature obscuring the light from the laser could loss of correlation over time, which will ultimately reduce the LSE resolution. In order to ascertain the practical strain rate resolution of the LSE, a series of benchmarking tests were conducted.

The first benchmarking test was a simple thermal expansion test to quantify the addition noise from pump vibration and light saturation at high temperatures. The T91 sample was taken up from room temperature to 550^{o}C using only the back heater, and compared with known quantities of thermal expansion of T91. The results of thermal expansion measurements were illustrated in Figure 4.28. The maximum error between measured thermal expansion and values reported in literature was less than 0.2% strain. In addition, the thermal expansion measurements consistently overestimated the literature data, which could be the result of the small load applied to the sample that was necessary for heat conduction. The thermal expansion experiment showed that the LSE is accurate to at least 0.2% strain if not more.

The second benchmarking test was conducted by looking at a zero strain sample over long period of time under vacuum. This benchmark was meant to quantify the loss of LSE resolution from pump vibration and correlation loss over time. A 1mm grid paper was attached to the vacuum chamber as a replacement for the T91 as target for the LSE, in order to ensure no physical movement was possible from the target. The LSE measured the 5mm gage length for an extended amount of time to quantify the minimum strain rate that can be measured given the noise in the system. Figure 4.29 plots the LSE noise measured over time for a zero strain sample.

By taking the line fit to the noise of the LSE, a strain rate due to the random walk of the noise was found to be around 10^{-10} s^{-1} over 10 hours. The strain rate from random walk of the noise in the experimental setup effectively defined the practical resolution of the LSE. The implication of the practical resolution has impact on the experimental limitations of the setup. The LSE will not be able to resolve any strain rate that was lower than 10^{-10} s^{-1} in less than 10 hours.

The LVDT used in this creep experiment was specially designed for the high vacuum and small space environment of the lower creep chamber. The instrument was formally called Microminiature DVRT ® manufactured by MicroStrain™ [75] with unique specifications to operate under harsh environments and resist deformation. The wiring and connections were hermetically sealed with metal shielding to prevent outgassing in the vacuum chamber. The LVDT had two distinct components. The LVDT rod consisted of a solid magnet sheathed in stainless steel. The LVDT core was a cylindrical component with a wire coil that was connected to a 5V DC voltage input and a 5V voltage output. As the magnetic LVDT rod was lowered into the coil, it will induce a change in voltage that will be registered in the 5V output. The LVDT rod was epoxy bonded to a #4-40 thread to be connected directly to the load-train, and aligned to the LVDT core so it will register the total displacement of the system as the sample strains.

A LVDT had no inherent resolution limit, but its experimental resolution was determined by the minimum change in voltage that can be measured. The voltage output from the LVDT was measured by the Data Acquisition (DAQ) card which fed the measured voltage to a computer running LabView®. The DAQ cards allowed flexibility in terms of the resolution of the LVDT measurement at the expense of total displacement. The 5V output of the LVDT corresponded to 6mm full stroke of the LVDT. The calibration of the linear relationship between voltage and displacement is shown in Figure 4.30. By using a 1V module for the DAQ card, the entire full stroke of the LVDT was measured to an accuracy of 0.001 volt which corresponds to Y displacement. However, by using a 100mV module, the maximum voltage that can be measured was 1.4V, but it will increase the resolution by a factor of 10. Since the gage length of the sample was 5mm, it was highly unlikely that the strain will be more than 1mm for the creep experiment. Therefore, the 100mV module was used to measure the LVDT output voltage during irradiation. However, during loading procedures, the 1V module was used to make sure the LVDT rod is in the correct position and other troubleshooting procedures that might arise during the experiment.

The two strain measurement techniques provided independent data on the strain of the sample overtime. Their simultaneous implementation did not overlap due to the limitation of their respective measurement methods. The LVDT was a reliable measurement of the strain in the system via a physical connection to the sample. However, due to the complicated temperature gradient the sample experiences during irradiation, the total strain LVDT measured included all the thermal expansion in the unirradiated region as well as any strain changes that were not related to the sample. This resulted in the decision to use the LVDT as a qualitative measurement of the strain behavior to support those of the LSE. The LVDT was used to judge when the sample strain has reached a relative steady state so a strain rate can be reliably measured. It was also used to ensure the entire irradiation creep setup was behaving as it should during unexpected failures. In contrast, the LSE measured only the gage length, and was used as the primary data for strain rate analysis. However, its tendency to lose correlation made it less reliable than the LVDT. The LVDT was used to determine if the LSE data was measuring strain rate at steady state conditions. When the LVDT was showing little change, any changes in the LSE data was considered to be real and used towards strain rate calculations. When the LVDT showed great disturbance from either a beam loss or power outage as shown in Figure 4.31, the LSE data during the disturbance was not used towards strain rate calculations. Instead, only the highlighted portions where LVDT was showing a stable trend was the LSE data used to determine the strain rates. If the data during the outages were not removed, the LSE would grossly underestimate the strain rates at stable conditions. By using the LVDT to determine which LSE readings were real, the local strain from the gage length was measured with the LSE without worrying about any false readings.

4.2.8 Irradiation Startup Procedure

In order to properly setup the irradiation creep experiment, a series of procedures must be followed precisely to avoid any premature failure, loss of temperature control, or misalignment of the sample. This section describes in detail the steps taken to put everything together, including the irradiation chamber, and the irradiation creep stage. The procedure should be followed in order, where the top irradiation chamber is set up first, followed by the bottom chamber, and lastly the irradiation creep stage.

Top irradiation chamber setup procedure is as follows:

1) Make sure all gate valves are closed and attach top creep chamber to the end of beam-line.
2) Use a lever to make sure the creep chamber is aligned perfectly perpendicular and vertical along the beam-line.
3) Attach the turbo pump bellows to the bottom left nipple, make sure the valve is closed.
4) Attach window vacuum flanges to the side ports.
5) Attach the LSE to the right hand nipple, connect the wires.
6) Attach the Stinger Pyrometer to the top left hand nipple, connect the wires.
7) Attach the wire of the current integrator to measure current.

Bottom irradiation chamber setup procedure is as follows:

1) Attach the LVDT to the loading tower using three set screws.
2) Completely raise the bottom feed-through, and attach the loading tower with the LVDT to the feed-through.
3) Connect wiring for LVDT and load cell to ensure the correct signals are sent to the computers.
4) Disconnect wiring for LVDT and load cell, and attach bottom creep chamber to the top creep chamber with the window port facing the outside.
5) Weigh the mass of tungsten blocks and weight rod used on a scale, to make sure the proper tensile stress will be applied.
6) Fully Insert the LVDT rod into the LVDT core with the weights attached.
7) Attach the load cell to the weight rod, and pull the wires from LVDT and load cell through the bottom right port.
8) Connect the wires to the 10 pin feed-through as color coded in Figure 4.32, and attach the feed-through to the bottom chamber.
9) Connect the wires from the feed-through into the computer, and ensure LVDT and load cell is still working properly.

10) Ensure the weight rod is loose when the system is completely unloaded so the LVDT rod will not be damaged. The fully completed bottom creep chamber should look like Figure 4.33.

Irradiation creep stage setup procedure is as follows:

1) Put dog-bone sample in the sample rig as shown in Figure 4.34.
2) Align the sample to the clamp using alignment pins, and firmly clamp the sample.
3) Use 4000 grit SiC paper to slightly rough the sample surface to ensure a good speckle pattern for LSE.
4) Attach the shim block to the creep stage.
5) Fill the reservoir on the shim block with solid indium and scrape off any excess with a razor blade to ensure a flat surface.
6) Use a heat gun to melt the solid indium on bench-top to ensure every part of the reservoir is filled.
7) Turn the irradiation creep stage horizontal, and attach the clamped sample onto the stage post.
8) Attach the loading pin to the sample clamp.
9) Use two C-clamps to fix the irradiation creep stage to the bench-top, and load the sample to ensure sample does not slip out of the clamps under load. Also, check the interface between the sample and the indium reservoir to ensure no leaks will occur. The bench-top loading is shown in Figure 4.35.
10) Unload the sample and remove the weights. Remove the C-clamps and move the irradiation creep stage in position to face the diffused laser for aperture alignment.
11) Configure the aperture to make a 5mm x 5mm window, and attach to the irradiation creep stage. Turn on the laser and center the red spot onto the sample gage length as seen in Figure 4.36.
12) Connect the aperture wires and thermocouple into the back of the irradiation creep stage.
13) Use a DC voltmeter to check that each aperture is electronically isolated from each other and the stage. Also use the voltmeter to induce a voltage to each aperture and identify which computer current reading correspond to which aperture.

14) Disconnect all the wires from the back of the creep chamber, and the stage is ready to be inserted into the creep chamber.

Pre-irradiation start up alignment procedure:

1) Put the tungsten weights inside the bottom creep chamber, reattach the load cell, and fully lower the loading feed-through.
2) Carefully insert the irradiation creep stage into the top creep chamber. Make sure the apertures are not bumped and the sample is vertical during insertion.
3) Use a level to ensure the irradiation creep stage is sitting perfectly horizontal such that the sample perfectly vertical over the reservoir.
4) Use a DC voltmeter to check the aperture pins from the back to insure all the apertures are still electrically isolated from each other and the rest of the stage.
5) Turn on the LSE, and align the camera and laser to obtain a good speckle pattern on the gage length of the sample. The image should be focused that the boundary of the sample is clear so the reservoir is completely covered.
6) Looking through the window ports, slowly raise the feed-through and hook the weight rod onto the loading pin without actually loading the sample.
7) Recheck the LSE to make sure hooking the weight rod has not misaligned the sample. Turn on the LVDT with 1V module to make sure the LVDT rod is fully inserted into the coil. Turn on the load cell to make sure the sample is fully unloaded.
8) Slowly lower the feed-through until the sample is partially loaded. Recheck alignment of the sample on the LSE.
9) Tighten all the bolts in the system. Connect the pins for apertures and the compressed air hose. Insert the back thermocouple and the cartridge heater.
10) Fully load the sample by lowering the feed-through until LVDT reads close to zero. Switch the 1V module for 100mV module to increase LVDT resolution.

Irradiation startup procedure:

1) Open bellows valve, and turn on turbo pump.
2) When the ion gage shows bellows vacuum is under 50mtorr, close bellows valve and turn off turbo pump. The vacuum should stay around 50mtorr if there are vacuum leaks.

3) Open target chamber valve to expose the irradiation creep chamber to the accelerator. The pressure of the entire system should be around 10^{-6}torr and dropping.
4) Wait until pressure drops below 10^{-8}torr. Turn the air pressure to 1 psi to allow for emergency cooling and heating. Slowly ramp up the heater by 5V increments until target irradiation temperature. During this procedure, care must be taken that the pressure inside the accelerator does not increase higher than 10^{-6}torr to avoid oxidation.
5) Once the sample has reached irradiation temperature, turn on the Stinger thermal imager and calibrate the emissivity of each AOI to match the temperature of the thermocouple.
6) Once the sample emissivity has been calibrated, lower the sample temperature down by ~250^{o}C to anticipate for heating from proton beam.
7) Ramp up the accelerator voltage to the target proton energy, and condition to source to give the total current needed for the irradiation.
8) Focus the beam using the beam profile monitor and ensure the beam is 3mm at full width half max.
9) Put in the high energy faraday cup and ensure the total current is as expected.
10) Turn on the beam scanner and broaden the beam so the sample experiences minimal thermal shock as proton beam strikes it.
11) Open gate valve and take out faraday cup. The sample temperature should rise and the current should be distributed on all the apertures. Use the beam steer to center the proton beam by balancing the aperture currents.
12) Slowly increase the amplitude of the beam scanner to reduce the current on the apertures and increase the current on the stage. As stage current rises, the sample temperature should rise accordingly.
13) Once the stage current reaches the target value, increase or decrease the heater voltage and air pressure to bring the sample temperature to the target temperature.
14) Once the temperature have reached steady state, the conditions are kept constant as the sample strains over time for measurement of irradiation creep strain.

Irradiation creep watch procedure:

1) Turn on temperature alarms to alert when the sample deviates ±10^{o}C from target temperature.
2) Turn on current alarm to alert when the sample deviates ±0.2μA from target current.
3) Use small adjustments of the air pressure (around 0.02 psi for 1^{o}C) to control the sample temperature.
4) Use beam scanner to keep stage current at target. If total current drops, lower the filament current from the source.
5) Check the LSE every 30 minutes to ensure correlation strength is strong. If the correlation peaks drop below 20, restart the LSE and start a new file.

Accelerator based irradiation creep experiments were complex in nature and required a precise setup procedure to achieve the control needed for a successful experiment. The procedure outlined in this section was developed through both theoretical design considerations, and practical experience. If the procedure was properly followed, the irradiation creep experimental setup could measure in-situ the temperature, current, stress and strain over time for each irradiation condition. The next section will describe the statistical analysis used to determine the characteristic strain rate of each irradiation creep condition from the data.

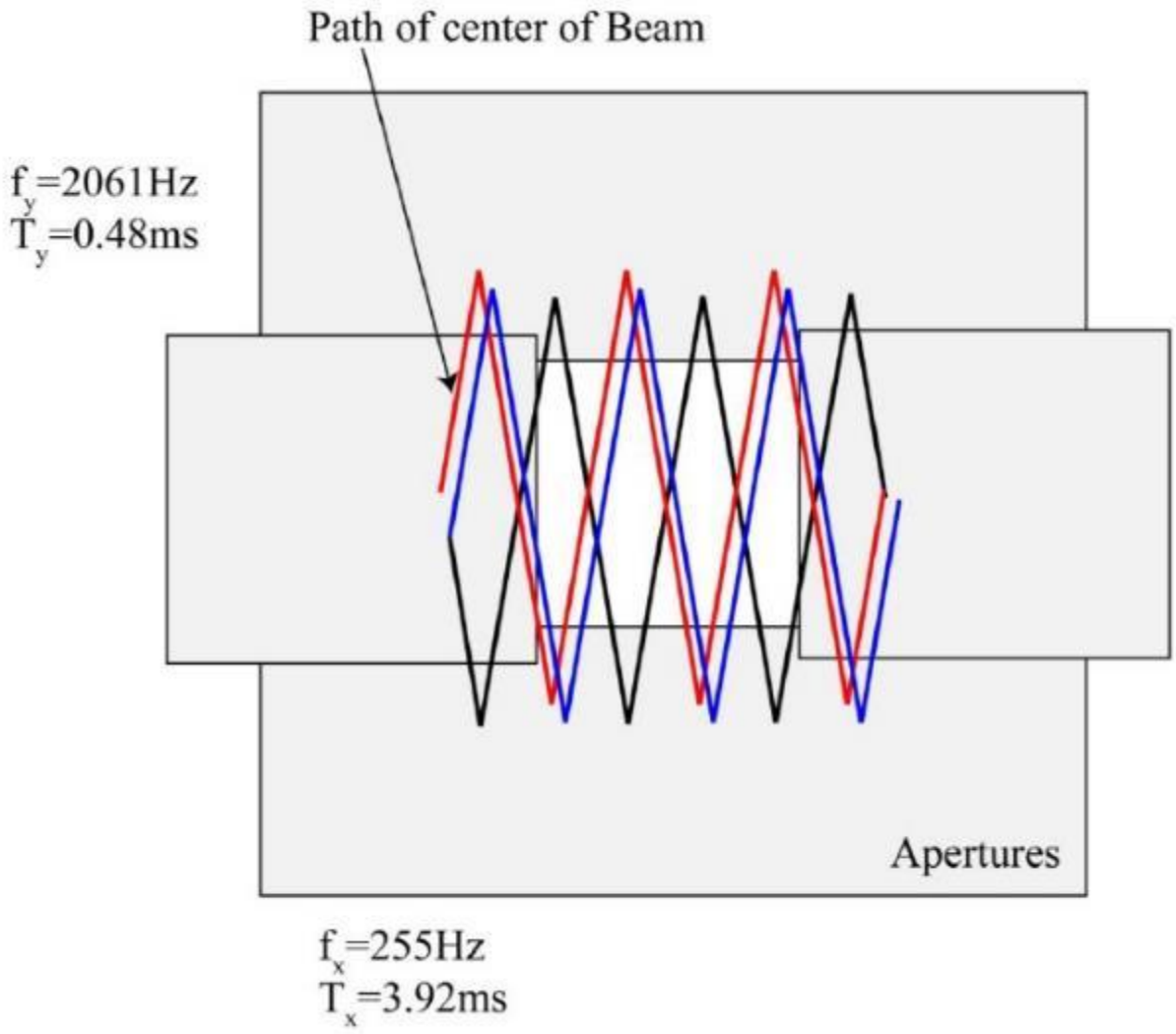

Figure 4.8 Pattern of the raster scanner during proton beam irradiation.

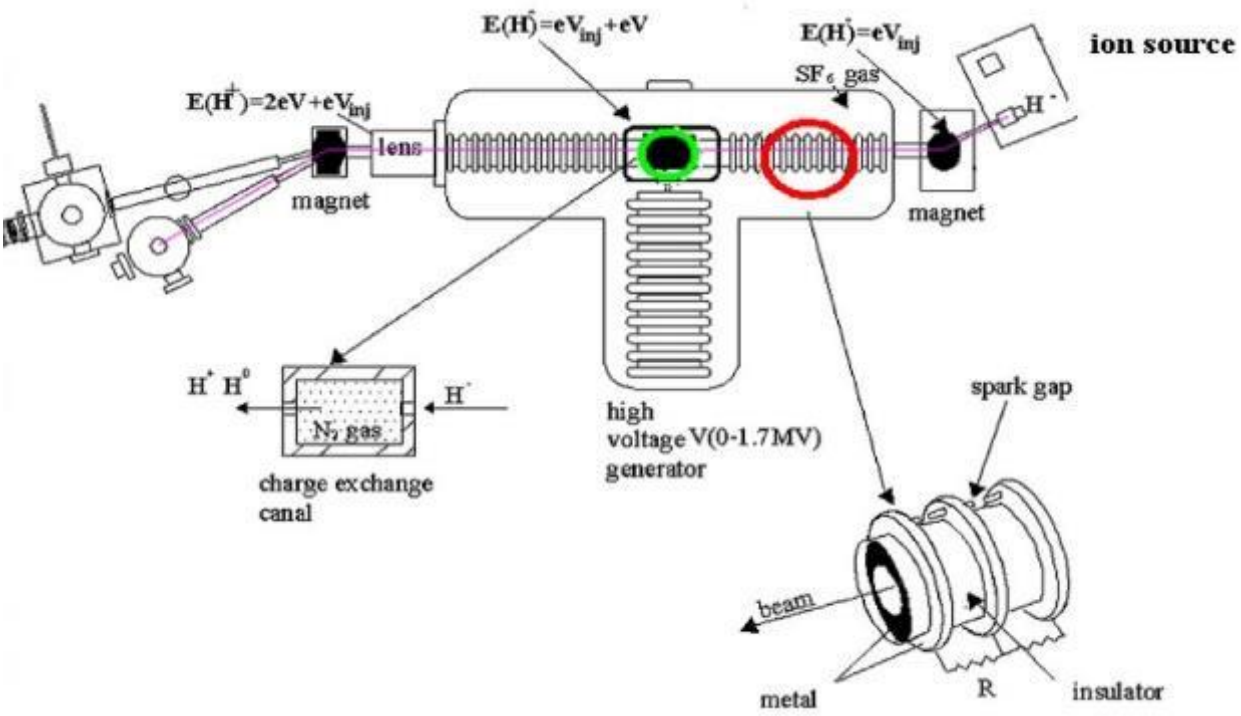

Figure 4.9 Overview of the General Ionex Tandetron accelerator at Michigan Ion Beam Laboratory (MIBL) and the components attached to the beam line to provide 3.2MeV protons necessary for irradiation creep experiments.

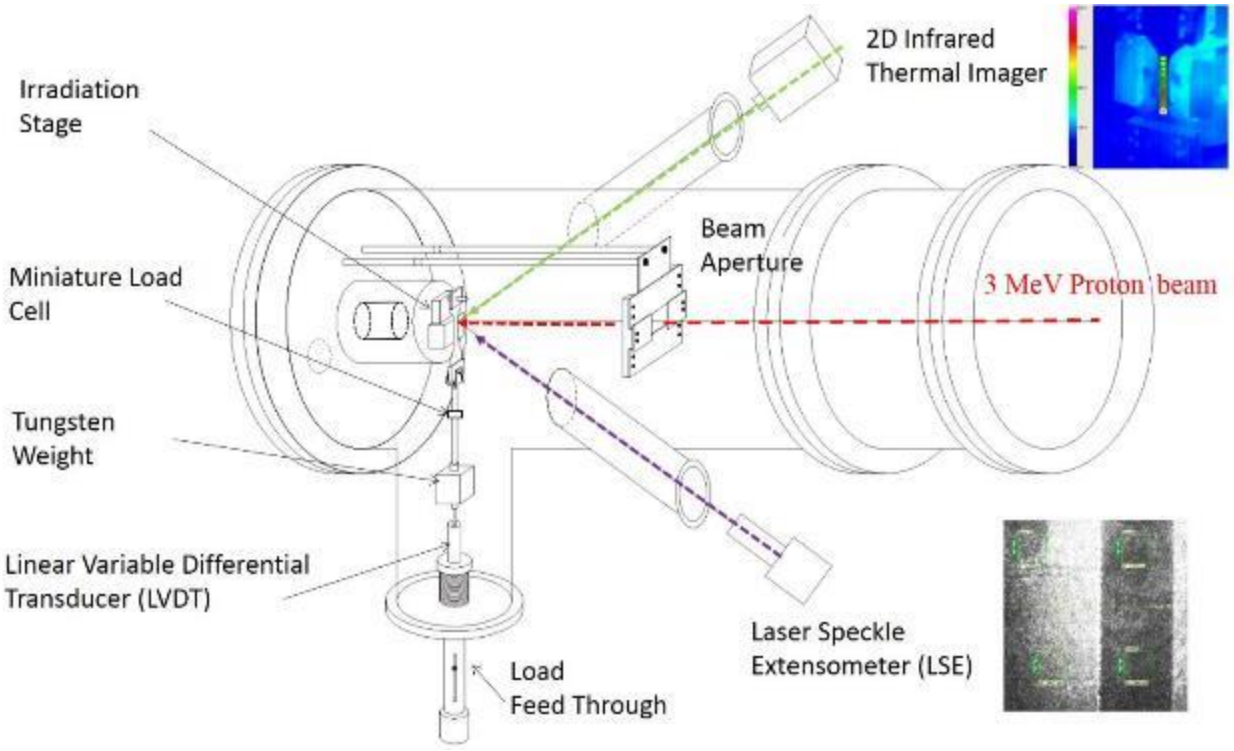

Figure 4.10 Schematic of irradiation creep chamber attached to the accelerator beam line with all measurement instruments.

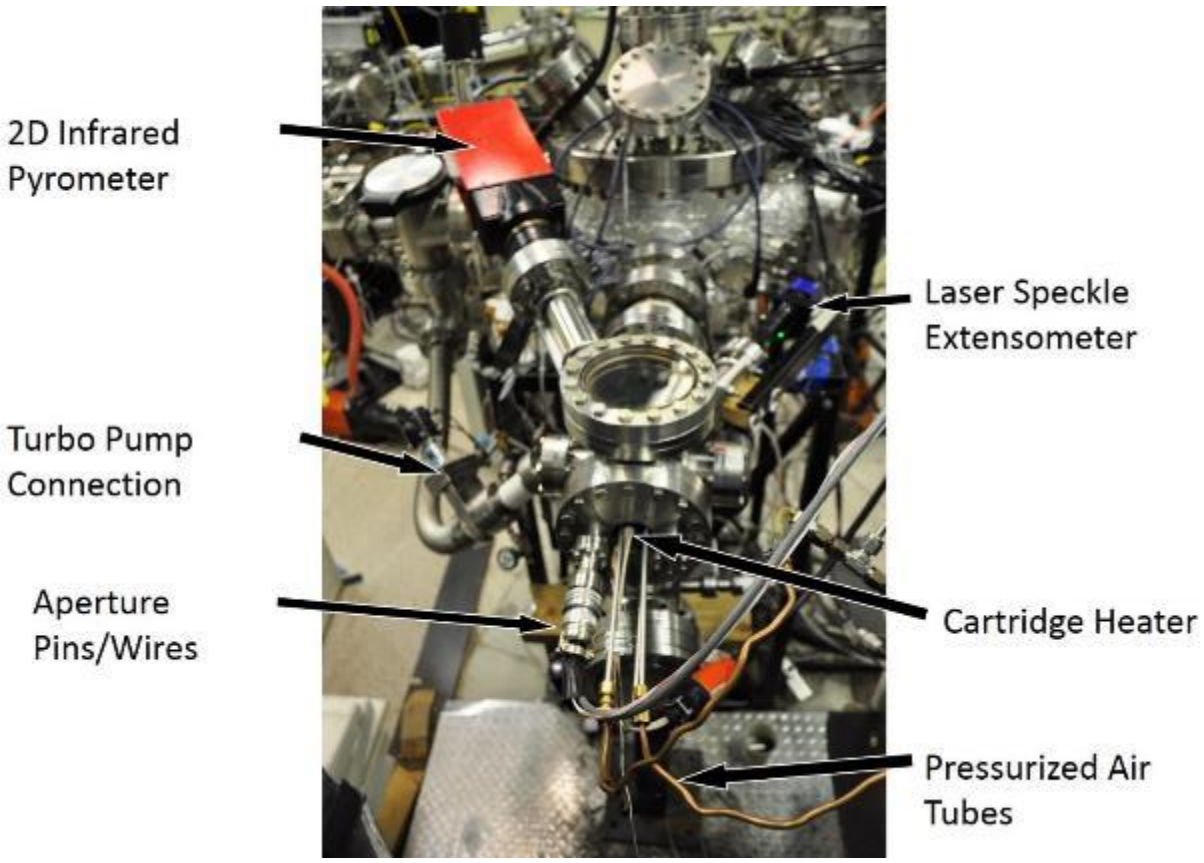

Figure 4.11 Photograph of irradiation creep chamber from above, showing laser speckle extensometer, pressurized air tubes, cartridge heater, aperture pins and infrared pyrometer.

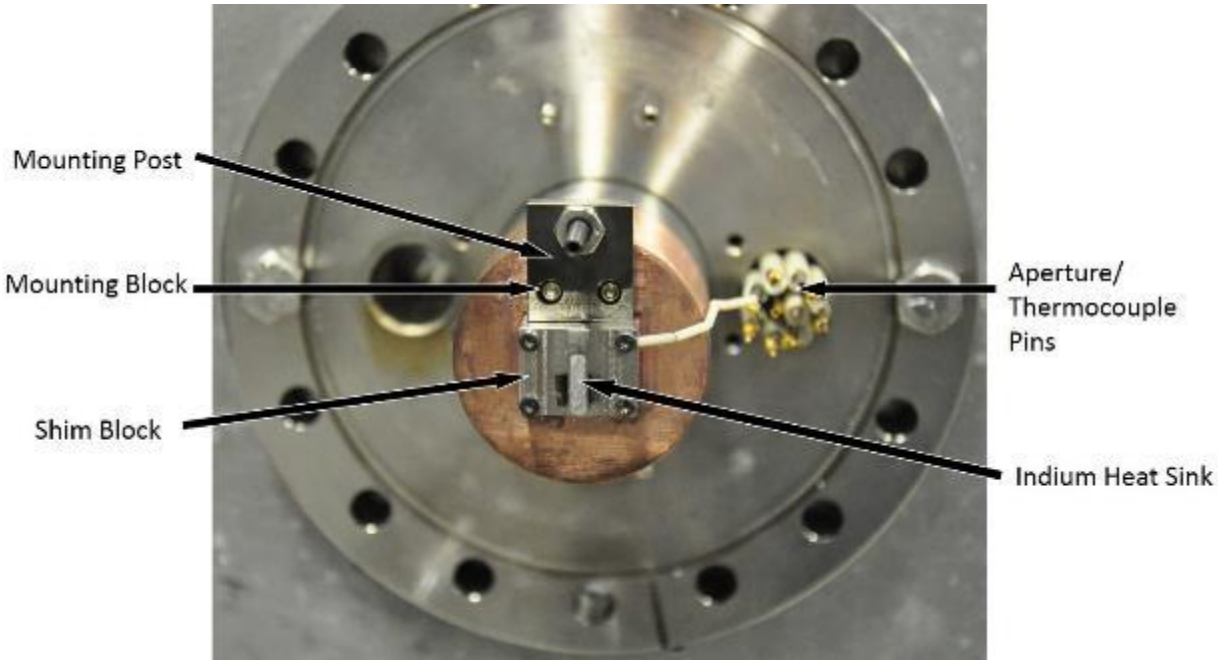

Figure 4.12 Photograph of the irradiation creep stage showing shim block with indium heat sink, sample mounting post, and aperture pins.

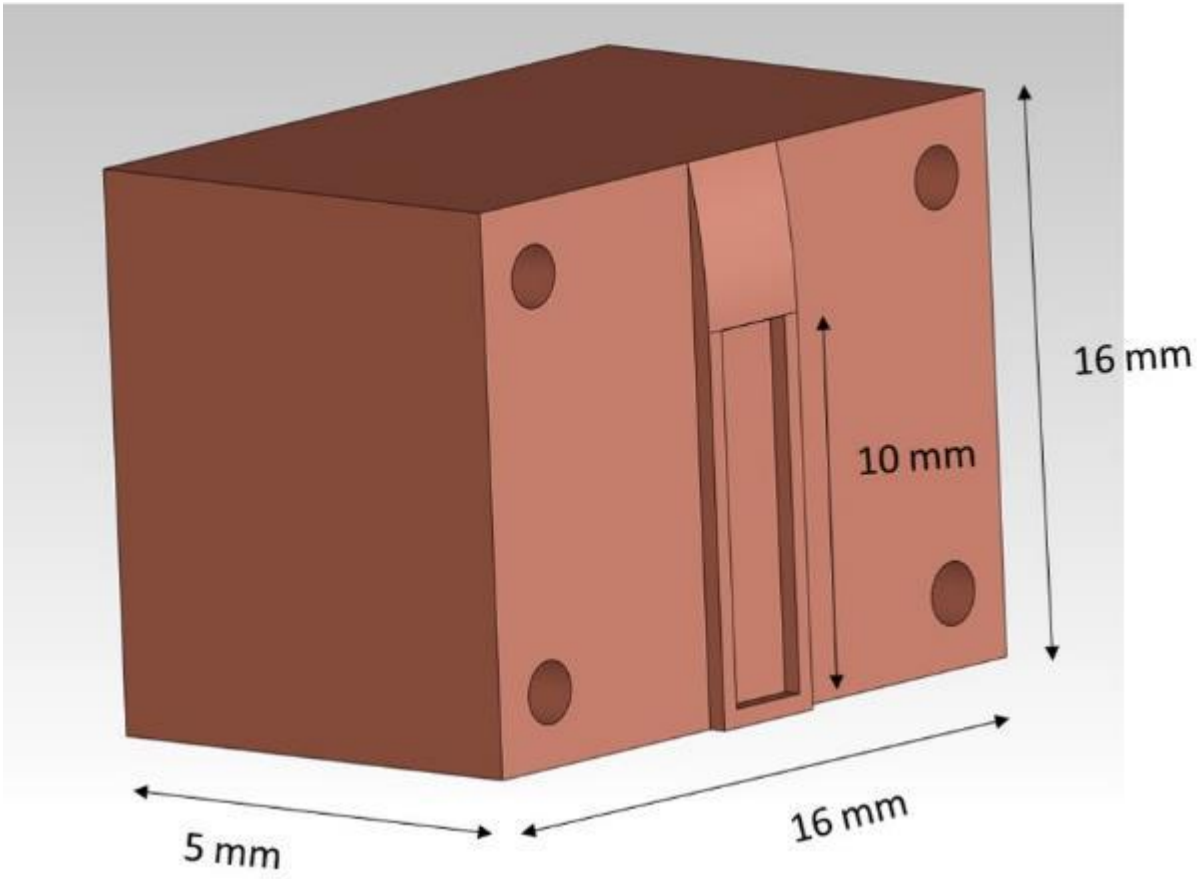

Figure 4.13 Drawing of the shim block showing critical dimensions to ensure thermal contact between the heat sink and the irradiated sample.

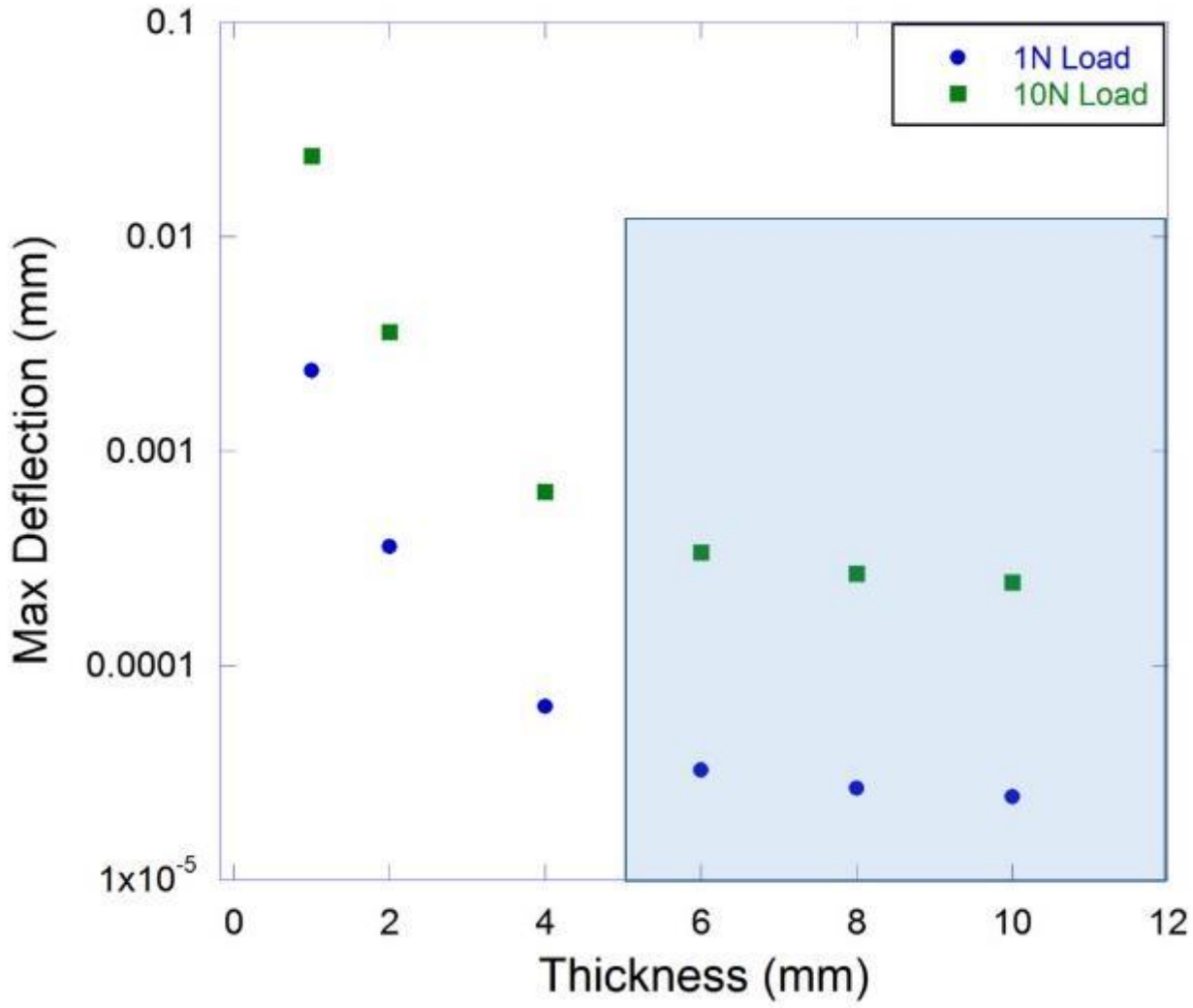

Figure 4.14 Result of calculated deflections of the shim block under load from screws as a function of thickness. The calculations show the deflection becomes minimal for a block that is more than 5mm thick, ensuring good thermal contact between the shim block and the rest of the irradiation creep stage.

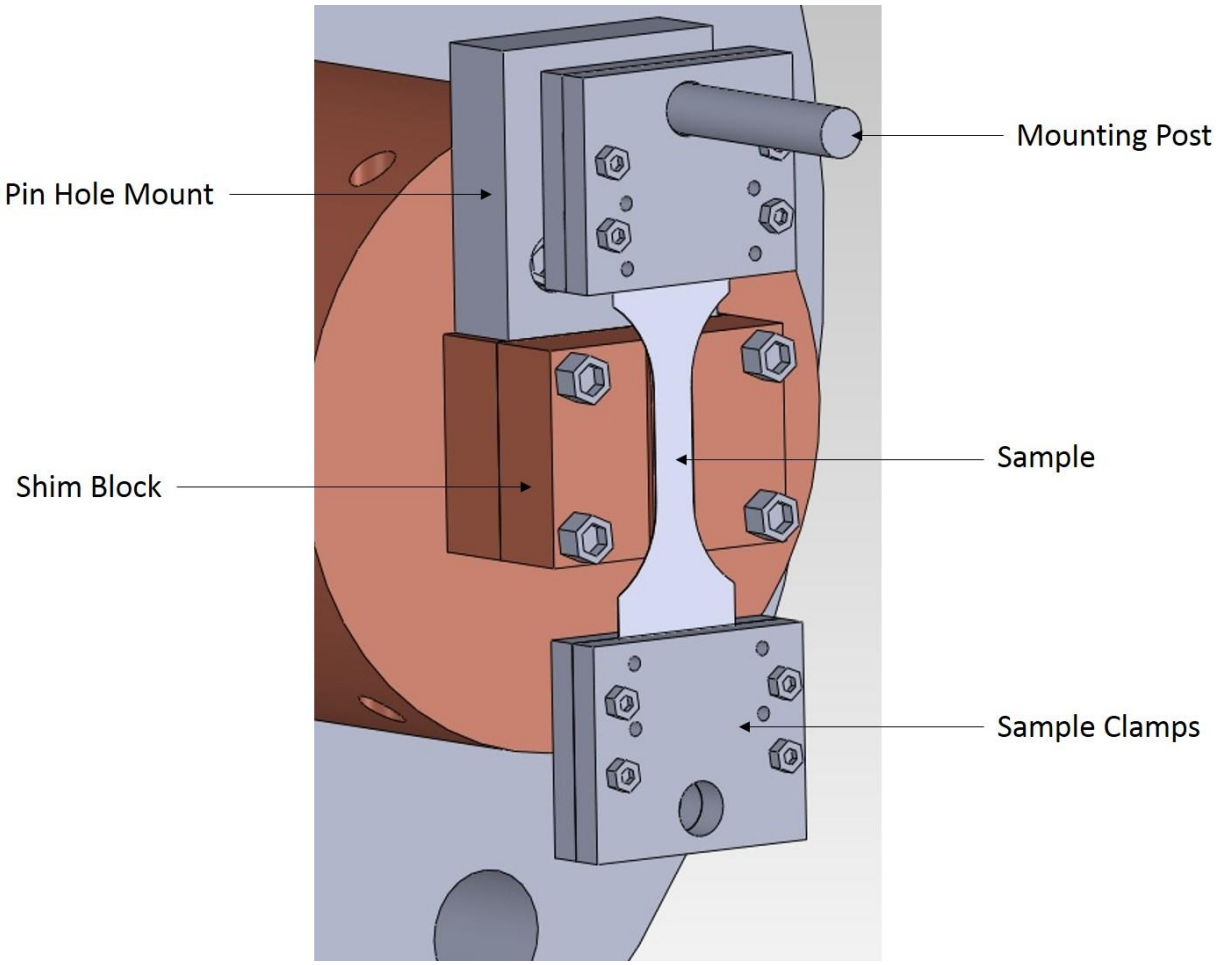

Figure 4.15 Schematic of irradiation creep stage sample mounting and shim block.

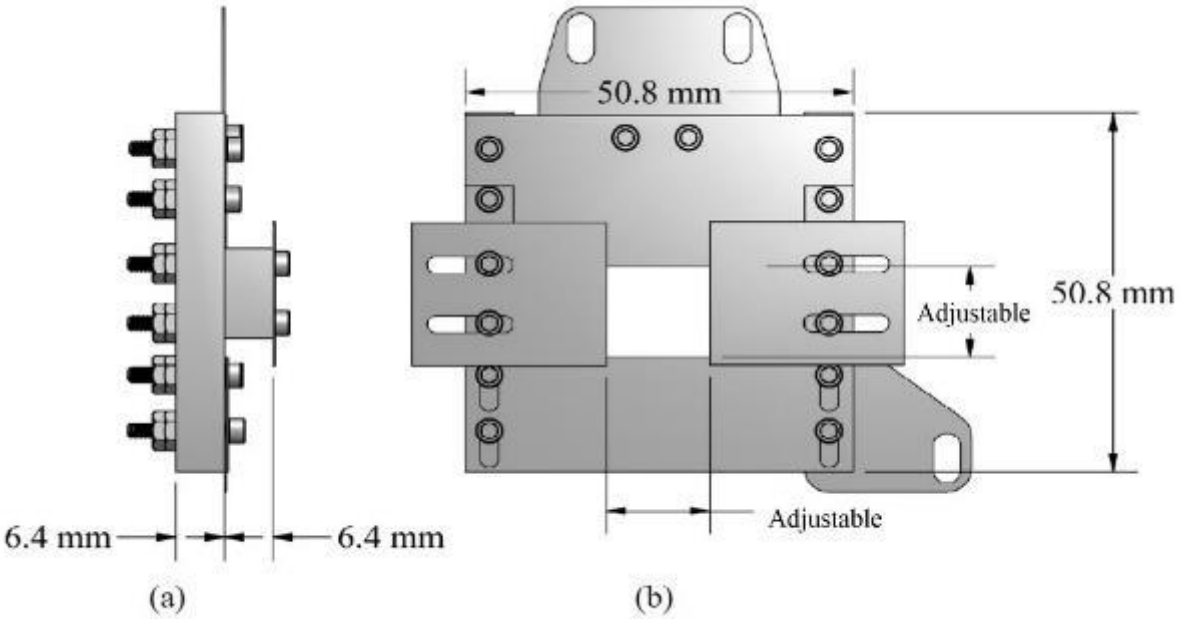

Figure 4.16 Tantalum aperture used to define the irradiation area and measure proton beam current for irradiation creep experiments.

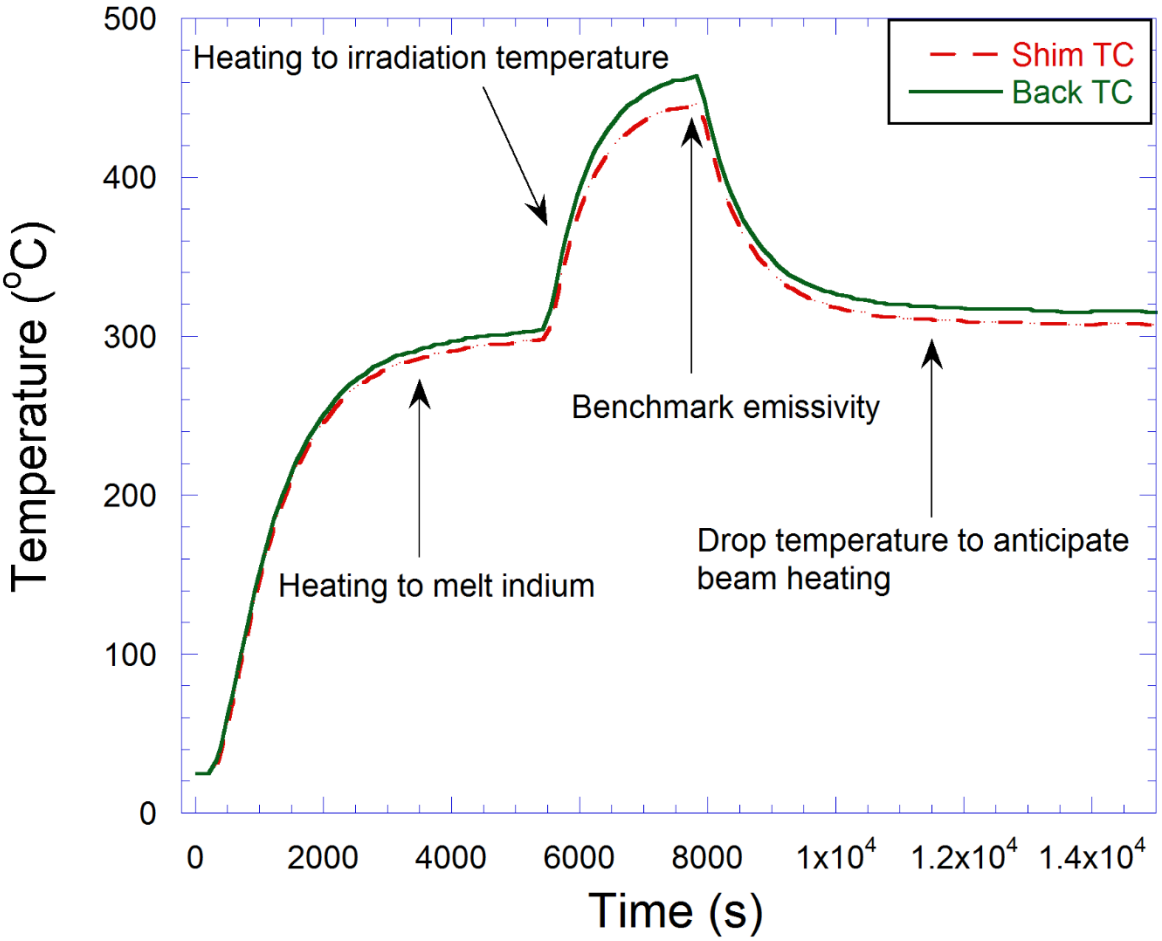

Figure 4.17 Thermocouple readings for benchmarking emissivity for an irradiation creep experiment at 450°C.

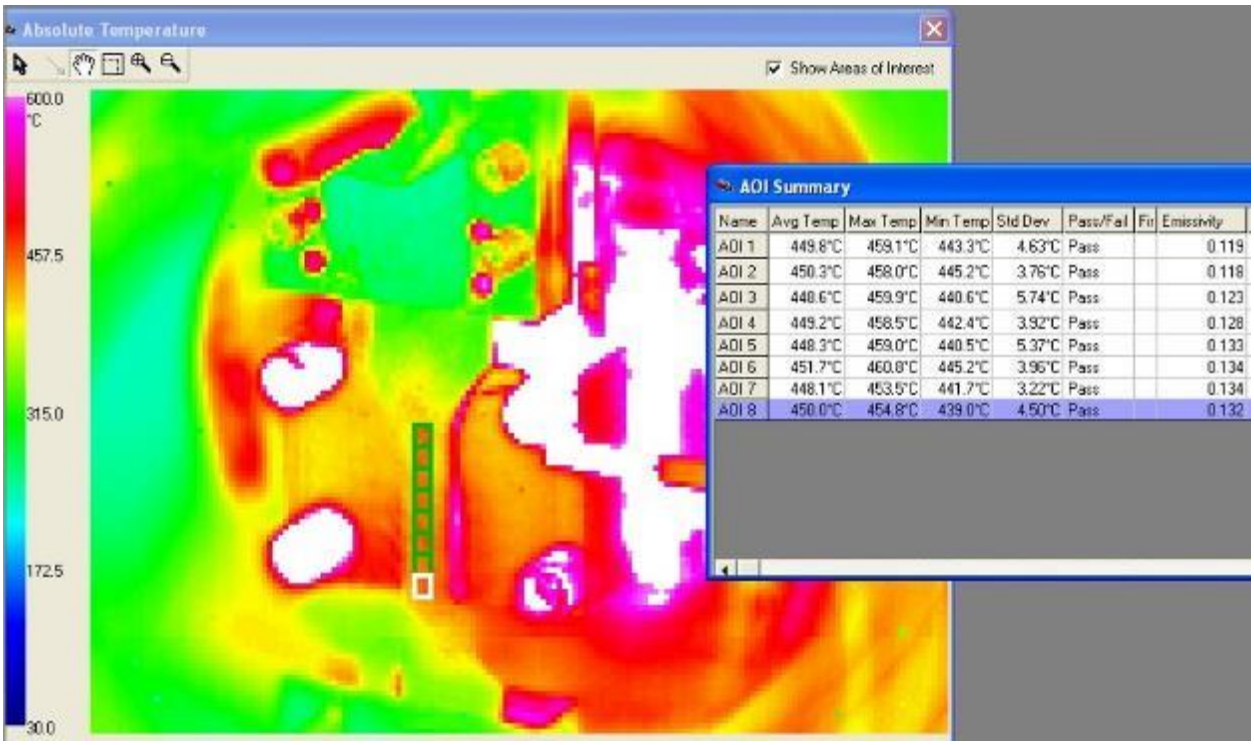

Figure 4.18 Infrared pyrometer image of the irradiation creep sample inside the chamber at 450°C.

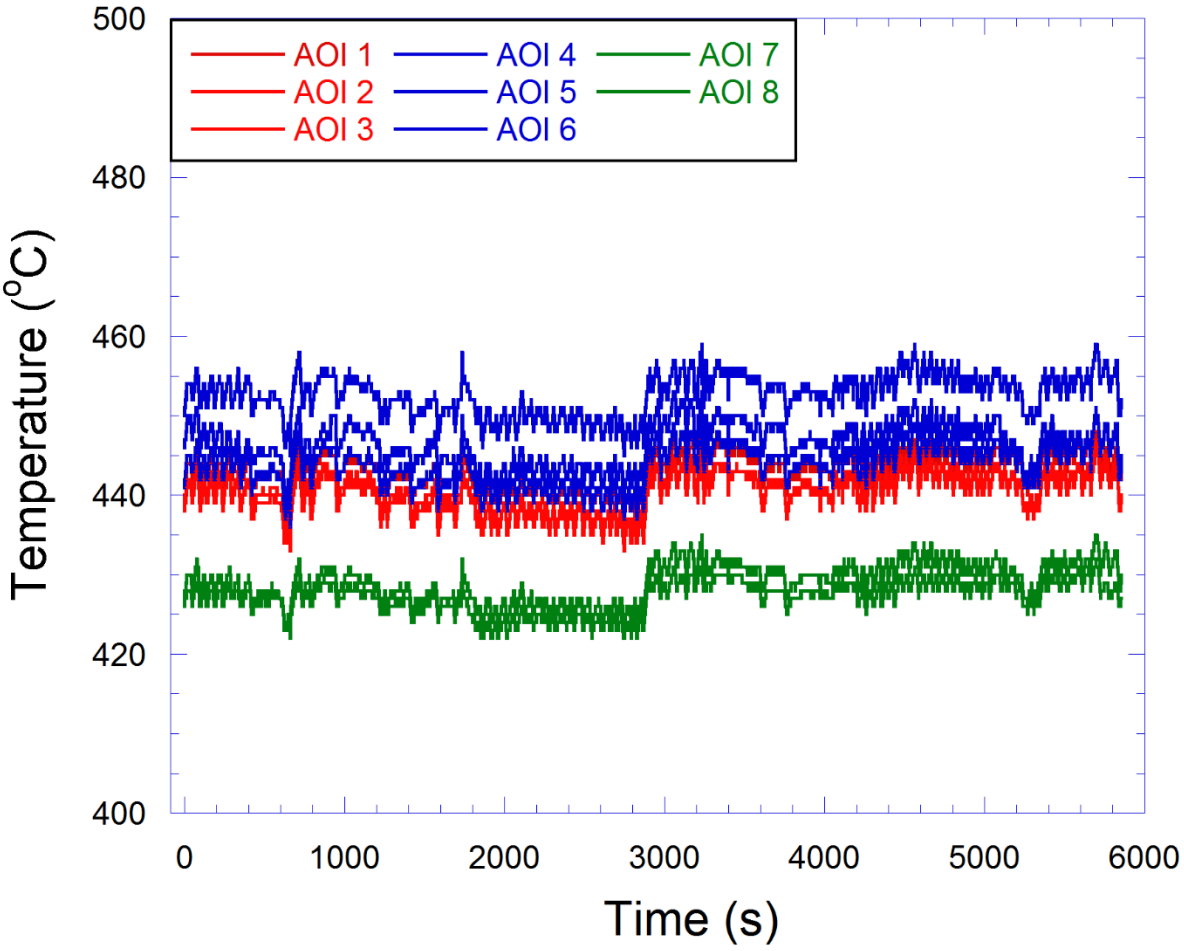

Figure 4.19 Temperature variation between different areas of interest (AOI) during irradiation creep at 450°C.

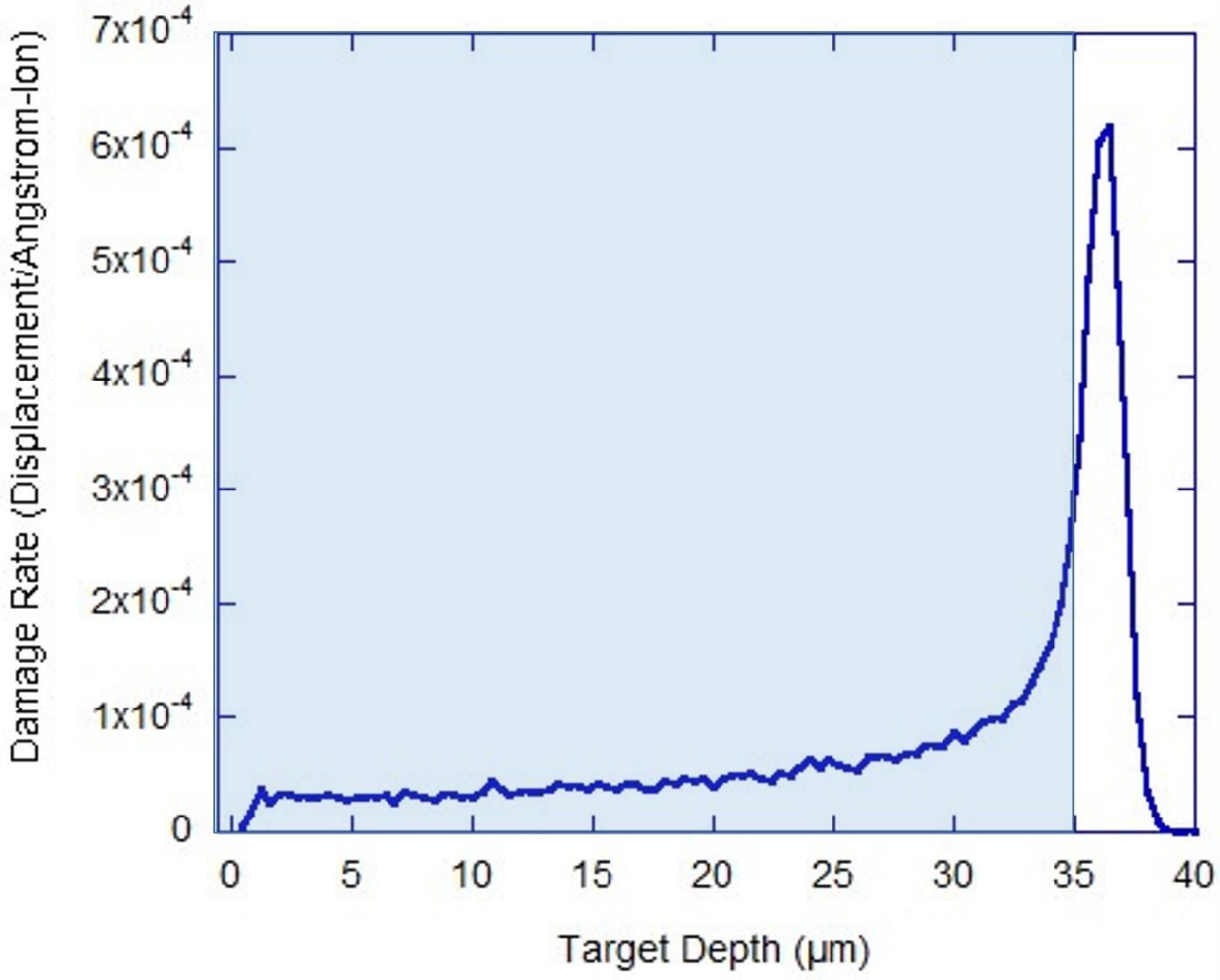

Figure 4.20 SRIM result of 3MeV proton beam incident on T91 target. Damage peak occurs around 37µm into the sample. Nominal sample thickness of 35µm was used to avoid the damage peak and any proton implantation.

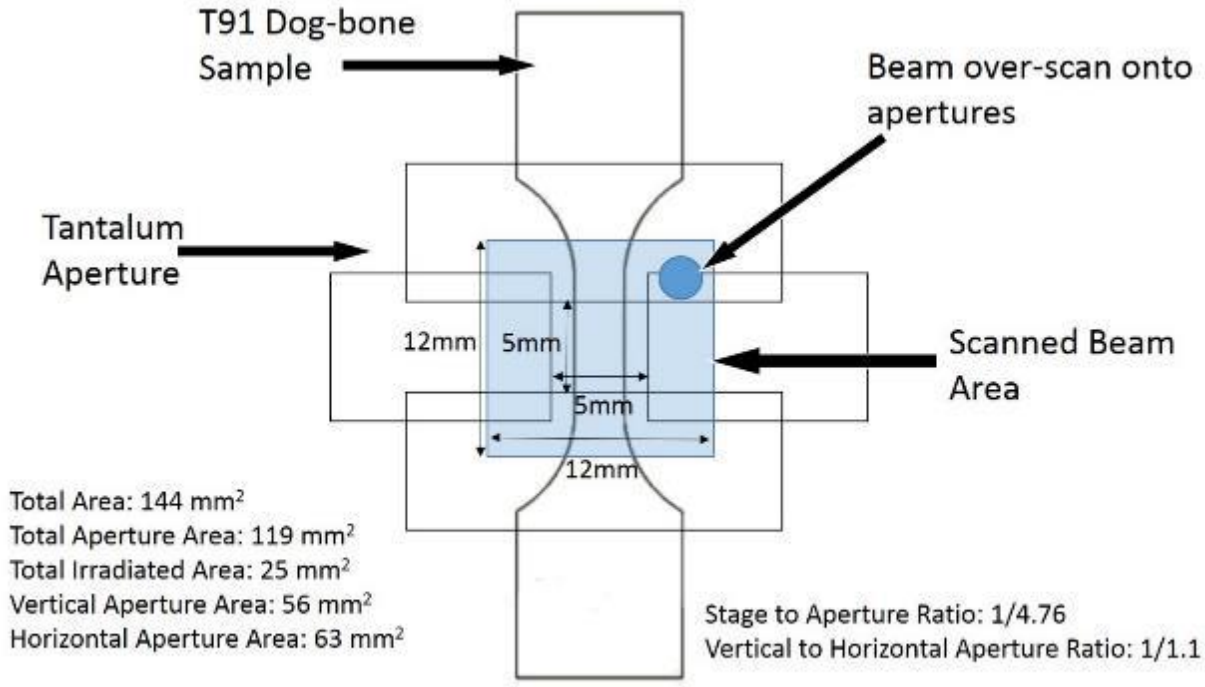

Figure 4.21 Schematic of scanned beam area for irradiation creep experiments, and the current ratios used to control dose rate.

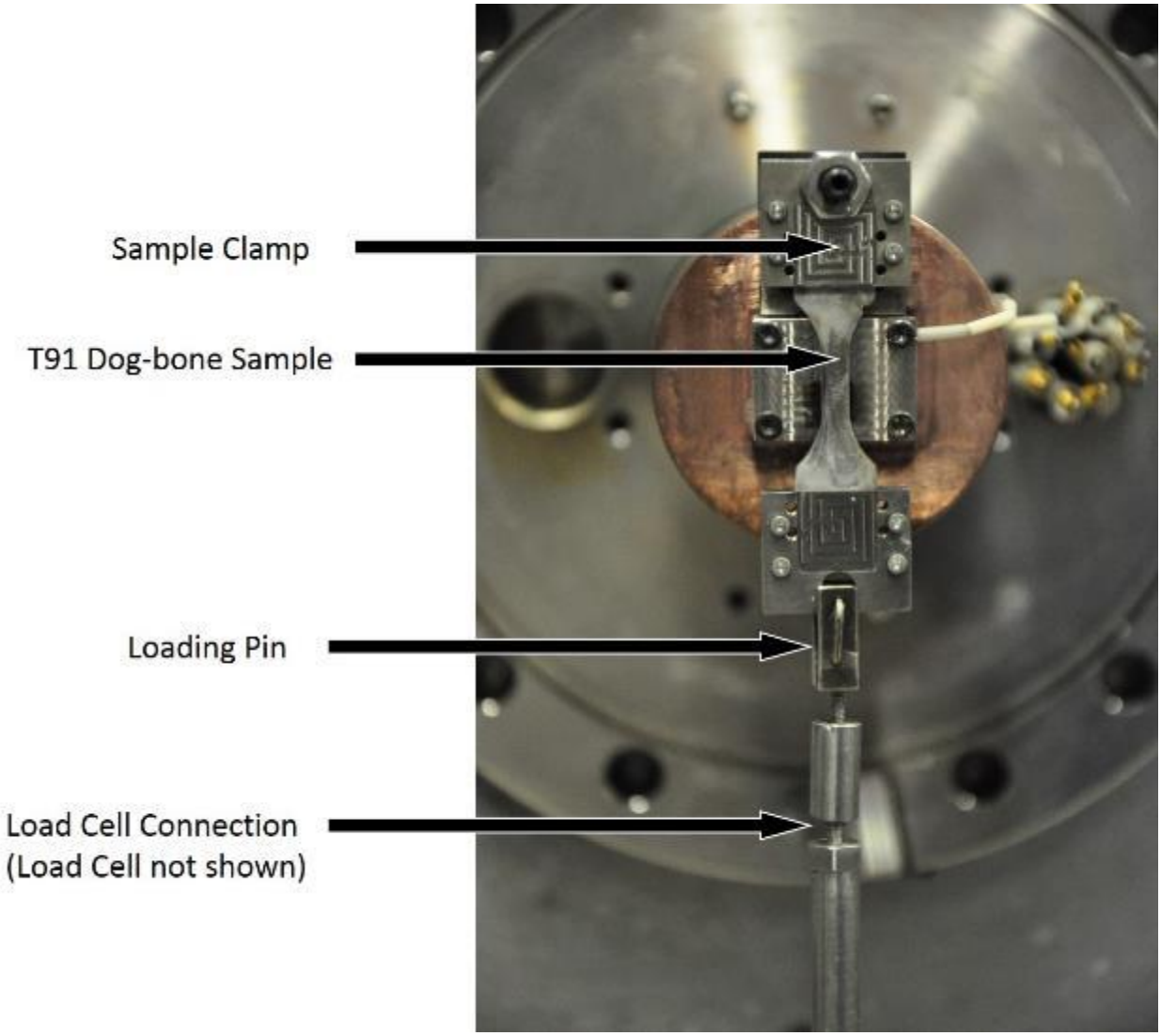

Figure 4.22 Detailed view of the clamped T91 sample on the irradiation creep stage.

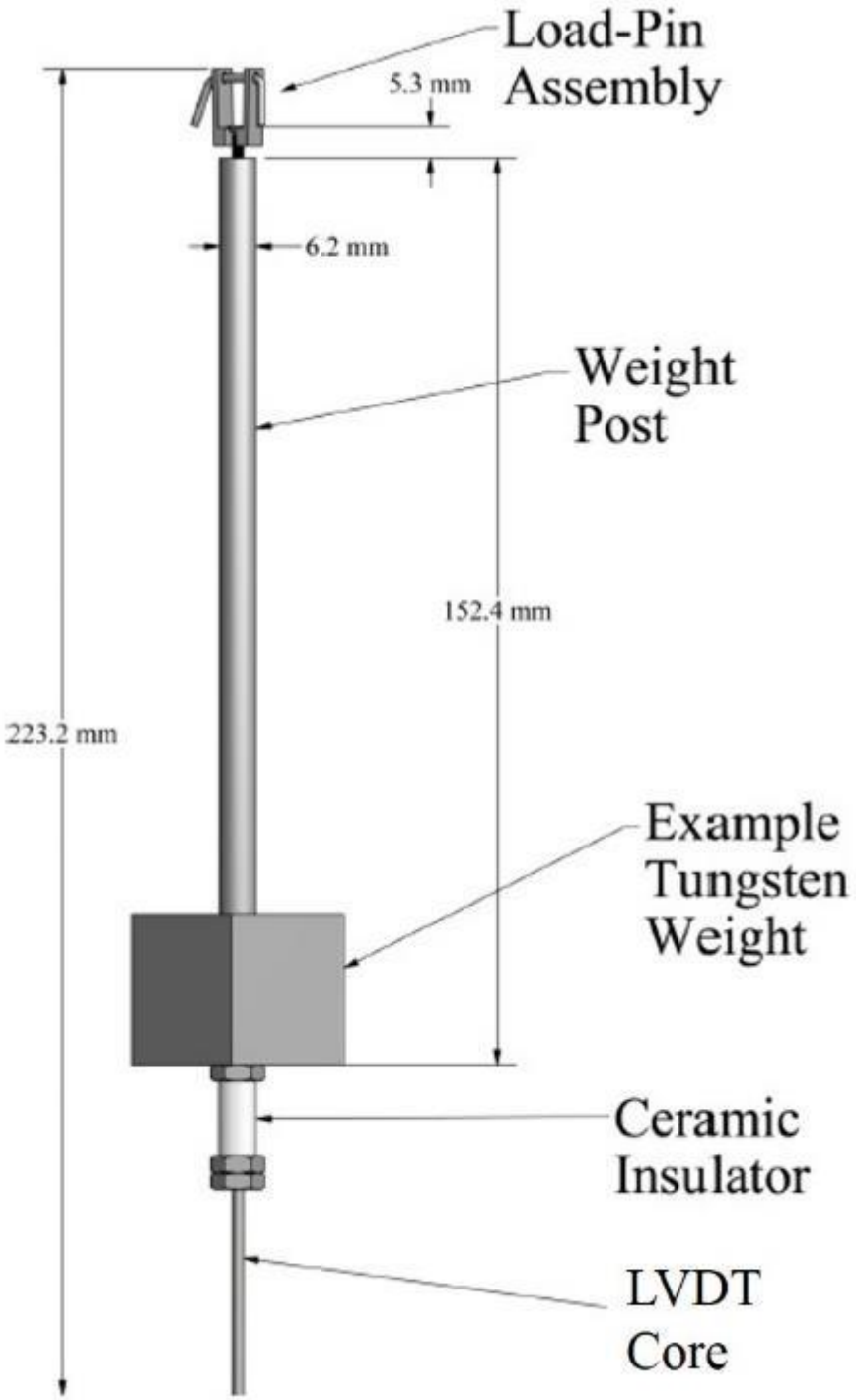

Figure 4.23 Schematic of the loading apparatus attached to the bottom of the sample.

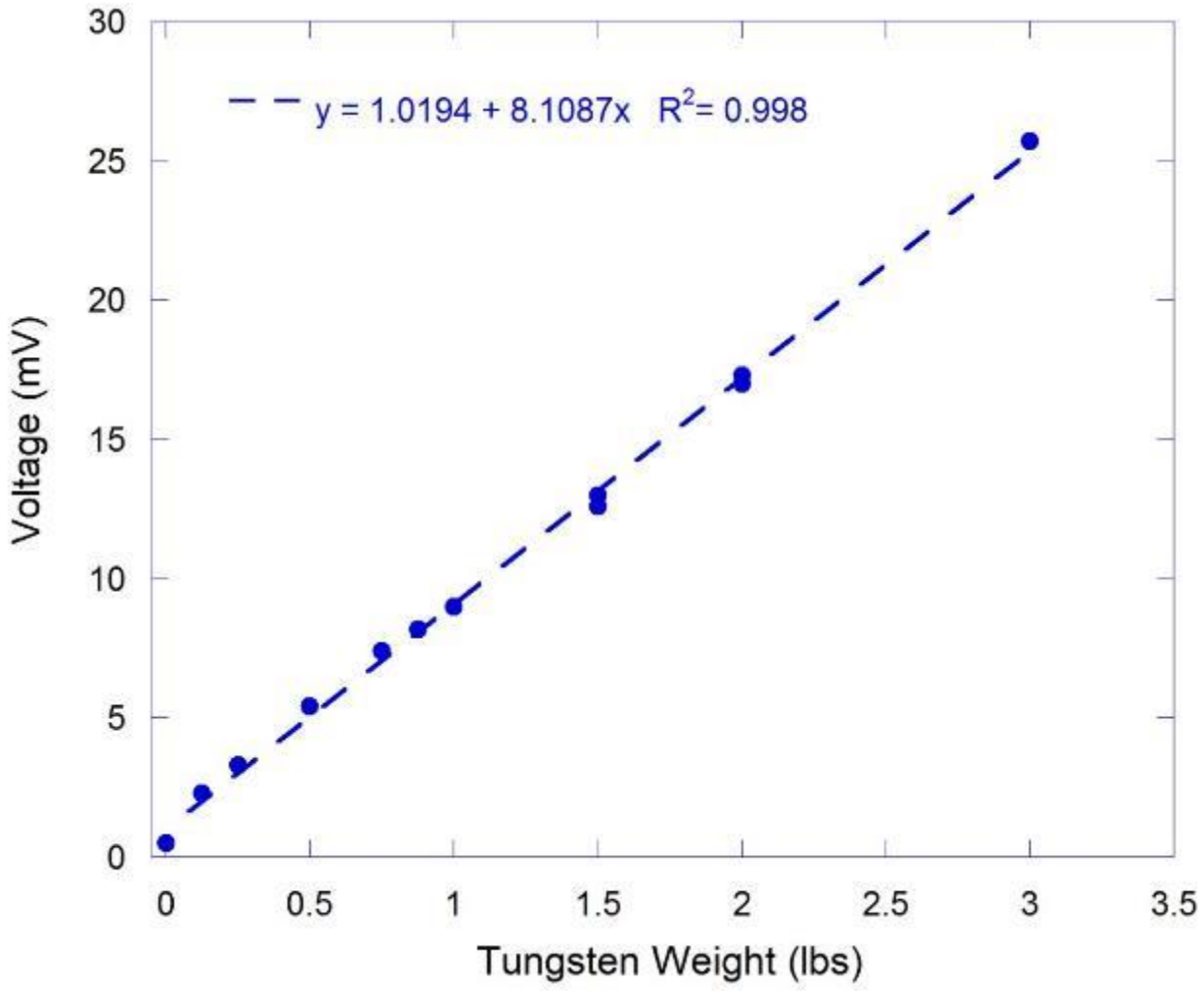

Figure 4.24 Calibration of the load cell voltage output as a function of tungsten weight mass.

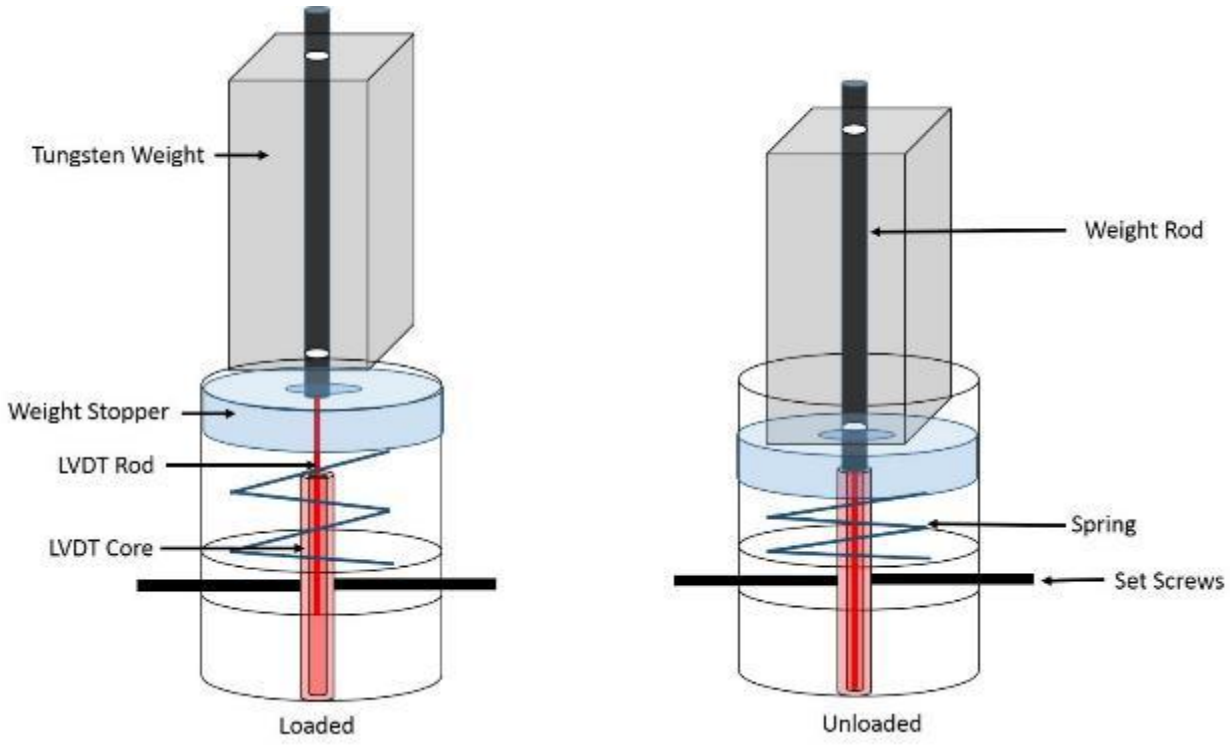

Figure 4.25 Schematic of the loading tower inside the bottom irradiation creep chamber. The loading tower is used to align the LVDT and provide buffer for the tungsten weights for sudden unload.

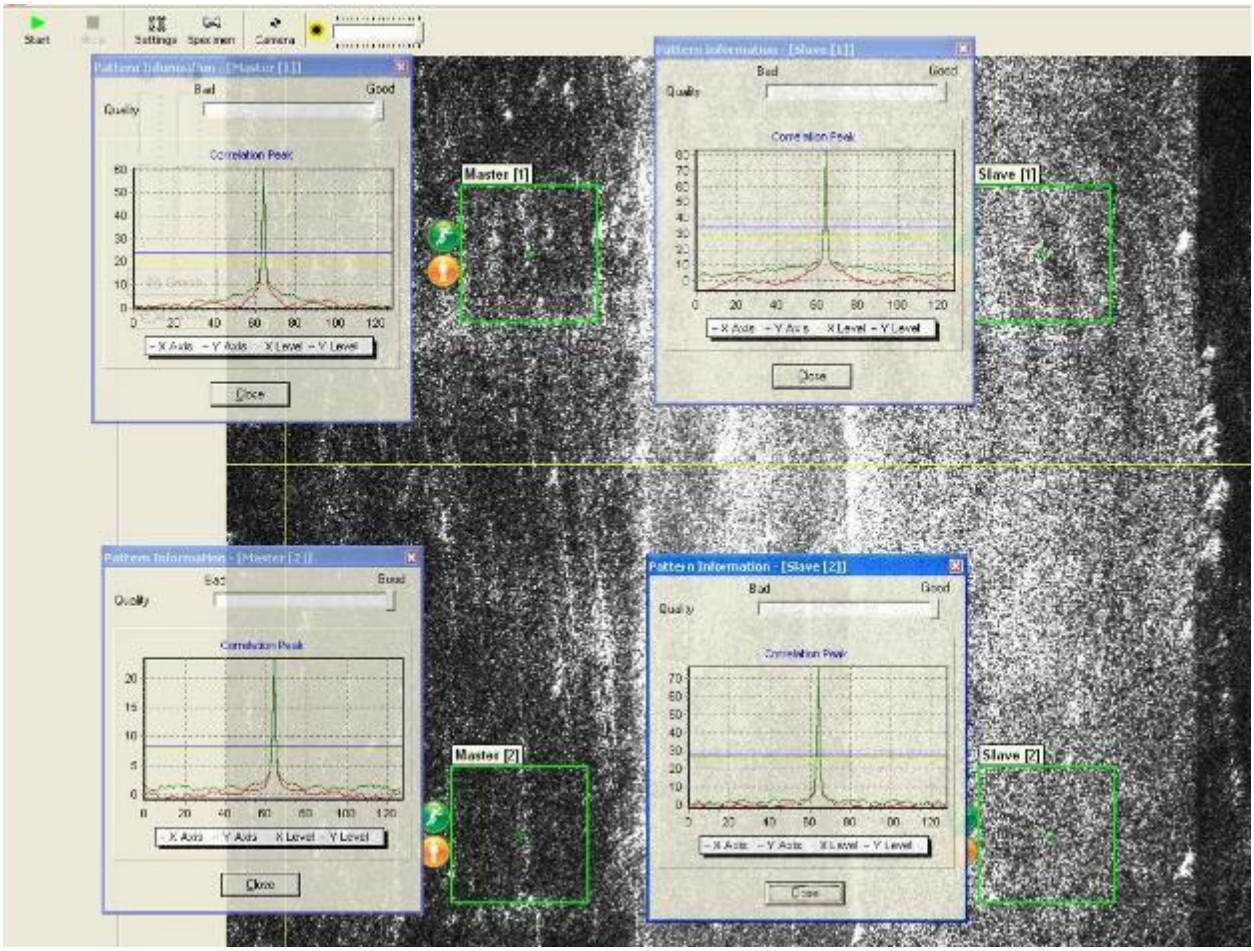

Figure 4.26 Screenshot of the LSE speckle patterns and correlation peaks for an irradiation creep experiment.

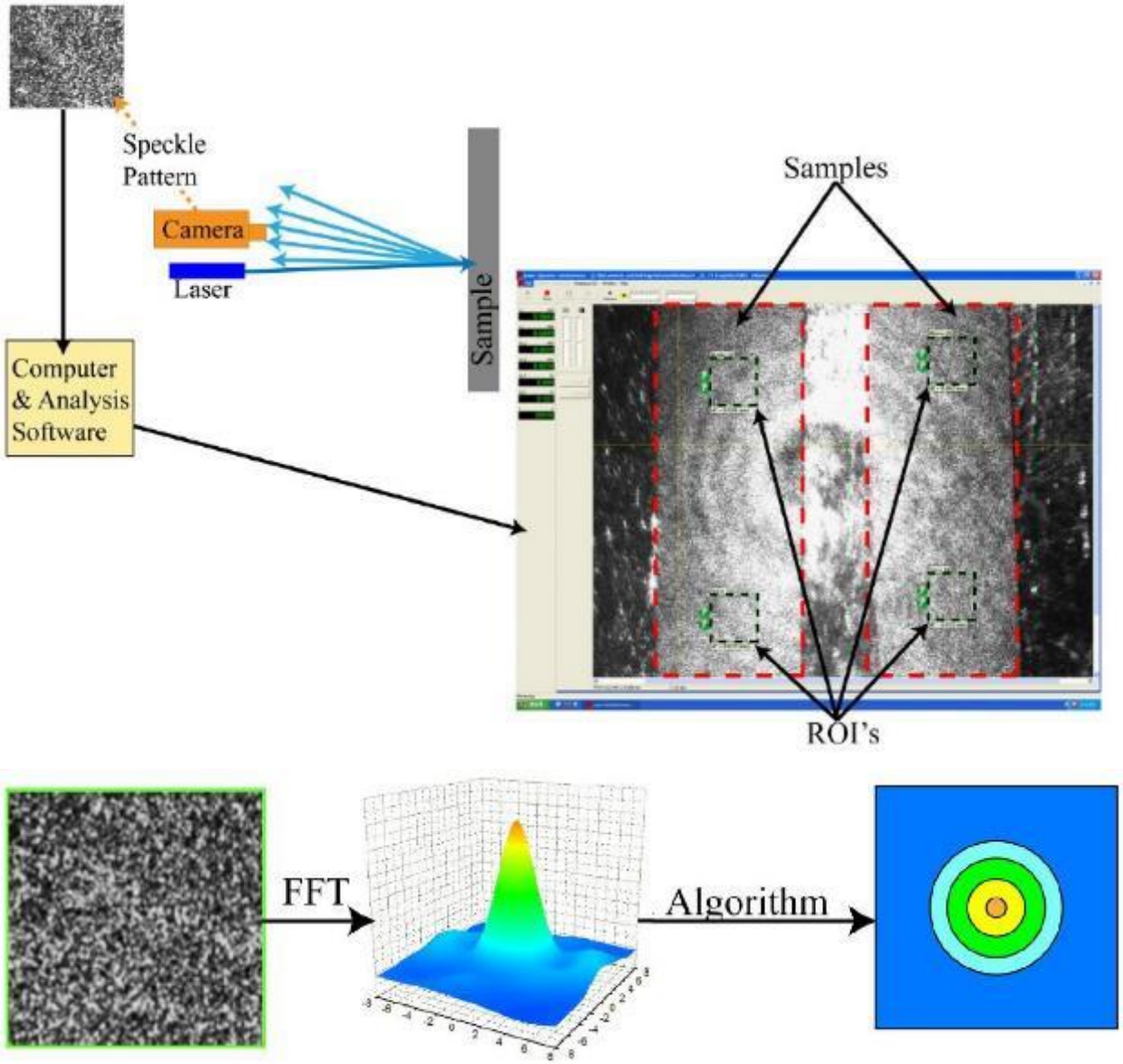

Figure 4.27 Schematic of the principle behind the LSE strain measurement system.

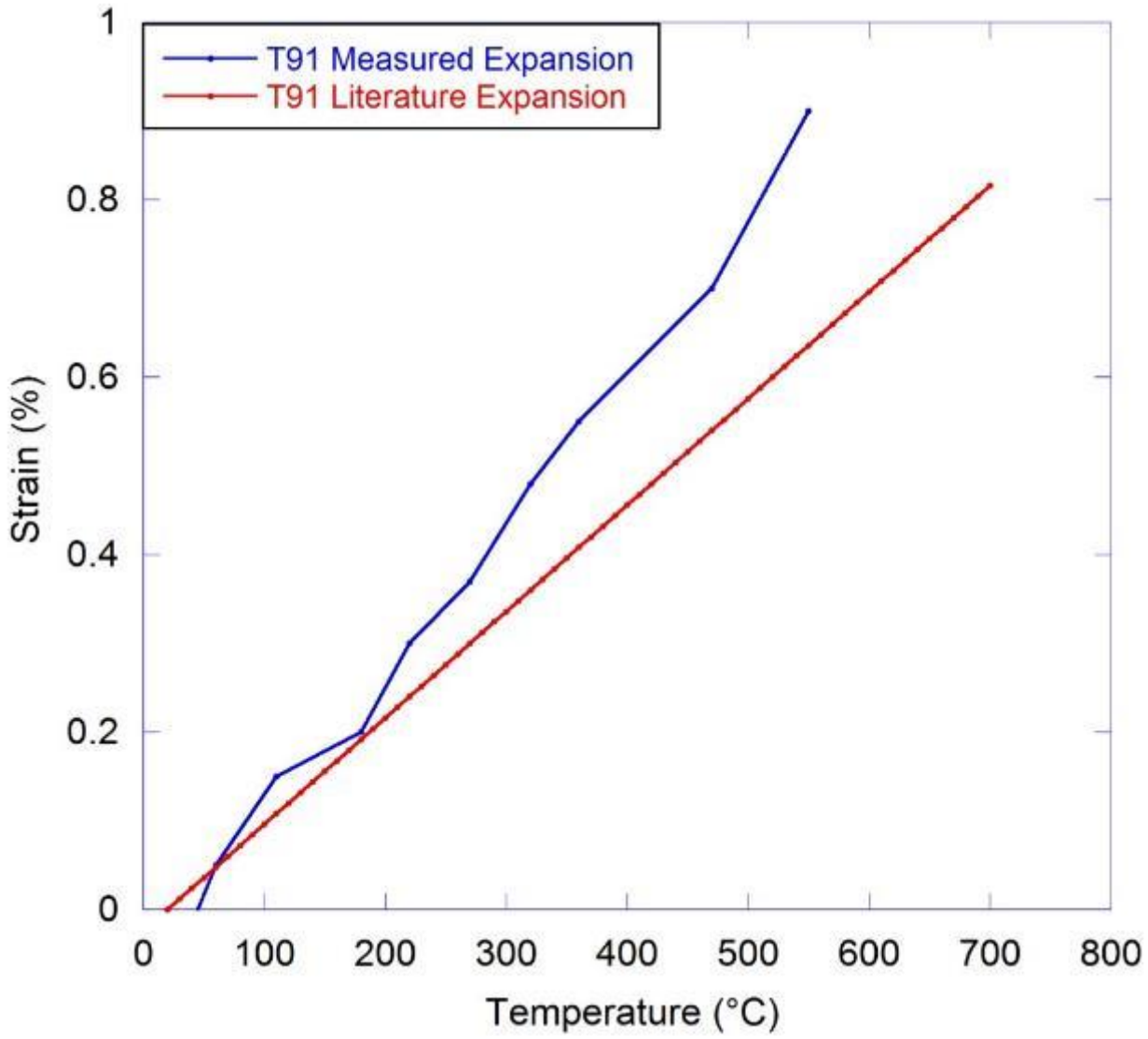

Figure 4.28 Thermal expansion results of T91 as a function of temperature compared to those predicted in literature [42].

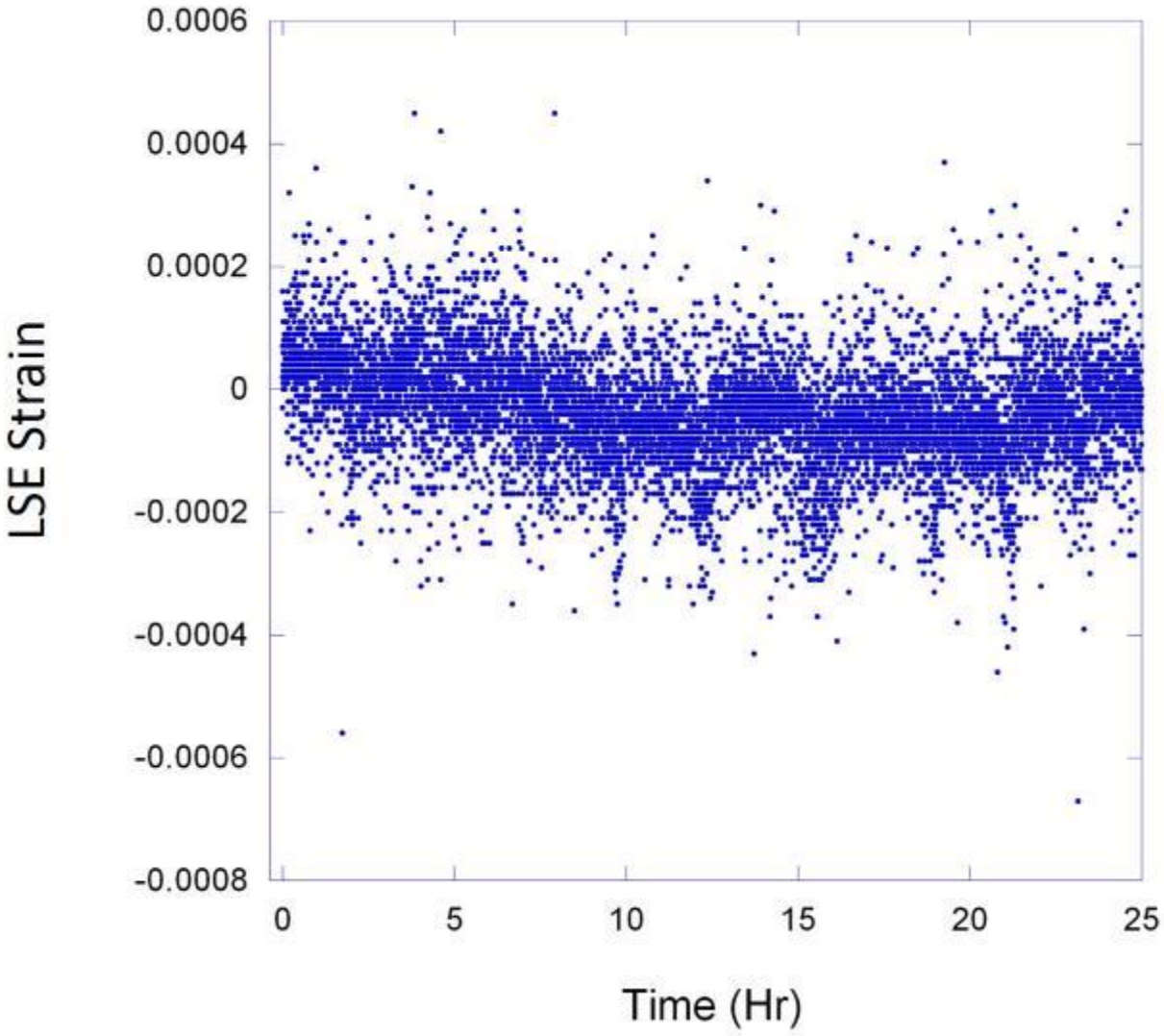

Figure 4.29 Noise of the LSE over 25 hours with pump vibration at room temperature. The LSE noise is on the order of ±0.02%.

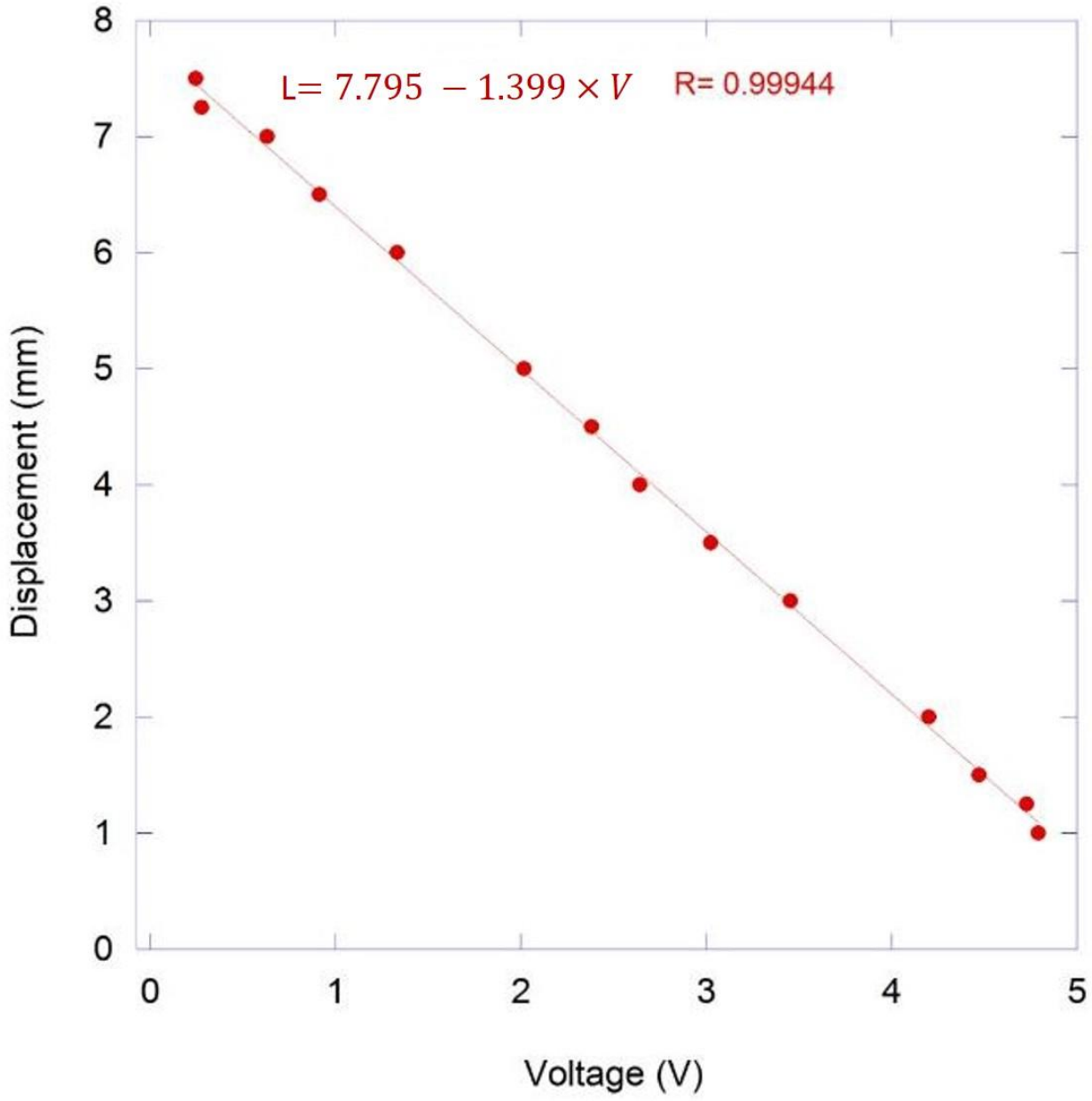

Figure 4.30 Displacement to voltage relationship of the LVDT as obtained by calibration blocks.

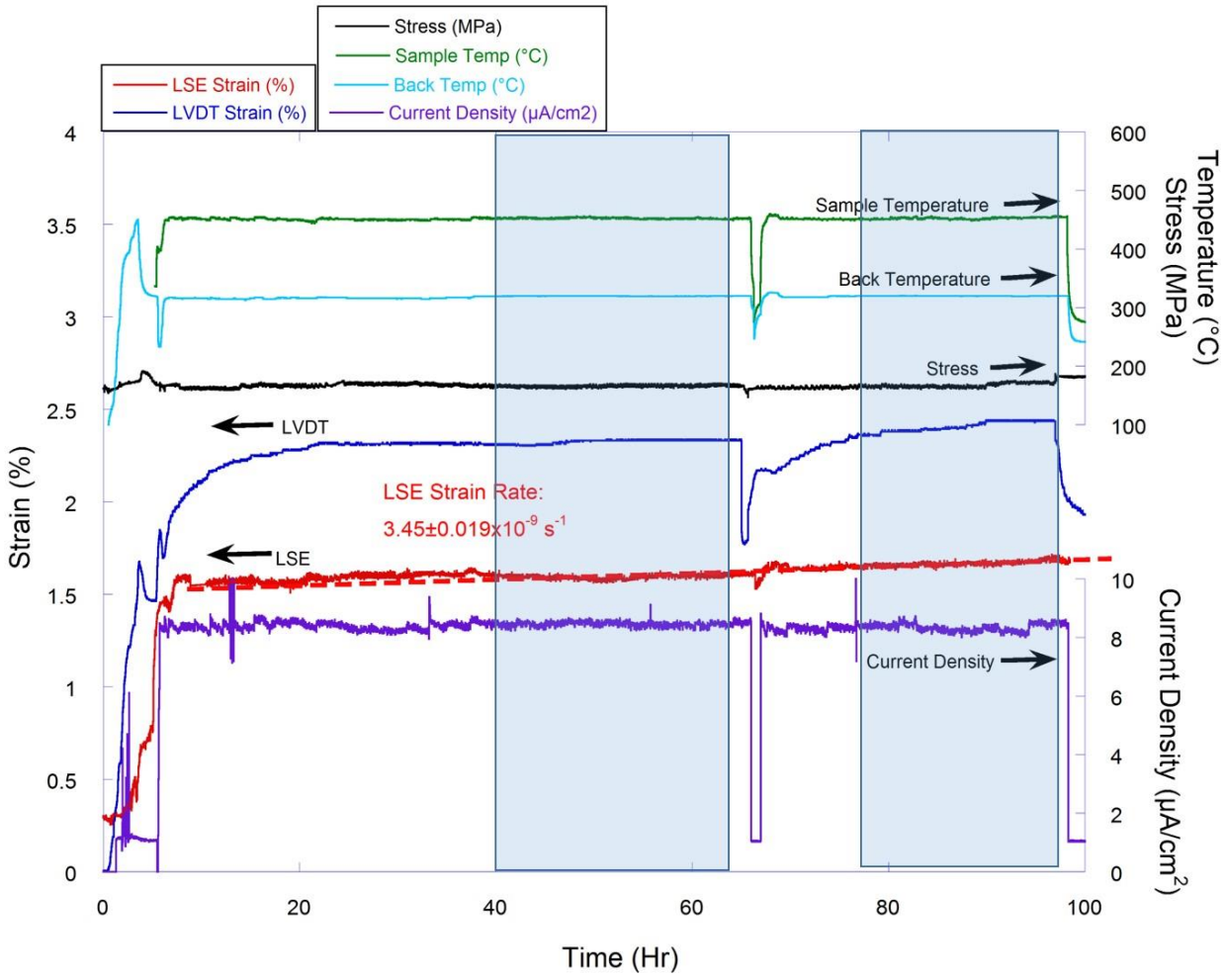

Figure 4.31 Irradiation creep experiment with power outages. The portions where LVDT showed stable behavior is highlighted. Only the LSE data from the highlighted portions were used to calculate the strain rates.

A - LVDT Ground

B - LVDT Input Voltage

C - LVDT Output Voltage

D - Load Cell Ground

E - Load Cell Input

F - Load Cell Output

G - Load Cell Signal Conditioner Input

H - Load Cell Signal Conditioner Output

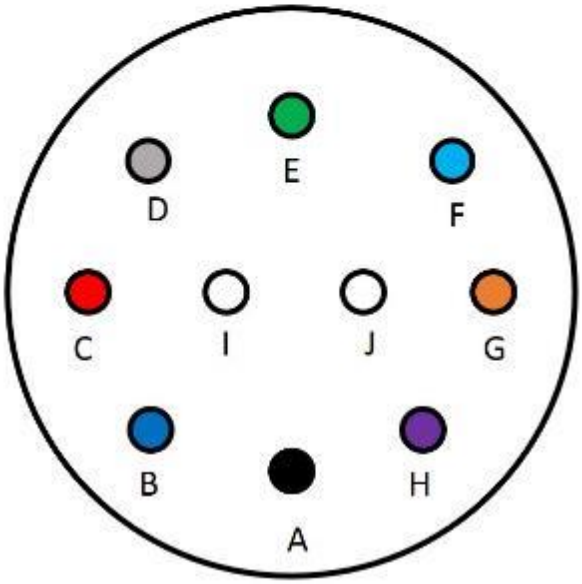

Figure 4.32 Color coded schematic of the 10 pin feed-through used as input/output connection for the LVDT and load cell.

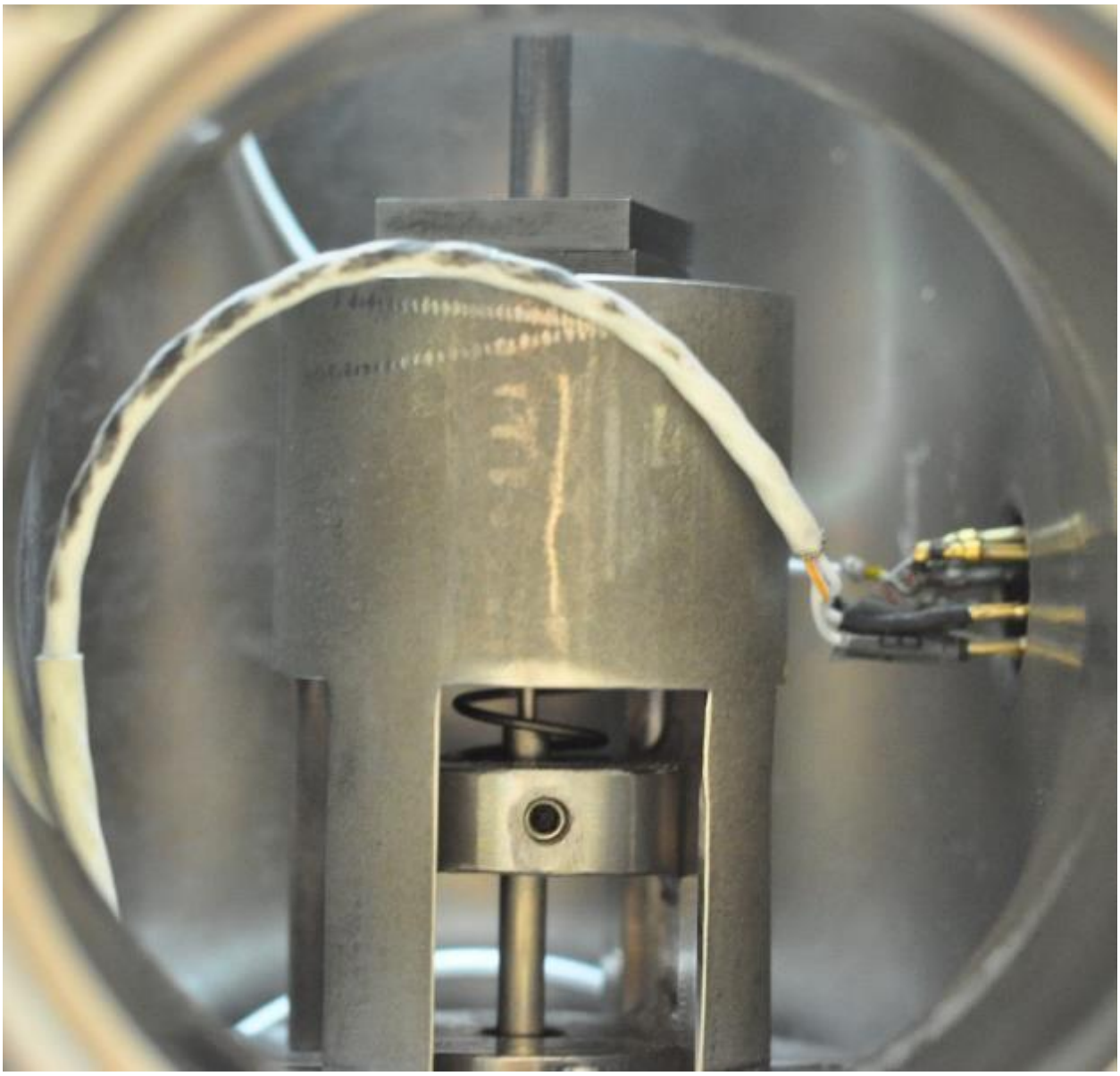

Figure 4.33 Inside of the bottom creep chamber with the LVDT and load cell pins connected to the feed-through.

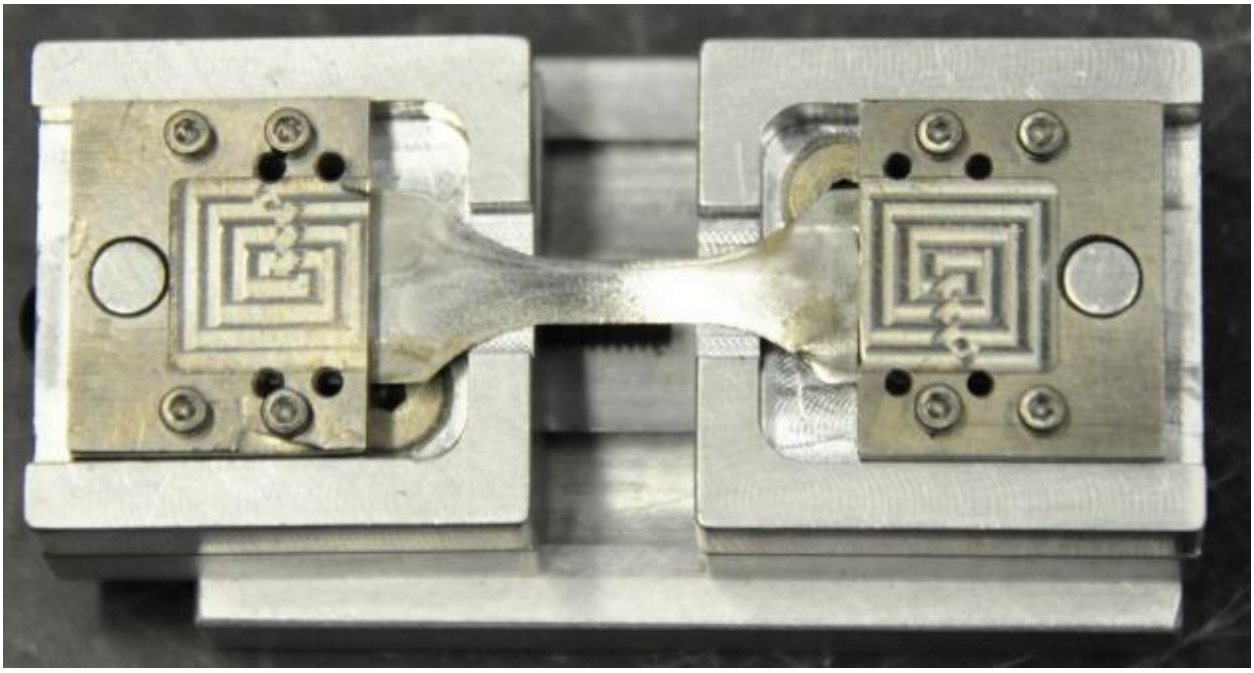

Figure 4.34 Irradiation creep sample clamped in the sample alignment rig.

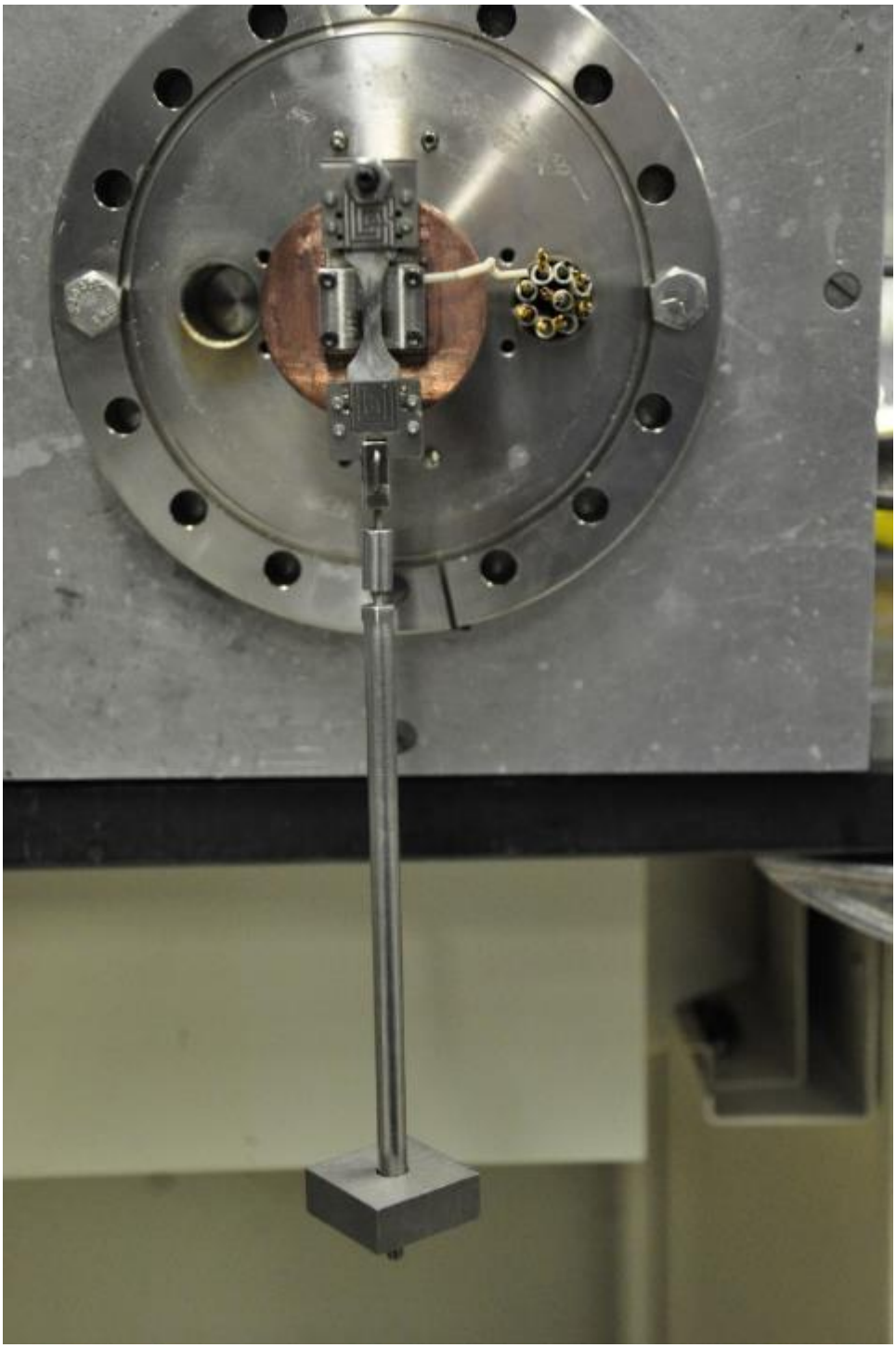

Figure 4.35 Bench-top loading to ensure sample clamp integrity and sample alignment to the indium heat sink.

a)

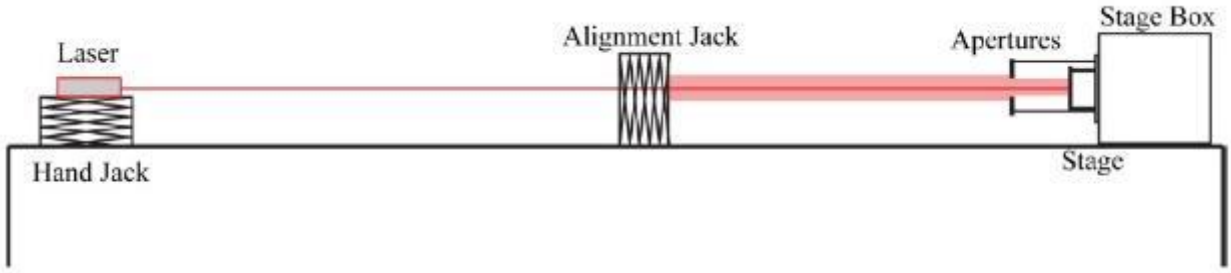

b)

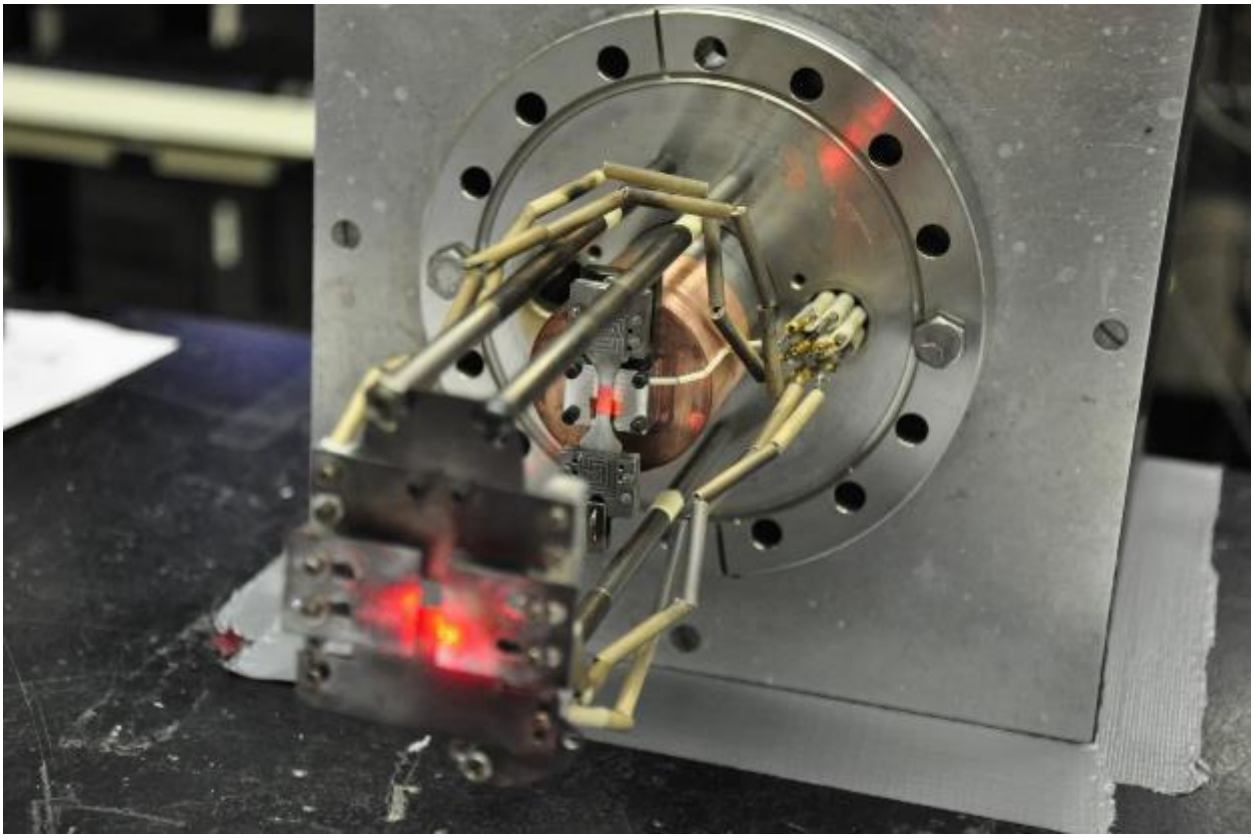

Figure 4.36 Laser beam alignment on the bench-top to ensure proton beam strikes sample gage length during irradiation a) schematic of alignment setup, b) picture of stage during alignment.

4.3 Irradiation Creep Strain Rate Analysis

Determining a strain rate from a creep curve was not a trivial matter. For ferritic martensitic steels, it was documented that no clear secondary creep was observable, but the creep rate will constantly decrease until it reached a minimum value, and then go into tertiary creep [34]. In order to capture the relevant transient microstructure, the microstructure analysis needed to be done before the strain rate hits the minimum creep rate. However, for adequate comparison of strain rate data under different conditions, there must be a standardized method for determining when the sample has entered into a regime where strain rate measurements can be made. The strain rates were determined by linear statistical fits to the sample strain over time. The errors in the strain rate were given by the statistical analysis in combination with zero-strain bench-top experiments used to determine measurement error. This section illustrated both the method for obtaining the irradiation creep strain rate of each sample, as well as the error analysis that accompanied that data.

4.3.1 Creep Rate and Error Determination

A typical strain vs. time curve of an irradiation creep experiment is illustrated in Figure 4.37. The transient behavior at the start of irradiation can be easily observed in all the data collection systems. Because the LVDT measurements took into account the effect of the entire experimental system, the LVDT transient was used to determine whether the creep system has reached a steady state. This was achieved by taking the instantaneous creep rate of the LVDT data over one hour for every hour, and plotted the changes in the creep rate. When the changes in the creep rate fell below an order of magnitude of the measured strain rate, the rate was considered to have reached a quasi-steady state such that rigorous statistical analysis may be done on the data henceforth. The normalized change in strain rate as a function of time is plotted in Figure 4.38. It was observed that in general, the system consistently reached a quasi-steady state at around 40 hours after the start of irradiation. The 40 hours was needed for the liquid indium to recover from the thermal instabilities induced by the proton beam. Other transients

such as vibrations as a result of changing pressure were also eliminated by only considering LSE data after 40 hours.

The strain data from the LSE taken after 40 hours until end of irradiation was used as input for the PRISM™ statistical analysis program. The analysis program would take in two data columns, x being time in seconds, and y being strain in percent as measured by the LSE. The analysis program generated a best linear fit of the data with the slope being the strain rate measured in percent per second. This strain rate from the linear fit is taken to be the characteristic strain rate of the sample for that specific irradiation condition.

The PRISM™ program utilized the Gauss-Markov formula to put the linear model through Chi squared testing in order to arrive at a set of constants that will minimize the variance. The Chi squared analysis consisted of first choosing a χ^2 value such that there was an equal chance that the next measurement taken will fall above or below the predictive model. The χ^2 value was derived by the following equation [76]:

$$\chi^2 = \sum \frac{(y_i - Y_i)^2}{V_i} \tag{4.2}$$

Where y_i is the observed value of y, Y_i is the predicted value of y, and V_i is the variance of y_i. For a linear line fit. Y_i is derived by the following equation:

$$Y_i = A + B \cdot x_i \tag{4.3}$$

Combining the two equations, Equation 4.1.1 becomes the following:

$$\chi^2 = \sum \frac{(y_i - A - B \cdot x_i)^2}{V_i} \tag{4.4}$$

The optimized constants A and B were found by taking the derivative of χ^2 with respect to A and B. The derivatives will generate two simultaneous equations that could be solved numerically.

$$\frac{\delta \chi^2}{\delta A} = 0 = \sum \frac{-2}{V_i} (y_i - A - B \cdot x_i)^2 \tag{4.5}$$

$$\frac{\delta \chi^2}{\delta B} = 0 = \sum \frac{-2x_i}{V_i} (y_i - A - B \cdot x_i)^2 \tag{4.6}$$

Through matrix manipulation by Cramer's rule, the simultaneous equation can be solved analytically, and the solutions were described below:

$$A = \frac{\sum({x_i}^2/V_i)\sum(y_i/V_i) - \sum(x_i/V_i)\sum(x_i y_i/V_i)}{\sum(1/V_i)\sum({x_i}^2/V_i) - (\sum(x_i/V_i))^2} \tag{4.7}$$

$$B = \dot{\varepsilon} = \frac{\sum(1/V_i)\sum(x_i y_i/V_i) - \sum(x_i/V_i)\sum(y_i/V_i)}{\sum(1/V_i)\sum({x_i}^2/V_i) - (\sum(x_i/V_i))^2} \tag{4.8}$$

The solution to the Gauss-Markov formula was an iterative one. The PRISM™ program had an algorithm to pick the values of the variance to calculate the constants. The constants were then used to inform the model such that a new set of variance can be calculated. The program iterated through the constants until all the variances converge. The final B calculated was the slope of the line fit which corresponds to the characteristic strain rate of the sample.

The statistical analysis of the characteristic strain rates also calculated the statistical error that was associated with the creep rates. The Gauss-Markov analysis used to calculate the strain rate also defined the error of the calculated constants by its variance. The statistical error of the strain rate was derived as follows:

$$\epsilon_{\dot{\varepsilon}} = \frac{\sum(1/V_i)}{\sum(1/V_i)\sum({x_i}^2/V_i) - (\sum(x_i/V_i))^2} \tag{4.9}$$

The statistical error on the strain rate was the function of the combination of noise of the entire system for a single experiment, including the fluctuations in temperature, beam current, pump vibration, light saturation, and loss of correlation over time. It did not include the error that arise between separate experiments. The largest error that dominated the difference between experiments was due to the thickness variation of the sample that will create uncertainty in the applied stress. The stress of the sample was derived by the formula below:

$$\sigma = \frac{mg}{tw} \tag{4.10}$$

where *m* is the mass of the tungsten weights as measured by scale, *g* is the acceleration constant of gravity, *w* is the width of the sample at the gage length, and *t* is the nominal thickness as measured by micrometer.

The percent error can be found by normalizing the error to the applied stress, which was equivalent to the percent error of the thickness variation.

$$\pm\frac{\Delta\sigma}{\sigma}=\pm\frac{\Delta t}{t} \tag{4.11}$$

Section 4.1.2 described in detail the sample preparation method and observed sample thickness variation to be around ±2μm. For a standard sample with target thickness of 35μm, ±2μm error will result in around ±6% error in the applied stress.

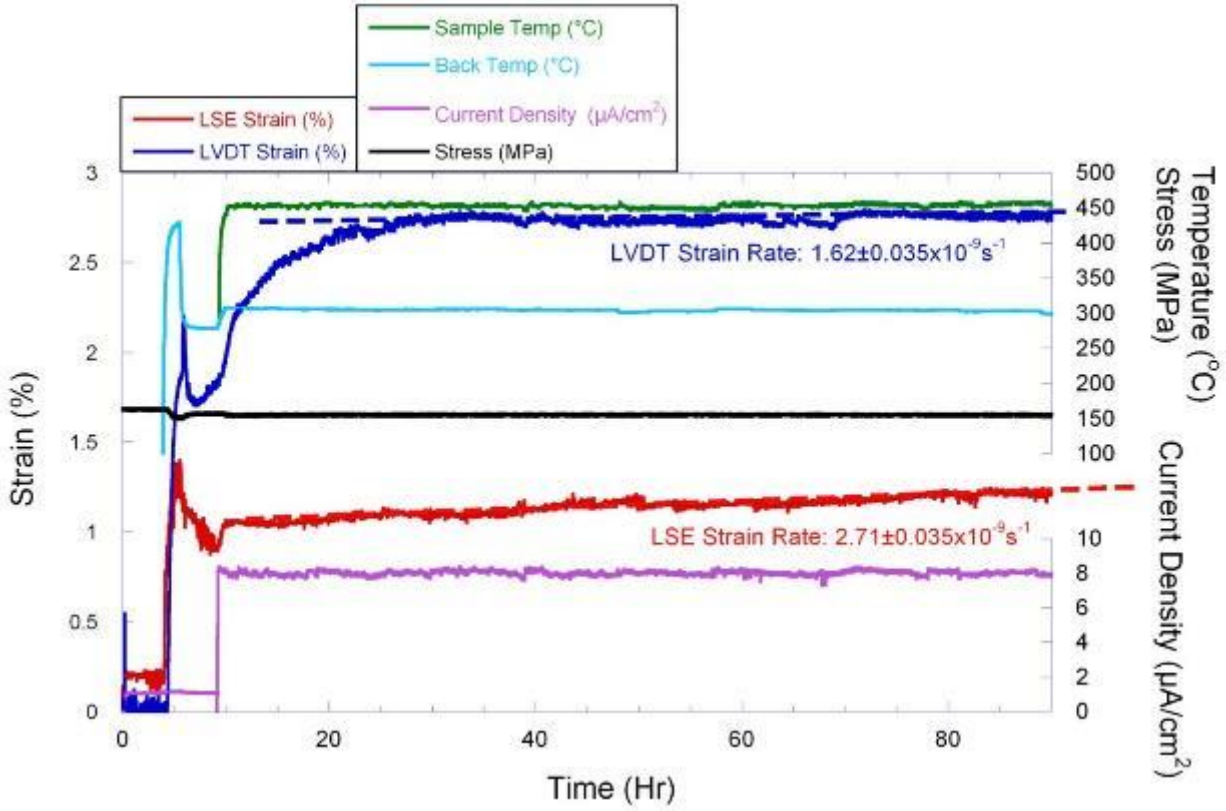

Figure 4.37 Representative creep curve of an irradiation creep experiment, including the strain from both LVDT and LSE, temperature, stress and beam current density as a function of time.

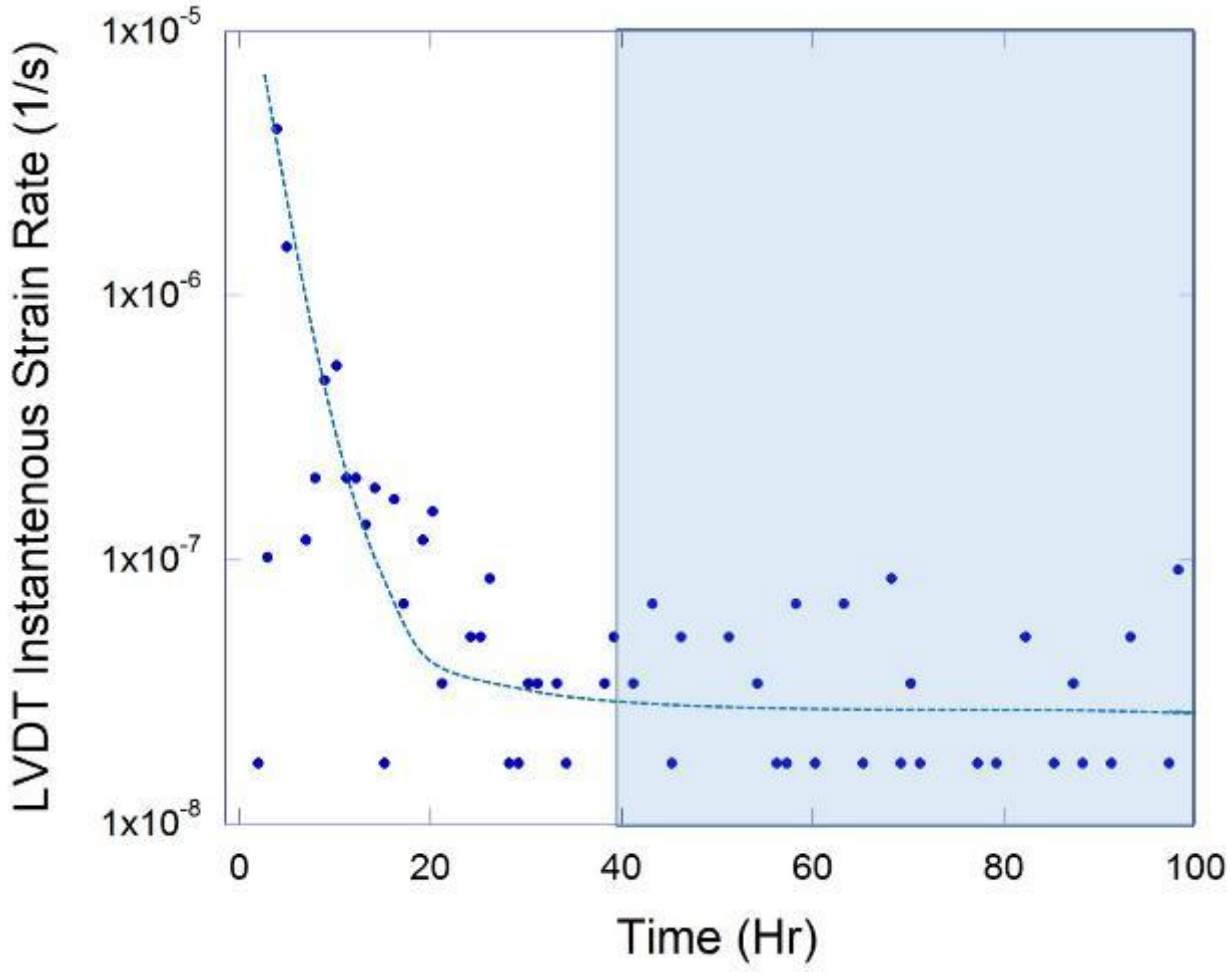

Figure 4.38 Instantaneous strain rates corresponding to the LVDT creep curve. Strain rate is seen to decrease and reach a relative steady state up to 40 hours.

4.4 Irradiation Creep Microstructure Analysis

Microstructure analysis of the irradiated creep samples was an important and intricate aspect of determining irradiation creep mechanisms. The microstructure analysis was conducted with Transmission Electron Microscope (TEM), and aimed specifically at imaging dislocation loops and dislocation lines to quantify any anisotropy formed under irradiation creep. The unique objective of the TEM analysis in this project required careful tracking of the sample orientation through all stages of analysis. This chapter will describe in detail the processes of 1) TEM sample preparation, 2) TEM dislocation loop imagining procedure, 3) Dislocation loop analysis procedure.

4.4.1 TEM Sample Preparation

Focused Ion Beam (FIB) milling was the method of choice for TEM sample preparation for this project. Compared to conventional jet thinning method, FIB samples will have better uniform thickness over the entire sample so a good image can be obtained even at high tilt angles. FIB also had the advantage of precisely identifying the orientation and location of the sample. This was essential in dislocation loop analysis where the direction of the tensile axis must be clearly identified under the TEM.

Figure 4.39 illustrates how the FIB samples were made from the irradiation creep samples. A 3mm by 5mm rectangular section was cut by diamond blade from the irradiated area, with the 5mm length being parallel to the tensile axis. A 15μm by 5μm FIB lift-out sample was then cut out from the section with the 15μm length aligned to the tensile axis.

The FIB first deposited a layer of platinum that was about 20μm by 2μm over the bulk sample surface to identify the TEM sample edge and protected the sample surface. A 20keV gallium ion beam was then used to dig out 15μm by 20μm trench that was 10μm deep on both sides of the platinum deposition. Once the trench was made, the energy of the gallium ion beam was dropped down to about 10keV to precisely cut out the FIB sample from the bulk. A lift-out needle was inserted and the sample attached to the needle via platinum deposition. The FIB sample was then lifted out of the bulk and attached to a half TEM grid. Once the FIB sample was

attached, it was thinned down to a final thickness of 100nm using 5keV beam. A typical FIB sample after final thinning is shown in Figure 4.40.

The FIB samples for this project were prepared on the Nova SEM located in the Electron Microbeam Analysis Laboratory (EMAL) at University of Michigan, the Quanta SEM located in Center for Materials and Sensor Characterization (CMSC) at University of Toledo, and some were professionally manufactured by Semion. Co.

4.4.2 TEM Dislocation Loop Imaging Procedure

TEM imaging of dislocation networks and dislocation loops required understanding of the nature of dislocations in the bcc martensitic structure. Many theoretical calculations had been done to predict the nature of the dislocation loops that form in FM steels [77], [78]. Some experimental observations on irradiated FM alloys [41] also provided clues to what imagining conditions should be used to get unique orientation information.

There was ample evidence to suggest that dislocation loops in FM steels were dominated by a_o<100> large loops with lower density of smaller $a_o/2$<111> loops. These loops can be seen in the TEM under a variety of conditions. Figure 4.41 illustrates the orientation of the two loop types when tilted to one of the major zone axis for a bcc crystal lattice. However, depending on the g vector chosen for the two beam condition, some of the loops will satisfy the g·b=0 invisibility criterion and will not show up under the TEM [79].

By looking at the possible combinations of g·b and orientations, the <100> zone axis double beam with g=<011> was chosen as the best imaging condition for determining orientation of the dislocation loops with respect to the tensile axis. Under this condition, two sets of a_o<100> loops were viewed completely edge on, allowing precise measurement of the loop plane angle to the tensile axis. It was the image condition where two sets of perpendicular loops in a single grain were both clearly visible, so a direct comparison between two orientations can be made. If the grain was oriented such that one set of edge on loops saw more of the tensile stress than the other, shown in Figure 4.42 as blue rectangles compared to the red rectangles, a ratio of the loops can be taken as a measurement of loop anisotropy for that specific grain orientation. This method was chosen for understanding the dislocation loop distribution with respect to the tensile stress within a single grain. A representative TEM image viewed under the two beam condition with g=<011> is shown in Figure 4.43.

The dislocation loop images were taken on the JEOL 3011 and JEOL 2010 at Electron Microbeam Analysis Laboratory (EMAL) at University of Michigan, the FEI Tecnai located in NanoTech User Facility (NTUF) at University of Washington, and the JEOL 2100 at Boise State Center for Materials Characterization (BSCMC) at Boise State University. The TEMs available at these facilities have double tilt capability to high angles that was required to reach the specific imaging condition outlined in this project. The following procedure was developed to most efficiently obtain the TEM image of value for orientation analysis:

- Align the TEM at 125k magnification to ensure good image quality
- Find the sample, take low magnification image of the sample length to identify the tensile direction.
- Increase magnification to 25k, focus the transmission beam, and turn to diffraction mode to obtain Kikuchi patterns.
- Look for Kikuchi patterns that are close to major zone axis by moving around the sample.
- Once a satisfactory Kikuchi pattern has been identified, put in the objective aperture in bright field mode to identify which grain produced the pattern.
- Tilt the sample while keeping track of the grain in question. The contrast should get darker as the grain is tilted towards the zone axis.
- Occasionally recheck the Kikuchi pattern to ensure the direction of the tilt moves the zone axis closer to the center of the screen.
- Take a diffraction pattern of the zone axis to ensure it is <100>. The <100> zone axis diffraction pattern is shown in Figure 4.44.
- Tilt off the zone axis in the <110> direction until the diffraction pattern shows equal intensity between the transmission beam and the g=110 diffraction spot.
- Take a diffraction pattern of the two beam condition, and center the objective aperture on the transmission beam for bright field image.
- Every picture taken will be associated with both the x and y tilt angles of the TEM for the sample to reach its <100> zone axis.

4.4.3 TEM Dislocation Loop Analysis Procedure and Error Analysis

Dislocation loop analysis in this project extracted information on the loop density, loop size, and orientation of the loop to the tensile axis. Every TEM image were analyzed using the ImageJ® software in the original .dm3 format so all the information during the TEM imaging process were preserved. The size of the loops were measured directly through the software, and the number of loops for each TEM image were counted and divided by the area and thickness of the image to arrive at a loop density.

Determining the loop orientation was especially difficult, because the bcc crystalline lattice of any specific grain were at arbitrary angles to the tensile axis as shown in Figure 4.45. The orientation of the dislocation loop to the tensile axis were defined by the angle θ between the normal vector to the loop plane and the tensile axis. This angle can be found by the dot product of the two vectors expressed in the same basis.

The basis chosen for this project was one where the electron beam direction was along the z-axis, hereon called the imaging basis. When the sample was tilted to the <100> zone axis, the three <100> directions will become the xyz primary axis, allowing for analysis to take advantage of the symmetry in the crystal lattice. In this basis, the edge on dislocation loop normal vectors will not have any z-component, and the vector that described the tensile axis will need to be calculated. This was done by rotating the tensile axis vector by the appropriate Euler angles to express its vector orientation in the imaging basis. The series of rotations were defined by the rotational matrix described below:

$$R_x = \begin{bmatrix} 1 & 0 & 0 \\ 0 & \cos(\theta_x) & -\sin(\theta_x) \\ 0 & \sin(\theta_x) & \cos(\theta_x) \end{bmatrix} \tag{4.12}$$

$$R_y = \begin{bmatrix} \cos(\theta_y) & 0 & \sin(\theta_y) \\ 0 & 1 & 0 \\ -\sin(\theta_y) & 0 & \cos(\theta_y) \end{bmatrix}$$

θ_x is the value of x-tilt, and θ_y is the value of y-tilt. Similarly, the tensile axis in the coordinates before tilting was represented by the following vector:

$$T_{BT} = \begin{bmatrix} \cos(\theta_T) \\ \sin(\theta_T) \\ 0 \end{bmatrix} \tag{4.13}$$

θ_T is the angle of the tensile axis to the x-axis before tilting to the zone axis.

The TEM sample was made so the tensile direction was easily identifiable and lied on the x-y plane, hence the z component of the tensile axis was 0 in the standard coordinates. By applying the rotational matrix to the tensile axis, the resulting vector were represented in the coordinates of the image basis rather than the coordinates before tilting.

$$T_{AT} = R_x \times R_y \times T_{BT} \tag{4.14}$$

In addition to the tensile axis vector, the normal vector of the dislocation loops must also be defined. The vectors L denoted the normal vector of the loops in the imaging basis. The L vectors were unit vectors derived by the angle $\varphi_{<100>}$ as measured in ImageJ®.

$$L_{<100>} = \begin{bmatrix} \cos(\varphi_{<100>}) \\ \sin(\varphi_{<100>}) \\ 0 \end{bmatrix} \tag{4.15}$$

By knowing the vector of the tensile axis, the cosine of the angle θ were found by taking the dot product of the two vectors by the following equation.

$$\cos(\theta_{<100>}) = \frac{T_{AT} \cdot L_{<100>}}{|T_{AT}| \cdot |L_{<100>}|} \tag{4.16}$$

Both the tensile and loop normal vectors were unit vectors, therefore the denominator comes out to be unity. The equation can be simplified to the following.

$$\cos(\theta_{<100>}) = T_{AT} \cdot L_{<100>} \tag{4.17}$$

The angle determined from equation 4.4.7 was used as the independent variable to describe loop anisotropy. An angle of zero described the case where the normal vector of the loop was exactly in the tensile direction, meaning the loop plane was perfectly perpendicular to the tensile axis. Conversely, an angle of 90° described the case where the loop plane was parallel to the tensile axis. For a single grain, two sets of loops will have different angles to the tensile axis. The difference in loop density and loop size between the two sets of loops were used as the dependent variable to describe the anisotropy in the microstructure.

The error associated with the loop density was calculated using normal counting statistics as outlined in Knoll et al [80]. The counting error associated with the number n of dislocation loops counted were expressed as:

$$\epsilon = \sqrt{n} \tag{4.18}$$

The counting error propagated through the equations as the counts were converted into a density. Unlike the number densities, the dislocation loop size had a spectrum that will generally follow a normal distribution. Due to the resolution limit of the TEM, any dislocation loops smaller than 5nm was not counted but considered as a defect cluster, causing the distribution to be skewed to the right. However, the standard error of the mean can still be used to describe the bounds around the average loop size. The equation that bounds 95% confidence interval for the dislocation loop size is shown below:

$$SD = 1.96 \times \frac{\sigma}{\sqrt{n}} \tag{4.19}$$

The σ denotes the standard deviation of the loop size spectrum, and n is the total number of loops counted.

4.4.4 Other Microstructure Analysis Procedure

In addition to dislocation loops, dislocation network density and lathe grain size were also needed as input for detailed analysis of irradiation creep mechanisms. The dislocation network densities were imaged in the TEM on both <100> and <111> zone axis in double beam conditions to get strain contrast. The grain size measurements were made on low magnification TEM images with zero x and y tilt.

The method for determining dislocation network density was a statistical method outlined in Smith et al [81] utilizing equidistant circular grid to quantify the intersection points between the grid and the dislocation lines to obtain a planar density. The schematic of the dislocation network density analysis was shown in Figure 4.46. The probability p of a randomly oriented line segment intersecting a grid is derived from the length of the line segment L_i, and spacing of the grid d_c:

$$p = \frac{2}{\pi}\frac{L_i}{d_c} \tag{4.20}$$

If L_i were much smaller than d_c and L was made up of M segments of L_i, then the number of intersections will be pM, and Equation 4.4.10 becomes the following:

$$N = \frac{2}{\pi}\frac{L}{d_c} \tag{4.21}$$

The 2D planar density was derived from the total length of the line over the effective area of the grid with units of m^{-1}:

$$\rho_{2D} = \frac{L}{A} \tag{4.22}$$

For a circular grid with number of concentric lines n_c and spacing d_c, the effective area would be the following:

$$A = \pi(n_c d_c)^2 \tag{4.23}$$

Combining Equations 4.4.11-13 gave the following description planar density with units of m^{-1}:

$$\rho_{2D} = \frac{N}{2{n_c}^2 d_c} \tag{4.24}$$

Because there was a finite sample thickness in the TEM image, it was necessary to convert the planar density into a volume density. The length of the projection of a dislocation in a TEM image was related to the actual length by a factor of $2/\pi$. By taking into consideration of the dislocation projection, the volumetric density was the following with units of m^{-2}:

$$\rho_{3D} = \frac{N\pi}{4{n_c}^2 d_c t} \tag{4.25}$$

The average sub-grain diameter was estimated by using a variation of the linear intercept procedure as outlined by ASTEM E112 [82]. Because sample polishing and etching was not possible post irradiation creep, low magnification TEM images of 9000x and 7600x were used instead of SEM images. For each image, four lines were randomly laid on top of the image. The intersections of the random lines for the sub-grain boundaries were counted. The average sub-grain diameter d_{grain} can be determined by the following equation

$$d_{grain} = \frac{N_{grain}}{L_{grain}} \tag{4.26}$$

where N_{grain} is the total number of intersects the lines made to the sub-grain boundary, and L_{grain} is the total length of the lines.

The values measured using these analysis methods were used as inputs for irradiation creep equations of various mechanisms to provide a link between theoretical mechanisms and empirical data.

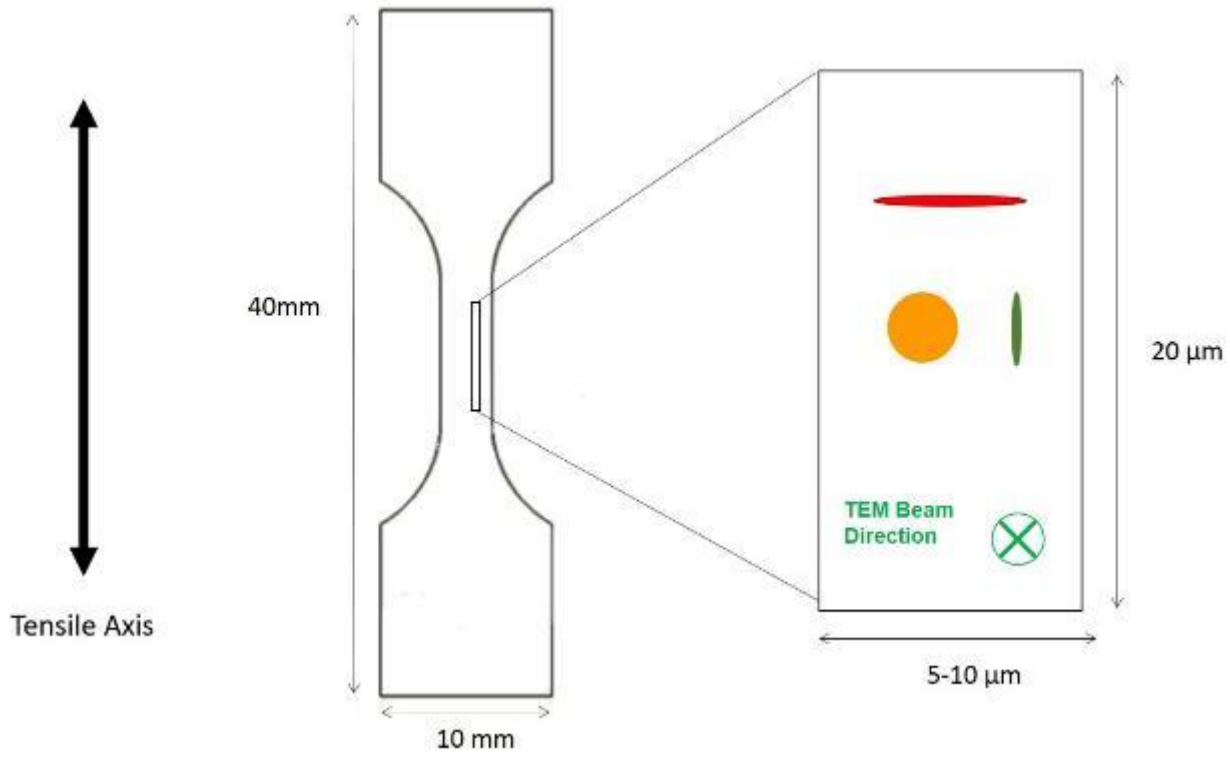

Figure 4.39 Schematic of the orientation of how FIB sample are machined and lifted out of the irradiation creep dog-bone sample.

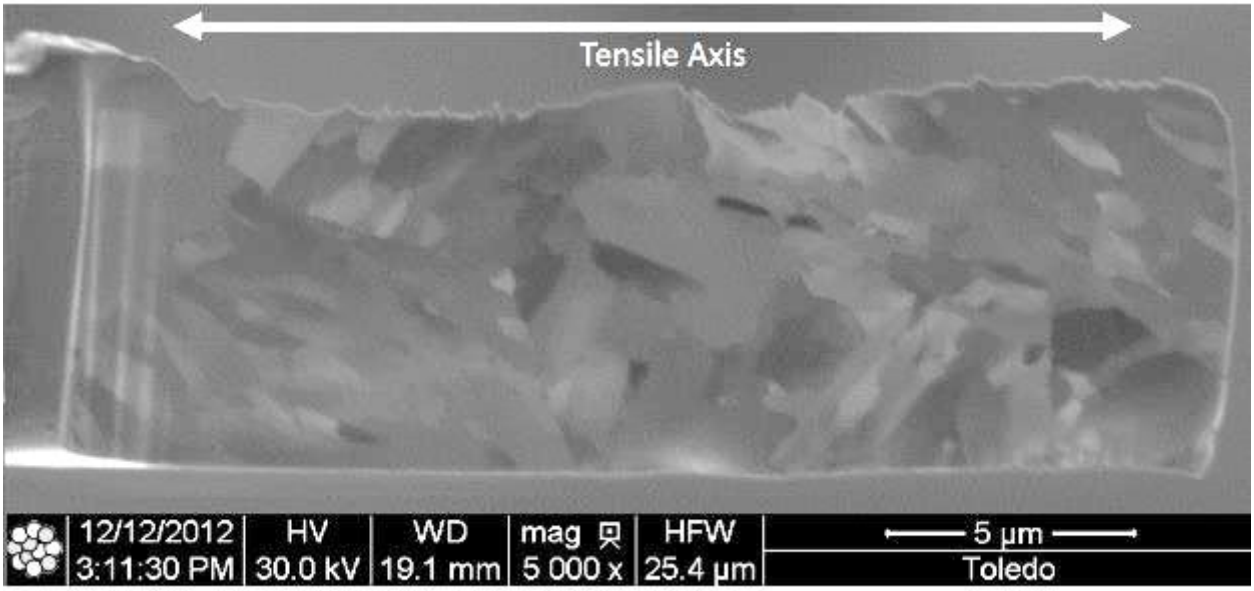

Figure 4.40 Heavy ion image of a FIB sample after it has been lifted out of the irradiation creep sample.

a)

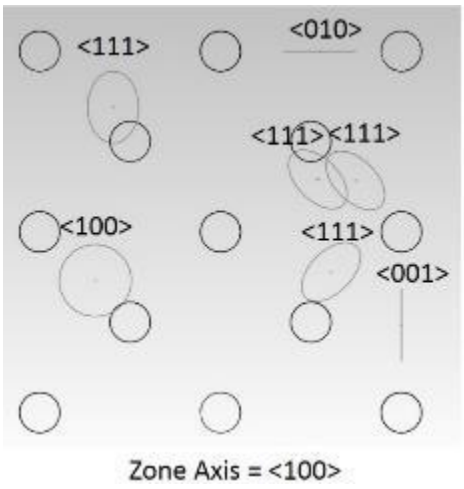

b)

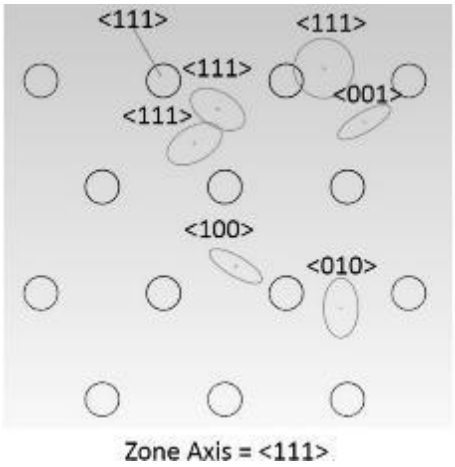

c)

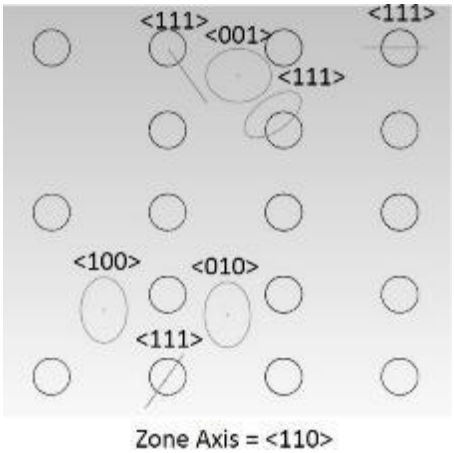

Figure 4.41 Schematic of loop images for both <100> and <111> loops as seen from a) <100> zone axis, b) <111> zone axis, c) <110> zone axis.

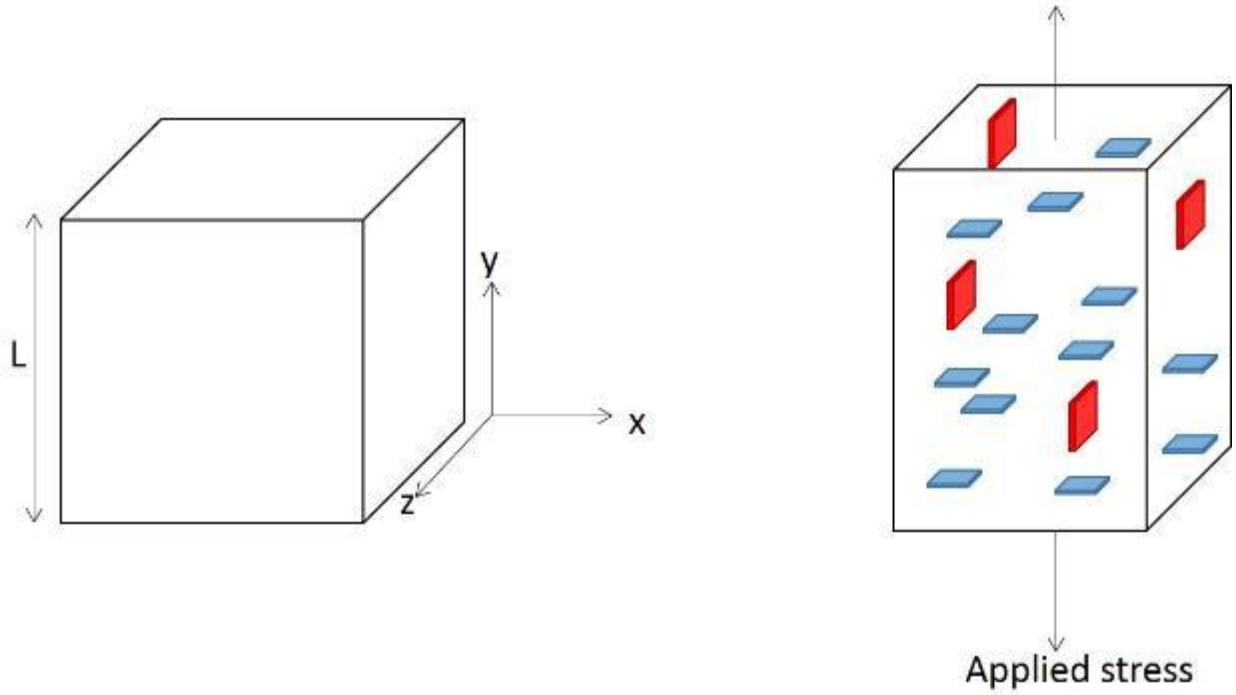

Figure 4.42 Illustration of the SIPN strain contribution theory and how it would appear under microstructural investigation.

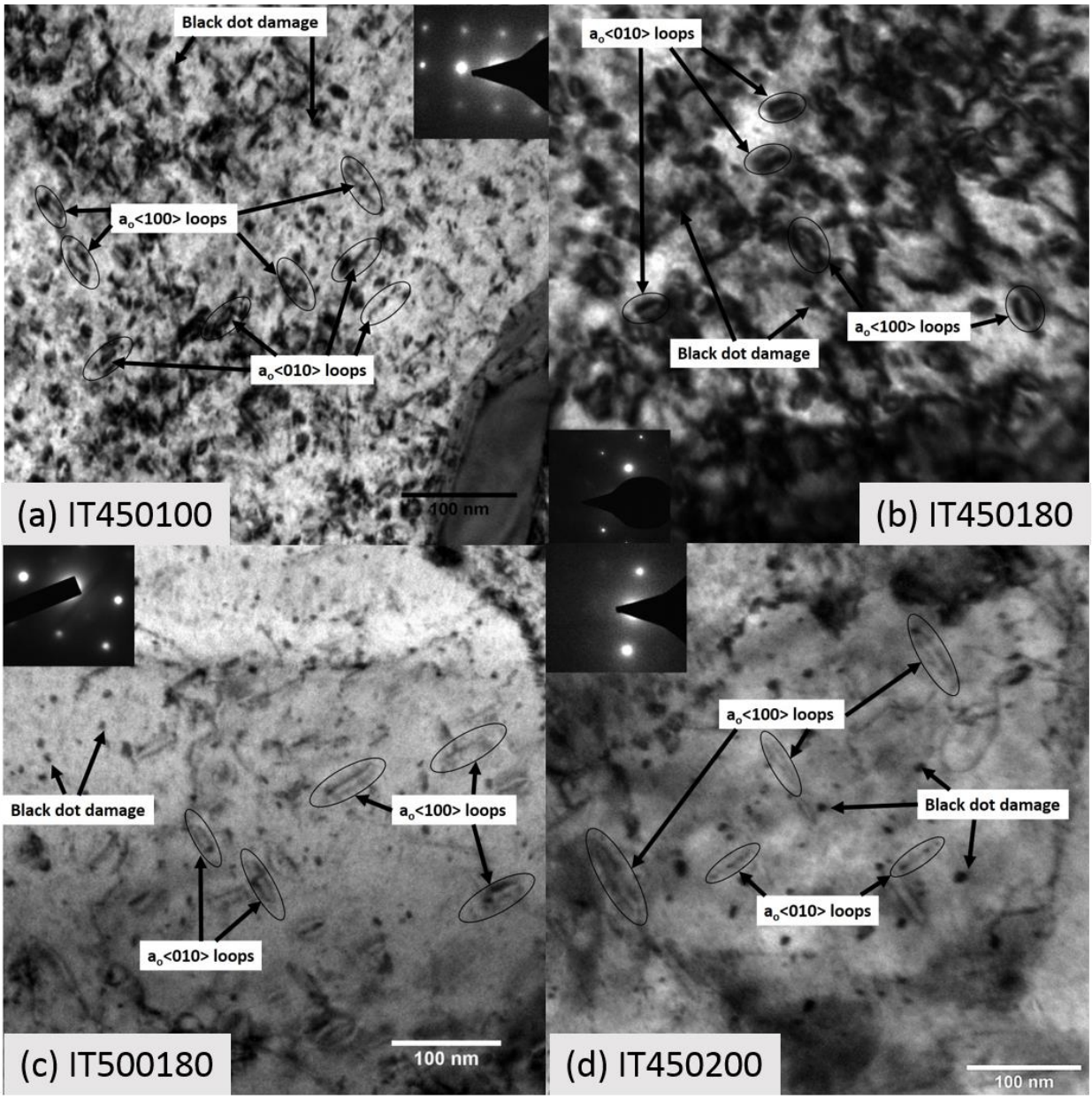

Figure 4.43 Representative TEM image of an irradiation creep sample on the <100> zone axis showing two sets of edge on <100> loops for samples a)IT450100, b)IT450180, c)IT500180, d)IT450200.

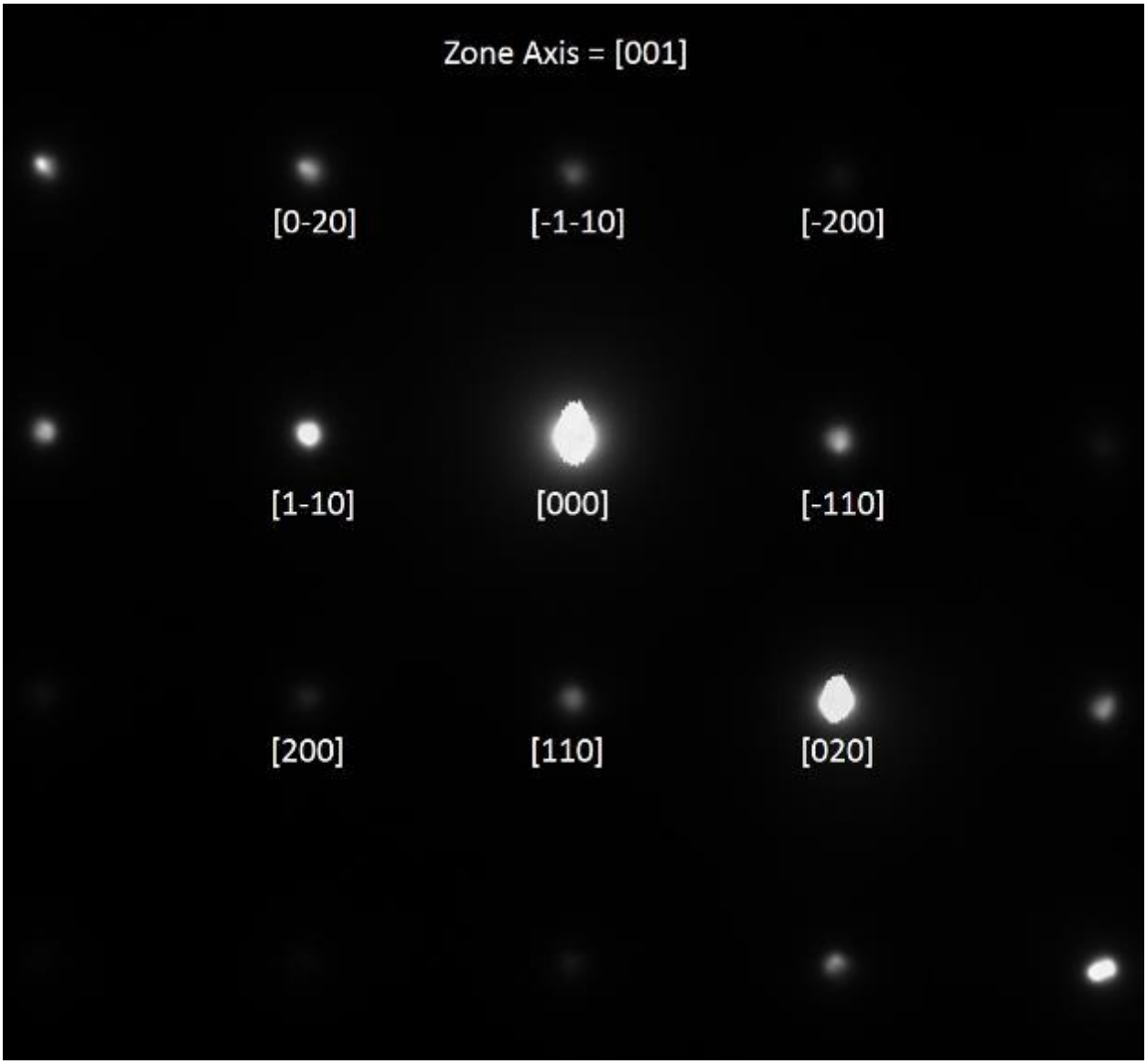

Figure 4.44 Diffraction pattern of the bcc crystal lattice from the <100> zone axis taken from an irradiation creep sample.

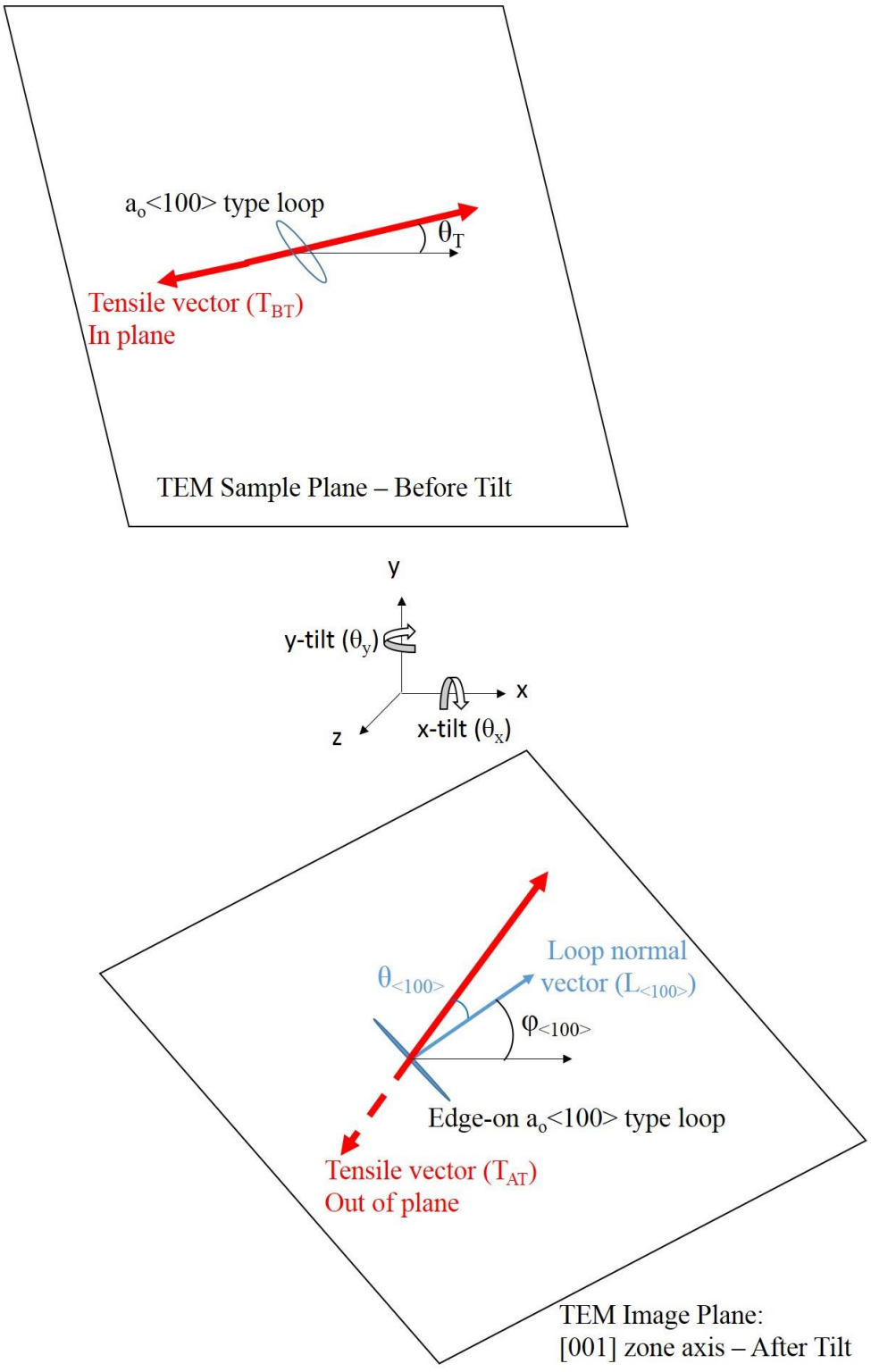

Figure 4.45 Schematic of dislocation loops at arbitrary angle to the tensile axis T, and the relevant angles that defines the orientation $\theta_{<100>}$ of the dislocation loop normal vector to the tensile axis.

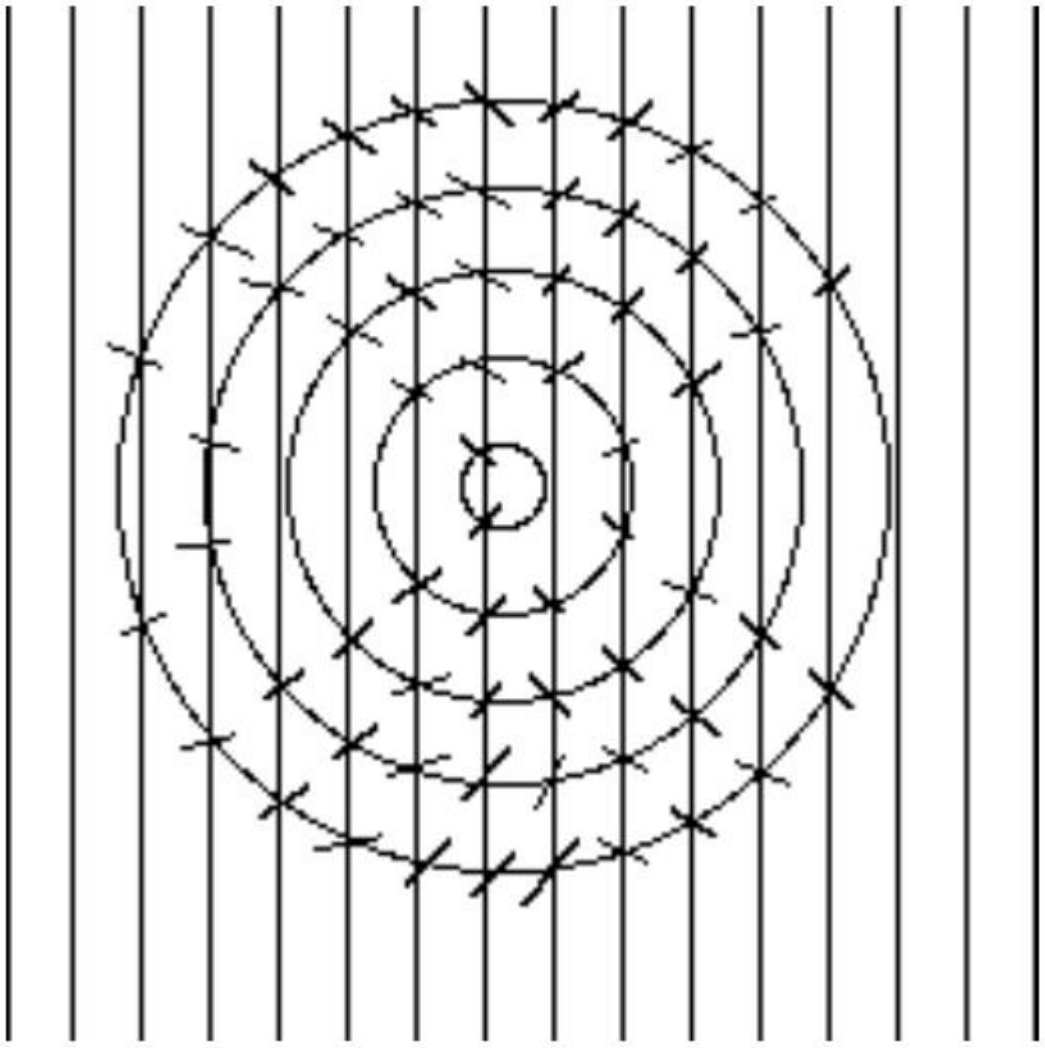

Figure 4.46 Schematic of a statistical method for determining planar dislocation network density by counting the intersections between the line segments and a superimposed circular grid [81].

CHAPTER 5 Results

The experiments were aimed at obtaining irradiation creep strain at well controlled stress, temperature, and dose rate conditions along with their related microstructure characteristics. Therefore, the results chapter will be organized into the following sections: (1) description of irradiation creep data, and (2) description of irradiation creep microstructure. The first section of the chapter describes in detail each irradiation creep experiment, and the strain rate observed for each irradiated condition. The second section of the chapter contains TEM characterization of the microstructure that informs calculations of strain contributions from theoretical irradiation creep mechanisms.

Each dog-bone specimen that was exposed to irradiation creep conditions was assigned a sample designation that reflected its irradiation conditions and alloy composition. The convention used is: irradiation/thermal_alloy_temperature_stress, such that IT450180 indicates a T91 sample irradiated at 450^{o}C under 180MPa. Similarly TT500200 denotes a T91 sample irradiated under thermal conditions of 500^{o}C at 200MPa. The list of samples irradiated and analyzed in this study is tabulated in Table 5.1. These sample designations are used throughout the thesis.

Twelve irradiation creep experiments on T91 were conducted for this thesis to obtain the stress dependence, dose rate dependence, and temperature dependence of irradiation creep. In addition, three thermal creep experiments were conducted for benchmark purposes. Two irradiation creep experiments were conducted on HT9 and HCM12A as a preliminary exploration of the effect of composition on creep rates. Out of seventeen total experiments, three conditions were repeated to confirm the repeatability of the experiments.

Table 5.1 Sample designation and conditions of all irradiation creep experiments

Sample Name	Alloy	Temperature (°C)	Stress (MPa)	Dose Rate (dpa/s)	Dose (dpa)
IT450200-A	T91	450	200	$3.4x10^{-6}$	1
IT450200-B	T91	450	200	$3.4x10^{-6}$	1
IT450180-A	T91	450	180	$3.4x10^{-6}$	1
IT450180-B	T91	450	180	$3.4x10^{-6}$	1
IT450160-A	T91	450	160	$3.4x10^{-6}$	1
IT450140-A	T91	450	140	$3.4x10^{-6}$	1
IT450120-A	T91	450	120	$3.4x10^{-6}$	1
IT450100-A	T91	450	100	$3.4x10^{-6}$	2
IT450000-A	T91	450	0	$3.4x10^{-6}$	1
IT400160-A	T91	400	160	$2.6\ x10^{-6}$	1
IT500180-A	T91	500	180	$1x10^{-5}$	1
IT500160-A	T91	500	160	$*3x10^{-6}$	1.5
IT500160-A	T91	500	160	$*3.4x10^{-6}$	0.8
IT500160-A	T91	500	160	$*4.8x10^{-6}$	1.2
TT450200-A	T91	450	200	0	0
TT500200-A	T91	500	200	0	0
TT500200-B	T91	500	200	0	0
IH450160-A	HT9	450	160	$3.4x10^{-6}$	1
IA450160-A	HCM12A	450	160	$3.4x10^{-6}$	1

5.1 Irradiation Creep Rates

This section presents in detail the results and errors of individual irradiation creep experiment, and demonstrate that the observed irradiation creep rates reported in this thesis are self-consistent and reflect realistic behavior. The irradiation creep experiments described in this section are organized by their significance as shown in Table 5.1. The total results of the irradiation temperature, stress, strain over time, strain rate, and their associated errors are reported in this section.

5.1.1 Irradiation Creep Experiments

The irradiation creep experiments were designed to explore the temperate, stress, dose rate dependence of the strain rates at constant dose, in addition to quantify the total error of repeated experiments. Alloy T91 has been irradiated over a range of temperatures between 400^{o}C-500^{o}C, doses rates between $2.6x10^{-6}$ – $1.0x10^{-5}$ dpa/s, and stresses from 0-200MPa. The creep behavior of representative experiments are outlined in this section. The creep curve of every irradiation creep experiment are recorded in Appendix A.

Typical irradiation creep experiments were conducted under constant temperature, stress, and dose rate conditions over around 100 hours. Figure 5.1 illustrates the creep curve of the experiment conducted on sample IT450180B. The data collection started at the beginning of chamber heating, and the system was allowed to bake out at high temperature for around 20 hours. The peak temperature seen at hour 20 in Figure 5.1 indicate emissivity calibrations and the start of data collection for the 2D pyrometer. The data also clearly tracked the lowering of temperature after emissivity calibration in anticipation of beam heating. The instantaneous increase in current density signals the start of irradiation. Irradiation on the target sample can cause transient behavior in the temperature, chamber pressure, and instability of the liquid indium heat sink to various degrees, depending on the stability of the beam, and the small differences in initial alignment. The LVDT measured the strain of the entire load train, therefor the LVDT data was used to determine the time when the system has reached stability, typically at around 40 hours.

The fluctuations in the beam current were adjusted manually and the corresponding changes in heater temperature to compensate were observed in the back temperature measured by thermocouples. Occasionally, beam loss events can occur either due to sparks or outages as is shown in Figure 5.1 at around hour 50. Short beam loss events were recovered quickly, and did not affect the strain rate measurements. However, beam loss events that lasted longer than an hour required the system to re-establish stability, therefore the data during long beam loss were removed when calculating the strain rates. An example of such an experiment is shown in Figure 5.2a for sample IT450120A, where consecutive power outages due to weather and a source failure caused transients in the data that adversely affected the strain rate calculations. Figure 5.2b shows how the data during the outages were removed, and a creep rate was determined from the remaining data. The strain rates of the irradiation creep experiments were determined by linear line fit to the strain over time data taken by the LSE under stable conditions.

Two irradiation creep experiments were uniquely different from the rest in their test conditions. IT500160A irradiation creep condition experiment was designed to test the effect of in-situ changes in dose rate. Figure 5.3 illustrates the creep curve of the experiment over 90s hours. The system leaved transient at around 45 hours. The LSE data shows stable strain for around 30 hours at dose rate of $3.4x10^{-6}$dpa/s. The dose rate increased to $4.8x10^{-6}$dpa/s at 75 hours, and the strain rate increased accordingly. At 100 hours, the beam current density was dropped down again to $3x10^{-6}$dpa/s. Three unique strain rates were determined from this single experiment where the only difference was the dose rate and initial microstructure of each dose rate condition. IT450000A irradiation creep condition experiment was designed to provide a microstructure comparison between the stressed and unstressed conditions. The liquid indium heat sink behind the sample, which was normally kept from flowing due to the normal force applied by the loaded sample, relied solely on its own viscosity to keep its stability in this experiment. This made the unloaded sample especially sensitive to small temperature variations and inherent system vibrations. Figure 5.4 illustrates the creep curve of IT450000. Due to the low stress applied, the strain measured by the LSE couldn't be distinguished from the noise due to vibrations in the system. Because there was not enough stress to keep the sample completely stable during the irradiation, the strains measurements followed the noise measured in the load cell. Therefore, the strain rate of this experiment was not measured and used in any strain rate analysis.

Thermal creep experiments were also conducted to provide a point of comparison to the irradiation creep experiments. Unlike the irradiation creep experiments, thermocouples were used to measure temperature instead of the pyrometer because there was no temperature difference between the sample gage length and the sample stage without irradiation beam heating. Figure 5.5 illustrates the thermal creep experiment conducted on sample TT450200. The thermal creep experiments were ran for much longer time, typically around 200 hours, than irradiation creep experiments. The longer time experiments were necessary due to the lower creep rates of thermal creep in comparison to irradiation creep.

The strain rates measured for every irradiation creep and thermal creep experiment are tabulated in Table 5.2 with sample ID and irradiation creep conditions. The detailed creep curves of each creep experiment are recorded in Appendix A.

Table 5.2 Strain rate results of irradiation creep experiments.

Sample Name	Temperature (°C)	Stress (MPa)	Dose Rate (dpa/s)	Dose (dpa)	Strain Rate ($10^{-9}s^{-1}$)	Statistic Error ($10^{-9}s^{-1}$)
IT450200-A	450	200	$3.4x10^{-6}$	1	12.5	0.053
IT450200-B	450	200	$3.4x10^{-6}$	1	11.5	0.032
IT450180-A	450	180	$3.4x10^{-6}$	1	4.67	0.037
IT450180-B	450	180	$3.4x10^{-6}$	1	5.00	0.03
IT450160-A	450	160	$3.4x10^{-6}$	1	2.7	0.035
IT450140-A	450	140	$3.4x10^{-6}$	1	2.05	0.04
IT450120-A	450	120	$3.4x10^{-6}$	1	1.9	0.025
IT450100-A	450	100	$3.4x10^{-6}$	2	1.67	0.06
IT450000-A	450	0	$3.4x10^{-6}$	1	N/A	N/A
IT400160-A	400	160	$2.6\ x10^{-6}$	1	~2.9	0.11
IT500180-A	500	180	$1x10^{-5}$	1	5.78	0.25
IT500160-A	500	160	$*3x10^{-6}$	1.5	1.78	0.16
IT500160-A	500	160	$*3.4x10^{-6}$	0.8	2.33	0.096
IT500160-A	500	160	$*4.8x10^{-6}$	1.2	5.08	0.13
TT450200-A	450	200	0	0	1.38	0.002
TT500200-A	500	200	0	0	12.8	0.032
TT500200-B	500	200	0	0	11.5	0.042
IH450160-A	450	160	$3.4x10^{-6}$	1	3.45	0.07
IA450160-A	450	160	$3.4x10^{-6}$	1	5.85	0.02

* Experiment conducted on the same sample at different conditions.

~ Experimental condition difficult to control due to low temperature.

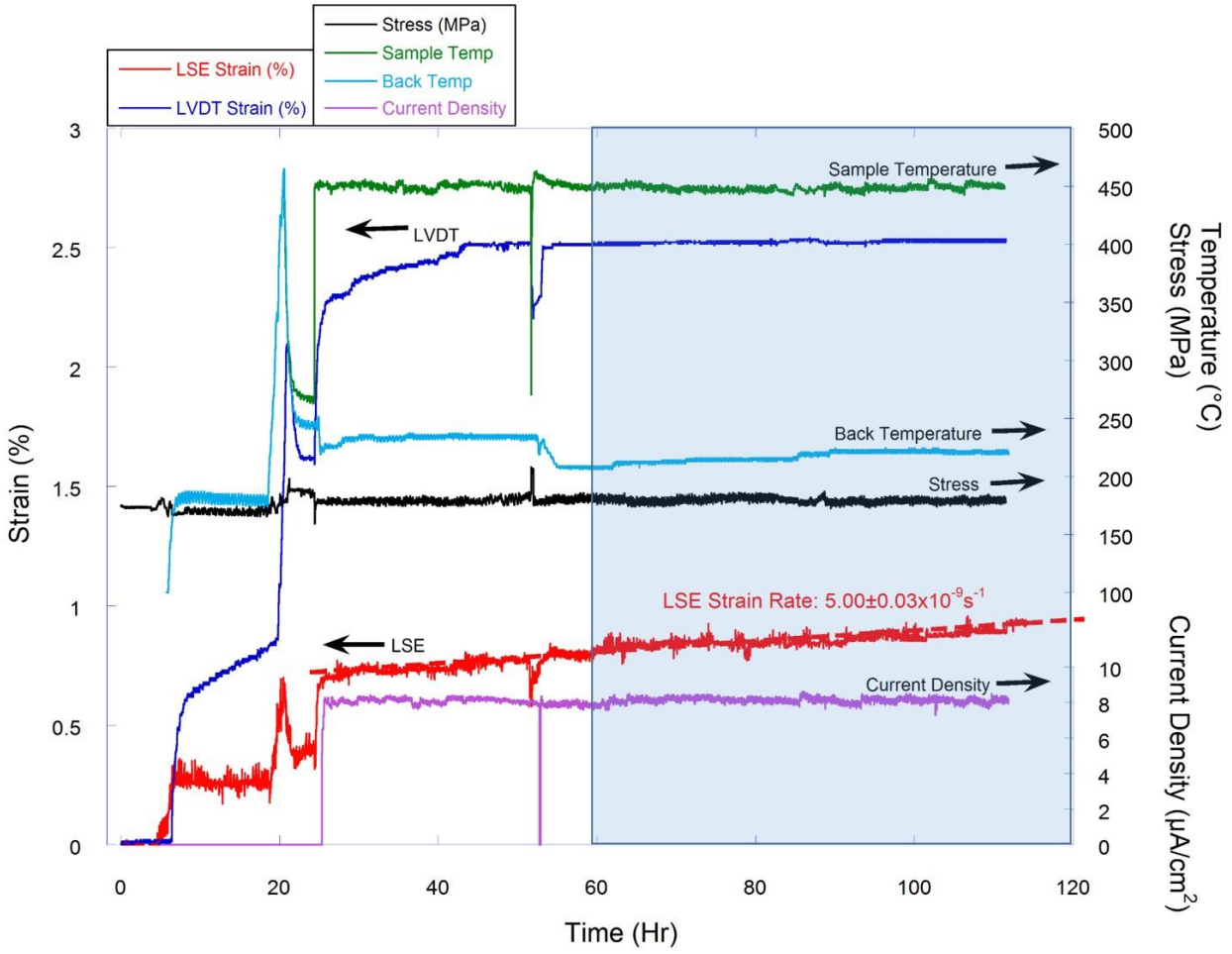

Figure 5.1 Irradiation creep curve of sample IT450180B. Irradiation temperature was at 450^{o}C, applied stress was at 180MPa, dose rate was constant at 3.4x10^{-6}dpa/s.

a)

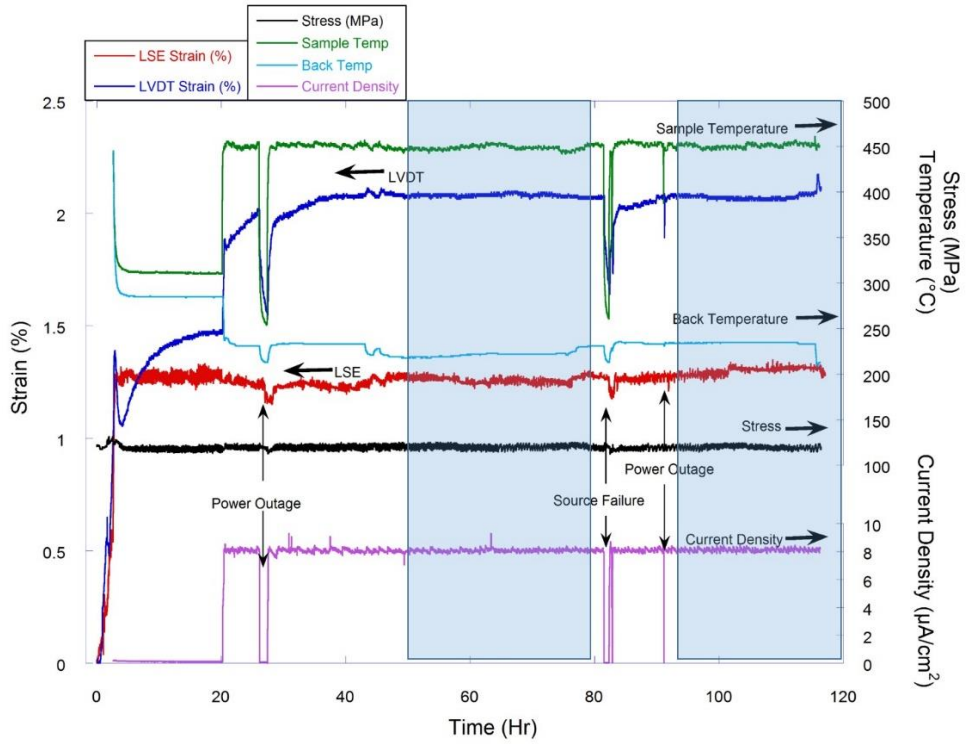

b)

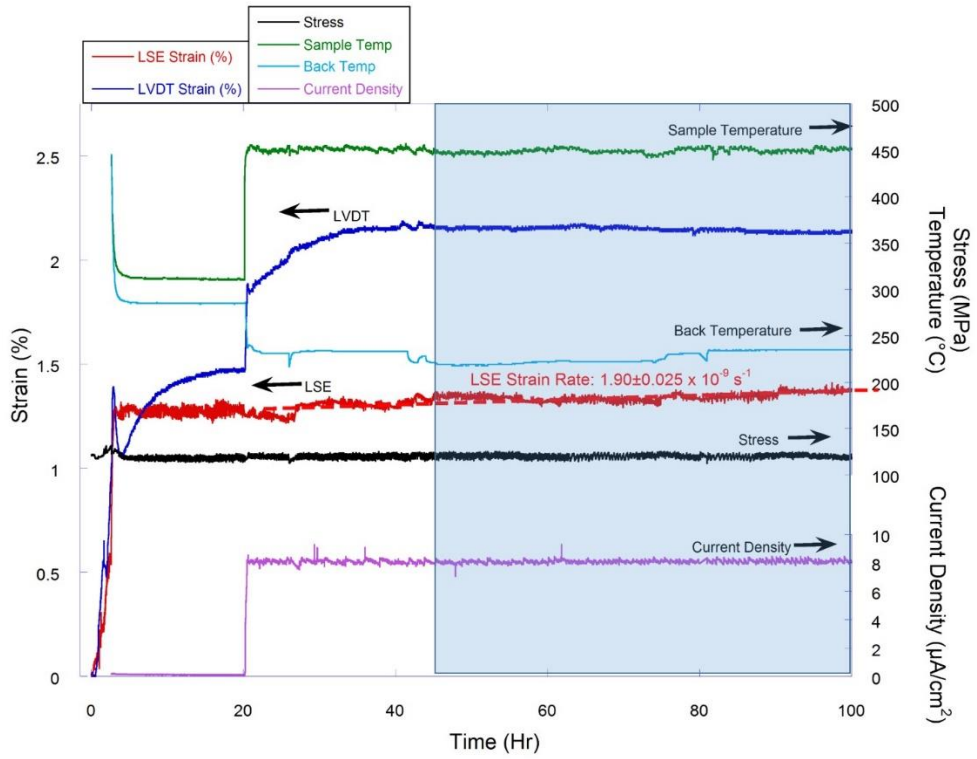

Figure 5.2 Irradiation creep curve of IT450120A. Irradiation temperature was at 450°C, applied stress at 120MPa, dose rate at 3.4×10^{-6}dpa/s. a) with power outage, b) without outage.

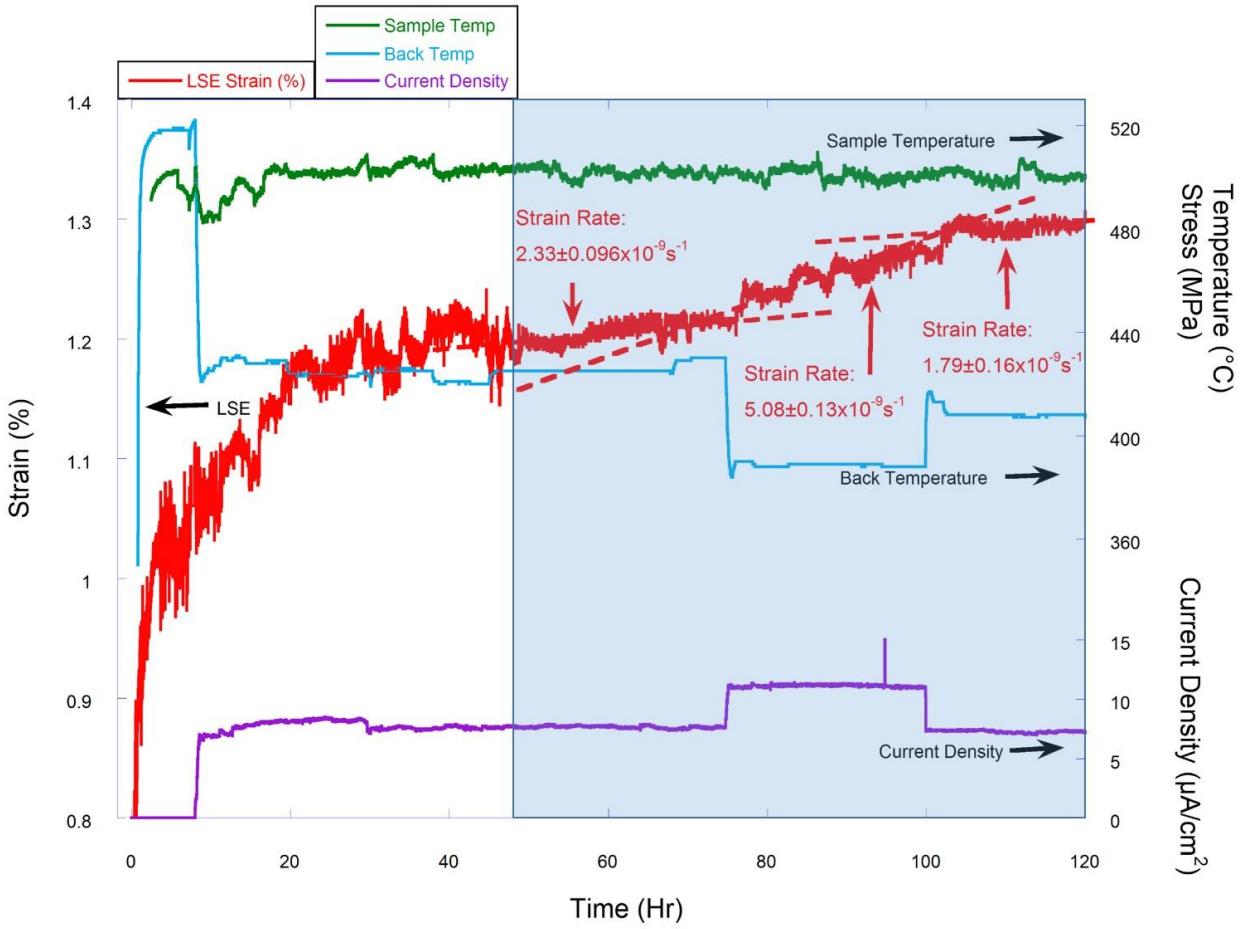

Figure 5.3 Irradiation creep curve of IT500160A. Irradiation temperature was at 500ºC, applied stress at 160MPa, dose rate varied from $3x10^{-6}$dpa/s – $4.8x10^{-6}$dpa/s.

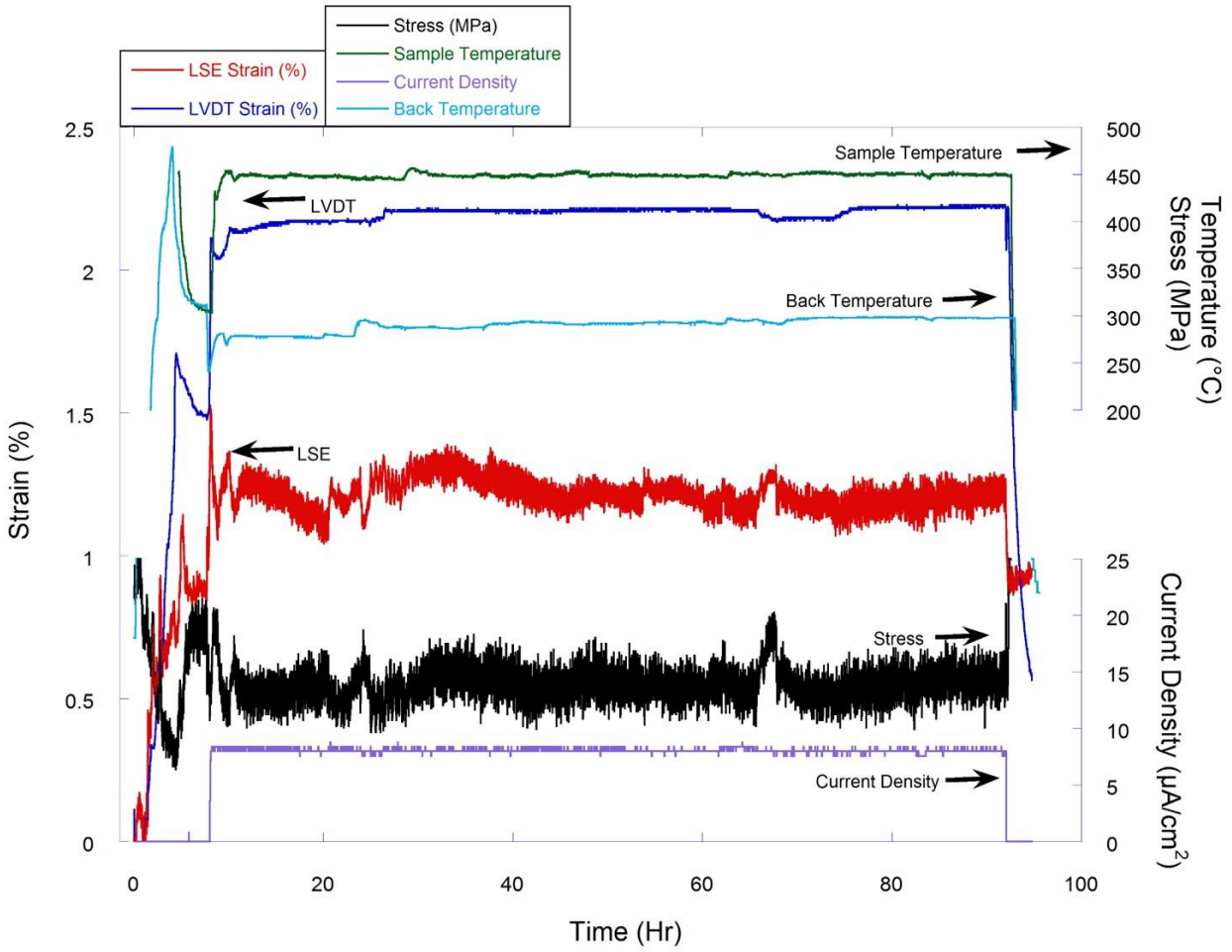

Figure 5.4 Irradiation creep curve of IT450000A. Irradiation temperature was at 450°C, with an applied stress of <15MPa, dose rate constant at 3.4×10^{-6} dpa/s.

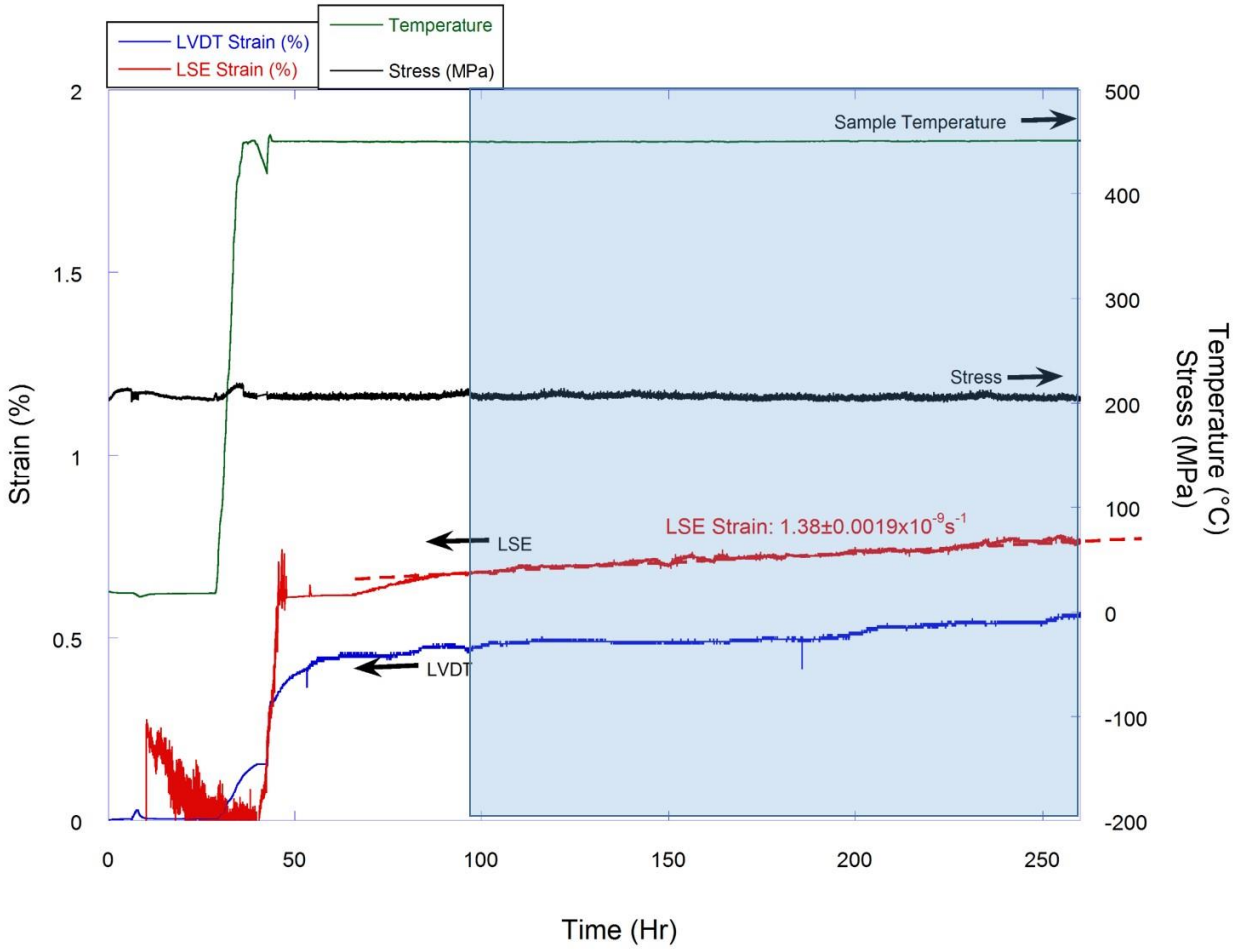

Figure 5.5 Thermal creep curve of TT450200A. Sample temperature was at 450°C, applied stress at 200MPa.

5.1.2 Error from repeated irradiation creep experiments

Three sets of experiments were repeated to quantify the error of the creep rates from different samples irradiated under the same conditions. The error of creep rate from each experiment was determined by statistical analysis of the line fit to the strain over time data. The errors are reported in column 3 of Table 5.3 and range from 0.2% to 8.9% of the measured creep rate. However, a single experiment cannot capture the effect of variations in sample thickness, beam history, and other random factors that arise between experiments. The error in the strain rates between different experiments under the same conditions requires that multiple experiments be conducted under the same conditions.

The thermal creep test condition of 500^{o}C and 200MPa was conducted twice for error measurements from repeated experiments. Two irradiation creep test conditions were also repeated, the 450^{o}C 200MPa condition and the 450^{o}C 180MPa condition. Repeated experiments over three unique creep conditions provided a basis for calculating the error over a wide range of conditions. Statistical analysis of error due to repeated data collection was outlined in chapter 2.6.3.2 of the NIST statistical handbook [83], where the standard deviation was calculated from the data set, and the 95% confidence interval was determined by utilizing the t-distribution.

The standard deviation of repeated experiments are tabulated in Table 5.3. Each experimental condition was repeated once, therefore this analysis has one degree of freedom. The equation for the standard error of repeated experiments is as follows:

$$SE = 6.31 \times \frac{\sigma}{\sqrt{n}} \tag{5.1}$$

The σ is the calculated standard deviation of the experiments done at the same conditions. The n is the degree of freedom of the analysis. The value of 6.31 is taken directly from the t-distribution table for statistical analysis on data with one degree of freedom for the 95% confidence. The standard error calculated for the three conditions are tabulated in Table 5.3.

The standard error calculated in this analysis represent the range of creep rates that will be measured 95% of the time if experiments were conducted under the same conditions. However, because the creep rates themselves change as the conditions change, a better representation of the standard error would be a percentage of the measured creep rate. The calculated standard errors were found to vary from 29.4% to 50.5% of the measured creep rates. The largest percentage error was chosen as a conservative estimate of the error from repeated

experiments. Unlike the measurement error taken from a single experiment, errors from repeated experiments include any difference that may arise between sample preparation and data collection as well as those from random factors such as power outages, LSE instability, and ion beam instabilities between experiments. Therefore, these errors are the largest error associated with the creep rate measurements in these experiments on the order of 30-50%. Since only three creep conditions have unique repeatability errors associated with it, the experiments that were not repeated will appear to have much lower error than reality. In order to avoid misrepresenting the error of the irradiation creep experiments that were not repeated, the maximum repeatability error was assumed to be a conservative representative error for all creep experiments conducted in this study. The error of ±50% in the strain rate is also consistent with recent evaluations of uniaxial tensile creep where the error factor was found to be around 1.7 and 2.5. [84] It is typical for uniaxial creep tests to have strain rate errors around a factor of 2. Table 5.2 tabulates the results of the irradiation temperature, stress, strain rate, and the total errors of every creep test conducted in this study.

Table 5.3 Strain rate results of irradiation creep experiments with repeatability error.

Sample Name	Strain Rate ($10^{-9}s^{-1}$)	Single Experiment Error ($10^{-9}s^{-1}$)	Repeated Experiment Error ($10^{-9}s^{-1}$)
IT450200-A	12.5	0.053	4.46
IT450200-B	11.5	0.032	4.46
IT450180-A	4.67	0.037	1.47
IT450180-B	5.00	0.03	1.47
IT450160-A	2.7	0.035	1.35
IT450140-A	2.05	0.04	1.02
IT450120-A	1.9	0.025	0.95
IT450100-A	1.67	0.06	0.83
IT450000-A	N/A	N/A	N/A
IT400160-A	~2.9	0.11	1.45
IT500180-A	5.78	0.25	2.89
IT500160-A	1.78	0.16	0.89
IT500160-A	2.33	0.096	1.16
IT500160-A	5.08	0.13	2.54
TT450200-A	1.38	0.002	0.69
TT500200-A	12.8	0.032	5.80
TT500200-B	11.5	0.042	5.80
IH450160-A	3.45	0.07	1.72
IA450160-A	5.85	0.02	2.92

* Experiment conducted on the same sample at different conditions.

~ Experimental condition difficult to control due to low temperature.

5.1.3 Dose rate dependence of irradiation creep rates

. An experiment to explore the dose rate dependence was conducted at 500°C and 160MPa for sample IT500160. The experiment was done on a single sample to take advantage of the in-situ strain measurement capability, such that the change in strain rate due to changes in the dose rate can be observed in real time. The high irradiation temperature was necessary to compensate for the large range of beam heating from changing the dose rates. Three dose rate conditions were used in this experiment as calculated by full cascade mode under SRIM: $3x10^{-6}$dpa/s, $3.4x10^{-6}$dpa/s, and $4.8x10^{-6}$dpa/s. The corresponding strain rates were found to be $1.78\pm0.89x10^{-9}s^{-1}$, $2.33\pm1.67x10^{-9}s^{-1}$, and $5.08\pm2.54x10^{-9}s^{-1}$. In addition, the thermal creep rate at 500°C and 160MPa was extrapolated from the 500°C 200MPa condition, and found to be around $2x10^{-10}$dpa/s. This strain rate was used as the strain rate at 0 dpa/s.

Recent studies have shown that SRIM Kinchin Pease (KP) model was the more appropriate dose rate calculation for comparison with neutron irradiations [72]. The KP model predict dose rates a factor of 2 lower than the full cascade calculations. Because the dose rate dependence serves as a means for extrapolation to neutron irradiation dose rates, the strain rates are plotted against the KP calculated dose rates, Figure 5.6. A linear best fit, shown in red, with slope of 0.001769 (dpa^{-1}) can be fitted to the data with an R squared value of 0.86. The implications of a linear dose rate dependence will be discussed in Section 6.1.1.

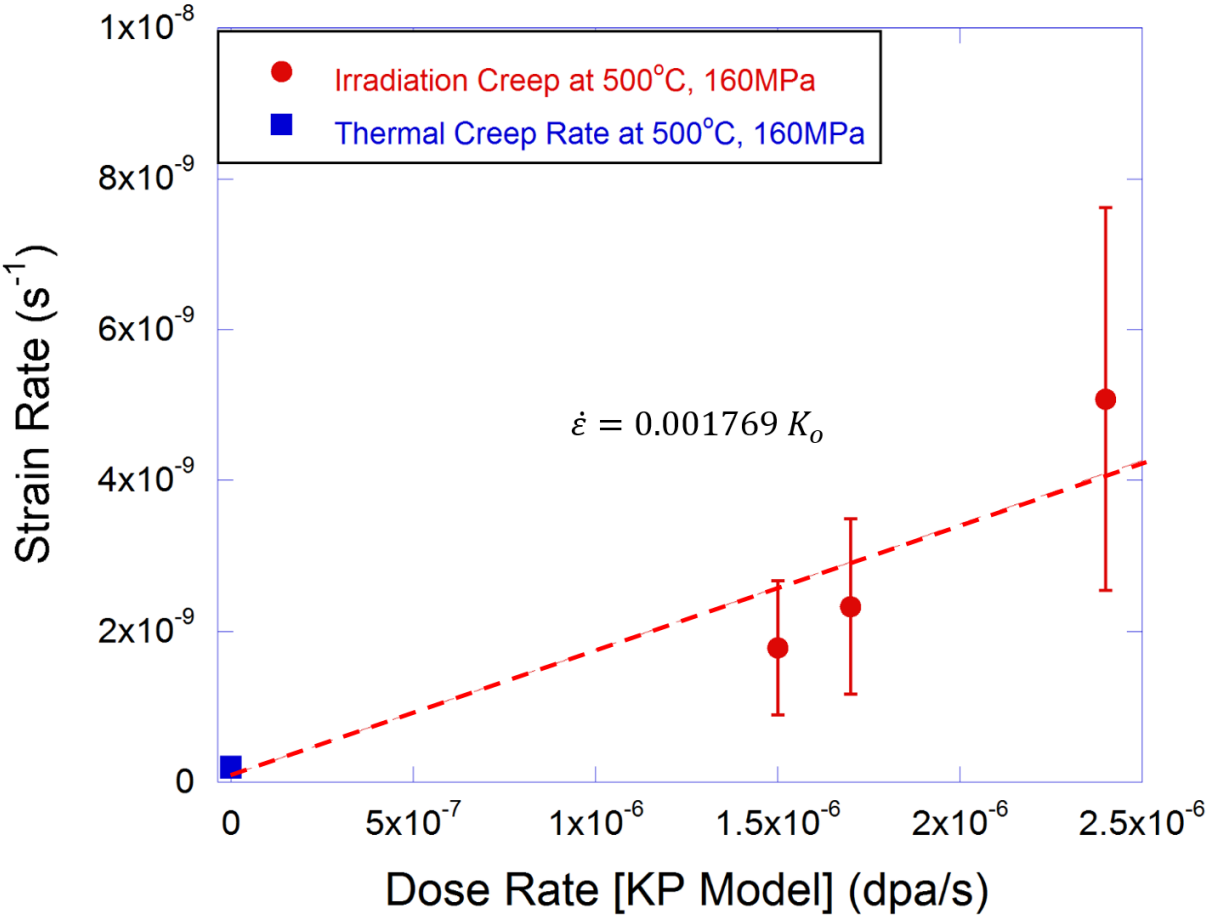

Figure 5.6 Dose rate dependence of irradiation creep strain rate for IT500160 and the best linear fit to the data. Sample IT500160 was irradiated at temperature of 500ºC, and stress of 160MPa.

5.1.4 Temperature dependence of irradiation creep rates

Irradiation creep experiments were conducted at 400ºC, 450ºC, and 500ºC at 160MPa to explore the temperature dependence. The dose rates of the experiments were kept at the nominal value of $3.4x10^{-6}$dpa/s with the exception of the 400ºC experiment where a lower dose rate was needed to maintain the lower temperatures. The strain rates measured for the experiments at 400ºC, 450ºC, and 500ºC were $2.9\pm1.45x10^{-9}s^{-1}$, $2.7\pm1.35x10^{-9}s^{-1}$, and $2.33\pm1.17x10^{-9}s^{-1}$ respectively. The measured strain rates plotted as a function of time are shown in Figure 5.7.

Various temperature dependencies were fit to the observed data in order to explore its consistency with current irradiation creep theory. The linear best fit to the data are shown in red in Figure 5.7. The linear fit suggest irradiation creep has a very weak inverse temperature dependence. However, because of the error associated with the creep rate results, a zero slope creep rate, can also be satisfactorily fit to the data. In addition to the zero slope and linear fit, an Arrhenius temperature dependence was also explored to see if the creep rates followed any simple diffusion mechanism. The activation energy of Q=240kJ was chosen as it is energy for lattice self-diffusion of iron. However, the Arrhenius temperature dependence with the activation energy of iron self-diffusion predicted more than an order of magnitude increase in creep rate between 400ºC and 450ºC. This temperature dependence is so large that it can't be fit to the data within the error. In order for an Arrhenius temperature dependence to be reasonably fit to the experimental data, an activation energy of less than 38kJ must be used. Such a low activation energy does not correspond to any known diffusion mechanisms in FM steels, therefore it is unlikely that the temperature dependence observed in this study is Arrhenius. The implications of each temperature dependence in relation to irradiation creep mechanisms will be discussed in detail in Section 6.1.2.

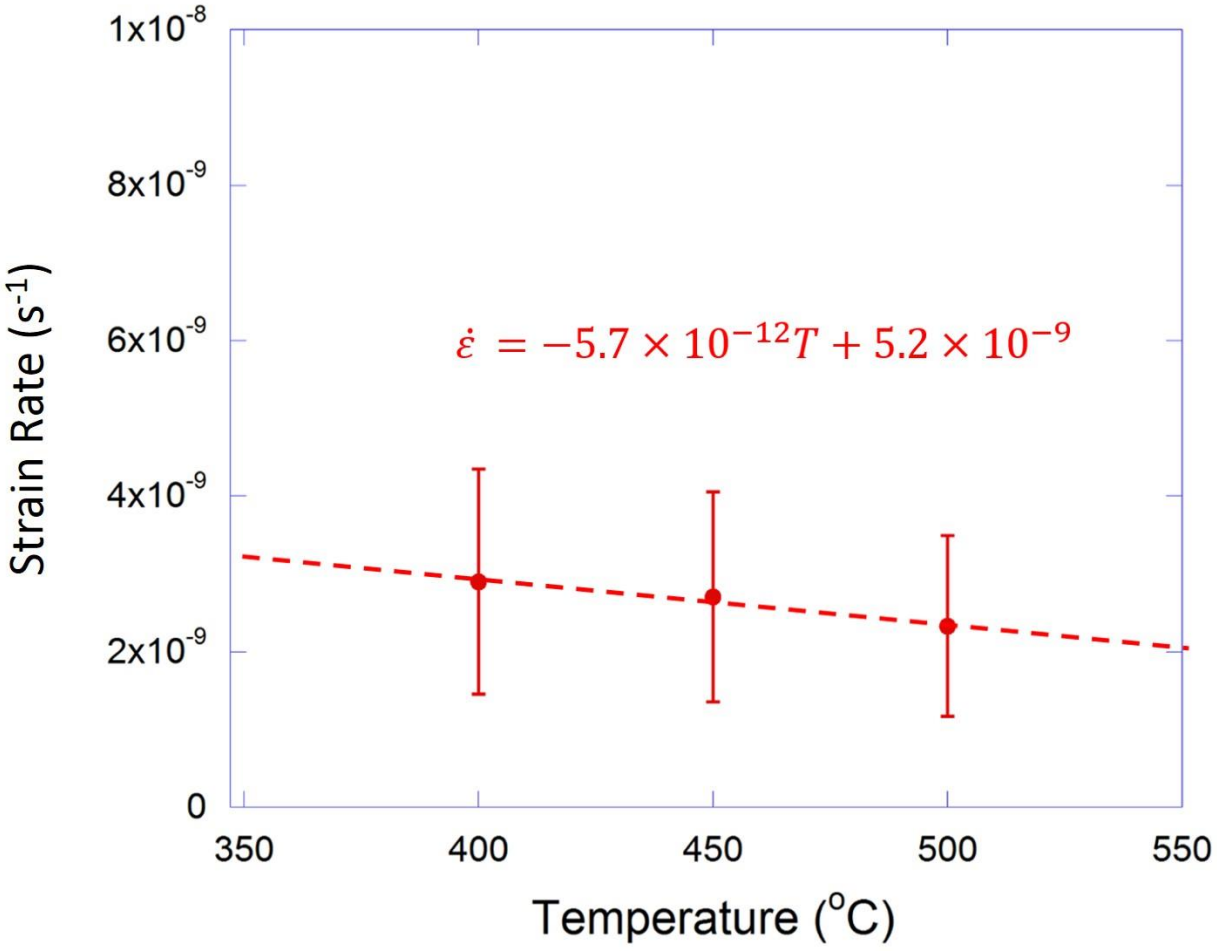

Figure 5.7 Temperature dependence of irradiation creep experiments done at 400°C, 450°C, and 500°C at applied stress of 160MPa and dose rate of 3.4×10^{-6}dpa/s. Equation describes the linear best fit to the data.

5.1.5 Stress dependence of irradiation creep rates

To fully explore the stress dependence of irradiation creep, seven experiments were conducted at constant temperature of 450°C and dose rate of 3.4×10^{-6}dpa/s. The applied stress of these experiments ranged from 100MPa to 200MPa at 20MPa intervals. The stress dependence appeared to follow a low stress exponent trend from 100MPa to 160MPa, and then increases sharply at stress above 180MPa.

Determination of the exact stress exponents was done recursively by minimizing the residuals of the line fit and the data. The data is first separated into two groups, the low stress and the high stress group. The low stress group included data from 100MPa to 160MPa, and the high stress group included data from 160MPa to 200MPa. The equation of the line fit was assumed to be similar to the empirical creep equations:

$$\dot{\varepsilon} = B\sigma^n \tag{5.2}$$

where B is an effective creep compliance, σ is the applied stress, and n is the stress exponent. The stress exponent n was varied between 0 and 1, and the corresponding B with the smallest residual was found for each stress exponent. The smallest residual fit for the low stress data (shown in red) between 100MPa - 160MPa was found to be n=0.86 and B=3.2×10^{-11}. Then, the strain rates from 160MPa – 200MPa was added to the data, and a high stress fit (shown in green) was determined by minimizing the total residual. The stress exponent for the high stress regime was found to be n=14, and B=5.4×10^{-41}. The best fit for the total strain rate data (shown in blue) as a function of stress becomes the following:

$$\dot{\varepsilon} = 3.2 \times 10^{-11}\sigma^{0.86} + 5.4 \times 10^{-41}\sigma^{14} \tag{5.3}$$

The residuals of the fits were calculated by subtracting the model fit by the experimental data. Figure 5.9 shows the residuals for model that is a combination of low stress exponent and high stress exponent in red. The residuals for this combined model are generally within 10% of the strain rate. In comparison, the residuals for the quadratic fit are much larger, about 50% under-prediction of the creep rate at 200MPa, making the quadratic stress dependence a worse fit compared to the combination of low stress and high stress fits. The mechanistic implications of the stress dependence will be discussed in Section 6.1.3.

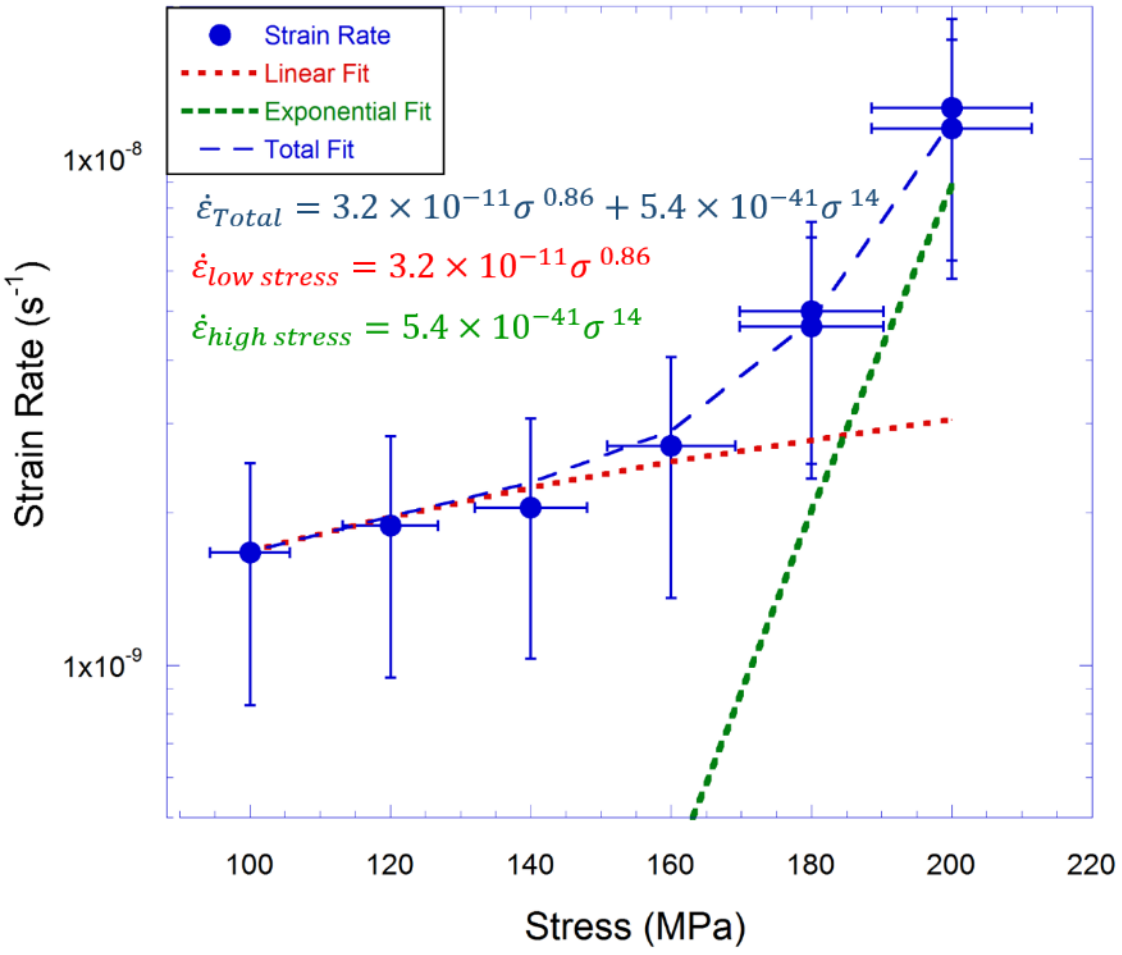

Figure 5.8 Stress dependence of irradiation creep rates of T91 at 450°C, 3.4x10^{-6}dpa/s and the best line fits to the data.

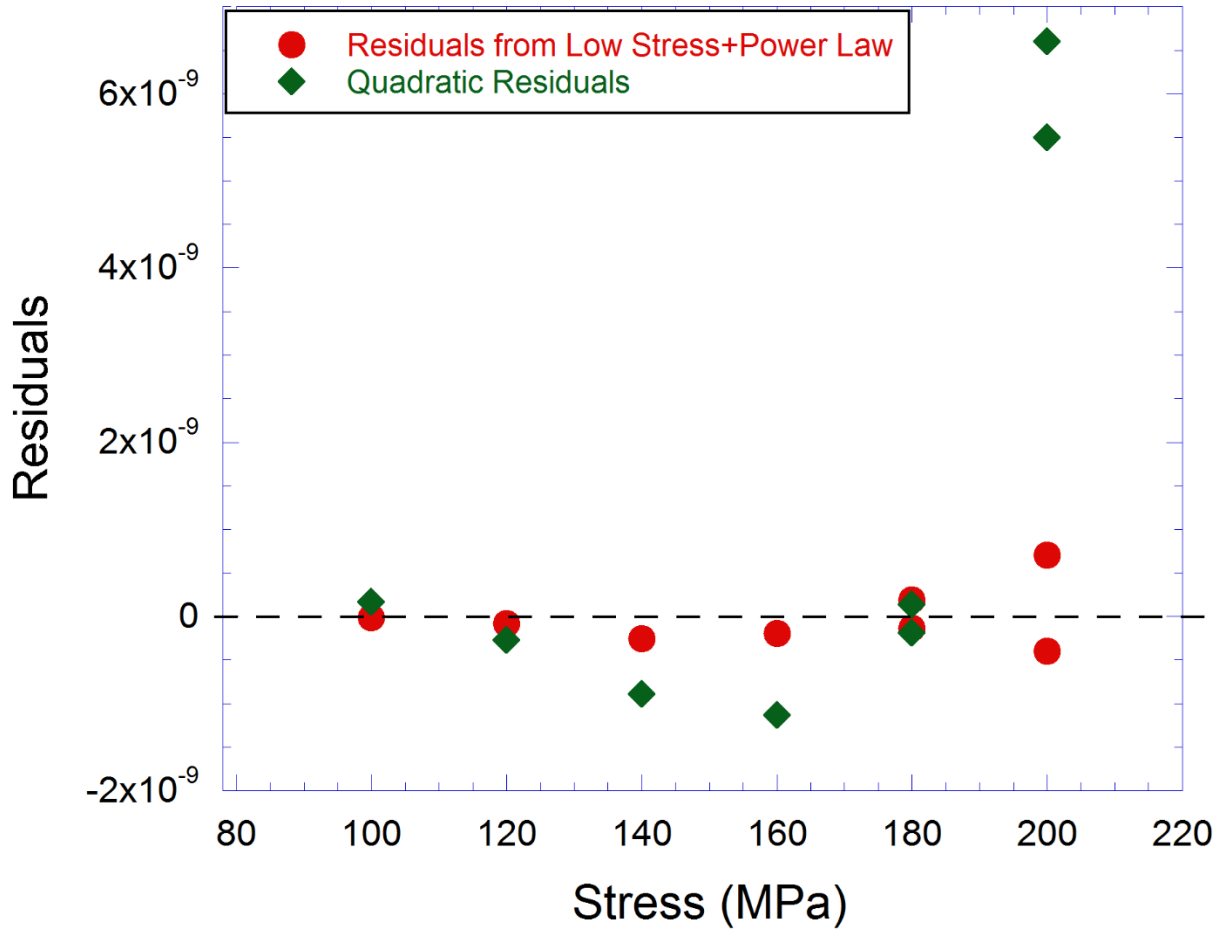

Figure 5.9 Residual plot of irradiation creep rates and the best line fits to the data.

5.2 Microstructure

This section presents the microstructure observations found for selected conditions of irradiation creep samples. Six samples were chosen for extensive microstructure analysis: IT450000-A, IT450100-A, IT450180-A, IT450200-A, IT500180-A, and TT450200-A. These samples span across a wide range of stress, temperature and dose conditions. The microstructure analysis included anisotropy measurements of dislocation loop density, dislocation loop size, dislocation network density, and sub-grain size. A separate analysis of dislocation loop nature was also conducted to determine whether the dislocation loops imaged were interstitial or vacancy in nature. This section is organized into five sections: dislocation loop image, dislocation loop size spectrum, dislocation network image, sub-grain size image, and dislocation loop nature image.

5.2.1 Dislocation Loop Image

An analysis method was developed to preserve the tensile direction under TEM to specifically target the relationship of the loop normal vector to the tensile axis. The sample was machined using focused ion beam (FIB) milling such that the length of the sample was in the direction of the tensile axis, so the tensile axis vector can be uniquely identified in the plane of the sample under low magnification. Each grain was then imaged on the <001> family of zone axes in the g=<110> two beam condition such that two sets of a_o<100> type loops can be seen edge-on. Because only edge-on loops were analyzed, the loop normal vectors of each set of loops were in-plane in the image. With two uniquely defined vectors, the angle between the two vectors can be calculated as a measure of the orientation of the loop to the tensile axis. An angle θ of 0 denotes loops oriented with their normal in the tensile direction, and an angle θ of 90 denotes loops with their normal perpendicular to the tensile axis. Because two sets of edge on loops were visible in a single grain, each TEM image provided dislocation loop data for two values of θ. Figure 5.10 illustrates the relationship between the loop normal and the tensile axis as seen from a typical TEM image.

Bright field TEM images were accompanied by the corresponding diffraction patterns of the imaging condition. The <100> loops in the bright field images were highlighted to show the loop orientation. For every image, four angles were recorded. The first two angles x-tilt, and y-tilt defined the rotation of the tensile axis from being on the x-y plane in the lab reference frame

into its new direction, making the tensile vector uniquely defined in the image reference frame. In the image reference frame, the loop normal vectors of two sets of <100> loops sat on the image plane. Therefore, the loop normal vector of two sets of <100> loops imaged were also uniquely defined by measuring the angle between its in-plane loop normal to the horizontal x-axis. The detailed information for all the TEM images are tabulated in Appendix B.

Four irradiation creep conditions were examined for dislocation loop anisotropy: IT450200A, IT450180A, IT450100A, and IT500180A. The samples were chosen to compare irradiation creep microstructure between different stress and temperature conditions. For sample IT450200, 286 loops were analyzed over 8 grains. The dislocation loops observed range from 10-120nm in diameter. Average dislocation loop density from all eight grains were found to be around $1x10^{21}m^{-3}$. For sample IT450180, 490 loops were analyzed over 10 grains. The dislocation loops observed range from 10-80nm in diameter. Average dislocation loop density from all eight grains were found to be around $1.3x10^{21}m^{-3}$. For sample IT450100, 434 loops were analyzed over 5 grains. The dislocation loops observed range from 10-65nm in diameter. Average dislocation loop density from all eight grains were found to be around $1.6x10^{21}m^{-3}$. For sample IT500180, 346 loops were analyzed over 6 grains. The dislocation loops observed range from 10-120nm in diameter. Average dislocation loop density from all eight grains were found to be around $1.4x10^{21}m^{-3}$.

Dislocation loop analysis was also conducted on the unstressed sample IT450000. However, the dislocation loops were too small in the edge-on configuration to allow any meaningful analysis on their anisotropy. Although dislocation loops were often observed under proton irradiation to low dose at around 400^{o}C [41], [69], their diameter was found to average around 15nm. Because any edge-on loops smaller than 10nm can't be distinguished from black dot damage, too few loops of adequate size were observed for the zero stress condition. In addition, molecular dynamics (MD) simulations have shown that dislocation loops in bcc steels evolved originally from interstitial clusters. The interstitial clusters grow into small glissile $a_o/2<111>$ loops, which then interact to become sessile $a_o<100>$ loops. The lack of $a_o<100>$ loops in the unstressed condition suggested that applied stress had an effect in increasing $a_o/2<111>$ loop interactions resulting in a higher density of larger $a_o<100>$ loops in the material.

Figure 5.11-14 illustrate two representative grains from each sample conditions, one with dislocation loops roughly at the same angle to the tensile axis showing minimal anisotropy in the

loop distribution, and another showing clear anisotropic dislocation distribution due to large angle θ for one set of loops but not the other. If we assume the images were taken on the [001] zone axis, then both a_o[100] loops and a_o[010] loops with distinct values of θ can be observed, and each grain will give a direct comparison between two sets of loops with two distinct angles $\theta_{[100]}$ and $\theta_{[010]}$. Due to symmetry of the bcc lattice, the a_o[100] loops are equivalent to a_o[010] or a_o[001] if imaged from [100] or [010] zone axes, respectively. As long as the images were taken from the <100> family of zone axes, then two of the three angles $\theta_{[100]}$, $\theta_{[010]}$, and $\theta_{[001]}$ could be tallied together and treated as a single variable θ denoting the angle between loop normal of any a_o<100> type loop to the tensile axis for the polycrystalline bulk material.

The total number of loops within each grain can vary depending on the size of the grain imaged. In order to make appropriate comparisons between the loop densities from different grains, the loop density for each orientation of a_o <100> loops was normalized by the total number of visible a_o <100> loops in that grain. The anisotropy in the loop density was defined by the fraction of one set of a_o <100> loops with angle θ over the entire visible a_o <100> loop population of that grain. This normalized dislocation loop density is plotted against angle θ for all samples in Figure 5.15. Each data point in Figure 5.15 describes one set of loops, and each grain provides two data points at two different values of θ by virtue of having two sets of loops. The average loop size of a set of loops is shown in red, and the grain normalized dislocation loop density is shown in blue.

The measurements showed that the dislocation loop size was not dependent on the angle between the loop plane normal and the tensile axis. In contrast, there was a strong dependence of the dislocation loop density on the angle between the loop plane normal and the tensile axis, as shown by the blue line fits in Figure 5.15. The dependence of the loop density on the angle between the loop plane normal and the tensile axis can be described by the simple linear relationship given by:

$$\frac{N(\theta)}{N} = \beta\theta + \alpha \tag{5.4}$$

The constants α, and β are fitting constants, and θ is defined as the angle between the loop normal to the tensile axis as shown in Figure 5.10. The equation describes the anisotropy of dislocation loops in a given irradiation creep sample. N denotes the total number of dislocation loops within the grain, and $N(\theta)$ is the number of dislocation loops with angle θ between its loop

normal and the tensile axis. The term on the left hand side describes the fraction of the loops that had an angle θ to the tensile axis. The anisotropy becomes larger as the externally applied stress increases at a constant temperature and dose rate, which is reflected by the larger slope of the relationship with increasing stress in Figure 5.15. The slope of the line fits are an indication of the strength of the anisotropy, and are tabulated in Table 5.4.

Table 5.4 Characterization of loop in irradiation creep samples.

Sample Name	Number of Loops Analyzed	Average Loop Size (nm)	Dislocation Loop Number Density (m^{-3})	Constants for Loop Anisotropy	
				α	β
IT450100-A	434	24.3	$1.6x10^{21}$	0.64	-0.0032
IT500180-A	346	23.3	$1.5x10^{21}$	0.95	-0.010
IT450180-A	490	24.9	$1.3x10^{21}$	0.78	-0.006
IT450200-A	286	42.3	$1.0x10^{21}$	1.16	-0.014

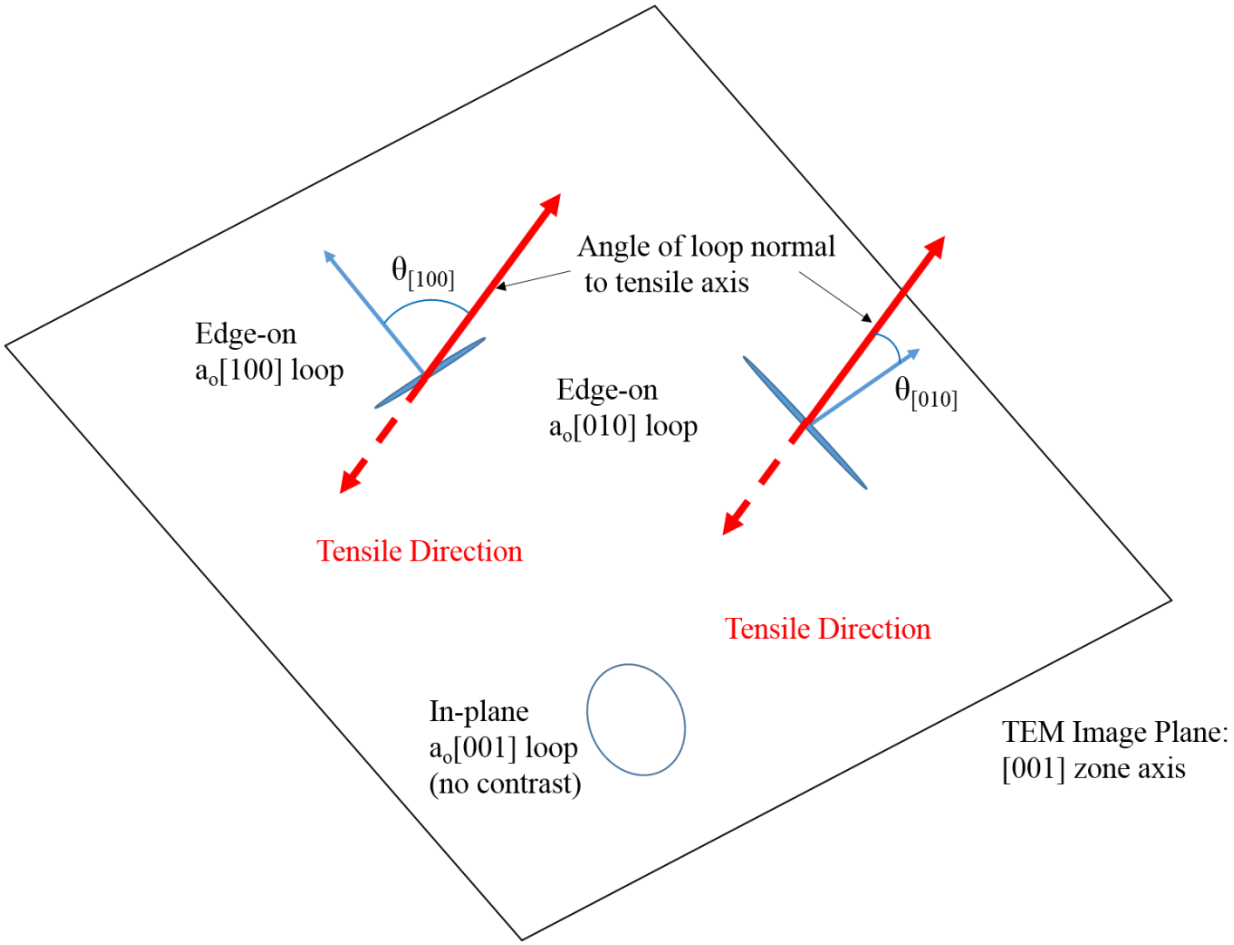

Figure 5.10 Schematic of dislocation loop image method and geometry. The tensile direction can be at any angle to any <001> image plane, and the angle between the loop normal vector of any a_o<100> type loop to the tensile axis is defined as θ. The angle θ is empirically measured in the analysis.

a)

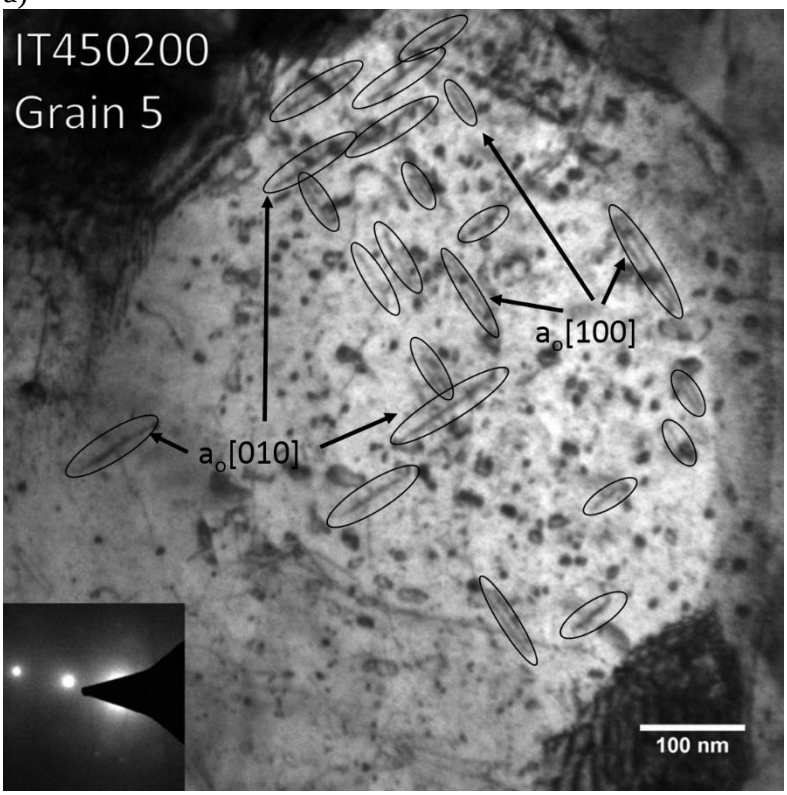

b)

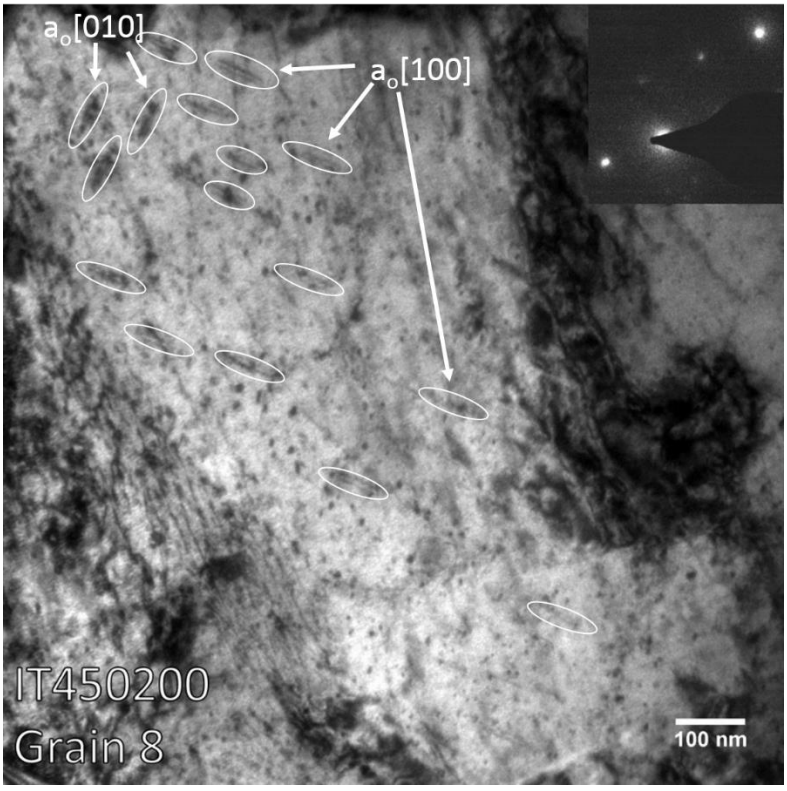

Figure 5.11 TEM image of a grain from sample IT450200 after irradiation creep at 450ºC, 200MPa and 1dpa with (a) $\theta_{[100]}$ = 48º, $\theta_{[010]}$ = 42º (b) $\theta_{[100]}$ = 66º, $\theta_{[010]}$ = 24º

a)

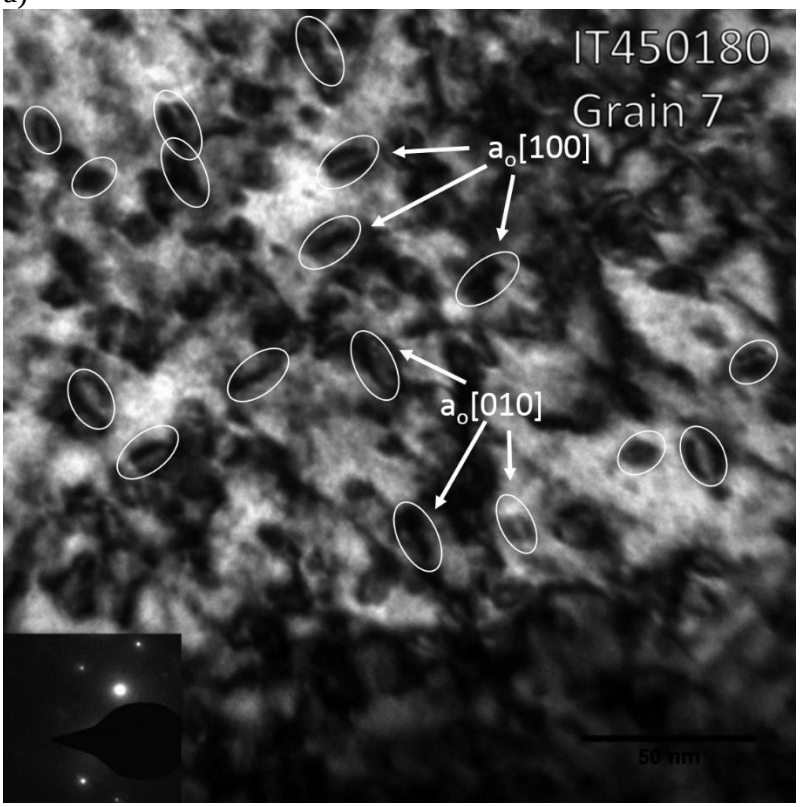

b)

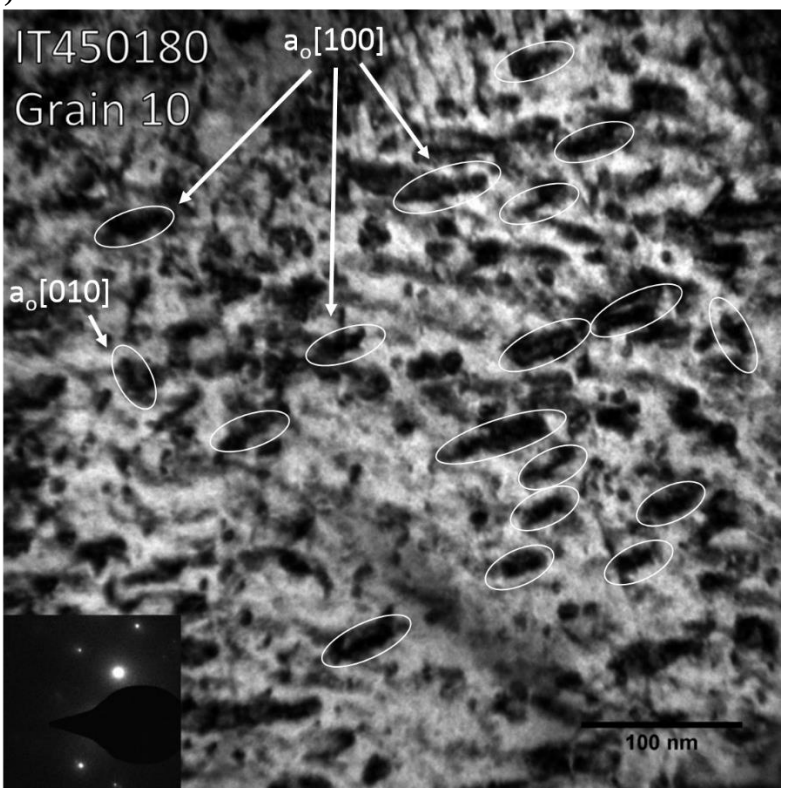

Figure 5.12 TEM image of a grain from sample IT450180 after irradiation creep at 450ºC, 180MPa and 1dpa with (a) $\theta_{[100]}$ = 48º, $\theta_{[010]}$ = 42º, (b) $\theta_{[100]}$ = 79º, $\theta_{[010]}$ = 11º

a)

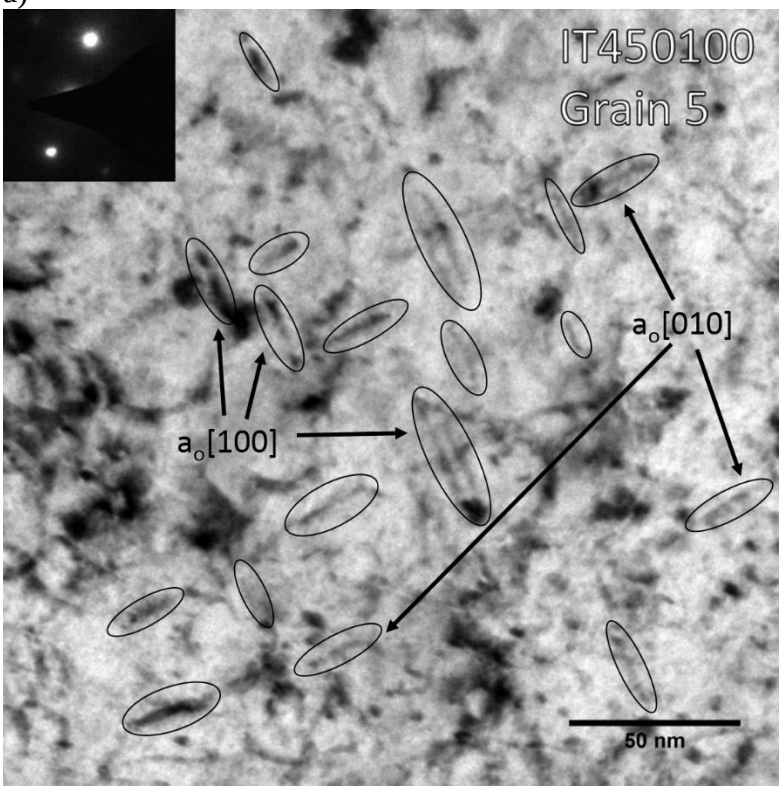

b)

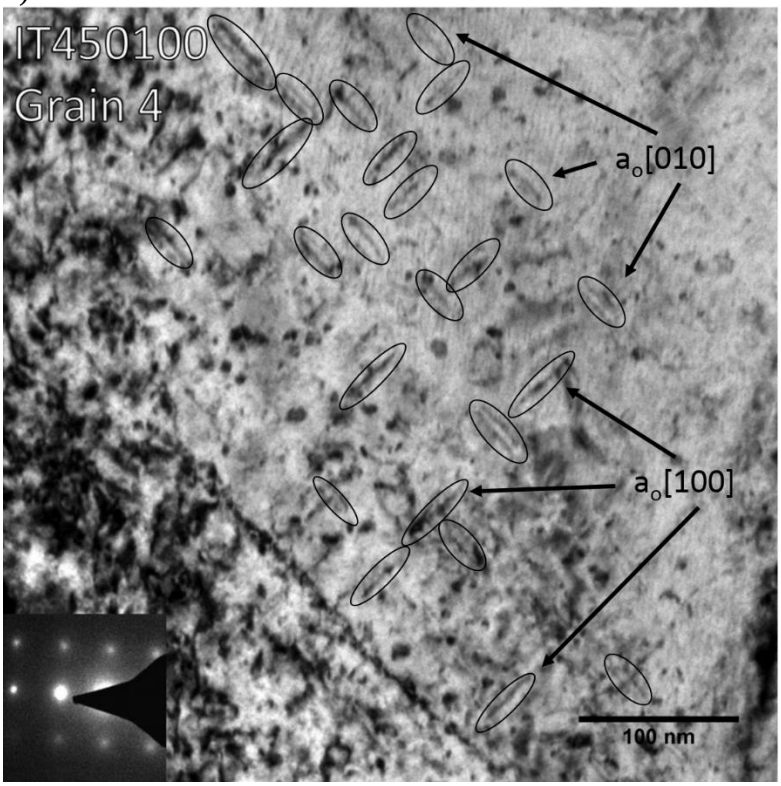

Figure 5.13 TEM image of a grain from sample IT450100 after irradiation creep at 450°C, 100MPa and 2dpa with (a) $\theta_{[100]}$ = 55°, $\theta_{[010]}$ = 35°, (b) $\theta_{[100]}$ = 7°, $\theta_{[010]}$ = 83°

a)

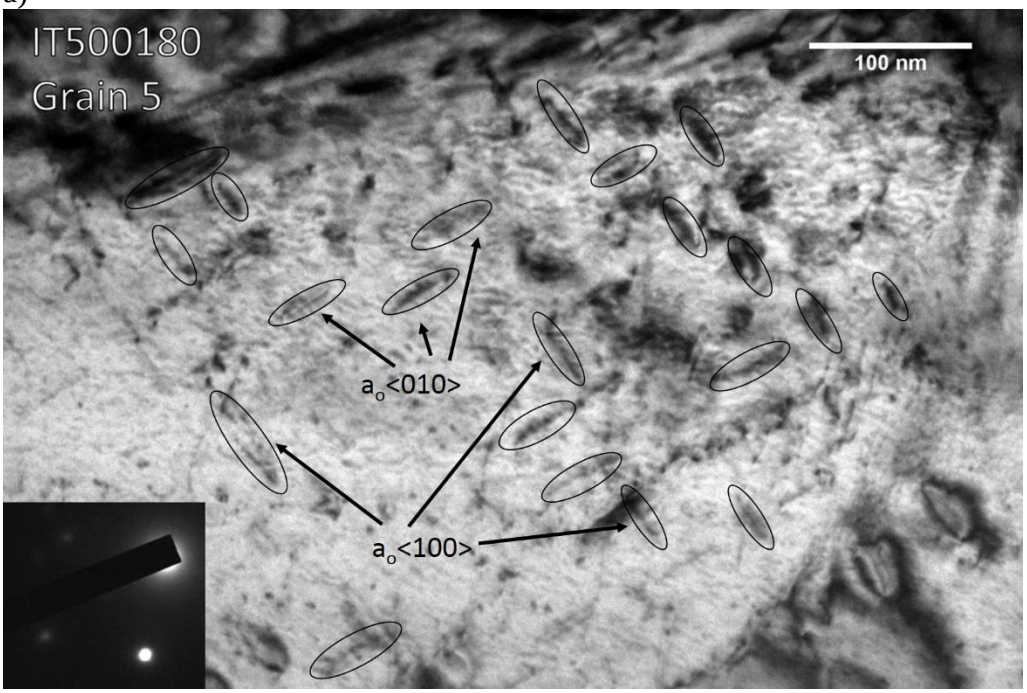

b)

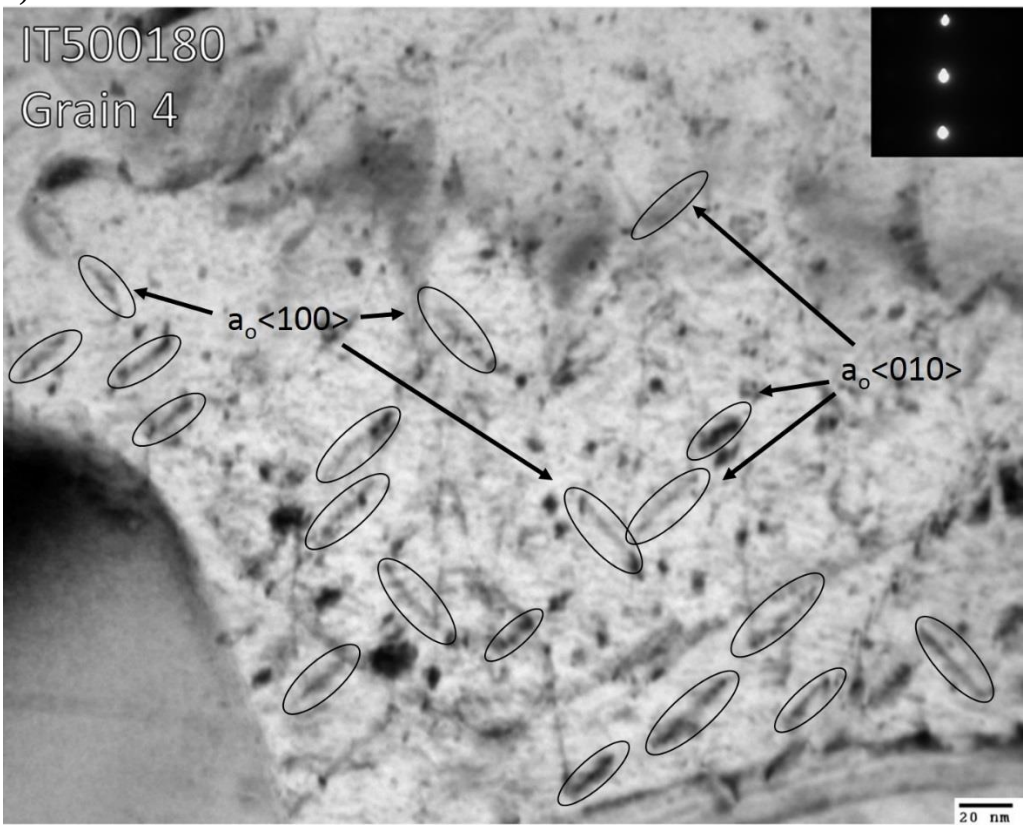

Figure 5.14 TEM image of a grain from sample IT500180 after irradiation creep at 500°C, 180MPa and 1dpa with (a) $\theta_{[100]} = 50^o$, $\theta_{[010]} = 40^o$, (b) $\theta_{[100]} = 20^o$, $\theta_{[010]} = 70^o$

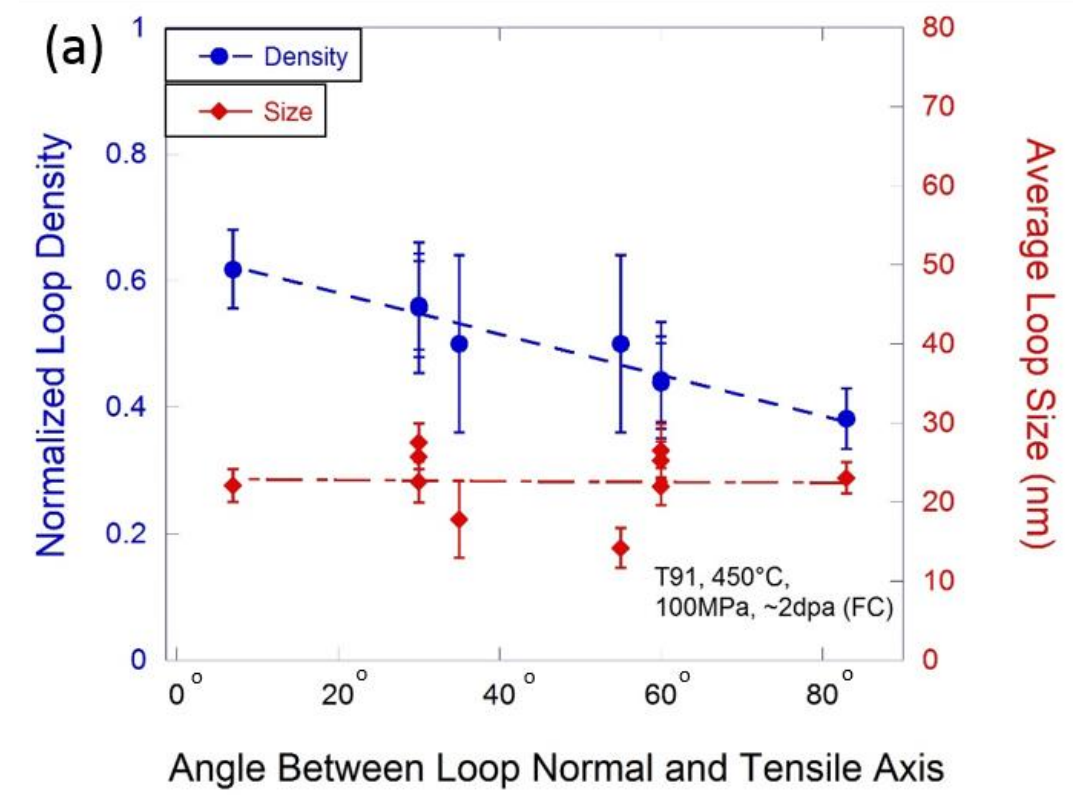
(a)
Density
Size
Normalized Loop Density
Average Loop Size (nm)
T91, 450°C,
100MPa, ~2dpa (FC)
Angle Between Loop Normal and Tensile Axis

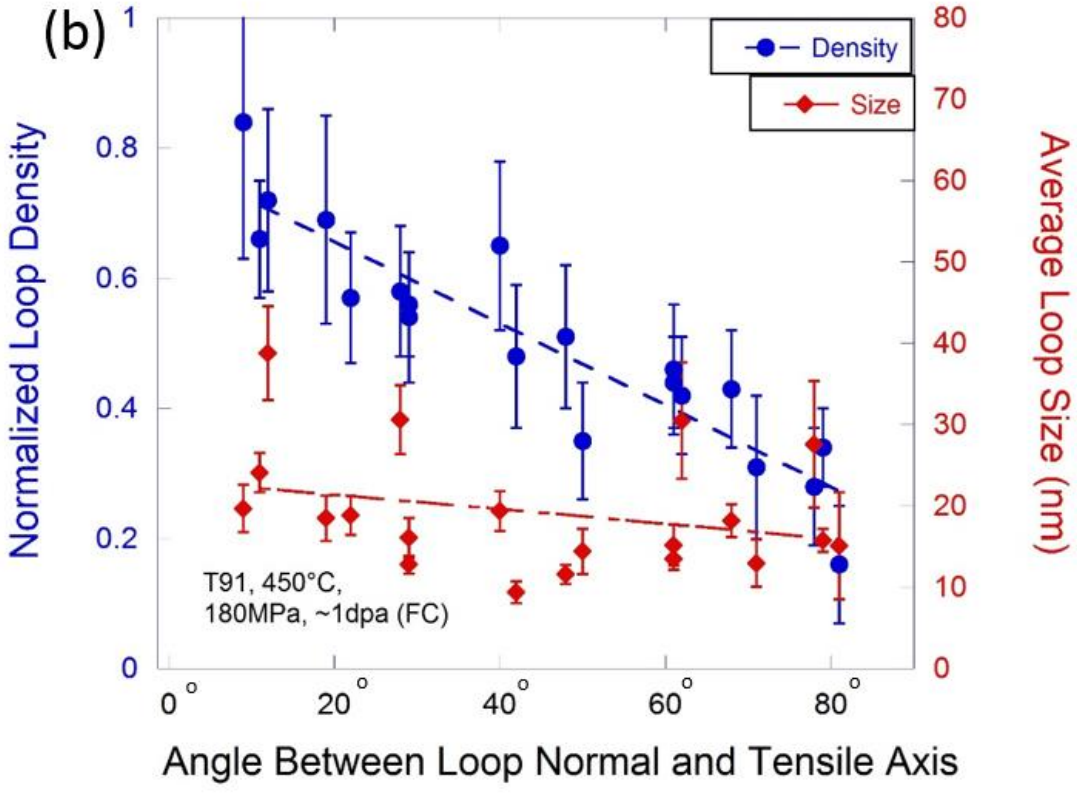
(b)
Density
Size
Normalized Loop Density
Average Loop Size (nm)
T91, 450°C,
180MPa, ~1dpa (FC)
Angle Between Loop Normal and Tensile Axis

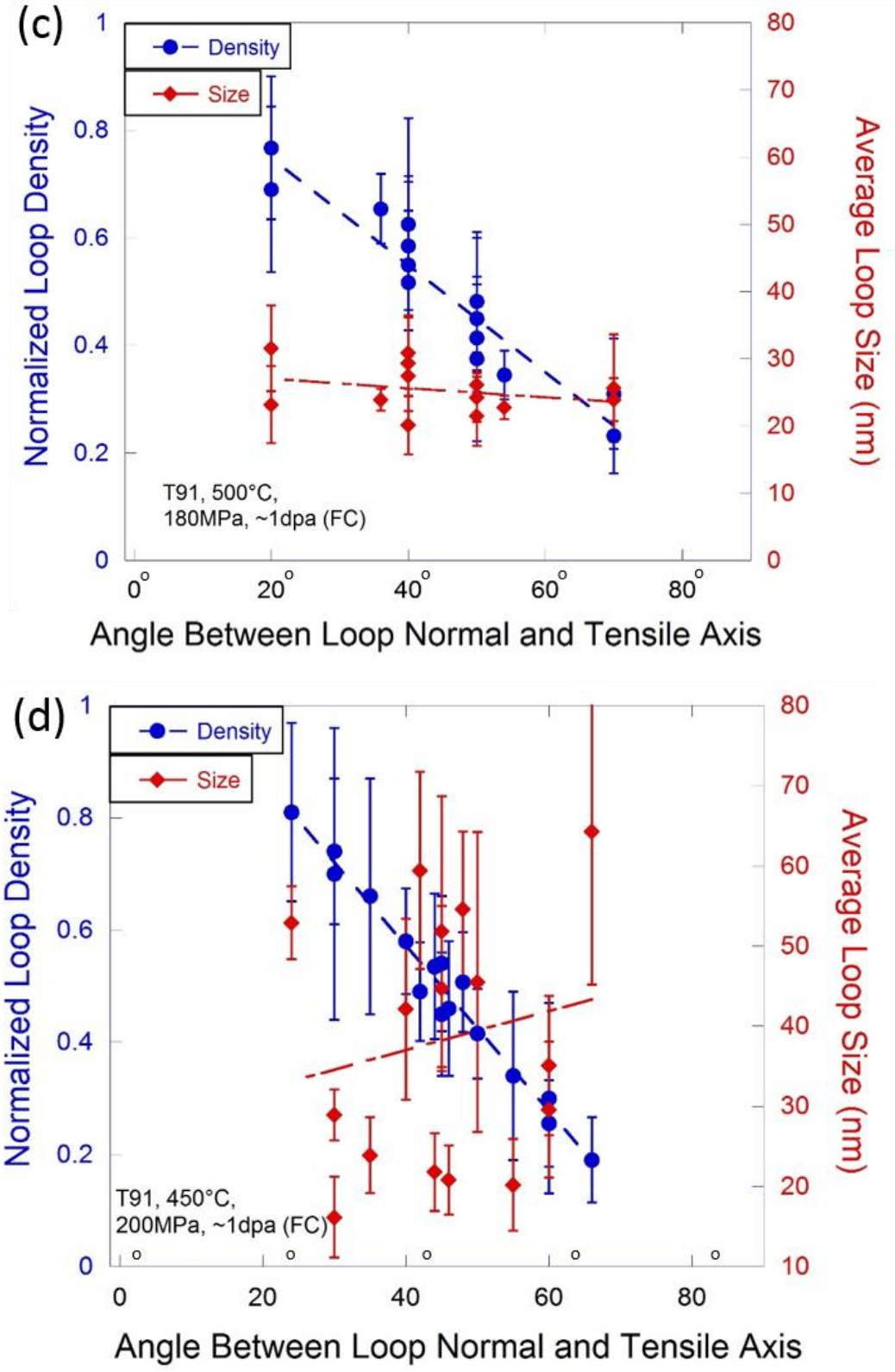

Figure 5.15 Loop anisotropy plot of the irradiation creep experiments for a) IT450100, b) IT450180, c) IT500180, d) IT450200. The normalized loop

5.2.2 Dislocation Loop Size Spectrum

Although there were no observable difference in the diameter of different dislocation loops of different orientation to the tensile axis within a single grain, the magnitude of the applied tensile stress could still affect the overall dislocation loop size in the bulk material. Table 5.5 tabulates the number of loops for each loop diameter for each sample condition. The dislocation loop size spectrums are plotted in Figure 5.16 for the four irradiation creep samples: IT450100, IT450180, IT450200, and IT500180. Any differences in loop diameter due to temperature will be reflected by comparison between IT500180 irradiated and IT450180, both irradiated at 180MPa with one at sample temperature of 500^{o}C and the other at 450^{o}C. Comparisons between the samples irradiated at 450^{o}C under 100MPa, 180MPa, and 200MPa will reveal any stress effects on the average dislocation loop diameter.

The histograms show that the average dislocation loop size distributions of irradiation creep samples with an applied stress below 180MPa are very similar. All three samples show that dislocation loop size follow a skewed distribution that peaks around 20nm with a maximum of around 80nm. The calculated full width half maximum (FWHM) of the histograms were also very similar at around 20-25nm. In contrast, sample IT450200 with an applied stress of 200MPa showed a higher fraction of larger loops. The average loop size for the 200MPa condition was found to be much larger at around 40nm, and the FWHM at around 50nm. This difference in loop size distribution suggested that dislocation loops were growing larger under high stress irradiation creep.

Table 5.5 Dislocation loop diameter

Dislocation Loop Diameter (nm)	IT450200 Loop Number	IT450180 Loop Number	IT450100 Loop Number	IT500180 Loop Number
10	3	63	5	1
15	14	138	54	31
20	22	123	101	86
25	30	57	103	67
30	29	52	63	65
35	26	22	54	48
40	36	9	29	28
45	17	3	18	11
50	26	10	5	3
55	18	5	1	3
60	14	3	0	1
65	12	2	1	1
70	14	2	0	0
75	11	0	0	0
80	7	1	0	1
85	4	0	0	0
90	2	0	0	0
95	0	0	0	0
100	1	0	0	0
105	3	0	0	0
110	5	0	0	0

a)

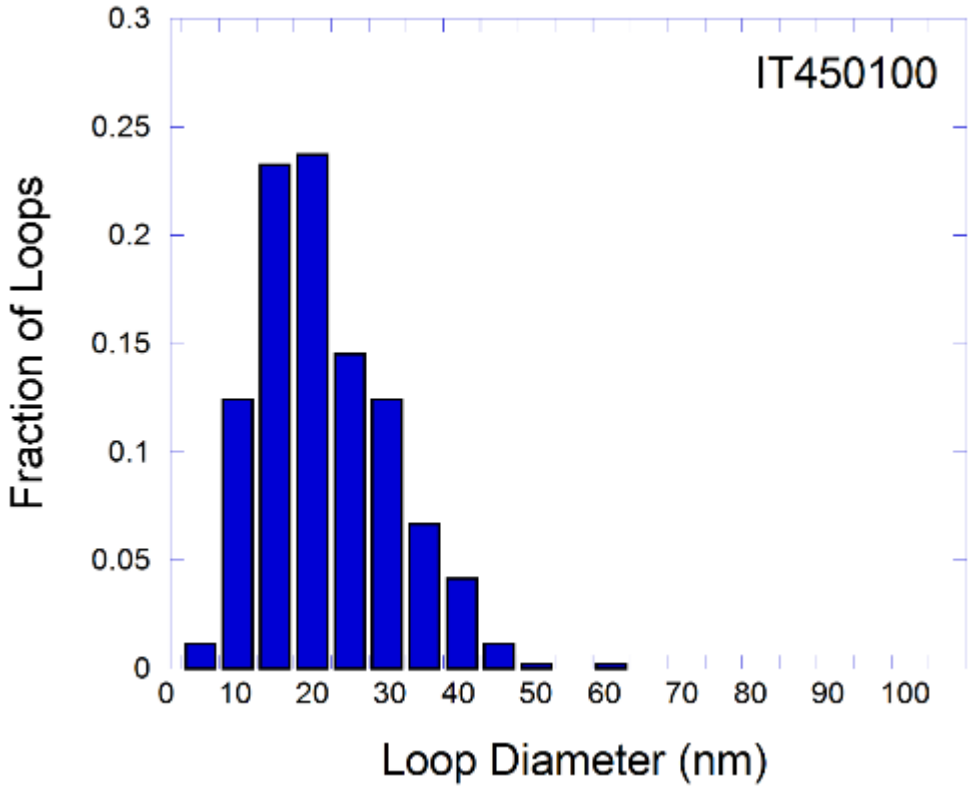
IT450100
Fraction of Loops
0.3
0.25
0.2
0.15
0.1
0.05
0
0 10 20 30 40 50 60 70 80 90 100
Loop Diameter (nm)

b)

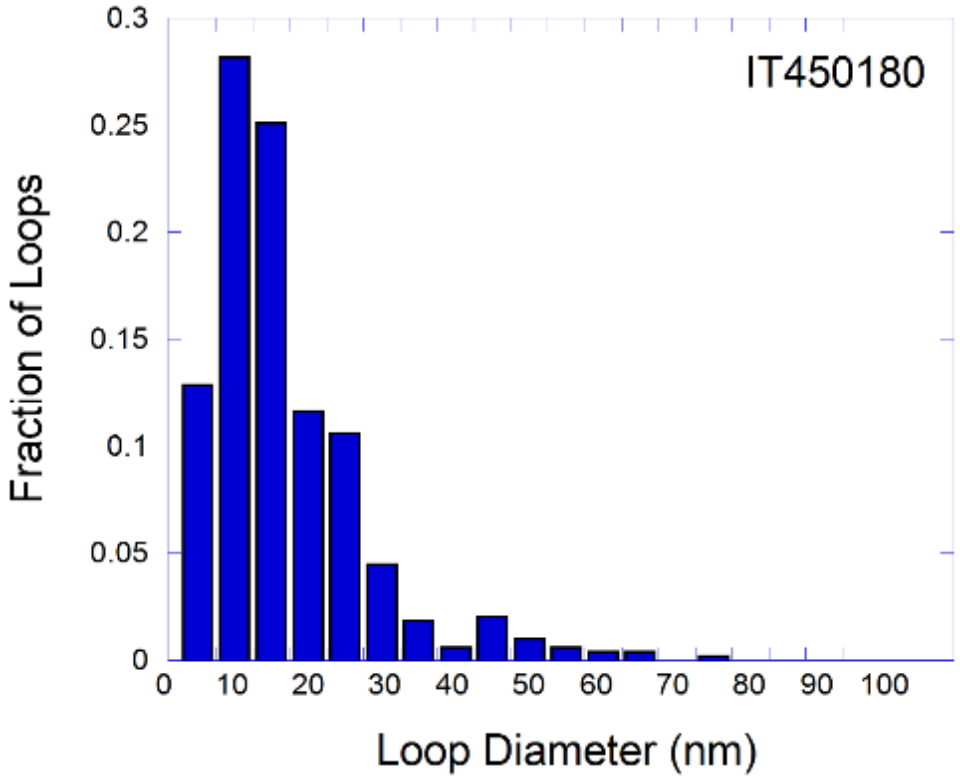
IT450180
Fraction of Loops
0.3
0.25
0.2
0.15
0.1
0.05
0
0 10 20 30 40 50 60 70 80 90 100
Loop Diameter (nm)

c)

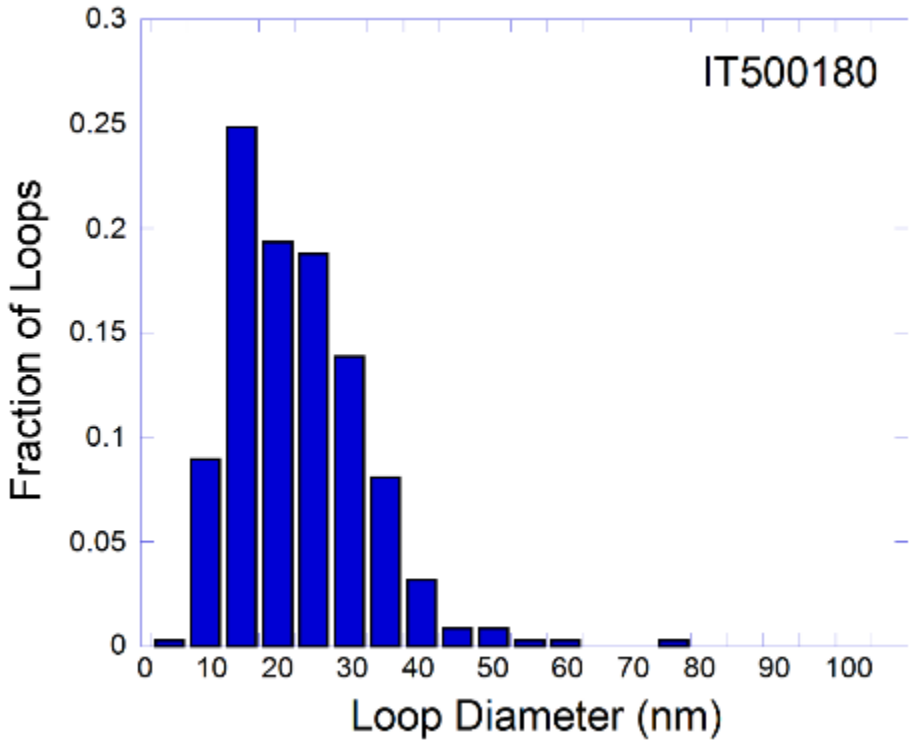

d)

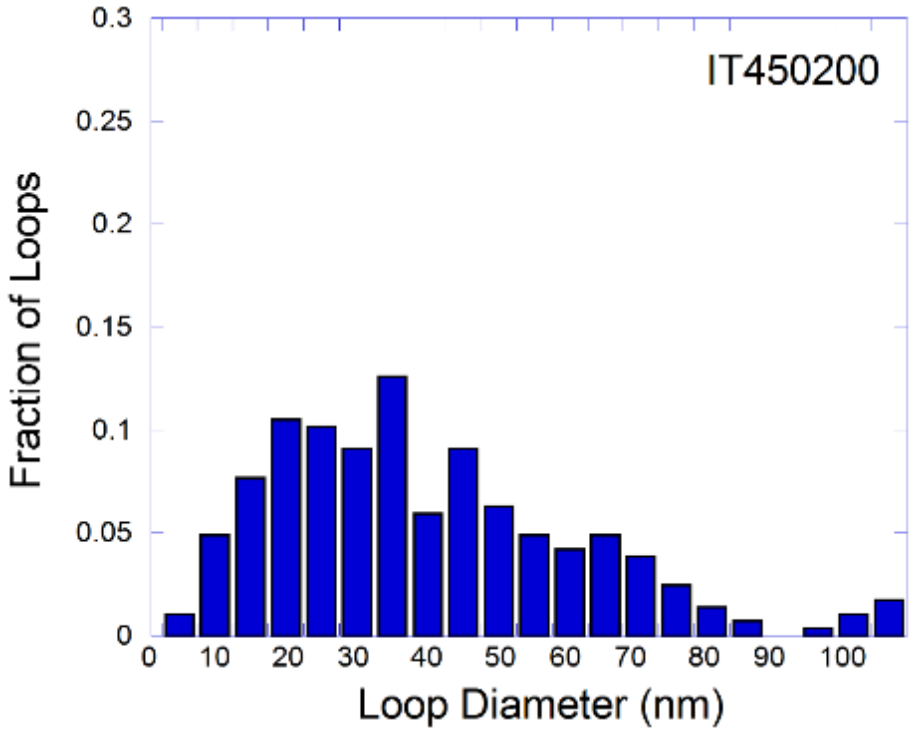

Figure 5.16 Loop size distributions of irradiation creep samples, a) IT450100, b) IT450180, c) IT500180, d) IT450200.

5.2.3 Analysis of Dislocation Loop Nature

The TEM analysis to distinguish a dislocation as either interstitial or vacancy type utilized the inside-outside contrast technique. A dislocation loop with an interstitial core will show outside contrast when $b \cdot g > 0$ and g is positive, while a vacancy loop will show outside contrast when g is negative. Figure 5.17 shows a schematic of the relationship between the dislocation loop nature and its contrast under TEM [79].

The procedure for determining the dislocation loop nature is twofold. First, the zone axis was indexed so the g vector for two beam condition could be uniquely defined. Figure 5.18 shows a series of TEM images, their corresponding diffraction and Kikuchi patterns of the grain being analyzed. The grain was tilted from the [-110] Kikuchi line near the [001] zone axis to the [-200] Kikuchi line near the [013] zone axis. Seven images in total were taken to chart the zone axis, and the position of the transmission beam on the zone axis is shown as a star on the Kikuchi map for each image. The zone axis for the grain was defined as [001], and all loop analysis will be conducted in this grain with a known zone axis.

Secondly, the dislocation loops were imaged in both positive and negative g two beam conditions to determine the sense of the loop Burgers vector. Two dislocation loops were imaged separately inside the grain. The [010] dislocation loop imaged with g=020 showed outside contrast, and showed inside contrast when imaged with g=0-20. The [100] dislocation loop was imaged with g=1-10 and showed outside contrast, and the same loop was imaged with g=-110 and showed inside contrast. The TEM loop images with their corresponding Kikuchi and diffraction pattern are shown in Figure 5.19. In both cases, the dislocation loops showed outside contrast when imaged with a positive g vector. These observations suggest the dislocation loops imaged were interstitial in nature as predicted by theory.

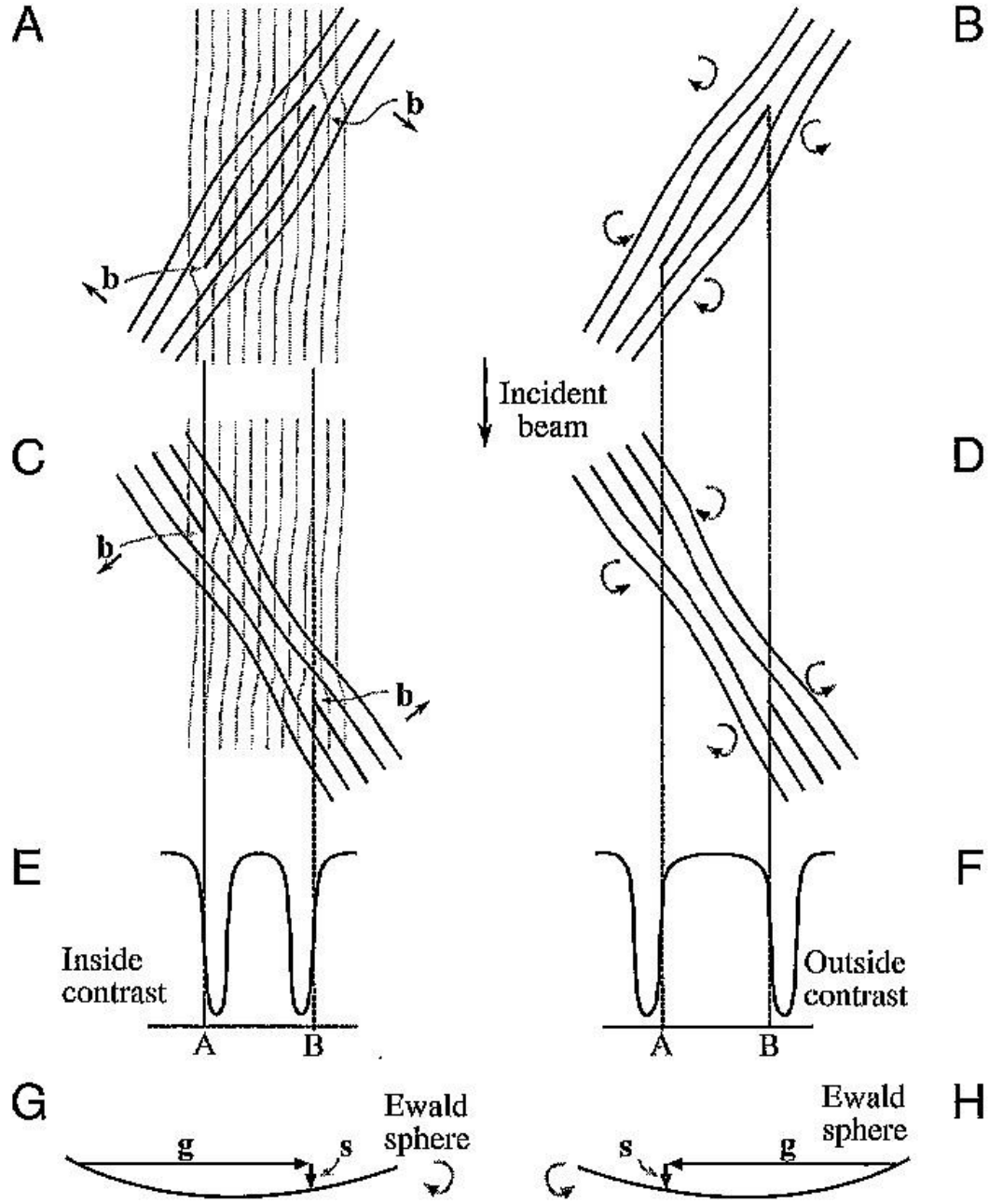

Figure 5.17 (A) Structure of an interstitial loop relative to the diffracting planes. (B) Arrows show the rotation of the diffraction planes around the dislocation. (C, D) Vacancy loops. (E, F) Position of the image contrast relative to the projected dislocation position. Inside contrast occurs when clockwise rotation of the diffracting planes brings them into the Bragg condition. Outside contrast occurs for the counter-clockwise case. (G, H) The relationship between g, s, and the sense of the rotation. [79]

a)

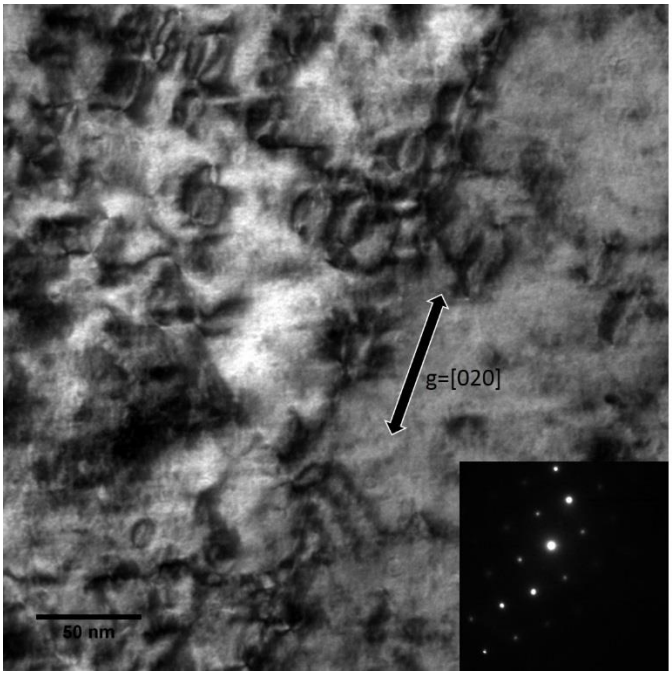

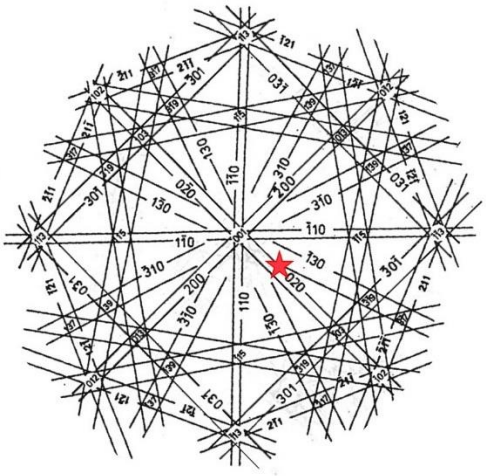

X-tilt = -7.7
Y-tilt = 0.11

b)

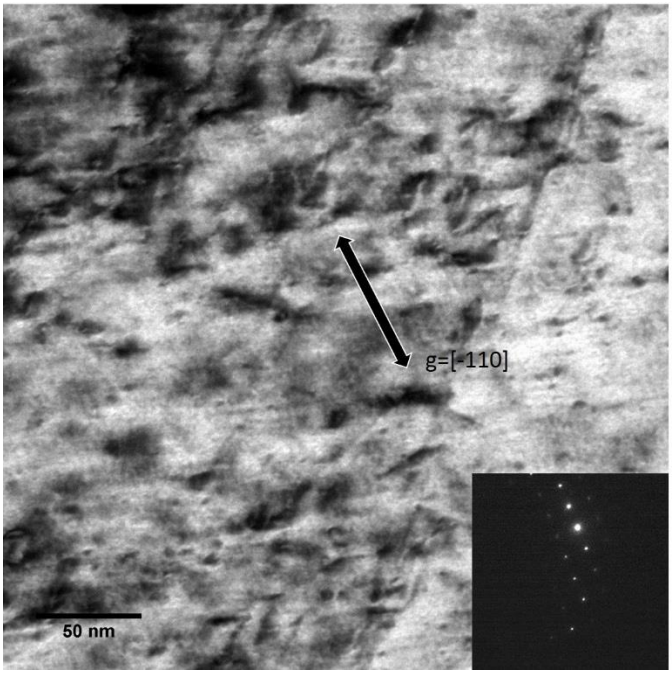

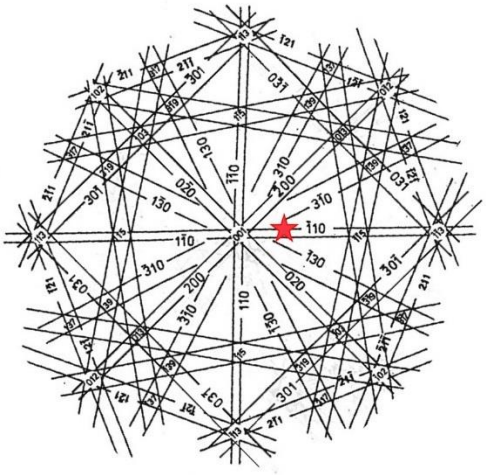

X-tilt = -12.1
Y-tilt = 0.11

c)

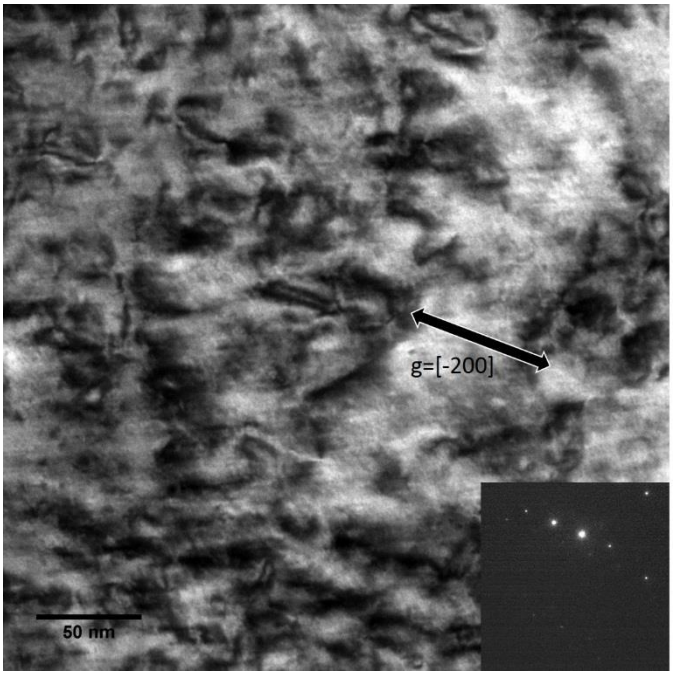

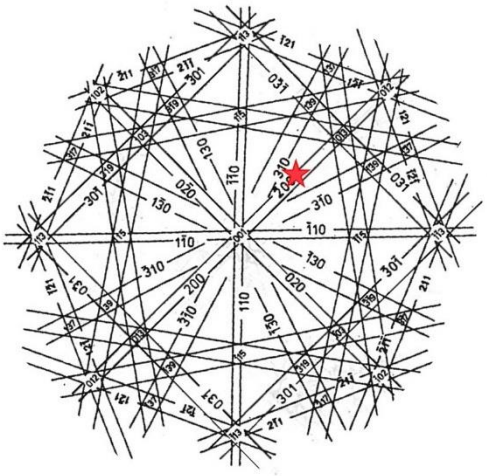

X-tilt = -22.1
Y-tilt = 0.11

d)

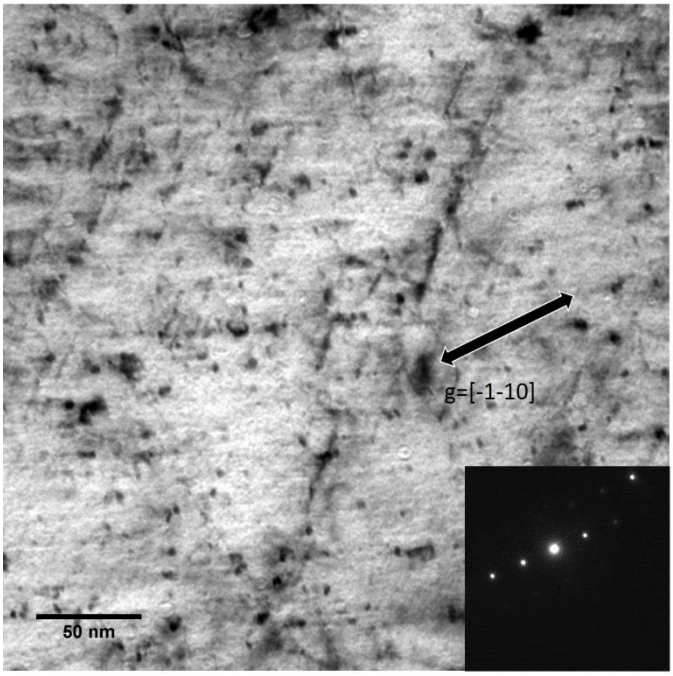

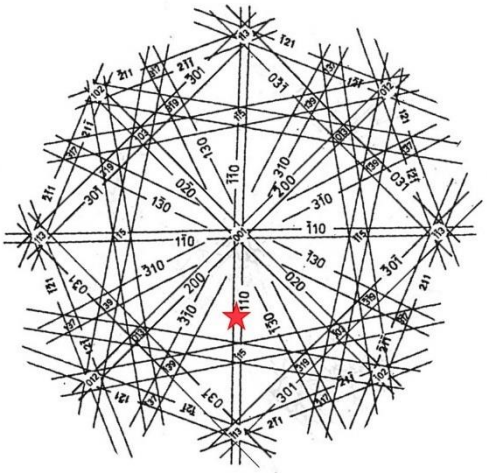

X-tilt = 2.3
Y-tilt = 0.11

e)

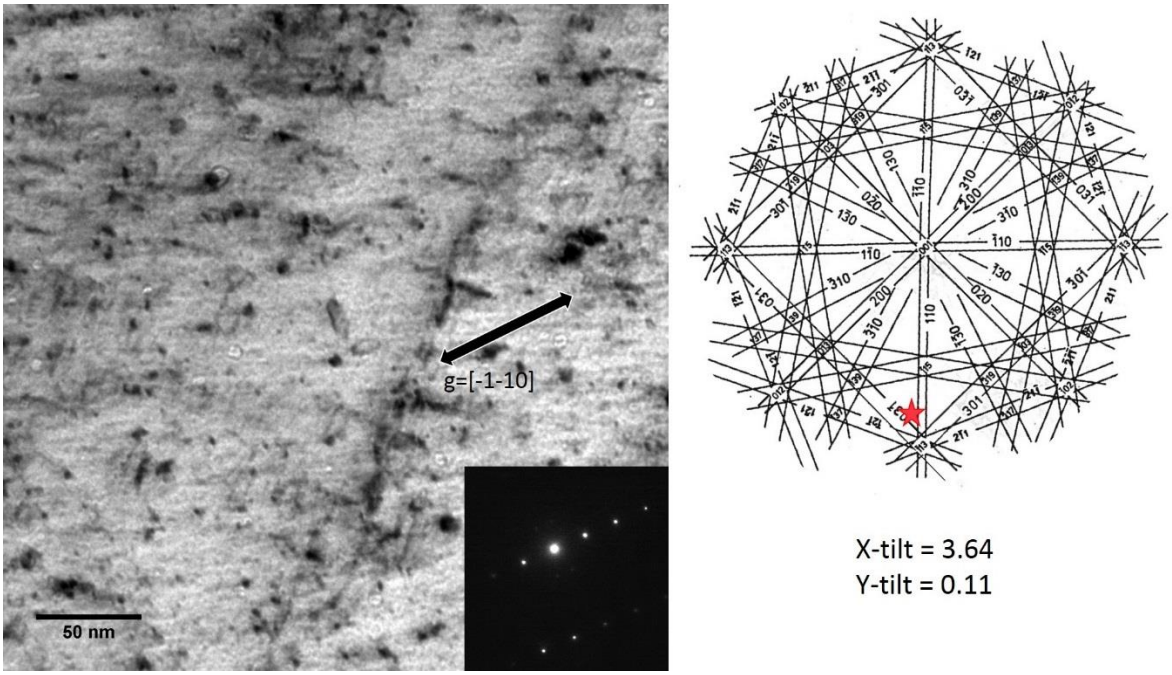

Figure 5.18 TEM images of a grain tilted around its [001] zone axis with their corresponding diffraction pattern a) x-tilt = -7.7, y-tilt=0.11, b) x-tilt = -12.1, y-tilt=0.11, c) x-tilt = -22.1, y-tilt=0.11, d) x-tilt = 2.3, y-tilt=0.11, e) x-tilt = 3.64, y-tilt=0.11.

a)

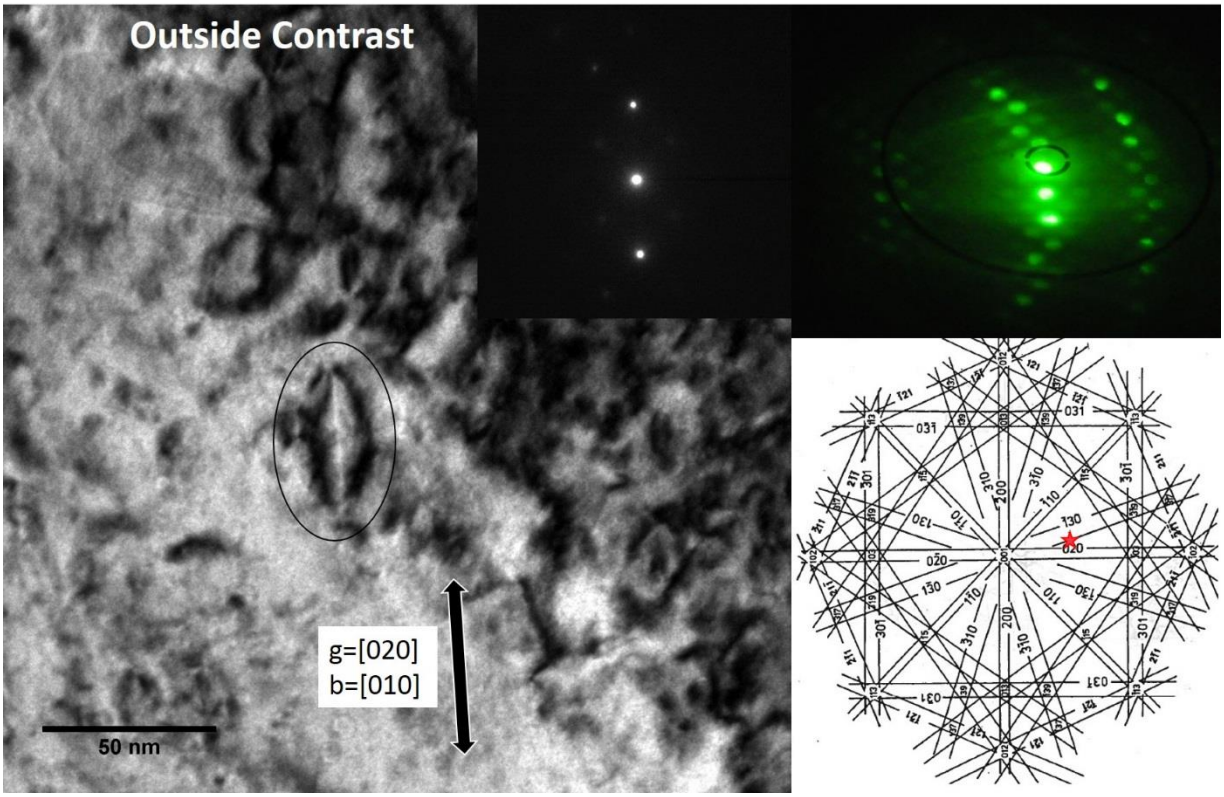
Outside Contrast
g=[020]
b=[010]
50 nm

b)

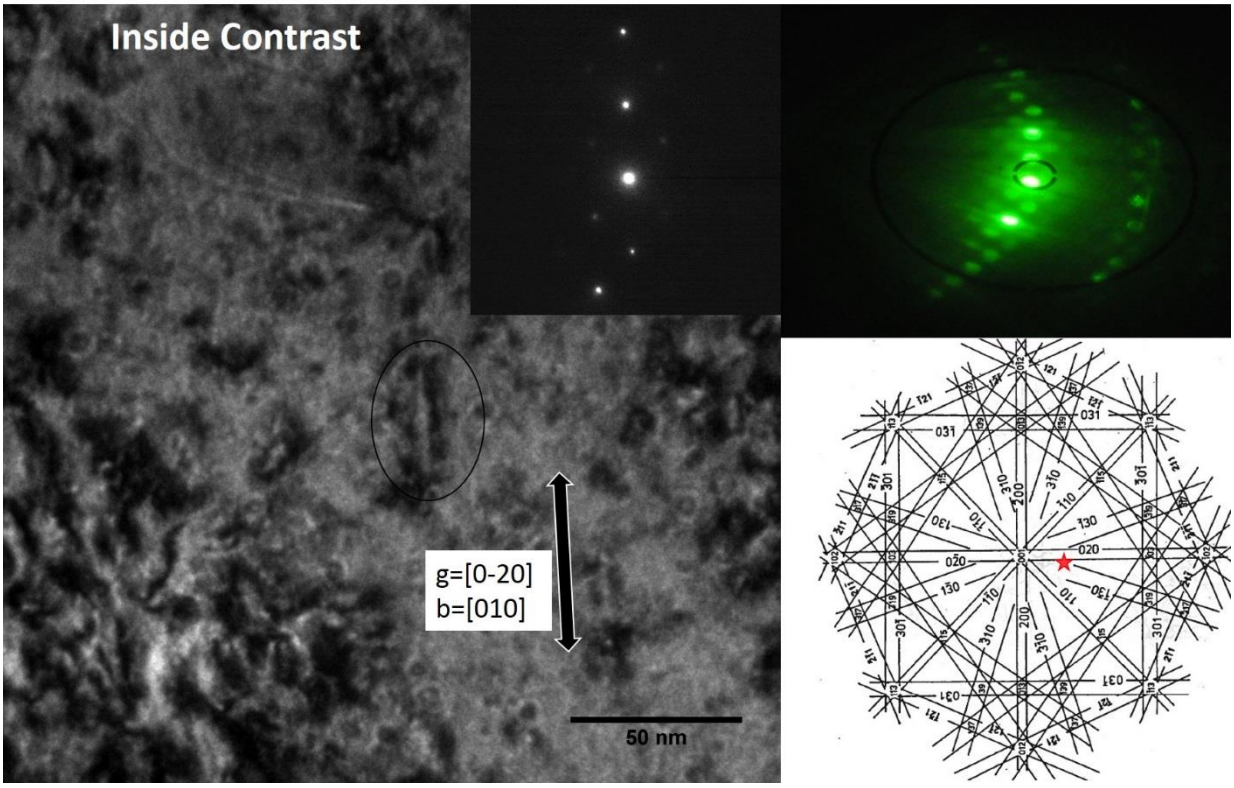
Inside Contrast
g=[0-20]
b=[010]
50 nm

c)

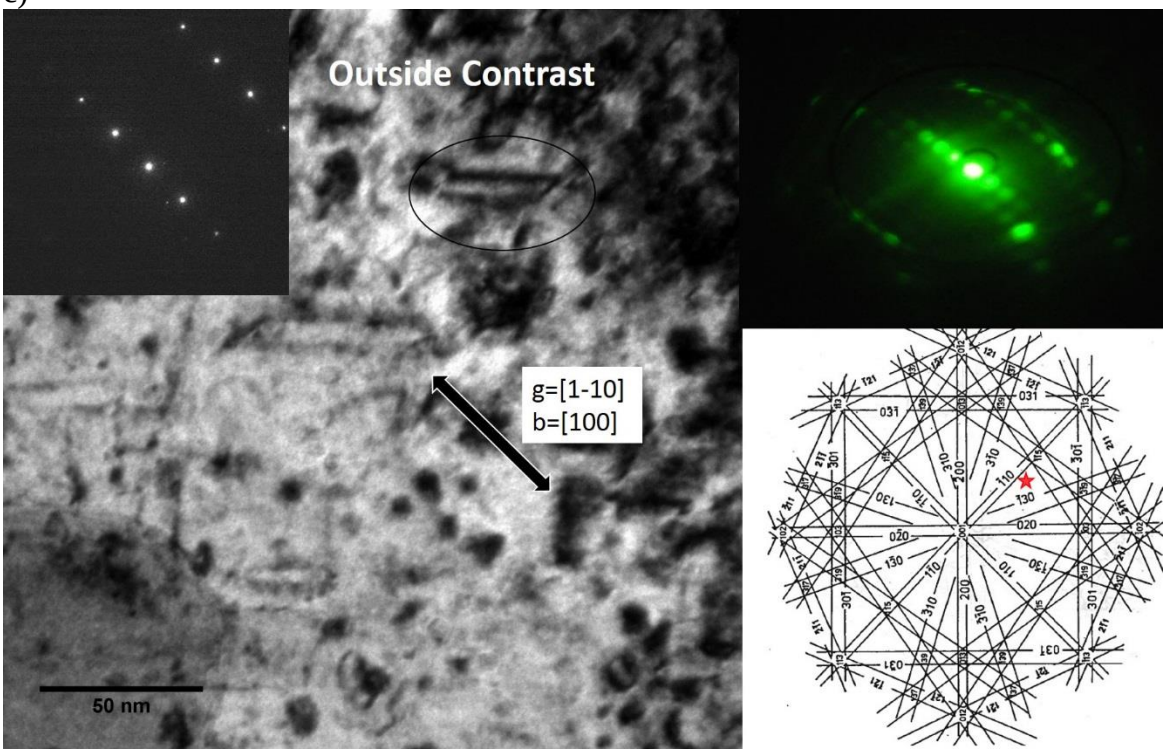

d)

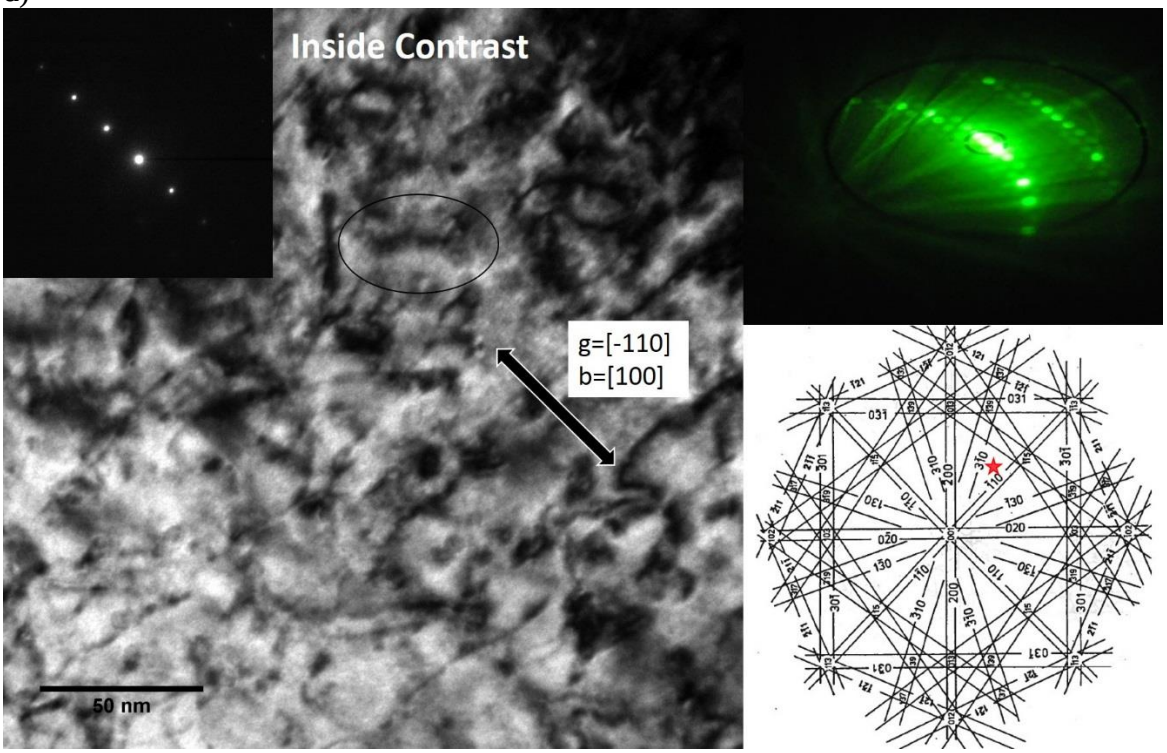

Figure 5.19 TEM image and Kikuchi line of an a_o<100> loop under two beam condition a) g=[020] showing outside contrast, b) g=[0-20] showing inside contrast, c) g=[1-10] showing outside contrast, d) g=[-110] showing inside contrast.

5.2.4 Dislocation Network Density

The dislocation network density is an important quantity in analyzing irradiation creep mechanisms. Dislocation network density measurements were done on three samples to quantify the difference between thermal creep, irradiation, and irradiation creep samples. The three samples chosen for dislocation network analysis are: TT450200 for thermal creep, IT450000 for irradiation, and IT450200 for irradiation creep. The sample thickness was estimated by SEM measurements looking edge on the FIB sample foil. The method used to determine dislocation density was outlined in section 4.4.3 of this thesis.

Three samples were chosen for dislocation network density analysis to compare the effects of stress, and irradiation on the dislocation microstructure. Sample IT450200A was chosen as the sample for irradiation creep. 17 TEM images were analyzed and a dislocation density of $5.70\pm0.83x10^{14}m^{-2}$ was found. Sample IT450000A was chosen as the sample for the unstressed condition. 9 TEM images were analyzed and a dislocation density of $3.64\pm0.72x10^{14}m^{-2}$ was determined. Sample TT450200A was chosen as the sample for thermal creep. 9 TEM images were analyzed for and a dislocation density of $3.97\pm0.98x10^{14}m^{-2}$ was found. A representative dislocation network TEM image from each condition are shown in Figure 5.20. Every TEM imaged and analysis details for dislocation network density are recorded in Appendix C.

The dislocation densities are plotted in Figure 5.21 to compare the three test conditions against the as received T91. The sample TT450200 tested under thermal creep conditions was found to have a dislocation network density of $4.14\pm0.96x10^{14}m^{-2}$. Proton irradiation sample IT450000 have a dislocation network density of $3.64\pm0.72x10^{14}m^{-2}$. Irradiation creep sample IT450200 have a dislocation network density of $5.7\pm0.85x10^{14}m^{-2}$. The dislocation network density for all three samples were of the same order of magnitude, with the irradiation creep sample having a density slightly higher than the other two. The results of dislocation density analysis hint at a correlation between creep strain rate and dislocation network density. However, the trend is not strong enough to make any definitive quantitative statements.

Qualitative observations on the dislocation density also hint at some unique dislocation network behavior that has been previously observed. Figure 5.22 shows an image of a dislocation line bowing out in while being pinned by dislocation loops. This dislocation line behavior was

described as Orowan bowing, and serves as the basis for the dislocation climb and glide mechanism described by both I-creep and PAG [5], [17], [19], [85]. Although one would expect the dislocation to return straight after the removal of stress, it is possible residual stresses in the sample after the rapid cooling upon the removal of beam heating retained the evidence for Orowan glide. Figure 5.23 shows a large amount of dislocation line segments aligned in specific directions. Diffraction pattern analysis indicates that the dislocations appear to be in the <110> direction. This "self-ordering" behavior has also been reported in ion irradiation experiments on FM steels by Kaoumi et al. [86] The ordering of dislocation lines in specific directions coupled with evidence of dislocation glide suggested a more complex dislocation network behavior than what was described in conventional irradiation creep mechanisms. However, these observations were qualitative in nature and does not provide enough quantitative evidence for detailed analysis.

Table 5.6 Results of dislocation network analysis

Sample Name	Number of TEM Images	Sample Thickness (nm)	Total Intersects Counted	Average Dislocation Density (m^{-2})	Error (m^{-2})
IT450200	17	100	660	$5.7x10^{14}$	$8.5\ x10^{13}$
IT450000	9	100	187	$3.6x10^{14}$	$7.2\ x10^{13}$
TT450200	7	100	127	$4.1x10^{14}$	$9.6\ x10^{13}$

a)

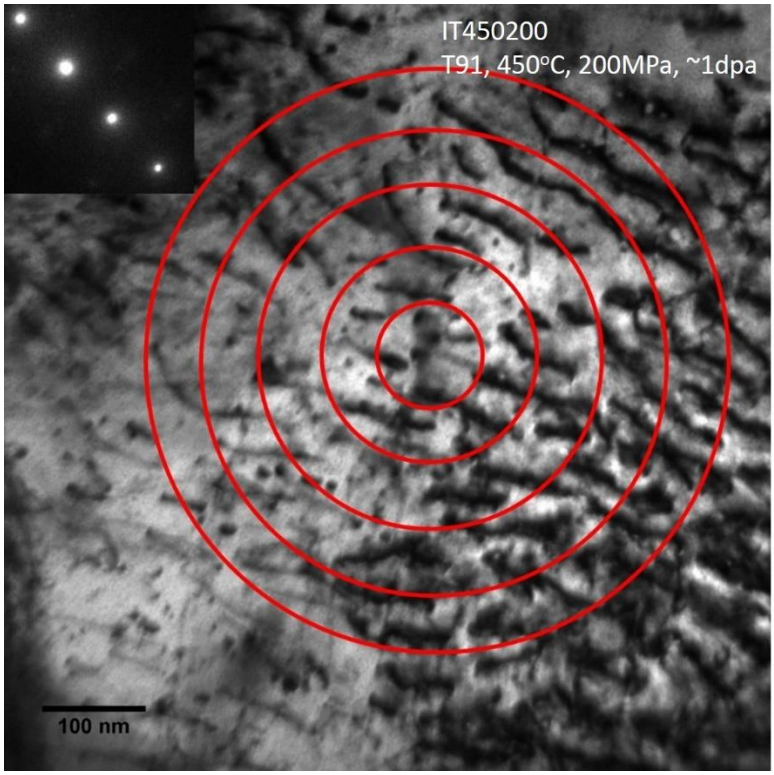
IT450200
T91, 450°C, 200MPa, ~1dpa
100 nm

b)

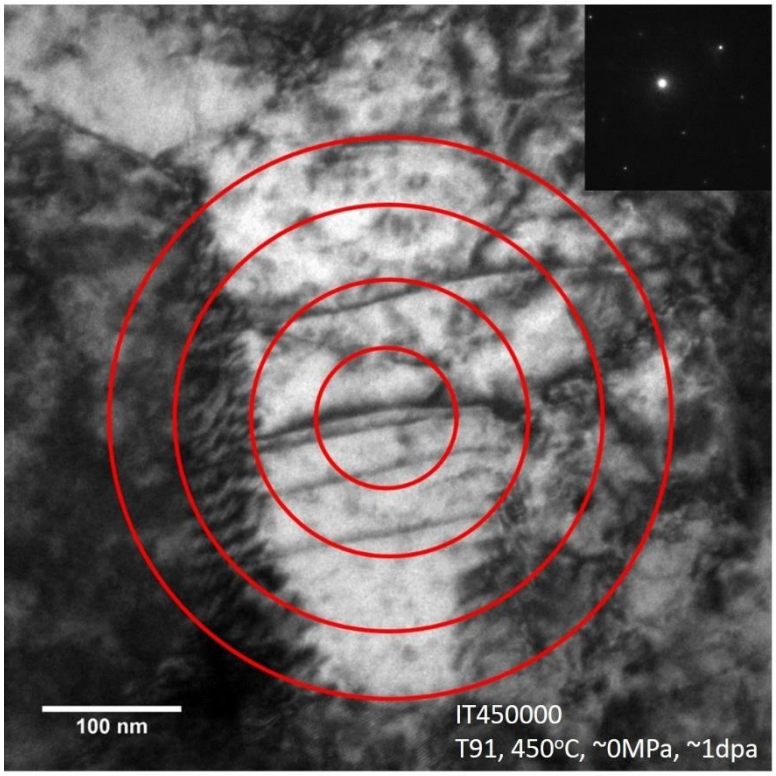
100 nm
IT450000
T91, 450°C, ~0MPa, ~1dpa

c)

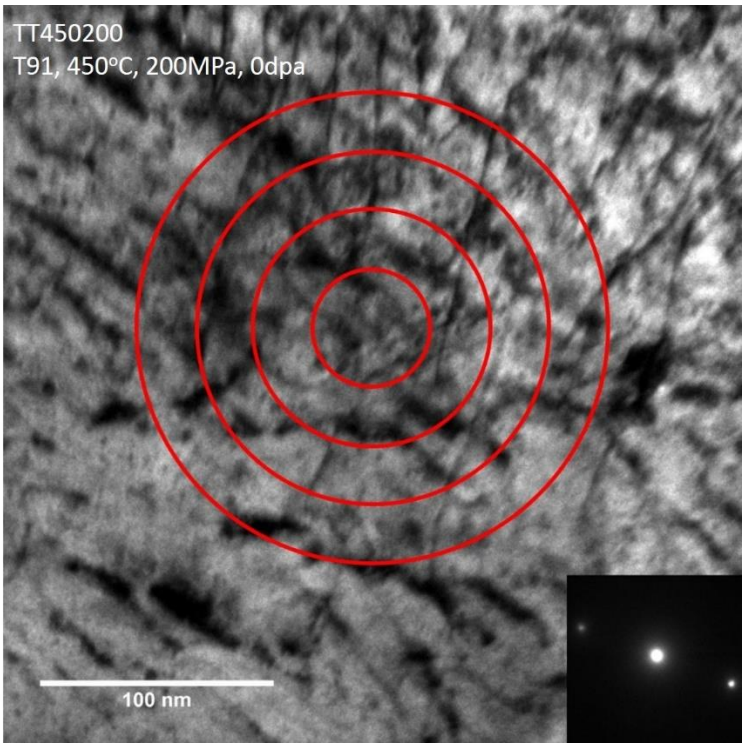

Figure 5.20 TEM image of dislocation networks for a) IT450200 irradiation creep sample, b) IT450000 unstressed irradiation sample, c) TT450200 thermal creep sample.

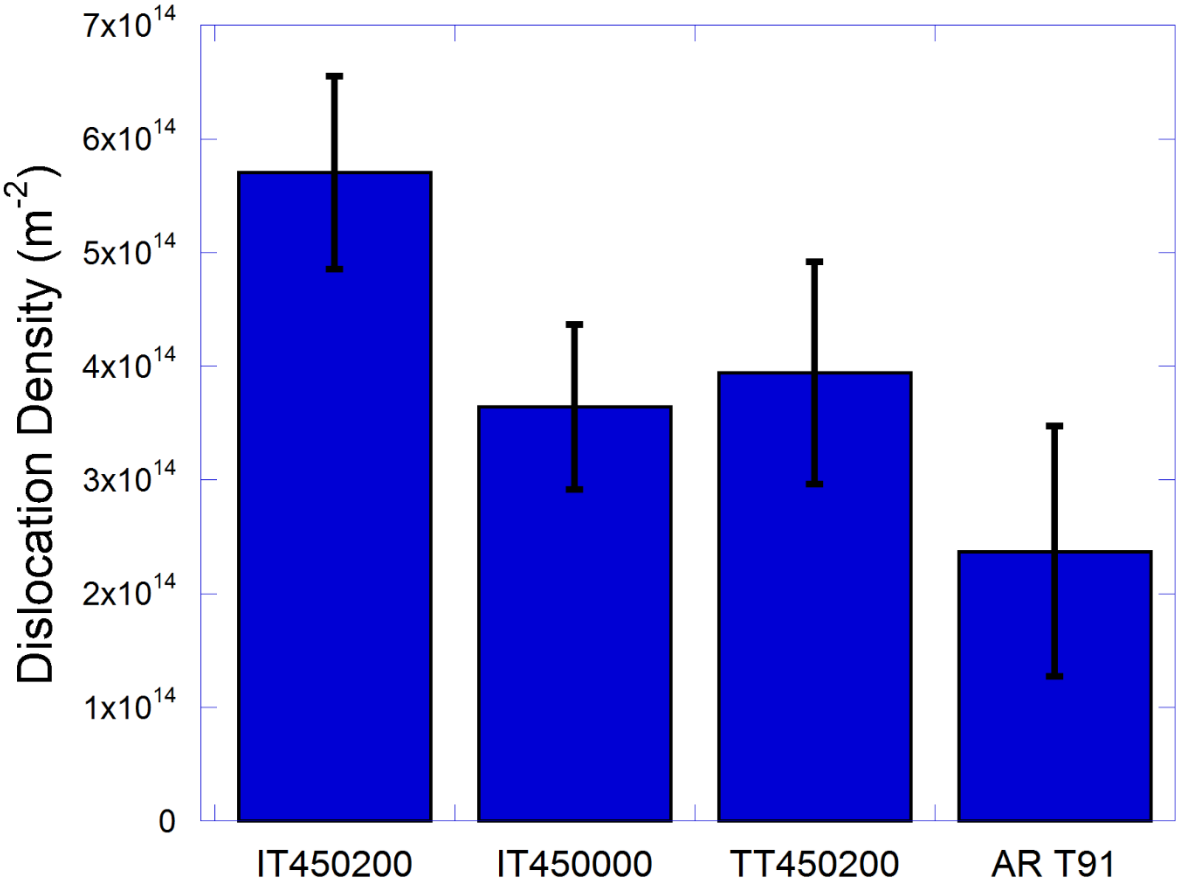

Figure 5.21 Dislocation network density of irradiation creep sample IT450200, proton irradiation sample IT450000, and thermal creep sample TT450200.

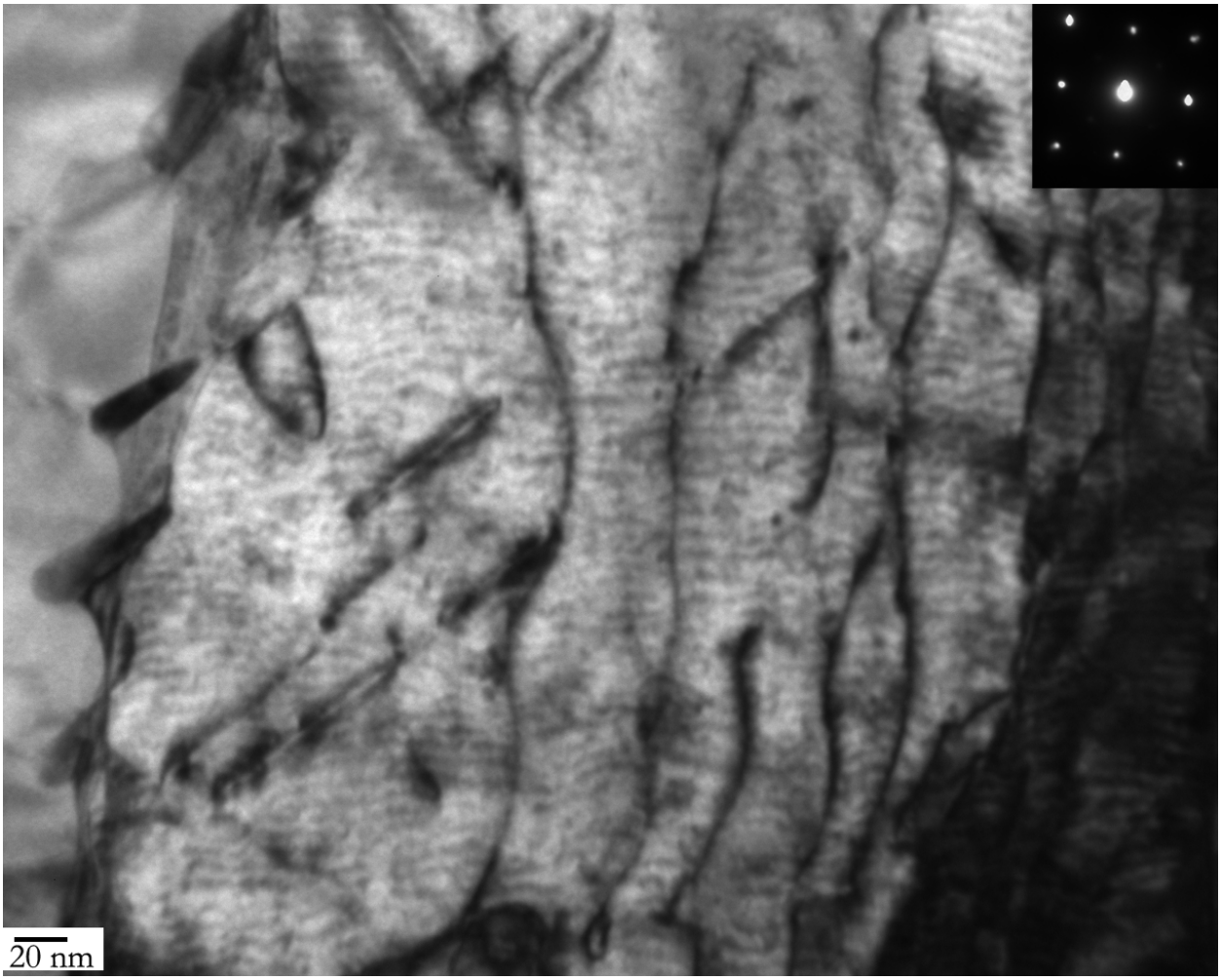

Figure 5.22 Dislocation network of irradiation creep sample IT500180. Orowan bowing of dislocation lines is clearly visible.

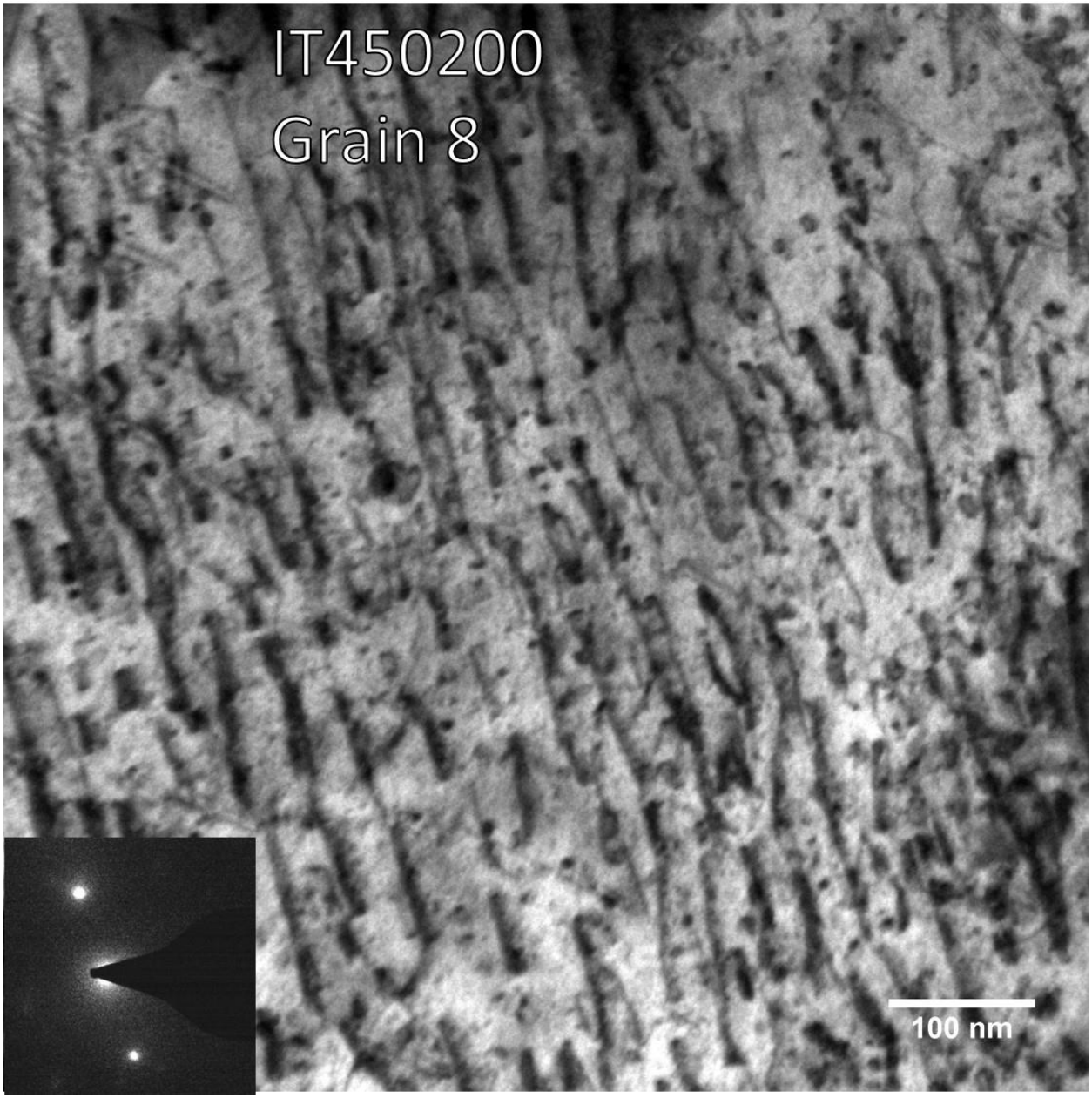

Figure 5.23 Self-ordered dislocation line segments in irradiation creep sample IT450200.

5.2.5 Sub-grain Size

Sub-grain boundaries are a major microstructure feature that acts as neutral sink for both interstitial and vacancy point defects. The sub-grain size need to be determined in order to perform theoretical calculations on the steady state point defect concentrations, which is the foundation for all irradiation creep mechanisms. FM steels have a complex microstructure where small sub-grains are formed inside martensitic lathes, multiple lathes form lathe packets, and multiple packets fill the large prior-austenite grains (PAG). To accurately reflect the sink density of the material, this analysis counts the smallest grain feature in the material, the sub-grain inside the lathe packets. This decision was informed by previous studies on thermal creep where the sub-grain structure were believed to be the dominating feature impacting creep behavior. [87]–[89]

The three samples chosen for sub-grain size analysis were: TT450200 for thermal creep, IT450000 for irradiation, and IT450200 for irradiation creep. Sample IT450200A was chosen as the sample for irradiation creep. 7 TEM images were analyzed and an average sub-grain size of 0.447±0.045μm was found. Sample IT450000A was chosen as the sample for the unstressed condition. 9 TEM images were analyzed and an average sub-grain size of 0.391±0.045μm was determined. Sample TT450200A was chosen as the sample for thermal creep. 8 TEM images were analyzed for and a dislocation density of 0.478±0.057μm was found. A representative TEM image of the sub-grains from each condition analyzed in this study are shown in Figure 5.24. Every TEM imaged and analysis details for sub-grain size are recorded in Appendix D. The sub-grain size are plotted in Figure 5.25 to compare the three test conditions. All three samples showed very similar sub-grain size within the error of each measurement. No significant difference was observed between the sub-grain sizes of the three samples analyzed.

Table 5.7 Results of sub-grain size analysis

Sample Name	Number of TEM Image	Number of Intercepts	Average Grain Size	Error
IT450200	7	118	0.447	0.045
IT450000	9	185	0.391	0.045
TT50200	8	103	0.478	0.057

a)

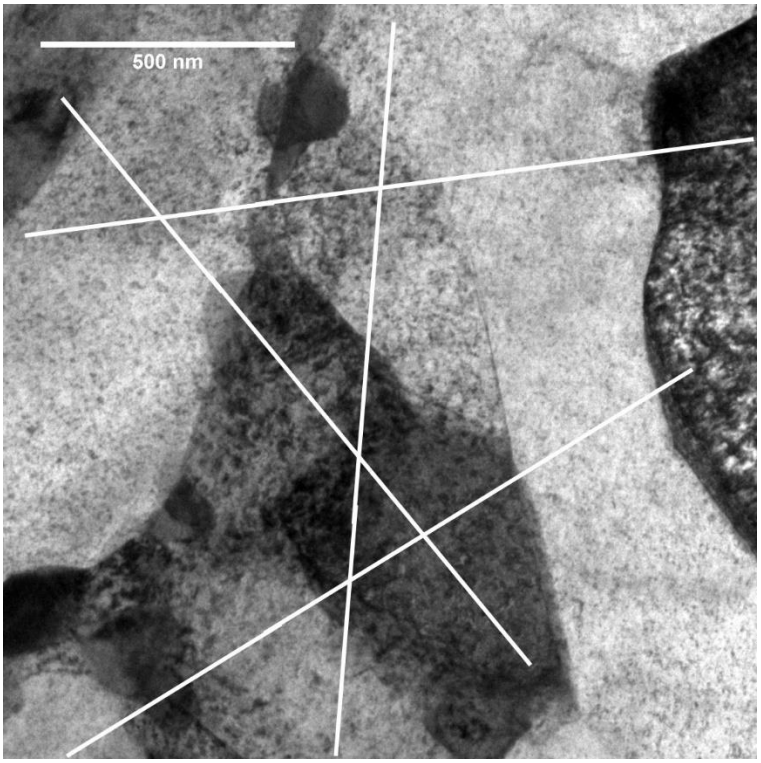

b)

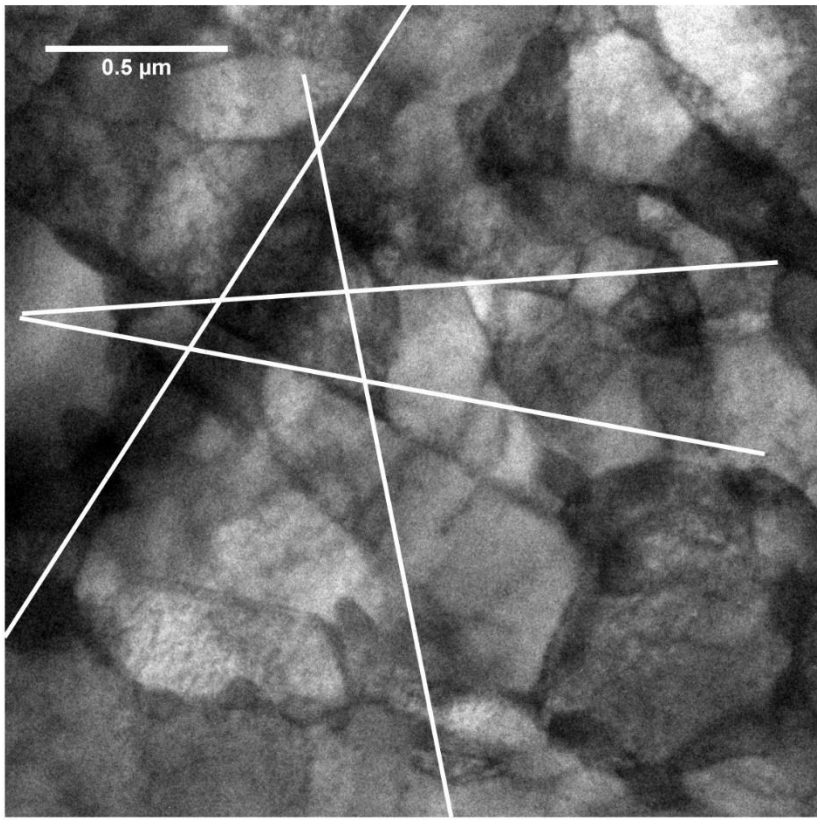

c)

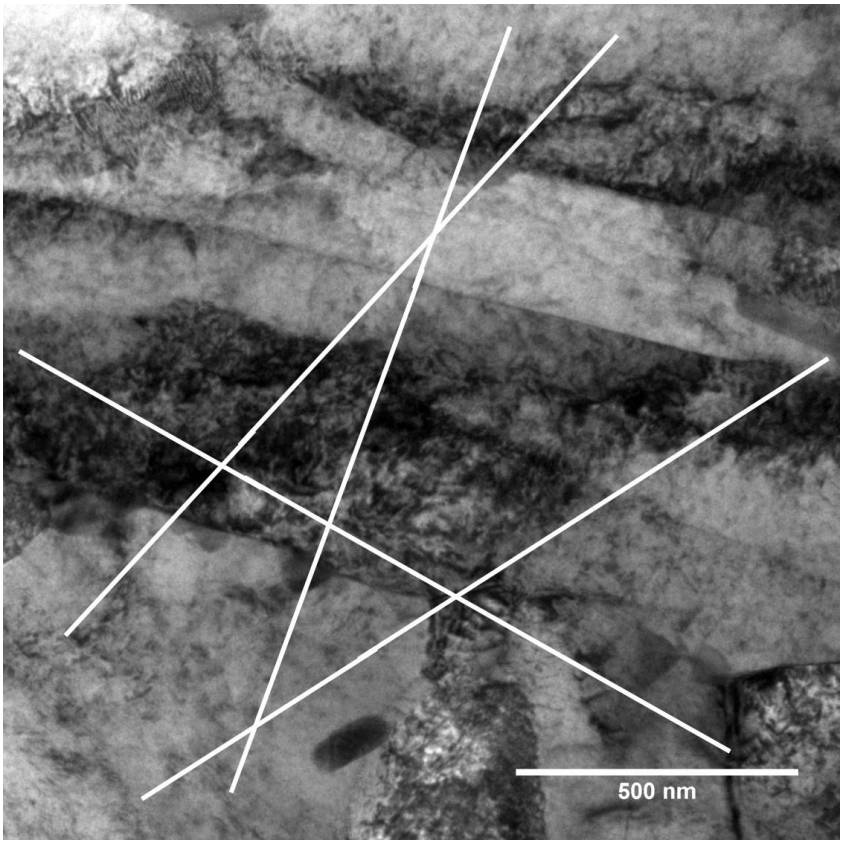

Figure 5.24 TEM image of grain size for a) IT450200 irradiation creep sample, b) IT450000 unstressed irradiation sample, c) TT450200 thermal creep sample.

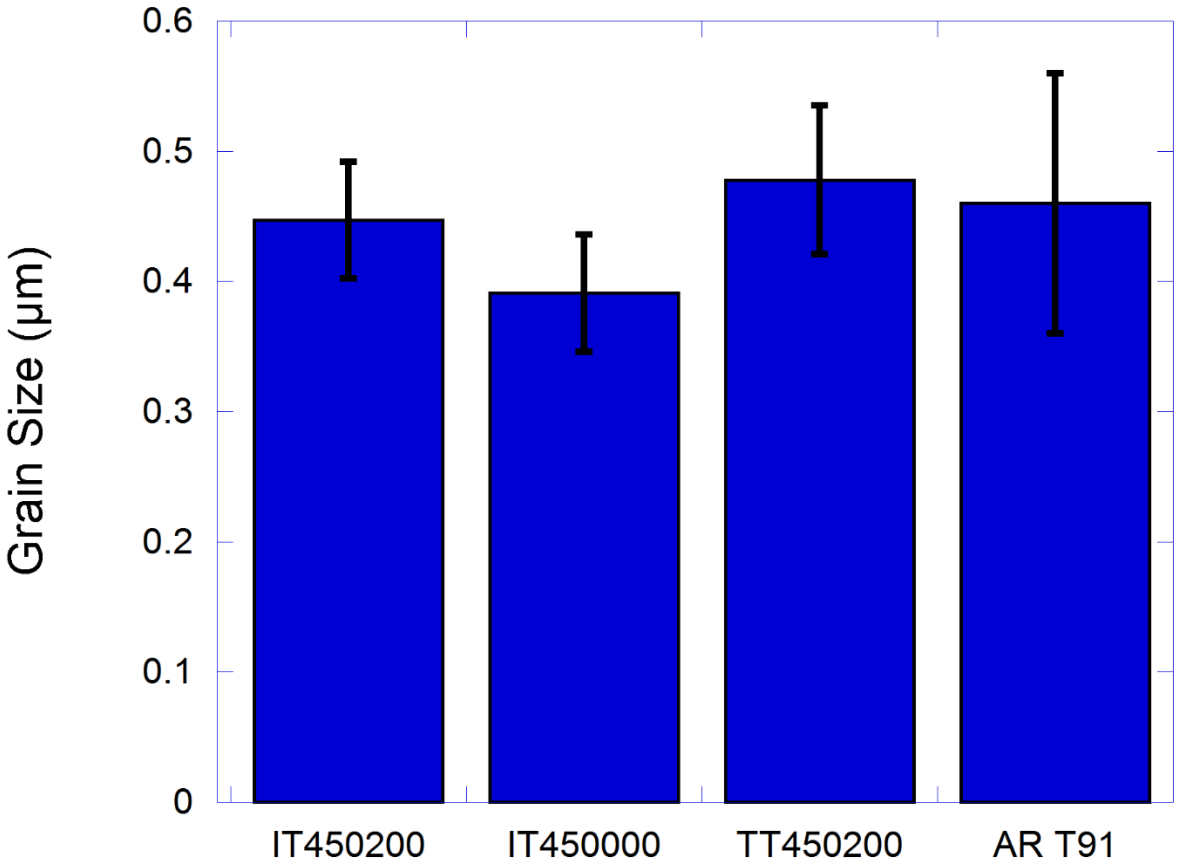

Figure 5.25 Average grain size of irradiation creep sample IT450200, proton irradiation sample IT450000, and thermal creep sample TT450200 from this study.

CHAPTER 6 Discussion

The previous chapters have presented the experimental measurements of irradiation creep strain rates, and microstructural features over a wide range of irradiation creep conditions. In this chapter, the results are analyzed under the paradigm of known theoretical irradiation creep mechanisms. This chapter systematically discusses the implications of the observed experimental results and identify any inconsistencies with current irradiation creep theories and past literature. Table 6.1 summarizes the irradiation creep theories and their unique dependencies on temperature, stress, dose rate, and microstructure features. This chapter targets the specific differences of each mechanism and discuss the implications of the experimental results from this study in light of the creep mechanisms. Section 6.1 focuses on the results of irradiation creep strain rates and their temperature, dose rate, and stress dependencies. Section 6.2 focuses on the result of key microstructure features observed that are unique to irradiation creep. Section 6.3 analyzes and calculates the strain due to observed anisotropy in the dislocation loop density. Section 6.4 subtracts out the strain contributions from known mechanisms and discuss the possibility of other theoretical mechanisms that may contribute to irradiation creep.

Table 6.1 Irradiation creep mechanisms and parameter dependencies.

Mechanism	Dose Rate dependence	Stress Exponent: n	Temperature dependence	Defining microstructure
SIPN (Stress Induced Preferential Nucleation)	1	1	1	Anisotropic loop density
SIPA (Stress Induced Preferential Absorption)	1	1	None	Anisotropic loop size distribution
PE (Preferential Emission)	None	Exponential	Arrhenius	Anisotropic loop size distribution
PAG (Preferential Absorption Glide)	1	2	None	Anisotropic dislocation glide
I-Creep	1	1	None	Voids and dislocation pinning
Proton Irradiation Creep Experiment	1	0.87/14 with PLB and Anisotropic loops	Negligible	Anisotropic loop density. No voids. Dislocation glide.

6.1 Irradiation Creep Strain Rate Dependencies

This section analyzes the strain rates of irradiation creep experiments conducted in this study and reviews their implications under current understanding of irradiation damage and creep theory. The creep rates are compared with empirical observations from neutron irradiations on similar alloys as well as calculations from fundamental theory.

6.1.1 Dose Rate Dependence of Irradiation Creep

An experiment to explore the dose rate dependence at 500ºC and 160MPa on a single sample, IT500160, to take advantage of the in-situ strain measurement capability, such that the change in strain rate due to changes in the dose rate can be observed in real time. A high irradiation temperature was necessary to accommodate for the large range of beam heating required for the different dose rates. Three dose rate conditions were used in this experiment: $1.5x10^{-6}$dpa/s, $1.7x10^{-6}$dpa/s, and $2.4x10^{-6}$dpa/s. The corresponding strain rates were found to be $1.78\pm0.89x10^{-9}s^{-1}$, $2.33\pm1.67x10^{-9}s^{-1}$, and $5.08\pm2.54x10^{-9}s^{-1}$. Thermal creep rate at 500ºC and 160MPa was added to the data as the strain rate at 0 dpa/s, shown in Figure 6.1.

Neutron irradiations are typically not able to isolate dose rate as a variable due to the complicated flux and temperature profiles in reactor and the limited space that could be used for testing. Therefore, the majority of irradiation creep experiments on FM steels only reported a range of dose rates for all irradiation conditions [11], [55], [90], [91]. Although there are no neutron irradiation creep experiments specifically targeting the dose rate dependence of FM steels, the dose rate dependence of irradiation creep of austenitic steels has been studied by Grossbeck et al. [92]. Figure 6.2 plots the strain rate as a function of dose rate for three cold-worked austenitic steels irradiated in different mixed spectrum reactors on a log-log plot. The slope of the fits were consistently at about 0.5, suggesting a square root dependence of the strain rate on the dose rate. In contrast, Lewthwaite and Mosedale [93] observed that creep compliance decreased as the dose rate increased. Woo and Garner et al. [94], [95] attempted to explain the findings by Lewthwaite and Mosedale by proposing a production bias model (PBM) which predicts an inverse square root dose rate dependence. Later interpretations of the Lewthwaite

data by Toloczko and Garner et al. [96] determined that there irradiation creep was insensitive to any changes to the dose rate up to an order of magnitude.

Much of the conflicting conclusions from analysis of irradiation creep of austenitic steels arose from the large swelling strain as well as densification from precipitation that accompanies irradiation creep in these steels. FM steels were designed to have negligible swelling and complex precipitate structure in the as-received condition, and therefore they should exhibit more consistent behavior. Klueh et al. [1] described the typical empirical equation used for neutron irradiation creep of FM steels as the following:

$$\dot{\varepsilon} = B'\sigma^n\varphi \tag{6.1}$$

Where *B'* was the temperature dependence creep compliance, *n* was the stress exponent, and φ was the flux of the reactor. In this form, the creep rate was linearly dependent on the flux which was proportional to the dose rate. This linear dose rate dependence was generally accepted in irradiation creep analysis of FM steels. Chen et al. [16], [65] normalized the strain rates of ferritic ODS alloys irradiated at STIP to obtain creep compliance by assuming a linear dose rate dependence. Chin et al. [97] also analyzed the temperature dependence of irradiation creep compliance for Sandvik HT9 irradiated in EBRII by assuming a linear dose rate dependence.

This study showed that the dose rate dependence of irradiation creep of T91 steel is most likely to be linear. This section conducts a rate theory analysis to determine which dependence makes the most theoretical sense for T91. The dose rate dependence of irradiation creep was understood to be a function of the balance of point defect kinetics generated by irradiation damage. For a given microstructure, the dose rate affects the steady state concentration of interstitials and vacancies, which then diffuse to various features that can ultimately lead to plastic deformation. The point defect concentrations were mathematically described by the chemical rate equations [17]:

$$\frac{dC_i}{dt} = K_o - K_{iv}C_iC_v - K_{is}C_sC_i, \tag{6.2}$$
$$\frac{dC_v}{dt} = K_o - K_{iv}C_iC_v - K_{vs}C_sC_v,$$

where C_v is the vacancy concentration, C_i is the interstitial concentration, K_o is the defect production rate, K_{iv} is the vacancy interstitial recombination rate coefficient, K_{is} is the interstitial sink reaction rate coefficient, and K_{vs} is the vacancy sink reaction coefficient. The equations are

non-linear differential equations and are not symmetric with respect to vacancy and interstitial concentrations, making analytical solutions difficult. Therefore, the equations were solved numerically through a Matlab® code in Appendix E to obtain the steady state point defect concentrations under different conditions.

The values for K_{is} and K_{vs} were calculated based on the observed microstructure of irradiation crept samples. Six distinct sink reaction rate coefficients were included in the calculations: vacancy to dislocations (K_{v_d}), interstitial to dislocation loops and networks (K_{i_d}), vacancy to grain boundaries (K_{v_gb}), and interstitial to grain boundaries (K_{v_gb}). The equations for reaction rate constants were as follows [17]:

$$K_{v\_d} = \frac{D_v}{\frac{\ln(R/R_d)}{2\pi}} \qquad K_{i\_d} = \frac{D_i}{\frac{\ln(R/R_d)}{2\pi}} \tag{6.3}$$

$$K_{v\_gb} = 6kD_v d^5 \qquad K_{i\_gb} = 6kD_i d^5$$

$$K_{v\_ppt} = 4\pi D_v R_{ppt} \qquad K_{i\_ppt} = 4\pi D_i R_{ppt}$$

The reaction rates are a function of the vacancy diffusion coefficient D_v, and the interstitial diffusion coefficient D_i. R_d is the radius of the dislocation core, and R is the radius of interaction of the dislocation core to interstitials and vacancies, d is the average sub-grain size, and k is the Boltzmann constant. The diffusion coefficients D_v and D_i were calculated assuming basic vacancy and interstitial self-diffusion in bcc crystal structure with corresponding migration energies [17], [69]:

$$D_v = a^2 10^{13} exp\left(\frac{-E_{vm}}{kT}\right) \tag{6.4}$$

$$D_i = \frac{a^2}{6} 10^{13} exp\left(\frac{-E_{im}}{kT}\right)$$

where the constant a is the lattice constant, E_{vm} is the vacancy migration energy, E_{im} is the interstitial migration energy. The migration energy for interstitial is much lower than those of vacancies, therefore with the same point defect concentration, interstitial migration is dominating as opposed to vacancy migration. Table 6.2 tabulates all the inputs necessary for calculating the diffusion rates and reactions rates of a typical T91 sample under irradiation creep. The total sink reaction rates were derived by combining the individual reaction of each sink and multiplying by

their corresponding sink densities. The sink densities used were from irradiation creep sample IT450200 to represent the irradiation creep microstructure.

$$K_{is}C_s = K_{i\_gb}C_{gb} + K_{i\_d}C_d + K_{i\_ppt}C_{ppt}$$
$$K_{vs}C_s = K_{v\_gb}C_{gb} + K_{v\_d}C_d + K_{v\_ppt}C_{ppt} \quad (6.5)$$

With the diffusion rates and reaction rates uniquely defined, the time constants for each rate limiting process in the point defect balance equation were calculated. Table 6.3 tabulates the time constant for the onset of mutual recombination (τ_1), onset of interstitial loss to sinks (τ_2), onset of vacancy loss to sinks (τ_3), and the point where mutual recombination dominates interstitial loss to sinks (τ_4). Assuming an irradiation temperature of 450°C and a dose rate of $3x10^{-6}$dpa/s, the interstitials start to be absorbed at sinks at around 1 μs. The vacancies absorption at sinks was an order of magnitude slower at around 30 μs. In contrast, the time constant for recombination was at around 200 μs. Therefore, we can safely assume that the typical condition for proton irradiation creep experiments will put the point defect concentration in the "high temperature high sink density regime" where the steady state point defect concentration was a linear function of the dose rate. This was confirmed by numerically solving equation 6.1, and the result of the analysis is plotted as the point defect concentration as a function of time, shown in Figure 6.3.

The analysis of point defect kinetics of the proton irradiation creep experiments confirmed that the experimental conditions in this study correspond to a high temperature and high sink density regime where the point defect concentrations are linearly dependent on the dose rate. This finding was consistent with majority of irradiation creep mechanisms where the creep rate were all linearly dependent on the point defect concentration, and therefore the dose rate. The only mechanism that the result of this study contradicts was the thermally driven preferential emission (PE). However, it did not preclude the possibility that PE was still operating in addition to another irradiation creep mechanisms.

Table 6.2 Inputs for calculating diffusivity and reaction rates.

Constant Inputs			
Parameter	Value	Units	Notes
T	400-500	^oC	Irradiation temperature
σ	100-200	MPa	Applied stress
K_o	$0 - 5x10^{-6}$	dpa/s	Irradiation dose rate
Ω	$1.23x10^{-23}$	cm^3/atom	Atomic volume
k	$1.38x10^{-23}$	Pa/K	Boltzmann constant
e_o	0.8	N/A	Interstitial relaxation volume [98]
ν	0.33	N/A	Poisson's Ratio
μ	$75x10^3$	MPa	Shear modulus
E	$200x10^3$	MPa	Elastic modulus
z_i	1.02	N/A	Dislocation bias for interstitials [98]
z_v	1	N/A	Dislocation bias for vacancies [98]
E_{if}	4.6	eV	Interstitial formation energy [69]
E_{vf}	1.7	eV	Vacancy formation energy [69]
E_{im}	0.2	eV	Interstitial migration energy [69]
E_{vm}	0.67	eV	Vacancy migration energy [69]
Measured Inputs: IT 450200			
d	0.45	µm	Sub-grain size
R_{ppt}	0.16	µm	Average precipitate radius [69]
C_{gb}	$2.1x10^{13}$	cm^{-3}	Sub-grain density
C_{loop}	$1.35\ x10^{10}$	cm^{-2}	Dislocation loop line density
$C_{network}$	$5.7x10^{10}$	cm^{-2}	Dislocation network line density
C_{ppt}	$1.16x10^{14}$	cm^{-3}	Precipitate density [69]
k_{ppt}	$1.4x10^{11}$	cm^{-2}	Precipitate sink strength
k_{gb}	$7.4x10^{10}$	cm^{-2}	Sub-grain sink strength
k_{loop}	$6.9x10^{10}$	cm^{-2}	Dislocation loop sink strength

$k_{network}$	$4.4x10^{11}$	cm^{-2}	Dislocation network sink strength
k_{total}	$7.3\ x10^{11}$	cm^{-2}	Total sink strength
$K_{is}\ C_s$	$2.4x10^{6}$	s^{-1}	Total reaction rate of interstitials to sinks
$K_{vs}C_s$	$6.7x10^{5}$	s^{-1}	Total reaction rate of vacancies to sinks

Table 6.3 Time constants for point defect kinetics of proton irradiation creep T91

Time constant	Equation	Process	Value
τ_1	$(K_oK_{iv})^{-1/2}$	Onset of mutual recombination	$3.06x10^{-4}$ s
τ_2	$(K_{is}C_s)^{-1}$	Onset of interstitial loss to sinks	$7.37x10^{-7}$ s
τ_3	$(K_{vs}C_s)^{-1}$	Onset of vacancy loss to sinks	$1.1x10^{-5}$ s
τ_4	$(K_{is}C_s)/(K_oK_{iv})$	Mutual recombination overtakes interstitial loss to sinks	0.127 s

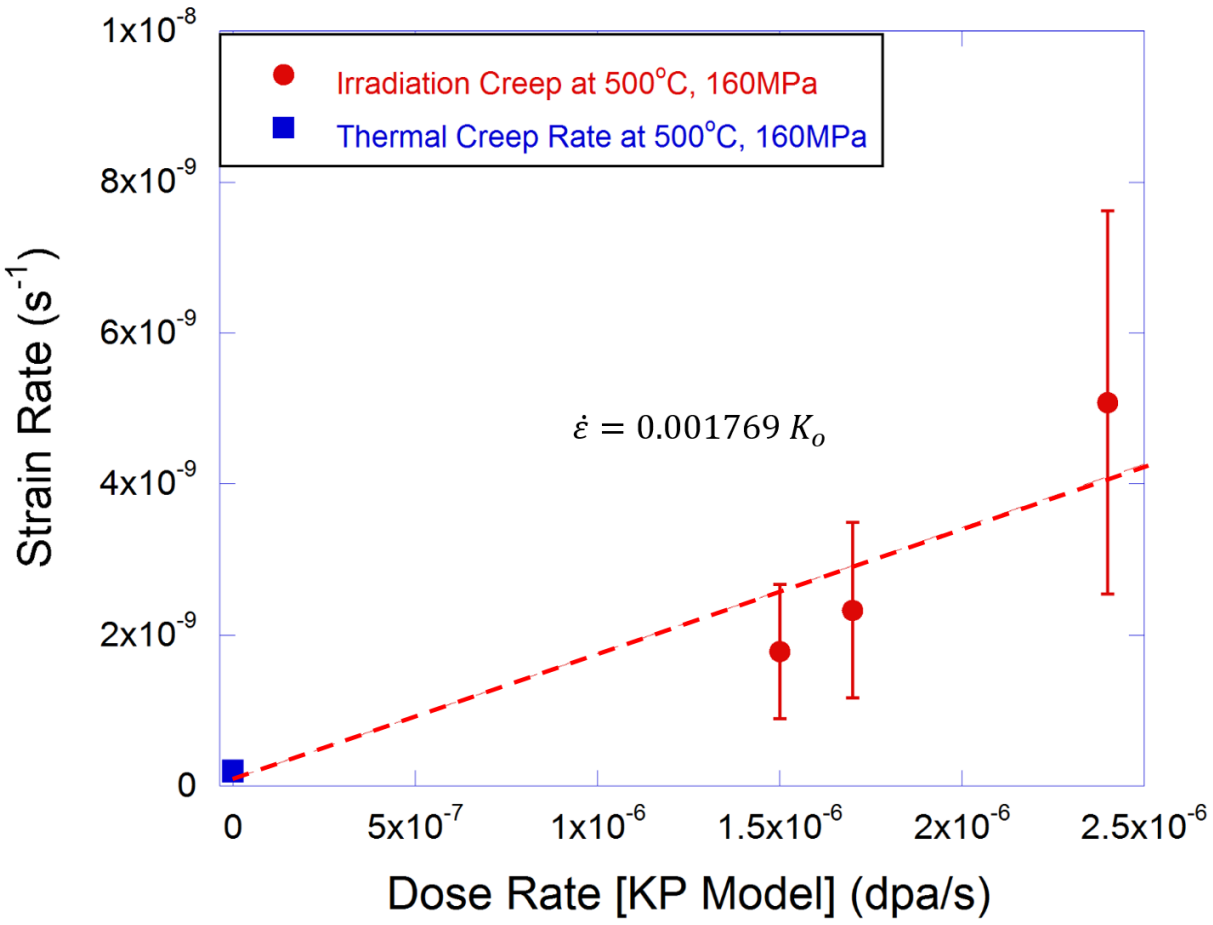

Figure 6.1 Dose rate dependence of irradiation creep strain rate for IT500160

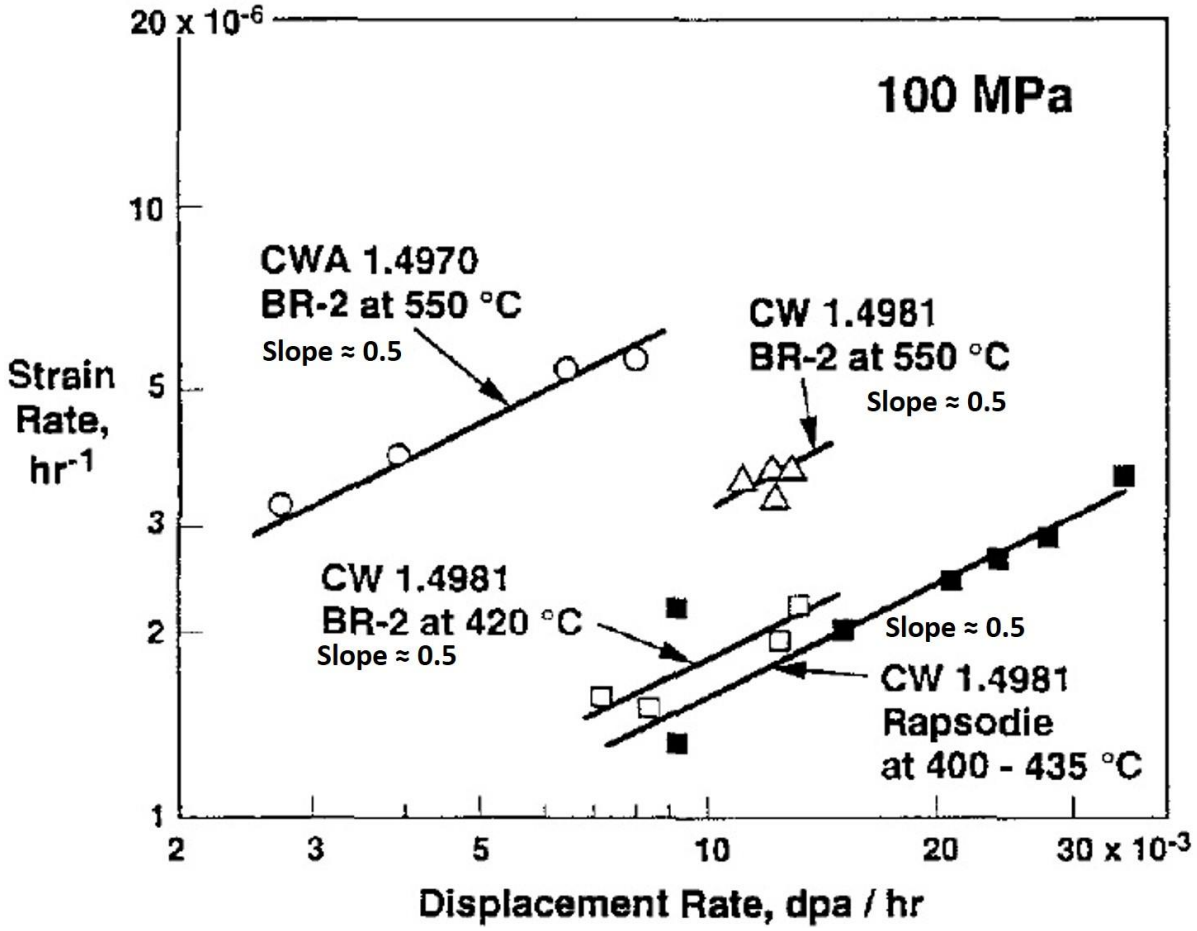

Figure 6.2 Dose rate dependence of cold-worked 316SS irradiated in fast and mix spectrum reactors. [92]

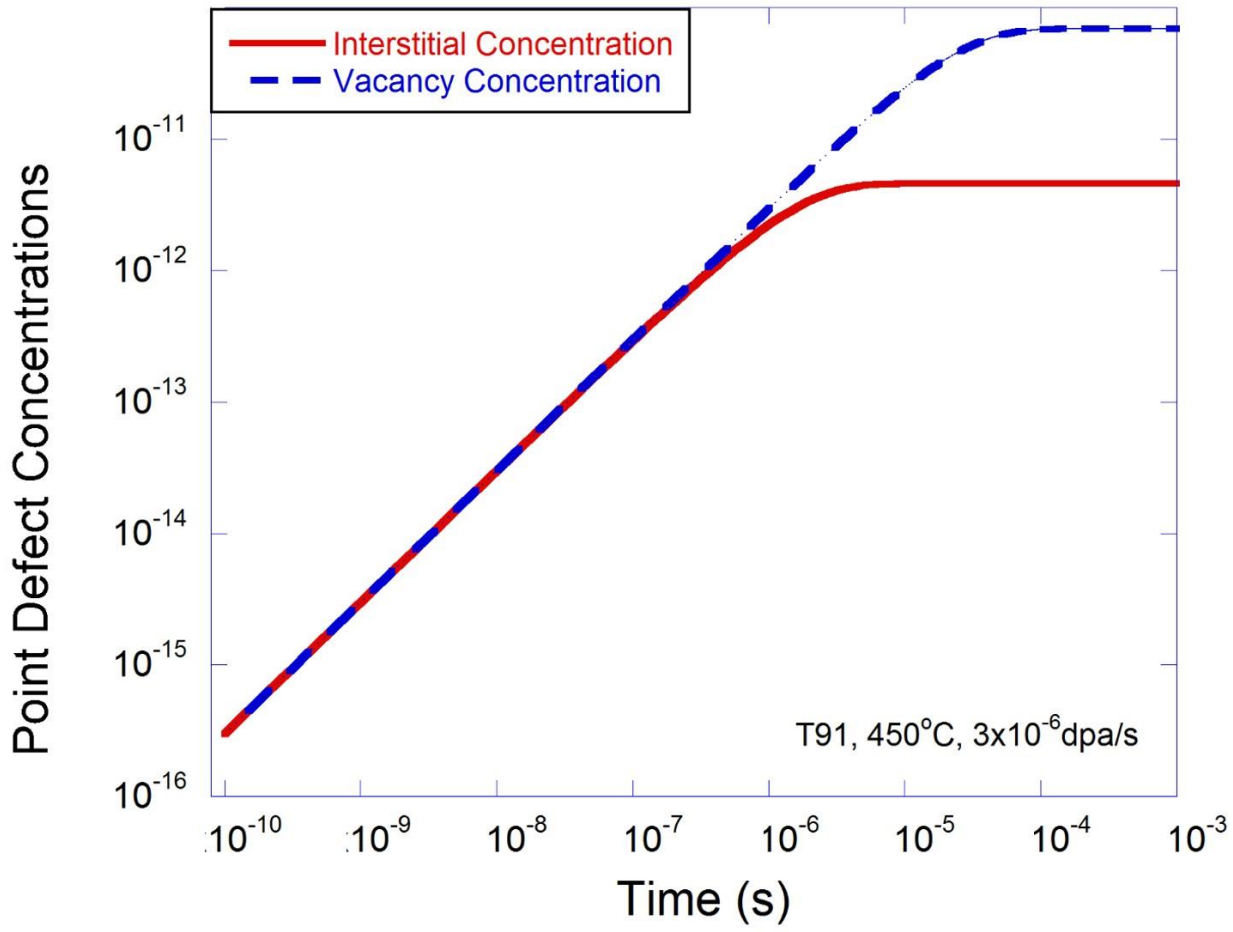

Figure 6.3 Point defect concentration of proton irradiation creep T91 at 450°C, $3x10^{-6}$dpa/s

6.1.2 Temperature Dependence of Irradiation Creep

Irradiation creep experiments were conducted at 400°C, 450°C, and 500°C at 160MPa to explore the temperature dependence. The dose rate was maintained at the nominal value of $3.4x10^{-6}$dpa/s with the exception of the 400°C experiment where a lower dose rate of $2.6x10^{-6}$ dpa/s was needed to maintain the temperature. The strain rates measured for the experiments at 400°C, 450°C, and 500°C were $2.9\pm1.45x10^{-9}s^{-1}$, $2.7\pm1.35x10^{-9}s^{-1}$, and $2.33\pm1.17x10^{-9}s^{-1}$, respectively. Extrapolation of the 400°C strain rate to $3.4x10^{-6}$dpa/s can be calculated using the 500°C dose rate dependence. The resulting strain rate would be higher than $2.9\pm1.45x10^{-9}s^{-1}$ but not significant enough to change the outcome of the analysis. The measured strain rates plotted as a function of time are shown in Figure 6.4. The three measured strain rates were very close to each other within the error. Although there appeared to be a small negative trend in the strain rate as temperature increased, the trend was weak enough to conclude that irradiation creep was independent of temperature. An Arrhenius temperature dependence with an activation energy lower than 38kJ could also be fitted to the experimental data, but such a low activation energy does not correspond to any realistic diffusion mechanisms. Therefore, the creep rates did not have an Arrhenius temperature dependence.

In neutron irradiation experiments, irradiation creep was found to be largely temperature independent, similar to those of proton irradiation creep experiments. Figure 6.5 plots the strain rates observed for a set of 9Cr-1Mo pressurized tube experiments conducted by Tolockzo et al [55] in FFTF. The neutron irradiation creep strain rates found below 500°C appeared to have a small negative temperature dependence similar to those found in this study. However, the difference in the strain rates were small enough that the temperature dependence of irradiation creep was often reported as negligible at low temperatures.

Although the temperature dependence of proton irradiation creep rates match very well to those of neutrons, the magnitude of the strain rates were about a factor of 100 higher. This large difference in strain rate is likely due to two major differences between neutron and proton irradiation creep experiments; the dose and the sample thickness.

FM steels follow a three stage creep curve with a very short secondary regime. Neutron irradiation creep experiments typically report the minimum creep rate, measured at doses above

100 dpa. In contrast, proton irradiation creep rates were measured at a dose of less than 1dpa in the primary creep regime. This difference in creep regime likely accounted for as much as a factor of 10 difference in the strain rates. In addition, the small thickness of the proton irradiation creep samples resulted in a large surface area to volume ratio and could have also contributed to the difference in strain rate.

Due to the difference in creep regime and sample thickness, proton irradiation creep experiments were not directly comparable to neutron data. However, because the differences were consistent in magnitude across all temperature, dose rate, and stress conditions, comparison of parameter dependencies and microstructure features are still valid.

The neutron irradiation creep strain rates found below 500^{o}C have no temperature dependence similar to those found in this study. However, the difference in the strain rates were small enough that the temperature dependence of irradiation creep were often reported as negligible at low temperatures. The creep rates at temperatures higher than 500^{o}C were found to increase as a function of temperature, but were not large enough to be explained by an Arrhenius behavior. At even higher temperatures, thermal creep start to dominate and the temperature dependence becomes Arrhenius in nature. In-reactor data on HT9 irradiated in EBRII [97] shown in Figure 6.6, and F82H irradiated in FFTF [99] shown in Figure 6.7 confirmed the negligible temperature dependence at low temperature and Arrhenius temperature dependence at high temperature for neutron irradiation creep.

The temperature independence of irradiation creep can be explained by considering the steady state point defect concentrations. Under thermal creep conditions, the point defect concentrations are governed by the equations for steady state thermal defect concentrations:

$$C_{vo} = \exp\left(\frac{-E_{vf}}{kT}\right), \qquad (6.6)$$

$$C_{io} = \exp\left(\frac{-E_{if}}{kT}\right),$$

where C_{vo} denotes the thermal vacancy concentration. The thermal vacancy concentrations is a function of the vacancy formation energy E_{vf}, temperature T, and Boltzmann's constant k. Similarly, the thermal interstitial concentration C_{io} is the function of the interstitial formation energy E_{if}.

In contrast, under proton irradiation creep conditions, the point defect concentrations are mainly a function of the dose rate and sink reaction rates as discussed in Section 6.1.1. The governing equations for their steady state quantity are described below:

$$C_v = \frac{K_o}{K_{vs}C_s}\ , \qquad (6.7)$$

$$C_i = \frac{K_o}{K_{is}C_s}.$$

The calculated thermal and irradiation point defect concentrations are plotted as a function of 1/T for T91 at 3.4x10^{-6}dpa/s between 300^{o}C and 600^{o}C in Figure 6.8. The solid lines denote irradiation induced point defects, and the dashed lines denote thermal defects. The red is for interstitial and blue is for vacancies. Thermal interstitial concentrations were so low between 300^{o}C and 600^{o}C that they do not contribute to the analysis. The thermal vacancy concentration followed a typical Arrhenius behavior where the concentration increased dramatically as a function of temperature. In contrast, the irradiation induced defects show a much weaker temperature dependence where the point defects were slightly higher at the lower temperatures. This was due to the fact that since FM alloys have such a high sink density, the faster diffusion to sinks with increasing temperature reduced the total steady state defect concentration under irradiation.

Figure 6.8 shows that at beyond 480^{o}C, the thermal vacancy concentration will start to overtake irradiation interstitial concentrations. Beyond 540^{o}C, thermal defects completely overtake irradiation defect populations. The temperature range of 400^{o}C to 500^{o}C for proton irradiation creep experiments are highlighted on the graph. Under those conditions, the point defects were mainly irradiation generated and not thermally generated.

However, temperature dependence of irradiation creep was not only a function of the steady state point defect concentration, but of the diffusivity at that temperature as well. Although vacancy concentrations were orders of magnitude higher than interstitial concentrations under these conditions, the interstitials diffused much faster and contribute significantly to irradiation creep. To understand the overall temperature dependence of these experiments, thermal and irradiation point defects were combined, and the total point defect flux ($C_iD_i+C_vD_v$) is plotted as a function of temperature in Figure 6.9. It can be observed that the

temperature dependence was essentially negligible in the highlighted region where proton irradiation creep experiments were conducted.

The temperature dependence observed in this study were largely consistent with what was reported in literature. [55], [59]. Although the temperature range in this study was limited to 400^{o}C to 500^{o}C, the results showed a weak negative temperature dependence that could be considered to be negligible given the associated error. A small negative temperature dependence in that temperature range was consistent with irradiation creep mechanism driven by irradiation induced point defect concentration. The analysis of point defect concentrations also correctly predicted that the temperature dependence of irradiation creep in T91 will change from negligible to Arrhenius at around 600^{o}C as seen in neutron irradiation creep studies. The low activation energy Arrhenius fit could potentially suggest the possibility of grain boundary diffusion creep (Coble Creep), but Coble creep was not compatible with irradiation enhancement of creep rate at 400-500^{o}C, since no driving force exist for irradiation to enhance diffusional creep [17].

The analysis on dose rate and temperature dependence concludes that the dominating irradiation creep mechanisms for T91 are governed by the irradiation induced steady state point defect concentrations. Although this conclusion does not preclude thermal emission mechanisms such as PE from operating, it does demonstrate that PE is not the dominating creep mechanism for the irradiation conditions conducted in this study.

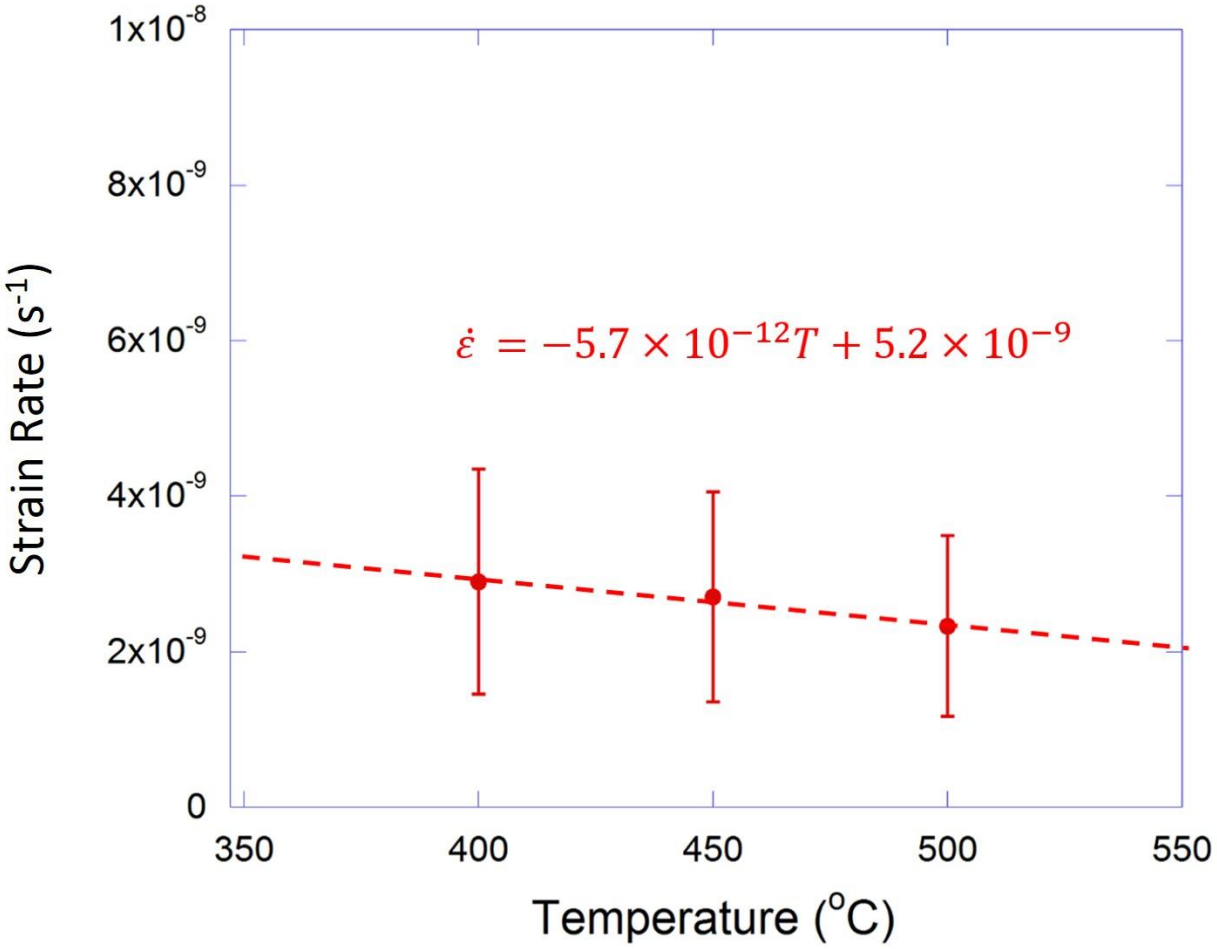

Figure 6.4 Temperature dependence of irradiation creep experiments done at 400°C, 450°C, and 500°C.

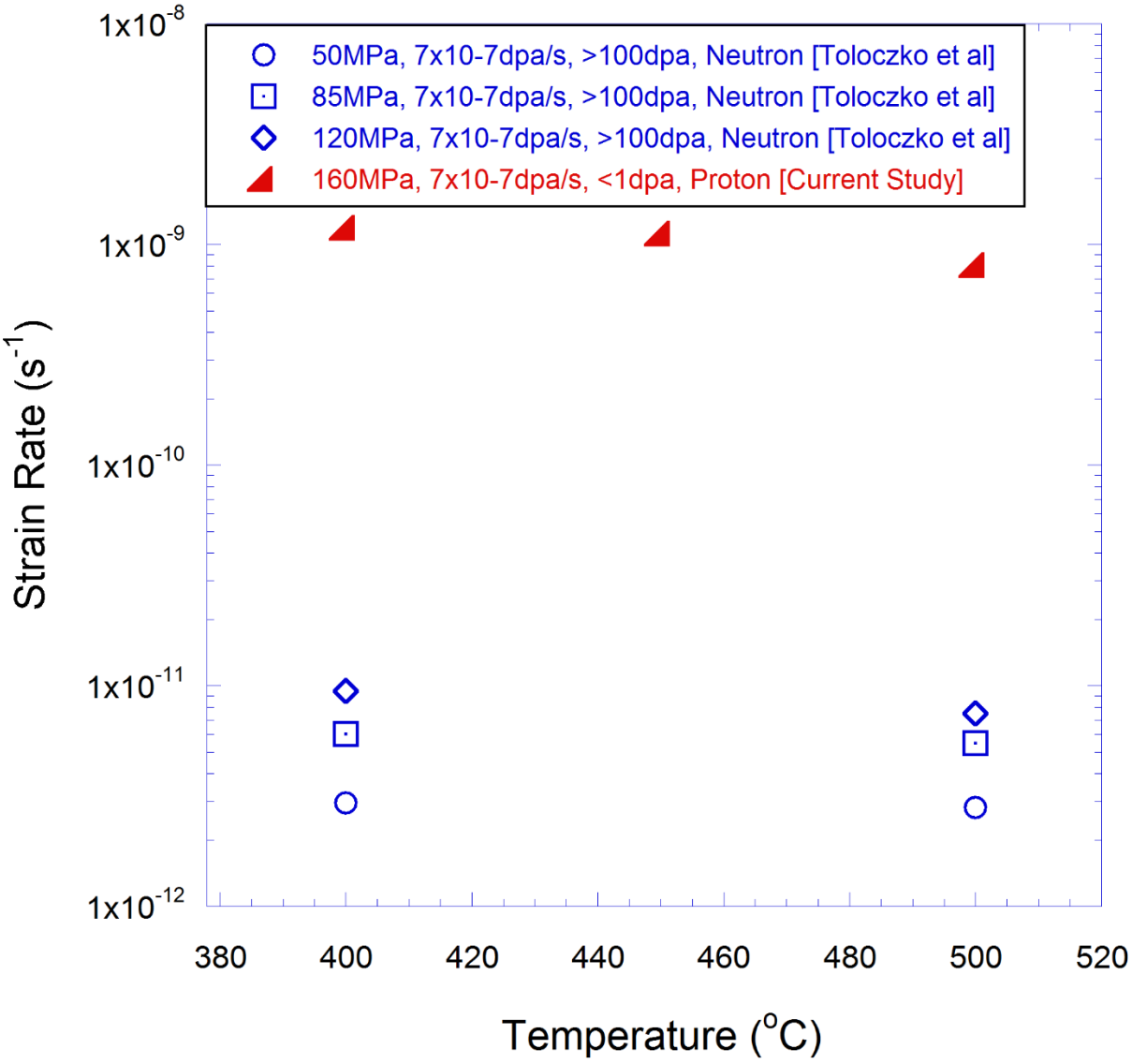

Figure 6.5 Neutron irradiation creep data of T91 by Tolockzo et al. [55] plotted as a function of irradiation temperature.

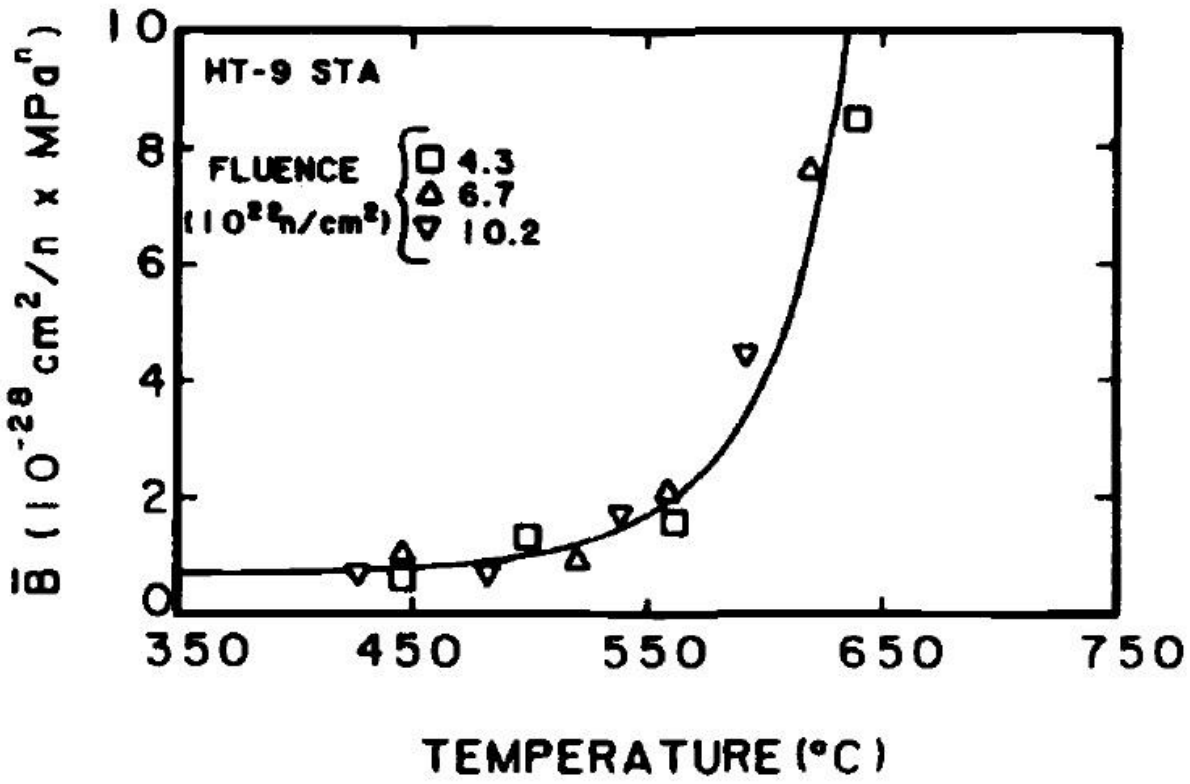

Figure 6.6 Neutron irradiation creep data of HT9 by Chin et al. [2], [97] plotted as a function of irradiation temperature.

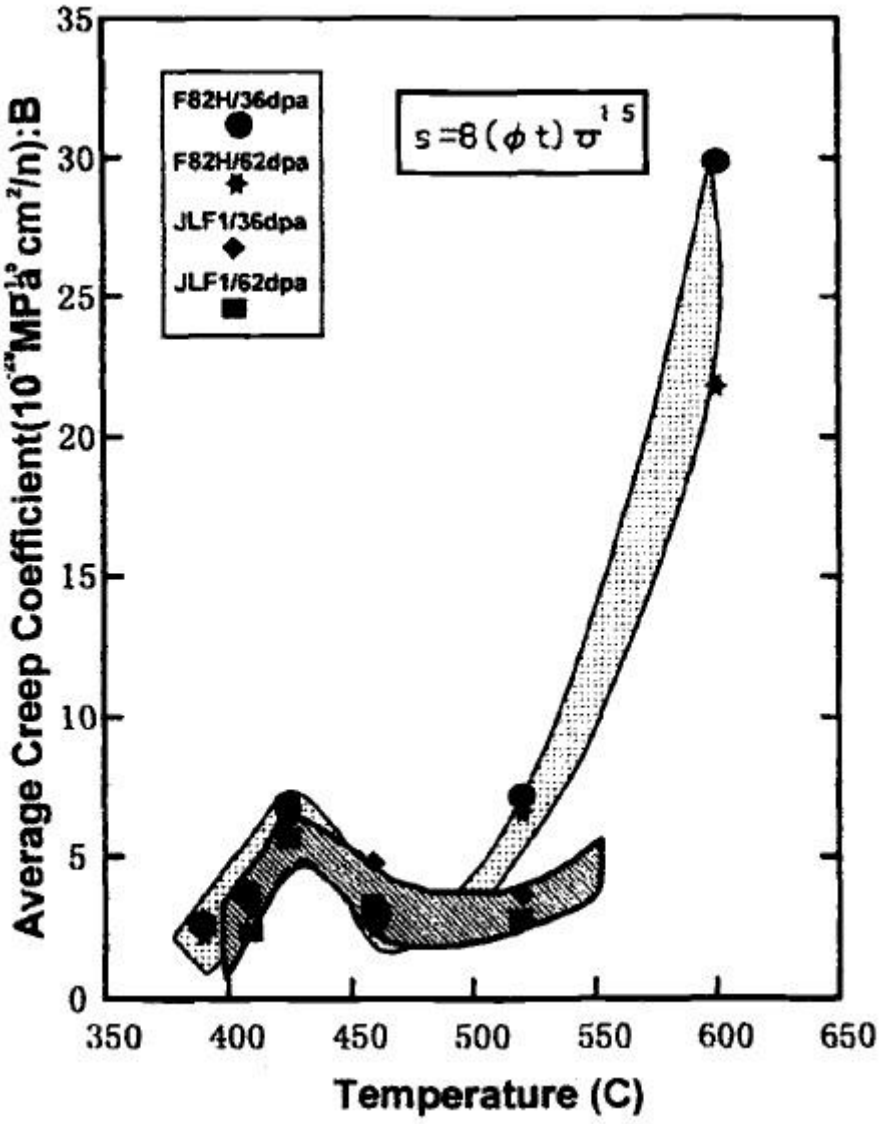

Figure 6.7 Neutron irradiation creep data of F82H by Kohyama et al. [2], [99] plotted as a function of irradiation temperature.

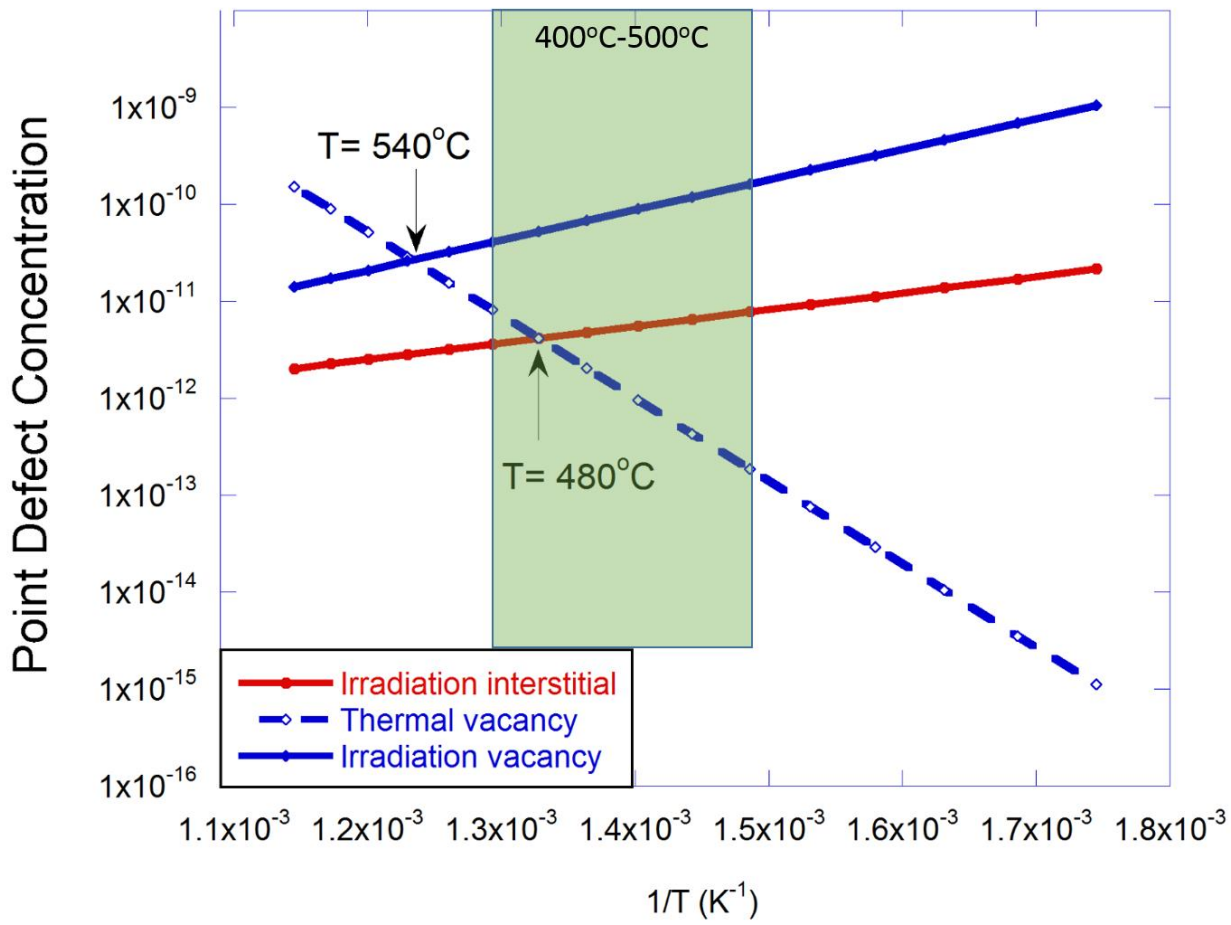

Figure 6.8 Point defect concentration of T91 under 3.4×10^{-6}dpa/s proton damage as a function of temperature.

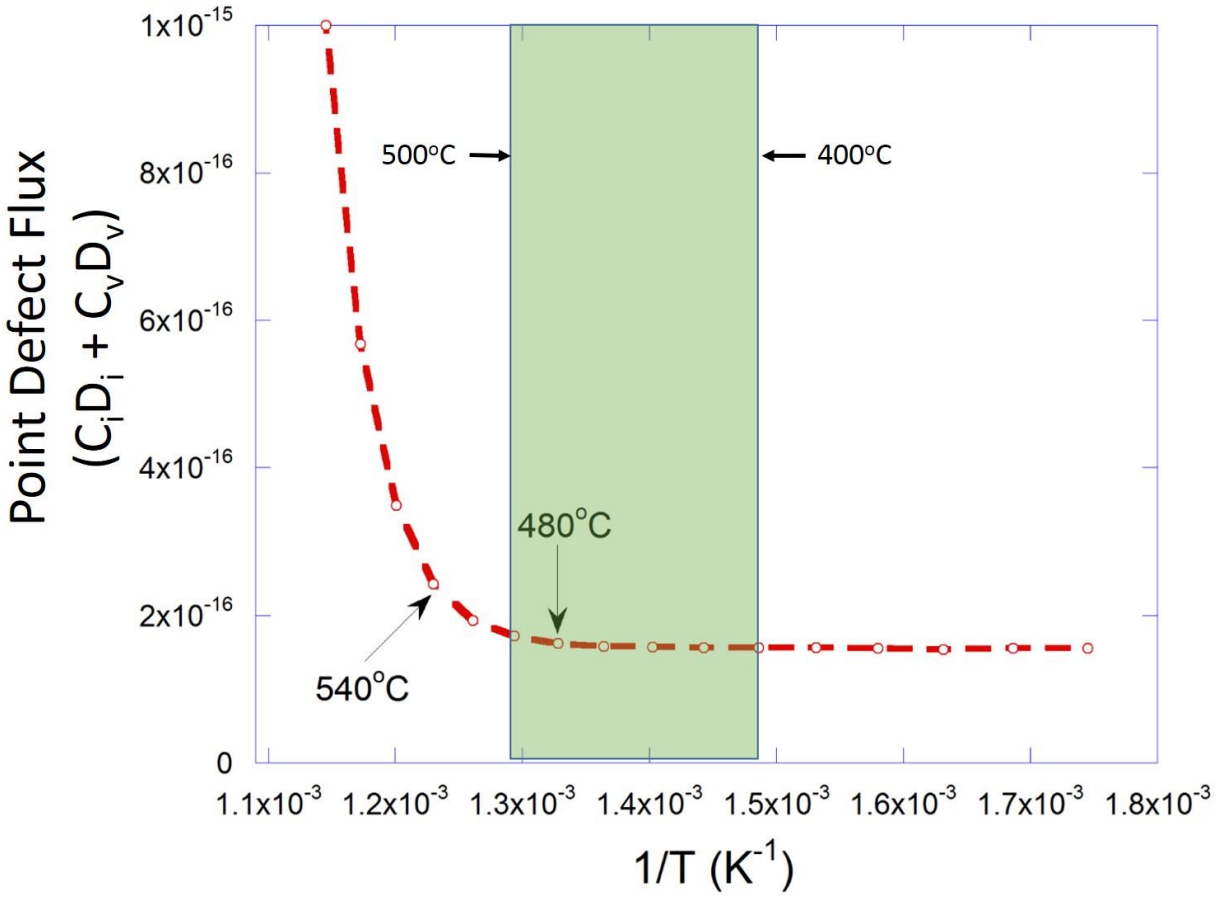

Figure 6.9 Point defect flux of T91 under 3.4x10^{-6}dpa/s proton damage as a function of temperature.

6.1.3 Stress Dependence of Irradiation Creep

To determine the stress dependence of irradiation creep, seven experiments were conducted at constant temperature of 450^{o}C and dose rate of 3.4x10^{-6}dpa/s. The applied stress of these experiments ranged from 100MPa to 200MPa at 20MPa intervals. The results of the irradiation creep experiments are plotted in Figure 6.10 on a logarithmic axis. The stress dependence appeared to have a low stress exponent between 100MPa to 160MPa, and then increased dramatically at stress above 180MPa. The best fit analysis conducted in section 5.1.7 determined that the stress exponent n=0.87 at low stress. At higher stress, the stress dependence followed a power law with stress exponent of n=14.

In general, neutron irradiation experiments have shown that irradiation creep exhibit anywhere between a linear to quadratic stress dependence. Figure 6.10 plots the proton irradiation creep rates using the dose rate dependence in Figure 6.1 to extrapolate the damage rates to that of the neutron irradiated data 9Cr-1Mo pressure tubes irradiated in FFTF [55]. The open symbols represent literature data, and filled data are the results of this study. The dependence on stress over the same stress range is very similar for both irradiations, but the proton irradiation creep rate was about a factor of 100 higher due to the difference in dose and sample thickness.

The near linear stress dependence of irradiation creep is consistent with the majority of creep theories where the deformation rates are controlled by pure diffusion mechanisms, either via mass transport or enabling dislocation movement. The high stress exponent observed for proton irradiation creep at stresses above 160MPa was beyond what was typically measured in neutron irradiation creep experiments below 500^{o}C, with the exception of an irradiation creep experiments on HT9 irradiated in HFIR at 400^{o}C that showed a dramatic increase in the strain under high stress conditions, shown in Figure 6.11 [100].

Deviations from linearity is often explained as thermal processes contributing to irradiation creep. A power law exponent of 10 or more was consistently observed in thermal creep of T91 at high stress [34], [51], suggesting that creep deformation rate is controlled by dislocation glide in the presence of long ranged internal stress. This high exponent regime was traditionally called "power law breakdown" (PLB), and has been well documented in literature [101]. The exact mechanisms behind PLB regime of thermal creep are currently still under debate. Studies on

thermal creep behavior showed that materials typically enter PLB at about 0.5 of the yield stress. [51], [102] Yield strength of FM steels at 450^{o}C-550^{o}C were found to be around 400MPa, therefore it is not surprising that PLB was observed at stresses near 200MPa.

With a stress dependence similar to power law breakdown observed under thermal creep conditions, an experiment was conducted at 450^{o}C and 200MPa without irradiation to directly compare the irradiation creep rate with thermal creep rate under the same conditions. The thermal creep experiment details were outlined in section 5.1.2. The creep rate of the thermal creep experiment was found to be $1.38\pm0.79\text{x}10^{-9}\text{s}^{-1}$, which is around an order of magnitude lower than the $12.5\pm6.25\text{x}10^{-9}\text{s}^{-1}$, and $11.5\pm5.75\text{x}10^{-9}\text{s}^{-1}$ values measured for two irradiation creep experiments conducted at the same temperature and stress. This direct comparison showed that the high stress dependence for irradiation creep rates measured in this experiment was not due to thermal creep alone. Instead, it supported the possibility of irradiation enhanced dislocation creep in conditions where both thermal creep and irradiation creep play an important role. Figure 6.12 plots the strain rates of irradiation creep experiments after subtracting out the high stress exponent contribution of the creep rate. The analysis of irradiation creep mechanisms henceforth will be conducted on the data without the PLB contributions.

The observation of power law stress dependence suggested that dislocation climb or glide in the presence of long range internal stress occurs under irradiation creep conditions. Although the precise mechanism for PLB are still under debate, there are many theories that exist which would be compatible with an irradiation environment. One such theory suggests that PLB is controlled by dislocation climb over sub-grain walls by absorbing vacancies resulting from plastic deformation [101]. This would be consistent with the enhancement of creep rate in the PLB regime with an oversaturation of vacancy concentration due to irradiation. Another explanation for the high stress exponent is that the strain hardening from thermal creep deformation will increase the dislocation network density, thus increase the long range internal stress in the material. Under irradiation, a similar mechanism could be operating where the dislocation network density increases as a result of irradiation hardening instead of strain hardening. However, without fully understanding the mechanisms behind PLB of thermal creep, any hypothesis about how a radiation-induced super-saturation of point defects can affect the creep rate in PLB would only be speculative.

The complex stress dependence observed in this study was not consistent with any current irradiation creep theory because of unforeseen strain contributions from a high stress exponent at high stress. It is clear that more than one creep mechanism could be contributing to the strain rates measured. Before any further analysis can be done on the stress dependence of irradiation creep in this study, contributions from other potential mechanisms must be subtracted from the data to isolate the stress dependence of the final mechanism. Figure 6.13 plots the irradiation creep rate after the PLB contribution had been subtracted from the total strain. The next section will explore the microstructure of the irradiation creep samples to identify any additional contributions from other creep mechanisms before revisiting the stress dependence for a final analysis to narrow down the dominating mechanism responsible for irradiation creep of FM steels.

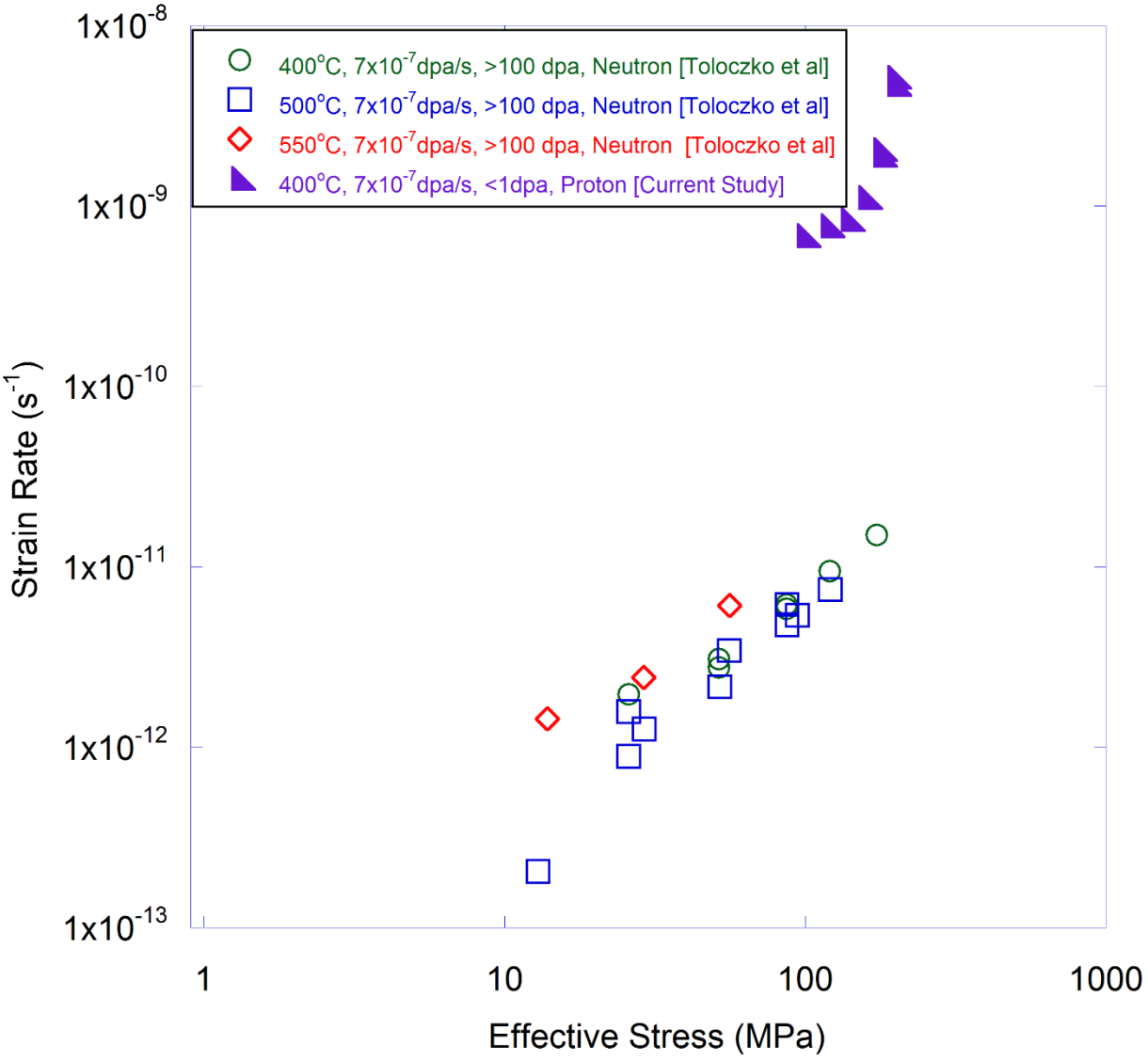

Figure 6.10 Neutron irradiation creep data on T91 by Tolockzo et al [55] plotted as a function of effective stress.

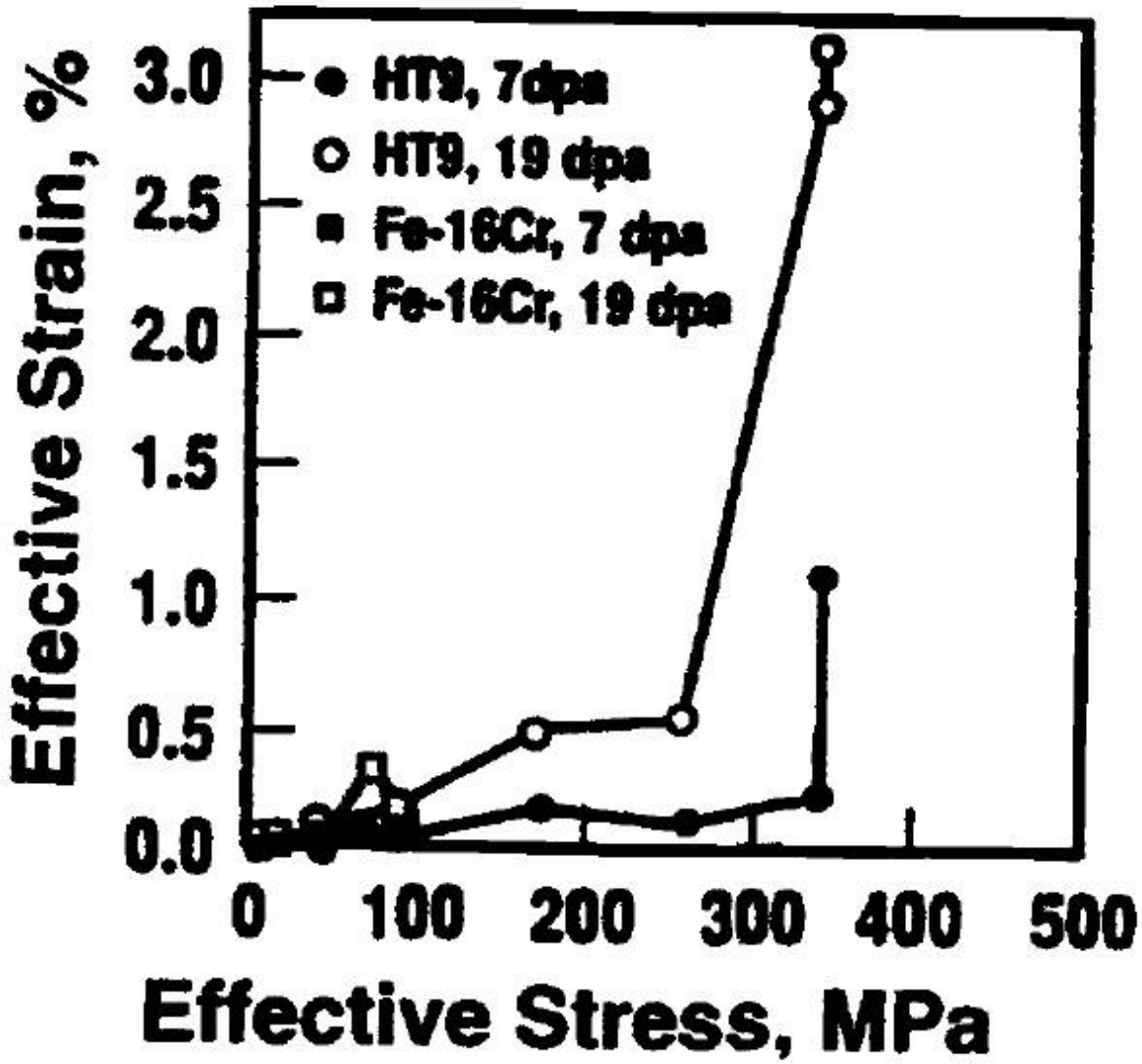

Figure 6.11 Neutron irradiation creep data on HT9 by Chin et al [103] plotted as a function of effective stress.

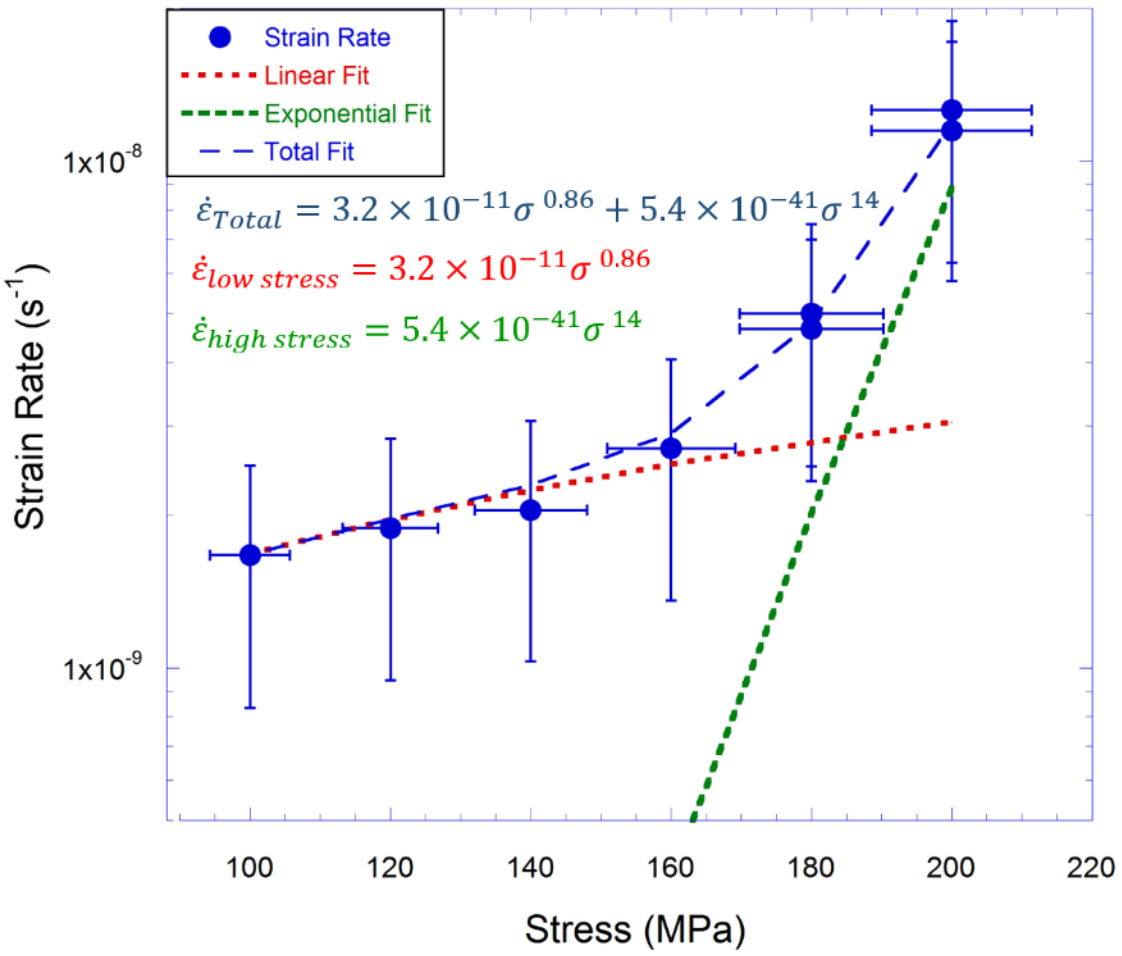

Figure 6.12 Stress dependence of irradiation creep rates of T91 at 450ºC and the best line fits to the data.

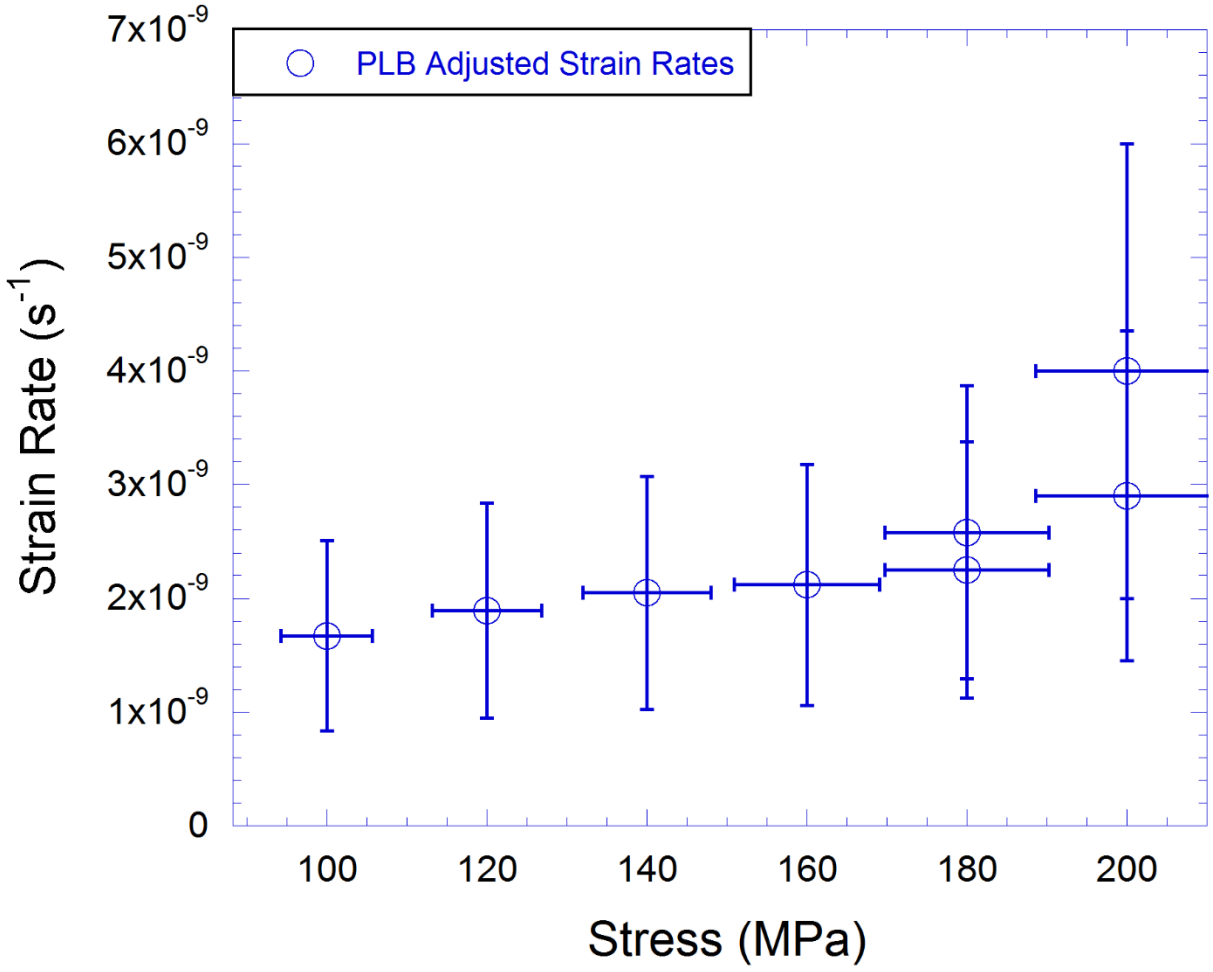

Figure 6.13 Strain rates of irradiation creep experiments at 450°C as a function of stress from 100MPa to 200MPa adjusted to exclude strain rate contributions from power law breakdown (PLB).

6.2 Irradiation Creep Microstructure

This section analyzes the microstructure of irradiation creep experiments conducted in this study, and reviews its implications under current understanding of irradiation damage and irradiation creep theory. Microstructure analysis of irradiation creep samples can reveal a snapshot of what was occurring inside the material and shed more light on the mechanism of deformation. Different irradiation creep theories predicted unique microstructure features as the result of different modes of deformation as previously discussed in Section 2.3.

I-creep relies on the intrinsic interstitial bias of dislocations to drive dislocation climb and glide to cause creep, with excess vacancy cluster to form voids. Therefore, if I-creep was dominating in the irradiation creep of FM steels, then a population of voids should be observed in the irradiation creep microstructure. Stress induced preferential absorption (SIPA) theorizes that the applied external stress causes point defects to be preferentially absorbed in dislocations of certain Burgers vector compared to others, therefore dislocation loops should grow larger in one direction compared to another depending on their orientation to the tensile axis. In contrast, stress induced preferential nucleation (SIPN) theorizes that the applied external stress causes dislocation loops to nucleate in favor of certain directions as opposed to others, therefore an anisotropy in the loop density should be observed after irradiation creep. Preferential absorption glide (PAG) is a dislocation climb glide mechanism similar to I-creep, but it incorporates the SIPA mechanism to describe how dislocations of certain directions can climb faster than others. If PAG is the dominating irradiation creep mechanism, there should be observable anisotropy in the dislocation network density of certain Burgers vector compared to others.

The analysis described in this chapter will target specifically the unique microstructure features predicted by the multitude of irradiation creep theories. The result of the analysis will be discussed to narrow down the potential irradiation mechanisms that were dominating under these experimental conditions.

6.2.1 Dislocation Network Density

Dislocation network density is a key microstructure feature that needed to be determined for any mechanistic calculations of irradiation creep rates. Three samples were used in this study to determine the dislocation network density of T91 under thermal creep conditions, proton irradiation conditions, and irradiation creep conditions. Section 5.2.2 described in detail the results and method of the dislocation network density analysis for samples TT450200, IT450000, and IT450200.

The dislocation densities are plotted in Figure 6.14 to compare the three test conditions. The sample TT450200 tested under thermal creep conditions was found to have a dislocation network density of $4.14\pm0.96\text{x}10^{14}\text{m}^{-2}$. Proton irradiation sample IT450000 had a dislocation network density of $3.64\pm0.72\text{x}10^{14}\text{m}^{-2}$. Irradiation creep sample IT450200 had a dislocation network density of $5.7\pm0.85\text{x}10^{14}\text{m}^{-2}$. The dislocation network density for all three samples were of the same order of magnitude, with the irradiation creep sample having a density slightly higher than the other two. The results of dislocation density analysis hint at a correlation between creep strain rate and dislocation network density. However, the trend was not strong enough to make any definitive quantitative conclusions.

High dose neutron irradiation experiments on FM steels in fast reactors consistently show (a/2)<111> type dislocation network structure with a<100> type dislocation loops. Sencer et al. [104], [105] observed a total dislocation network density of $3\text{x}10^{15}\text{m}^{-2}$ for HT9 irradiated up to 155 dpa at 443ºC. Dvoriashin et al. [106] also observed dislocation network densities of around $1\text{x}10^{15}\text{m}^{-2}$ for martensite grains and $2\text{x}10^{14}\text{m}^{-2}$ in ferrite grains in EP450 irradiated in BN-350, BN-600, and BR-10 reactors between 11-86 dpa.

The dislocation density for the irradiation creep experiment conducted in this study was lower than those observed in neutron irradiated samples. The major difference between the neutron and proton irradiation experiments is the different total dose to which the samples were exposed. Neutron experiments were irradiated to 11 – 155 dpa, proton irradiation creep experiments were irradiated to less than 1 dpa. The higher dose in neutron experiments were representative of a microstructure that has reached steady state. In contrast, the low dose proton irradiations represent early stages of irradiation creep where the microstructure was yet to reach steady state. The observation that a neutron irradiated microstructure had a higher dislocation network density suggests that irradiation creep can provide a mechanism for the generation of dislocation networks.

Alignment of the dislocation line segments were also observed in the high stress samples after irradiation. Figure 6.15 shows a large amount of dislocation line segments aligned in specific directions. Diffraction pattern analysis indicated that the dislocations appeared to be in the <110> direction. This "self-ordering" behavior has also been reported in ion irradiation experiments on FM steels by Kaoumi et al. [86]. The ordering of dislocation lines in specific directions coupled with evidence of dislocation glide suggested a more complex dislocation network behavior than what was described in conventional irradiation creep mechanisms. The exact cause of this microstructure feature are still under investigation. Similar features have also been reported in unstressed proton irradiated samples up to higher dose, therefore it is not yet conclusive that these alignments are induced by the externally applied stress. However, aligned network dislocations will have a large impact on theoretical calculations of SIPA, PE, and PAG. Quantitative analysis on these aligned network features are needed to arrive at a more accurate understanding of microstructural influence on irradiation creep.

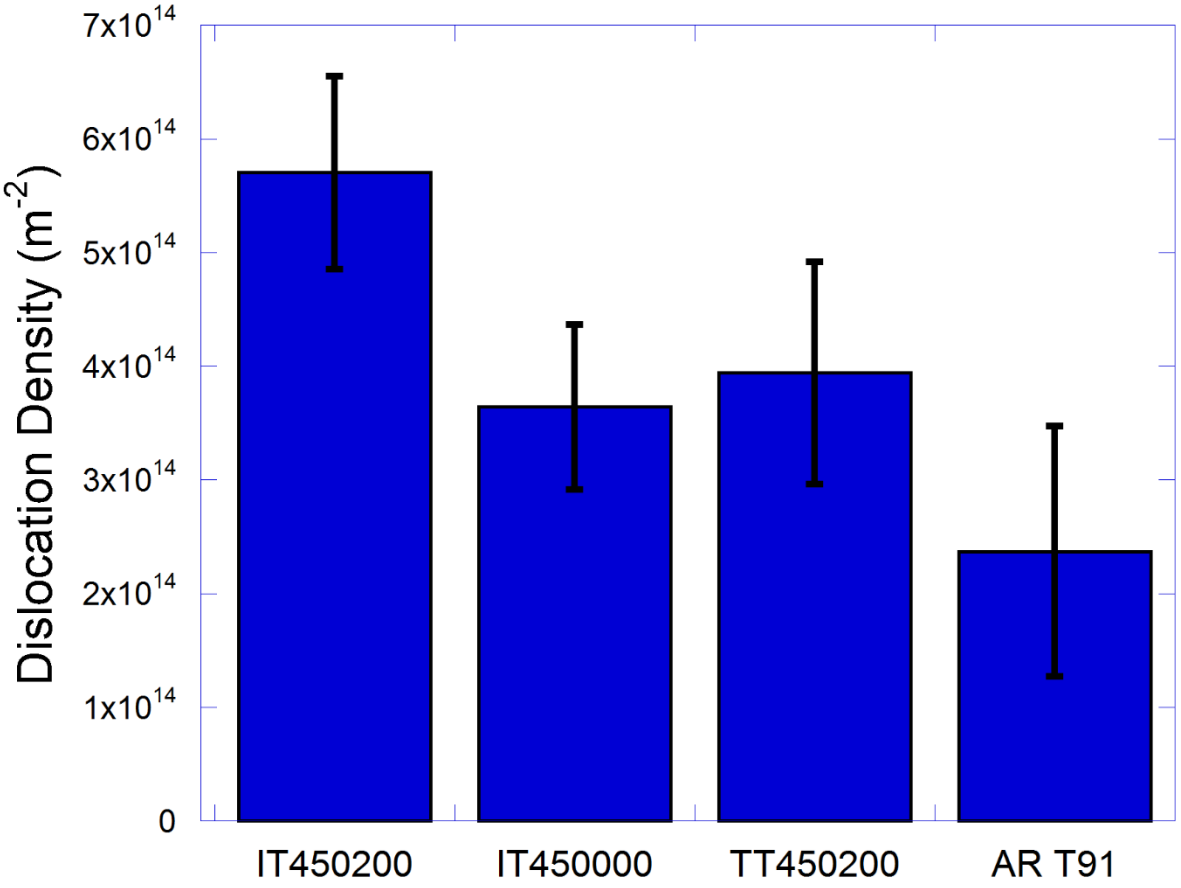

Figure 6.14 Dislocation network density of irradiation creep sample IT450200, proton irradiation sample IT450000, and thermal creep sample TT450200 from this study, and as received (AR) T91 sample analyzed by Gupta et al. [87]

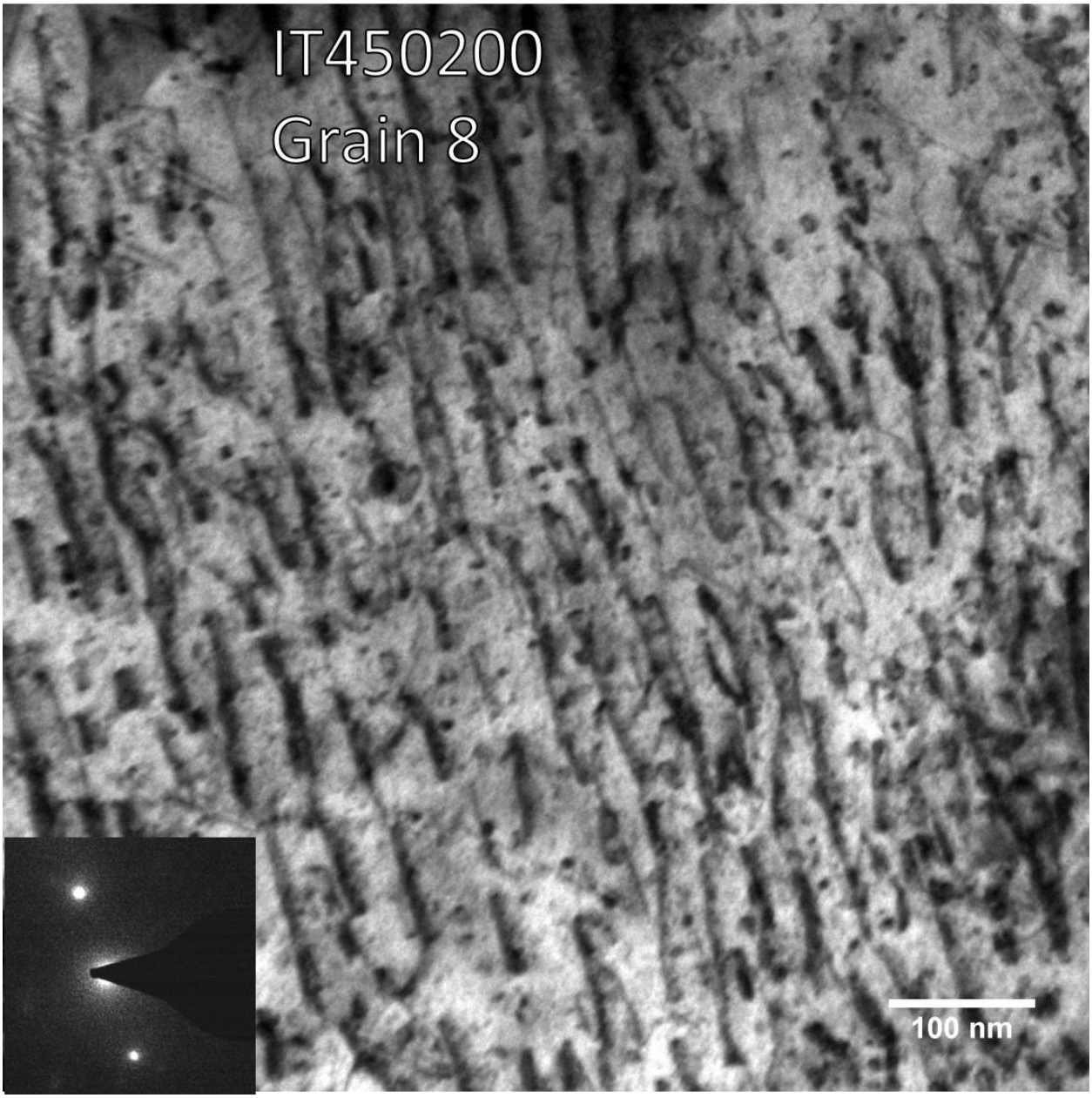

Figure 6.15 Self-ordered dislocation line segments in irradiation creep sample IT450200.

6.2.2 Sub-grain Size

Sub-grain size is also a key microstructure feature that needs to be accounted for in mechanistic calculations of irradiation creep rates. Three samples were used in this study to determine the effect of sub-grain size of T91 under thermal creep, proton irradiation without stress, and irradiation creep. Section 5.2.3 described in detail the results and method of the sub-grain size analysis for samples TT450200, IT450000, and IT450200.

The sub-grain size in the three test conditions is plotted in Figure 6.16. The sample TT450200 tested under thermal creep conditions was found to have a sub-grain size of 0.447±0.045μm. The unstressed, proton irradiated sample IT450000 had a sub-grain size of 0.391±0.045μm. The irradiation creep sample IT450200 had a sub-grain size of 0.478±0.057μm. No significant difference was observed between the sub-grain sizes of the three samples analyzed. These observation suggested that no significant grain growth or sub-grain formation occurred during the experiments. This was consistent with majority of neutron irradiation experiments where the martensitic grain structure generally remain unchanged as a function of dose.

The stability of the grain structure suggested that there was no grain coarsening occurring in the material nor is grain boundary sliding contributing to the creep deformation. The sub-grain boundaries merely act as neutral sinks or obstacles to dislocations. However, this does not preclude the possibility that formation of sub-grain boundaries or grain coarsening will occur at higher doses or temperatures. Thermal creep studies on FM steels conducted by Gupta et al. [41] showed that the internal stress created by sub-grain formation was directly correlated with the measured creep rates. Studies on power law breakdown (PLB) also point to the high density of sub-grain boundaries as the source of the long-range internal stress responsible for the high stress exponent seen in PLB [88], [89], [101]. The sub-grain structures observed in this study could be responsible for the unexpected large stress exponent observed for irradiation creep at stresses above 180MPa.

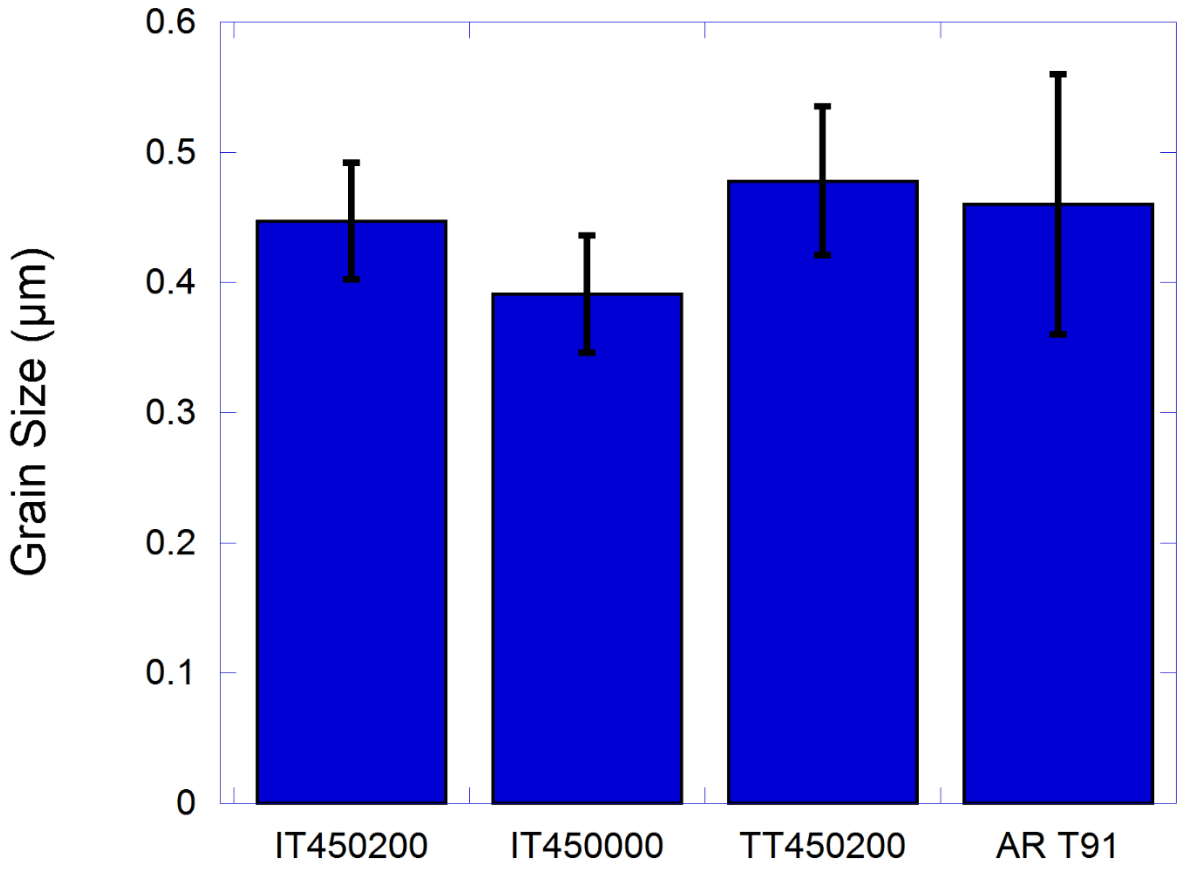

Figure 6.16 Average sub-grain size of irradiation creep sample IT450200, proton irradiation sample IT450000, and thermal creep sample TT450200 from this study, and as received (AR) T91 analyzed by Gupta et al. [87]

6.2.3 Voids

Historically, irradiation creep for austenitic steels was closely correlated with irradiation induced void swelling as predicted by the I-creep mechanism [19], [91], [107], [108]. However, this creep-swelling relationship became more complicated when dealing with FM steels. Because FM steels were designed to be swelling resistant, their void swelling is much less than in austenitic steels. If I-creep was the dominating mechanism, the suppression of void formation should also suppress irradiation creep in FM steels. However, significant irradiation creep was still observed in the absence of void swelling.

The irradiation creep samples showed no evidence of voids under TEM examination. Neutron irradiation experiments on FM steels typically do not exhibit void swelling until well above 100dpa [105], [109]–[111]. Therefore, the lack of voids was not surprising considering the low dose (typically around 1 dpa) in proton-irradiated samples. However, the lack of voids was evidence that irradiation creep can still occur in the absence of void swelling. The decoupling between void swelling and irradiation creep indicated that I-creep was not the dominant irradiation creep mechanism occurring in T91.

6.2.4 Dislocation Loops

Analysis of the dislocation loops of the irradiation creep samples revealed strong anisotropy in the dislocation loop density in relation to the tensile axis. The anisotropy in the dislocation loop were observed to increase as a function of the applied stress, and described by an inverse linear function with respect to its angle to the tensile axis. No clear anisotropy in the dislocation loop diameter were observed as a function of orientation, however the mean diameter showed a dramatic increase at higher stress conditions. The results of the anisotropy and dislocation loop size were described in detail in Section 5.2 and summarized in Table 6.4.

Interstitial loops had long been theorized to play an important role in the irradiation creep of nuclear materials. Loops can only contribute to creep if their orientations were anisotropic such that more were oriented with their habit planes normal to the applied stress than parallel to it. Hesketh et al. [112] first proposed the link between dislocation loops and irradiation creep in uranium. Lewthwaite et al. [113] extended the mechanism to austenitic steels where irradiation induced vacancies clustered to form voids that drive swelling, while interstitials clustered to form loops that drive irradiation creep. Herschbach et al. [114] further developed a method to calculate the strain contribution from dislocation loops while taking into account both the effect of irradiation and applied stress. However, the calculation of the loop contributions up to that point were based on the assumption that the dislocation loop density anisotropy would be proportional to a Boltzmann factor, where the external applied stress modified the loop nucleation energy in the exponential term of the expression for dislocation loop concentration [26]. The validity of the assumptions for loop anisotropy calculations have been debated and challenged [5], [115], [116].

Direct measurement of anisotropy in the dislocation loop density was first conducted by Okamoto et al. [7] in solution annealed (SA) 316 stainless steel irradiated in EBRII at 410^{o}C and 206.84 MPa (30ksi) hoop stress to a total fluence of 2.4x10^{21}n/cm^{2}. Four distinct loop orientations, [-1-11], [111], [-111], [1-11], were imaged under bright field and dark field conditions. It was found that the four loop orientations all had the same loop size within 5%. However, the loop concentration on different sets of {111} planes varied by as much as a factor of two. Okamoto et al. [7] concluded that his observations supported the stress-biased loop nucleation mechanism as playing a significant role in the irradiation creep of SA 316 stainless steels.

The effect of stress on dislocation loop microstructure of 316 stainless steel in both SA and 20% cold worked state were examined by Brager et al. [117]. Pressurized tube specimens of stainless steel were irradiated in EBRII to $3.0x10^{22}n/cm^2$ at 500°C and hoop stress as high as 327MPa. Loop number density measurements showed that, for a given Hoop stress condition, there was a clear preferential nucleation of loops on planes with a higher resolved normal stress. For the 20% coldworked 316 stainless steel, doubling the resolved normal stress (200MPa vs. 100MPa) doubled the measured loop density in the same sample. The conclusion for irradiated austenitic steels was that a higher resolved normal stress primarily enhanced the nucleation of dislocation loops, with a secondary effect of increasing the size of the defects.

Gelles et al. [9] confirmed the anisotropy of loops in 20% cold worked 316 stainless steel by conducting TEM analysis on pressurized tubes irradiated in FFTF to $8.0x10^{22}n/cm^2$ at 450°C and a hoop stress of 138MPa, and at 650°C with a hoop stress of 69MPa. It was observed that one set of <111> loops had a much higher density compared to another set of <111> loops in the sample depending on their Burgers vector orientation. The ratio of the one set of loop density to the other was interpreted to be the anisotropy factor. The anisotropy factor of the loop Burgers vector was reported to be 4.3 to 5.3 for these samples. In addition, Gelles et al. [9] also documented the anisotropy found in a duplex ferritic/martensitic alloy irradiated in FFTF at 407-520°C to $7.5x10^{22}n/cm^2$ with a stress up to 90MPa. The anisotropy factor for different orientations was reported to be as large as 7.3 for $a_o/2<111>$ loops and up to 2.7 for $a_o<100>$ loops. However, the analysis on the duplex steel was only done on the delta-ferrite regions and not the martensitic regions. Therefore, observations of dislocation loop anisotropy in tempered martensitic steels have yet to be documented.

Schaeublin et al. [111] conducted studies on the FM steel F82H irradiated up to 10 dpa also arrived at the same observations for dislocation loops. The study concluded that $a_o/2<111>$ glissile loops from under irradiation, then interact with each other to form $a_o<100>$ sessile loops or interact with other dislocation lines to form new helical dislocations. The $a_o<100>$ loops were interstitial in nature, observed to be immobile, and suspected to fill the entire matrix at high dose. Anisotropy of the dislocation loops were not analyzed in this study.

A recent detailed TEM analysis of ferritic RAFM steel irradiated to 3.9dpa in HFIR confirmed the previous results of anisotropy in the a_o <100> dislocation loop density [118]. This study confirmed that at temperatures above 400°C, the ferritic RAFM steel is dominated by a_o

<100> sessile dislocation loops rather than $a_o/2$<111> glissile loops. The ratio of the sessile loops with different orientations relative to glissile loops was reported to be as much as a factor of 5. The paper differentiated the anisotropy between the two loop types but made no attempt to quantify the relationship between the loop anisotropy to the applied stress.

The microstructure observations from this study on FM alloys confirmed majority of the past findings on austenitic steels. There existed many theories on the mechanistic significance for the anisotropic distribution of dislocation loops. The classic interpretation of the loop density anisotropy pointed to stress induced preferential nucleation (SIPN) as the dominating mechanism. However, SIPN had been criticized on the grounds that interstitial emission was not energetically favorable in bcc steels. This meant that SIPN did not allow loops to be dissolved in order for the density to reach steady state, making it incompatible with traditional nucleation theory. Two explanations were proposed to amend the SIPN mechanism in order to explain the observed anisotropy in loop density. [5] It was suggested that stress induced preference in the dislocation loops could occur during the very initial stages of loop nucleation, and its effect will persist as the loops grow at equal rates regardless of their orientation. This theory predicted that irradiation creep would persist even after the applied stress was removed because anisotropy would already exist during the initial nucleation stage. However, this phenomenon has not yet been observed because the capability of in-situ removal of stress during irradiation has not been satisfactorily developed. The second theory for SIPN was to allow preferential absorption of interstitials to occur in tandem with preferential nucleation of interstitials. This additional mechanism would be SIPA in nature, and would allow SIPN to be compatible with traditional nucleation theory where dislocation loops nucleate and dissolve to reach a steady state density. Anisotropic absorption of interstitials predicted anisotropy in the dislocation diameter as a function of their orientation to the tensile axis.

The effect of stress on the dislocation loop diameter in proton irradiation creep experiments were twofold. First, there was a lack of anisotropy as a function of orientation to the tensile axis. Second, an applied stress around 200MPa changed the size distribution of the dislocation loops to be much larger. These two observations suggested a dislocation loop evolution process where the applied stress affected the dislocation interactions rather than anisotropic diffusion. Preferential diffusion of interstitials towards dislocation loops of specific orientation was not observed because no difference in size was observed as a function of

orientation. The a_o<100> type loops imaged in this analysis were created by the interaction of $a_o/2$<111> glissile loops. Therefore, the anisotropic dislocation density distribution could be the result of anisotropic interaction between the $a_o/2$<111> loops as a function of applied stress. In addition, the large dislocation loops found for the 200MPa stress condition corresponded to strain rate regime dominated by dislocation glide by PLB. The onset of large amounts of glide can give rise to dislocation network and loop interactions to break apart the dislocation loops as seen in Figure 6.17. These broken loops imaged in the edge on condition would appear much larger than loops imaged under lower stress conditions.

Although the result of this study contradicted the predictions made by SIPA or SIPA-AD by preferential interstitial absorption, it did not completely eliminate the SIPA concept by other mechanisms such SIPA operating in an anisotropic dislocation network. Woo et al. [22], [119], [120] conducted many calculations on how SIPA could occur in the presence of an anisotropic dislocation microstructure. However, majority of these calculations were for zirconium alloys and austenitic steels. Additional work is needed to determine the Burgers vector distributions of the dislocation networks in addition to the analysis on dislocation loops done in this study to validate every aspect of the SIPA theory for FM steels.

The observation of anisotropic dislocation loop density and the lack of anisotropy in the dislocation loop diameter provided valuable evidence narrowing down certain aspects of the irradiation creep mechanisms. The result of this study supported a classical interpretation of SIPN theory in FM that had been observed for austenitic steels, but did not address the criticisms against the theory. Qualitative observations of the dislocation network may suggest a potential solution to the criticism by allowing interaction of a_o<100> loops with dislocation networks, but more study is needed to confirm the hypothesis. The results of this study also contradicted the SIPA theory of preferential absorption of vacancies, but SIPA could still be operating indirectly via mechanisms other than the preferential absorption of vacancies. Although the anisotropy analysis did not definitively determine whether SIPA or SIPN was dominating during irradiation creep, it revealed that anisotropy in the microstructure existed in FM steels and should be taken into account in analysis of creep rates. In addition, the anisotropic dislocation loop microstructure also contributed to the strain in the sample that will be measured as part of irradiation creep.

Table 6.4 Characterization of loops in irradiation creep samples

Sample Name	Number of Loops Analyzed	Average Loop Size (nm)	Dislocation Loop Density (m^{-3})	Constants for Loop Anisotropy	
				α	β
IT450100	434	24.3	$1.6x10^{21}$	0.64	-0.0032
IT500180	346	23.3	$1.5x10^{21}$	0.95	-0.010
IT450180	490	24.9	$1.3x10^{21}$	0.78	-0.006
IT450200	286	42.3	$1.0x10^{21}$	1.16	-0.014

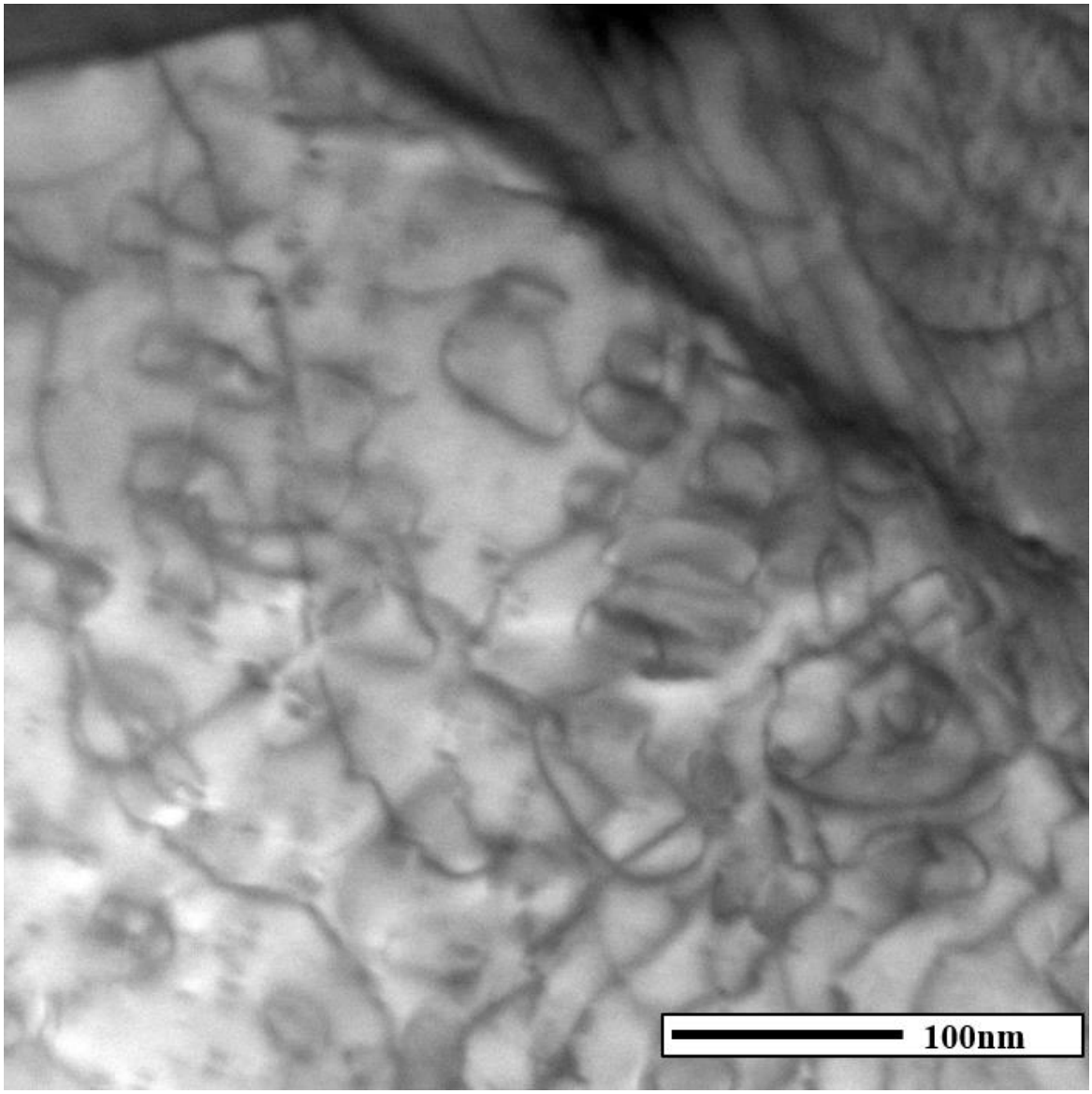

Figure 6.17 Dislocation loops interaction with network observed in sample IT500180.

6.3 Summary of Strain Rate Dependence and Microstructure Observations

The linear dose rate dependence analysis in this study found that irradiation creep was mainly a function of irradiation induced point defect concentration, eliminating thermal diffusion mechanisms such as PE as a dominating process. The lack of temperature dependence was found to be consistent with those findings, and creep mechanisms based on irradiation point defects such as SIPA, I-Creep, and PAG. Results of microstructure observations saw no voids which eliminated the I-Creep description of irradiation creep. SIPN mechanism was eliminated due to unfavorable energy for interstitial emission in bcc steels. The microstructure effect of SIPN, mainly the anisotropic dislocation loop distribution, was explained by a variant of the SIPA mechanism [121]. The stress dependence was found to be incompatible with all irradiation mechanisms, but further analysis was needed to subtract out specific strain contributions to further isolate the mechanism.

PAG and SIPA appeared to be the most compatible with every experimental observation with the exception of the stress dependence. However, the stress dependence of irradiation creep in this study was complicated by contribution from the anisotropic distribution dislocation of the loops and the power law breakdown observed at high stress. In order to properly isolate the stress dependence of the creep rates, these contributions should be subtracted from the creep strain. The next section will calculate the strain contribution from the anisotropic loop distribution based on the measured microstructure data.

6.4 Strain Contribution from Dislocation Loop Anisotropy to Irradiation Creep

Many studies have been conducted in an attempt to understand the anisotropy in the dislocation loop density. However, a standardized measurement or analysis technique of anisotropy had not yet been established. Investigators often reported an anisotropy factor based solely on observations of specific sets of dislocation loop density without taking into consideration the complex interdependent relationship between the external stress, grain orientation, and loop plane orientation. Although empirical observations on 316 stainless steel have consistently confirmed the existence of dislocation loop anisotropy, the magnitude of the anisotropy and its relationship with the applied stress are still not immediately clear.

Using the empirical observations of dislocation loop anisotropy described in Section 6.2.4, this section will determine the strain in the tensile direction associated with the observed loop anisotropy and compare the strain due to anisotropic dislocation distribution with the macroscopic creep strain measured in the samples. It will provide the first evaluation of loop strain in irradiation crept FM alloys.

Kroupa et al. [122] derived the strain in a volume due to a continuous distribution of dislocation loops as the following strain tensor:

$$\epsilon_{ij} = \sum_{k=1}^{N} \frac{S^{(k)} A^{(k)} n_i^{(k)} b_j^{(k)}}{\Delta V} \quad . \tag{6.7}$$

The equation describes the strain ε caused by N groups of loops in a volume ΔV, where the k^{th} group of loops all have the same Burgers vector b, area A, normal vector n and number density S. The subscript i denotes x, y, z directions of the loop normal vector, and subscript j denotes the contribution of loop Burgers vectors to the x, y, z directions

Each variable was measured in this study, yielding the following expression for a single group of loops in a single grain:

$$\epsilon_{ij}^{(k)} = \frac{N^{(k)} \pi \left(\frac{D}{2}\right)^2 n_i^{(k)} b_j^{(k)}}{\Delta V}, \tag{6.8}$$

where $N^{(k)}$ is the total number of the k^{th} loop in the volume ΔV. D is the measured loop diameter. Because only a_o<100> type loops were analyzed, the subscript on the Burgers vector can be dropped. Analysis of the anisotropy of the dislocation loops determined that $N^{(k)}/N = \beta\theta^{(k)}+\alpha$ as described by equation. (5.4). Let the bulk dislocation loop density, ρ, be derived as $N/\Delta V$, and equation (6.8) becomes:

$$\epsilon_i^{(k)} = b\rho\pi\left(\frac{D}{2}\right)^2 n_i^{(k)}(\beta\theta^{(k)} + \alpha). \tag{6.9}$$

If we define the coordinate axis such that the tensile axis is in the z-direction as shown in Figure 6.18, then the loop normal vector, n is derived by the following:

$$n^{(k)} = \begin{bmatrix} x \\ y \\ z \end{bmatrix} = \begin{bmatrix} \sin(\theta^{(k)})\cos(\phi^{(k)}) \\ \sin(\theta^{(k)})\sin(\phi^{(k)}) \\ \cos(\theta^{(k)}) \end{bmatrix}, \tag{6.10}$$

where the angle $\theta^{(k)}$ is the angle between the normal vector of the kth loop and the tensile axis, and $\phi^{(k)}$ is the azimuthal angle. Combining equations (6.8)-(6.10), the strain vector ε becomes only a function of the angles $\theta^{(k)}$ and $\phi^{(k)}$. The bulk strain can be determined by integrating over angles $\theta^{(k)}$ and $\phi^{(k)}$:

$$\epsilon_i = b\rho\pi\left(\frac{D}{2}\right)^2 \frac{1}{C}\int_{\phi=0}^{\pi/2}\int_{\theta=0}^{\pi/2} n_i(\beta\theta + \alpha)\, d\phi d\theta. \tag{6.11}$$

To avoid double counting the total number of loops when integrating across the angles, the integral is normalized by a constant C such that the sum of the densities of each set of loops with any normal vector, n becomes equal to the total loop density, ρ. The normalization constant C is derived as follows:

$$C = \int_{\phi=0}^{\pi/2}\int_{\theta=0}^{\pi/2}(\beta\theta + \alpha)\, d\phi d\theta\ . \tag{6.12}$$

Because the analysis by Kroupa et al. [122] assumed the loops were additional to the atoms in the matrix, the strains in all three directions were positive. The positive strains caused a volumetric expansion equal to the following:

$$\epsilon_{vol} = \epsilon_x+\epsilon_y+\epsilon_z\ . \tag{6.13}$$

This assumption violated the volume conservation of creep. In reality, the atoms that made up the dislocation loops originated from the matrix. For the purpose of this analysis, the atoms were assumed to originate equally from each of the x, y, and z directions. Therefore, one third of the

volumetric expansion from dislocation loops was subtracted from the strain of the three primary directions.

The final volume conservative strain calculated from the anisotropy of the loops becomes:

$$\varepsilon_i = b\rho\pi \left(\frac{D}{2}\right)^2 \frac{1}{C} \int_{\phi=0}^{\pi/2} \int_{\theta=0}^{\pi/2} n_i(\beta\theta + \alpha)\, d\phi d\theta - \frac{1}{3}\, \epsilon_{vol}. \qquad (6.14)$$

This integral was evaluated numerically using a Matlab® code developed at University of Michigan and provided in the Appendix E. The result of the calculations for the samples IT450200, IT450180, IT450100, and IT500180 are plotted in Figure 6.19. The total strain due to the anisotropy of the loops is compared to the total measured strain in the sample in Table 6.5.

The strain due to anisotropy of the dislocation loops observed in the samples was found to account for only 4-11% of the total strain measured in the samples. This observation was consistent with previous works that claimed strain due to anisotropy in the dislocation loops was much lower than the total measured strain [5], and suggesting that another deformation mechanism must be responsible for the irradiation creep behavior.

Table 6.5 tabulates the maximum strain in samples IT450100, IT450180, IT450200, and IT500180 in comparison to the macroscopic strain of the bulk sample. The macroscopic strain of the bulk sample is determined by multiplying the characteristic strain rate by the irradiation time. It is observed that the strain from anisotropic dislocation loops alone can't account for the total observed macroscopic strain of irradiation creep. Anisotropic loop strain is responsible for 4% to 11% of the total strain in the irradiation creep samples, depending on the irradiation condition. The result of the analysis showed that contribution from the anisotropic dislocation loops alone can't account for the total strain measured. Therefore, the SIPN mechanism was not the dominating mechanism for irradiation creep of this study.

Table 6.5 Strain due to anisotropic loop density and measured total strain

Sample Name	Loop Anisotropy Strain (%)	Irradiation Time (Hr)	Measured Total Strain (%)	Percent of Strain due to Anisotropy (%)
IT450100	0.006	170	0.10	6
IT450180	0.0056	80	0.13	4.3
IT450200	0.0158	80	0.36	4.4
IT500180	0.0067	30	0.06	11.2

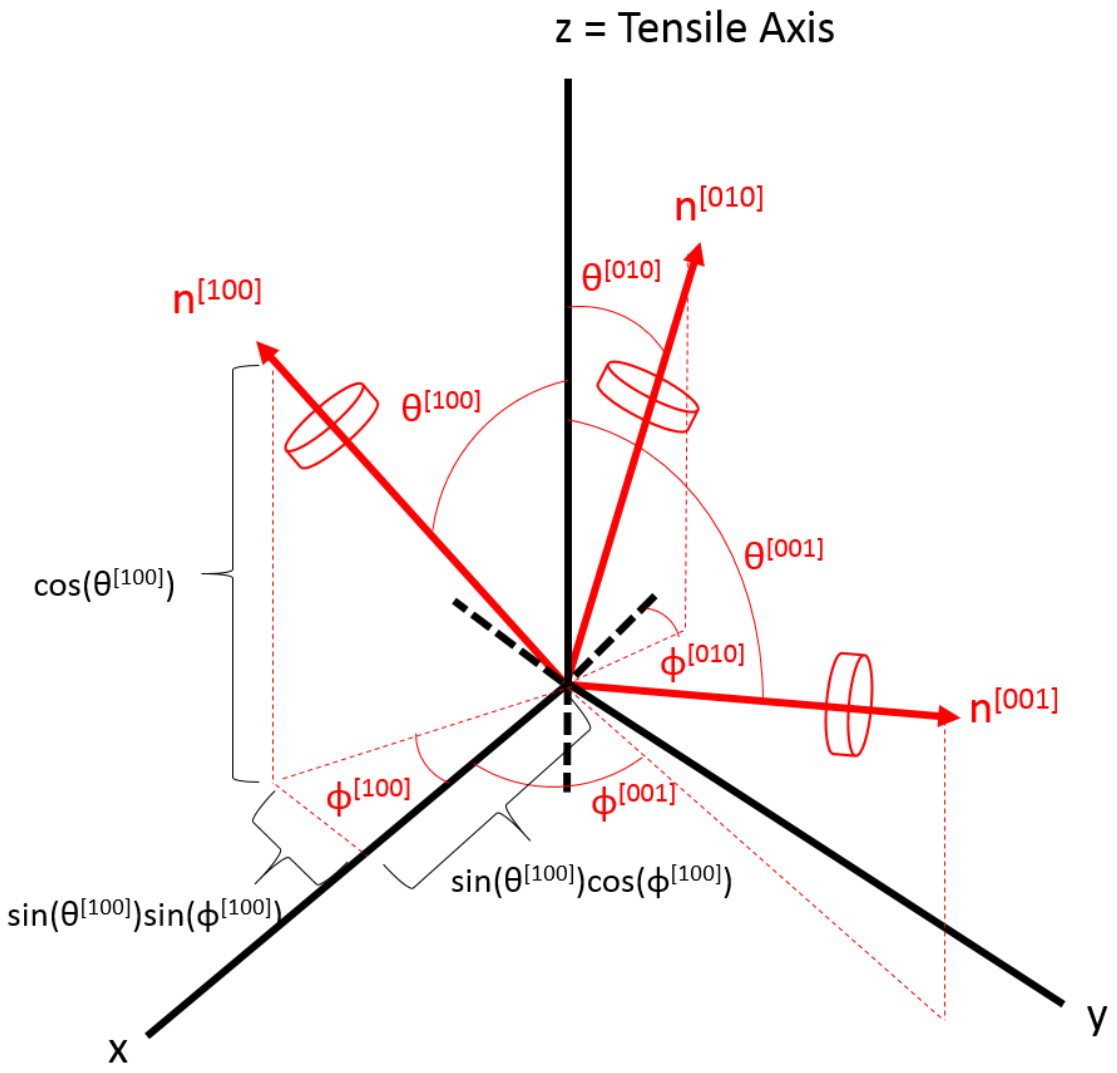

Figure 6.18 Schematic of the normal vectors n(k) of three sets of dislocation loops, where k= [100], [010], and [001]. The components of the n[100] are defined in the Cartesian coordinate where z-axis is the tensile axis.

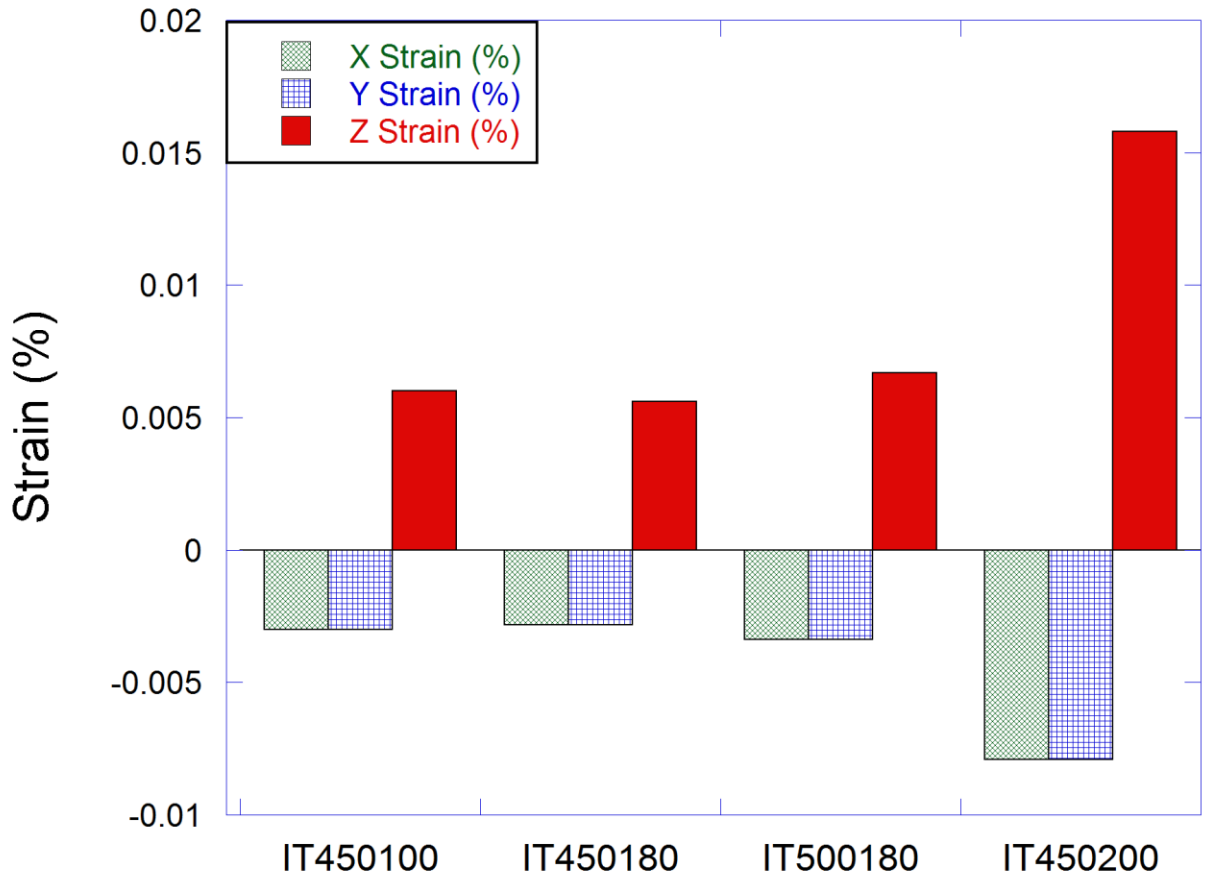

Figure 6.19 Result of analysis of the strain due to anisotropic dislocation loops observed in samples IT450100, IT450180, IT500180, and IT450200.

6.5 Analysis of Other Irradiation Creep Mechanisms

The observation of an anisotropic dislocation loop distribution under TEM analysis concluded that anisotropy in the loop density alone could not satisfactorily explain the total strains measured in the samples. The lack of large temperature dependence precluded preferential emission (PE) as a viable irradiation creep mechanism and the lack of voids eliminated I-Creep as the dominant irradiation creep mechanism. Stress induced preferential absorption (SIPA) and preferential absorption glide (PAG) are the two remaining irradiation creep mechanisms that could explain the creep rates that were observed experimentally.

The distinction between the two most viable creep mechanisms lies in their stress dependences, with SIPA being linearly dependent on applied stress and PAG having a quadratic stress dependence. Analysis of the stress dependence of the experimental creep rates conducted in Section 6.1.3 demonstrated that power-law breakdown (PLB) behavior at high stress complicated the picture and made it difficult to determine whether PAG or SIPA was active. In addition, any strain contribution from anisotropic loop distribution, however small, can also affect the stress dependence analysis on the irradiation creep rates. Therefore, the PLB and anisotropic loop contribution were both subtracted from the total strain. The adjusted strain rates are tabulated in Table 6.6, and plotted in Figure 6.20.

In order to determine whether PAG or SIPA was the dominant irradiation mechanism, this section will revisit the stress dependence of irradiation creep, and conduct the stress dependence analysis without the contributions from PLB and anisotropic loops. SIPA and PAG creep rates were calculated using literature formulas described by Mansur et al. [23], [123] and derived below:

$$\dot{\varepsilon}_{PAG} = \frac{4}{9}\frac{\epsilon}{b}(\pi L)^{1/2}\Omega D_i C_i \Delta Z_i \ , \tag{6.15}$$

$$\dot{\varepsilon}_{SIPA} = \frac{2}{9}\Omega \mathrm{L} D_i C_i \Delta Z_i. \tag{6.16}$$

The variable ϵ denotes elastic deflection, which is the applied stress over the modulus σ/E. L is the total dislocation density, Ω is the atomic volume, D_i is the interstitial diffusion coefficient, and C_i is the steady state interstitial concentration. ΔZ_i is the difference in stress induced

anisotropic sink strength for interstitials between aligned and unaligned sinks such that $\Delta Z_i = Z_{aligned} - Z_{unaligned}$. The sink strengths are a linear function of stress as defined by Savino et al. [8]:

$$Z_{aligned} = z_i \left(1 + \frac{5\sigma(2-\nu)}{2\mu e_o(7-5\nu)}\right) \tag{6.17}$$

$$Z_{unaligned} = z_i \left(1 - \frac{5\sigma(1+\nu)}{2\mu e_o(7-5\nu)}\right) \tag{6.18}$$

The μ is the shear modulus, ν the Poisson's ratio, z_i the interstitial bias for the dislocation in a stress-free lattice and e_o is the stress relaxation volume induced by the defect.

Since the defect concentrations are proportional to the dose rate, the dose rate dependence of the creep rate for both SIPA and PAG is also linear. The temperature dependence of the diffusion coefficient D_i cancels the temperature dependence of the reaction rate constants causing both PAG and SIPA to have no temperature dependence. In previous work by Savino et al. [8], [98], the stress induced anisotropic sink strength ΔZ_i was found to be a linear function of stress, making the SIPA mechanism linear in stress dependence and PAG quadratic in stress dependence.

Both linear and quadratic fits were made to the PLB- and anisotropic loop-adjusted strain rates to determine whether SIPA or PAG was dominating. The fits were forced through zero since irradiation creep goes to zero in the absence of stress. Figure 6.21 plots the creep strain rates, adjusted for PLB and anisotropic loop strain, as a function of stress. The plot shows that a linear fit goes through the majority of the data well within the experimental error, suggesting the experimental data can be explained by a linear stress dependence. Similarly, the quadratic fit also falls within the experimental error of the irradiation creep data. The analysis of the stress dependence suggests that both SIPA and PAG are viable irradiation creep mechanisms for FM steels.

Both qualitative and quantitative analysis of irradiation creep mechanisms by low dose proton irradiation showed that anisotropic dislocation microstructure was created during irradiation creep in FM steel T91. Analysis of the stress dependence revealed the operation of dislocation glide at high stress. Further analysis of the creep rates based on SIPA and PAG theory showed that both mechanisms provided satisfactory predictions on the stress dependence.

The dose rate dependence of irradiation creep suggests that it is directly related to the point defect concentrations under irradiation. Analysis on the temperature dependence showed that

diffusion of thermal vacancies alone had no effect on the strain rates. However, the observation of thermal dislocation glide by PLB accounted for the contribution from both thermal and irradiation vacancies. The PLB – and anisotropic loop adjusted - strain rates showed stress dependence that were consistent with both dislocation climb and glide enabled by the stress biased interstitial absorption by dislocations. These observations suggest a process where point defects were generated by irradiation, and the applied stress cause preferential interaction between dislocation networks and dislocation loops of certain orientations to generate an anisotropic dislocation microstructure. The anisotropic dislocation microstructure then will climb and glide by further absorption of interstitials to cause irradiation creep. Under high stress, the glide enabled by vacancies will further contribute to irradiation creep to cause the deviation from linear stress dependence at high stress.

Table 6.6 Experimental strain rates after adjustment to subtract out the strain contribution from PLB and SIPN.

Sample Name	Strain Rate ($10^{-9}s^{-1}$)	PLB Adjusted Strain Rate ($10^{-9}s^{-1}$)	SIPN Contribution (% Strain Rate)	SIPN+PLB Adjusted Strain Rate ($10^{-9}s^{-1}$)
IT450200-A	12.5	4.00	11.9	3.52
IT450200-B	11.5	2.90	11.9	2.55
IT450180-A	4.67	2.25	4	2.16
IT450180-B	5.00	2.58	4	2.47
IT450160-A	2.7	2.12	4.2*	2.03
IT450140-A	2.05	2.05	4.4*	1.95
IT450120-A	1.9	1.9	4.6*	1.81
IT450100-A	1.67	1.67	4.8	1.6

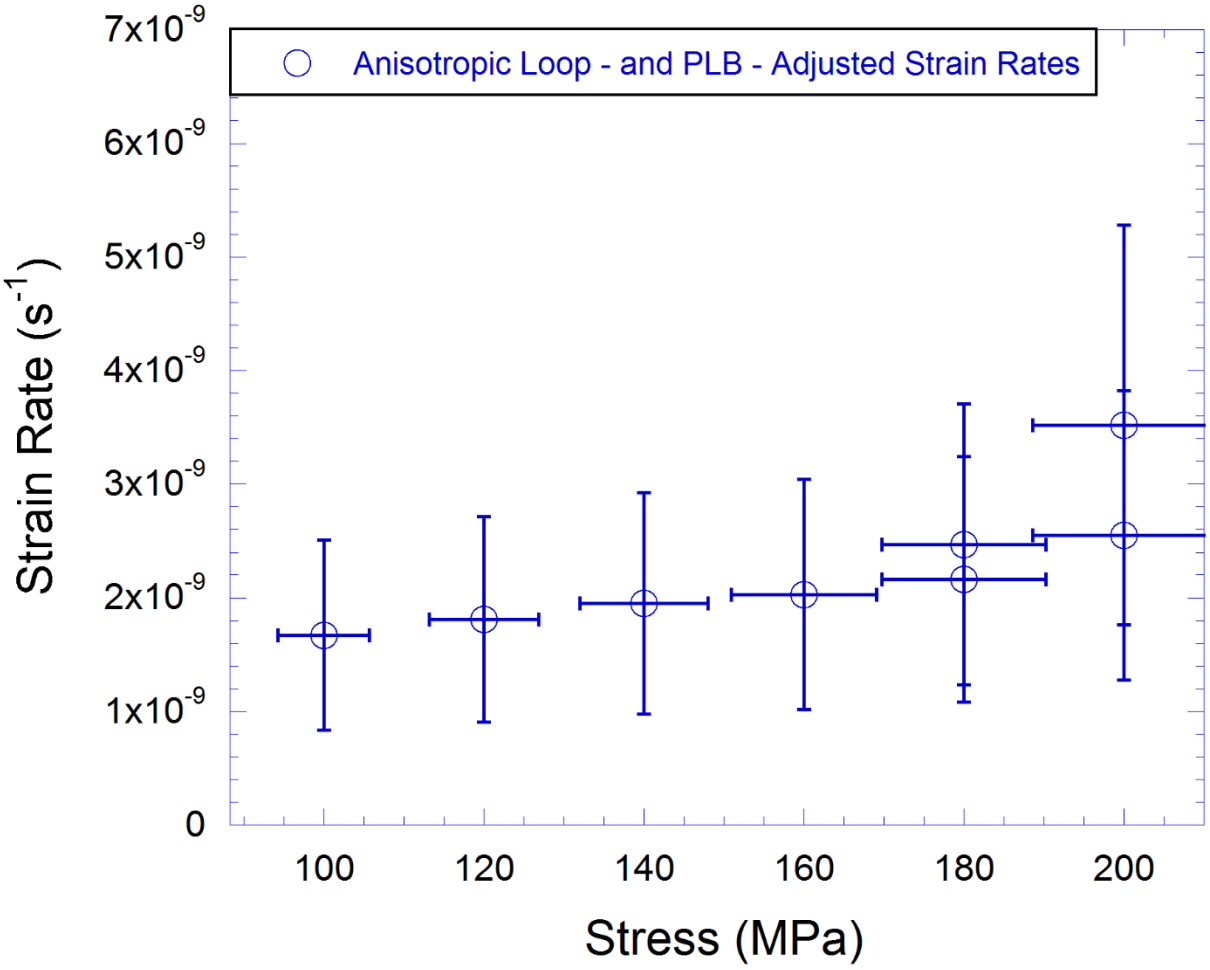

Figure 6.20 Experimental strain rates after adjustment to subtract out the strain contribution from PLB and SIPN.

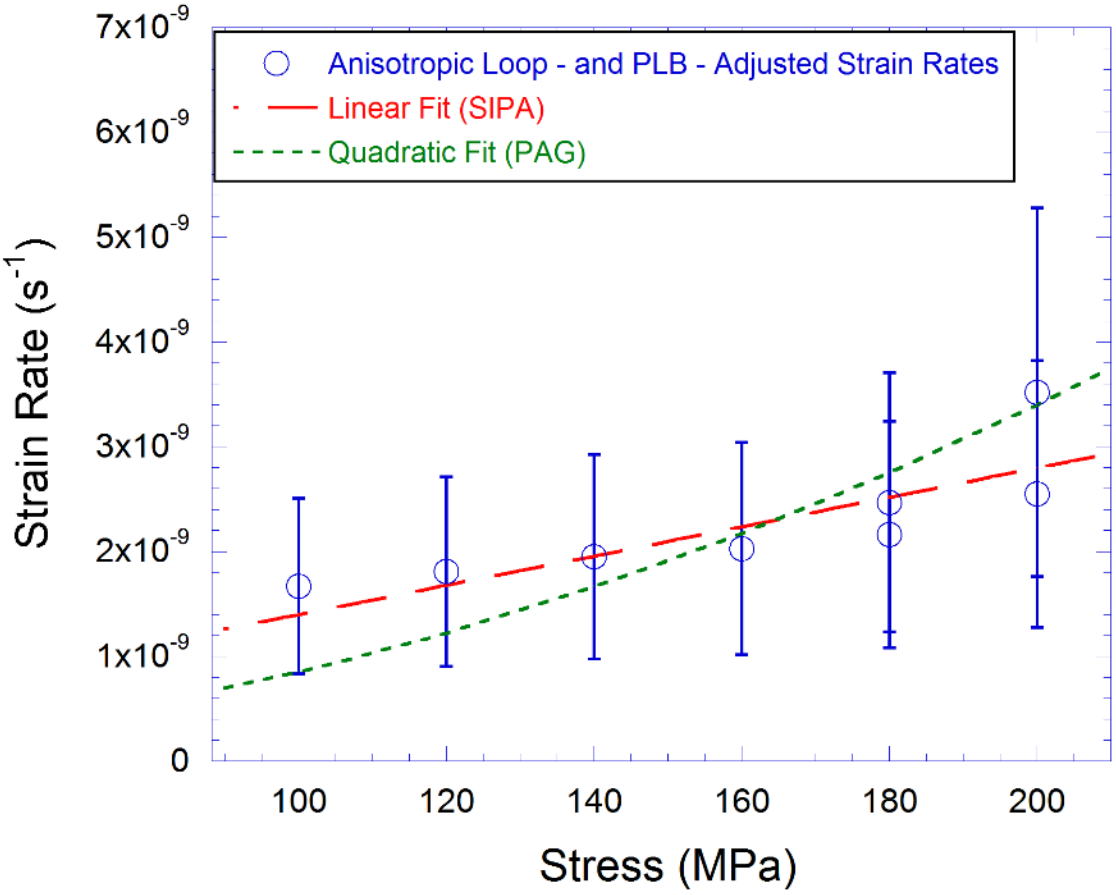

Figure 6.21 Stress dependence of proton irradiation creep rates without contribution from anisotropic dislocation loops and power law breakdown with linear and quadratic fits.

CHAPTER 7 Conclusion and Future Work

This thesis has reached the following conclusions:

1) Proton irradiation creep of T91 steel exhibits linear dose rate dependence. Analysis has shown that T91 steel under proton irradiation at temperatures above 400^{o}C fell under the high sink density, high temperature regime where the steady state point defect concentrations are a linear function of dose rate. The linear dose rate dependence of the experiment showed that irradiation creep strain rate was controlled by the steady state point defect concentrations.

2) Proton irradiation creep of T91 steel exhibited negligible temperature dependence. Point defect concentration analysis showed that thermal vacancy concentrations will start to overtake all irradiation induced point defects at temperatures above 540^{o}C. The three strain rates measured at 400^{o}C, 450^{o}C, and 500^{o}C were very close to each other and suggested no strong temperature dependence. This was consistent with neutron irradiation experiments, and confirmed theoretical predictions of all irradiation creep mechanism except preferential emission (PE). The lack of temperature dependence from this experiment eliminated PE as the dominant irradiation creep mechanism.

3) Power law breakdown behavior was observed during irradiation creep at high stress. This observation suggests that dislocation glide is operating at high stress, which is not typical of irradiation creep. The results of the stress dependence provided evidence that dislocation glide was contributing to the deformation of irradiation and thermal creep of FM steels.

4) No voids were observed in TEM analysis of low dose irradiation creep samples. This eliminated the I-creep as a viable irradiation creep mechanism in this study.

5) Anisotropic dislocation loop density was observed in proton irradiation creep. Anisotropic loop density have been well documented in neutron irradiated fcc austenitic steels,

but not in bcc FM alloys. Detailed characterization of the anisotropic loop microstructure yielded a linear relationship between the loop angle to the tensile axis and the local loop density.

6) Calculation of strain from loops using the most conservative assumptions suggest dislocation loops can only contribute 4%-11% of the total irradiation creep strain. Thus, anisotropic dislocation loop density alone can't account for the total strain measured in irradiation creep samples. The calculation of anisotropic dislocation loop strain eliminated SIPN as the dominating irradiation creep mechanism in this study.

7) No anisotropic distribution of dislocation loop diameter was observed. Traditional SIPA suggests preferential absorption of vacancies should result in an anisotropic distribution of loop diameters as a function of orientation to the tensile axis. The lack of an anisotropic distribution of dislocation loop diameter is evidence against the traditional SIPA mechanism. However, dislocation climb of anisotropic network density due to SIPA remains a viable irradiation creep mechanism.

8) PAG and SIPA stress dependence both match well with experimental data adjusted for contribution from power law breakdown and anisotropic dislocation loops. An irradiation creep mechanism based on both dislocation climb (SIPA) and glide (PAG) is the best explanation for the measured creep rates found in this study.

9) The overall contribution of irradiation creep of low dose proton irradiation creep of FM alloys included PAG, SIPA, anisotropic dislocation loop density, and PLB at high stress.

While significant conclusions have been drawn from this study, there are still unanswered questions that deserve further investigation:

1) The source of the anisotropic dislocation loop density is still not fully understood. This study suggested the anisotropy arise in the initial stages of loop formation and persists until the loops grow large enough to become part of the dislocation network. This hypothesis suggested that the loop anisotropy would continue to exist even if the tensile stress is removed in the middle of the irradiation creep experiment. Therefore, one should be able to measure significant strain from dislocation loops after the stress was removed and the loops continue to grow. In-situ irradiation creep experiments where stress can be readily removed would be ideal to test this hypothesis.

2) The effect of irradiation on dislocation creep mechanism in the thermal creep regime was still not well understood. Historically, irradiation creep and thermal creep were considered completely separate mechanisms. However, this study showed that there existed certain combinations of stress and temperature conditions where both irradiation creep and thermal creep were significant. The interactions between thermal mechanisms and irradiation mechanisms need to be studied in depth to arrive at a complete mechanistic understanding of creep behavior.

3) In-situ TEM investigation of dislocation loop evolution under applied stress, high temperature, and irradiation will be useful to determine how loops nucleate and interact with dislocation networks. This study observed significant anisotropy in the dislocation loop density at the end of irradiation. The snapshot of the final microstructure raised more questions regarding the evolution of the dislocation loops that can only be answered by in-situ TEM investigation and observing dislocation interactions in real time.

Appendix A: Irradiation Creep Strain Rates

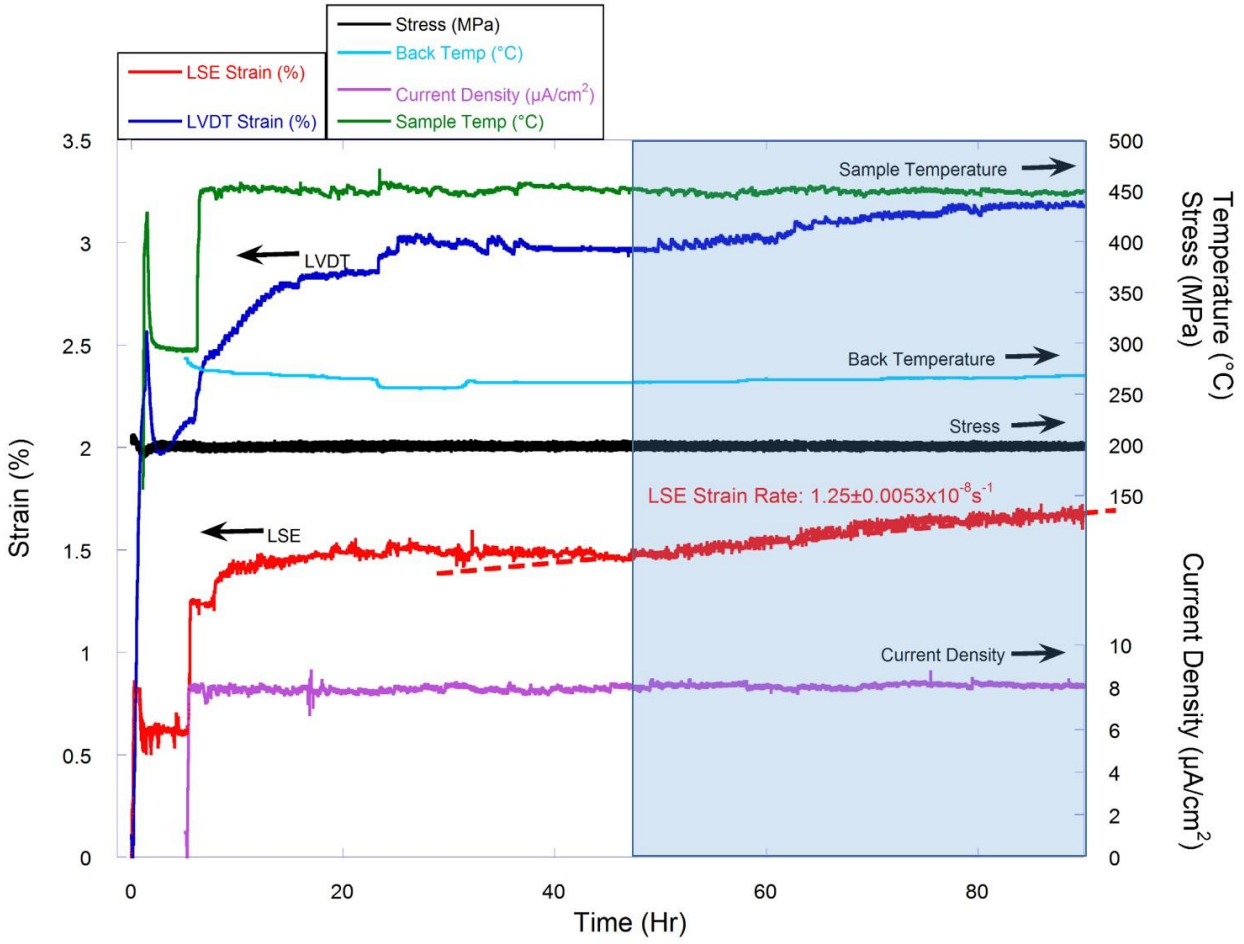

Figure A. 1 Irradiation creep curve of IT450200-A.

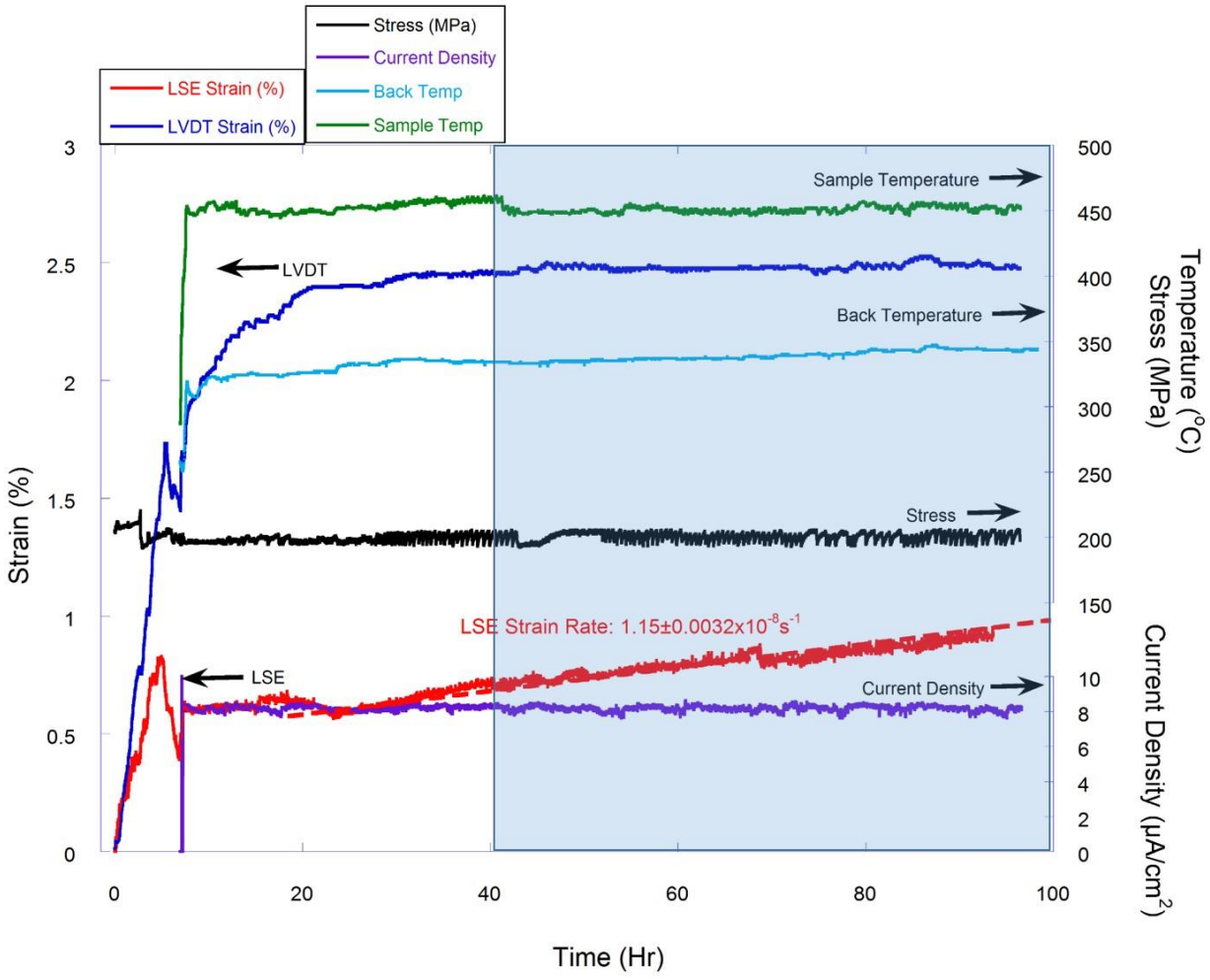

Figure A. 2 Irradiation creep curve of IT450200-B.

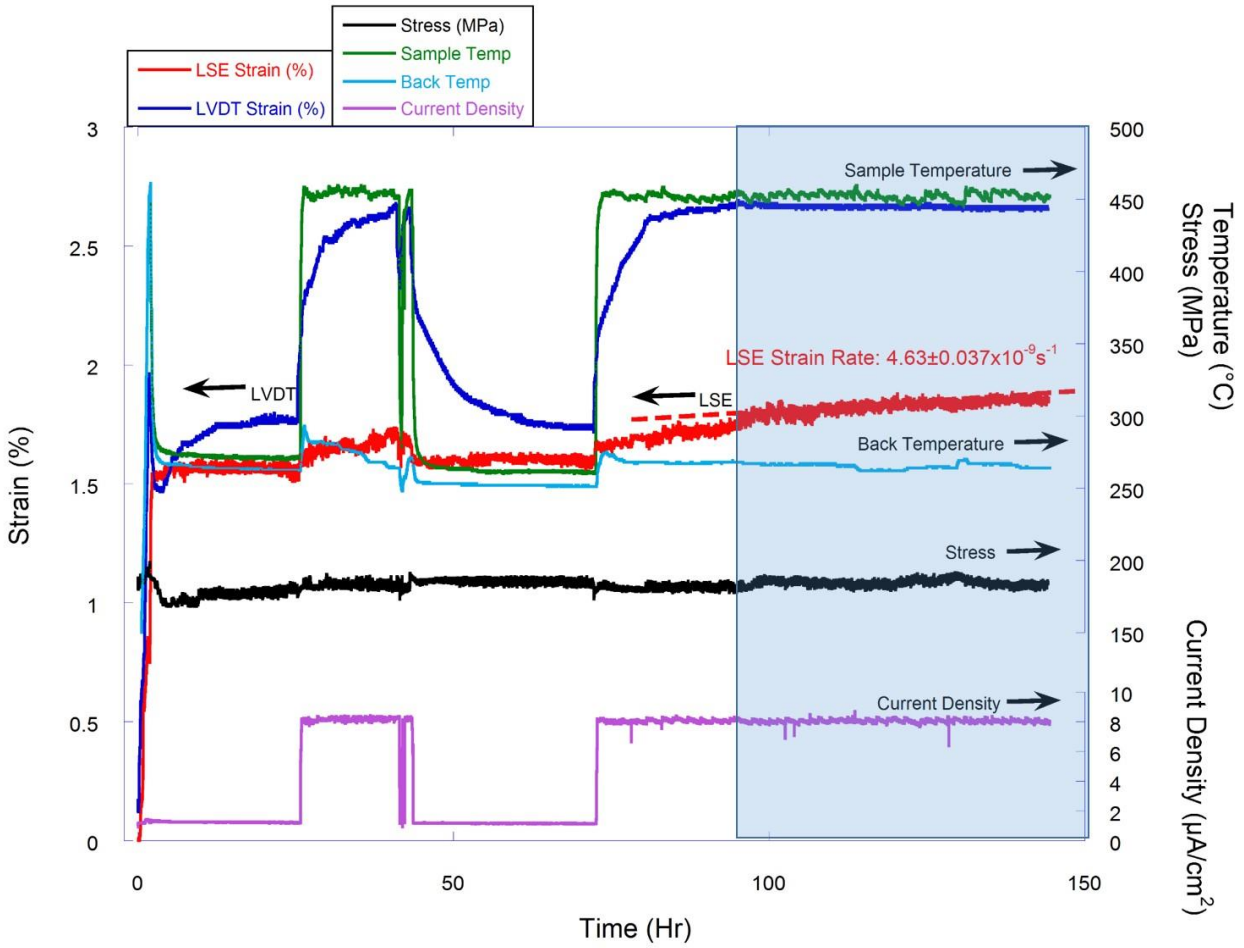

Figure A. 3 Irradiation creep curve of IT450180-A.

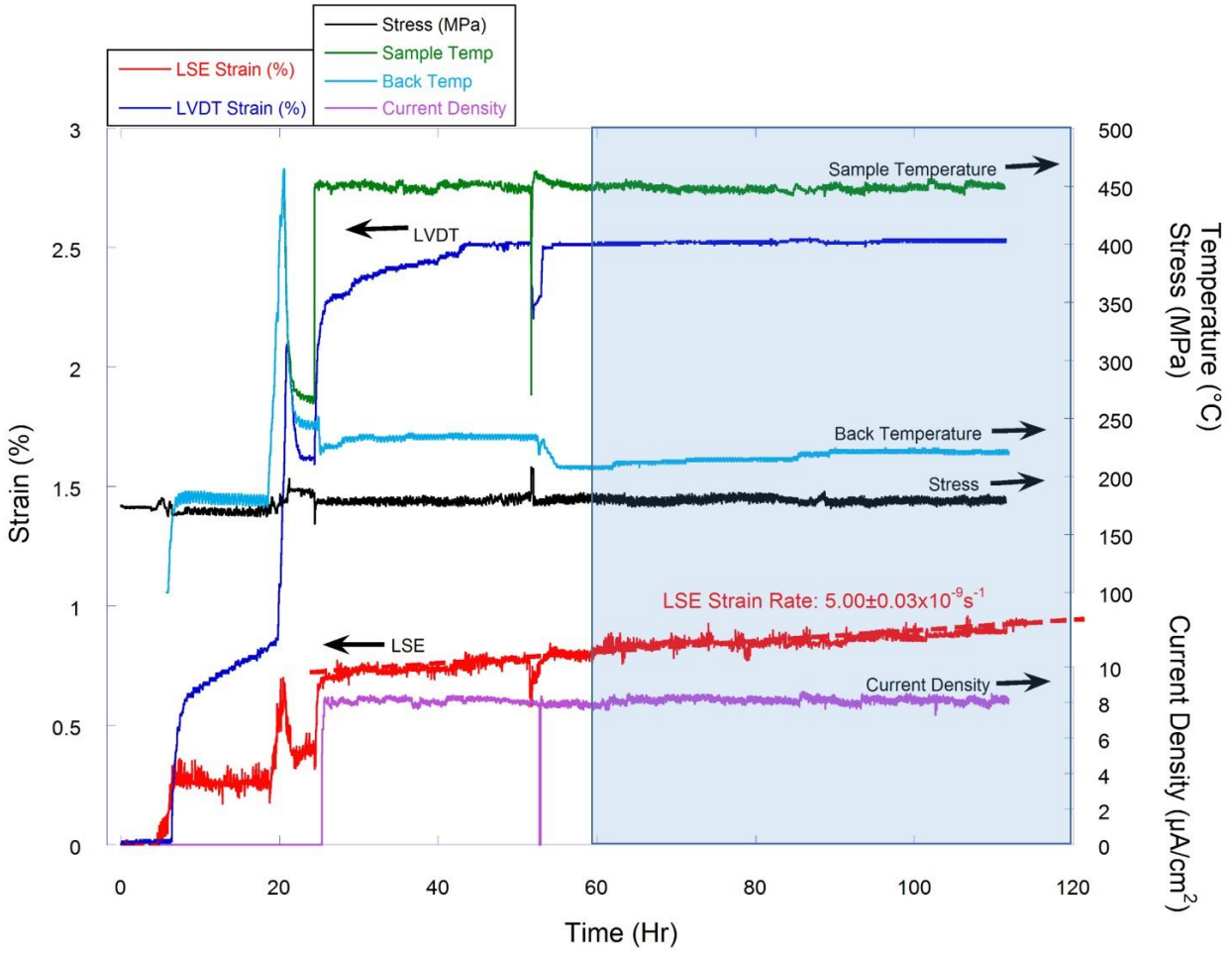

Figure A. 4 Irradiation creep curve of IT450180-B.

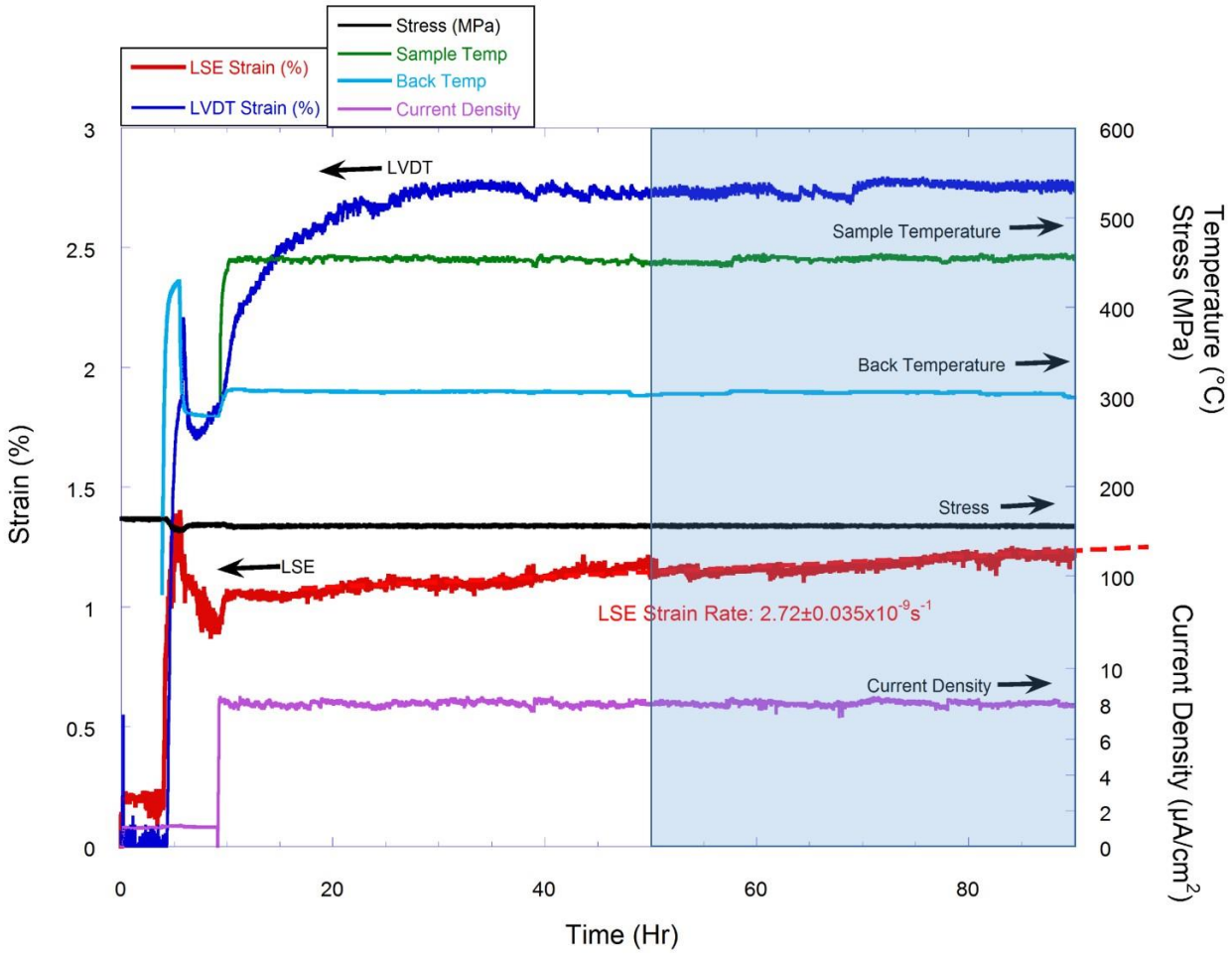

Figure A. 5 Irradiation creep curve of IT450160-A.

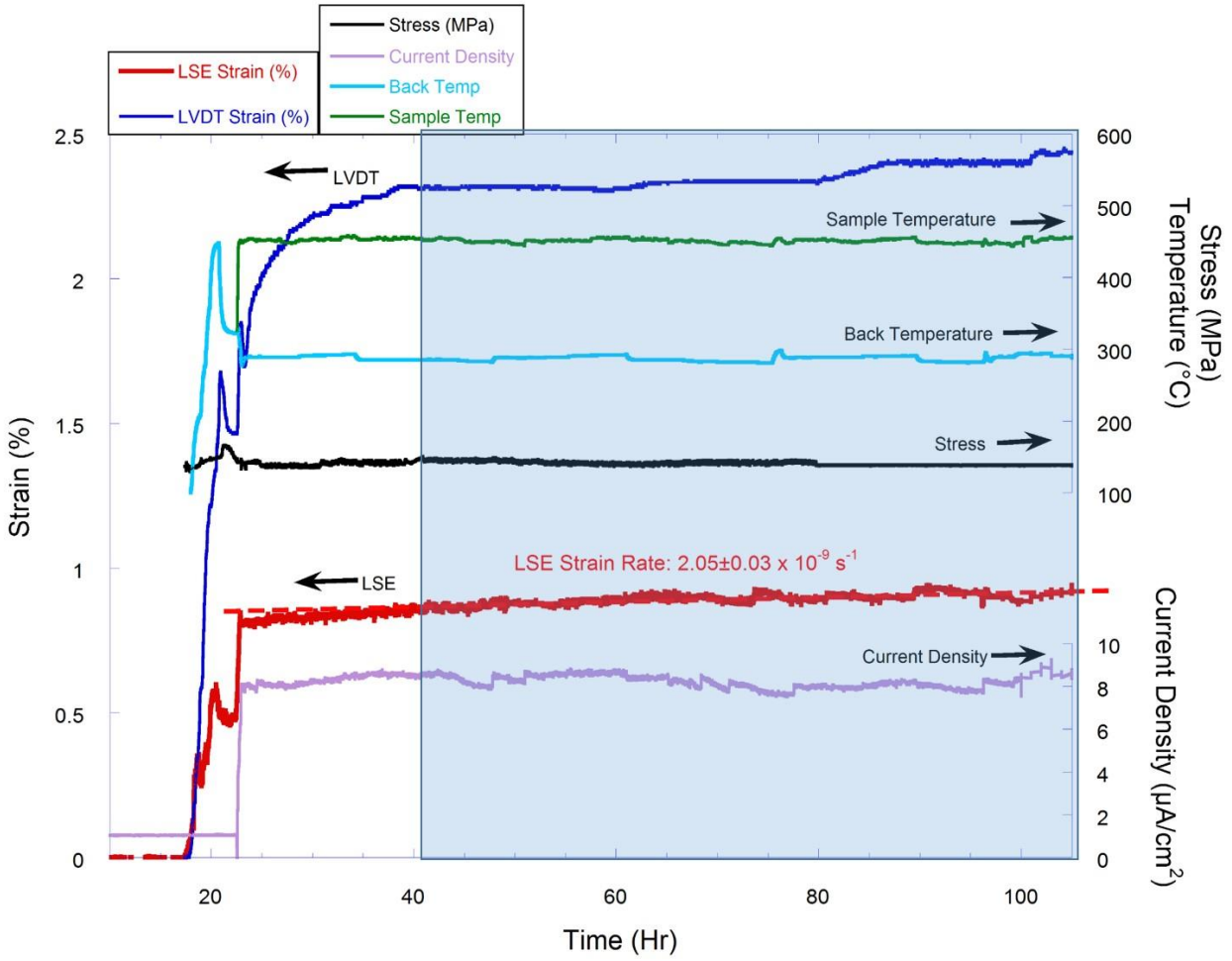

Figure A. 6 Irradiation creep curve of IT450140-A.

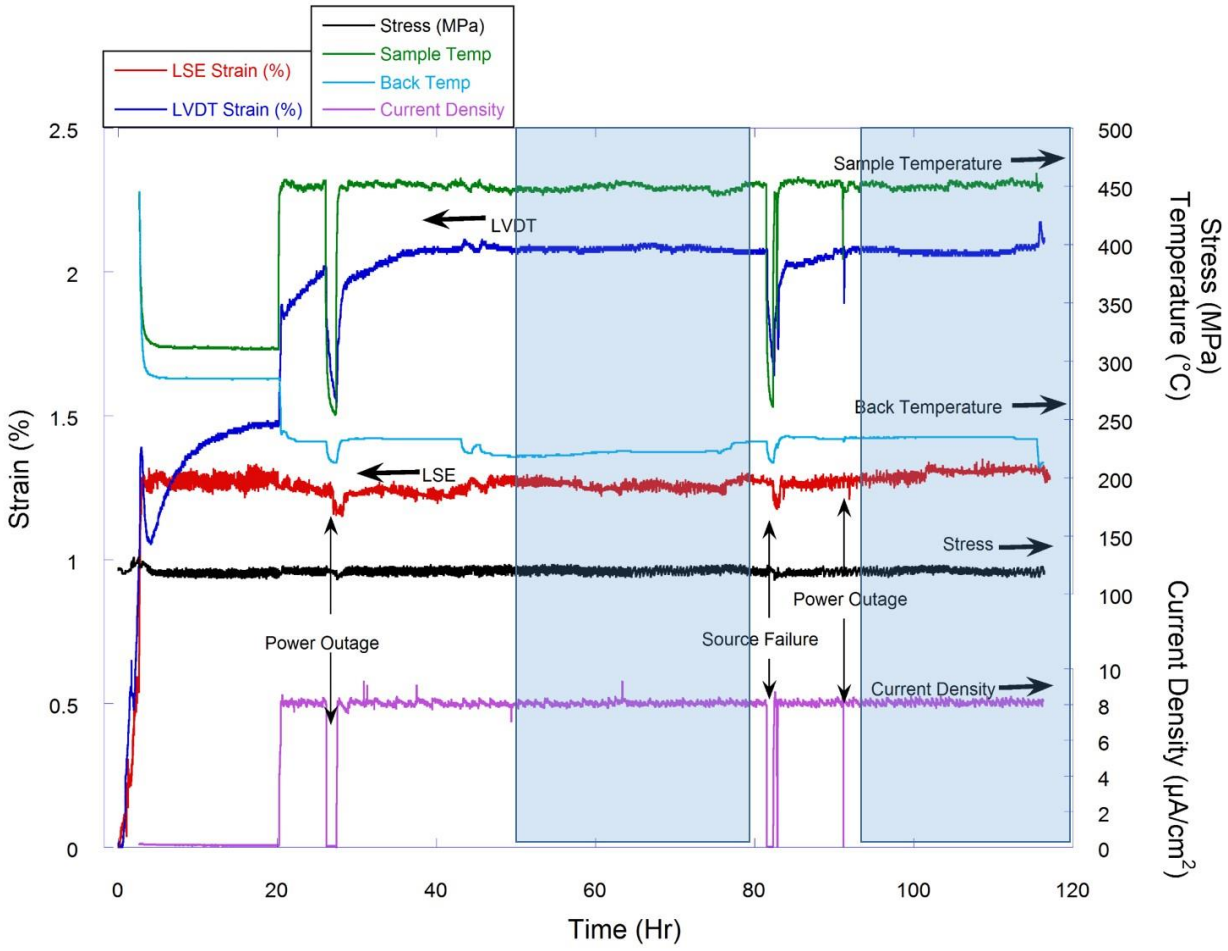

Figure A. 7 Irradiation creep curve of IT450120-A with outage.

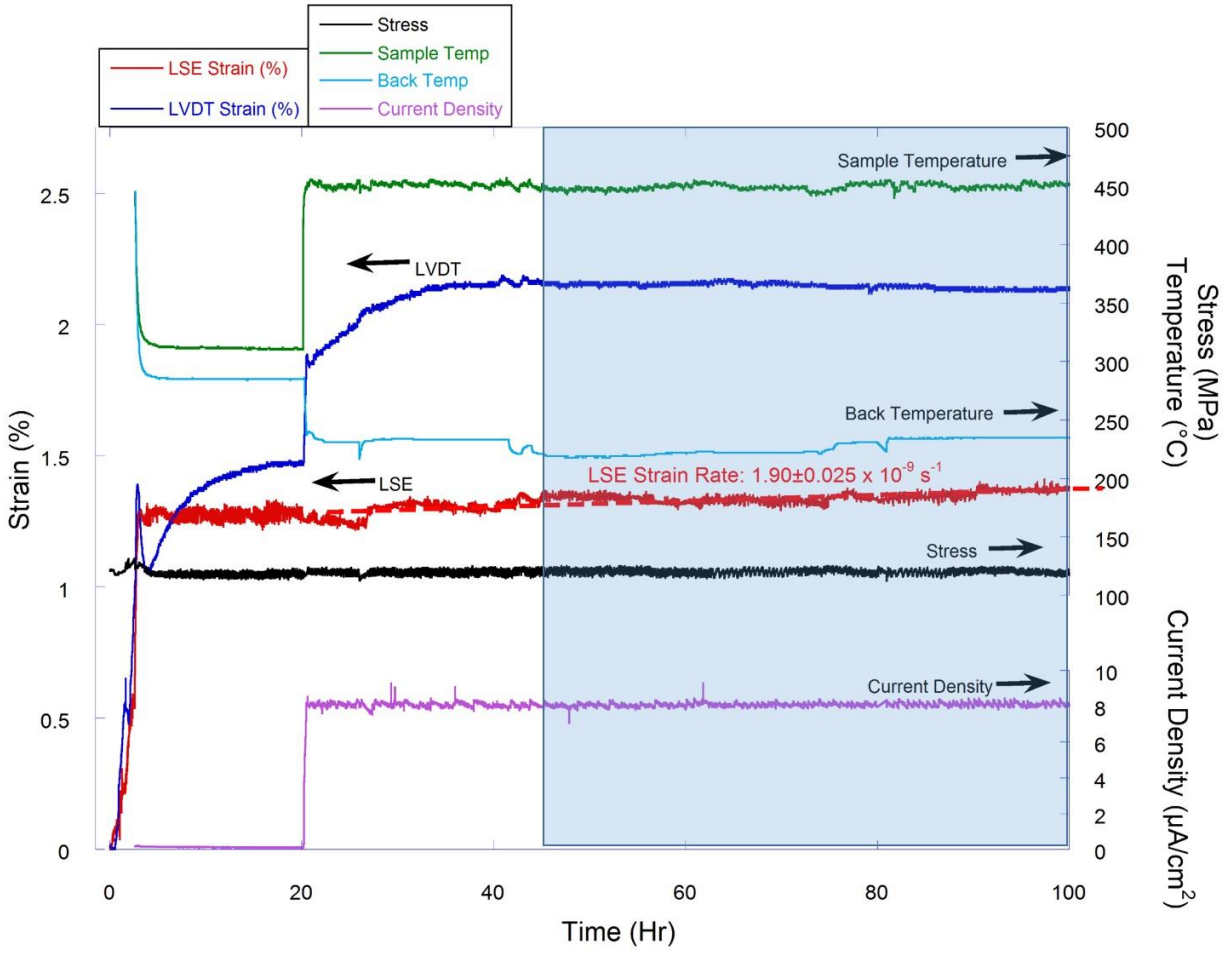

Figure A. 8 Irradiation creep curve of IT450120-A without outage.

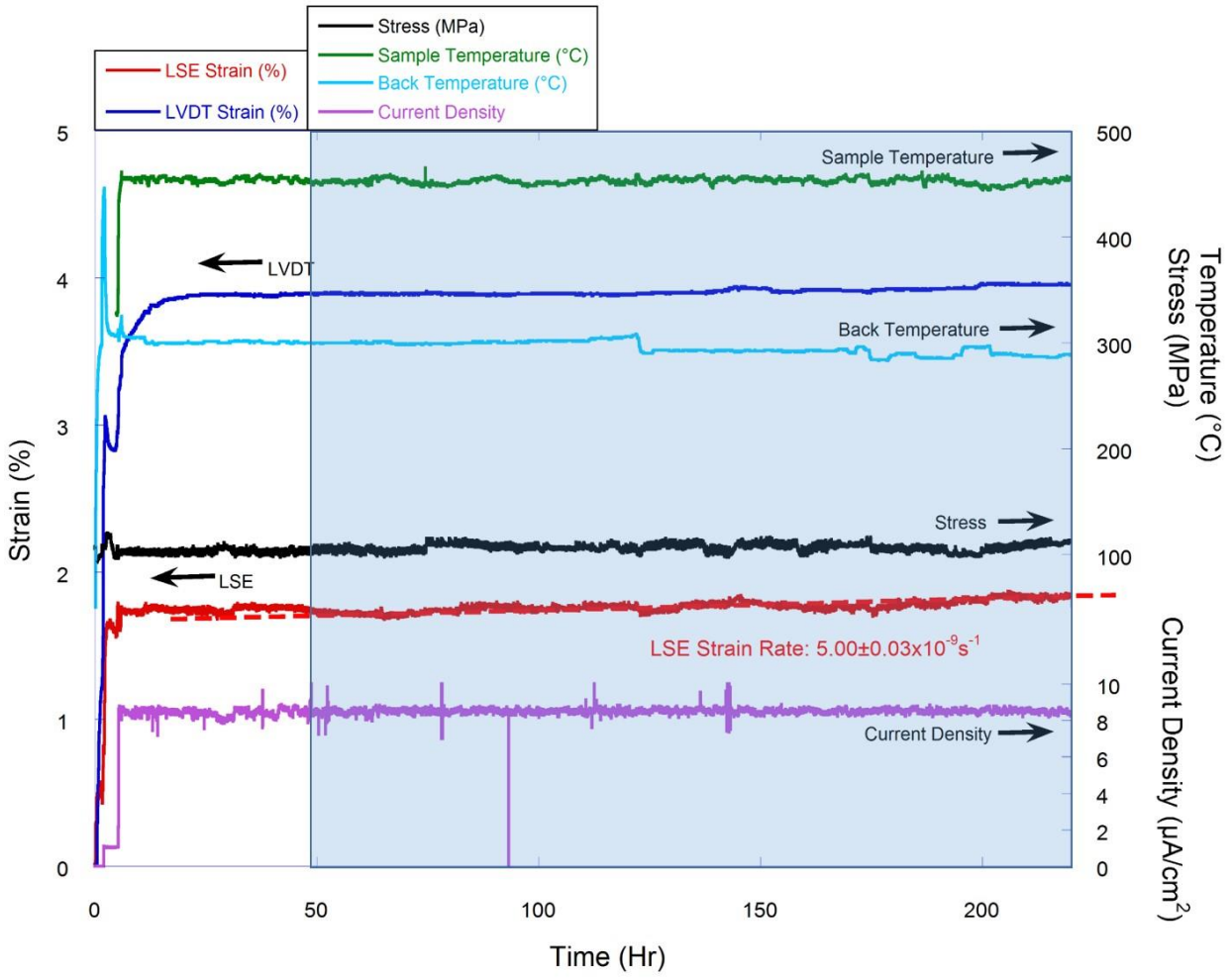

Figure A. 9 Irradiation creep curve of IT450100-A.

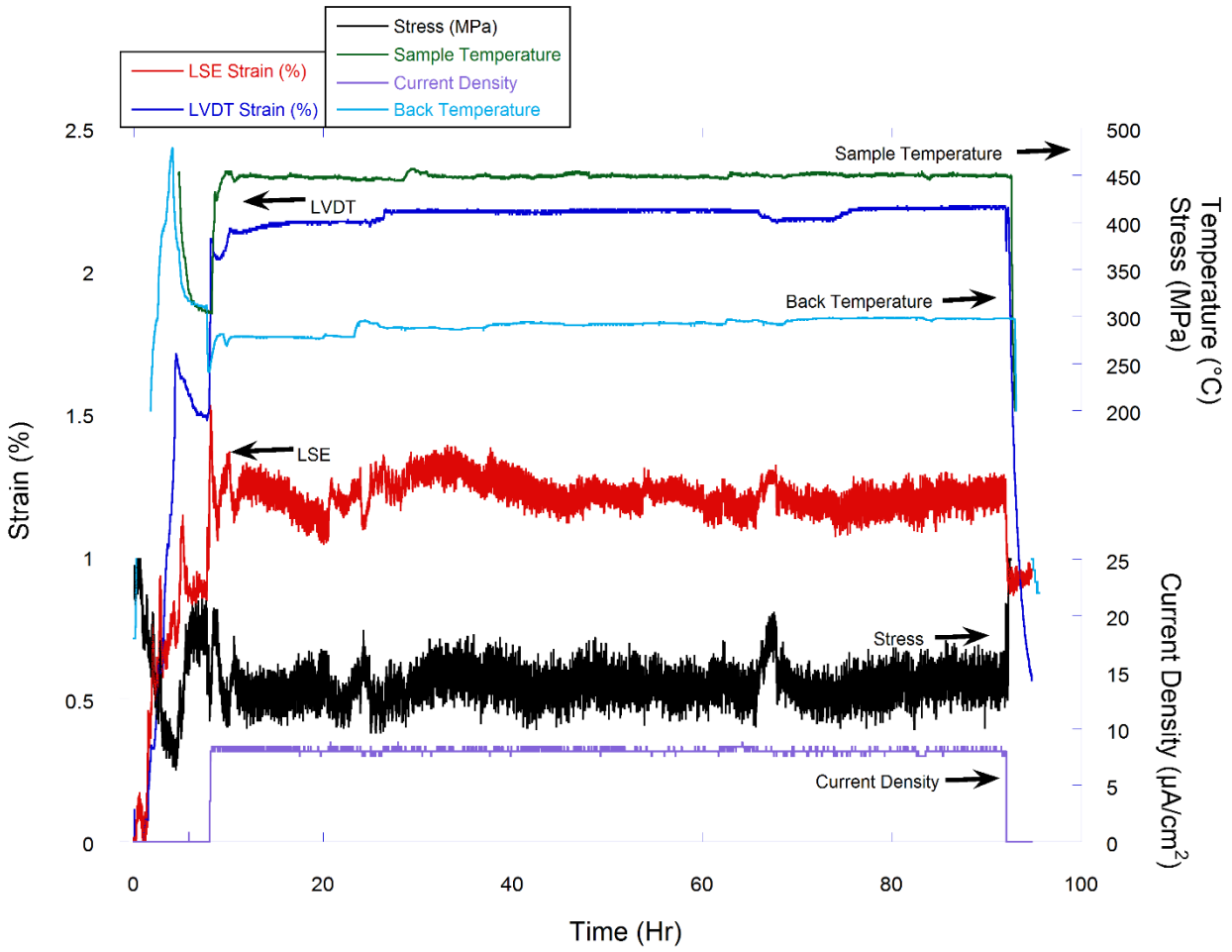

Figure A. 10 Irradiation creep curve of IT450000-A.

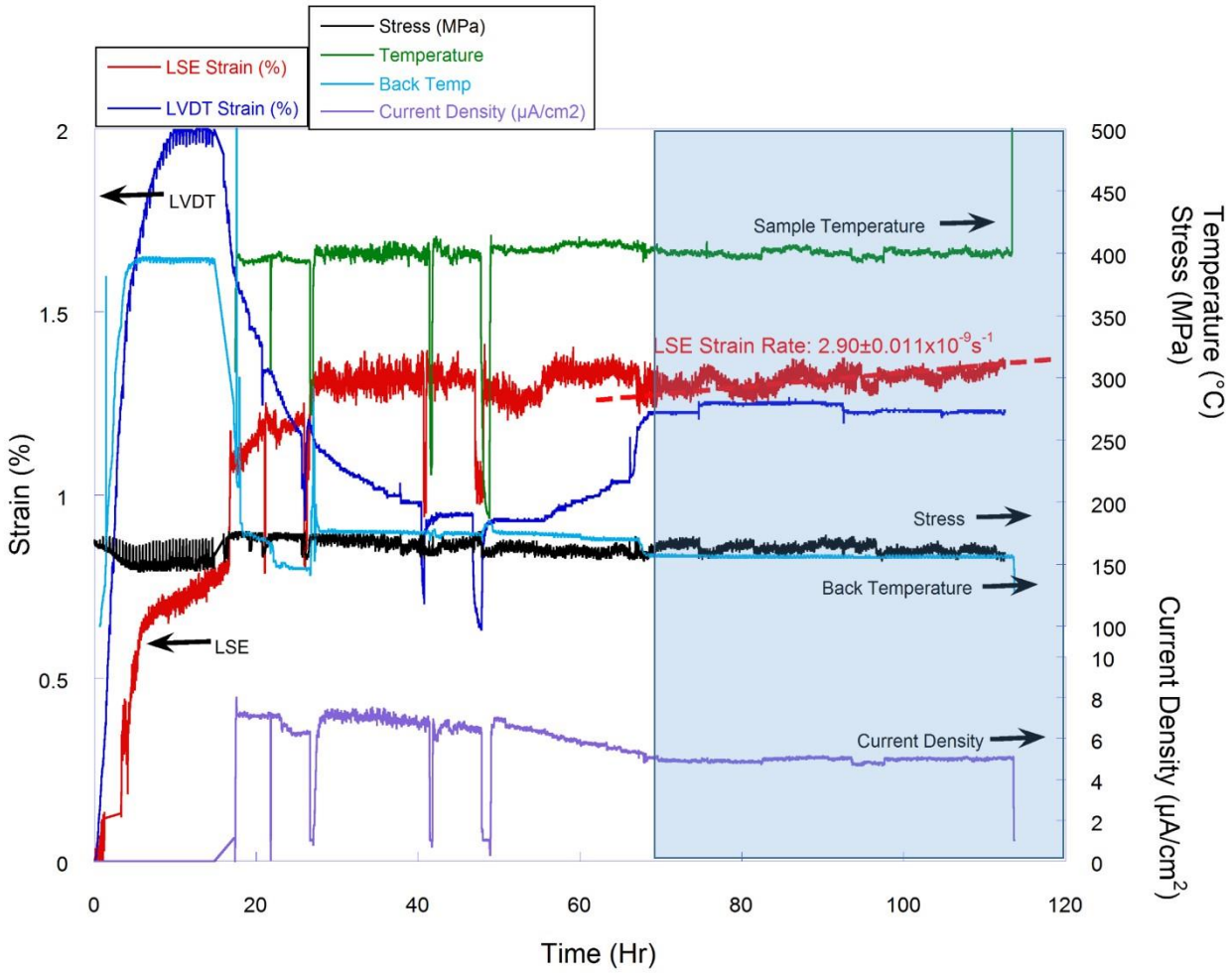

Figure A. 11 Irradiation creep curve of IT400160-A.

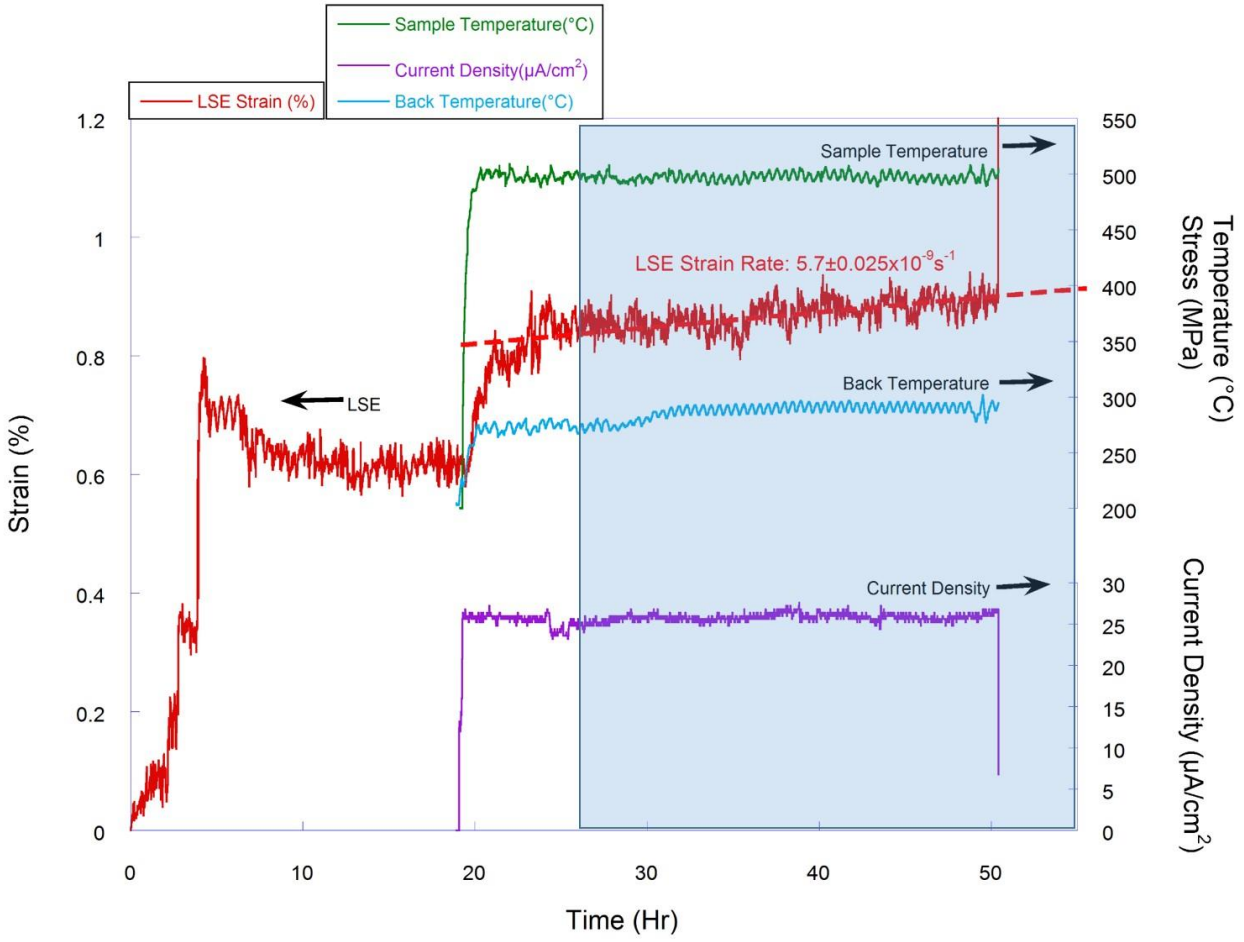

Figure A. 12 Irradiation creep curve of IT500180-A.

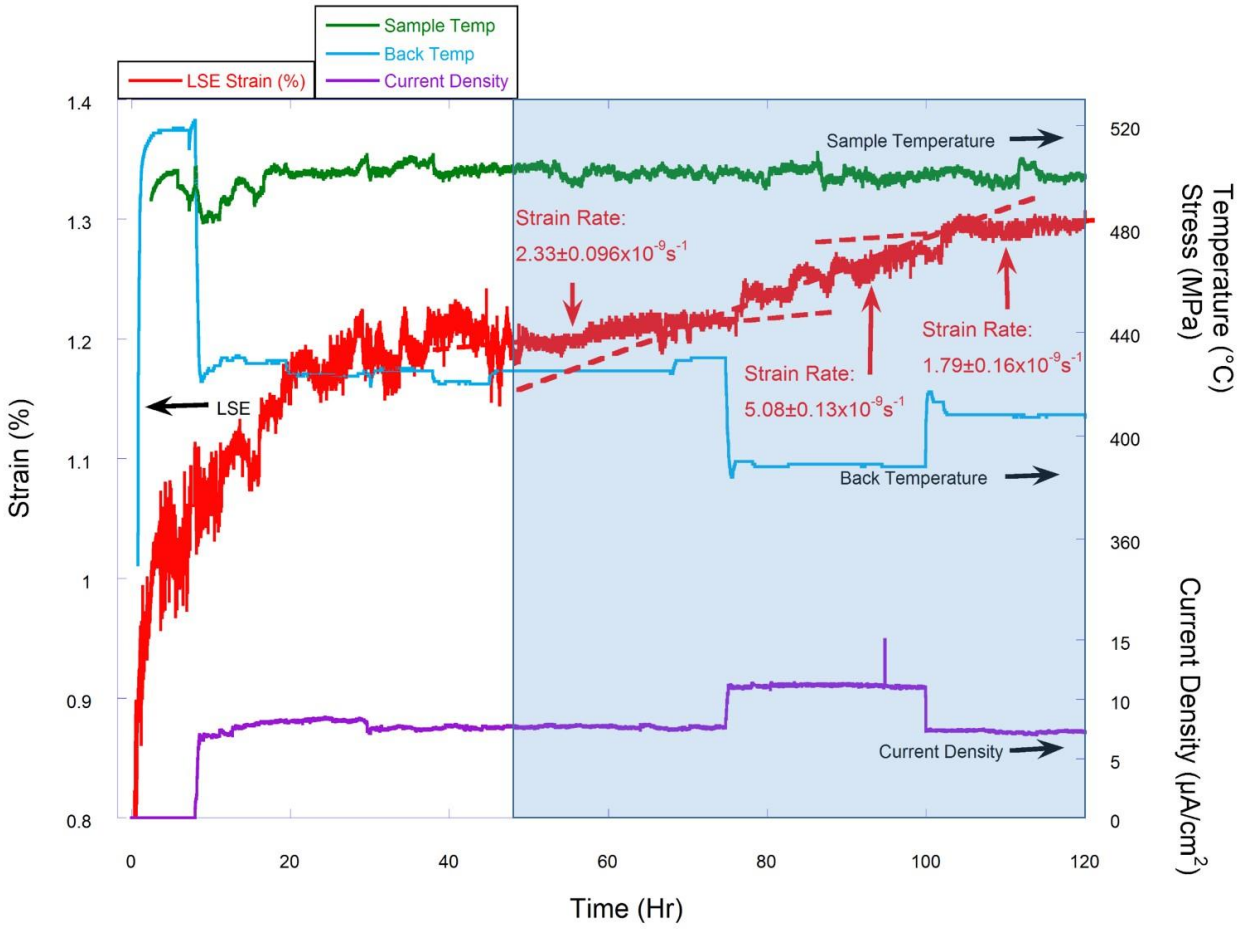

Figure A. 13 Irradiation creep curve of IT500160-A.

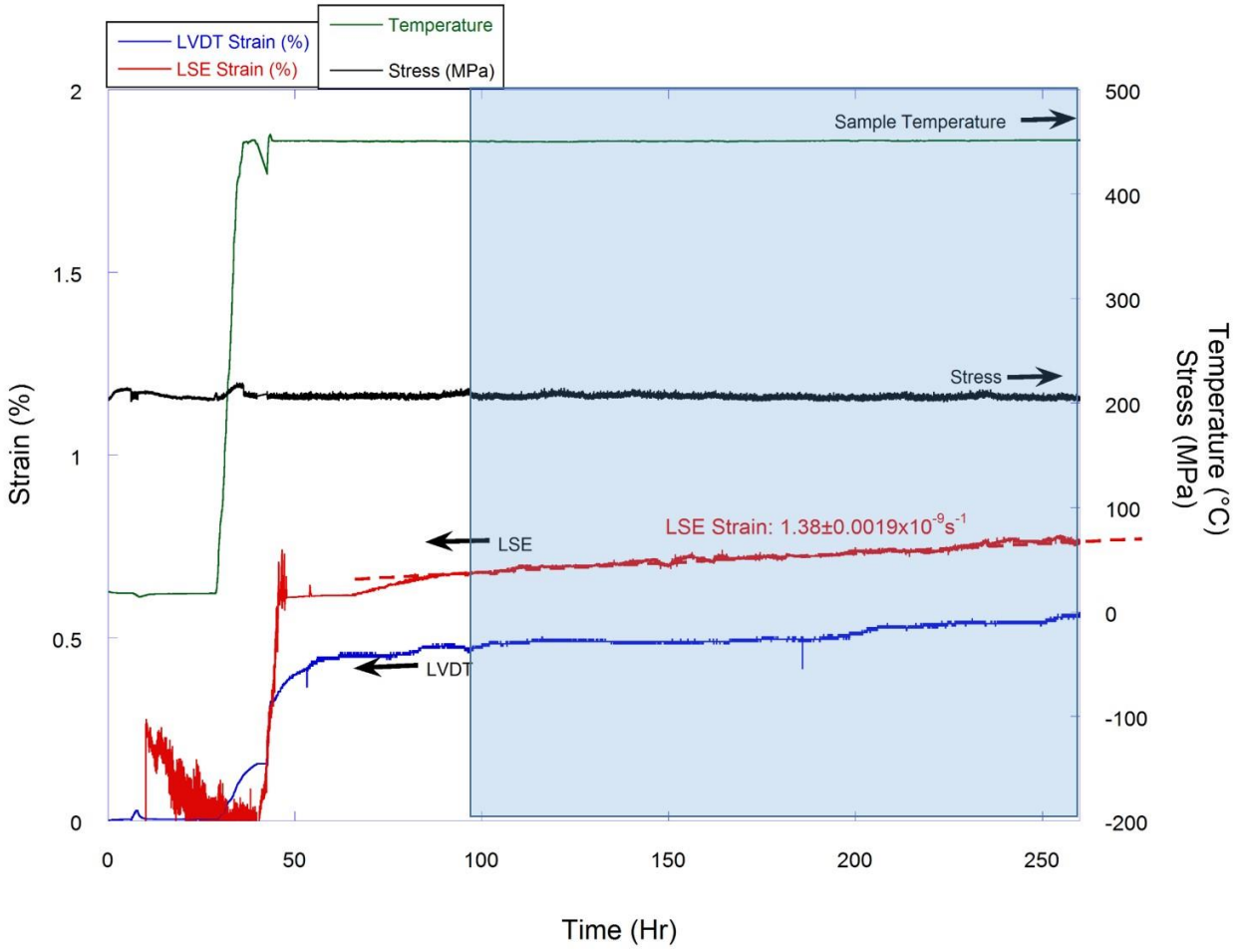

Figure A. 14 Irradiation creep curve of TT450200-A.

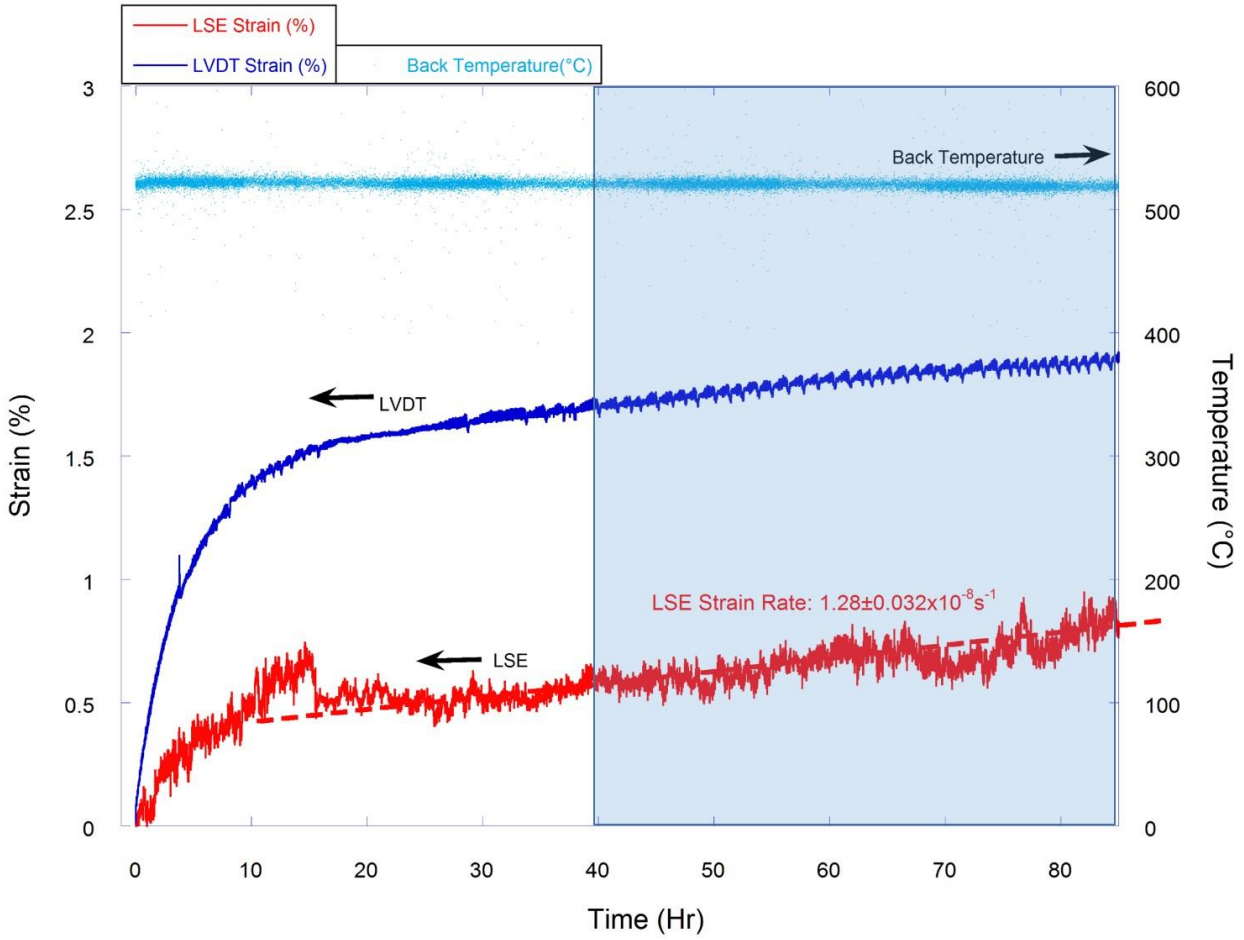

Figure A. 15 Irradiation creep curve of TT500200-A.

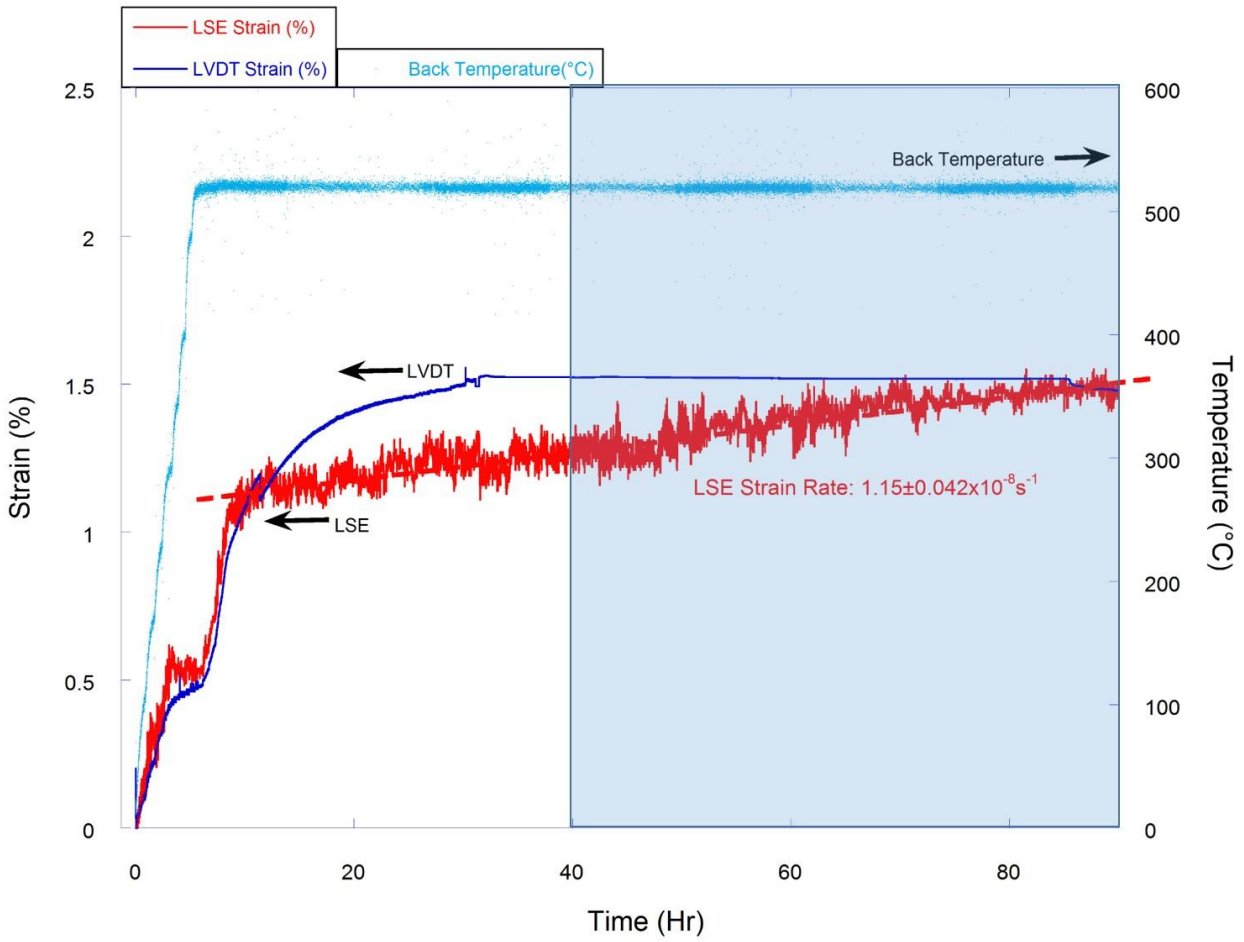

Figure A. 16 Irradiation creep curve of TT500200-B.

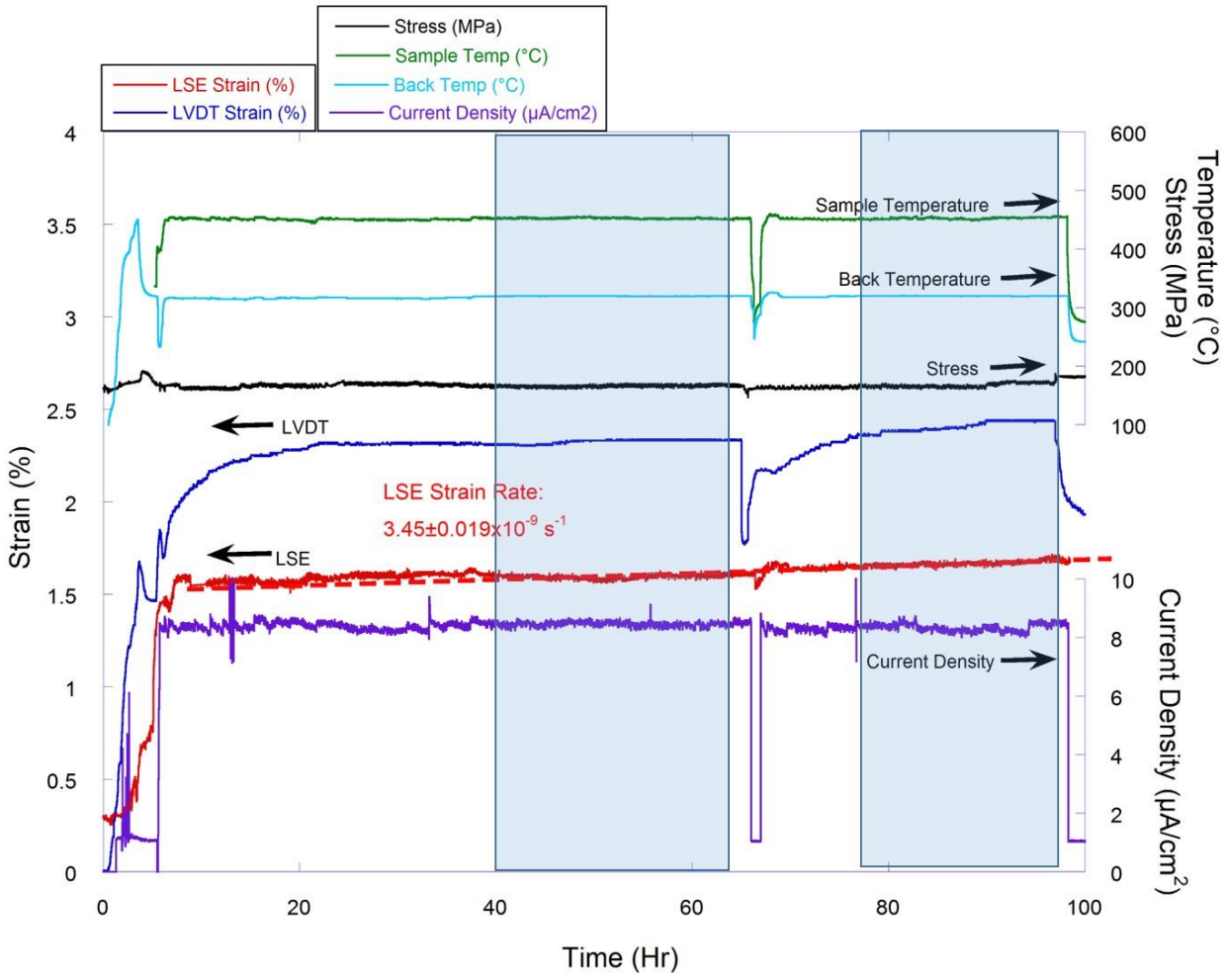

Figure A. 17 Irradiation creep curve of IH450160-A.

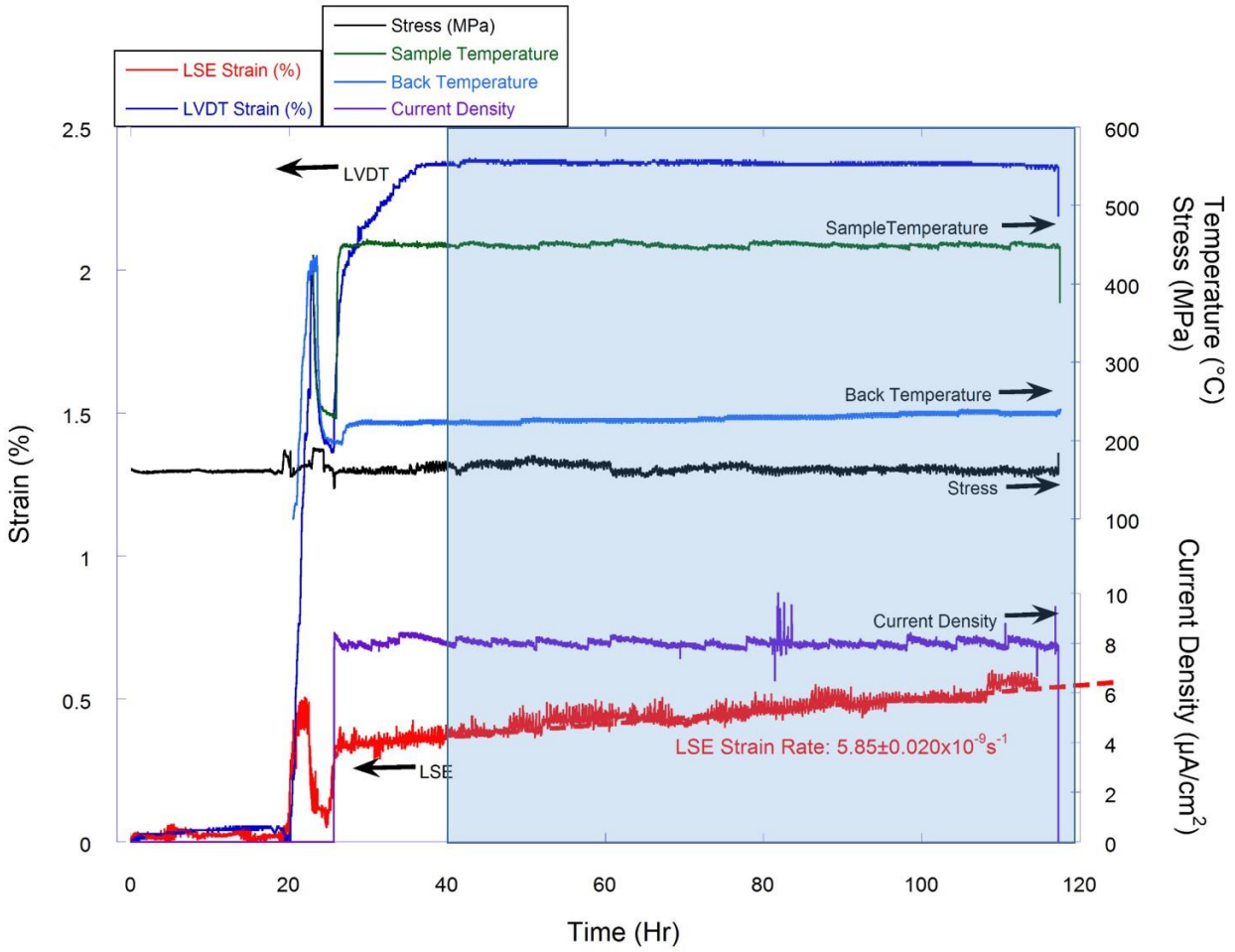

Figure A. 18 Irradiation creep curve of IA450160-A.

Appendix B: Dislocation Loop TEM Image

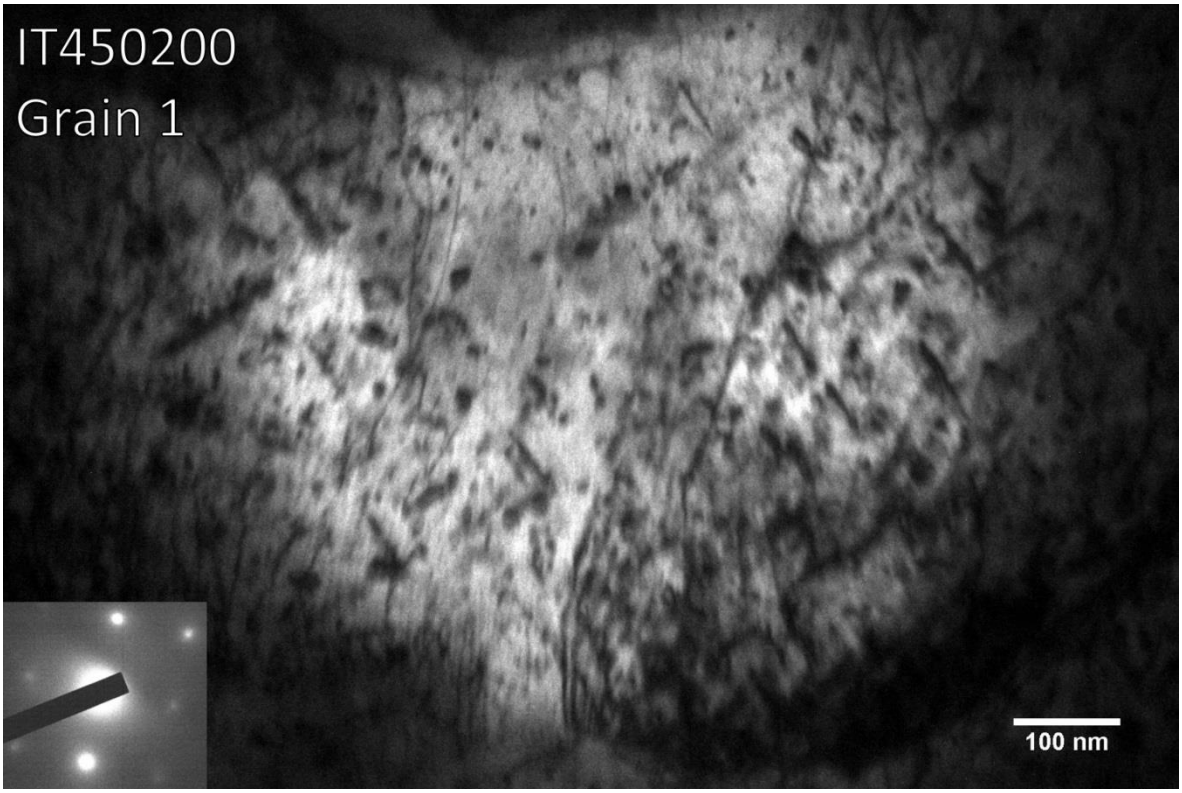
IT450200
Grain 1
100 nm

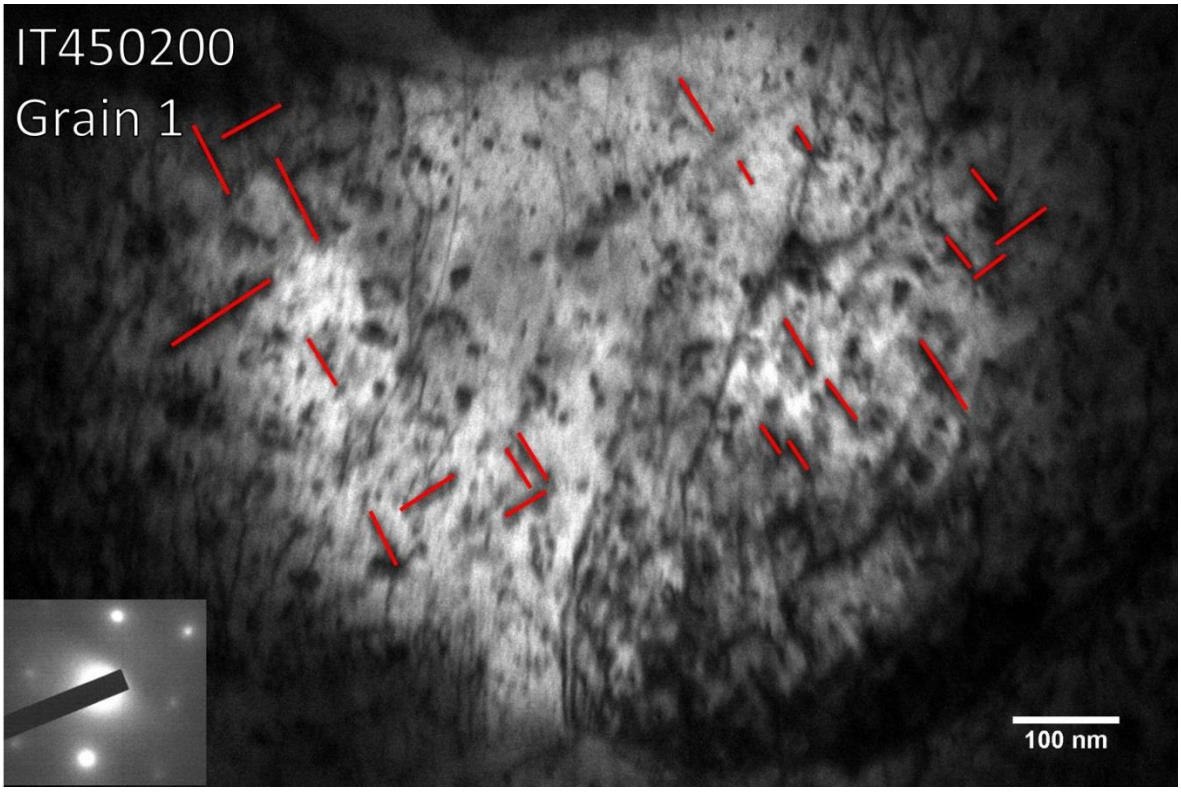
IT450200
Grain 1
100 nm

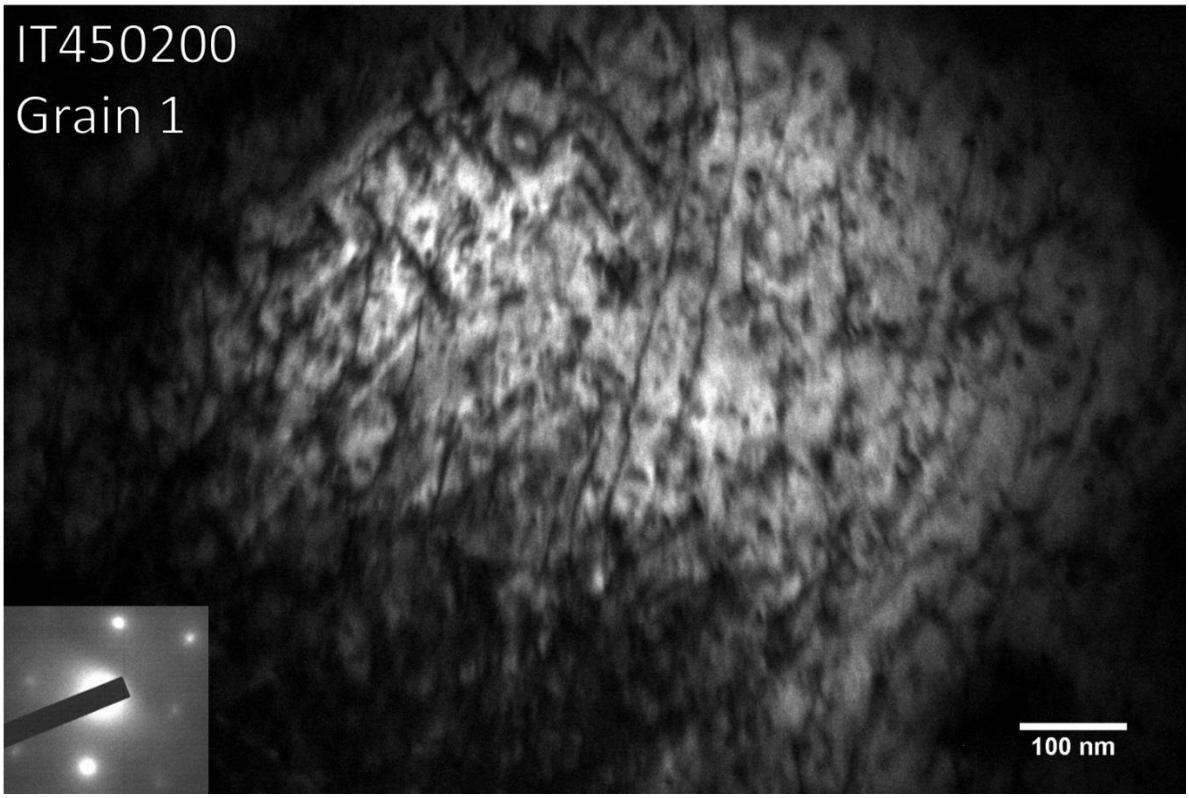
IT450200
Grain 1
100 nm

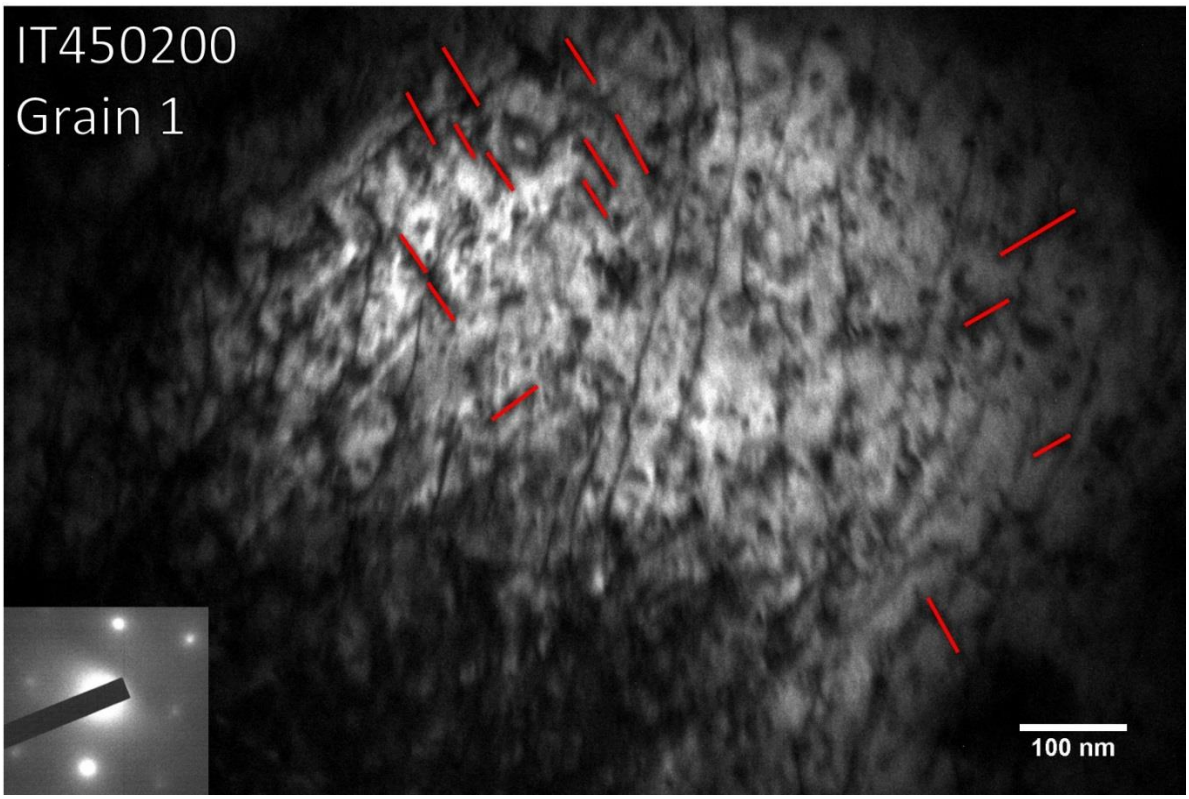
IT450200
Grain 1
100 nm

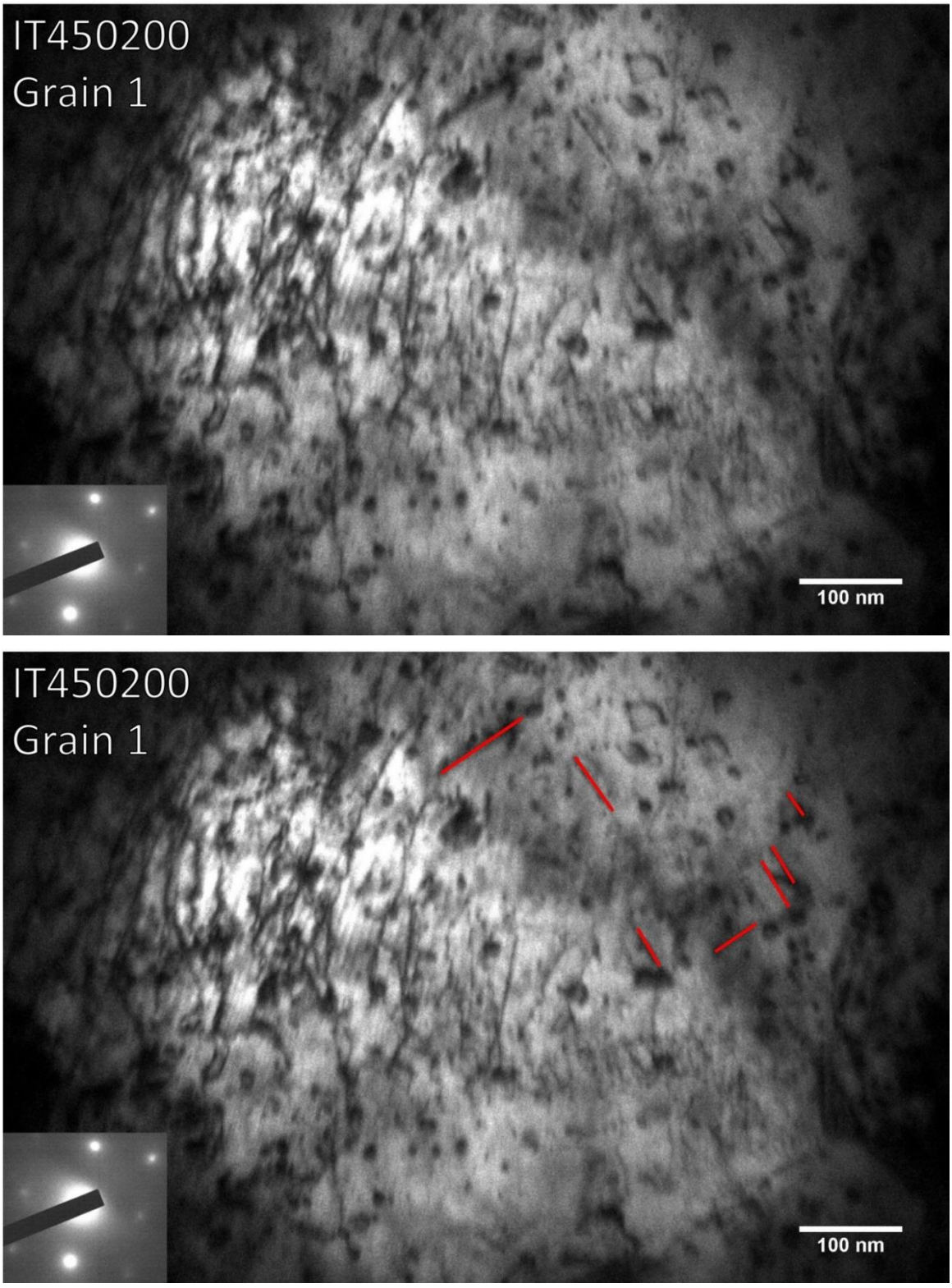

Figure B.1. 1 TEM image of grain #1 from irradiation creep sample IT450200, a_o<100> type edge on dislocation loops are highlighted in red.

Table B.1. 1 Results from dislocation loop analysis on grain #1 from irradiation creep sample IT450200.

Xtilt (θ_x)	Ytilt (θ_y)	TV Ztilt (θ_T)	LV Ztilt ($\theta_{<100>}$)			
13.9	3.9	-23.7	32.34			
Loop Normal angle to Tensile Axis	Number Density	Number Density Error	Size	Size Error	Fraction of Loops	Error in Fraction of loops
($\theta_{<100>}$)=30	32	5.656854	28.95833	3.186195	0.744186047	0.131555
($\theta_{<010>}$)=60	11	3.316625	35.08333	8.690665	0.255813953	0.077131

Orientation	Size (nm)	Actual Size (nm)	Orientation	Size (nm)	Actual Size (nm)	Scale Bar Ratio	Area (m^2)	Loop Density (1/m^3)
30	43	43	60	33	33	1	2.61E-20	1.65E+21
30	51	51	60	62	62			
30	32	32	60	33	33			
30	35	35	60	23	23			
30	26	26	60	20	20			
30	30	30	60	31	31			
30	35	35	60	29	29			
30	16	16	60	26	26			
30	16	16	60	46	46			
30	25	25	60	22	22			
30	22	22	60	64	64			
30	30	30	60	32	32			
30	46	46						
30	28	28						
30	19	19						
30	20	20						
30	32	32						
30	36	36						
30	27	27						
30	19	19						
30	23	23						
30	21	21						
30	28	28						
30	35	35						
30	24	24						
30	22	22						

30	33	33						
30	44	44						
30	30	30						
30	35	35						
30	28	28						
30	16	16						

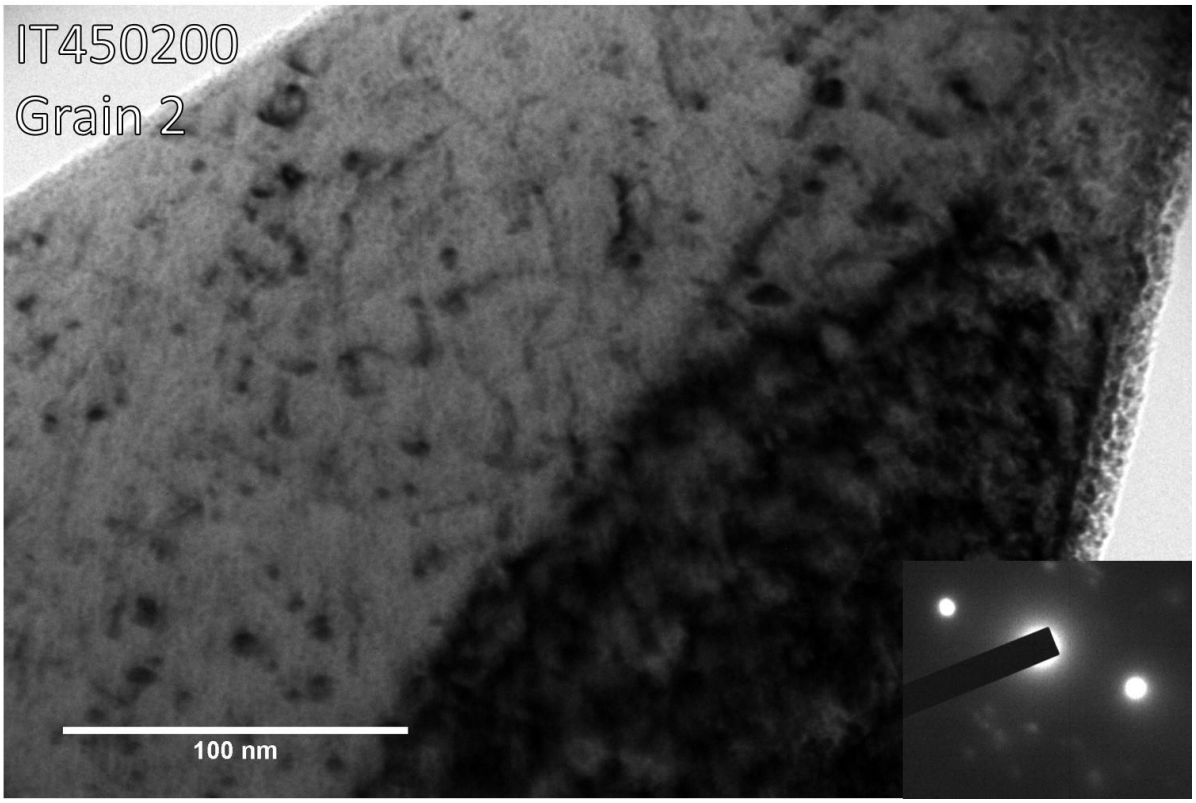
IT450200
Grain 2
100 nm

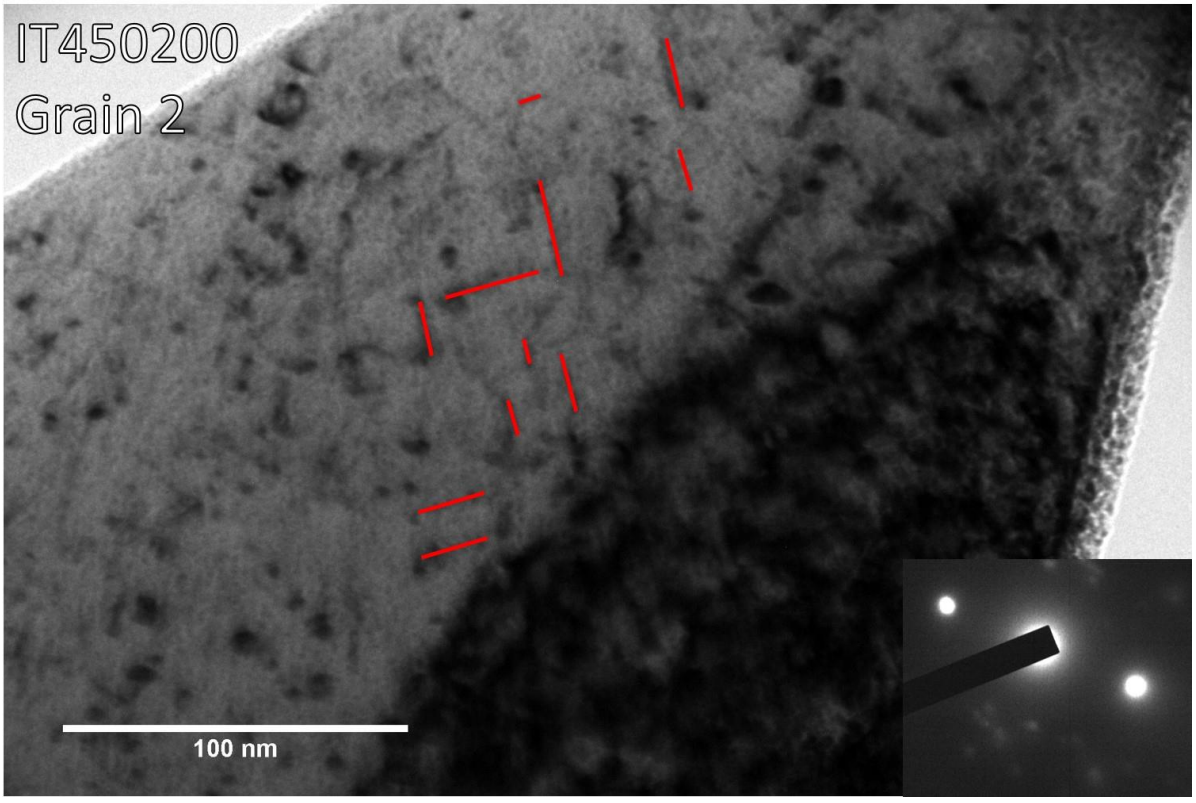
IT450200
Grain 2
100 nm

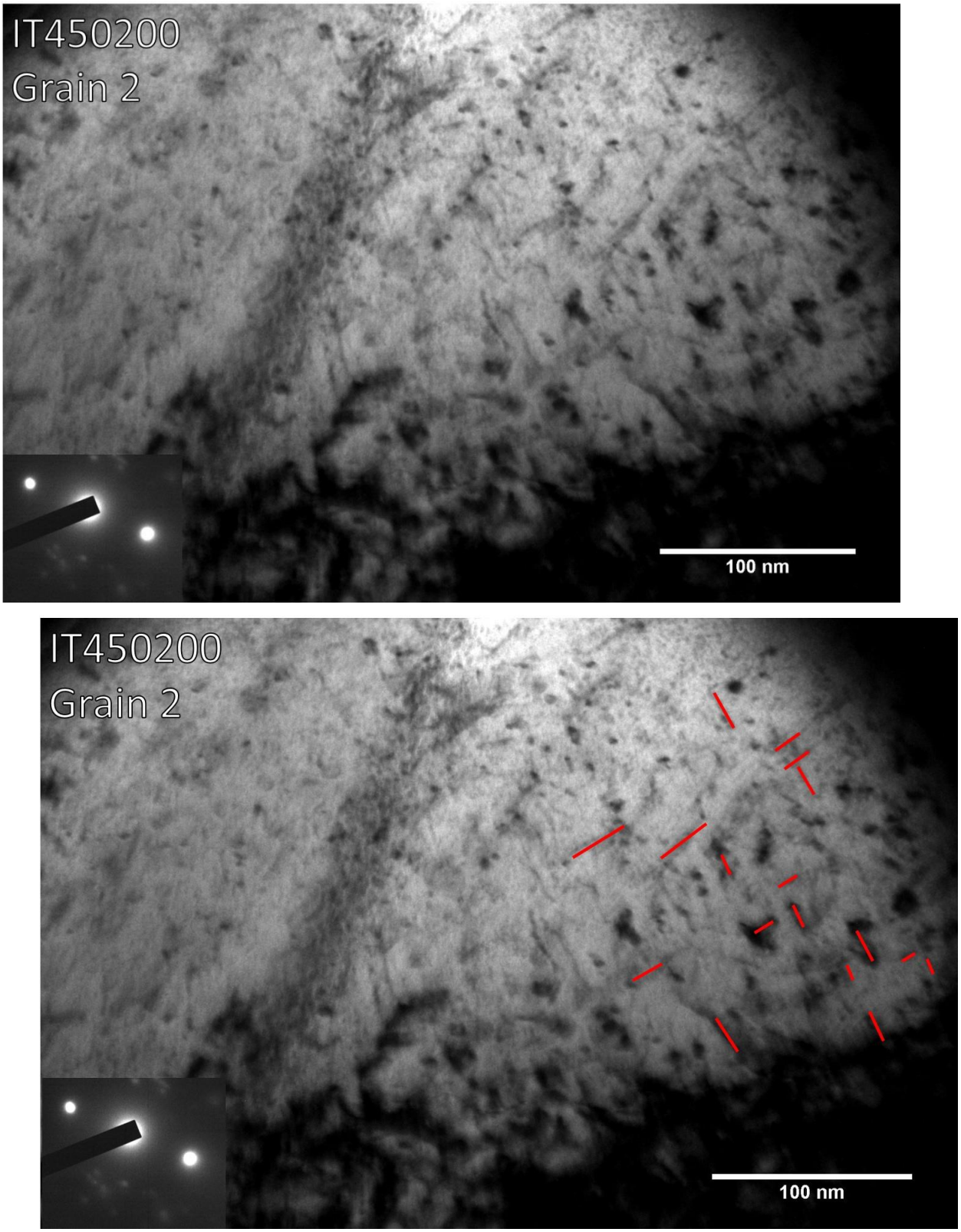

Figure B.1. 2 TEM image of grain #2 from irradiation creep sample IT450200, a_o<100> type edge on dislocation loops are highlighted in red.

Table B.1. 2 Results from dislocation loop analysis on grain #2 from irradiation creep sample IT450200.

Xtilt (θ_x)	Ytilt (θ_y)	TV Ztilt (θ_T)	LV Ztilt ($\theta_{<100>}$)			
15.8	-23.1	-23.7	22.2			
Loop Normal angle to Tensile Axis	Number Density	Number Density Error	Size	Size Error	Fraction of Loops	Error in Fraction of loops
($\theta_{<100>}$)=44	15	3.872983	21.8	4.854805	0.535714286	0.138321
($\theta_{<010>}$)=46	13	3.605551	20.80769	4.342529	0.464285714	0.12877

Orientation	Size (nm)	Actual Size (nm)	Orientation	Size (nm)	Actual Size (nm)	Scale Bar Ratio	Area (m^2)	Loop Density (1/m^3)
44	38	38	46	26	26	1	7.83E-20	3.57E+20
44	38	38	46	21	21			
44	18	18	46	15	15			
44	18	18	46	18	18			
44	22	22	46	27	27			
44	15	15	46	10	10			
44	12	12	46	25	25			
44	10	10	46	11	11			
44	24	24	46	22	22			
44	14	14	46	25	25			
44	12	12	46	26	26			
44	25	25	46	36	36			
44	37	37	46	8.5	8.5			
44	27	27						
44	17	17						

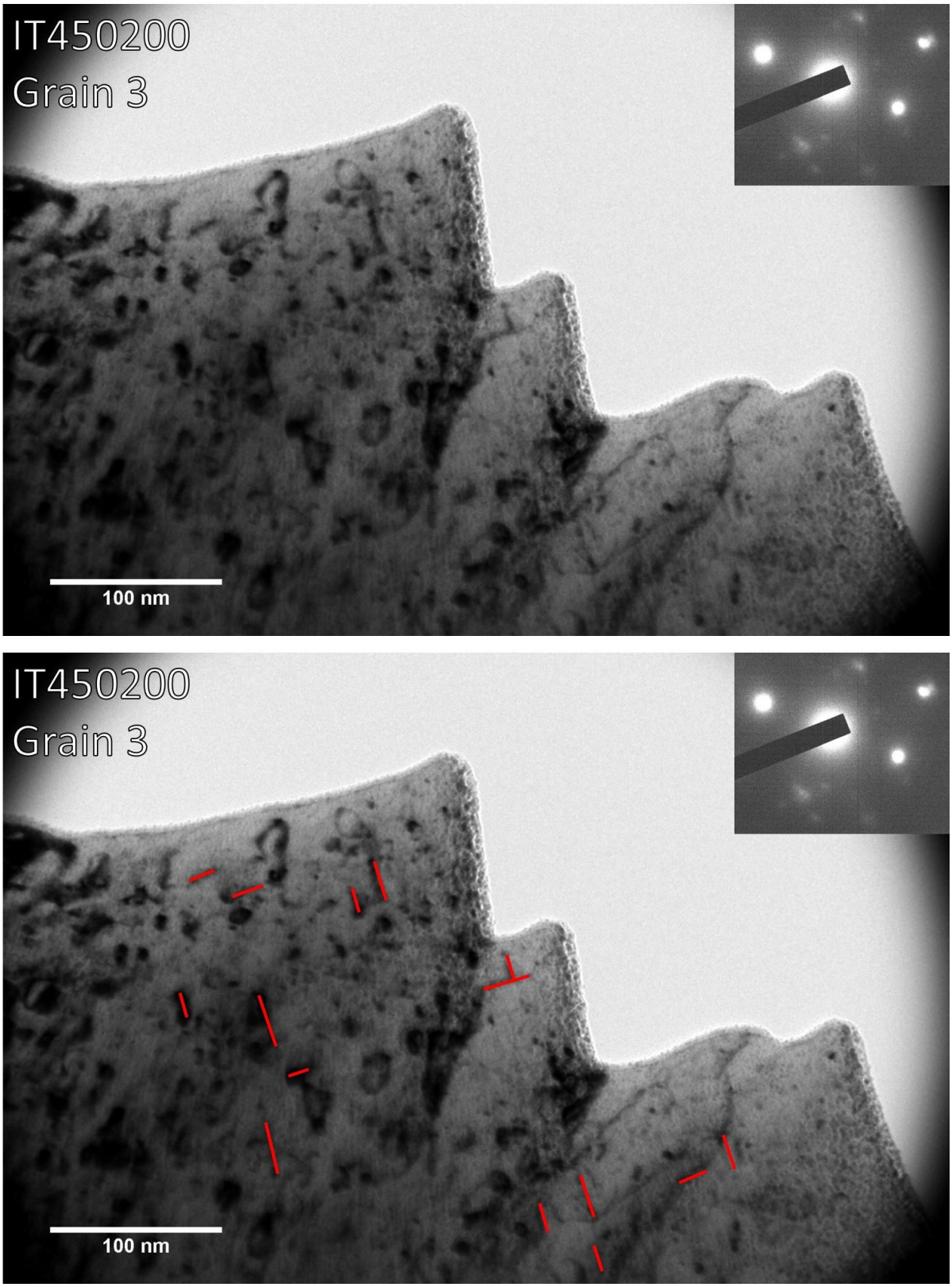

Figure B.1. 3 TEM image of grain #3 from irradiation creep sample IT450200, a_o<100> type edge on dislocation loops are highlighted in red.

Table B.1. 3 Results from dislocation loop analysis on grain #3 from irradiation creep sample IT450200.

Xtilt (θ_x)	Ytilt (θ_y)	TV Ztilt (θ_T)	LV Ztilt ($\theta_{<100>}$)			
18.4	-20.3	-23.7	21			
Loop Normal angle to Tensile Axis	Number Density	Number Density Error	Size	Size Error	Fraction of Loops	Error in Fraction of loops
($\theta_{<100>}$)=35	10	3.162278	23.9	4.769333	0.666667	0.21081851
($\theta_{<010>}$)=55	5	2.236068	20.2	5.727763	0.333333	0.1490712

Orientation	Size (nm)	Actual Size (nm)	Orientation	Size (nm)	Actual Size (nm)	Scale Bar Ratio	Area (m^2)	Loop Density (1/m^3)
35	17	17	55	18	18	1	2.61E-20	5.74E+20
35	36	36	55	21	21			
35	18	18	55	14	14			
35	27	27	55	31	31			
35	15	15	55	17	17			
35	37	37						
35	20	20						
35	27	27						
35	22	22						
35	20	20						

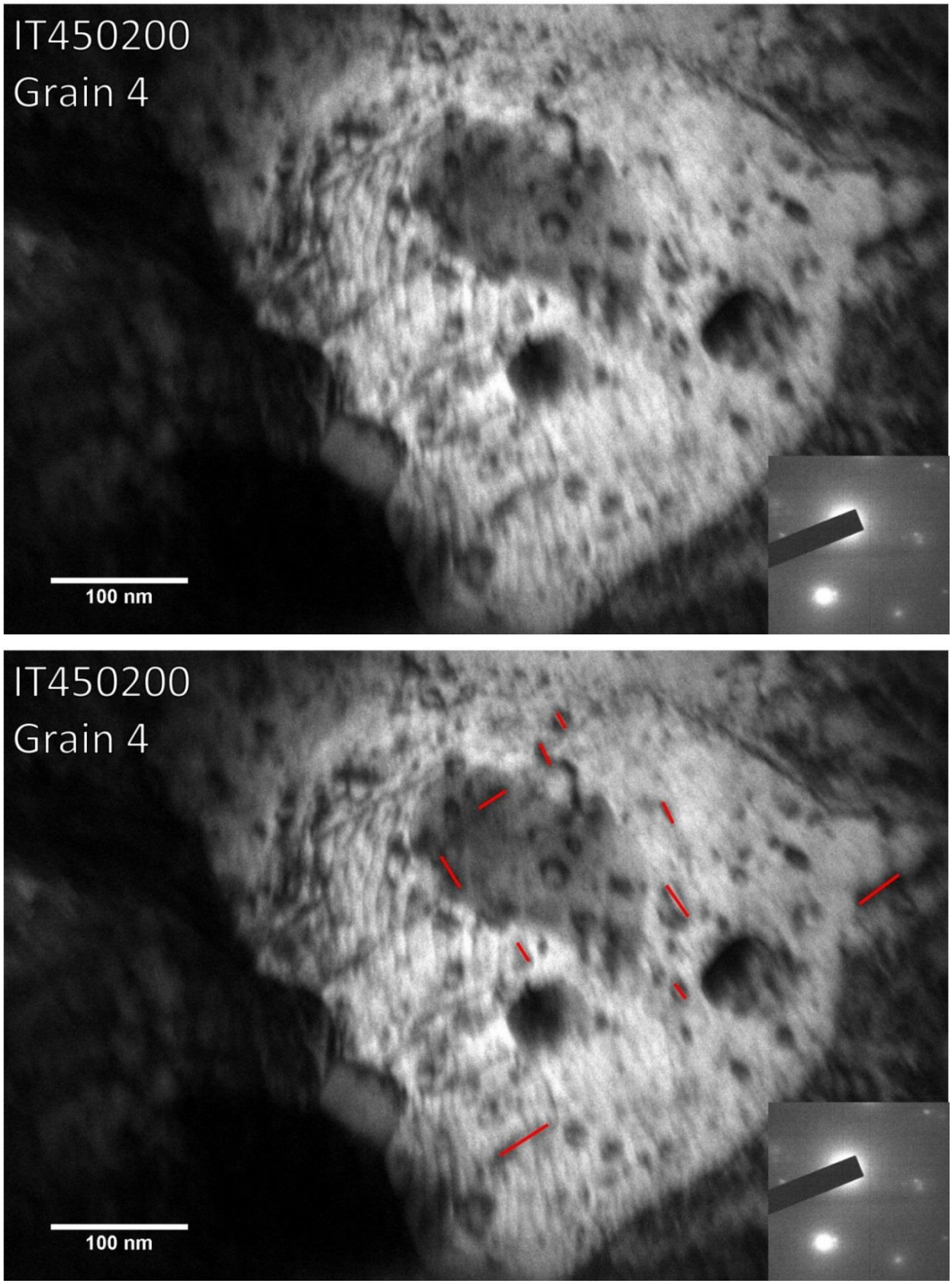

Figure B.1. 4 TEM image of grain #4 from irradiation creep sample IT450200, a_o<100> type edge on dislocation loops are highlighted in red.

Table B.1. 4 Results from dislocation loop analysis on grain #4 from irradiation creep sample IT450200.

Xtilt (θ_x)	Ytilt (θ_y)	TV Ztilt (θ_T)	LV Ztilt ($\theta_{<100>}$)			
-25.1	6.1	-23.7	33.3			
Loop Normal angle to Tensile Axis	Number Density	Number Density Error	Size	Size Error	Fraction of Loops	Error in Fraction of loops
($\theta_{<100>}$)=30	7	2.645751	16.14286	5.05036	0.7	0.264575
($\theta_{<010>}$)=60	3	1.732051	29.66667	8.493333	0.3	0.173205

Orientation	Size (nm)	Actual Size (nm)	Orientation	Size (nm)	Actual Size (nm)	Scale Bar Ratio	Area (m^2)	Loop Density (1/m^3)
30	26	26	60	21	21	1	2.61E-20	3.83E+20
30	14	14	60	34	34			
30	11	11	60	34	34			
30	13	13						
30	12	12						
30	11	11						
30	26	26						

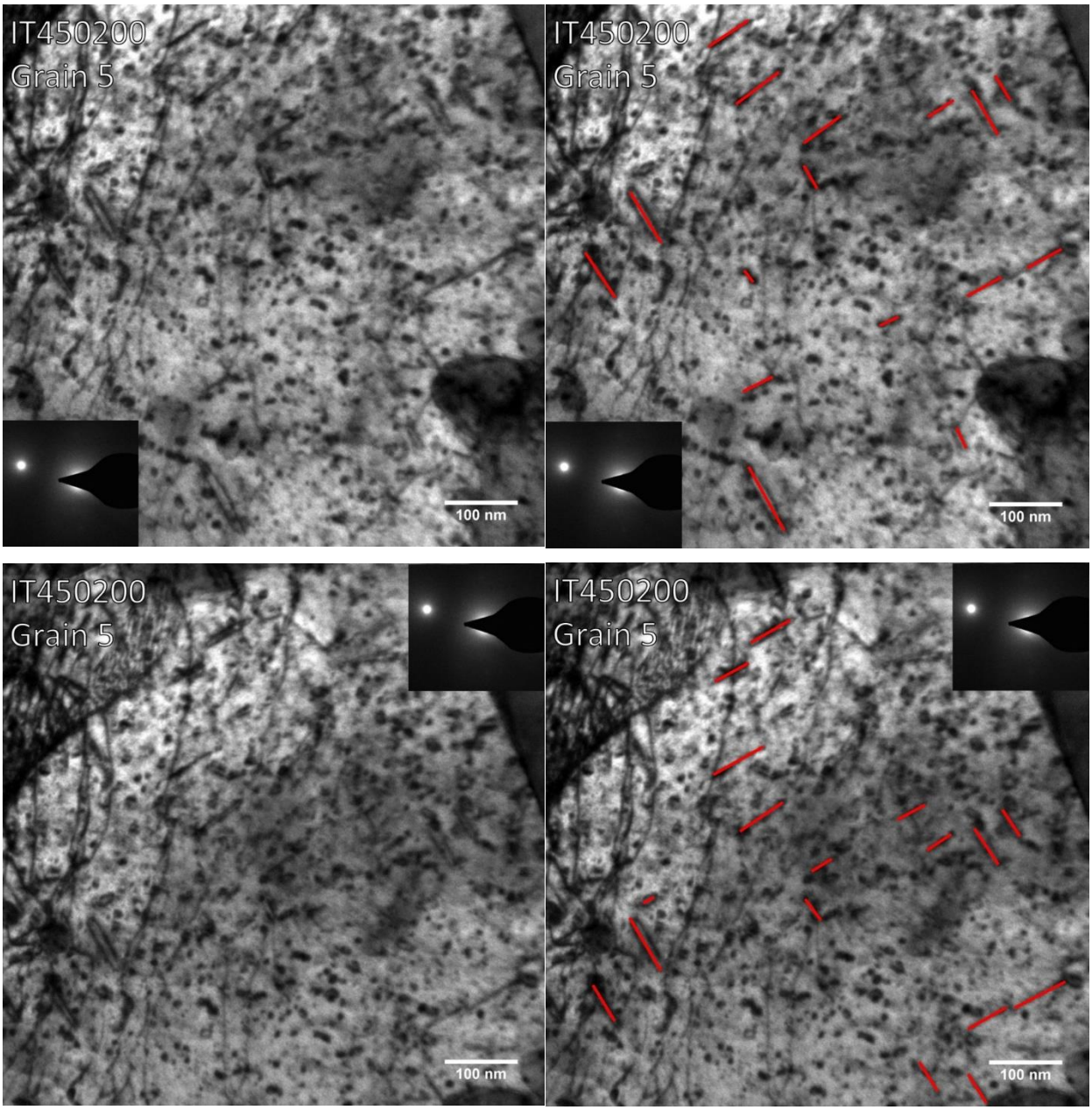
IT450200
Grain 5
100 nm
IT450200
Grain 5
100 nm
IT450200
Grain 5
100 nm
IT450200
Grain 5
100 nm

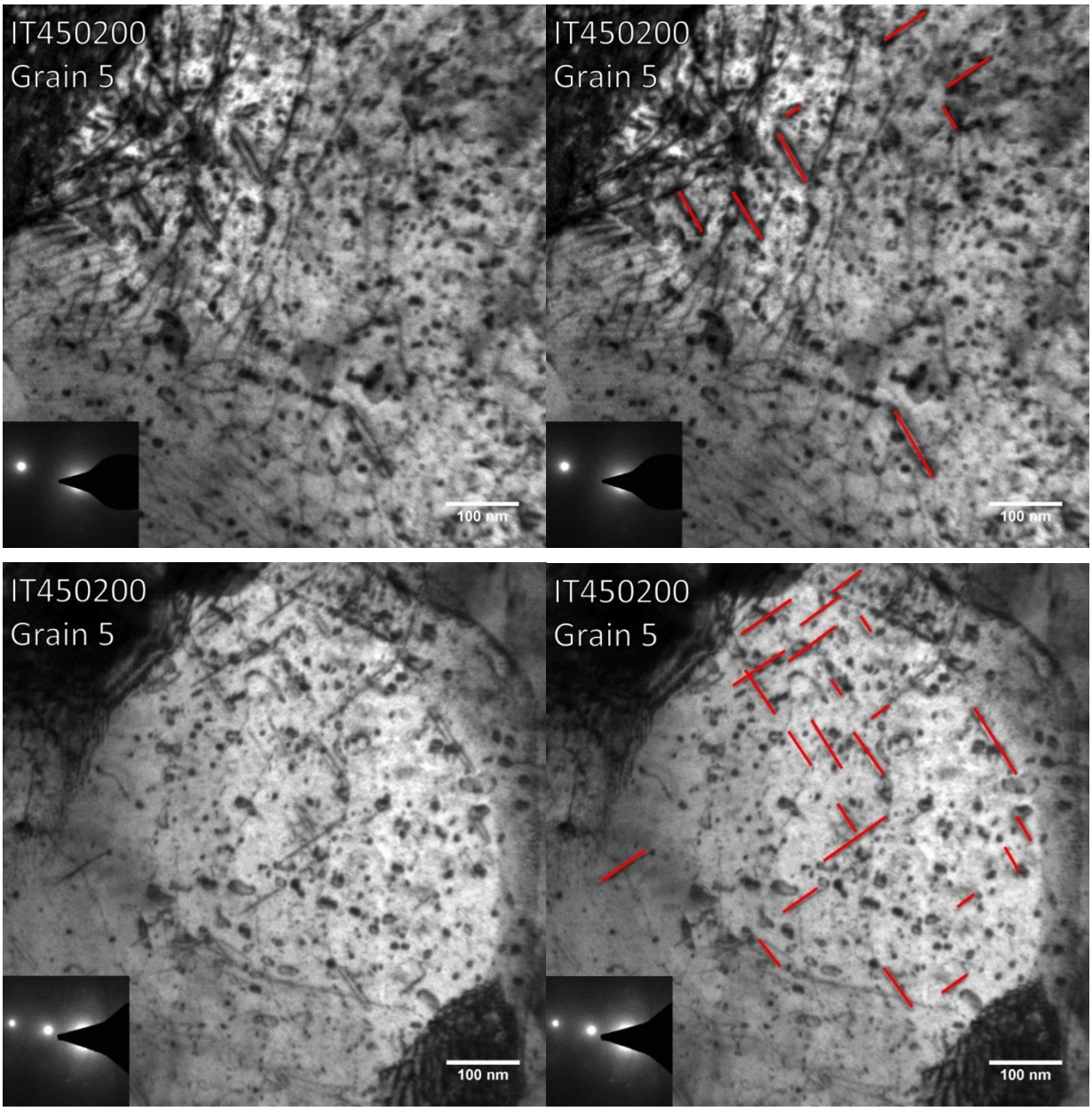

Figure B.1. 5 TEM image of grain #5 from irradiation creep sample IT450200, a_o<100> type edge on dislocation loops are highlighted in red.

Table B.1. 5 Results from dislocation loop analysis on grain #5 from irradiation creep sample IT450200.

Xtilt (θ_x)	Ytilt (θ_y)	TV Ztilt (θ_T)	LV Ztilt ($\theta_{<100>}$)			
-5.92	-4.56	-5	35.9			
Loop Normal angle to Tensile Axis	Number Density	Number Density Error	Size	Size Error	Fraction of Loops	Error in Fraction of loops
($\theta_{<100>}$)=42	31	5.567764	59.39785	12.36774	0.492063	0.088377
($\theta_{<010>}$)=48	32	5.656854	54.6875	9.663448	0.507937	0.089791

Orientation	Size (nm)	Actual Size (nm)	Orientation	Size (nm)	Actual Size (nm)	Scale Bar Ratio	Area (m^2)	Loop Density (1/m^3)
42	110	73.33	48	98	65.33	0.67	2.61E-20	2.41+21
42	121	80.66	48	110	73.33			
42	28	18.66	48	92	61.33			
42	55	36.66	48	54	36			
42	105	70	48	67	44.66			
42	158	105.33	48	39	26			
42	53	35.33	48	82	54.66			
42	86	57.33	48	79	52.66			
42	127	84.66	48	26	17.33			
42	57	38	48	86	57.33			
42	88	58.66	48	78	52			
42	68	45.33	48	118	78.66			
42	76	50.66	48	99	66			
42	75	50	48	58	38.66			
42	98	65.33	48	49	32.66			
42	111	74	48	58	38.66			
42	114	76	48	81	54			
42	55	36.66	48	117	78			
42	160	106.66	48	36	24			
42	109	72.66	48	104	69.33			
42	41	27.33	48	100	66.66			
42	36	24	48	106	70.66			
42	123	82	48	119	79.33			
42	106	70.66	48	120	80			
42	71	47.33	48	97	64.66			
42	159	106	48	117	78			

42	60	40	48	61	40.66			
42	60	40	48	31	20.66			
42	103	68.66	48	161	107.33			
42	71	47.33	48	77	51.33			
42	78	52	48	44	29.33			
			48	61	40.66			

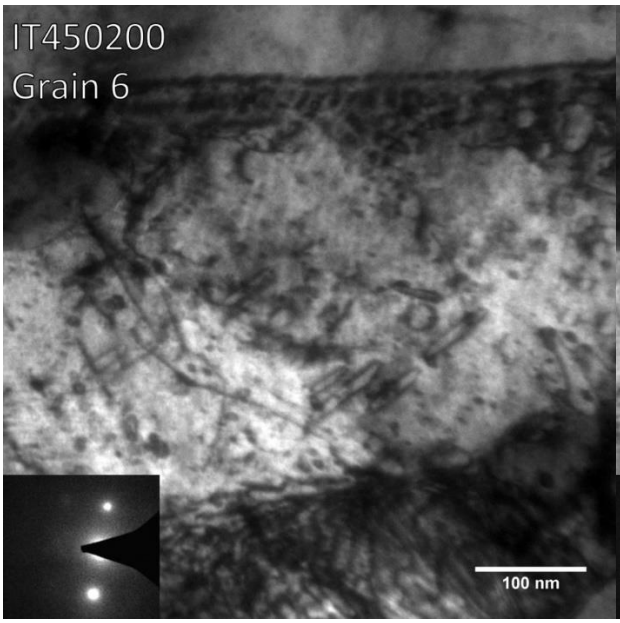
IT450200
Grain 6
100 nm

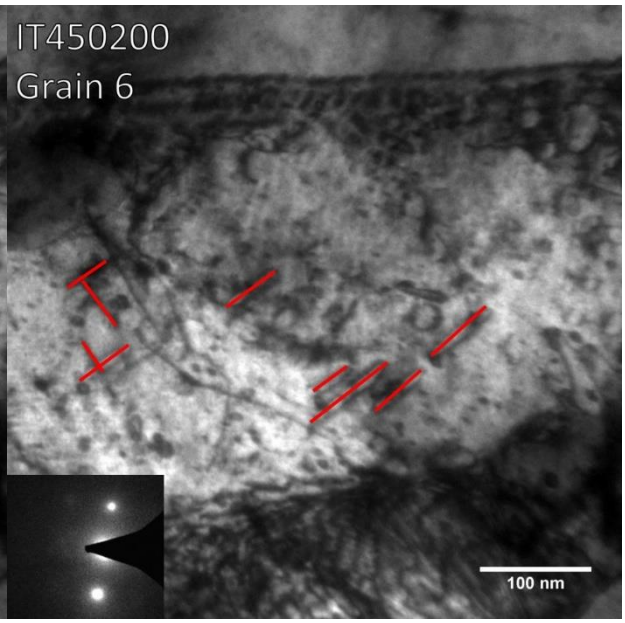
IT450200
Grain 6
100 nm

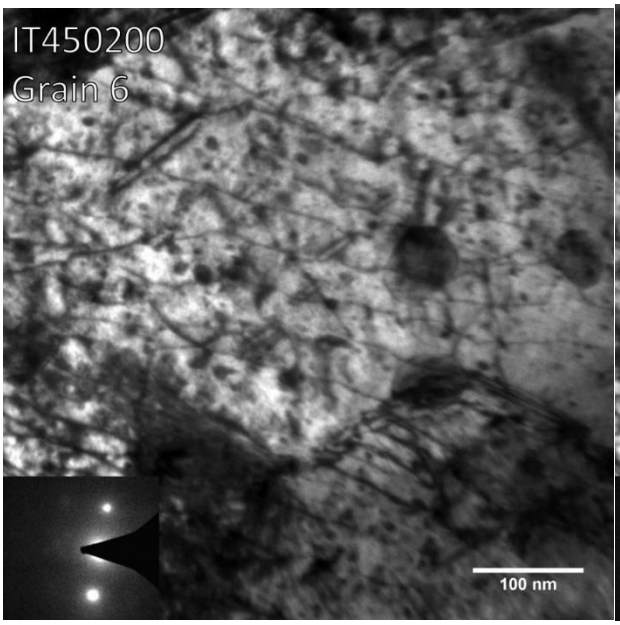
IT450200
Grain 6
100 nm

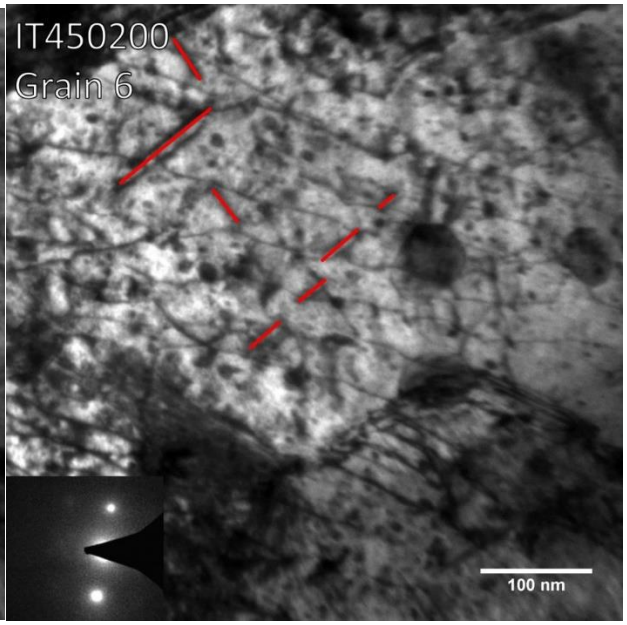
IT450200
Grain 6
100 nm

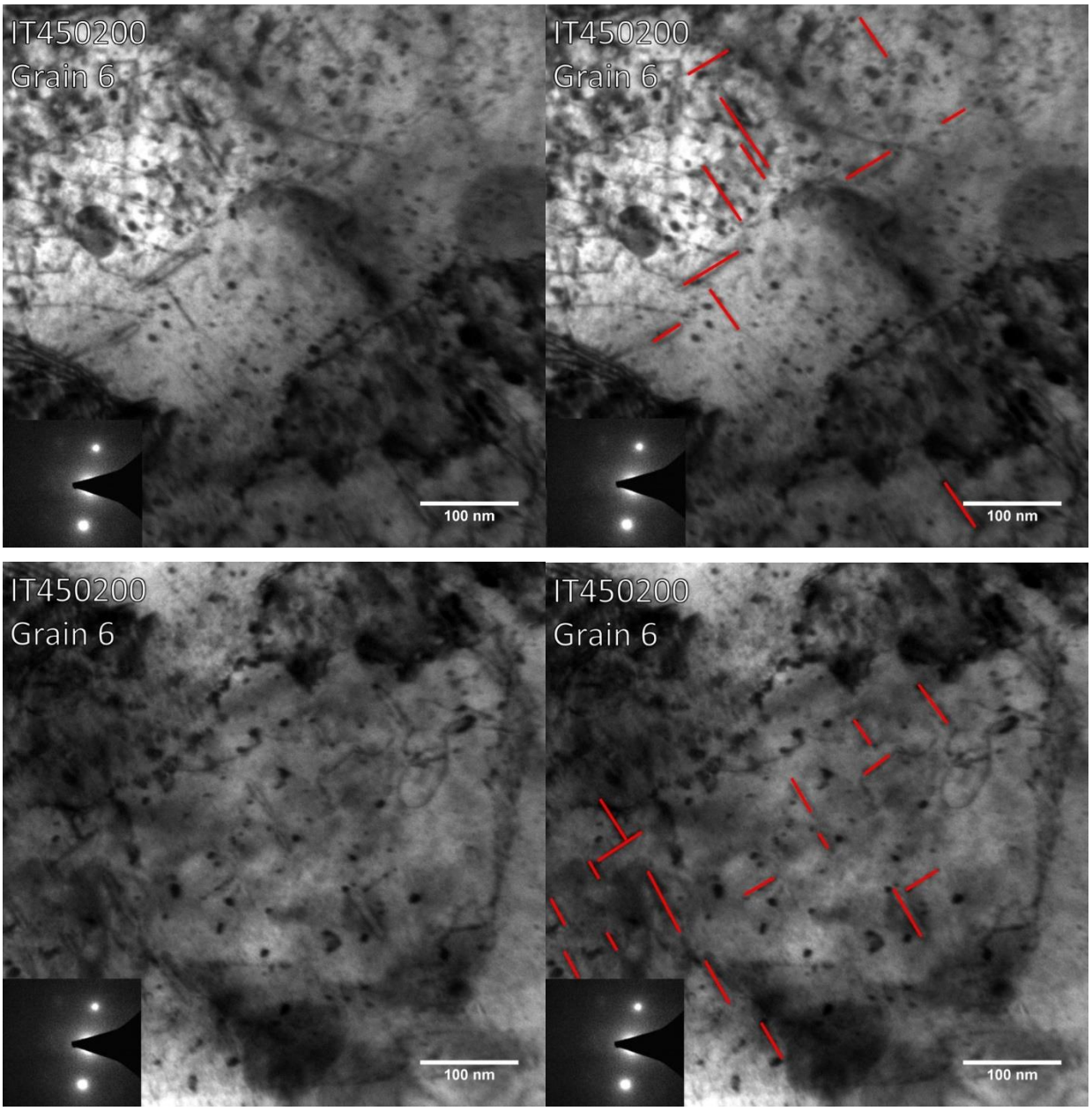
IT450200
Grain 6
100 nm
IT450200
Grain 6
100 nm
IT450200
Grain 6
100 nm
IT450200
Grain 6
100 nm

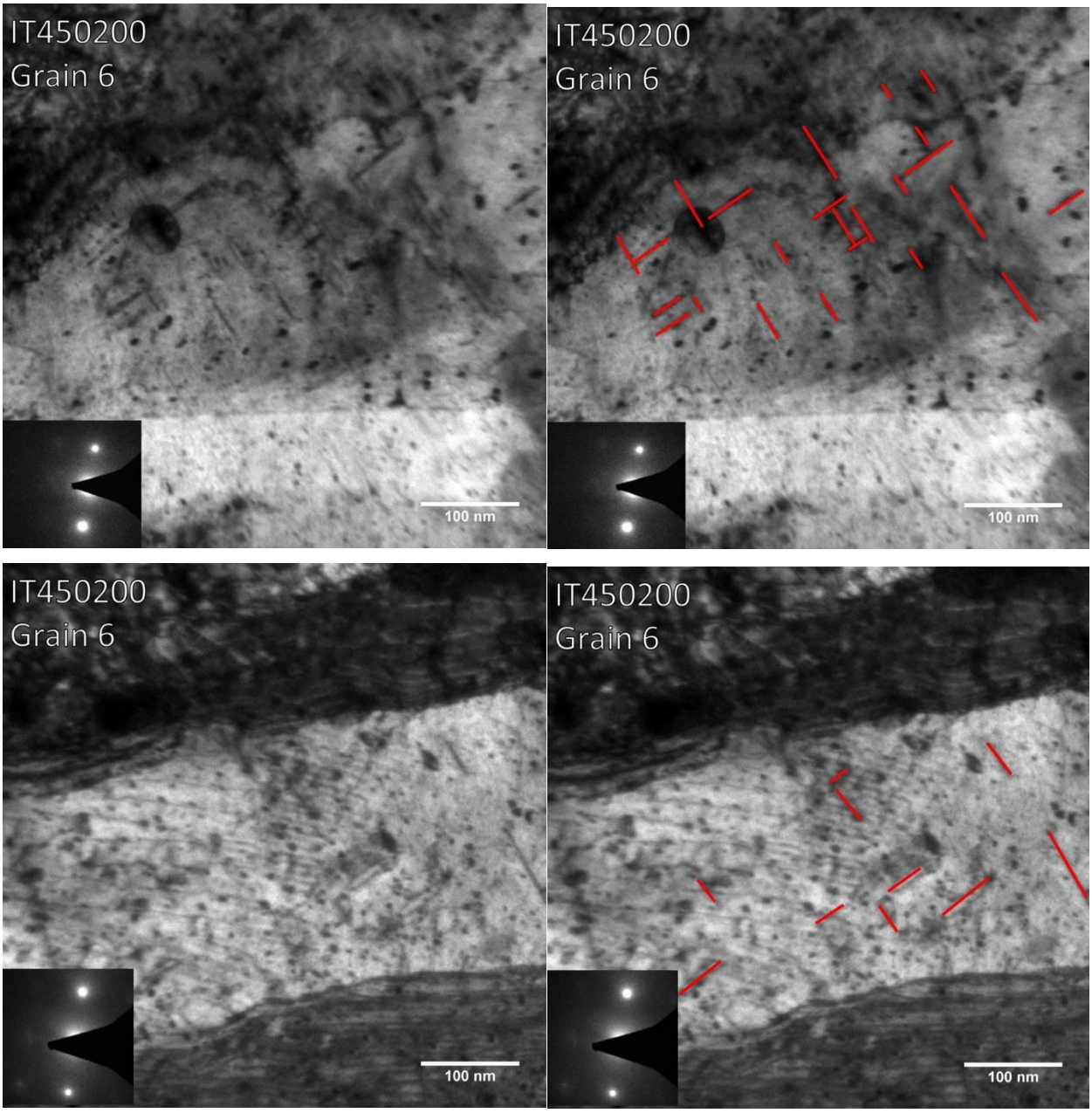

Figure B.1. 6 TEM image of grain #6 from irradiation creep sample IT450200, a_o<100> type edge on dislocation loops are highlighted in red.

Table B.1. 6 Results from dislocation loop analysis on grain #6 from irradiation creep sample IT450200.

Xtilt (θ_x)	Ytilt (θ_y)	TV Ztilt (θ_T)	LV Ztilt ($\theta_{<100>}$)			
-15.3	-8.58	-5	34			
Loop Normal angle to Tensile Axis	Number Density	Number Density Error	Size	Size Error	Fraction of Loops	Error in Fraction of loops
($\theta_{<100>}$)=40	38	6.164414	42.10526	11.27898	0.584615	0.094837
($\theta_{<010>}$)=50	27	5.196152	45.58148	18.71592	0.415385	0.079941

Orientation	Size (nm)	Actual Size (nm)	Orientation	Size (nm)	Actual Size (nm)	Scale Bar Ratio	Area (m^2)	Loop Density (1/m^3)
40	64	32	50	111.6	55.8	0.5	2.61E-20	2.49E+21
40	87	43.5	50	112.8	56.4			
40	72	36	50	76	38			
40	175	87.5	50	178	89			
40	92	46	50	110	55			
40	145	72.5	50	134	67			
40	100	50	50	210	105			
40	105	52.5	50	72	36			
40	113	56.5	50	60	30			
40	99	49.5	50	87	43.5			
40	45	22.5	50	29	14.5			
40	61	30.5	50	97	48.5			
40	62	31	50	107	53.5			
40	41	20.5	50	52	26			
40	144	72	50	69	34.5			
40	100	50	50	100	50			
40	91	45.5	50	75	37.5			
40	110	55	50	63	31.5			
40	88	44	50	72	36			
40	42	21	50	78	39			
40	60	30	50	63	31.5			

40	100	50	50	75	37.5			
40	95	47.5	50	107	53.5			
40	115	57.5	50	80	40			
40	29	14.5	50	44	22			
40	83	41.5	50	117	58.5			
40	51	25.5	50	82	41			
40	71	35.5						
40	130	65						
40	78	39						
40	85	42.5						
40	43	21.5						
40	43	21.5						
40	35	17.5						
40	50	25						
40	41	20.5						
40	130	65						
40	125	62.5						

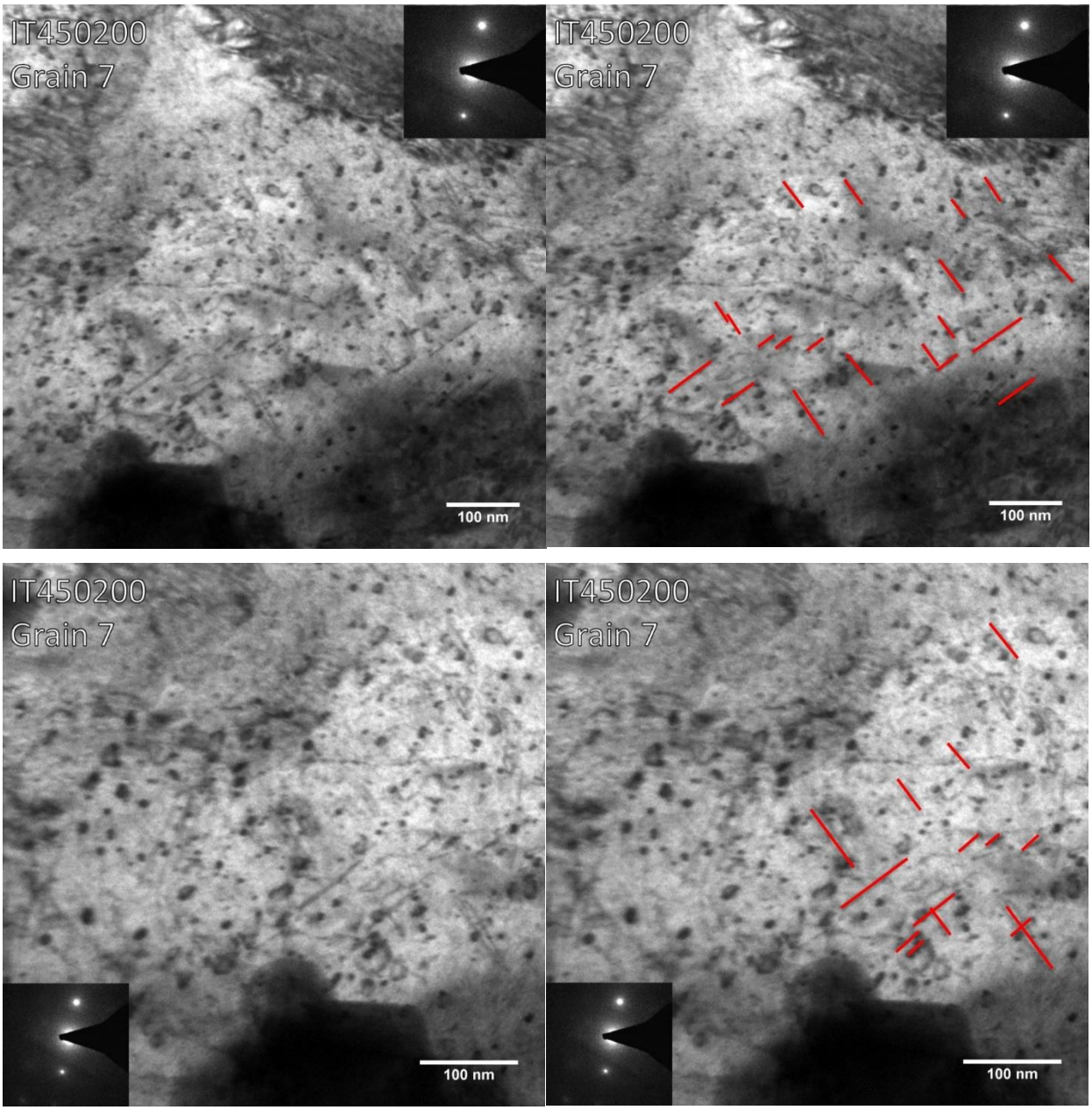

Figure B.1. 7 TEM image of grain #7 from irradiation creep sample IT450200, a_o<100> type edge on dislocation loops are highlighted in red.

Table B.1. 7 Results from dislocation loop analysis on grain #7 from irradiation creep sample IT450200.

Xtilt (θ_x)	Ytilt (θ_y)	TV Ztilt (θ_T)	LV Ztilt ($\theta_{<100>}$)			
-13.6	-9.73	-5	37			
Loop Normal angle to Tensile Axis	Number Density	Number Density Error	Size	Size Error	Fraction of Loops	Error in Fraction of loops
($\theta_{<100>}$)=45	19	4.358899	51.81667	16.9391	0.542857	0.12454
($\theta_{<010>}$)=45	16	4	44.77193	10.37552	0.457143	0.114286

Orientation	Size (nm)	Actual Size (nm)	Orientation	Size (nm)	Actual Size (nm)	Scale Bar Ratio	Area (m^2)	Loop Density (1/m^3)
45	108	72	45	46	30.66667	0.67	2.61E-20	1.34E+21
45	77.6	51.73333	45	43	28.66667			
45	40	26.66667	45	109	72.66667			
45	35	23.33333	45	85	56.66667			
45	30	20	45	61	40.66667			
45	45	30	45	62	41.33333			
45	53	35.33333	45	63	42			
45	114	76	45	46	30.66667			
45	91	60.66667	45	69	46			
45	47	31.33333	45	83	55.33333			
45	144	96	45	57	38			
45	80	53.33333	45	55	36.66667			
45	65	43.33333	45	165	110			
45	93	62	45	55	36.66667			
45	67	44.66667	45	101	67.33333			
45	154	102.6667	45	60	40			
			45	30	20			
			45	40	26.66667			
			45	46	30.66667			

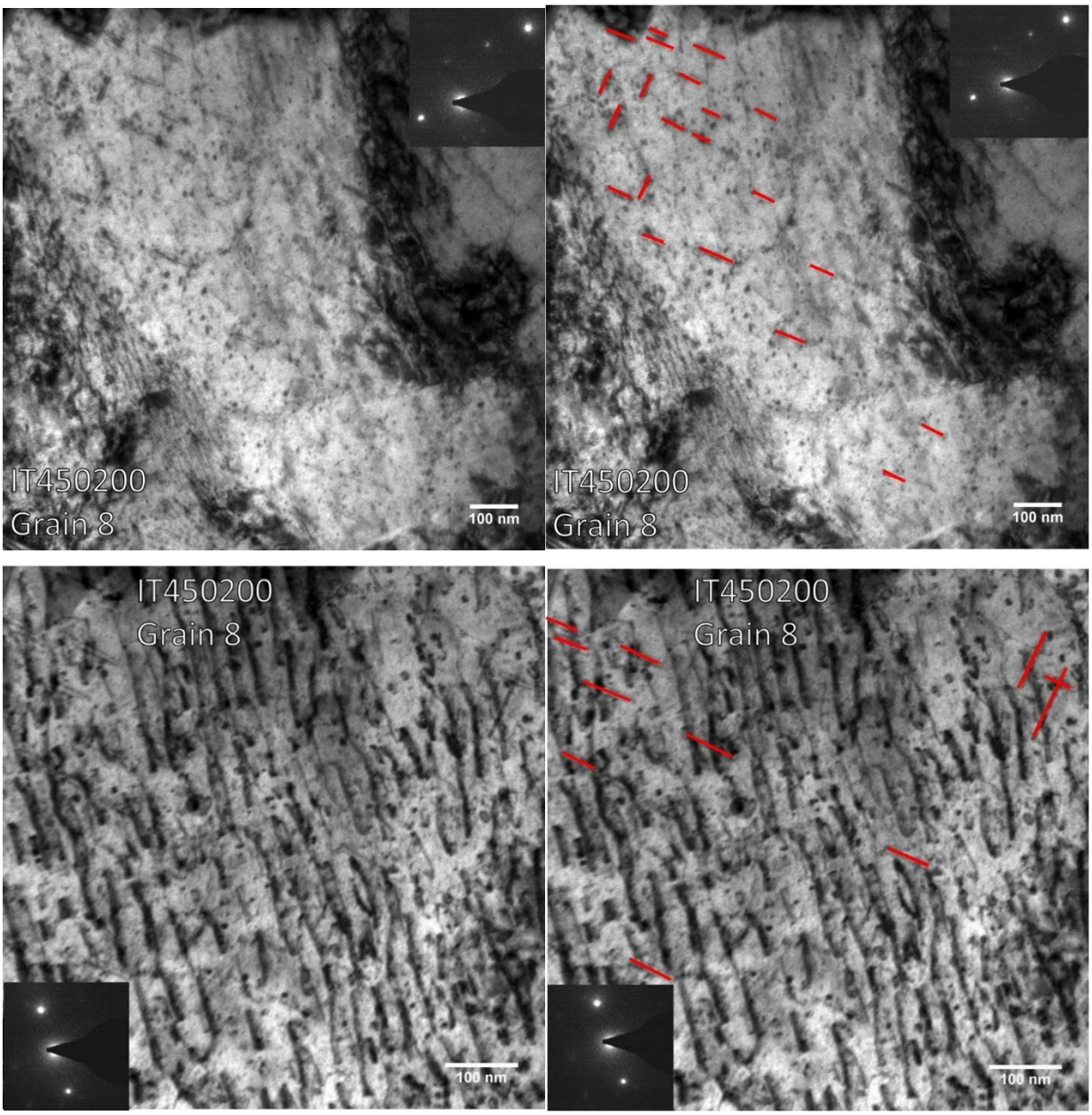

Figure B.1. 8 TEM image of grain #8 from irradiation creep sample IT450200, a_o<100> type edge on dislocation loops are highlighted in red.

Table B.1. 8 Results from dislocation loop analysis on grain #8 from irradiation creep sample IT450200.

Xtilt (θ_x)	Ytilt (θ_y)	TV Ztilt (θ_T)	LV Ztilt ($\theta_{<100>}$)			
-10.1	0.77	45	-21			
Loop Normal angle to Tensile Axis	Number Density	Number Density Error	Size	Size Error	Fraction of Loops	Error in Fraction of loops
($\theta_{<100>}$)=24	26	5.09902	53.04731	4.578806	0.8125	0.159344
($\theta_{<010>}$)=66	6	2.44949	64.49	19.30179	0.1875	0.076547

Orientation	Size (nm)	Actual Size (nm)	Orientation	Size (nm)	Actual Size (nm)	Scale Bar Ratio	Area (m^2)	Loop Density (1/m^3)
24	68	68	66	126	84.42	1	2.61E-20	1.22E+21
24	36	36	66	156	104.52	0.67		
24	50	50	66	52	52			
24	69	69	66	48	48			
24	52	52	66	50	50			
24	38	38	66	48	48			
24	34	34						
24	48	48						
24	37	37						
24	37	37						
24	48	48						
24	52	52						
24	70	70						
24	55	55						
24	61	61						
24	56	56						
24	53	53						
24	60	40.2						
24	96	64.32						
24	75	50.25						
24	100	67						

24	78	52.26						
24	94	62.98						
24	107	71.69						
24	98	65.66						
24	61	40.87						

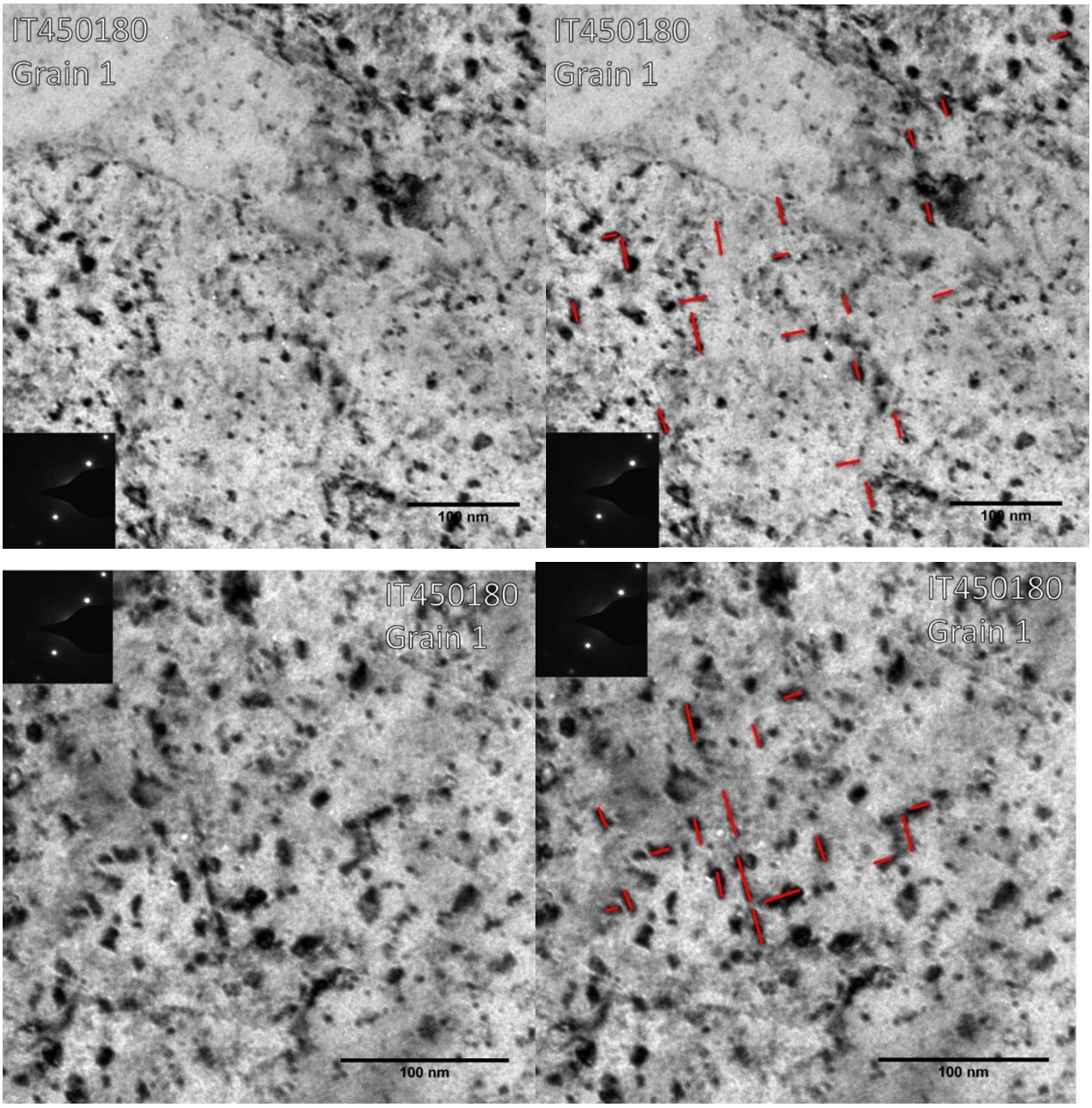

Figure B.2. 1 TEM image of grain #1 from irradiation creep sample IT450180, a_o<100> type edge on dislocation loops are highlighted in red.

Table B.2. 1 Results from dislocation loop analysis on grain #1 from irradiation creep sample IT450180.

Xtilt (θ_x)	Ytilt (θ_y)	TV Ztilt (θ_T)	LV Ztilt ($\theta_{<100>}$)			
5.33	-3.12	-37	13			
Loop Normal angle to Tensile Axis	Number Density	Number Density Error	Size	Size Error	Fraction of Loops	Error in Fraction of loops
($\theta_{<100>}$)=40	25	5	19.41714	2.468092	0.657894737	0.131579
($\theta_{<010>}$)=50	13	3.605551	14.43223	2.764646	0.342105263	0.094883

Orientation	Size (nm)	Actual Size (nm)	Orientation	Size (nm)	Actual Size (nm)	Scale Bar Ratio	Area (m^2)	Loop Density (1/m^3)
40	36	16.00	50	33	14.67	0.444444444	2.5E-20	7.6E+20
40	37	16.44	50	55	24.44	0.285714286		
40	63	28.00	50	26	11.56			
40	52	23.11	50	40	17.78			
40	77	34.22	50	40	17.78			
40	71	31.56	50	35	15.56			
40	52	23.11	50	35	15.56			
40	39	17.33	50	27	7.71			
40	30	13.33	50	33	9.43			
40	51	22.67	50	77	22.00			
40	51	22.67	50	35	10.00			
40	29	12.89	50	37	10.57			
40	38	16.89	50	37	10.57			
40	31	13.78						
40	43	12.29						
40	46	13.14						
40	49	14.00						
40	50	14.29						
40	71	20.29						
40	92	26.29						
40	95	27.14						

40	67	19.14						
40	45	12.86						
40	51	14.57						
40	68	19.43						

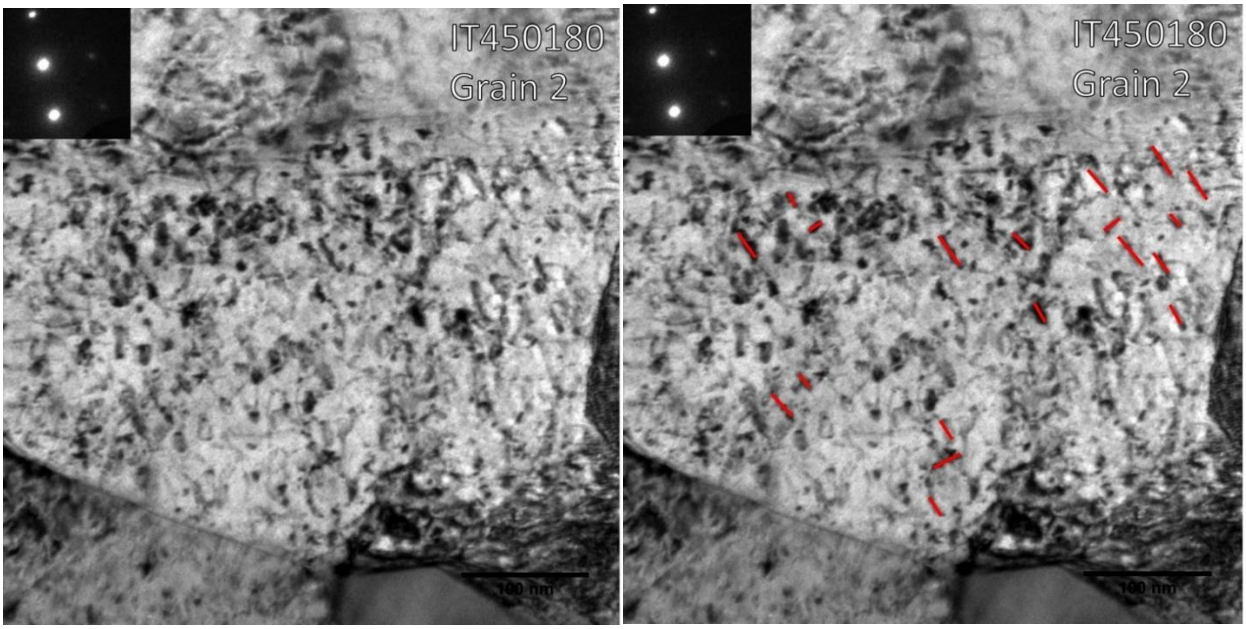

Figure B.2. 2 TEM image of grain #2 from irradiation creep sample IT450180, a_o<100> type edge on dislocation loops are highlighted in red.

Table B.2. 2 Results from dislocation loop analysis on grain #2 from irradiation creep sample IT450180.

Xtilt (θ_x)	Ytilt (θ_y)	TV Ztilt (θ_T)	LV Ztilt ($\theta_{<100>}$)			
34.67	-1.15	-37	58			
Loop Normal angle to Tensile Axis	Number Density	Number Density Error	Size	Size Error	Fraction of Loops	Error in Fraction of loops
($\theta_{<100>}$)=9	16	4	19.72222	2.92166	0.842105	0.210526
($\theta_{<010>}$)=81	3	1.732051	15.11111	6.595947	0.157895	0.091161

Orientation	Size (nm)	Actual Size (nm)	Orientation	Size (nm)	Actual Size (nm)	Scale Bar Ratio	Area (m^2)	Loop Density (1/m^3)
9	58	25.78	81	20	8.89	0.444444	2.5E-20	7.6E+20
9	56	24.89	81	46	20.44			
9	23	10.22	81	36	16.00			
9	34	15.11						

9	36	16.00						
9	37	16.44						
9	58	25.78						
9	34	15.11						
9	36	16.00						
9	49	21.78						
9	63	28.00						
9	37	16.44						
9	45	20.00						
9	60	26.67						
9	24	10.67						
9	60	26.67						

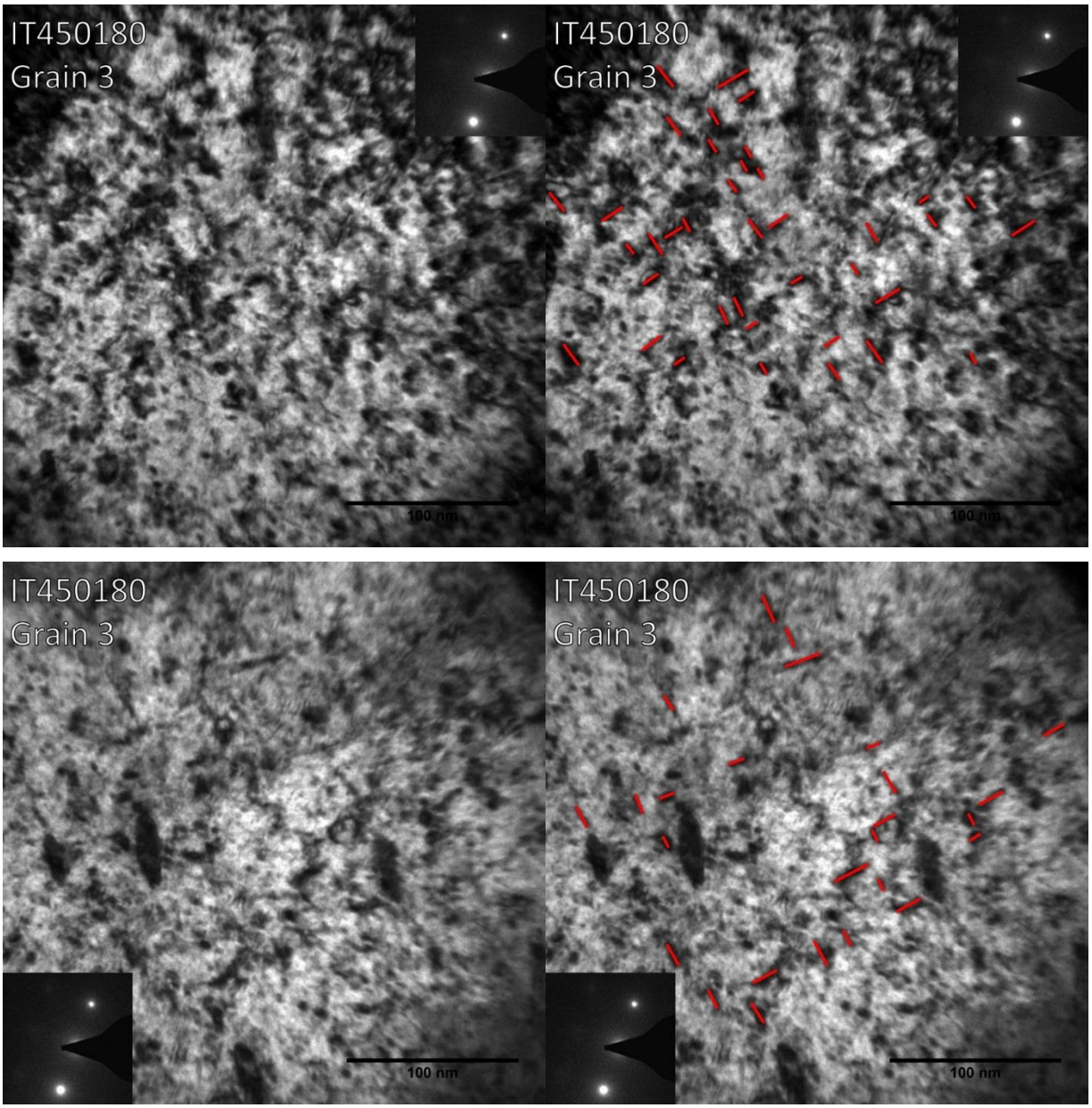
IT450180
Grain 3
100 nm
IT450180
Grain 3
100 nm
IT450180
Grain 3
100 nm
IT450180
Grain 3
100 nm

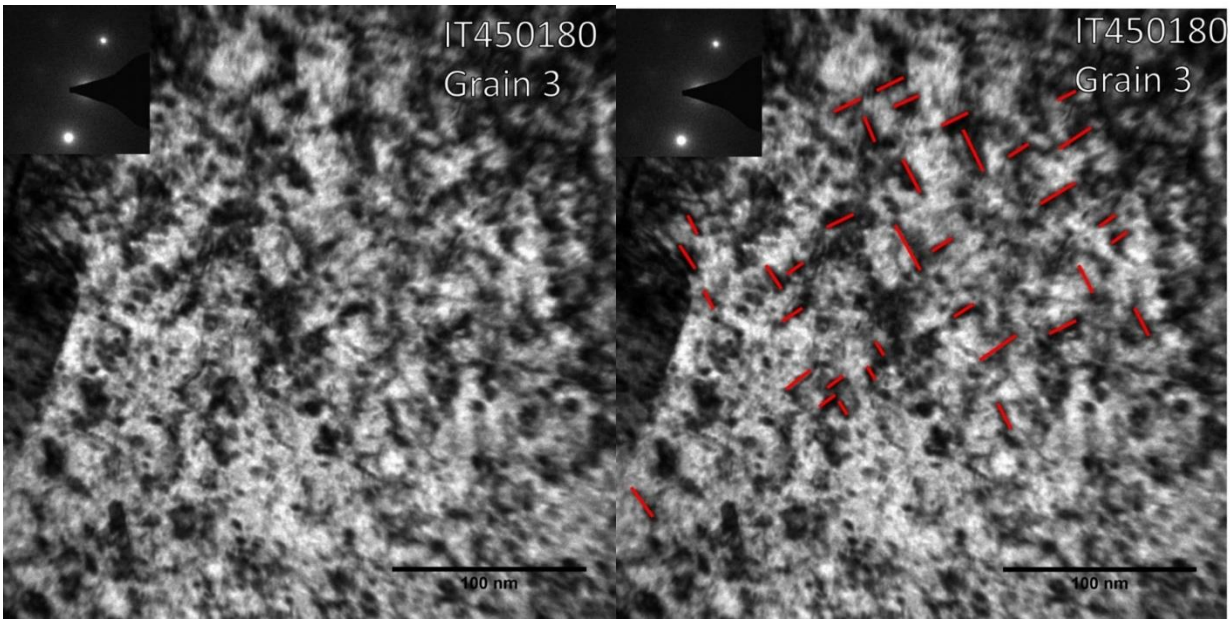

Figure B.2. 3 TEM image of grain #3 from irradiation creep sample IT450180, a_o<100> type edge on dislocation loops are highlighted in red.

Table B.2. 3 Results from dislocation loop analysis on grain #3 from irradiation creep sample IT450180.

Xtilt (θ_x)	Ytilt (θ_y)	TV Ztilt (θ_T)	LV Ztilt ($\theta_{<100>}$)			
-1.18	-5.55	-37	25			
Loop Normal angle to Tensile Axis	Number Density	Number Density Error	Size	Size Error	Fraction of Loops	Error in Fraction of loops
($\theta_{<100>}$)=29	50	7.071068	12.81714	1.107358	0.555556	0.078567
($\theta_{<010>}$)=61	40	6.324555	13.49286	1.273132	0.444444	0.070273

Orientation	Size (nm)	Actual Size (nm)	Orientation	Size (nm)	Actual Size (nm)	Scale Bar Ratio	Area (m^2)	Loop Density (1/m^3)
29	47	13.43	61	51	14.57	0.285714	1.03E-20	2.90E+21
29	53	15.14	61	41	11.71			
29	36	10.29	61	42	12.00			
29	51	14.57	61	26	7.43			

29	34	9.71	61	42	12.00			
29	40	11.43	61	26	7.43			
29	37	10.57	61	70	20.00			
29	26	7.43	61	33	9.43			
29	50	14.29	61	50	14.29			
29	45	12.86	61	25	7.14			
29	38	10.86	61	34	9.71			
29	32	9.14	61	60	17.14			
29	30	8.57	61	25	7.14			
29	30	8.57	61	56	16.00			
29	30	8.57	61	31	8.86			
29	33	9.43	61	59	16.86			
29	44	12.57	61	72	20.57			
29	44	12.57	61	77	22.00			
29	30	8.57	61	43	12.29			
29	55	15.71	61	52	14.86			
29	41	11.71	61	51	14.57			
29	32	9.14	61	49	14.00			
29	32	9.14	61	55	15.71			
29	30	8.57	61	44	12.57			
29	51	14.57	61	33	9.43			
29	42	12.00	61	33	9.43			
29	48	13.71	61	52	14.86			
29	45	12.86	61	59	16.86			
29	47	13.43	61	52	14.86			
29	40	11.43	61	45	12.86			
29	44	12.57	61	55	15.71			
29	57	16.29	61	44	12.57			
29	65	18.57	61	39	11.14			
29	42	12.00	61	77	22.00			
29	46	13.14	61	54	15.43			
29	62	17.71	61	67	19.14			
29	53	15.14	61	64	18.29			

29	41	11.71	61	35	10.00			
29	36	10.29	61	33	9.43			
29	47	13.43	61	33	9.43			
29	51	14.57						
29	98	28.00						
29	70	20.00						
29	80	22.86						
29	56	16.00						
29	60	17.14						
29	52	14.86						
29	30	8.57						
29	30	8.57						
29	30	8.57						

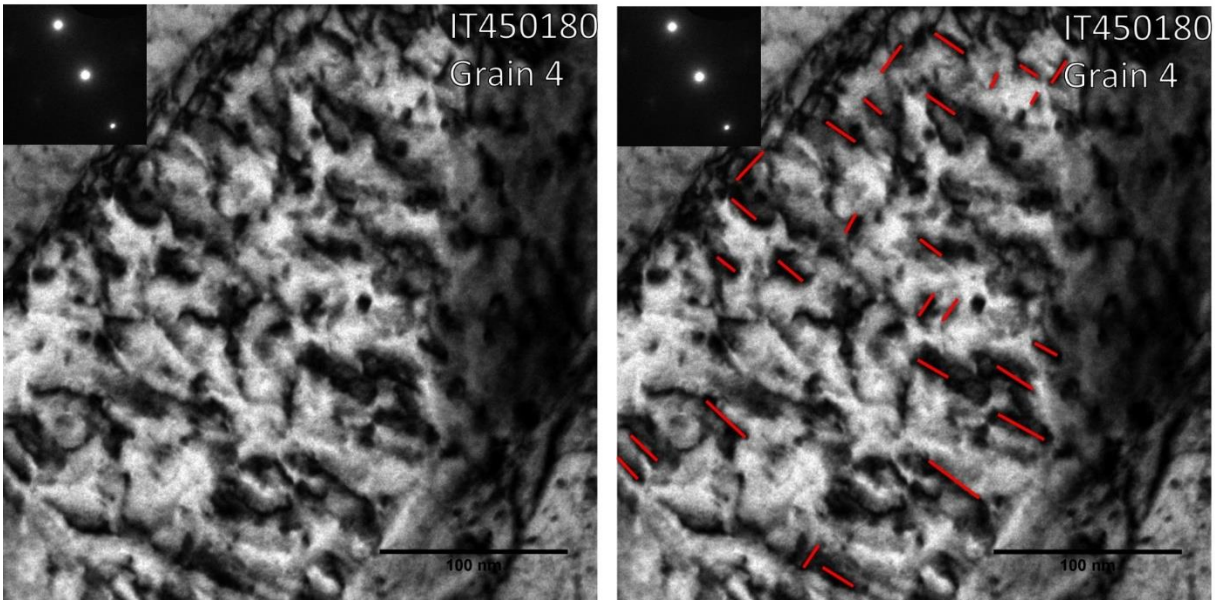

Figure B.2. 4 TEM image of grain #4 from irradiation creep sample IT450180, a_o<100> type edge on dislocation loops are highlighted in red.

Table B.2. 4 Results from dislocation loop analysis on grain #3 from irradiation creep sample IT450180.

Xtilt (θ_x)	Ytilt (θ_y)	TV Ztilt (θ_T)	LV Ztilt ($\theta_{<100>}$)			
32.08	-4.67	54	-17			
Loop Normal angle to Tensile Axis	Number Density	Number Density Error	Size	Size Error	Fraction of Loops	Error in Fraction of loops
($\theta_{<100>}$)=19	18	4.242641	18.49206	2.833403	0.692308	0.163178
($\theta_{<010>}$)=71	8	2.828427	12.96429	2.932729	0.307692	0.108786

Orientation	Size (nm)	Actual Size (nm)	Orientation	Size (nm)	Actual Size (nm)	Scale Bar Ratio	Area (m^2)	Loop Density (1/m^3)
19	59	16.86	71	51	14.57	0.285714	1.03E-20	2.52E+21
19	66	18.86	71	47	13.43			
19	96	27.43	71	43	12.29			
19	65	18.57	71	34	9.71			

19	115	32.86	71	74	21.14			
19	101	28.86	71	54	15.43			
19	67	19.14	71	30	8.57			
19	80	22.86	71	30	8.57			
19	51	14.57						
19	40	11.43						
19	55	15.71						
19	61	17.43						
19	64	18.29						
19	47	13.43						
19	40	11.43						
19	61	17.43						
19	35	10.00						
19	62	17.71						

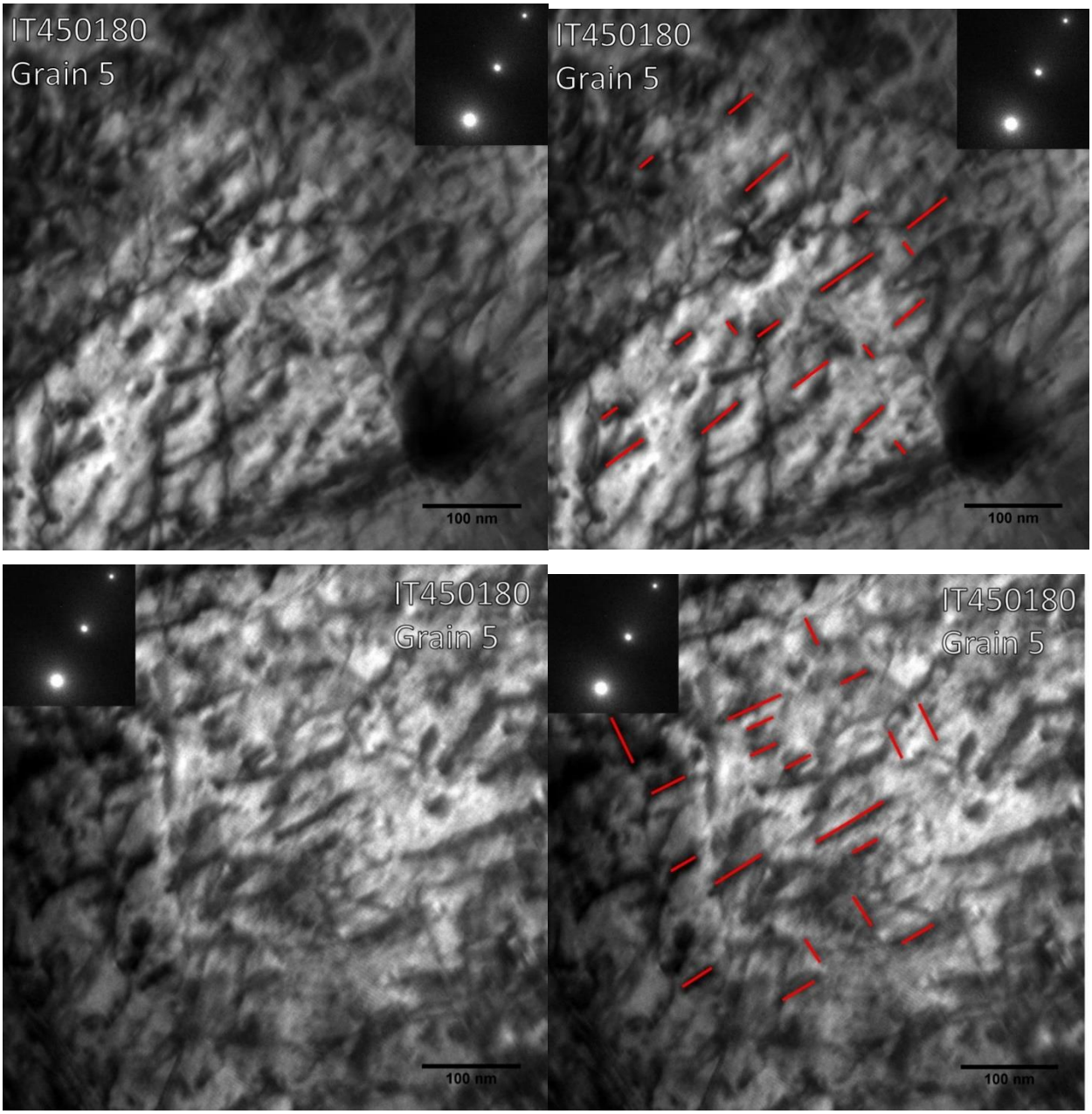

Figure B.2. 5 TEM image of grain #5 from irradiation creep sample IT450180, a_o<100> type edge on dislocation loops are highlighted in red.

Table B.2. 5 Results from dislocation loop analysis on grain #5 from irradiation creep sample IT450180.

Xtilt (θ_x)	Ytilt (θ_y)	TV Ztilt (θ_T)	LV Ztilt ($\theta_{<100>}$)			
-10.07	2.31	-60	18			
Loop Normal angle to Tensile Axis	Number Density	Number Density Error	Size	Size Error	Fraction of Loops	Error in Fraction of loops
($\theta_{<100>}$)=12	26	5.09902	38.80769	5.8044	0.722222	0.141639
($\theta_{<010>}$)=78	10	3.162278	27.65	7.774461	0.277778	0.087841

Orientation	Size (nm)	Actual Size (nm)	Orientation	Size (nm)	Actual Size (nm)	Scale Bar Ratio	Area (m^2)	Loop Density (1/m^3)
12	41	20.5	78	34	17	0.5	3.16E-20	1.13E+21
12	93	46.5	78	31	15.5			
12	95	47.5	78	27	13.5			
12	45	22.5	78	31	15.5			
12	52	26	78	102	51			
12	90	45	78	55	27.5			
12	75	37.5	78	70	35			
12	75	37.5	78	80	40			
12	129	64.5	78	53	26.5			
12	100	50	78	70	35			
12	115	57.5						
12	59	29.5						
12	38	19						
12	63	31.5						
12	70	35						
12	70	35						
12	110	55						
12	161	80.5						
12	50	25						
12	55	27.5						
12	73	36.5						

12	119	59.5						
12	60	30						
12	60	30						
12	60	30						
12	60	30						

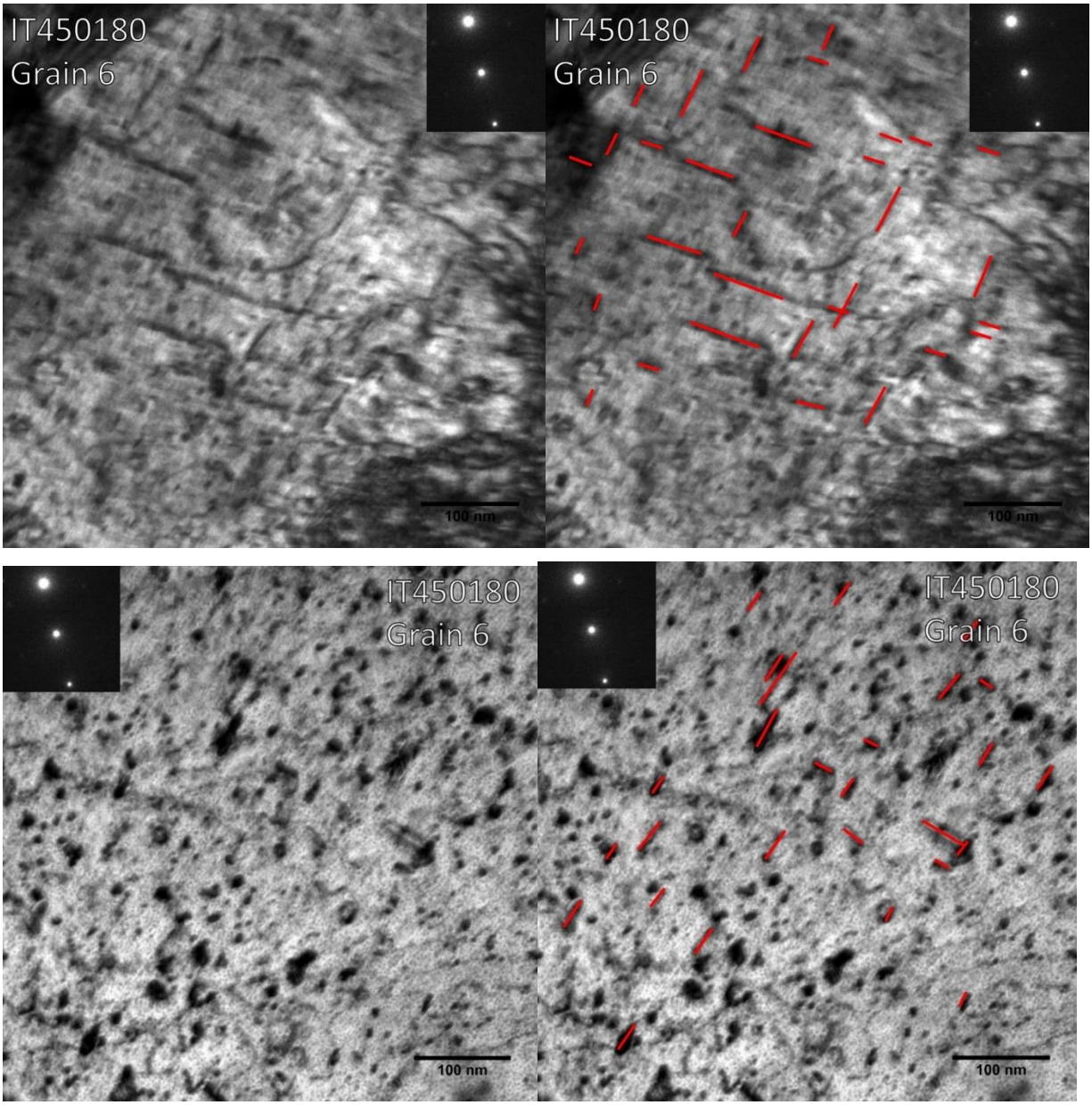

Figure B.2. 6 TEM image of grain #6 from irradiation creep sample IT450180, a_o<100> type edge on dislocation loops are highlighted in red.

Table B.2. 6 Results from dislocation loop analysis on grain #6 from irradiation creep sample IT450180.

Xtilt (θ_x)	Ytilt (θ_y)	TV Ztilt (θ_T)	LV Ztilt ($\theta_{<100>}$)			
2.71	6.16	-60	58			
Loop Normal angle to Tensile Axis	Number Density	Number Density Error	Size	Size Error	Fraction of Loops	Error in Fraction of loops
($\theta_{<100>}$)=28	33	5.744563	30.65152	4.23655	0.578947	0.100782
($\theta_{<010>}$)=62	24	4.898979	30.54167	7.16879	0.421053	0.085947

Orientation	Size (nm)	Actual Size (nm)	Orientation	Size (nm)	Actual Size (nm)	Scale Bar Ratio	Area (m^2)	Loop Density (1/m^3)
28	48	24	62	57	28.5	0.5	3.16E-20	9.01E+20
28	50	25	62	50	25			
28	29	14.5	62	40	20			
28	30	15	62	120	60			
28	33	16.5	62	98	49			
28	105	52.5	62	110	55			
28	75	37.5	62	45	22.5			
28	60	30	62	143	71.5			
28	58	29	62	145	72.5			
28	85	42.5	62	41	20.5			
28	100	50	62	40	20			
28	100	50	62	40	20			
28	94	47	62	42	21			
28	80	40	62	45	22.5			
28	57	28.5	62	43	21.5			
28	35	17.5	62	40	20			
28	44	22	62	40	20			
28	40	20	62	55	27.5			
28	54	27	62	39	19.5			
28	63	31.5	62	47	23.5			
28	130	65	62	32	16			

28	88	44	62	30	15			
28	45	22.5	62	94	47			
28	64	32	62	30	15			
28	56	28						
28	68	34						
28	47	23.5						
28	52	26						
28	66	33						
28	52	26						
28	51	25.5						
28	32	16						
28	32	16						

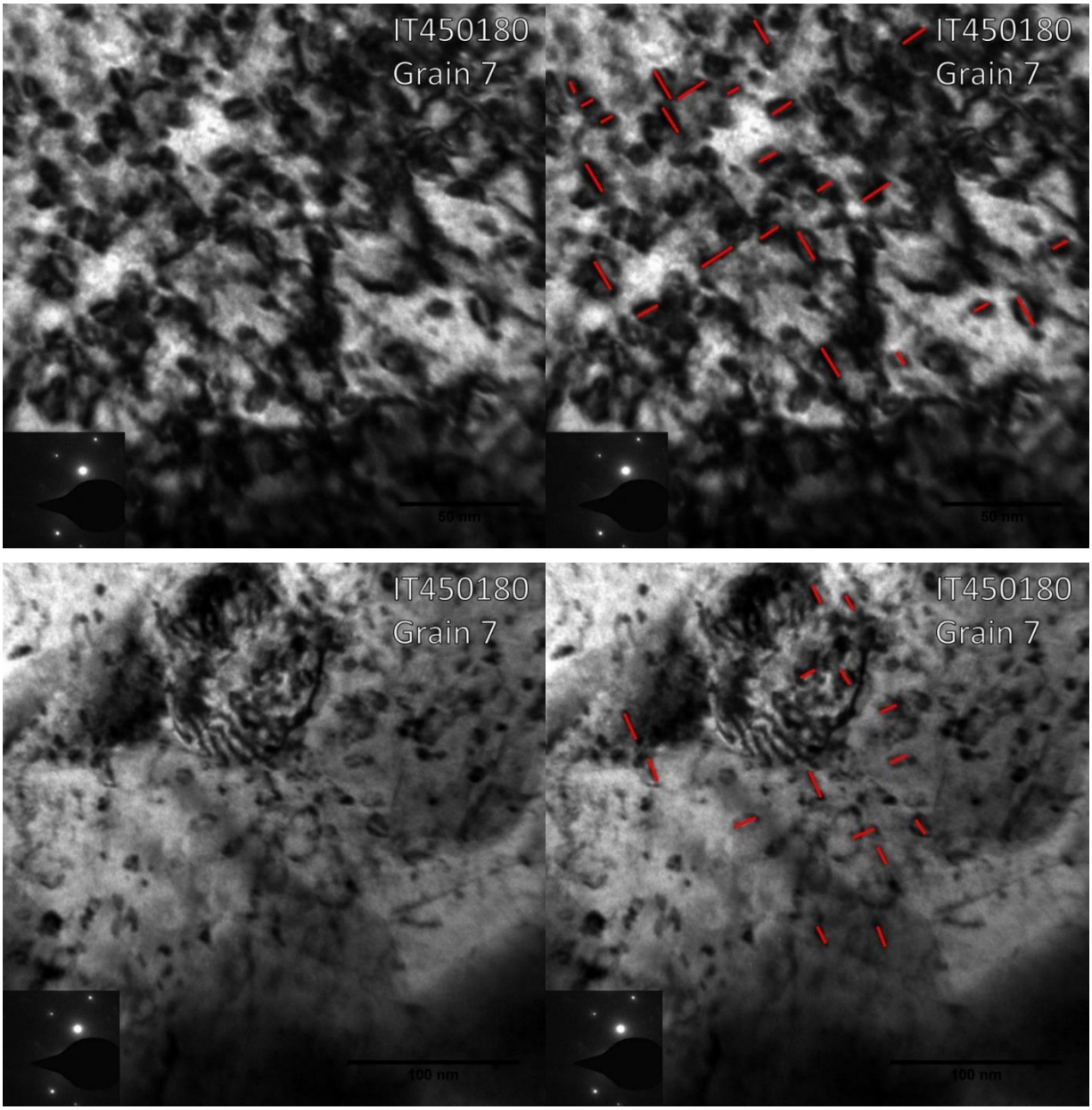

Figure B.2. 7 TEM image of grain #7 from irradiation creep sample IT450180, a_o<100> type edge on dislocation loops are highlighted in red.

Table B.2. 7 Results from dislocation loop analysis on grain #7 from irradiation creep sample IT450180.

Xtilt (θ_x)	Ytilt (θ_y)	TV Ztilt (θ_T)	LV Ztilt ($\theta_{<100>}$)			
24.7	1.8	58	20			
Loop Normal angle to Tensile Axis	Number Density	Number Density Error	Size	Size Error	Fraction of Loops	Error in Fraction of loops
($\theta_{<100>}$)=48	20	4.472136	11.6006	1.176572	0.512821	0.11467
($\theta_{<010>}$)=42	19	4.358899	9.402882	1.363399	0.487179	0.111767

Orientation	Size (nm)	Actual Size (nm)	Orientation	Size (nm)	Actual Size (nm)	Scale Bar Ratio	Area (m^2)	Loop Density (1/m^3)
48	26	5.42	42	27	5.63	0.208333	1.03E-20	1.88E+21
48	64	13.33	42	25	5.21	0.285714		
48	60	12.50	42	44	9.17			
48	61	12.71	42	70	14.58			
48	61	12.71	42	60	12.50			
48	50	10.42	42	26	5.42			
48	65	13.54	42	46	9.58			
48	68	14.17	42	35	7.29			
48	30	6.25	42	43	8.96			
48	65	13.54	42	33	6.88			
48	54	15.43	42	60	12.50			
48	46	13.14	42	52	10.83			
48	37	10.57	42	33	6.88			
48	33	9.43	42	32	6.67			
48	35	10.00	42	46	13.14			
48	54	15.43	42	32	9.14			
48	34	9.71	42	36	10.29			
48	35	10.00	42	32	9.14			
48	45	12.86	42	52	14.86			
48	38	10.86						

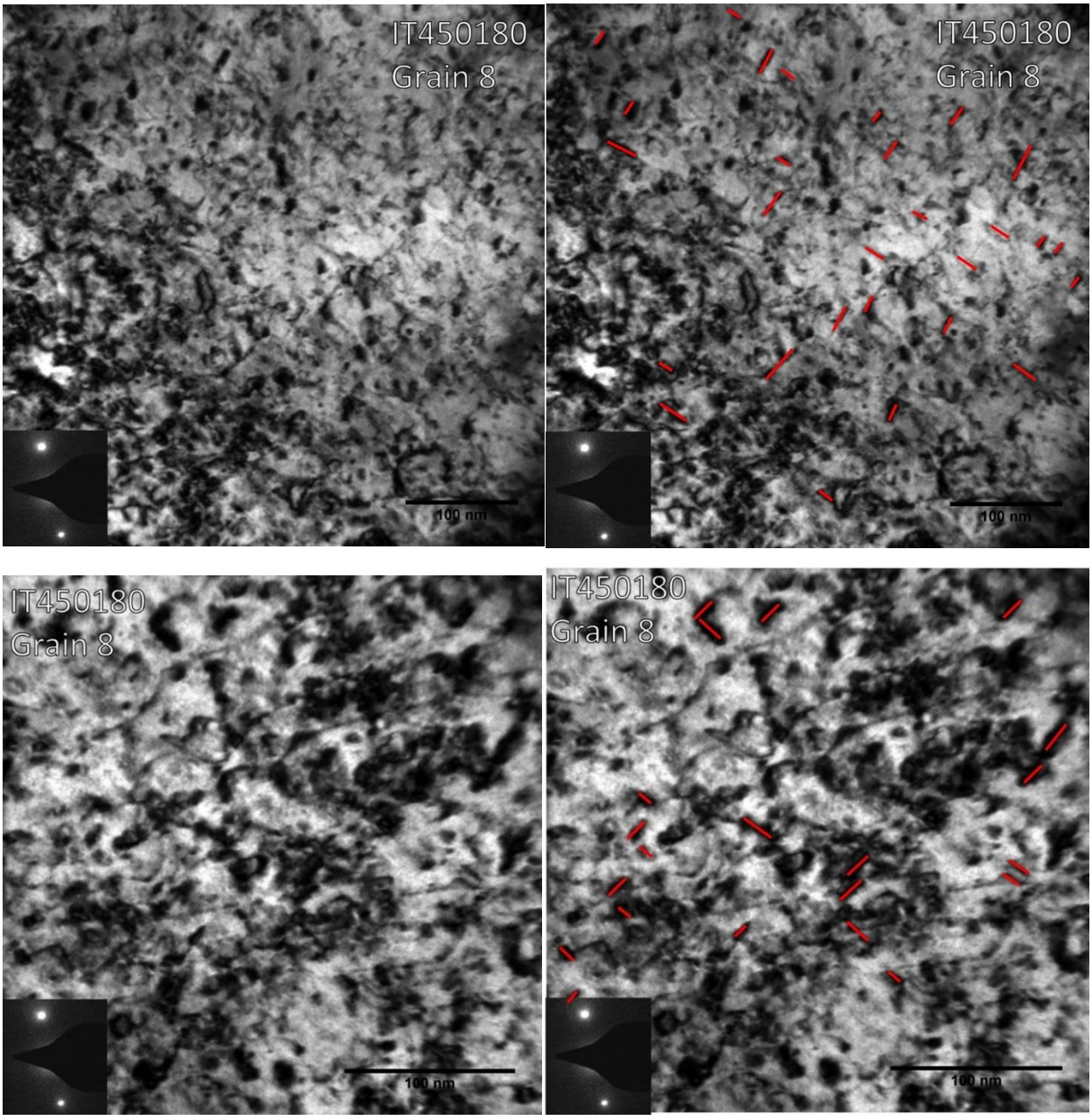

Figure B.2. 8 TEM image of grain #8 from irradiation creep sample IT450180, a_o<100> type edge on dislocation loops are highlighted in red.

Table B.2. 8 Results from dislocation loop analysis on grain #8 from irradiation creep sample IT450180.

Xtilt (θ_x)	Ytilt (θ_y)	TV Ztilt (θ_T)	LV Ztilt ($\theta_{<100>}$)			
-14.44	-19.25	-61	58			
Loop Normal angle to Tensile Axis	Number Density	Number Density Error	Size	Size Error	Fraction of Loops	Error in Fraction of loops
($\theta_{<100>}$)=29	27	5.196152	16.17284	2.470603	0.54	0.103923
($\theta_{<010>}$)=61	23	4.795832	15.24224	2.513814	0.46	0.095917

Orientation	Size (nm)	Actual Size (nm)	Orientation	Size (nm)	Actual Size (nm)	Scale Bar Ratio	Area (m^2)	Loop Density (1/m^3)
29	33	14.67	61	60	26.67	0.444444	2.5E-20	1E+21
29	32	14.22	61	28	12.44	0.285714		
29	50	22.22	61	28	12.44			
29	57	25.33	61	27	12.00			
29	24	10.67	61	27	12.00			
29	40	17.78	61	63	28.00			
29	42	18.67	61	62	27.56			
29	76	33.78	61	30	13.33			
29	47	20.89	61	42	18.67			
29	34	15.11	61	37	16.44			
29	78	34.67	61	42	18.67			
29	33	14.67	61	32	14.22			
29	35	15.56	61	53	23.56			
29	24	10.67	61	48	13.71			
29	24	10.67	61	32	9.14			
29	25	11.11	61	26	7.43			
29	46	13.14	61	31	8.86			
29	53	15.14	61	36	10.29			
29	39	11.14	61	65	18.57			
29	48	13.71	61	51	14.57			
29	26	7.43	61	31	8.86			

29	32	9.14	61	47	13.43			
29	56	16.00	61	34	9.71			
29	53	15.14	61					
29	48	13.71						
29	63	18.00						
29	47	13.43						

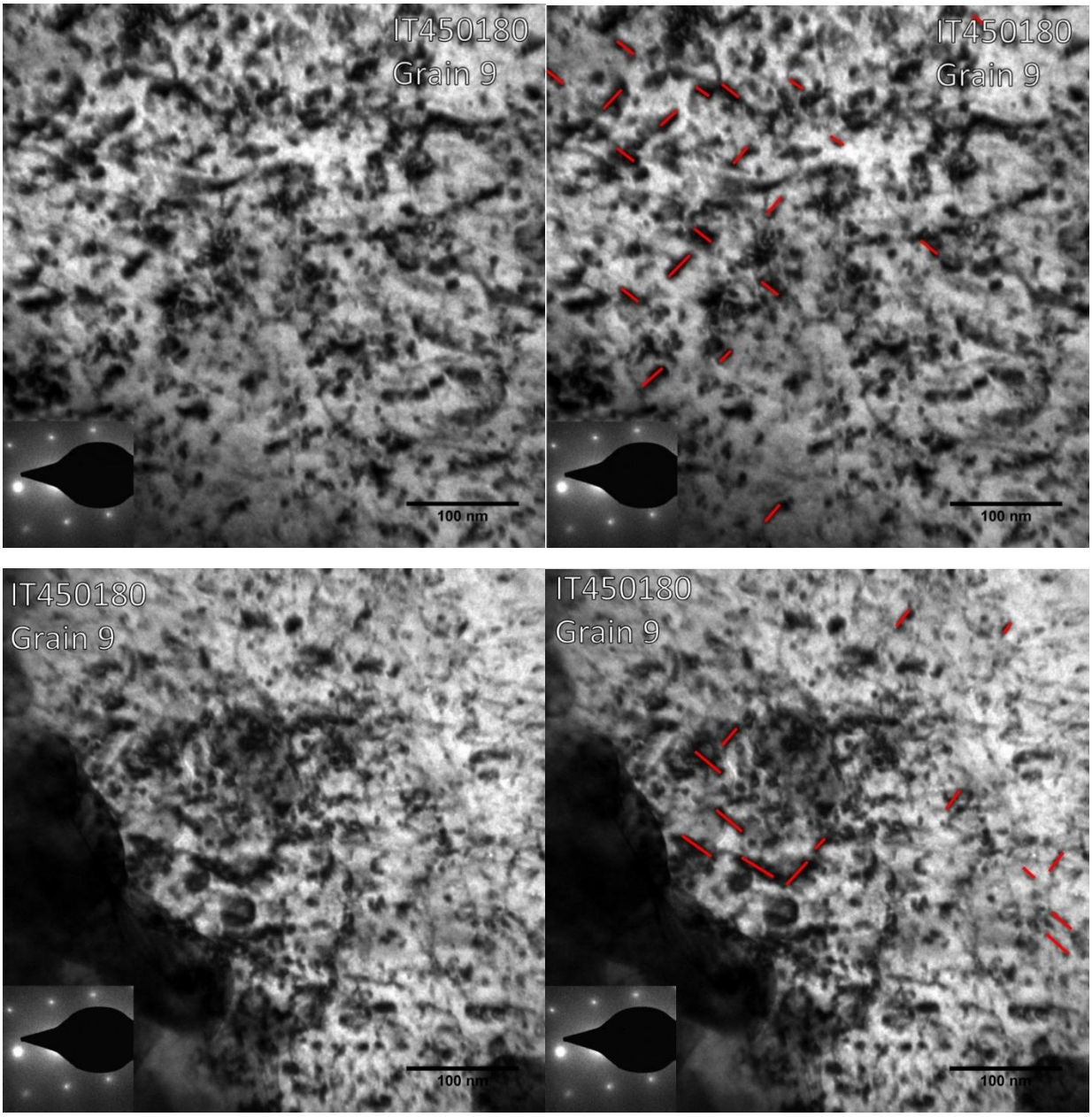
IT450180
Grain 9
100 nm
IT450180
Grain 9
100 nm
IT450180
Grain 9
100 nm
IT450180
Grain 9
100 nm

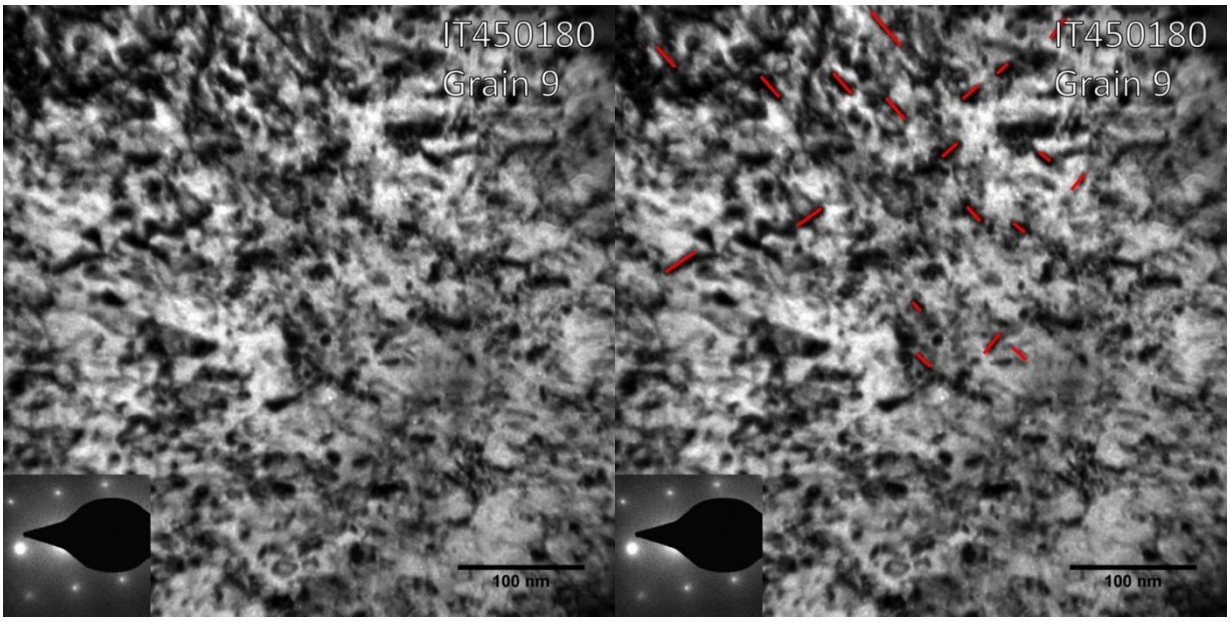

Figure B.2. 9 TEM image of grain #9 from irradiation creep sample IT450180, a_o<100> type edge on dislocation loops are highlighted in red.

Table B.2. 9 Results from dislocation loop analysis on grain #9 from irradiation creep sample IT450180.

Xtilt (θ_x)	Ytilt (θ_y)	TV Ztilt (θ_T)	LV Ztilt ($\theta_{<100>}$)			
-6.13	-27.55	-61	55			
Loop Normal angle to Tensile Axis	Number Density	Number Density Error	Size	Size Error	Fraction of Loops	Error in Fraction of loops
($\theta_{<100>}$)=22	30	5.477226	18.9037	2.427761	0.566038	0.103344
($\theta_{<010>}$)=68	23	4.795832	18.28019	2.013958	0.433962	0.090487

Orientation	Size (nm)	Actual Size (nm)	Orientation	Size (nm)	Actual Size (nm)	Scale Bar Ratio	Area (m^2)	Loop Density (1/m^3)
22	42	18.67	68	45	20.00	0.444444	2.5E-20	7.06667E+20
22	42	18.67	68	42	18.67			
22	45	20.00	68	55	24.44			
22	30	13.33	68	39	17.33			
22	40	17.78	68	55	24.44			
22	29	12.89	68	42	18.67			
22	30	13.33	68	32	14.22			
22	30	13.33	68	45	20.00			
22	42	18.67	68	47	20.89			
22	42	18.67	68	41	18.22			
22	42	18.67	68	18	8.00			
22	41	18.22	68	28	12.44			
22	62	27.56	68	60	26.67			
22	64	28.44	68	47	20.89			
22	66	29.33	68	46	20.44			
22	73	32.44	68	57	25.33			
22	31	13.78	68	53	23.56			
22	48	21.33	68	30	13.33			
22	59	26.22	68	35	15.56			
22	45	20.00	68	21	9.33			
22	49	21.78	68	35	15.56			

22	50	22.22	68	35	15.56			
22	78	34.67	68	38	16.89			
22	45	20.00						
22	21	9.33						
22	30	13.33						
22	26	11.56						
22	16	7.11						
22	28	12.44						
22	30	13.33						

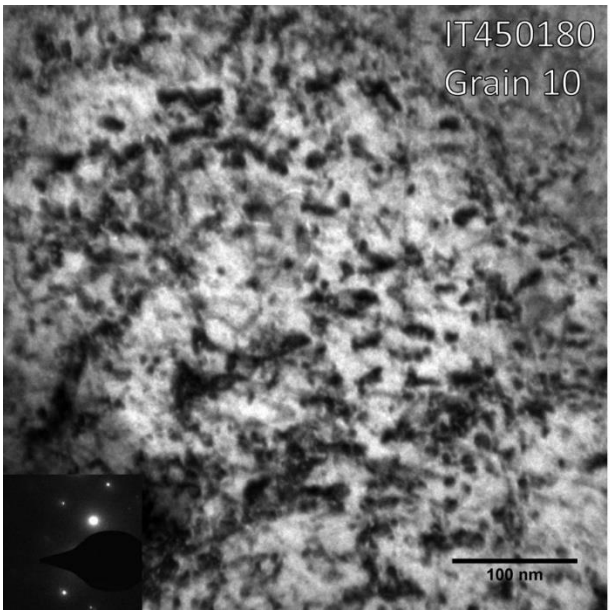
IT450180
Grain 10
100 nm

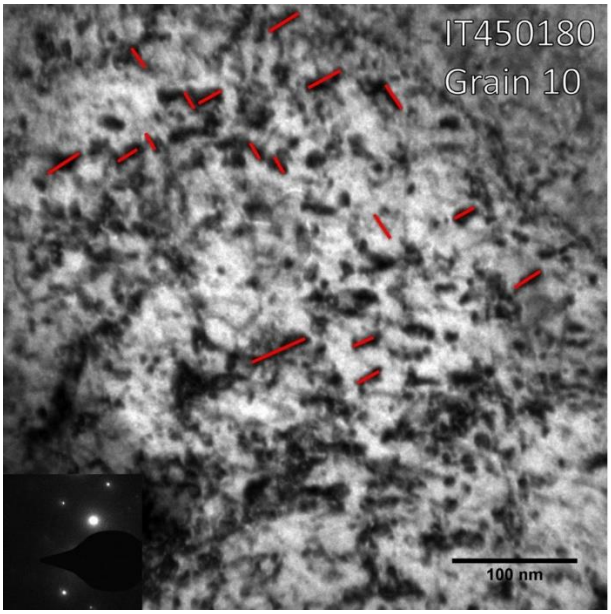
IT450180
Grain 10
100 nm

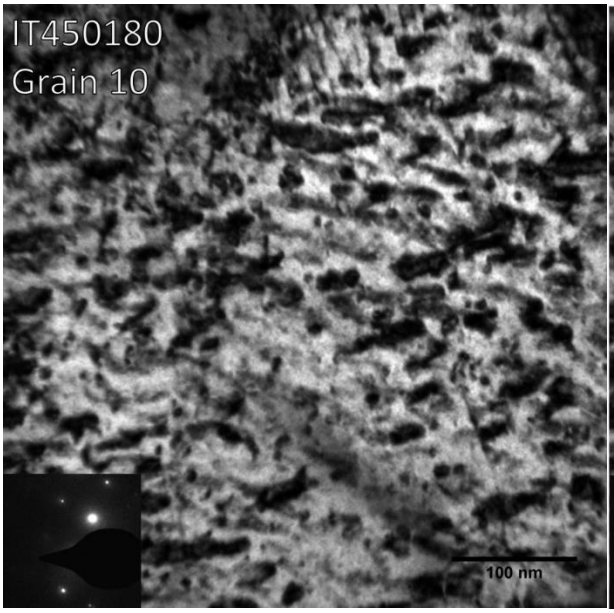
IT450180
Grain 10
100 nm

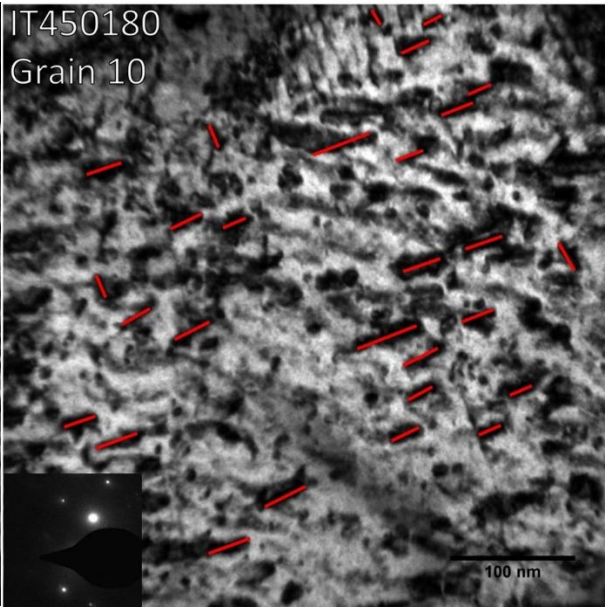
IT450180
Grain 10
100 nm

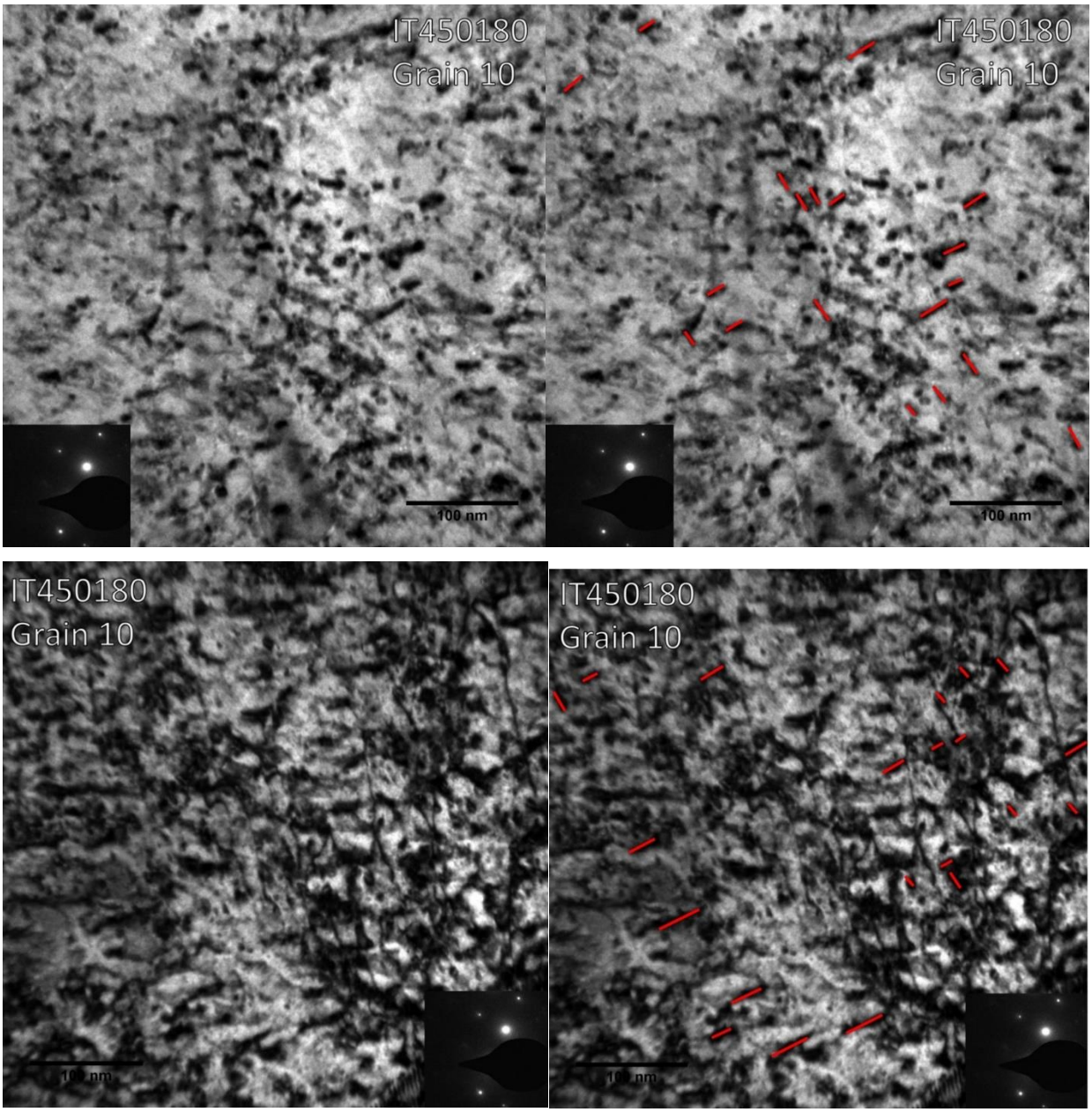

Figure B.2. 10 TEM image of grain #10 from irradiation creep sample IT450180, a_o<100> type edge on dislocation loops are highlighted in red.

Table B.2. 10 Results from dislocation loop analysis on grain #10 from irradiation creep sample IT450180.

Xtilt (θ_x)	Ytilt (θ_y)	TV Ztilt (θ_T)	LV Ztilt ($\theta_{<100>}$)			
-6.13	-27.55	-61	20			
Loop Normal angle to Tensile Axis	Number Density	Number Density Error	Size	Size Error	Fraction of Loops	Error in Fraction of loops
($\theta_{<100>}$)=11	55	7.416198	24.10505	2.38911	0.662651	0.089352
($\theta_{<010>}$)=79	28	5.291503	15.85714	1.420438	0.337349	0.063753

Orientation	Size (nm)	Actual Size (nm)	Orientation	Size (nm)	Actual Size (nm)	Scale Bar Ratio	Area (m^2)	Loop Density (1/m^3)
11	62	27.56	79	44	19.56	0.444444	2.5E-20	8.3E+20
11	38	16.89	79	32	14.22			
11	43	19.11	79	32	14.22			
11	60	26.67	79	50	22.22			
11	63	28.00	79	27	12.00			
11	102	45.33	79	35	15.56			
11	34	15.11	79	52	23.11			
11	43	19.11	79	30	13.33			
11	40	17.78	79	40	17.78			
11	52	23.11	79	41	18.22			
11	61	27.11	79	49	21.78			
11	39	17.33	79	33	14.67			
11	53	23.56	79	35	15.56			
11	109	48.44	79	35	15.56			
11	39	17.33	79	28	12.44			
11	61	27.11	79	50	22.22			
11	52	23.11	79	45	20.00			
11	63	28.00	79	38	16.89			
11	41	18.22	79	28	12.44			
11	58	25.78	79	37	16.44			
11	71	31.56	79	47	20.89			

11	59	26.22	79	31	13.78			
11	74	32.89	79	24	10.67			
11	79	35.11	79	29	12.89			
11	78	34.67	79	24	10.67			
11	113	50.22	79	28	12.44			
11	61	27.11	79	31	13.78			
11	68	30.22	79	24	10.67			
11	49	21.78						
11	54	24.00						
11	49	21.78						
11	45	20.00						
11	45	20.00						
11	36	16.00						
11	57	25.33						
11	35	15.56						
11	34	15.11						
11	49	21.78						
11	36	16.00						
11	42	18.67						
11	30	13.33						
11	60	26.67						
11	29	12.89						
11	48	21.33						
11	46	20.44						
11	23	10.22						
11	24	10.67						
11	57	25.33						
11	90	40.00						
11	20	8.89						
11	44	19.56						
11	70	31.11						
11	38	16.89						
11	80	35.56						

11	77	34.22						

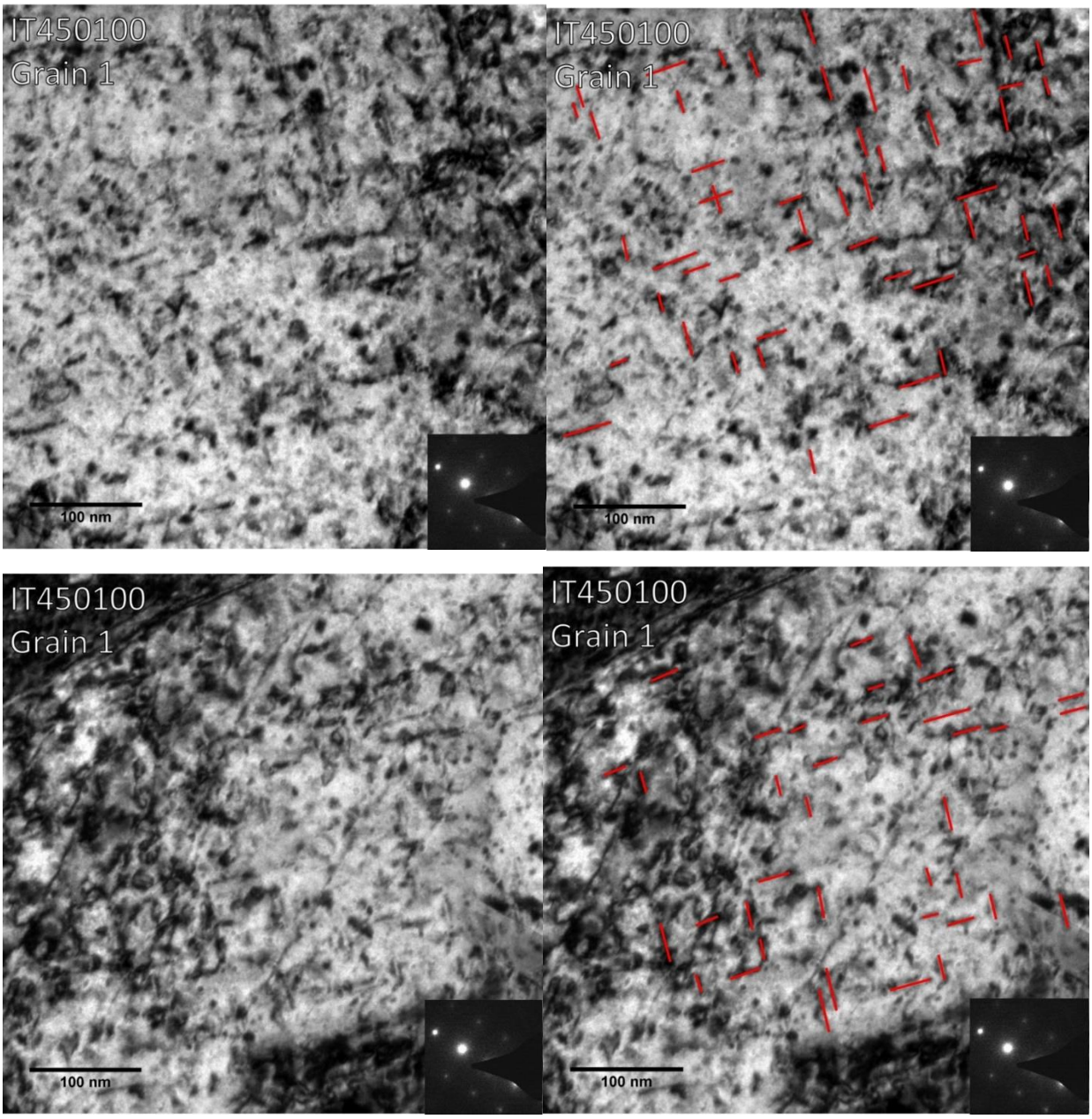
IT450100
Grain 1
100 nm
IT450100
Grain 1
100 nm
IT450100
Grain 1
100 nm
IT450100
Grain 1
100 nm

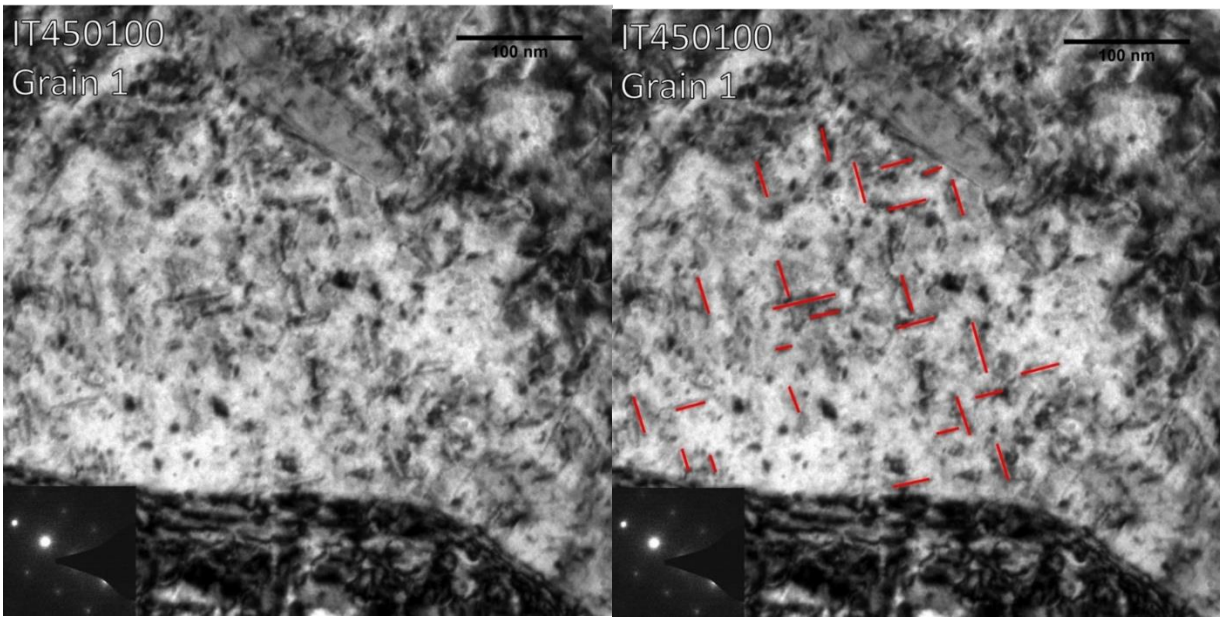

Figure B.3. 1 TEM image of grain #1 from irradiation creep sample IT450100, a_o<100> type edge on dislocation loops are highlighted in red.

Table B.3. 1 Results from dislocation loop analysis on grain #1 from irradiation creep sample IT450100.

Xtilt (θ_x)	Ytilt (θ_y)	TV Ztilt (θ_T)	LV Ztilt ($\theta_{<100>}$)			
4.23	0.22	45	106			
Loop Normal angle to Tensile Axis	Number Density	Number Density Error	Size	Size Error	Fraction of Loops	Error in Fraction of loops
($\theta_{<100>}$)=30	64	8	25.74437	1.582695	0.561403509	0.070175
($\theta_{<010>}$)=60	50	7.071068	25.25322	2.422985	0.438596491	0.062027

Orientation	Size (nm)	Actual Size (nm)	Orientation	Size (nm)	Actual Size (nm)	Scale Bar Ratio	Area (m^2)	Loop Density (1/m^3)
30	47	20.17	60	98	42.06	0.42	7.01E-20	1.62E+21
30	35	15.02	60	35	15.02			
30	58	24.89	60	88	37.77			
30	50	21.46	60	65	27.90			
30	38	16.31	60	65	27.90			
30	74	31.76	60	90	38.63			
30	46	19.74	60	55	23.61			
30	50	21.46	60	37	15.88			
30	54	23.18	60	55	23.61			
30	50	21.46	60	50	21.46			
30	62	26.61	60	50	21.46			
30	34	14.59	60	65	27.90			
30	57	24.46	60	90	38.63			
30	51	21.89	60	51	21.89			
30	71	30.47	60	85	36.48			
30	73	31.33	60	83	35.62			
30	62	26.61	60	85	36.48			
30	62	26.61	60	48	20.60			
30	80	34.33	60	46	19.74			
30	90	38.63	60	40	17.17			
30	53	22.75	60	46	19.74			

30	53	22.75	60	52	22.32			
30	55	23.61	60	48	20.60			
30	70	30.04	60	63	27.04			
30	75	32.19	60	62	26.61			
30	78	33.48	60	54	23.18			
30	65	27.90	60	31	13.30			
30	53	22.75	60	48	20.60			
30	68	29.18	60	82	35.19			
30	42	18.03	60	46	19.74			
30	65	27.90	60	26	11.16			
30	49	21.03	60	49	21.03			
30	39	16.74	60	72	30.90			
30	47	20.17	60	100	42.92			
30	80	34.33	60	50	21.46			
30	39	16.74	60	33	14.16			
30	57	24.46	60	49	21.03			
30	49	21.03	60	53	22.75			
30	39	16.74	60	51	21.89			
30	43	18.45	60	116	49.79			
30	65	27.90	60	26	11.16			
30	90	38.63	60	50	21.46			
30	90	38.63	60	58	24.89			
30	69	29.61	60	34	14.59			
30	43	18.45	60	70	30.04			
30	56	24.03	60	71	30.47			
30	70	30.04	60	65	27.90			
30	50	21.46	60	37	15.88			
30	50	21.46	60	49	21.03			
30	73	31.33	60	70	30.04			
30	74	31.76						
30	39	16.74						
30	36	15.45						
30	68	29.18						

30	73	31.33						
30	70	30.04						
30	52	22.32						
30	67	28.76						
30	72	30.90						
30	64	27.47						
30	69	29.61						
30	72	30.90						
30	98	42.06						
30	66	28.33						

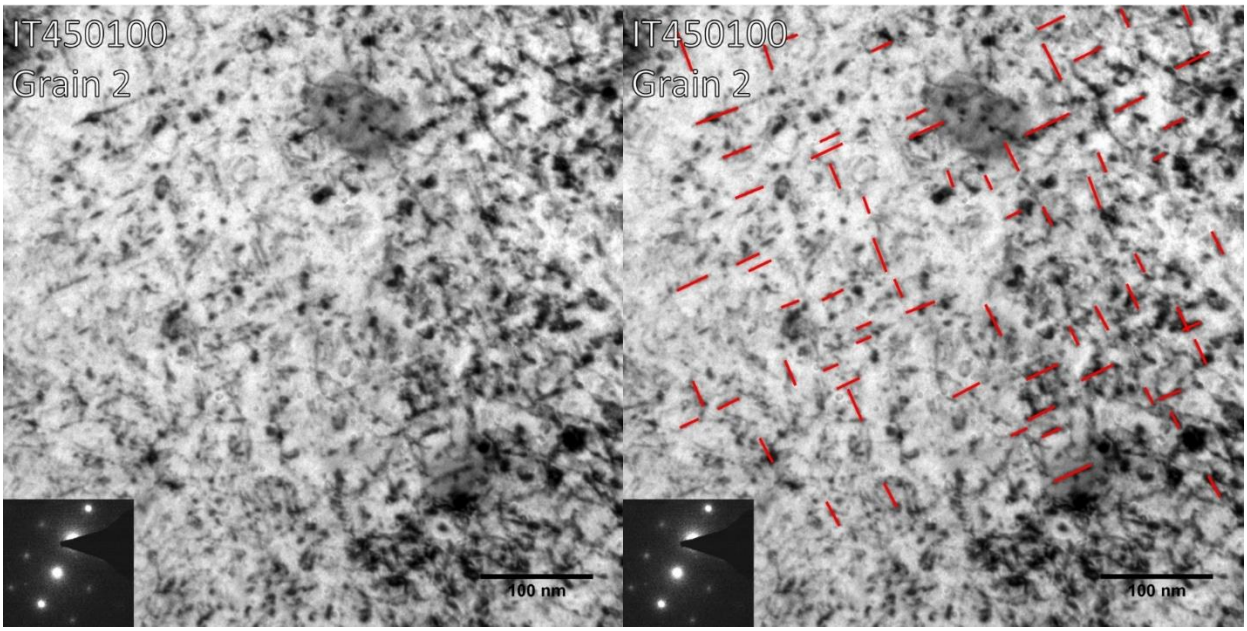

Figure B.3. 2 TEM image of grain #2 from irradiation creep sample IT450100, a_o<100> type edge on dislocation loops are highlighted in red.

Table B.3. 2 Results from dislocation loop analysis on grain #2 from irradiation creep sample IT450100.

Xtilt (θ_x)	Ytilt (θ_y)	TV Ztilt (θ_T)	LV Ztilt ($\theta_{<100>}$)			
4.23	0.22	45	106			
Loop Normal angle to Tensile Axis	Number Density	Number Density Error	Size	Size Error	Fraction of Loops	Error in Fraction of loops
($\theta_{<100>}$)=30	29	5.385165	22.53448	2.59098	0.557692308	0.103561
($\theta_{<010>}$)=60	23	4.795832	26.52174	3.400673	0.442307692	0.092228

Orientation	Size (nm)	Actual Size (nm)	Orientation	Size (nm)	Actual Size (nm)	Scale Bar Ratio	Area (m^2)	Loop Density (1/m^3)
30	93	46.5	60	81	40.5	0.5	3.16E-20	1.64E+21
30	52	26	60	27	13.5			
30	47	23.5	60	40	20			
30	48	24	60	52	26			

30	38	19	60	68	34			
30	72	36	60	50	25			
30	34	17	60	64	32			
30	46	23	60	31	15.5			
30	56	28	60	43	21.5			
30	44	22	60	38	19			
30	50	25	60	48	24			
30	50	25	60	72	36			
30	31	15.5	60	32	16			
30	26	13	60	56	28			
30	69	34.5	60	59	29.5			
30	35	17.5	60	60	30			
30	45	22.5	60	36	18			
30	37	18.5	60	32	16			
30	30	15	60	88	44			
30	50	25	60	66	33			
30	47	23.5	60	50	25			
30	51	25.5	60	60	30			
30	41	20.5	60	67	33.5			
30	40	20						
30	34	17						
30	30	15						
30	37	18.5						
30	31	15.5						
30	43	21.5						

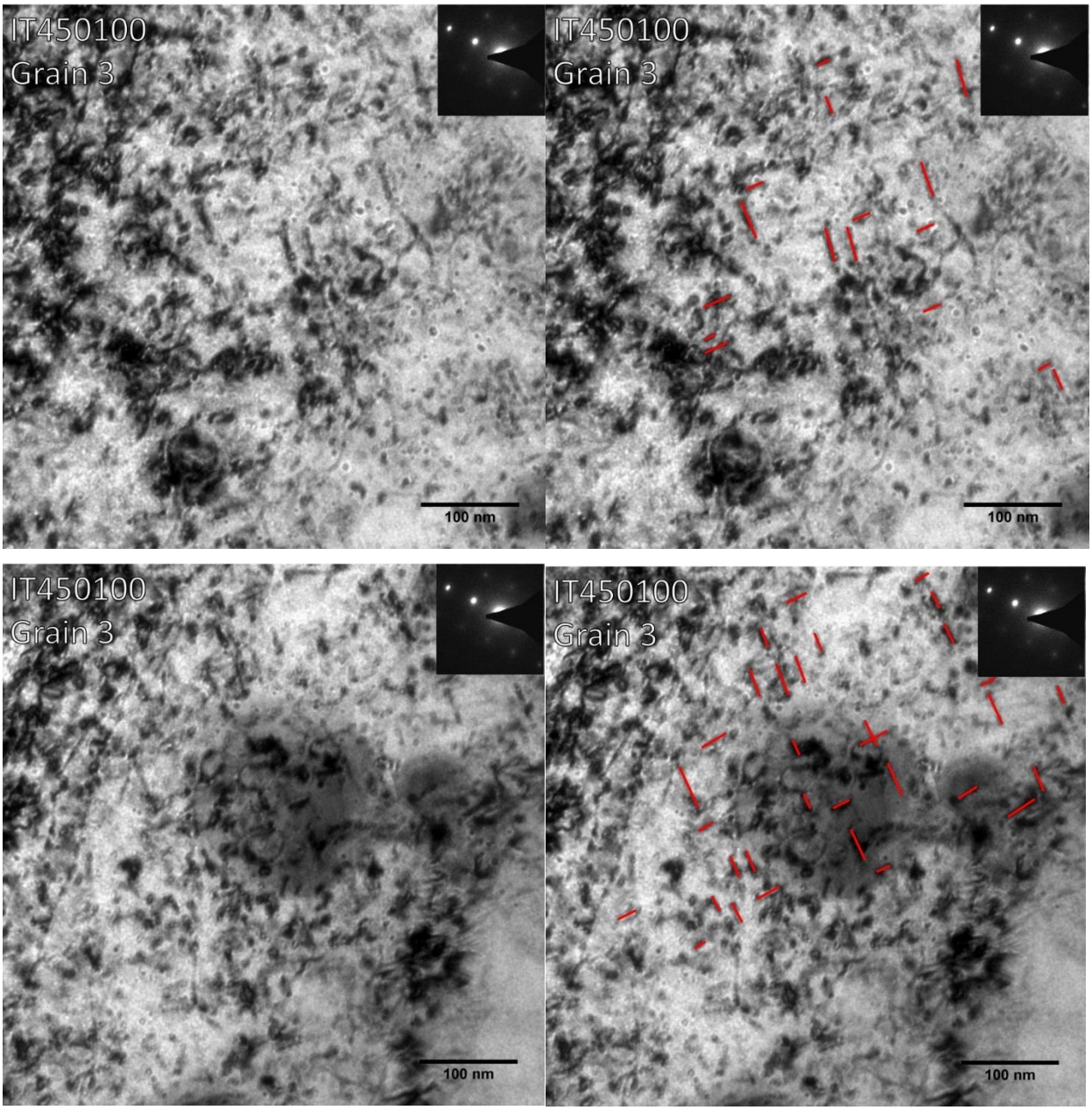
IT450100
Grain 3
100 nm
IT450100
Grain 3
100 nm
IT450100
Grain 3
100 nm
IT450100
Grain 3
100 nm

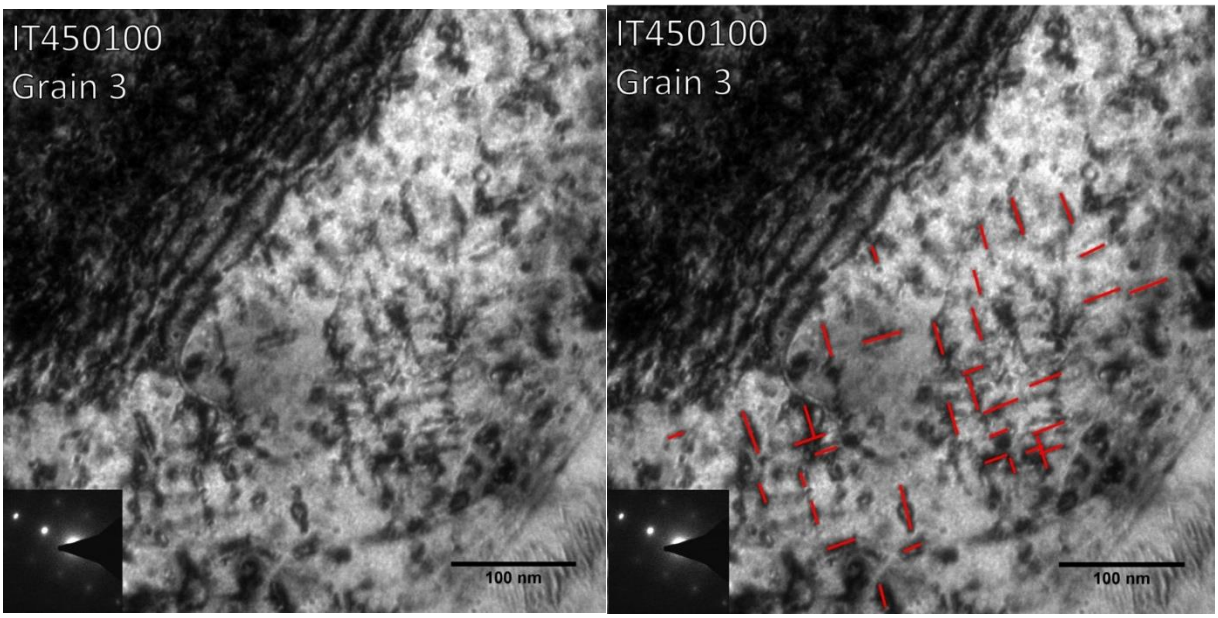

Figure B.3. 3 TEM image of grain #3 from irradiation creep sample IT450100, a_o<100> type edge on dislocation loops are highlighted in red.

Table B.3. 3 Results from dislocation loop analysis on grain #3 from irradiation creep sample IT450100.

Xtilt (θ_x)	Ytilt (θ_y)	TV Ztilt (θ_T)	LV Ztilt ($\theta_{<100>}$)			
0.7	3.13	45	22			
Loop Normal angle to Tensile Axis	Number Density	Number Density Error	Size	Size Error	Fraction of Loops	Error in Fraction of loops
($\theta_{<100>}$)=30	46	6.78233	27.5434783	2.402398	0.560976	0.08271134
($\theta_{<010>}$)=60	36	6	21.9444444	2.362986	0.439024	0.07317073

Orientation	Size (nm)	Actual Size (nm)	Orientation	Size (nm)	Actual Size (nm)	Scale Bar Ratio	Area (m^2)	Loop Density (1/m^3)
30	84	42	60	60	30	0.5	6.33E-20	1.29E+21
30	70	35	60	22	11			
30	38	19	60	50	25			
30	70	35	60	34	17			

30	73	36.5	60	32	16			
30	75	37.5	60	30	15			
30	42	21	60	32	16			
30	34	17	60	28	14			
30	44	22	60	22	11			
30	97	48.5	60	43	21.5			
30	44	22	60	22	11			
30	45	22.5	60	32	16			
30	60	30	60	53	26.5			
30	34	17	60	50	25			
30	34	17	60	37	18.5			
30	40	20	60	31	15.5			
30	65	32.5	60	48	24			
30	57	28.5	60	60	30			
30	68	34	60	31	15.5			
30	43	21.5	60	45	22.5			
30	60	30	60	65	32.5			
30	74	37	60	30	15			
30	40	20	60	57	28.5			
30	40	20	60	40	20			
30	67	33.5	60	50	25			
30	55	27.5	60	64	32			
30	40	20	60	30	15			
30	82	41	60	38	19			
30	39	19.5	60	62	31			
30	27	13.5	60	56	28			
30	45	22.5	60	48	24			
30	57	28.5	60	70	35			
30	60	30	60	75	37.5			
30	47	23.5	60	56	28			
30	85	42.5	60	37	18.5			
30	29	14.5	60	40	20			
30	66	33						

30	64	32						
30	64	32						
30	58	29						
30	31	15.5						
30	50	25						
30	50	25						
30	59	29.5						
30	68	34						
30	60	30						

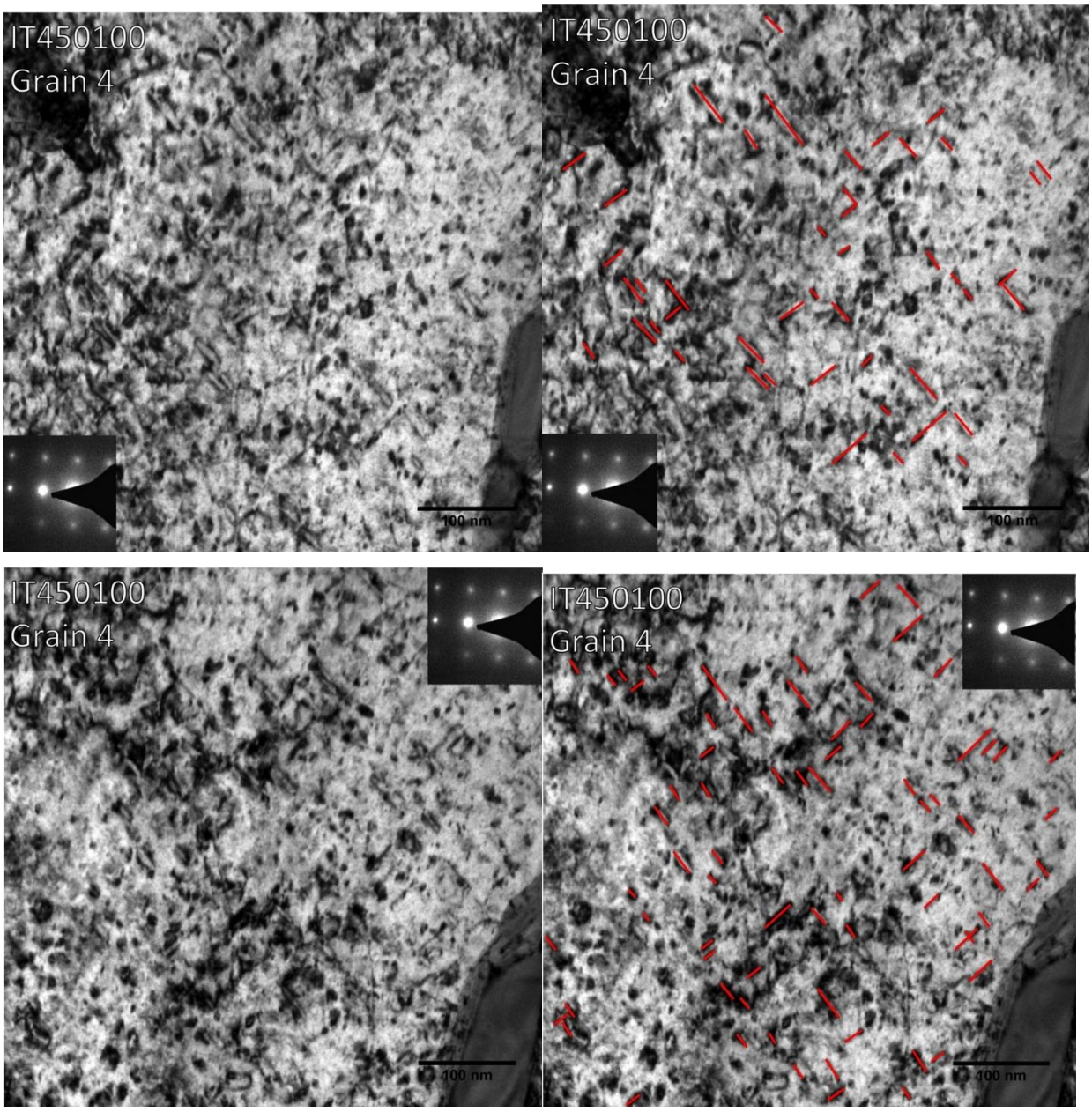
IT450100
Grain 4
100 nm
IT450100
Grain 4
100 nm
IT450100
Grain 4
100 nm
IT450100
Grain 4
100 nm

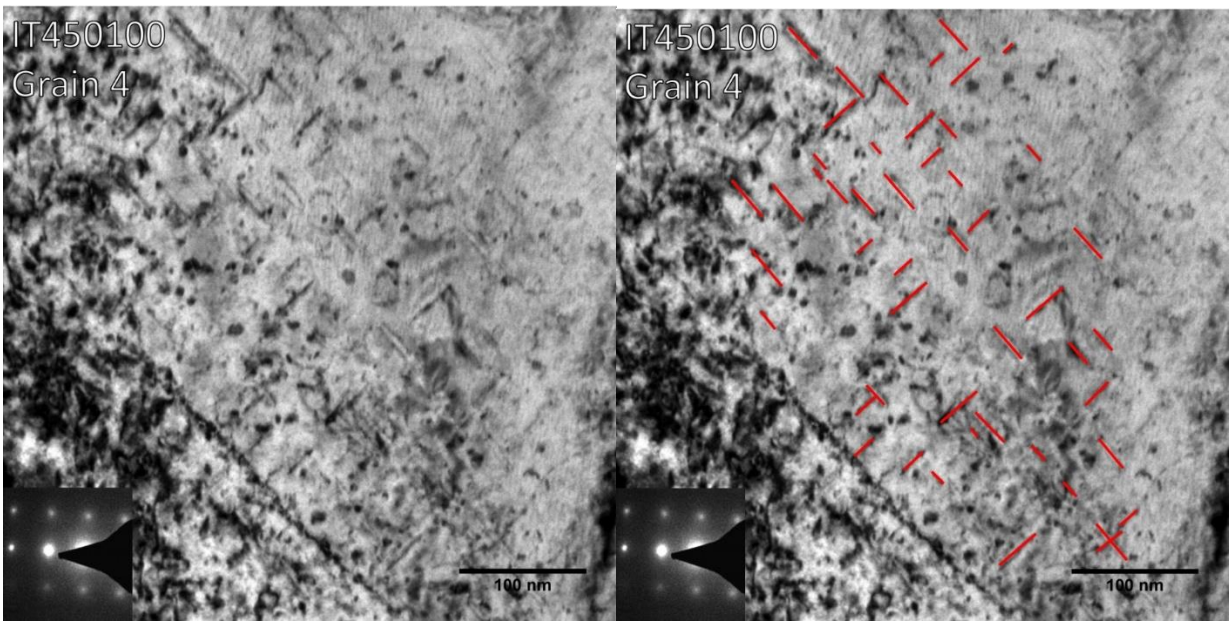

Figure B.3. 4 TEM image of grain #4 from irradiation creep sample IT450100, a_o<100> type edge on dislocation loops are highlighted in red.

Table B.3. 4 Results from dislocation loop analysis on grain #4 from irradiation creep sample IT450100.

Xtilt (θ_x)	Ytilt (θ_y)	TV Ztilt (θ_T)	LV Ztilt ($\theta_{<100>}$)			
2.74	-3.1	45	22			
Loop Normal angle to Tensile Axis	Number Density	Number Density Error	Size	Size Error	Fraction of Loops	Error in Fraction of loops
($\theta_{<100>}$)=7	100	10	22.07609	2.086371	0.617284	0.061728
($\theta_{<010>}$)=83	62	7.874008	23.06944	1.991396	0.382716	0.048605

Orientation	Size (nm)	Actual Size (nm)	Orientation	Size (nm)	Actual Size (nm)	Scale Bar Ratio	Area (m^2)	Loop Density (1/m^3)
7	40	20	83	60	30	0.5	9.50E-20	1.7E+21
7	67	33.5	83	51	25.5			
7	66	33	83	57	28.5			
7	29	14.5	83	42	21			

7	31	15.5	83	35	17.5			
7	33	16.5	83	55	27.5			
7	75	37.5	83	60	30			
7	63	31.5	83	89	44.5			
7	65	32.5	83	29	14.5			
7	24	12	83	93	46.5			
7	95	47.5	83	26	13			
7	50	25	83	38	19			
7	25	12.5	83	45	22.5			
7	53	26.5	83	52	26			
7	29	14.5	83	44	22			
7	34	17	83	30	15			
7	25	12.5	83	30	15			
7	80	40	83	36	18			
7	58	29	83	29	14.5			
7	26	13	83	33	16.5			
7	127	63.5	83	38	19			
7	44	22	83	43	21.5			
7	50	25	83	40	20			
7	43	21.5	83	76	38			
7	43	21.5	83	35	17.5			
7	27	13.5	83	49	24.5			
7	27	13.5	83	44	22			
7	52	26	83	44	22			
7	66	33	83	59	29.5			
7	31	15.5	83	38	19			
7	31	15.5	83	53	26.5			
7	47	23.5	83	65	32.5			
7	33	16.5	83	34	17			
7	35	17.5	83	32	16			
7	35	17.5	83	34	17			
7	21	10.5	83	43	21.5			
7	21	10.5	83	35	17.5			

7	35	17.5	83	101	50.5			
7	42	21	83	48	24			
7	27	13.5	83	80	40			
7	31	15.5	83	56	28			
7	34	17	83	75	37.5			
7	58	29	83	30	15			
7	30	15	83	72	36			
7	47	23.5	83	24	12			
7	26	13	83	70	35			
7	56	28	83	51	25.5			
7	28	14	83	31	15.5			
7	28	14	83	49	24.5			
7	40	20	83	46	23			
7	70	35	83	55	27.5			
7	30	15	83	82	41			
7	30	15	83	43	21.5			
7	44	22	83	48	24			
7	32	16	83	48	24			
7	37	18.5	83	89	44.5			
7	87	43.5	83	82	41			
7	63	31.5	83	54	27			
7	42	21	83	36	18			
7	36	18	83	60	30			
7	40	20	83	82	41			
7	69	34.5	83	50	25			
7	73	36.5						
7	40	20						
7	52	26						
7	36	18						
7	36	18						
7	36	18						
7	51	25.5						
7	68	34						

7	37	18.5						
7	66	33						
7	41	20.5						
7	85	42.5						
7	88	44						
7	43	21.5						
7	28	14						
7	84	42						
7	69	34.5						
7	35	17.5						
7	63	31.5						
7	77	38.5						
7	72	36						
7	73	36.5						
7	72	36						
7	49	24.5						
7	36	18						
7	38	19						
7	77	38.5						
7	56	28						
7	76	38						
7	69	34.5						
7	83	41.5						
7	40	20						
7	21	10.5						
7	21	10.5						
7	27	13.5						
7	33	16.5						
7	34	17						

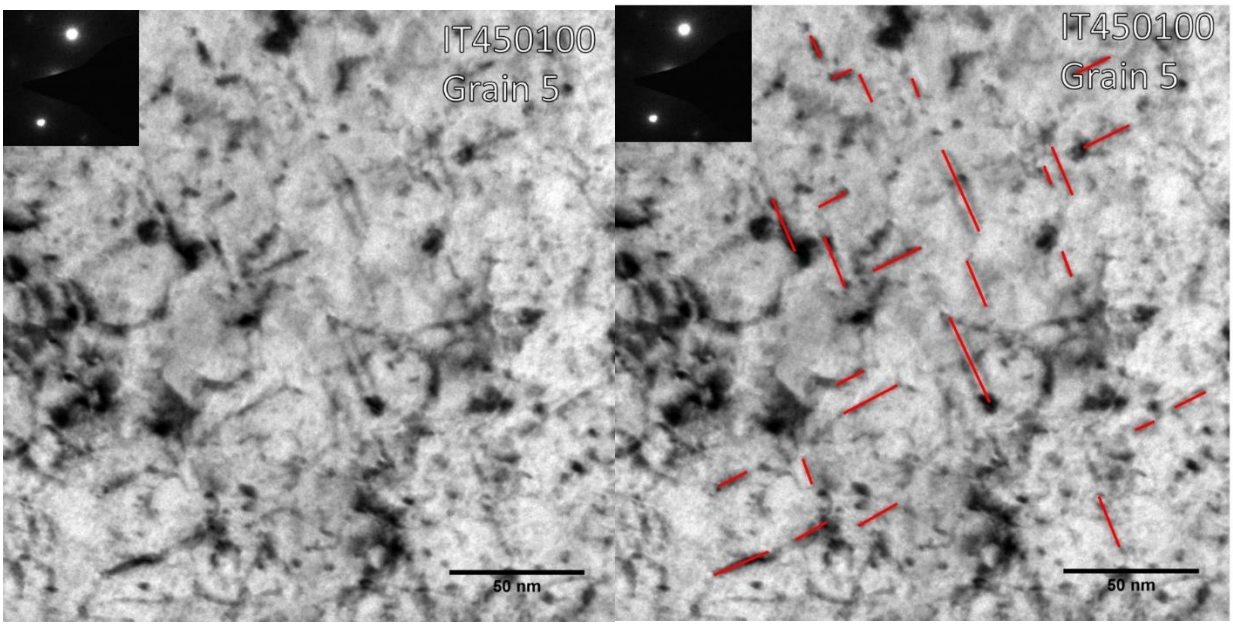

Figure B.3. 5 TEM image of grain #5 from irradiation creep sample IT450100, a_o<100> type edge on dislocation loops are highlighted in red.

Table B.3. 5 Results from dislocation loop analysis on grain #5 from irradiation creep sample IT450100.

Xtilt (θ_x)	Ytilt (θ_y)	TV Ztilt (θ_T)	LV Ztilt ($\theta_{<100>}$)			
2.74	-3.1	-10	22			
Loop Normal angle to Tensile Axis	Number Density	Number Density Error	Size	Size Error	Fraction of Loops	Error in Fraction of loops
($\theta_{<100>}$)=35	13	3.605551	17.82051	4.858735	0.5	0.138675
($\theta_{<010>}$)=55	13	3.605551	14.18269	2.513933	0.5	0.138675

Orientation	Size (nm)	Actual Size (nm)	Orientation	Size (nm)	Actual Size (nm)	Scale Bar Ratio	Area (m^2)	Loop Density (1/m^3)
35	105	21.88	55	53	11.04	0.21	1.65E-20	1.57E+21
35	50	10.42	55	100	20.83			
35	98	20.42	55	60	12.50			
35	50	10.42	55	78	16.25			

35	55	11.46	55	103	21.46			
35	42	8.75	55	58	12.08			
35	167	34.79	55	48	10.00			
35	95	19.79	55	35	7.29			
35	160	33.33	55	91	18.96			
35	101	21.04	55	74	15.42			
35	37	7.71	55	86	17.92			
35	52	10.83	55	57	11.88			
35	100	20.83	55	42	8.75			

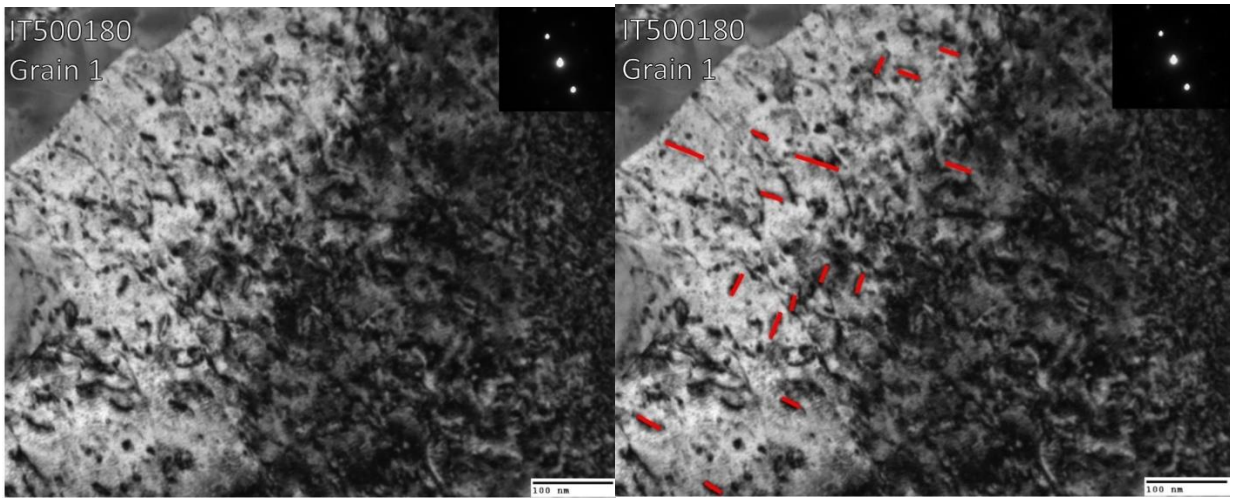

Figure B.4. 1 TEM image of grain #1 from irradiation creep sample IT500180, a_o<100> type edge on dislocation loops are highlighted in red.

Table B.4. 1 Results from dislocation loop analysis on grain #1 from irradiation creep sample IT500180.

Xtilt (θ_x)	Ytilt (θ_y)	TV Ztilt (θ_T)	LV Ztilt ($\theta_{<100>}$)			
-5.3	-2	111	71			
Loop Normal angle to Tensile Axis	Number Density	Number Density Error	Size	Size Error	Fraction of Loops	Error in Fraction of loops
($\theta_{<100>}$)=40	10	3.162	29.33	7.114	0.625	0.197
($\theta_{<010>}$)=50	6	2.449	21.47	4.424	0.375	0.153

Orientation	Size (nm)	Actual Size (nm)	Orientation	Size (nm)	Actual Size (nm)	Scale Bar Ratio	Area (m^2)	Loop Density (1/m^3)
40	19	18.27	50	20	19.23	1.85	4.57912E-20	4.579E+20
40	44	42.31	50	22	21.15			
40	38	36.54	50	32	30.77			
40	14	13.46	50	15	14.42			
40	28	26.92	50	20	19.23			
40	53	50.96	50	25	24.04			
40	33	31.73						
40	21	20.19						

40	30	28.85						
40	25	24.04						

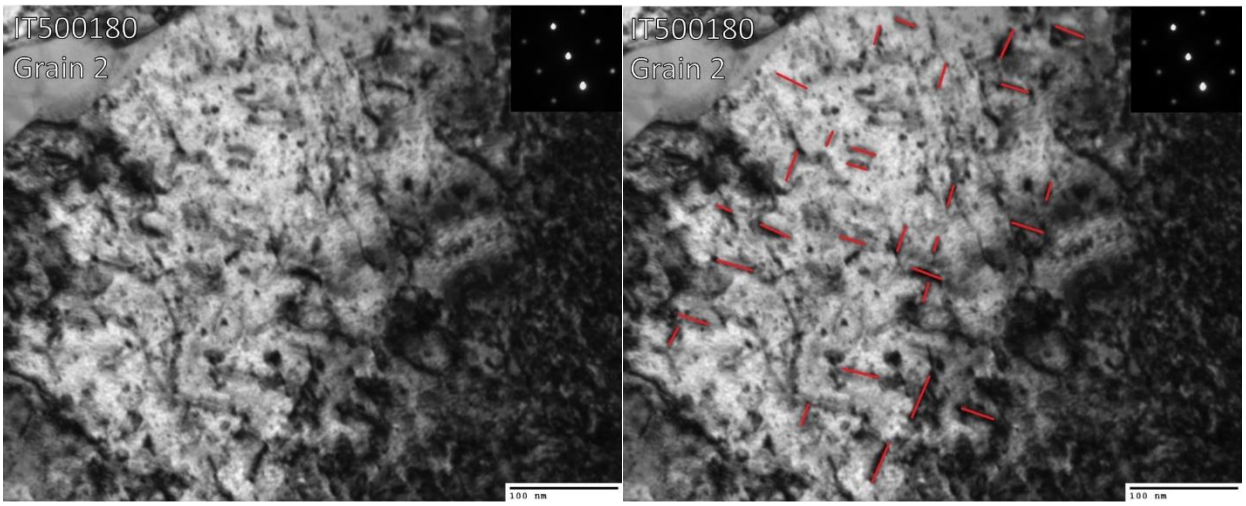

Figure B.4. 2 TEM image of grain #2 from irradiation creep sample IT500180, a_o<100> type edge on dislocation loops are highlighted in red.

Table B.4. 2 Results from dislocation loop analysis on grain #2 from irradiation creep sample IT500180.

Xtilt (θ_x)	Ytilt (θ_y)	TV Ztilt (θ_T)	LV Ztilt ($\theta_{<100>}$)			
-5.2	-5.8	111	71			
Loop Normal angle to Tensile Axis	Number Density	Number Density Error	Size	Size Error	Fraction of Loops	Error in Fraction of loops
($\theta_{<100>}$)=40	15	3.872983	27.46	2.953792	0.517241	0.133551
($\theta_{<010>}$)=50	14	3.741657	24.25	3.053178	0.482759	0.129023

Orientation	Size (nm)	Actual Size (nm)	Orientation	Size (nm)	Actual Size (nm)	Scale Bar Ratio	Area (m^2)	Loop Density (1/m^3)
40	43	32.09	50	27	20.15	1.34	2.58868E-20	1.12E+21
40	22	16.42	50	40	29.85			
40	40	29.85	50	26	19.40			
40	47	35.07	50	21	15.67			
40	42	31.34	50	33	24.63			
40	26	19.40	50	35	26.12			
40	28	20.90	50	32	23.88			
40	27	20.15	50	38	28.36			

40	34	25.37	50	31	23.13			
40	47	35.07	50	20	14.93			
40	38	28.36	50	24	17.91			
40	37	27.61	50	48	35.82			
40	37	27.61	50	57	42.54			
40	42	31.34	50	23	17.16			
40	42	31.34						

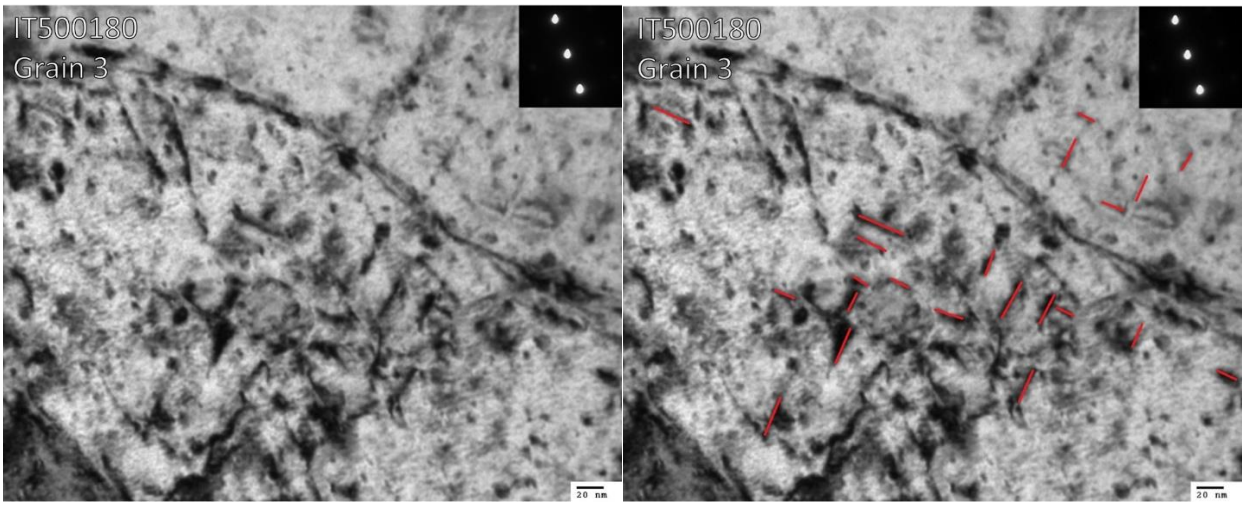

Figure B.4. 3 TEM image of grain #3 from irradiation creep sample IT500180, a_o<100> type edge on dislocation loops are highlighted in red.

Table B.4. 3 Results from dislocation loop analysis on grain #3 from irradiation creep sample IT500180.

Xtilt (θ_x)	Ytilt (θ_y)	TV Ztilt (θ_T)	LV Ztilt ($\theta_{<100>}$)			
-2.8	-5.8	111	71			
Loop Normal angle to Tensile Axis	Number Density	Number Density Error	Size	Size Error	Fraction of Loops	Error in Fraction of loops
($\theta_{<100>}$)=40	11	3.316625	20.11	4.366307	0.55	0.165831
($\theta_{<010>}$)=50	9	3	24.25	3.629567	0.45	0.15

Orientation	Size (nm)	Actual Size (nm)	Orientation	Size (nm)	Actual Size (nm)	Scale Bar Ratio	Area (m^2)	Loop Density (1/m^3)
40	50	29.41	50	54	31.76	1.7	2.19451E-20	9.11365E+20
40	28	16.47	50	27	15.88			
40	60	35.29	50	51	30.00			
40	46	27.06	50	38	22.35			
40	22	12.94	50	52	30.59			
40	26	15.29	50	40	23.53			
40	38	22.35	50	42	24.71			
40	25	14.71	50	35	20.59			

40	30	17.65	50	32	18.82			
40	25	14.71						
40	26	15.29						

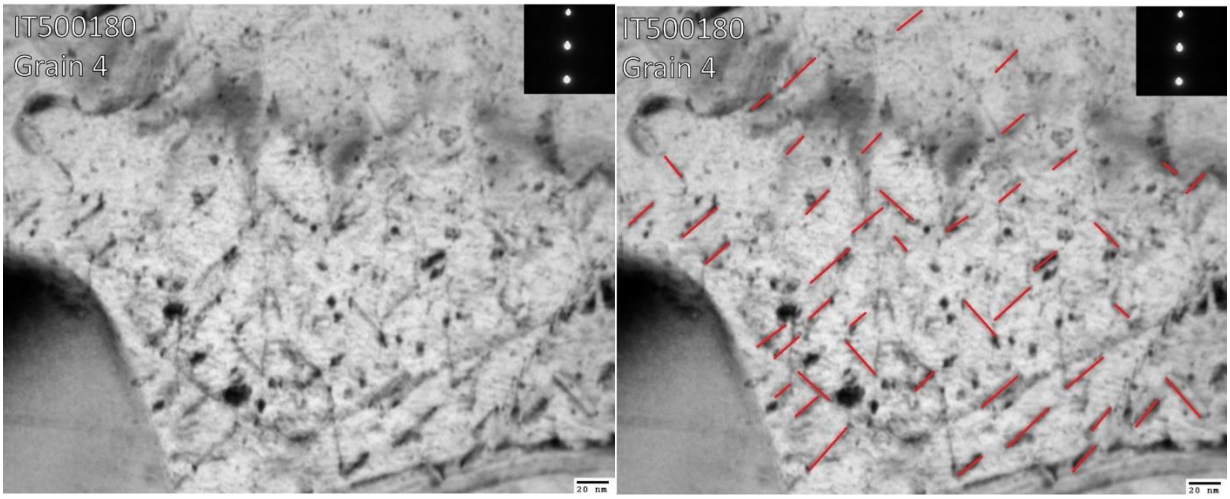

Figure B.4. 4 TEM image of grain #4 from irradiation creep sample IT500180, a_o<100> type edge on dislocation loops are highlighted in red.

Table B.4. 4 Results from dislocation loop analysis on grain #4 from irradiation creep sample IT500180.

Xtilt (θ_x)	Ytilt (θ_y)	TV Ztilt (θ_T)	LV Ztilt ($\theta_{<100>}$)			
-4.8	3.8	111	41			
Loop Normal angle to Tensile Axis	Number Density	Number Density Error	Size	Size Error	Fraction of Loops	Error in Fraction of loops
($\theta_{<100>}$)=20	33	5.744563	23.17	1.792106	0.767442	0.133594
($\theta_{<010>}$)=70	10	3.162278	23.95	5.198263	0.232558	0.073541

Orientation	Size (nm)	Actual Size (nm)	Orientation	Size (nm)	Actual Size (nm)	Scale Bar Ratio	Area (m^2)	Loop Density (1/m^3)
20	43	22.63	70	33	17.37	1.9	1.70853E-20	2.51678E+21
20	30	15.79	70	55	28.95			
20	56	29.47	70	24	12.63			
20	41	21.58	70	56	29.47			
20	61	32.11	70	58	30.53			
20	34	17.89	70	66	34.74			
20	43	22.63	70	44	23.16			
20	43	22.63	70	26	13.68			

20	37	19.47	70	25	13.16			
20	40	21.05	70	68	35.79			
20	46	24.21						
20	69	36.32						
20	52	27.37						
20	38	20.00						
20	43	22.63						
20	41	21.58						
20	34	17.89						
20	37	19.47						
20	40	21.05						
20	28	14.74						
20	29	15.26						
20	37	19.47						
20	36	18.95						
20	63	33.16						
20	36	18.95						
20	37	19.47						
20	61	32.11						
20	41	21.58						
20	74	38.95						
20	60	31.58						
20	41	21.58						
20	37	19.47						
20	45	23.68						

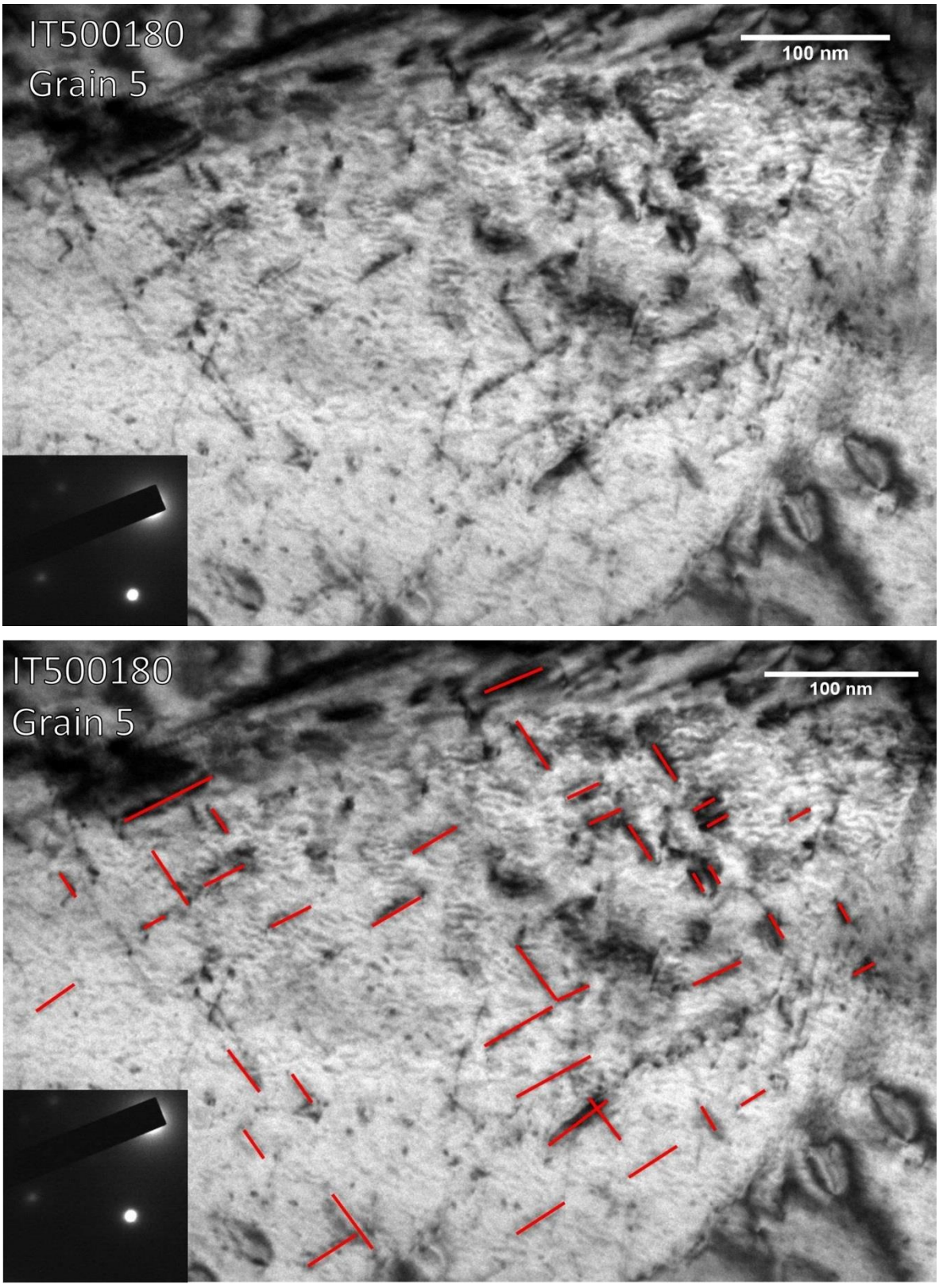

Figure B.4. 5 TEM image of grain #5 from irradiation creep sample IT500180, a_o<100> type edge on dislocation loops are highlighted in red.

Table B.4. 5 Results from dislocation loop analysis on grain #5 from irradiation creep sample IT500180.

Xtilt (θ_x)	Ytilt (θ_y)	TV Ztilt (θ_T)	LV Ztilt ($\theta_{<100>}$)			
3.1	5.8	-98	32			
Loop Normal angle to Tensile Axis	Number Density	Number Density Error	Size	Size Error	Fraction of Loops	Error in Fraction of loops
($\theta_{<100>}$)=40	24	4.898979	30.875	5.331662	0.585366	0.119487
($\theta_{<010>}$)=50	17	4.123106	26.11765	4.862043	0.414634	0.100564

Orientation	Size (nm)	Actual Size (nm)	Orientation	Size (nm)	Actual Size (nm)	Scale Bar Ratio	Area (m^2)	Loop Density (1/m^3)
40	30	30	50	17	17	1	2.6125E-20	1.57E+21
40	16	16	50	42	42			
40	64	64	50	18	18			
40	31	31	50	35	35			
40	36	36	50	25	25			
40	28	28	50	29	29			
40	35	35	50	44	44			
40	32	32	50	31	31			
40	49	49	50	22	22			
40	34	34	50	22	22			
40	54	54	50	15	15			
40	47	47	50	15	15			
40	37	37	50	20	20			
40	21	21	50	15	15			
40	33	33	50	33	33			
40	39	39	50	43	43			
40	22	22	50	18	18			
40	22	22						
40	15	15						
40	15	15						
40	15	15						
40	34	34						
40	14	14						
40	18	18						

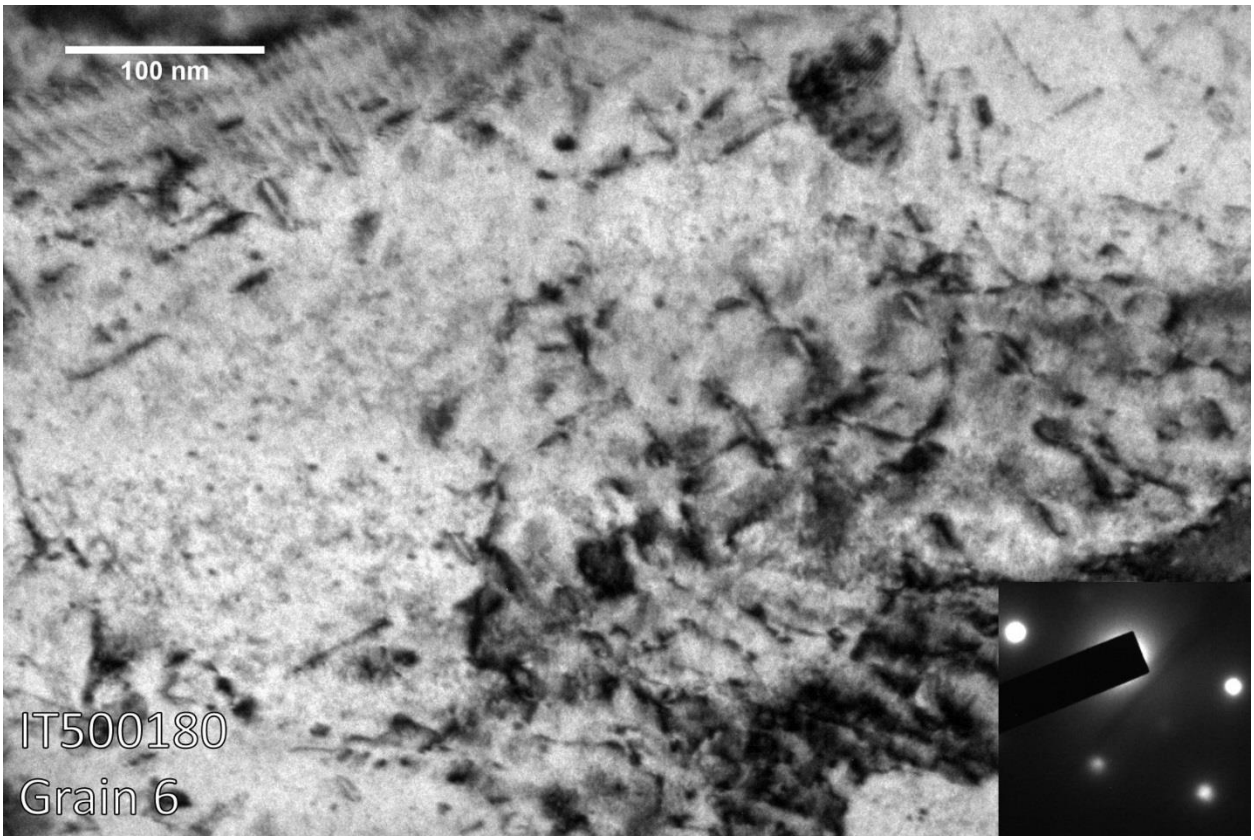
100 nm
IT500180
Grain 6

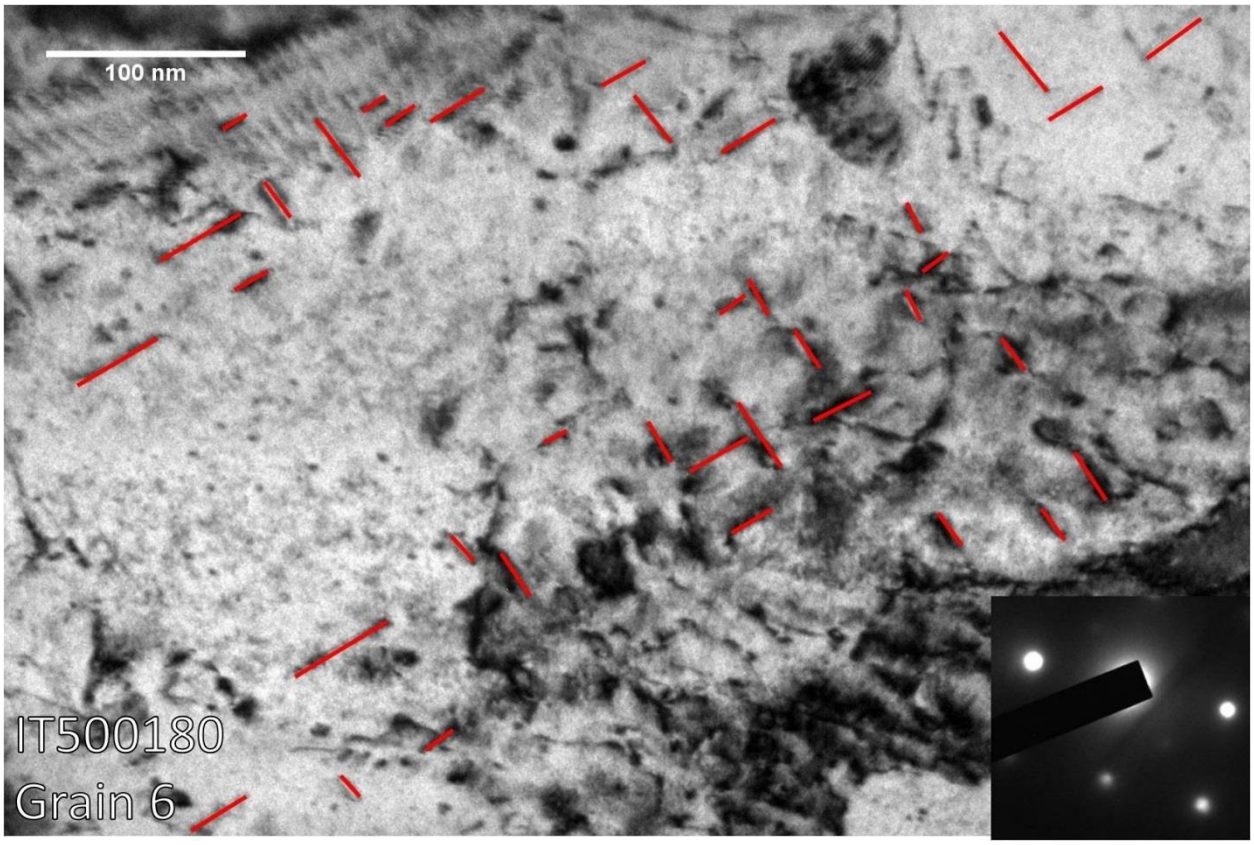
100 nm
IT500180
Grain 6

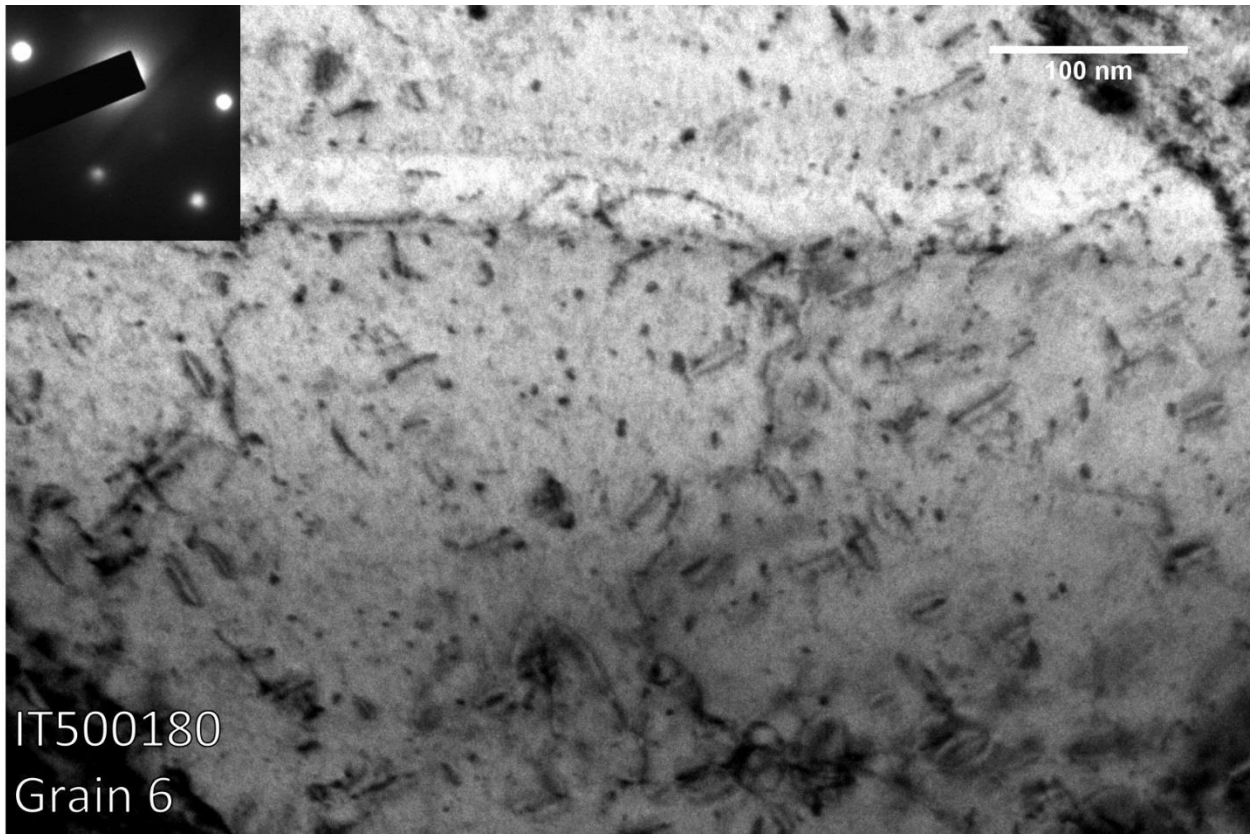
100 nm
IT500180
Grain 6

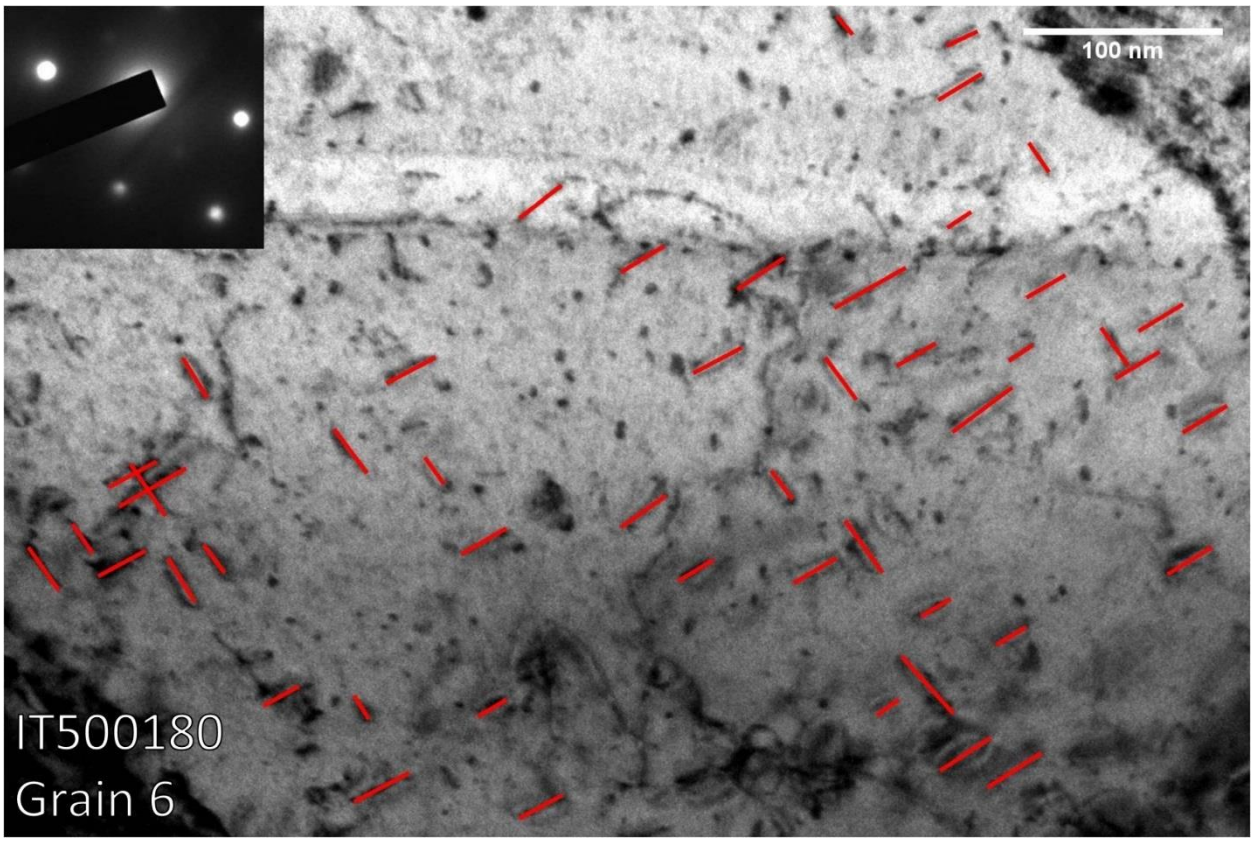
100 nm
IT500180
Grain 6

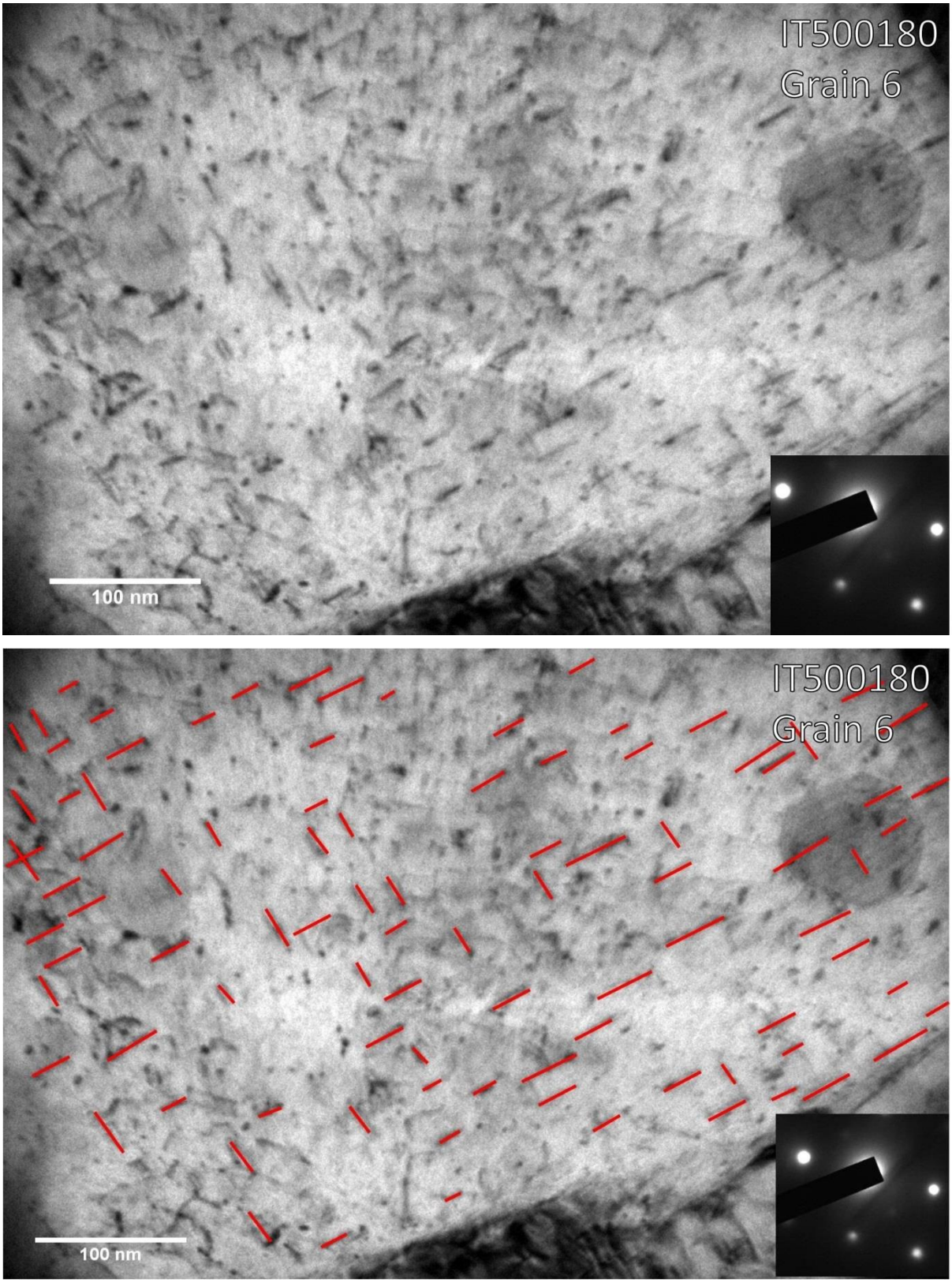

Figure B.4. 6 TEM image of grain #6 from irradiation creep sample IT500180, a_o<100> type edge on dislocation loops are highlighted in red.

Table B.4. 6 Results from dislocation loop analysis on grain #6 from irradiation creep sample IT500180.

Xtilt (θ_x)	Ytilt (θ_y)	TV Ztilt (θ_T)	LV Ztilt ($\theta_{<100>}$)			
7.5	2.2	-98	28			
Loop Normal angle to Tensile Axis	Number Density	Number Density Error	Size	Size Error	Fraction of Loops	Error in Fraction of loops
($\theta_{<100>}$)=36	110	10.48809	23.91818	1.62052	0.654762	0.062429
($\theta_{<010>}$)=54	58	7.615773	22.7931	1.753315	0.345238	0.045332

Orientation	Size (nm)	Actual Size (nm)	Orientation	Size (nm)	Actual Size (nm)	Scale Bar Ratio	Area (m^2)	Loop Density (1/m^3)
36	38	38	54	21	21	1	7.8375E-20	2.14E+21
36	44	44	54	36	36			
36	47	47	54	29	29			
36	12	12	54	39	39			
36	18	18	54	16	16			
36	13	13	54	19	19			
36	17	17	54	15	15			
36	30	30	54	22	22			
36	27	27	54	19	19			
36	33	33	54	27	27			
36	31	31	54	17	17			
36	32	32	54	18	18			
36	15	15	54	39	39			
36	13	13	54	23	23			
36	15	15	54	26	26			
36	36	36	54	17	17			
36	34	34	54	13	13			
36	23	23	54	26	26			
36	24	24	54	15	15			
36	40	40	54	31	31			
36	27	27	54	28	28			
36	19	19	54	16	16			
36	31	31	54	23	23			
36	16	16	54	27	27			
36	22	22	54	12	12			
36	26	26	54	17	17			

36	25	25	54	17	17			
36	26	26	54	40	40			
36	26	26	54	35	35			
36	29	29	54	26	26			
36	18	18	54	12	12			
36	24	24	54	19	19			
36	23	23	54	22	22			
36	13	13	54	21	21			
36	30	30	54	23	23			
36	32	32	54	26	26			
36	16	16	54	29	29			
36	16	16	54	32	32			
36	27	27	54	24	24			
36	38	38	54	33	33			
36	24	24	54	25	25			
36	37	37	54	24	24			
36	15	15	54	22	22			
36	11	11	54	16	16			
36	18	18	54	21	21			
36	24	24	54	18	18			
36	25	25	54	21	21			
36	25	25	54	19	19			
36	25	25	54	20	20			
36	25	25	54	22	22			
36	13	13	54	18	18			
36	16	16	54	15	15			
36	16	16	54	21	21			
36	15	15	54	22	22			
36	27	27	54	17	17			
36	15	15	54	19	19			
36	21	21	54	31	31			
36	31	31	54	21	21			
36	36	36						
36	9	9						
36	17	17						
36	17	17						
36	23	23						
36	30	30						
36	16	16						
36	12	12						
36	14	14						

36	33	33						
36	15	15						
36	25	25						
36	25	25						
36	25	25						
36	25	25						
36	25	25						
36	25	25						
36	37	37						
36	25	25						
36	16	16						
36	12	12						
36	12	12						
36	25	25						
36	26	26						
36	26	26						
36	15	15						
36	12	12						
36	15	15						
36	11	11						
36	15	15						
36	28	28						
36	39	39						
36	27	27						
36	20	20						
36	25	25						
36	25	25						
36	27	27						
36	14	14						
36	15	15						
36	32	32						
36	39	39						
36	15	15						
36	14	14						
36	26	26						
36	34	34						
36	43	43						
36	28	28						
36	44	44						
36	25	25						
36	26	26						

36	34	34						
36	23	23						

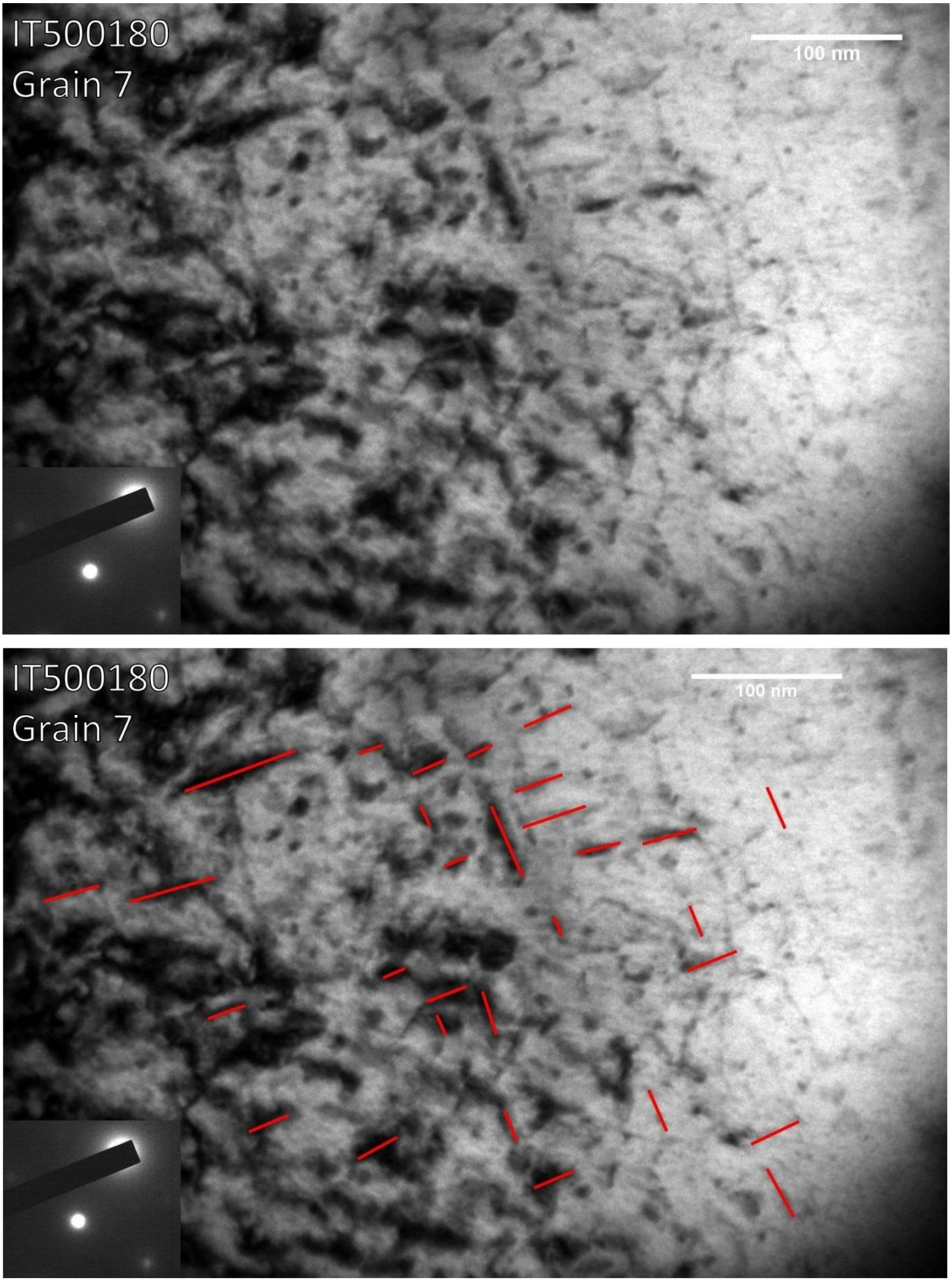

Figure B.4. 7 TEM image of grain #7 from irradiation creep sample IT500180, a_o<100> type edge on dislocation loops are highlighted in red.

Table B.4. 7 Results from dislocation loop analysis on grain #7 from irradiation creep sample IT500180.

Xtilt (θ_x)	Ytilt (θ_y)	TV Ztilt (θ_T)	LV Ztilt ($\theta_{<100>}$)			
-15	10.5	-98	-78			
Loop Normal angle to Tensile Axis	Number Density	Number Density Error	Size	Size Error	Fraction of Loops	Error in Fraction of loops
($\theta_{<100>}$)=20	20	4.472136	31.55	6.408922	0.689655	0.154212
($\theta_{<010>}$)=70	9	3	25.66667	7.97495	0.310345	0.103448

Orientation	Size (nm)	Actual Size (nm)	Orientation	Size (nm)	Actual Size (nm)	Scale Bar Ratio	Area (m^2)	Loop Density (1/m^3)
20	39	39	70	14	14	1	2.61E-20	1.11E+21
20	56	56	70	14	14			
20	76	76	70	30	30			
20	24	24	70	24	24			
20	26	26	70	50	50			
20	30	30	70	22	22			
20	16	16	70	30	30			
20	15	15	70	35	35			
20	21	21	70	12	12			
20	16	16						
20	27	27						
20	28	28						
20	34	34						
20	32	32						
20	44	44						
20	26	26						
20	37	37						
20	34	34						
20	33	33						
20	17	17						

Appendix C: Dislocation Network TEM Image

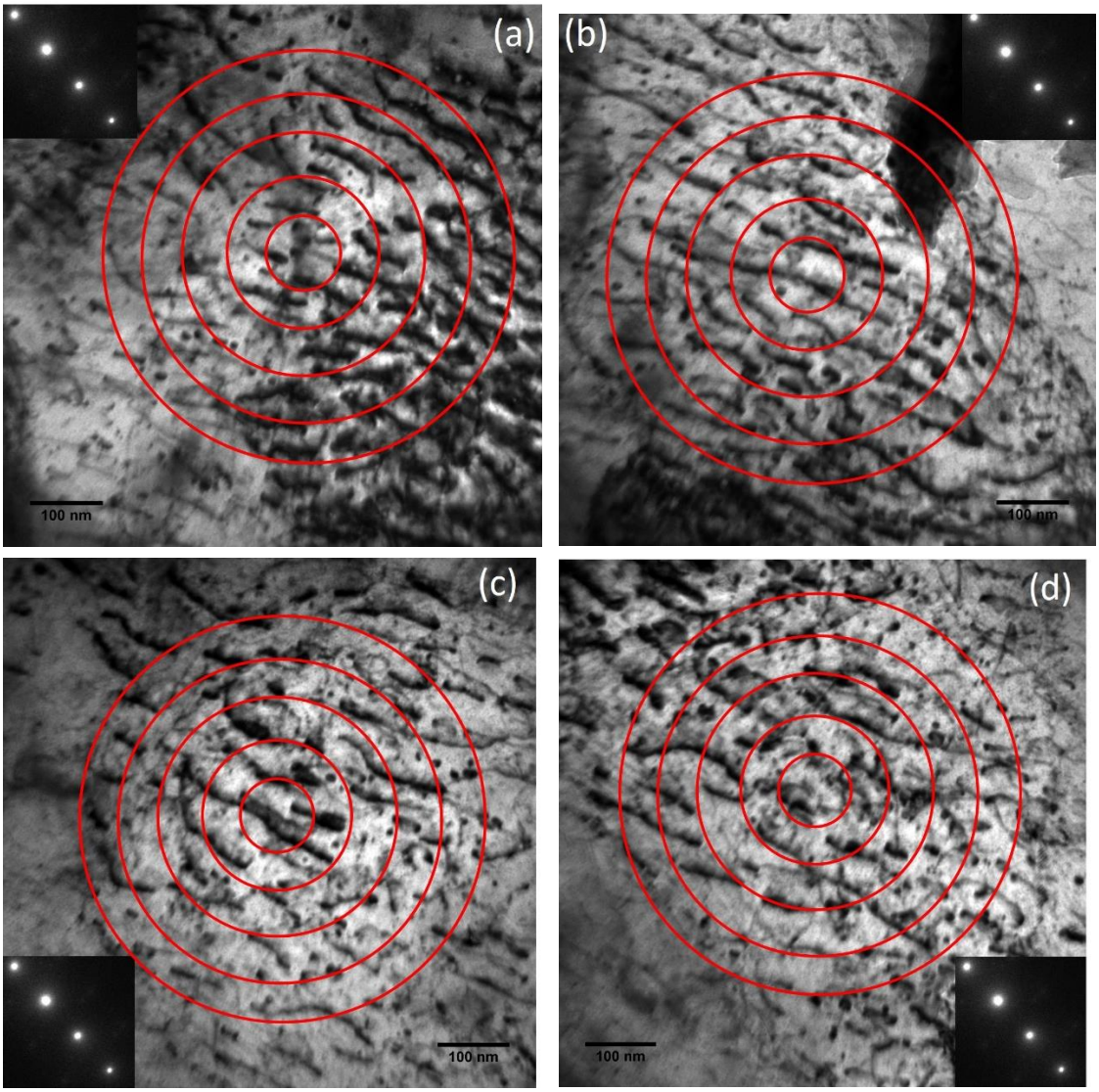
(a)
100 nm
(b)
100 nm
(c)
100 nm
(d)
100 nm

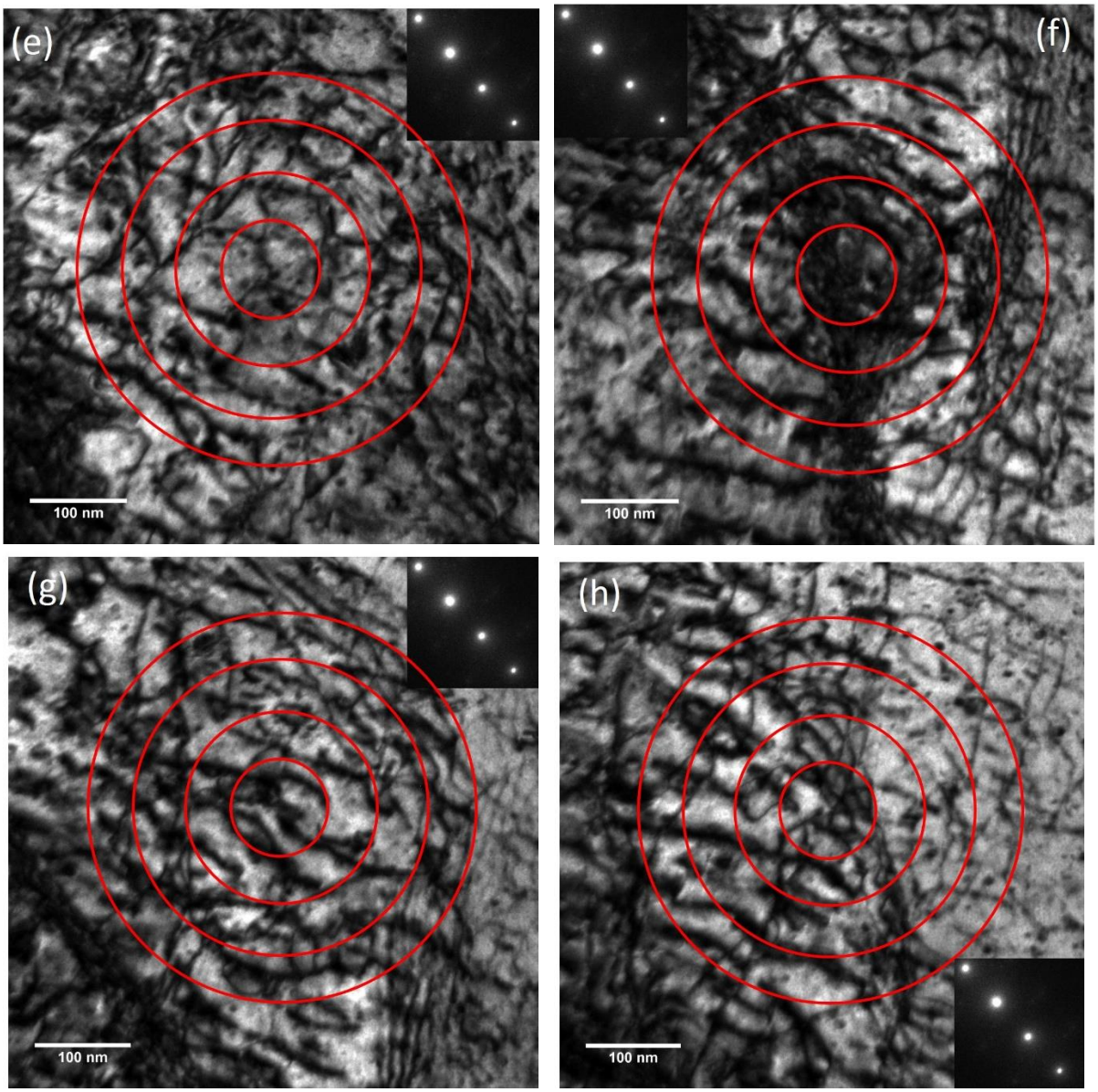
(e)
100 nm
(f)
100 nm
(g)
100 nm
(h)
100 nm

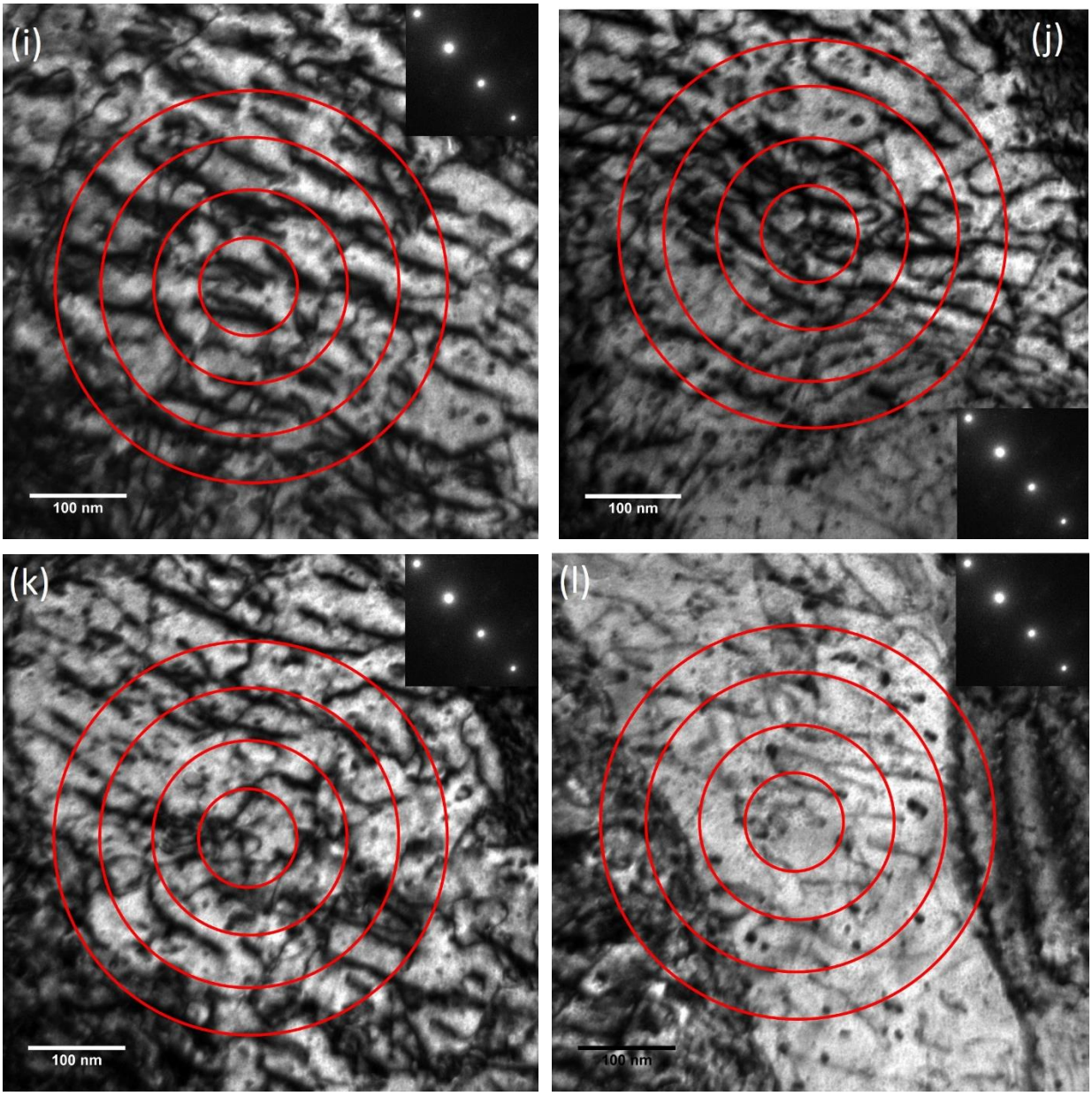
(i)
100 nm
(j)
100 nm
(k)
100 nm
(l)
100 nm

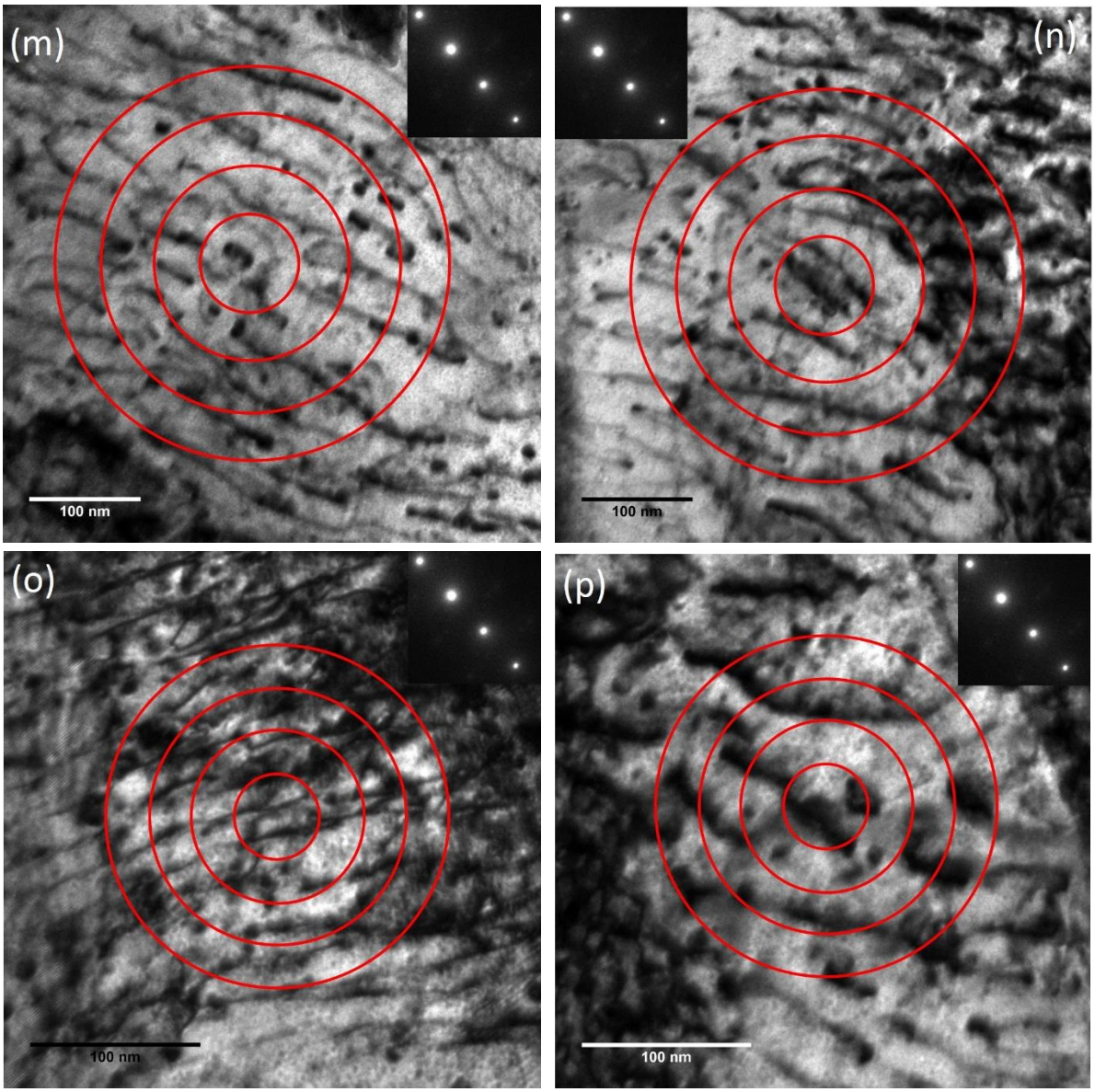
(m)
100 nm
(n)
100 nm
(o)
100 nm
(p)
100 nm

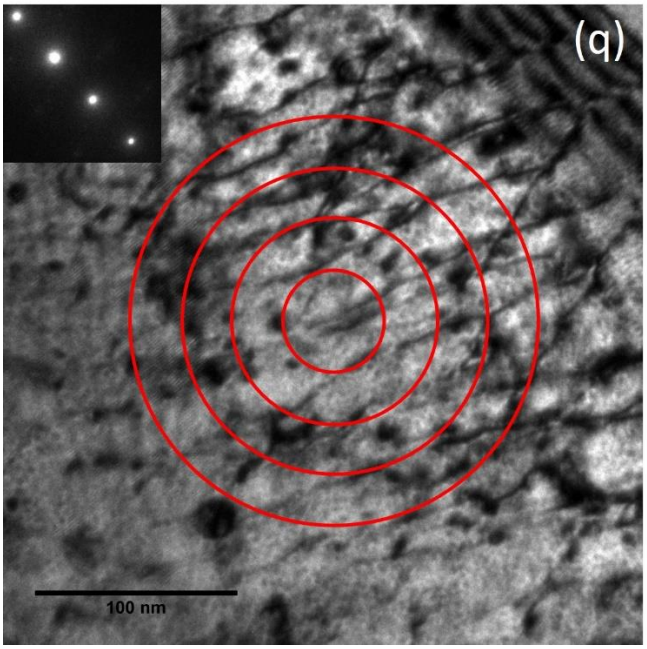

Figure C. 1 TEM images of dislocation network density imaged in the <200> two beam condition for sample IT450200.

Table C. 1 Results of dislocation network density measured for irradiation creep sample IT450200

Image #	N_c	D_c	N	Thickness (nm)	Network Density ($1/m^2$)	Average Density ($1/m^2$)	Error
a	5	50	50	100	4.7124E+14	5.7E+14	8.55E+13
b	5	50	49	100	4.6181E+14		
c	5	50	26	100	2.4504E+14		
d	5	50	30	100	2.8274E+14		
e	4	50	41	100	6.0377E+14		
f	4	50	37	100	5.4487E+14		
g	4	50	41	100	6.0377E+14		
h	4	50	52	100	7.6576E+14		
i	4	50	49	100	7.2158E+14		
j	4	50	43	100	6.3323E+14		
k	4	50	44	100	6.4795E+14		
l	4	50	39	100	5.7432E+14		
m	4	50	37	100	5.4487E+14		
n	4	50	29	100	4.2706E+14		
o	4	50	39	100	5.7432E+14		
p	4	25	19	100	5.596E+14		
q	4	25	35	100	1.0308E+15		

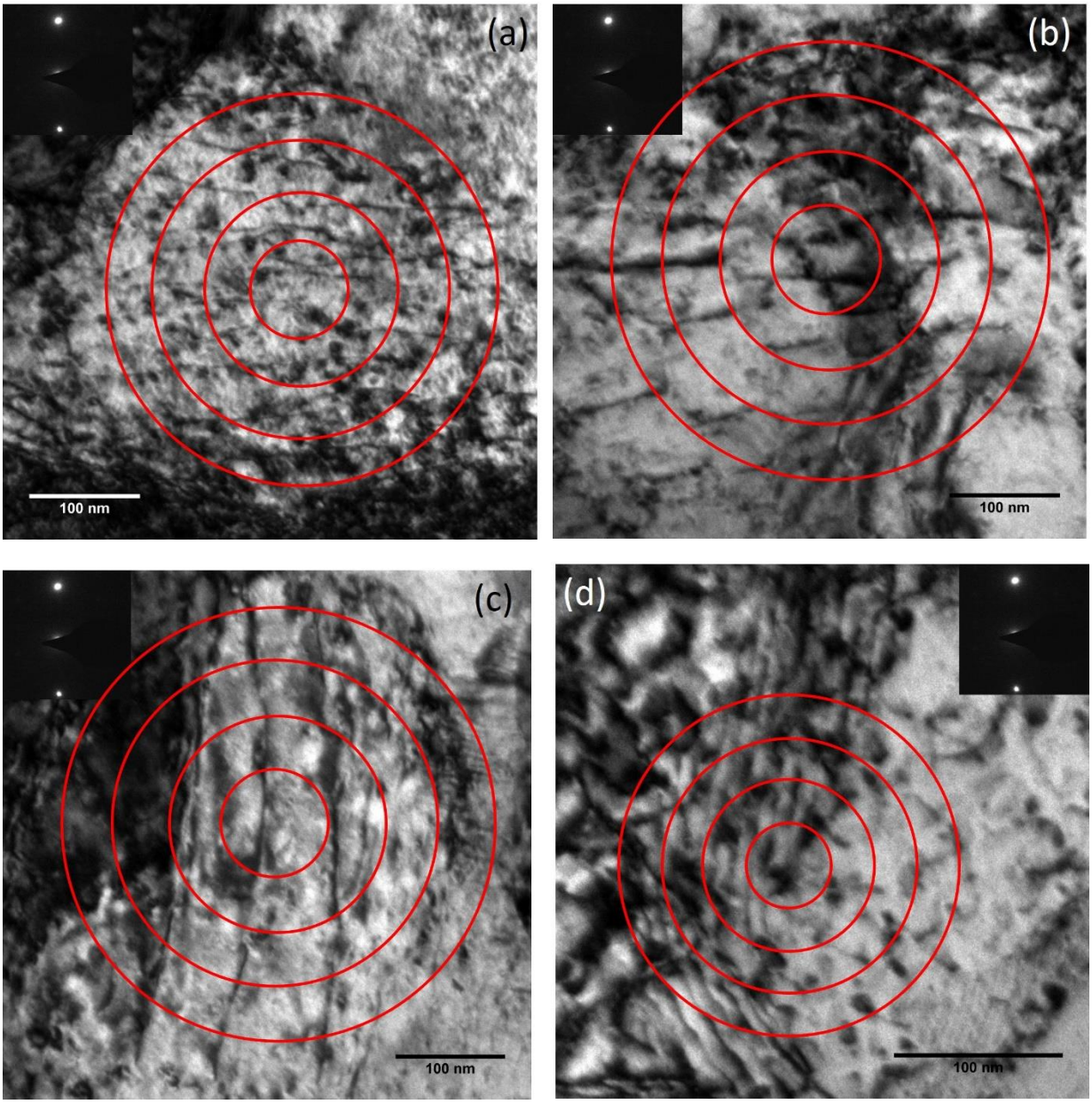
(a)
100 nm
(b)
100 nm
(c)
100 nm
(d)
100 nm

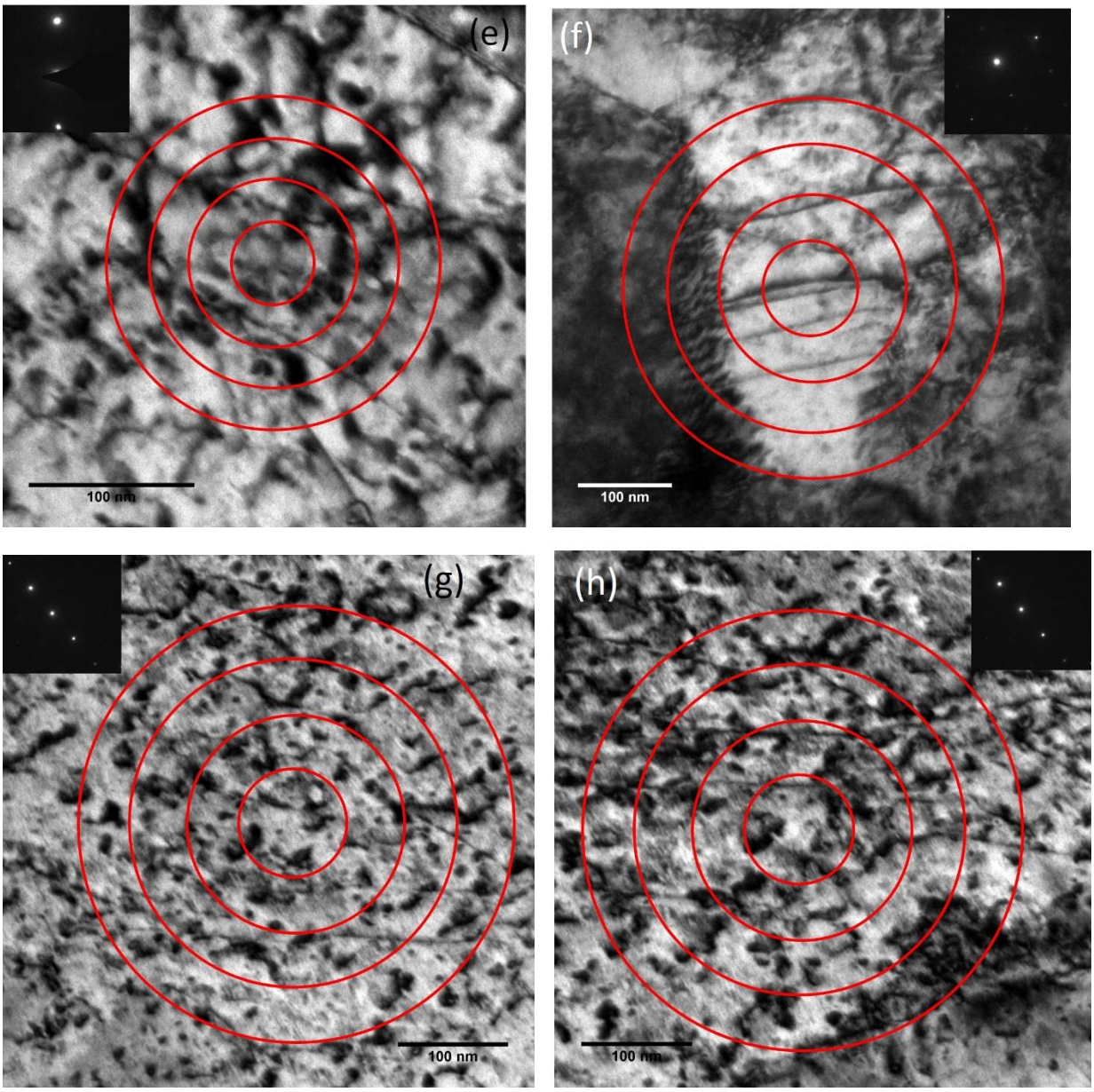
(e)
100 nm
(f)
100 nm
(g)
100 nm
(h)
100 nm

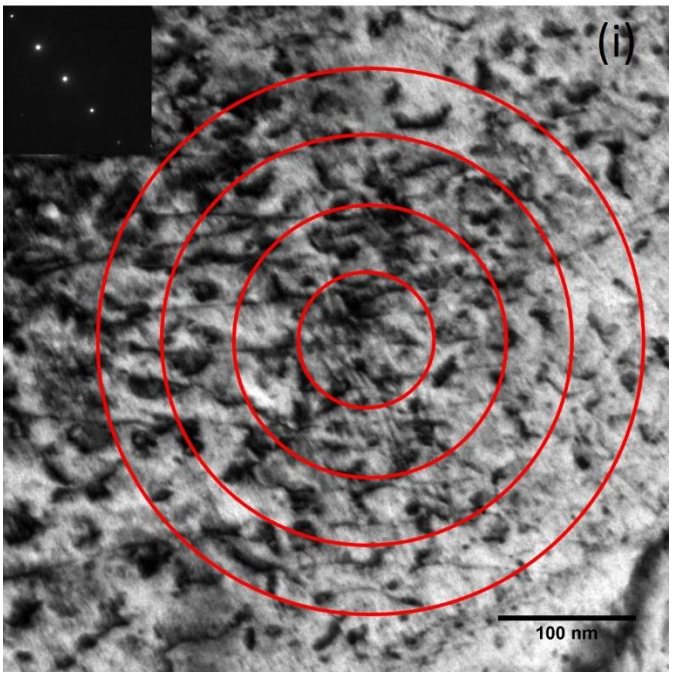

Figure C. 2 TEM images of dislocation network density imaged in the <200> two beam condition for sample IT450000.

Table C. 2 Results of dislocation network density measured for irradiation sample IT450000

Image #	N_c	D_c	N	Thickness (nm)	Network Density ($1/m^2$)	Average Density ($1/m^2$)	Error
a	4	50	28	100	4.12E+14	3.64E+14	7.26E+13
b	4	50	21	100	3.09E+14		
c	4	50	23	100	3.39E+14		
d	4	25	18	100	5.3E+14		
e	4	25	18	100	5.3E+14		
f	4	50	19	100	2.8E+14		
g	4	50	16	100	2.36E+14		
h	4	50	17	100	2.5E+14		
i	4	50	27	100	3.98E+14		

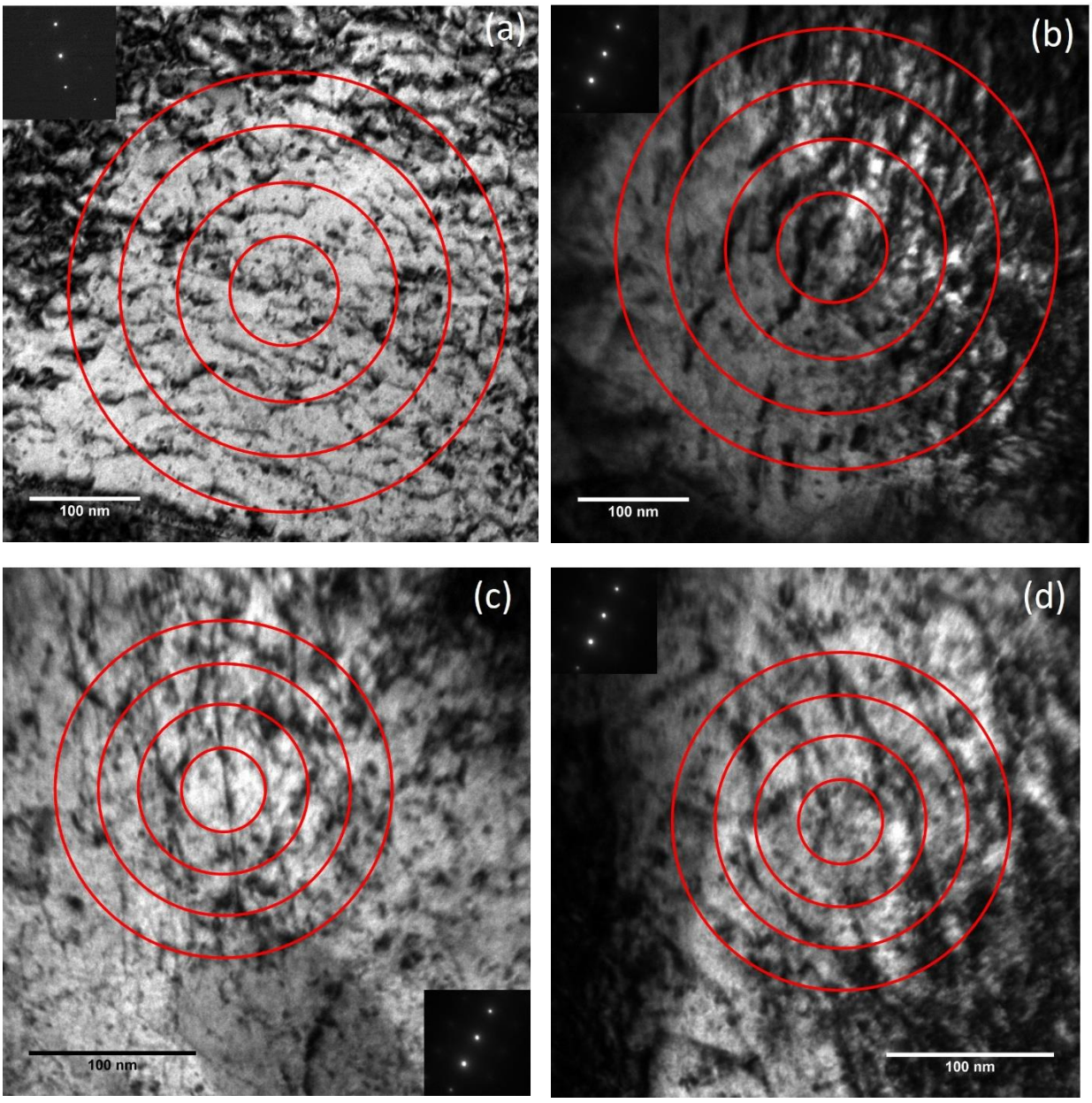
(a)
100 nm
(b)
100 nm
(c)
100 nm
(d)
100 nm

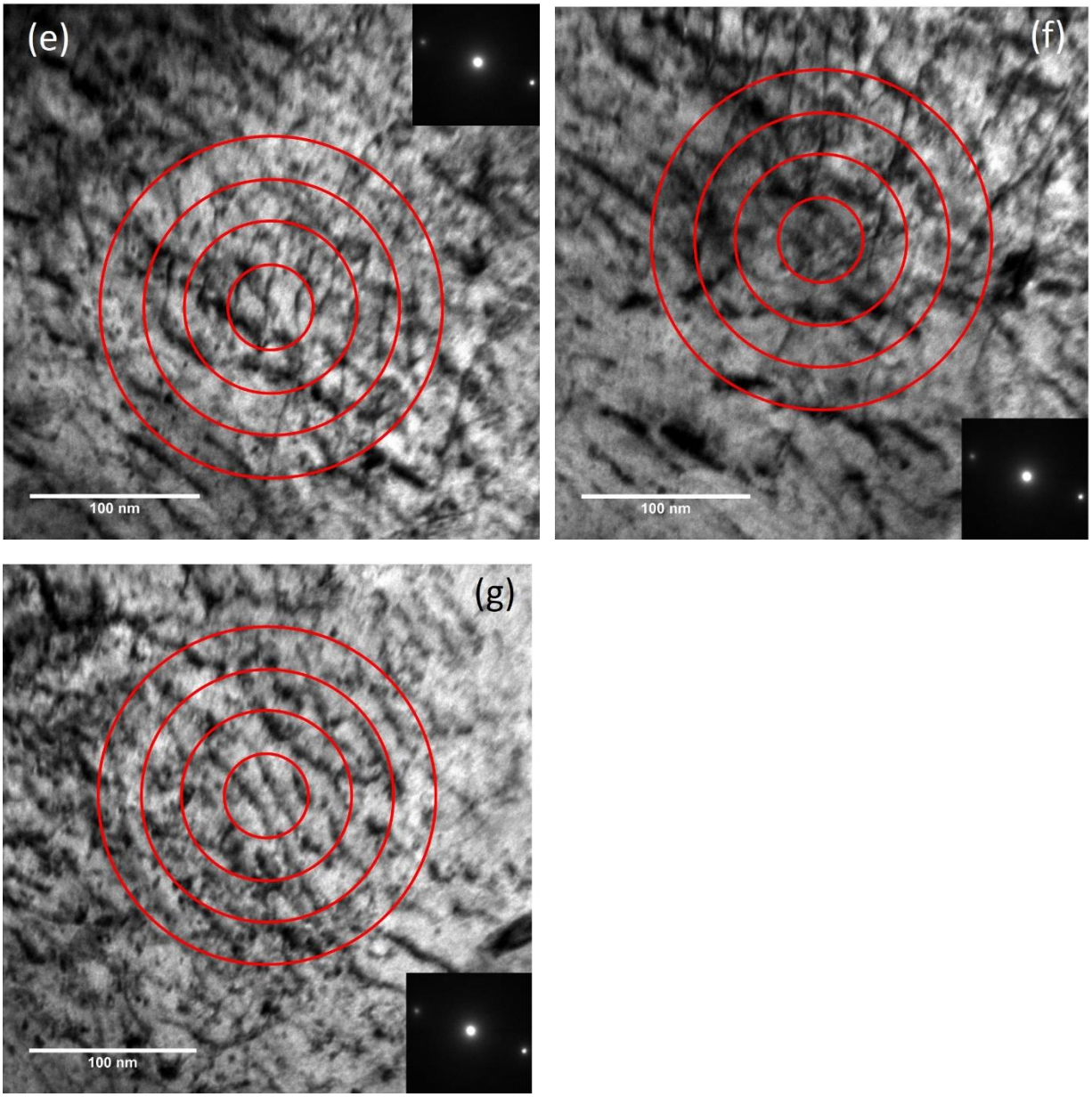

Figure C. 3 TEM images of dislocation network density imaged in the <200> two beam condition for sample TT450200.

Table C. 3 Results of dislocation network density measured for thermal creep sample TT450200

Image #	N_c	D_c	N	Thickness (nm)	Network Density ($1/m^2$)	Average Density ($1/m^2$)	Error
a	4	50	22	100	3.24E+14	4.14E+14	9.65E+13
b	4	50	18	100	2.65E+14		
c	4	25	18	100	5.3E+14		
d	4	25	16	100	4.71E+14		
e	4	25	15	100	4.42E+14		
f	4	25	21	100	6.19E+14		
g	4	50	17	100	2.5E+14		

Appendix D: Sub-grain Size TEM Image

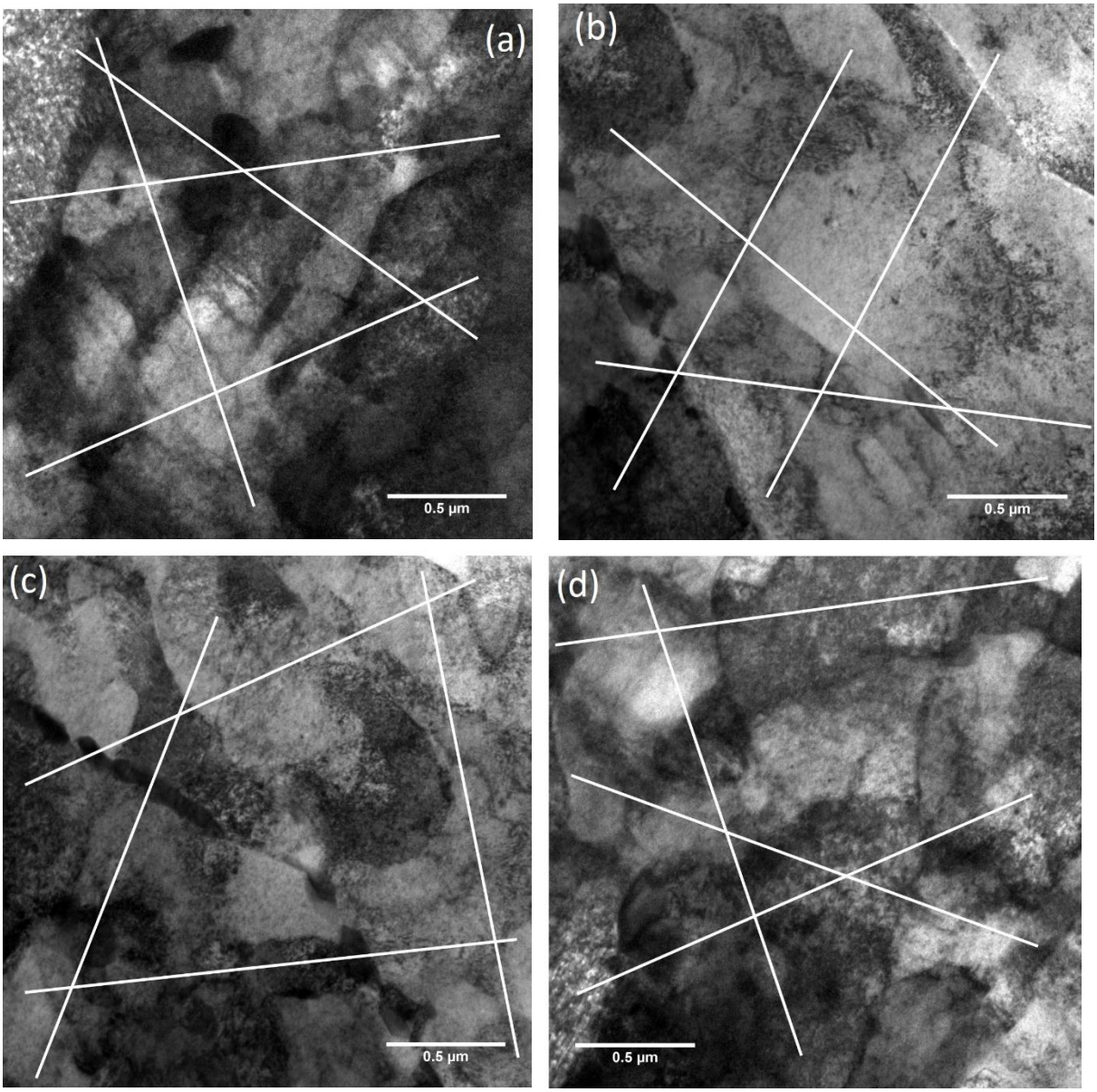
(a)
0.5 µm
(b)
0.5 µm
(c)
0.5 µm
(d)
0.5 µm

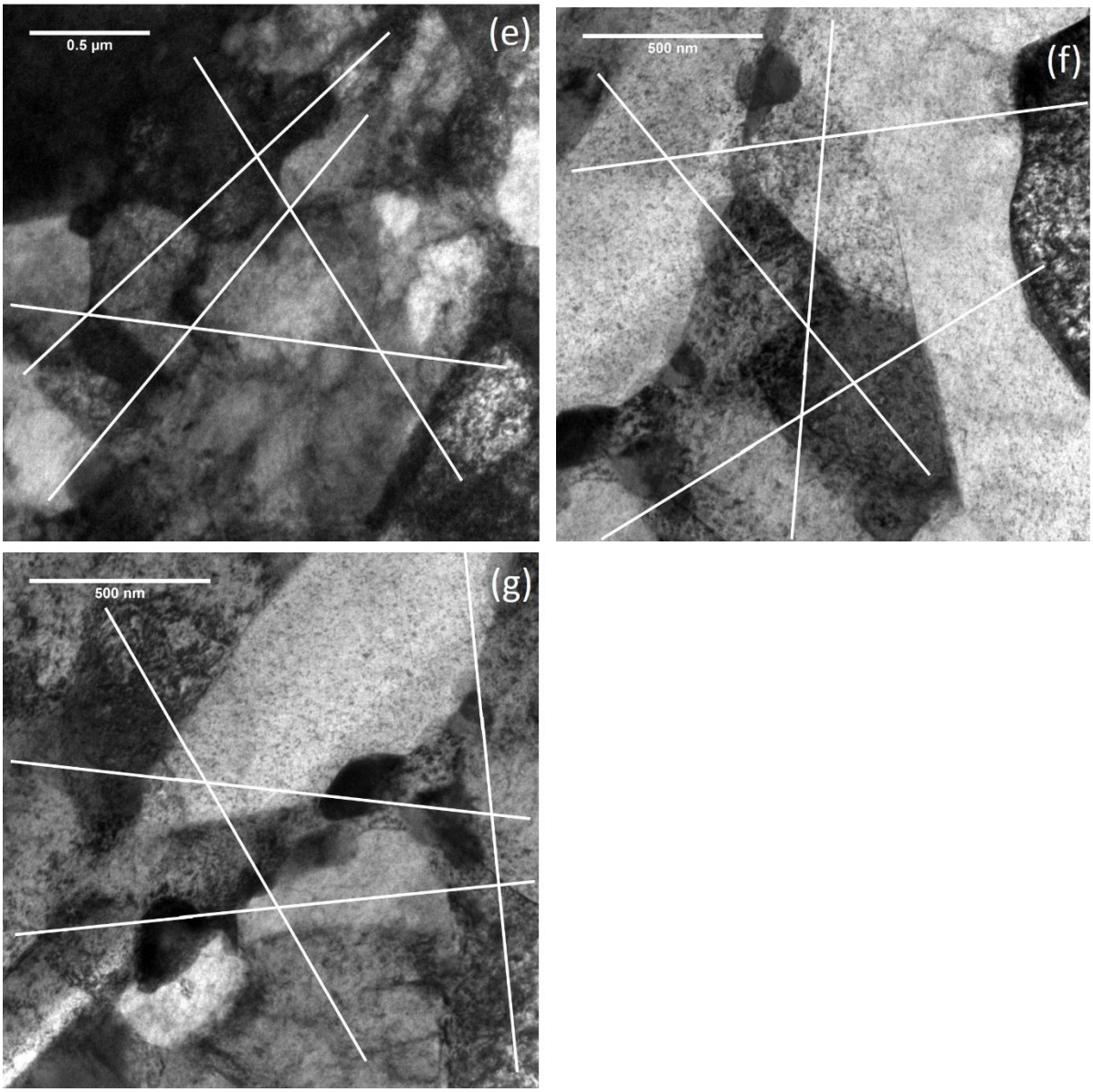

Figure D. 1 TEM images at zero tilt for sub-grain size measurements of irradiation creep sample IT450200.

Table D. 1 Results of sub-grain size measurements for irradiation creep sample IT450200.

Image #	L (nm)	N (#)	D (nm)	Average N	Average D (nm)	Error
a	8000	22	363.63	16.85	447.34	45.83
b	8000	18	444.44			
c	8000	15	533.33			
d	8000	18	444.44			
e	8000	17	470.58			
f	6000	12	500			
g	6000	16	375			

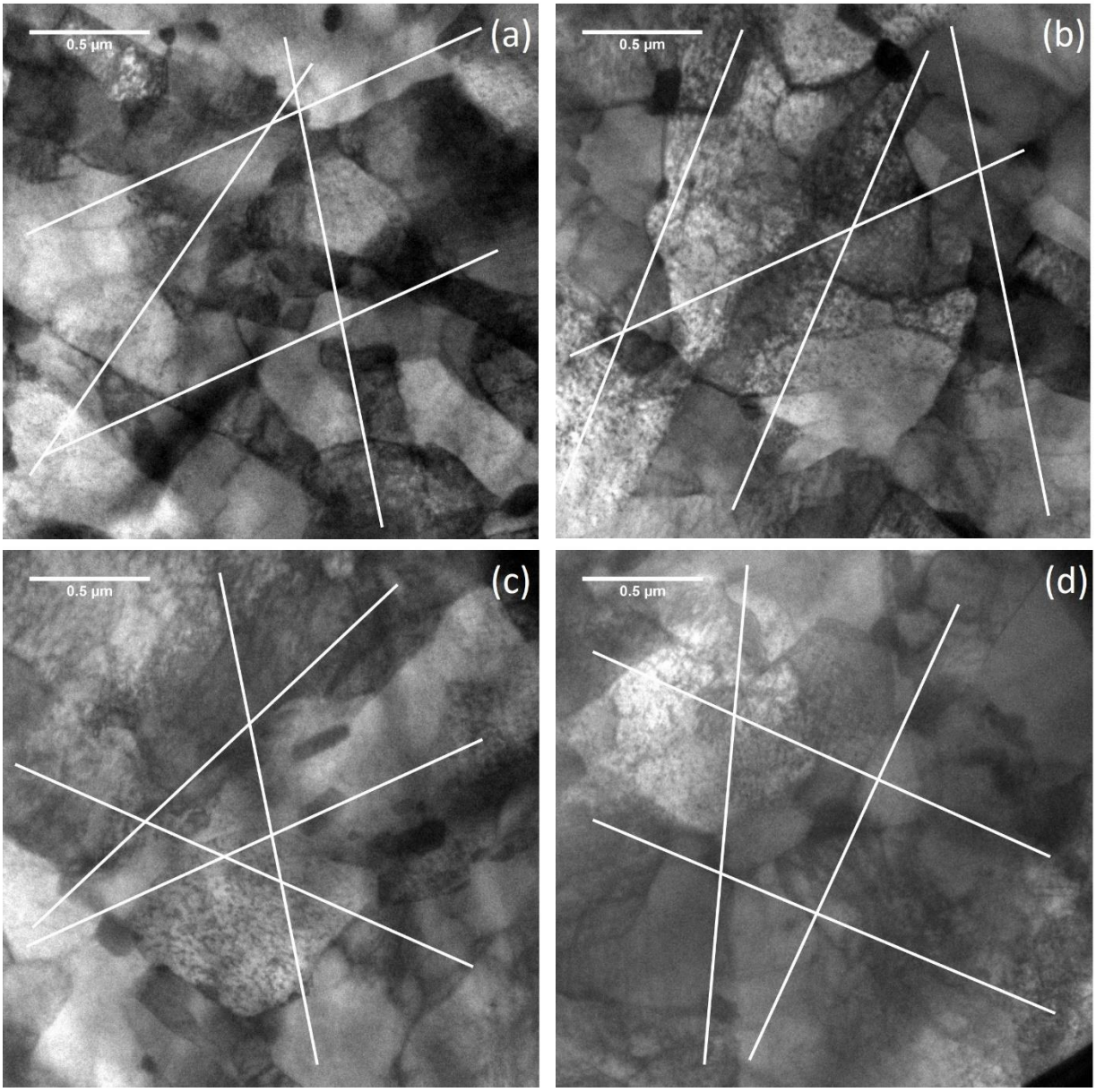
0.5 µm
(a)
0.5 µm
(b)
0.5 µm
(c)
0.5 µm
(d)

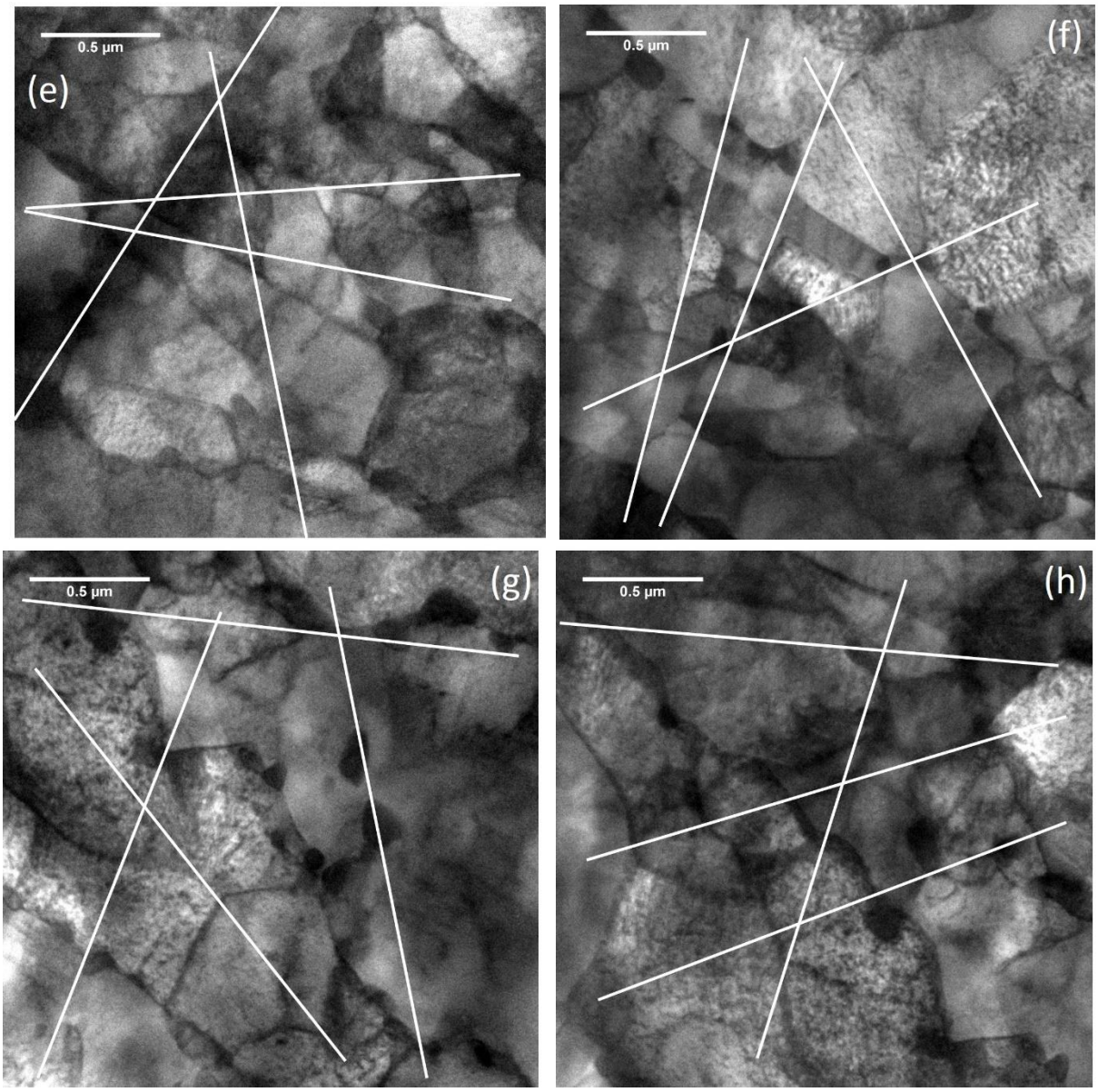
0.5 µm
(e)
0.5 µm
(f)
0.5 µm
(g)
0.5 µm
(h)

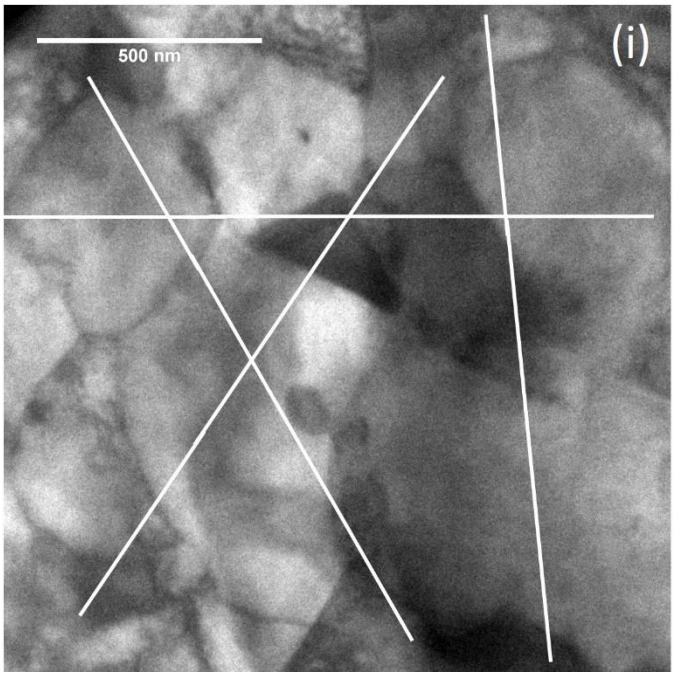

Figure D. 2 TEM images at zero tilt for sub-grain size measurements of irradiation sample IT450000.

Table D. 2 Results of sub-grain size measurements for irradiation sample IT450000.

Image #	L (nm)	N (#)	D (nm)	Average N	Average D (nm)	Error
a	8000	25	320	20.55	391.69	45.07
b	8000	26	307.69			
c	8000	17	470.58			
d	8000	17	470.58			
e	8000	20	400			
f	8000	28	285.71			
g	8000	17	470.58			
h	8000	20	400			
i	6000	15	400			

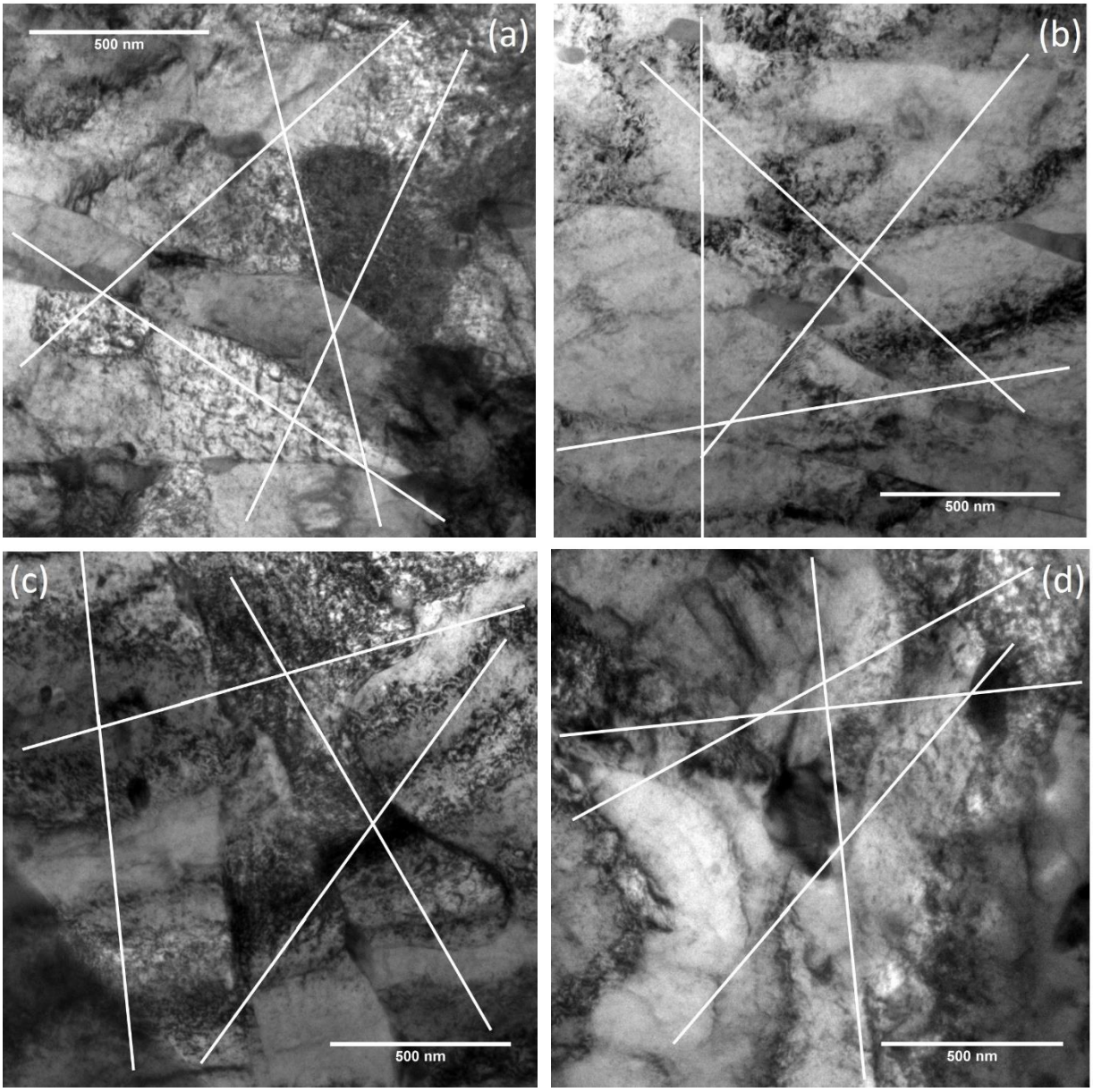
500 nm
(a)
(b)
500 nm
(c)
500 nm
(d)
500 nm

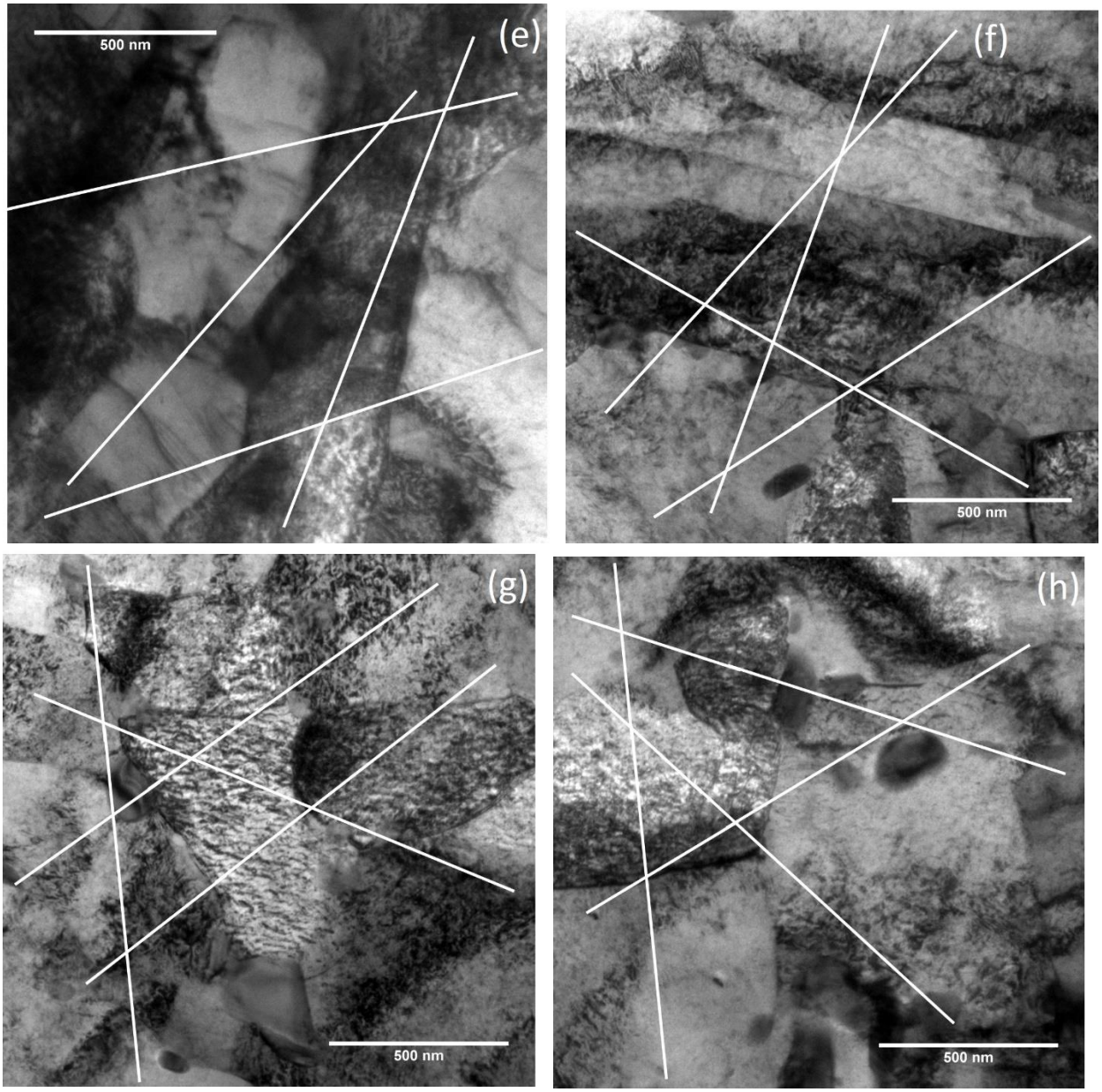

Figure D. 3 TEM images at zero tilt for sub-grain size measurements of thermal creep sample TT450200.

Table D. 3 Results of sub-grain size measurements for thermal creep sample TT450200.

Image #	L (nm)	N (#)	D (nm)	Average N	Average D (nm)	Error
a	6000	16	375	12.87	478.87	57.61
b	6000	16	375			
c	6000	10	600			
d	6000	13	461.5385			
e	6000	11	545.4545			
f	6000	12	500			
g	6000	14	428.5714			
h	6000	11	545.4545			

Appendix E: MATLAB Code

Code 1: Calculate angle θ

```
function orientation=orientationcalc(xtilt,ytilt,tvtilt,lvtilt)

%Calculates the angle theta between the tensile axis and the loop normal

%Rotational matrix for x-tilt
Rx=[1, 0, 0;
    0, cosd(xtilt), -sind(xtilt);
    0, sind(xtilt), cosd(xtilt);];
%Rotational matrix for y-tilt
Ry=[cosd(ytilt), 0, sind(ytilt);
             0,   1,    0;
    -sind(ytilt), 0, cosd(ytilt)];
%Tensile vector before tilting
TV=[cosd(tvtilt), -sind(tvtilt), 0;
          sind(tvtilt), cosd(tvtilt), 0;
          0,0,1]*[0;1;0];
%Loop normal vector after tilting
LV1=[cosd(lvtilt), -sind(lvtilt), 0;
          sind(lvtilt), cosd(lvtilt), 0;
          0,0,1]*[0;1;0];
%Tensile vector after tilting
TV=Rx*Ry*TV;
%Projection of loop normal vector onto tensile vector
ori1=sum(TV.*LV1);
%Angle between tensile vector and loop normal
orientation1=acosd(sum(TV.*LV1))
```

Code 2: Plot point defect concentrations

```
function output=pt_defect
%Plot point defect concentration as a function of time

%Typical sink densities for FM steels
sink_dens=[5*10^10, 10^15, 25*10^-7, 0, 0.5*10^-4]
%Define temperature in celcius
T=450
%convert temperature to Kelvin
T=T+273
%define dose rate in dpa/s
K=3*10^-6; %dpa/s
density=7.67; %g/cm^3
weight=56; %g/mol
omega=1.23*10^-23; %cm^3/atom
Eif=4.6; %interstitial formation energy
Evf=1.7; %vacancy formation energy
Eim=0.34; %interstitial migration energy
Evm=0.62; %vacancy migration energy
a= 4.59*10^-8; %cm, lattice constant
b= 4.59*10^-8; %ao <100>
ro_d = sink_dens(1); %dislocation density in 1/cm2
loop_d = sink_dens(2); %loop density in 1/cm3
loop_s = sink_dens(3); %loop diameter in cm
void_d = sink_dens(4); %void density in 1/cm3
gb_s= sink_dens(5); %sub-grain boundary size in cm
k=8.617*10^-5; % eV/K
k_1=1.38*10^-23; %pa/k
Cio= exp(-Eif/k/T);%thermal interstitial
Cvo= exp(-Evf/k/T);%thermal vacancy
Di= a^2/6*10^13*exp(-Eim/k/T) %interstitial diffusivity
Dv=a^2*10^13*exp(-Evm/k/T) %vacancy diffusivity
Kiv=500*Di/a^2; %recombination reaction rate
Kis_d= Di/(1/1.4)*ro_d %reaction rate interstitial dislocation
Kvs_d= Dv/(1/1.4)*ro_d %reaction rate vacancy dislocation
Kis_l= Di/(1/1.4)*loop_d*(pi*loop_s) %reaction rate interstitial loop
Kvs_l= Dv/(1/1.4)*loop_d*(pi*loop_s) %reaction rate vacancy loop
Kigb=4*Di*gb_s*6/pi/gb_s^3*pi %reaction rate interstitial gb
Kvgb=4*Dv*gb_s*6/pi/gb_s^3*pi %reaction rate vacancy gb
Kis_eff=(Kis_d+Kis_l+Kigb); %effective reaction rate interstitial
Kvs_eff=(Kvs_d+Kvs_l+Kvgb); %effectiv reaction rate vacancy
t1=(K*Kiv)^-0.5 %time constant for recombination
t2=1/Kis_eff %time constant for interstital to sinks
t4=Kis_eff/K/Kiv %time constant for vacancy and interstitial to sinks
t3=1/Kvs_eff %time constant for vacancy to sinks
t=0; %initial condition for time
i=1; %counter
Ci(1)=0; %initial condition for interstital concentration
Cv(1)=0; %initial condition for vacancy concentration
dt=10^-12; %change in time

%while loop to run through time
while t>=0 & t<10^-3
    di_net(i)=Kis_d*Ci(i);
    di_loop(i)=Kis_l*Ci(i);
```

```
    di_gb(i)=Kigb*Ci(i);
    dv_net(i)=Kvs_d*Cv(i);
    dv_loop(i)=Kvs_l*Cv(i);
    dv_gb(i)=Kvgb*Cv(i);
    recomb(i)=Kiv*Ci(i)*Cv(i);
    dCv(i)=K-recomb(i)-(dv_net(i)+dv_loop(i)+dv_gb(i));
    dCi(i)=K-recomb(i)-(di_net(i)+di_loop(i)+di_gb(i));
    Ci(i+1)=Ci(i)+dCi(i)*dt(i);
    Cv(i+1)=Cv(i)+dCv(i)*dt(i);
    if dt(i)<5*10^-7
        dt(i+1)=dt(i)*1.1;
    elseif dt(i)>5*10^-7
        dt(i+1)=dt(i);
    end
    t(i+1)=t(i)+dt(i);
    i=i+1;
end

%plot interstitial and vacancy concentrations
loglog (t,Ci,'b')
hold on
loglog (t,Cv,'r')
hold off
```

Code 3: Evaluate integral for anisotropic dislocation loops

```
function plotSIPN
%Calculate integral for strain contribution from anisotropic loop density
%define theta
theta=linspace(0,90,91)
%define phi
phi=linspace(0,90,91)
%define change in theta
dtheta=theta(end)-theta(end-1);
%define change in phi
dphi=phi(end)-phi(end-1);
%empirically measured anisotropy constants
a=0.99;
b=0.011;
%Burgers vector
B=4.59*10^-10;
%Dislocation loop diameter
D=23.3*10^-9;
%Average dislocation loop density
ro=1.5*10^21;
%Size of the dislocation loop
size=pi*(D/2)^2*B*ro;
%Volume of dislocation loop
A=B*ro*pi*(D/2)^2
%Numerical integration of integral
for i=1:length(theta)
    for j=1:length(phi)
        ex(i,j)=A*sind(theta(i))*cosd(phi(j))*(a-b*theta(i))*dtheta*dphi;
        ey(i,j)=A*sind(theta(i))*sind(phi(j))*(a-b*theta(i))*dtheta*dphi;
        ez(i,j)=A*cosd(theta(i))*(a-b*theta(j))*dtheta*dphi;
        C(i,j)=(a-b*theta(i))*dtheta*dphi;
    end
end
%Normalizing constant
Csum=sum(sum(C));
%Normalize strain in 3 cartesian coordinates
strainx=ex/Csum;
strainy=ey/Csum;
strainz=ez/Csum;
%Total strain in 3 cartesian coordinates
totalx=sum(sum(strainx))
totaly=sum(sum(strainy))
totalz=sum(sum(strainz))
%Total volumetric strain
strainvol=totalx+totaly+totalz
%Volume conservation of strain
strain_x=totalx-1/3*strainvol
strain_y=totaly-1/3*strainvol
strain_z=totalz-1/3*strainvol
```

Code 4: Calculating SIPA and PAG predictions on strain rates

```
function output=SIPA_PAG(T,stress)
sink_dens=[5.7*10^14*10^-4, 10^21*10^-6, 42.3*10^-7, 0, 0.73*10^-4]
%measured sink densities from IT450200
T=T+273 %Temperature
K=3.4*10^-6; %dpa/s
density=7.67; %g/cm^3
weight=56; %g/mol
omega=1.23*10^-23; %cm^3/atom
Eif=4.6; %interstitial formation energy
Evf=1.7; %vacancy formation energy
Eim=0.2; %interstitial migration energy
Evm=0.67; %vacancy migration energy
a= 4.59*10^-8; %cm, lattice constant
b= 4.59*10^-8; %ao <100>
ro_d = sink_dens(1) %dislocation density in 1/cm2
loop_d = sink_dens(2); %loop density in 1/cm3
loop_s = sink_dens(3); %loop diameter in cm
void_d = sink_dens(4); %void density in 1/cm3
gb_s= sink_dens(5); %sub-grain boundary size in cm
eo= 0.8; %interstitial relaxation vol
v= 0.33; %poisson's ratio
u= 75*10^3; %shear modulus in MPA
E= 200*10^3; %elastic modulus in MPA
zi= 1.02; %dislocation bias
zv= 1; %vacancy bias
ziA= zi*(1+5*stress*(2-v)/2/u/eo/(7-5*v)) %aligned interstitial bias
ziN= zi*(1-5*stress*(1+v)/2/u/eo/(7-5*v)) %none aligned interstitial bias
k=8.617*10^-5; % eV/K
k_1=1.38*10^-23; %pa/k
Rd=4.59*10^-8; %dislocation core radius
R=100*Rd; %capture radius
Cio= exp(-Eif/k/T)%thermal interstitial
Cvo= exp(-Evf/k/T)%thermal vacancy
Di= a^2/6*10^13*exp(-Eim/k/T) %interstitial diffusivity
Dv=a^2*10^13*exp(-Evm/k/T)  %vacancy diffusivity
Kis_d= Di/(1/(2*pi/log(R/Rd)))*ro_d %reaction rate of dislocations and
interstitials
Kvs_d= Dv/(1/(2*pi/log(R/Rd)))*ro_d %reaction rate of dislocations and
vacancies
Kis_l= Di/(1/(2*pi/log(R/Rd)))*loop_d*(pi*loop_s) %reaction rate of loops and
interstitials
Kvs_l= Dv/(1/(2*pi/log(R/Rd)))*loop_d*(pi*loop_s) %reaction rate of loops and
vacancies
Kigb=4*Di*gb_s*6/pi/gb_s^3*pi %reaction rate of grain boundaries and
interstitials
Kvgb=4*Dv*gb_s*6/pi/gb_s^3*pi %reaction rate of grain boundaries and
vacancies
Kis_eff=(Kis_d+Kis_l+Kigb); %reaction rate total interstitial
Kvs_eff=(Kvs_d+Kvs_l+Kvgb); %reaction rate total vacancy
Ci= K/Kis_eff %interstitial concentration
Cv= K/Kvs_eff %vacancy concentration
ro_tot= ro_d+loop_d*(pi*loop_s); %Total dislocation density
Vi= 1/b*(zi*Di*Ci-zv*Dv*Cv) %Dislocation climb rate
SIPA = 2/9*ro_tot*((ziA-ziN)*Di*Ci)
PAG = 4/9*stress/E/b*sqrt(pi*ro_tot)*Di*Ci*(ziA-ziN)
```

Bibliography

[1] R. . Klueh and D. . Harris, *High Chromium Ferritic Martensitic Materials for Nulcear Applications*. ASTM International, 2001, p. 221.

[2] R. L. Klueh, B. Van Der Schaaf, and M. Victoria, "Ferritic / martensitic steels – overview of recent results," *J. Nucl. Mater.*, vol. 311, no. 2002, pp. 455–465, 2008.

[3] S. . Zinkle, "Advanced Materials for Future Nuclear Plants," in *Fission Energy Workshop*, 2007.

[4] R. L. Klueh and a. T. Nelson, "Ferritic/martensitic steels for next-generation reactors," *J. Nucl. Mater.*, vol. 371, no. 1–3, pp. 37–52, Sep. 2007.

[5] J. . Matthews and M. . Finnis, "Irradiation Creep Models - An Overview," *J. Nucl. Mater.*, vol. 159, pp. 257–285, 1988.

[6] P.T. HEALD and J. E. HARBOTTLE, "Irradiation Creep Due to Dislocation Climb and Glide," *J. Nucl. Mater.*, vol. 67, pp. 229–233, 1977.

[7] P. R. Okamoto and S. D. Harkness, "Stress-biased Loop Nucleation in Irradiated Type 316 Stainless Steel," *J. Nucl. Mater.*, vol. 48, pp. 204–206, 1973.

[8] E. J. SAVINO and C. N. TOME, "Irradiation Creep by Stress-induced Preferential Attraction due to Anisotropic Diffsion (SIPA-AD)," *J. Nucl. Mater.*, vol. 109, pp. 405–416, 1982.

[9] D. S. Gelles, "Effects of stress on microstructural evolution during irradiation.," *J. Nucl. Mater.*, vol. 5, pp. 146–161, 1993.

[10] F. A. Garner and D. S. Gelles, "Irradiation Creep Mechanisms: An Experimental Perspective," *J. Nucl. Mater.*, vol. 159, pp. 286–309, 1988.

[11] F. A. Garner and M. . Toloczko, “Irradiation creep and void swelling of two LMR heats of HT9 at ~400°C and 165 dpa,” *J. Nucl. Mater.*, vol. 237, pp. 289–292, 1996.

[12] F. A. Garner and R. J. Puigh, “Irradiation creep and swelling of the fusion heats of PCA, HT9 and 9Cr-1Mo irradiated to high neutron fluence,” *J. Nucl. Mater.*, vol. 179–181, pp. 577–580, Mar. 1991.

[13] M. Ando, M. Li, H. Tanigawa, M. L. Grossbeck, S. Kim, T. Sawai, K. Shiba, Y. Kohno, and a. Kohyama, “Creep behavior of reduced activation ferritic/martensitic steels irradiated at 573 and 773K up to 5dpa,” *J. Nucl. Mater.*, vol. 367–370, pp. 122–126, Aug. 2007.

[14] J. A. Hudson, R. S. Nelson, and R. J. Mcelroy, “The Irradiation Creep of Nickel and AISI 321 Stainless Steel During 4 MeV Proton Bombardment,” *J. Nucl. Mater.*, vol. 65, pp. 279–294, 1977.

[15] H. Tanigawa, A. Kohyama, and Y. Katoh, “A modeling of radiation induced microstructural evolution under applied stress in austenitic alloys,” *J. Nucl. Mater.*, vol. 239, pp. 80–84, Dec. 1996.

[16] J. Chen, M. a. Pouchon, a. Kimura, P. Jung, and W. Hoffelner, “Irradiation creep and microstructural changes in an advanced ODS ferritic steel during helium implantation under stress,” *J. Nucl. Mater.*, vol. 386–388, pp. 143–146, Apr. 2009.

[17] G. S. Was, *Fundamentals of Radiation Materials Science*. Springer, 2007.

[18] A. C. Roberts and A. H. Cottrell, “Creep of Alpha Uranium During Irradiation with Neutrons,” *Philos. Mag.*, vol. 1, p. 711, 1958.

[19] J. H. Gittus, “Theory of Dislocation Creep for a Material Subjected to Bombardment by Energetic Particles,” *Philos. Mag.*, vol. 25, p. 345, 1972.

[20] P.T. HEALD and M. V Speightt, “.,” *Philos. Mag.*, vol. 29, p. 1075, 1974.

[21] R. Bullough and J. R. Willis, “.,” *Philos. Mag.*, vol. 31, p. 855, 1975.

[22] C. H. Woo, “Creep due to elastodiffusion *,” *J. Nucl. Mater.*, vol. 120, pp. 55–64, 1984.

[23] L. K. Mansur and T. C. Reiley, “Irradiation creep by dislocation glide enabled by preferred absorption of point defects - theory and experiment,” *J. Nucl. Mater.*, vol. 90, pp. 60–67, 1980.

[24] L. K. Mansur, “Irradiation creep by climb-enabled glide of dislocations resulting from preferred absorption of point defects,” *Philos. Mag.*, vol. A39, p. 497, 1979.

[25] H. R. Brager and F. A. Garner, “The effect of stress on the microstructure of neutron irradiated type 316 stainless steel,” *J. Nucl. Mater.*, vol. 66, pp. 301–321, 1977.

[26] W. G. Wolfer, “Correlation of radiation creep theory with experimental evidence,” *J. Nucl. Mater.*, vol. 90, pp. 175–192, 1980.

[27] A. D. Brailsford and R. Bullough, “Irradiation creep Due to the Growth of Interstitial Loops,” *Philos. Mag.*, vol. 27, p. 49, 1973.

[28] M. B. Bever, *Encyclopedia of Materials Science and Engineering*. Cambridge, Mass: MIT Press, 1986.

[29] H. S. Forgings, S. S. Bars, T. P. Qualifications, and N. Facilities, “Standard Specification for Austenitic and Martensitic Stainless Steel Bars , Billets , and Forgings for Liquid Metal Cooled Reactor Core,” vol. 01, no. Reapproved 2000, pp. 1–5, 2011.

[30] M. Hansen and K. Anderko, *Constitution of Binary Alloys*. IIT Research Institute, 1958, p. 1305.

[31] M. A. Shtremel, V. G. Andreev, and D. A. Kozlov, *Structure and Strength of Lath Martensite*. Metal Science and Heat Treatment, 1999, pp. 140–145.

[32] G. V. Kurdyumov, L. M. Utevskii, and R. I. Entin, *Transformation in Iron and Steels*. Moscow, 1977.

[33] M. Durand-Charre, *Microstructure of Steels and Cast Irons*. Springer, 2004.

[34] G. Gupta, “Irradiation Creep Behavior of Ferritic-martensitic Alloy T91 by Subgrain Boundary Desnity Enhancement,” University of Michigan, 2007.

[35] I. . Gorynin, V. V. Rybin, and V. A. Malyshevskii, “Transformation of Dislocation Martensite in Tempering Secondary-Hardening Steel,” *Met. Sci. Heat Treat.*, vol. 41, pp. 13–19, 1999.

[36] R. Schaublin, P.Spatig, and M. Victoria, “Microstructure Assessment of the Low Activation Ferritic/Martensitic Steel F82H,” *J. Nucl. Mater.*, vol. 258–263, pp. 1178–1182, 1998.

[37] A. F. Padilha and P. R. Rios, “Decomposition of Austenite in Austenitic Stainless Steels,” *ISII Int.*, vol. 42, pp. 325–337, 2002.

[38] J. J. Kai and G. L. Kulcinski, “The Effects of Heat-Treatment on the Microstructural Evolution of HT-9,” *Scr. Metall.*, vol. 23, pp. 1151–1156, 1989.

[39] O. A. Atasoy, K. Ozbaysal, and O. T. Inal, “Precipitation of Vanadium Carbides in 0.8%C, 13%Mn, 1%V Austenitic Steel,” *J. Mater. Sci.*, vol. 24, pp. 1393–1398, 1989.

[40] S. Yamasaki and H. K. D. H. Bhadeshia, “Modelling and Characterisation of V4C3 Precipitation and Cementite Dissolution During Tempering of Fe-C-V Martensitic Steel,” *Mater. Sci. Technol.*, vol. 19, pp. 1335–1343, 2003.

[41] G. Gupta, G. S. Was, and Z. J. Jiao, “Microstructural Evolution of Proton Irradiated T91,” *J. Nucl. Mater.*, vol. 351, pp. 162–173, 2006.

[42] N. Yamanouchi, “Accumulation of Engineering Data for Practical Use of Reduced Activation Ferritic Steel 8%Cr-2%W-0.2%V-Ta-Fe,” *J. Mater. Sci.*, vol. 191, pp. 882–826, 1992.

[43] K. Haarmann and J. C. Vaillant, *The T91/P91 Book*. Vallourec & Mannesmann Tubes, 1999.

[44] a. a. F. Tavassoli, “Materials design data for fusion reactors,” *J. Nucl. Mater.*, vol. 258–263, pp. 85–96, Oct. 1998.

[45] A. A. F. Tavassoli, “Present Limits and Improvements of Structural Materials for Fusion Reactors - A Review,” *J. Nucl. Mater.*, vol. 302, pp. 73–88, 2002.

[46] S. J. Zinkle, J. P. Robertson, and R. L. Klueh, “Thermophysical and Mechanical Properties for Fe-(8-9)%Cr Reduced Activation Steels,” 1998.

[47] a. -a. . Tavassoli, a Alamo, L. Bedel, L. Forest, J.-M. Gentzbittel, J.-W. Rensman, E. Diegele, R. Lindau, M. Schirra, R. Schmitt, H. . Schneider, C. Petersen, a.-M. Lancha, P. Fernandez, G. Filacchioni, M. . Maday, K. Mergia, N. Boukos, P. Spätig, E. Alves, and E. Lucon, “Materials design data for reduced activation martensitic steel type EUROFER,” *J. Nucl. Mater.*, vol. 329–333, pp. 257–262, Aug. 2004.

[48] K. Sawada, “Effect of Microstructure on Elastic Property at High Temperatures in Ferritic Heat Resistant Steels,” *Mater. Sci. Eng. a - Struct. Mater. Prop. Microstruct. Process.*, vol. 394, pp. 36–42, 2005.

[49] M. Matijasevic and A. Almazouzi, “Behavior of Ferritic/Martensitic Steels after n-irradiation at 200 and 300°C,” *J. Nucl. Mater.*, vol. 377, pp. 101–108, 2008.

[50] Y. Dai, X. J. Jia, and K. Farrell, “Mechanical Properties of Modified 9Cr-1Mo (T91) Irradiated at 300°C in SINQ Target-3,” *J. Nucl. Mater.*, vol. 318, pp. 192–199, 2003.

[51] E. M. Haney, F. Dalle, M. Sauzay, L. Vincent, I. Tournié, L. Allais, and B. Fournier, “Macroscopic results of long-term creep on a modified 9Cr–1Mo steel (T91),” *Mater. Sci. Eng. A*, vol. 510–511, pp. 99–103, Jun. 2009.

[52] B. K. Choudhary and E. I. Samuel, “Creep Behaviour of Modified 9Cr-1Mo Ferritic Steel,” *J. Nucl. Mater.*, vol. 412, pp. 82–89, 2011.

[53] T. Shrestha, M. Basirat, I. Charit, G. P. Potirniche, K. K. Rink, and U. Sahaym, “Creep deformation mechanisms in modified 9Cr–1Mo steel,” *J. Nucl. Mater.*, vol. 423, no. 1–3, pp. 110–119, Apr. 2012.

[54] J. E. Bird, A. K. Mukherjee, and J. E. Dorn, *Quantitative Relation Between Properties and Microstructure*. 1969, pp. 255–342.

[55] M. B. Toloczko, F. A. Garner, and S. A. Maloy, “In-reactor Creep of Two Heats of T91 (Modified 9Cr-1Mo) from ~ 400 ° C to 600 ° C,” in *8th International Workshop on Spallation Materials Technology (IWSMT-8)*, 2006.

[56] M. B. Toloczko, F. A. Garner, and C. R. Eiholzer, “Irradiation creep and swelling of the US fusion heats of HT9 and 9Cr-1Mo to 208 dpa at - 4O0°C,” *J. Nucl. Mater.*, vol. 215, pp. 604–607, 1994.

[57] F. . Garner, M. . Toloczko, and B. . Sencer, “Comparison of swelling and irradiation creep behavior of fcc-austenitic and bcc-ferritic/martensitic alloys at high neutron exposure,” *J. Nucl. Mater.*, vol. 276, no. 1–3, pp. 123–142, Jan. 2000.

[58] M. B. Toloczko, F. a. Garner, and C. R. Eiholzer, “Irradiation creep of various ferritic alloys irradiated at ~400°C in the PFR and FFTF reactors,” *J. Nucl. Mater.*, vol. 258–263, pp. 1163–1166, Oct. 1998.

[59] M. . Toloczko, D. . Gelles, F. . Garner, R. . Kurtz, and K. Abe, “Irradiation creep and swelling from 400 to 600 °C of the oxide dispersion strengthened ferritic alloy MA957,” *J. Nucl. Mater.*, vol. 329–333, pp. 352–355, Aug. 2004.

[60] M. B. Toloczko, F. A. Garner, and S. A. Maloy, “Irradiation creep and density changes observed in MA957 pressurized tubes irradiated to doses of 40 – 110 dpa at 400 – 750 ° C in FFTF,” *J. Nucl. Mater.*, vol. 428, pp. 170–175, 2012.

[61] A. Kohyama, Y. Kohno, K. Asakura, M. Yoshino, C. Namba, and C. R. Eiholzer, “Irradiation creep of low-activation ferritic steels in FFTF/ MOTA,” *J. Nucl. Mater.*, vol. 215, pp. 751–754, 1994.

[62] D. S. Gelles, A. Kimura, and T. Shibayama, “Effects of Radiation on Materials, 19th Symp., ASTM STP,” 2000, p. 535.

[63] P. Jung, “Investigations on creep and microstructure in proton-irradiated DIN 1.4914 martensitic stainless steel,” *J. Nucl. Mater.*, vol. 179–181, pp. 745–748, 1991.

[64] J. Chen, P. Jung, M. a. Pouchon, T. Rebac, and W. Hoffelner, “Irradiation creep and precipitation in a ferritic ODS steel under helium implantation,” *J. Nucl. Mater.*, vol. 373, no. 1–3, pp. 22–27, Feb. 2008.

[65] J. Chen, P.Jung, and W. Hoffelner, “Irradiation creep of Candidate Material for Advanced Nuclear Plants,” *J. Nucl. Mater.*, 2013.

[66] J. Nagakawa, S. Uchio, Y. Murase, N. Yamamoto, and K. Shiba, “Creep behavior of the F82H steel under irradiation with 17MeV protons at 300°C,” *J. Nucl. Mater.*, vol. 386–388, pp. 264–267, Apr. 2009.

[67] “Alloy Data Sheet for T91 Heat #C2269 Slab 7B Plate#A99532.”

[68] K. B. Small, D. A. Englehart, and T. A. Christman, “Guide to Etching Specialty Alloys,” *Adv. Mater. Process.*, p. 33, 2008.

[69] J. J. Penisten, “The Mechanism of Radiation-induced Segregation in Ferritic-Martensitic Steels,” University of Michigan, 2012.

[70] J. F. Ziegler, “The Stopping Range of Ions in Matter.” 2006.

[71] “Standard Practice for Neutron Radiation Damage Simulation by Charged-Particle Irradiation,” *ASTM Int.*, vol. E 521–96, 2003.

[72] R. E. Stoller, M. B. Toloczko, G. S. Was, a. G. Certain, S. Dwaraknath, and F. a. Garner, “On the use of SRIM for computing radiation damage exposure,” *Nucl. Instruments Methods Phys. Res. Sect. B Beam Interact. with Mater. Atoms*, vol. 310, pp. 75–80, Sep. 2013.

[73] “ELFF Load Cell,” *Measurement Specialties*, 2013. [Online]. Available: http://www.meas-spec.com/downloads/ELFF.pdf.

[74] Messphysik, “Laser Speckle Extensometer.” [Online]. Available: http://www.messphysik.com/index.php?id=111&L=1.

[75] MicroStrain, “Microminiature Displacement Sensor.” [Online]. Available: http://www.microstrain.com/displacement/dvrt.

[76] P. R. Bevington, *Data Reduction and Error Analysis for the Physical Sciences*. McGraw-Hill, 1969.

[77] J. Marian, B. D. Wirth, R. Schaublin, J. . Perlado, and T. D. de la Rubia, “<100>-Loop characterization in alpha iron: comparison between experiments and modeling,” *J. Nucl. Mater.*, vol. 307–311, pp. 871–875, 2002.

[78] B. . Wirth, G. R. Odette, J. Marian, L. Ventelon, J. A. Young-Vandersall, and L. A. Zepeda-Ruiz, “Multiscale modeling of radiation damage in Fe-based alloys in the fusion environment,” *J. Nucl. Mater.*, vol. 329–333, pp. 103–111, 2004.

[79] D. B. Williams and C. . Carter, *Transmission Electron Microscopy*. Springer, 1996, p. 410.

[80] G. F. Knoll, *Radiation Detection and Measurement*, 4th ed. Wiley, 2010.

[81] C. S. Smith and L. Guttman, "Measurement of Internal Boundaries in Three Dimensional Structures by Random Sectioning," *J. Met. Trans. AIME*, vol. 5, pp. 81–87, 1953.

[82] ASTM, "Standard Test Methods for Determining Average Grain Size," 2004.

[83] *NIST/SEMATECH e-Handbook of Statistical Methods*. .

[84] J. Larsson, "Evaluation of current methods for creep analysis and impression creep testing of power plant steels," Royal Institute of Technology (KTH), 2012.

[85] L. K. Mansur, "Irradiation Creep by Climb-Enabled Glide of Dislocations Resulting from Preferred Absorption of Point Defects," *Philos. Mag. A*, vol. 39, pp. 497–506, 1979.

[86] D. Kaoumi and J. Adamson, "Self-ordered defect structures in FM steels under in-situ ion irradiation," *J. Nucl. Mater.*, vol. 448, 2014.

[87] G. Gupta and G. S. Was, "Improved Creep Behavior of Ferritic-Martensitic Alloy T91 by Subgrain Boundary Density Enhancement," *Metall. Mater. Trans. A*, vol. 39, no. 1, pp. 150–164, Dec. 2007.

[88] J. R. Spingarn and W. D. Nix, "A Model for Creep Based on the Climb of Dislocations at Grain Boundaries," *Acta Metall.*, vol. 27, 1979.

[89] G. M. Pharr, "Some Observations on the Relation Between Dislocation Substructure and Power Law Breakdown in Creep," *Scr. Metall.*, vol. 15, 1981.

[90] M. B. Toloczko, F. A. Garner, and C. R. Eiholzer, "Irradiation Creep and Swelling of the U.S. Fusion Heats of HT9 and 9Cr-1Mo to 208 dpa at ~400C," in *Sixth International Conference on Fusion Materials*, 1993.

[91] M. B. Toloczko, "Irradiation Creep of Stainless Steels," Washington State, 1999.

[92] M. L. Grossbeck, K. Ehrlich, and C. Wassilew, "An Assessment of tensile, irradiation creep, creep rupture, and fatigue behavior in austenitic stainless steels with emphasis on spectral effects," *J. Nucl. Mater.*, vol. 174, 1990.

[93] G. W. Lewthwaite and D. Mosedale, "The effects of temperature and dose rate variations on the creep of austenitic stainless steels in the dounreay fast reactor," *J. Nucl. Mater.*, vol. 90, 1980.

[94] C.H.Woo, B. N. Singh, and A. A. Semenov, “Recent advances in the understanding of damage production and its consequences on void swelling, irradiation creep and growth,” *J. Nucl. Mater.*, vol. 239, 1996.

[95] C.H.Woo and F. A. Garner, “Displacement rate dependence of irradiation creep as predicted by the production bias model,” *J. Nucl. Mater.*, vol. 233–237, 1996.

[96] F. A. Garner and M. B. Toloczko, “Irradiation creep and void swelling of austenitic stainless steels at low displacement rates in light water energy systems,” *J. Nucl. Mater.*, vol. 251, pp. 252–261, 1997.

[97] B. A. Chin, “Topical Conference on Ferritic Steels for Use in Nuclear Energy Technologies,” in *The Metallurtical Society of AIME*, 1984, p. 593.

[98] E. J. Savino, “Stress-induced Preferred Absorption Due to Saddle-point,” vol. 116, pp. 17–28, 1983.

[99] A. Kohyama, “Irradiation Creep of Low-Activation Ferritic Steels in FFTF/MOTA,” *J. Nucl. Mater.*, vol. 212, pp. 751–754, 1994.

[100] R. E. Stoller, M. L. Grossbeck, and L. K. Mansur, “Effects of Radiation on Materials: 15th International Symposium,” 1999.

[101] M. Kassner, *Fundamentals of Creep in Metals and Alloys*, 2nd ed. Elsevier, 2009.

[102] K. Kimura, “Creep Deformation, rupture strength, and rupture ductility of grades T/P92 Steesl,” *ASME Symp. Elev. Temp. Appl. Mater. Foss. Nucl. Petrochemical Ind.*, 2014.

[103] B. A. Chin, “An Analysis of the Creep Properties of a 12Cr-1Mo-W-V Steel,” in *Topical Conference on Ferritic Alloys for Use in Nuclear Energies Technologies*, 1984.

[104] B. H. Sencer, J. R. Kennedy, J. I. Cole, S. a. Maloy, and F. a. Garner, “Microstructural analysis of an HT9 fuel assembly duct irradiated in FFTF to 155dpa at 443°C,” *J. Nucl. Mater.*, vol. 393, no. 2, pp. 235–241, Sep. 2009.

[105] B. H. Sencer, “Microstructural Stability of an HT-9 Fuel Assembly Duct Irradiated in FFTF,” *J. Nucl. Mater.*, vol. 414, pp. 237–242, 2011.

[106] a. . Dvoriashin, S. . Porollo, Y. . Konobeev, and F. . Garner, “Influence of high dose neutron irradiation on microstructure of EP-450 ferritic–martensitic steel irradiated in three Russian fast reactors,” *J. Nucl. Mater.*, vol. 329–333, pp. 319–323, Aug. 2004.

[107] F. A. Garner, M. . Toloczko, and B. . Sencer, “Comparison of swelling and irradiation creep behavior of fcc-austenitic and bcc-ferritic/martensitic alloys at high neutron exposure,” *J. Nucl. Mater.*, vol. 276, no. 1–3, pp. 123–142, Jan. 2000.

[108] M. B. Toloczko, F. A. Garner, and C. R. Eiholzer, “Irradiation creep and swelling of the US fusion heats of HT9 and 9Cr-1mo to 208 dpa at ~400C,” *J. Nucl. Mater.*, vol. 212–215, pp. 604–607, 1994.

[109] F. A. Garner and R. J. Puigh, “Irradiation Creep and Swelling of the Fusion Heats of PCA, HT9 and 9Cr-1Mo Irradiated to High Neutron Fluence,” *J. Nucl. Mater.*, vol. 179–181, pp. 577–580, 1991.

[110] D. S. Gelles and L. E. Thomas, “Microstructural Examination of HT-9 and 9Cr-1Mo Contained in the AD-2 Experiments,” 1982.

[111] R. Schaeublin, D. Gelles, and M. Victoria, “Microstructure of irradiated ferritic/martensitic steels in relation to mechanical properties,” *J. Nucl. Mater.*, vol. 307–311, pp. 197–202, Dec. 2002.

[112] R. V. Hesketh, “A Possible Mechanism of Irradiation Creep and its Reference to Uranium,” *Philos. Mag.*, vol. 7, 1962.

[113] G. W. Lewthwaite and K. J. Proctor, “Irradiation-creep in a materials testing reactor,” *J. Nucl. Mater.*, vol. 46, no. 1, 1973.

[114] K. Herschbach and W. Schneider, “Interconnection Between Irradiation Creep and Interstitial Loop Formation in fcc Metals,” *J. Nucl. Mater.*, vol. 51, pp. 215–220, 1974.

[115] W. G. Wolfer, J. P. Foster, and F. A. Garner, “The Interrelationship between Swelling and Irradiation Creep,” *Nucl. Technol.*, vol. 16, p. 55, 1972.

[116] G. W. Lewthwaite, “Interconnection between irradiation creep and interstitial loop formation in fcc metals,” *J. Nucl. Mater.*, vol. 54, no. 1, 1974.

[117] H. R. Brager, F. A. Garner, and G. L. Gutherie, “The Effect of Stress on the Microstructure of Neutron Irradiated Type 316 Stainless Steels,” *J. Nucl. Mater.*, vol. 66, pp. 301–321, 1977.

[118] B. Yao, D. J. Edwards, and R. J. Kurtz, “TEM characterization of dislocation loops in irradiated bcc Fe-based steels,” *J. Nucl. Mater.*, vol. 434, no. 1–3, pp. 402–410, Mar. 2013.

[119] C. H. Woo, “Intrinsic Bias Differential Interstitial Loops,” *J. Nucl. Mater.*, pp. 20–30, 1982.

[120] C. H. Woo, “Effects of an Anisotropic Dislocation Structure on Irradiation due to SIPA,” *J. Nucl. Mater.*, vol. 80, pp. 132–143, 1979.

[121] C. H. Woo and F. A. Garner, “A SIPA-based theory of irradiation creep in the low swelling rate regime,” *J. Nucl. Mater.*, vol. 194, pp. 1309–1312, 1992.

[122] K. Kroupa, “Dislocation Loops,” in *Theory of Crystal Defects - Proceedings of the Summer School held in Hrazany in September 1964*, 1966, pp. 308–313.

[123] L. K. Mansur, “Irradiation creep by climb-enabled glide of dislocations resulting from preferred absorption of point defects,” *Philos. Mag.*, vol. 39, p. 497, 1979.